BOUNDARY-LAYER TRANSITION WITH FLUIDS AT SUPERCRITICAL PRESSURE

Pietro Carlo Boldini

BOUNDARY-LAYER TRANSITION WITH FLUIDS AT SUPERCRITICAL PRESSURE

Pietro Carlo Boldini

BOUNDARY-LAYER TRANSITION WITH FLUIDS AT SUPERCRITICAL PRESSURE

Dissertation

for the purpose of obtaining the degree of doctor
at Delft University of Technology
by the authority of the Rector Magnificus, Prof. dr. ir. H. Bijl,
Chair of the Board for Doctorates,
to be defended publicly on
Friday 23 January 2026 at 12:30 o'clock

by

Pietro Carlo BOLDINI

Master of Science in Aerospace Engineering,
University of Stuttgart, Germany,
born in Pisa, Italy.

This disseration has been approved by the promotors.

Composition of the doctoral committee:

Rector Magnificus,	chairperson
Prof. dr. R. Pecnik,	Delft University of Technology, promotor
Dr. ir. J. W. R. Peeters,	Delft University of Technology, copromotor
Independent members:	
Prof. dr. M. Kotsonis,	Delft University of Technology
Prof. dr. J.-C. Robinet,	Arts et Métiers Institute of Technology, France
Prof. dr. V. Terrapon,	University of Liège, Belgium
Dr. A. Hanifi,	KTH Royal Institute of Technology, Sweden
Prof. dr. ir. B. J. Boersma,	Delft University of Technology, reserve member
Other member:	
Dr.-Ing. M. J. Kloker,	University of Stuttgart, Germany

The research was funded by the European Research Council under grant no. ERC-2019-CoG-864660 (CRITICAL). The author acknowledges the use of the computational facilities of the Dutch National Supercomputer Snellius (SURF) under grant nos. 2022/ENW/01251049 and 2024/ENW/01704792, and of the Delft High Performance Computing Centre (DHPC).

Keywords:	Boundary-Layer Stability, Transition to Turbulence, Supercritical Fluids, Direct Numerical Simulations
Printed by:	Ridderprint
Front, back, & spine:	Density billow in a transitional boundary layer under pseudo-boiling; isocontours of the Q-criterion coloured by the streamwise velocity for a K-type-like transition; pressure–specific-volume diagram with saturation curves (yellow), the critical point (white), and the Widom line (blue).

ISBN 978-94-6518-218-6

An electronic version of this dissertation is available at

`http://repository.tudelft.nl/`

[1]Author e-mail address: pietro.c.boldini@gmail.com

与天地准

'In accord with Heaven and Earth'

— *Book of Changes (I Ching)*

SUMMARY

Fluids at supercritical pressure are increasingly attractive for energy and propulsion technologies, from power cycles to advanced rocket engines. Their favourable thermophysical properties, notably high density combined with low viscosity, promise gains in efficiency and reduced environmental impact. Yet near the thermodynamic critical point, strong non-ideal gas effects arise: thermodynamic and transport properties vary abruptly across the pseudo-critical (Widom) line, profoundly altering hydrodynamic stability and transition to turbulence. Accurate prediction of the onset and extent of turbulence is therefore essential for the reliable design and control of supercritical-fluid systems.

To this end, the present thesis investigates laminar-to-turbulent transition in boundary layers of supercritical fluids, extending stability theory, as well as transition to turbulence, beyond the ideal-gas assumption. Classical stability methods, such as linear stability theory, non-modal analysis, and Floquet-based secondary instability theory, account here for non-ideal equations of state and variable thermodynamic and transport properties. To capture the nonlinear stages of transition and breakdown to turbulence, high-fidelity simulations are essential. Therefore, the CUBic Equation of state Navier–Stokes (CUBENS) solver is developed – a massively parallel GPU-accelerated, high-order solver for non-ideal compressible wall-bounded flows, leveraging state-of-the-art high-performance computing facilities.

The application of this framework to diabatic flat-plate boundary layers at supercritical pressure reveals that stability and transition differ fundamentally from those in ideal-gas boundary layers. Linear stability analysis shows that, under pseudo-boiling conditions, an inviscid instability arises from a generalised inflection point linked to a kinematic-viscosity minimum at the Widom line – a result universal to non-polar supercritical fluids. At low Mach numbers, two-dimensional modes dominate, while increasing compressibility promotes oblique perturbations. Non-modal analysis reveals that optimal disturbances become streamwise-modulated streaks driven by an interplay between lift-up and Orr mechanisms. Floquet-based secondary instability analysis demonstrates that two-dimensional subharmonic resonance is possible at moderate amplitudes, a behaviour characteristic of free shear layers. Direct numerical simulations show that the nonlinear development of the inviscid mode generates billow-like structures and near-wall flow reversals, enabling an earlier onset of transition even without oblique-wave forcing. The breakdown to turbulence is characterised by Λ-vortices and shear layers, resembling breakdown under adverse pressure gradient. Finally, in the fully turbulent region, variable-property scaling extended to supercritical fluids accurately predicts skin-friction and heat-transfer coefficients, in agreement with direct numerical simulations.

SAMENVATTING

Vloeistoffen bij superkritische druk zijn in toenemende mate aantrekkelijk voor energie- en voortstuwingstoepassingen, van thermodynamische kringprocessen tot geavanceerde raketmotoren. Hun gunstige thermofysische eigenschappen, met name hun hoge dichtheid in combinatie met hun lage viscositeit, kunnen leiden tot rendementswinst en een meer beperkte milieuimpact. In de nabijheid van het thermodynamische kritische punt treden echter sterke niet-ideale gaseffecten op: zo vertonen de thermodynamische en transporteigenschappen abrupte variaties over de pseudo-kritische (Widom) lijn, met belangrijke gevolgen voor de hydrodynamische stabiliteit en transitie naar turbulentie van stromingen. Het nauwkeurig voorspellen van het begin en het verloop van de laminair-turbulente transitie is daarom essentieel voor het betrouwbare ontwerp en de regeling van systemen met superkritische vloeistoffen.

Dit proefschrift onderzoekt de laminair-turbulente transitie in grenslagen van superkritieke fluïda, waarbij zowel stabiliteitstheorie als de beschrijving van de transitie naar turbulentie worden uitgebreid voorbij de aannames van de algemene ideale gaswet. Klassieke stabiliteitsmethoden, zoals lineaire stabiliteitstheorie, niet-modale analyse en Floquet-gebaseerde secundaire-instabiliteitstheorie, houden hierbij rekening met niet-ideale toestandsvergelijkingen en variërende thermodynamische en transporteigenschappen. Om de niet-lineaire stadia van transitie en breakdown naar turbulentie te beschrijven zijn high-fidelity simulaties vereist. Hierom is de CUBic Equation of state Navier–Stokes (CUBENS) solver ontwikkeld – een massaal parallelle, GPU-versnelde, hoge-orde solver voor niet-ideale compressibele wandgebonden stromingen, gebruikmakend van de modernste high-performance-computing faciliteiten.

De toepassing van deze methodologie op diabatische vlakke-plaats-grenslagen bij superkritische druk onthult fundamentele verschillen met stabiliteit en transitie in ideaal-gasgrenslagen. Lineaire stabiliteitsanalyse toont aan dat onder pseudo-boiling omstandigheden een niet-viskeuze instabiliteit ontstaat uit een gegeneraliseerd buigpunt, gekoppeld aan een minimum in kinematische viscositeit bij de Widom-lijn – een resultaat dat universeel is voor niet-polaire superkritische vloeistoffen. Bij lage Machgetallen domineren tweedimensionale modes, terwijl toenemende compressibiliteit schuine verstoringen bevordert. Niet-modale analyse laat zien dat optimale verstoringen stroomafwaarts gemoduleerde streaks worden, aangedreven door een wisselwerking tussen lift-up- en Orr-mechanismen. Floquet-gebaseerde secundaire-instabiliteitsanalyse toont aan dat tweedimensionale subharmonische resonantie mogelijk is bij gematigde amplituden – een gedrag kenmerkend voor schuiflagen. Directe

numerieke simulaties tonen aan dat de niet-lineaire ontwikkeling van de niet-viskeuze mode rolachtige structuren en nabij-wand stromingsomkeringen genereert, waardoor vroege transitie mogelijk is, zelfs zonder schuine-golfforcering. De breakdown tot turbulentie wordt gekenmerkt door Λ-structuren met schuiflagen, vergelijkbaar met grenslaag-breakdown bij een ongunstige drukgradiënt. Tot slot voorspelt een variabele-eigenschappenschaling, uitgebreid naar superkritische vloeistoffen, in het volledig turbulente gebied nauwkeurig de wrijvings- en warmteoverdrachtscoëfficiënten, in overeenstemming met directe numerieke simulaties.

CONTENTS

1

INTRODUCTION

'and so, once more, we do not obtain a critical Reynolds number. There seems to be a very nasty devil in turbulence so that all mathematical efforts are doomed to failure.'

L. Prandtl to T. von Kármán, 1921, as quoted in Davidson *et al.* (2011)

1.1 Motivation

The current global energy crisis is imposing an unprecedented economic burden. Global consumers spent nearly USD 10 trillion on energy in 2022 (International Energy Agency 2023). By 2049, climate-related damages are projected to cost the world economy around USD 38 trillion per year, reducing average global income by 19% compared to a climate-stable scenario (Kotz *et al.* 2024). Furthermore, Burke *et al.* (2015) showed that rising temperatures have a strong, nonlinear negative effect on economic productivity, which peaks at an annual average temperature of 13 °C and declines at higher temperatures. Their analysis suggests that climate change could reduce global incomes by more than 20% by 2100. Climate change is also expected to drastically cut agricultural yields, increase infrastructure damage from extreme weather events, and decrease labour productivity, especially in heat-exposed industries.

In response to these challenges, supercritical fluids emerge as a transformative technology for the energy sector (Brunner 2010; Lamanna 2024). Industrial applications operating at supercritical pressure achieve thermal efficiencies of 40–50% in power generation, outperforming traditional steam cycles by several percentage points through higher temperatures and pressures, while reducing the size of heat transfer equipment (Crespi *et al.* 2017). These advantages extend to concentrated solar-thermal power systems, where supercritical CO_2 Brayton cycles, analogous to subcritical Brayton cycles but with the working fluid in the supercritical phase, are increasingly employed. These cycles enable compact, high-efficiency operation (improving thermal efficiency from 33–46% to 40–52%) and robust handling of transient solar input, making such systems particularly well suited to intermittent renewable energy sources (Iverson *et al.* 2013). Recently commissioned in 2024, the world's largest supercritical CO_2 heat pump (using supercritical CO_2 as the refrigerant), a 70 MW system in Esbjerg, Denmark, delivers 280 000 MWh of climate-neutral heat annually to 25 000 households, reducing CO_2 emissions by 120 000 tons per year (Fig. 1.1a) (MAN Energy Solutions 2024). Supercritical fluids are also essential to carbon capture and storage technologies, as demonstrated by the Porthos project in the Port of Rotterdam (Fig. 1.1b) (Porthos CO_2 Transport and Storage 2024). Here, CO_2 is compressed from a vapour state at 35 bar to a supercritical liquid-like state at 130 bar for pipeline transport to permanently store up to 2.5 million tons annually in depleted gas fields beneath the North Sea. This corresponds to approximately 1.5% of the Netherlands' annual emissions. Finally, next-generation geothermal systems are targeting supercritical water, found at high temperatures and pressures deep within the Earth's crust, whose thermophysical properties markedly enhance heat and mass transfer (Reinsch *et al.* 2017).

Beyond their technological advantages, supercritical fluids also occur naturally in various planetary and geophysical environments. Supercritical CO_2, with high N_2 contents, has been identified below the seafloor in submarine hydrothermal vents in the Okinawa Trough (Zhang *et al.* 2020). Beyond Earth, supercritical CO_2 is present in Venus's dense atmosphere (Fig. 1.1c) at an altitude of 12 km, where temperatures exceed 700 K and pressures reach

Figure 1.1: (a) World's largest supercritical CO_2 heat pump in Esbjerg, Denmark (credit: `https://www.man-es.com/discover/esbjerg-heat-pump`); (b) the Porthos carbon capture and storage project in the Port of Rotterdam (credit: `https://www.porthosco2.nl/`); (c) Venera 14 Soviet lander on the surface of Venus in 1982 (credit: D. P. Mitchell & M. Carroll, NASA APOD).

approximately 75 bar (Lebonnois & Schubert 2017). The future DAVINCI mission is expected to improve existing models of Venus's deep atmosphere (Garvin *et al.* 2022).

The successful integration of supercritical fluids into advanced energy systems has sparked considerable interest in understanding their fundamental flow behaviour. These applications typically involve single-phase fluids operating at strongly non-ideal thermodynamic states, which has motivated a distinct field known as Non-Ideal Compressible Fluid Dynamics (NICFD) (aus der Wiesche 2023; Guardone *et al.* 2024). At supercritical pressures, steep gradients in thermophysical properties invalidate classical assumptions such as ideal-gas behaviour and linear thermodynamic relations. These non-ideal effects significantly influence heat transfer (Yoo 2013) and laminar-to-turbulent transition (Robinet & Gloerfelt 2019), creating new challenges for both fundamental science and industrial applications in this regime.

Flow instabilities and transition to turbulence are a particularly critical aspect of non-ideal flow behaviour, since multiple mechanisms may compete and determine when and how a laminar flow breaks down into turbulence, thereby affecting the performance, efficiency, and heat-transfer characteristics of supercritical-fluid systems. A pronounced influence of sharp property variations on linear stability was first reported for flows at supercritical pressure by Ren *et al.* (2019*a*). In flat-plate boundary layers with supercritical CO_2, the pivotal study of Ren *et al.* (2019*b*) – a first-of-its-kind linear stability analysis for this configuration – revealed a new type of flow instability with growth rates far exceeding those of previously known modes. This discovery raises fundamental questions, which the present thesis addresses for the first time in a unified framework: How universal is this result across other non-ideal fluids? How does external forcing affect laminar-flow dynamics? And how might non-ideal effects modify the nonlinear stages of transition to turbulence?

High-fidelity numerical simulations have become indispensable for investigating transitional and turbulent non-ideal fluid flows, particularly through Direct Numerical Simulation (DNS), due to the extreme experimental challenges posed by operating at supercritical condi-

tions. The high pressures and temperatures severely limit experimental capabilities, with restricted optical access and strict material constraints (Cinnella & Gloerfelt 2023). DNS offers a fully resolved approach that captures the complex interplay between thermodynamics and turbulence across all relevant flow scales, albeit at a high computational cost. Reduced-order models, such as Large-Eddy Simulation (LES) or Reynolds-Averaged Navier–Stokes (RANS), do not resolve the sharp property gradients and strong thermodynamic couplings characteristic of supercritical fluids and therefore generally fail to predict laminar-to-turbulent transition and reliably capture the resulting turbulent boundary layer. Even for ideal-gas boundary layers, LES transition predictions depend strongly on the subgrid scale closure (Sayadi 2012). Consequently, DNS is essential for developing improved turbulence closures for NICFD applications.

Overall, unlocking the full potential of supercritical fluids requires a comprehensive understanding of how non-ideal thermodynamic behaviour interacts with flow instabilities and the transition to turbulence – an understanding that remains limited, as systematic research in this direction is still in its early stages. This thesis contributes to closing this gap.

1.2 Supercritical Fluids

Every pure substance can exist in three principal states of matter (solid, liquid, and gas) depending on its thermodynamic conditions, specifically temperature and pressure. The transition between these states, referred to as phase transition, occurs when the Gibbs free energies of the phases become equal. At subcritical pressures and temperatures (subcritical conditions), these transitions involve distinct phase boundaries and are accompanied by latent heat exchange. For instance, at saturation conditions, heating a liquid induces a sharp transformation to the gaseous phase through vaporisation, characterised by a discontinuous change in density and enthalpy.

As temperature and pressure increase towards the liquid-vapour critical point, the distinctions between liquid and vapour phases gradually vanish. At the critical point, the two phases become thermodynamically indistinguishable, and the first-order phase transition disappears. Beyond this point lies the supercritical-fluid state, where the fluid exists as a single, continuous phase with no phase boundary, no latent heat, and no surface tension. Nevertheless, thermodynamic and transport properties may still undergo sharp, albeit continuous, variations, particularly near the critical point.

The thermodynamic characteristics of pure substances can be visualised in the reduced pressure–temperature (p_r–T_r) diagram, as shown in Fig. 1.2(a), where pressure and temperature are normalised by their respective critical values, p_c and T_c. The melting line (yellow) separates the solid and liquid phases and typically exhibits a positive slope for most substances. The saturation curve (purple) marks the boundary between subcritical liquid and vapour phases, ending at the critical point (black star), where the latent heat of vaporisation vanishes and the phase boundary disappears. Beyond this point, the fluid enters the supercritical-fluid region, where it does not undergo any discontinuous (first-order) phase

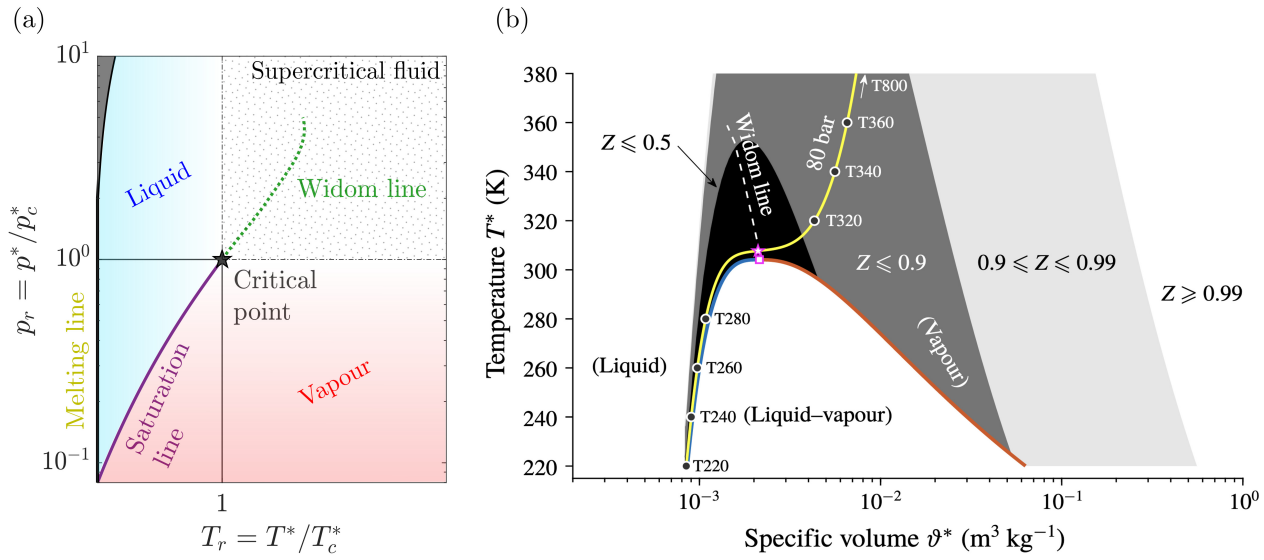

Figure 1.2: In (a), the reduced pressure–temperature diagram ($p_r = p/p_c$, $T_r = T/T_c$) shows the saturation curve (purple), the melting line (yellow), the critical point (black star), and the Widom line (green), defined as the locus of pseudo-critical temperatures where the specific heat capacity c_p reaches a maximum. In (b), the T–ϑ diagram (where ϑ denotes the specific volume) for supercritical CO_2 displays the critical point (magenta square), pseudo-critical point (magenta pentagram), Widom line (white dashed line), liquid and vapour saturation curves (thick blue and red lines), and an isobar at 80 bar (yellow line). The shaded region indicates contours of the compressibility factor Z. The figure is reproduced from Ren *et al.* (2019*b*).

transition. Experiments and simulations demonstrate that a supercritical analogue to the subcritical saturation line exists: a crossover line that marks a rapid but continuous transition between liquid-like and vapour-like behaviour over a small temperature interval (Simeoni *et al.* 2010; Banuti *et al.* 2017). This line coincides with the so-called Widom line, defined by H. E. Stanley and colleagues (Xu *et al.* 2005) in honour of B. Widom[1], as the locus of the maximum correlation length (i.e. the characteristic spatial scale over which thermodynamic fluctuations remain correlated). Because the correlation length cannot be directly measured from macroscopic data, the Widom line is typically approximated by the loci of extrema in thermodynamic response functions, defined as derivatives of the state functions with respect to temperature, e.g. the specific heat capacity $c_p = \partial h/\partial T|_p$. Among these, c_p most prominently exhibits a sharp peak at what is known as the pseudo-critical temperature for a given pressure, and the collection of such points defines the Widom line, shown in green in Fig. 1.2(a).

Different thermodynamic states can be classified with respect to the pseudo-critical

[1]Benjamin Widom (1927–2025) pioneered the scaling theory of 'critical phenomena'. In Widom (1965), he introduced the scaling hypothesis ('critical point scaling ansatz'), showing that, near the critical point, diverse thermodynamic quantities (e.g. compressibility, heat capacity, and the order parameter) follow universal power laws. The Widom line extends the concept of a diverging correlation length into the supercritical region.

temperature T_{pc}, all lying within the supercritical-fluid region where $p_r = p/p_c > 1$. In the context of this research, the term 'subcritical' refers to conditions with $T < T_{pc}$, where the fluid exhibits liquid-like behaviour, such as high density, low compressibility, and relatively low thermal expansion. Conversely, the 'supercritical' state with $T > T_{pc}$ is characterised by vapour-like behaviour, including lower density, higher diffusivity, and weaker intermolecular interactions. Between these two states lies the transcritical state, which involves crossing the Widom line and where pseudo-boiling occurs (Banuti 2015). Analogous to classical subcritical vaporisation, the supercritical (transcritical) state transition – occurring upon either heating or cooling across the Widom line – is associated with a sharp change in density and a peak in specific heat capacity (Banuti 2015). As a result, in the transcritical state, the critical temperature T_c loses its significance as a meaningful phase-transition point and is replaced by the pseudo-critical or pseudo-boiling temperature T_{pc}. Note that the Widom line vanishes for $p_r \gtrsim 3$ (Guardone *et al.* 2024).

When the fluid is in the supercritical region, its thermodynamic behaviour deviates significantly from that of an ideal gas, especially near the critical point. To quantify the deviation of a fluid from ideal-gas behaviour at supercritical pressures, the compressibility factor

$$Z = \frac{p}{\rho R_g T}, \tag{1.1}$$

is introduced, where ρ is the density and R_g is the specific gas constant. This quantity incorporates the effects of intermolecular forces and finite molecular size. For an ideal gas, where such effects are absent, $Z = 1$. However, in real fluids, especially near the critical point, intermolecular interactions lead to significant deviations from ideality. In supercritical CO_2 ($p_c = 73.8\,\text{bar}$, $T_c = 304.1\,\text{K}$), values of Z can fall well below 0.5 near the Widom line, indicating strong non-ideal fluid behaviour. These deviations, discussed more in detail in Chapter 2, are associated with large density gradients and sharp variations in response functions such as heat capacity. Figure 1.2(b) illustrates this phenomenon, showing how Z varies as a function of temperature and pressure in the vicinity of the pseudo-critical temperature T_{pc}.

1.3 Laminar-to-turbulent transition

In the 19th century, Euler's equations of fluid motion for incompressible, inviscid flow were believed to reasonably model the flow of low-viscosity fluids. However, observed phenomena often contradicted solutions to these equations. G. G. Stokes attributed these discrepancies to instabilities inherent in inviscid (Eulerian) flows. Since highly viscous flows were observed to be stable, while low-viscosity flows were often chaotic, the prevailing view emerged that viscosity acted purely as a stabilising mechanism – implying that inviscid flows would always be unstable.

This question motivated the first rigorous analyses of inviscid stability. Rayleigh's inflection point criterion (Rayleigh 1880) provides a necessary condition for instability in an incompressible, inviscid parallel flow, i.e. a flow where the velocity U has only a streamwise component and varies only with the wall-normal y coordinate, i.e. $\vec{u} = U(y)\vec{e}_x$. Rayleigh

demonstrated that D^2U must change sign within the flow for an inviscid instability to exist, where $\mathrm{D} \equiv \mathrm{d}/\mathrm{d}y$ and thus $\mathrm{D}^2U \equiv \mathrm{d}^2U/\mathrm{d}y^2$. This famous result contradicted the prevailing idea that inviscid flows are always linearly unstable. These findings were expected, yet they revealed a further mystery: if highly viscous flows are stable, and inviscid flows are also stable provided that D^2U does not change sign, then how do we explain the observed instability in flows with moderate viscosity? As Lord Rayleigh[2] remarked:

> *It seems very unlikely that the first effect of increasing viscosity should be to introduce an instability not previously existent, while, as observation shows, a large viscosity makes for stability.* (Rayleigh 1892)

It was L. Prandtl[3], together with his doctoral student O. Tietjens, who, through a simplified approach, first discovered that a flow that is inviscidly stable could become unstable when viscous effects are included. The significance of this result is reflected in Prandtl's reaction in the original Prandtl (1921) study:

> *At first we didn't want to believe this result and then we each calculated it three times independently in different ways. But the same sign came up again and again, meaning instability.* (Prandtl 1921)

Around the same time, Heisenberg (1924) found a stability limit for plane Poiseuille flow, also challenging the belief that flows without inflection points are always stable. Motivated by these issues, Prandtl initiated a new study of boundary-layer stability using more realistic velocity profiles. His work was continued by his students W. Tollmien and H. Schlichting, who found that the flat-plate (Blasius) boundary-layer stability depends on both Reynolds number and disturbance wavelength, identifying a critical Reynolds number[4] of 420 for the onset of instability. Indeed, they showed that a velocity profile without an inflection point can exhibit linear instability according to the Orr–Sommerfeld equation (Orr 1907; Sommerfeld 1908), which governs the stability of parallel, viscous flows. These are known as Tollmien–Schlichting instabilities or Tollmien–Schlichting waves (TS waves) (Schlichting & Gersten 2003). For nearly a decade, Tollmien and Schlichting's theory could not be verified due to excessive turbulence in wind tunnels. Schubauer & Skramstad (1947) eventually confirmed it by observing the amplification of controlled TS waves in a quiet wind tunnel using a vibrating ribbon, matching predictions from the Orr–Sommerfeld equation. In parallel, Lees & Lin (1946) extended Rayleigh's inviscid stability theory to compressible boundary layers,

[2]Lord Rayleigh (1842–1919) made key contributions to fluid mechanics, though his 1904 Nobel Prize in Physics was awarded for the discovery of argon. To date, no Nobel Prize has been awarded specifically for work in fluid dynamics.

[3]Ludwig Prandtl (1875–1953) is widely regarded as the central figure of the Göttingen school of fluid mechanics. After arriving in Göttingen in 1904, he introduced boundary-layer theory and helped establish the experimental tradition through the 'Göttinger Bauart' wind tunnel, which became a model for aerodynamic testing.

[4]The Reynolds number, introduced by Reynolds (1883), is here based on the incompressible displacement thickness δ_1 as $Re = u_\infty \delta_1/\nu_\infty$, where u_∞ is the velocity in the free stream, δ_1 is defined as $\int_0^\infty (1 - u/u_\infty)\,\mathrm{d}y$, and ν_∞ is the kinematic viscosity in the free stream.

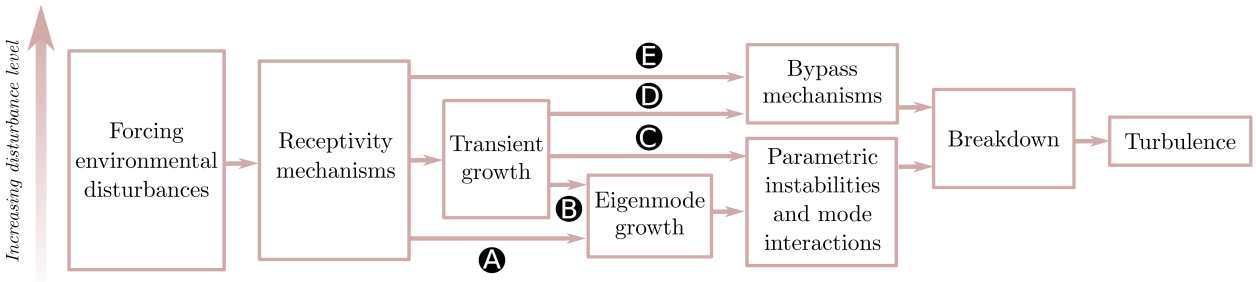

Figure 1.3: Transition road map, adapted from Morkovin (1969).

showing that the quantity $\mathrm{D}(\rho \mathrm{D}U)$ plays a role analogous to D^2U in the incompressible case and implying that compressible flat-plate boundary layers may admit purely inviscid unstable waves. Gaster (1962) connected the temporal growth predicted theoretically to the spatial growth observed experimentally and developed a relation connecting both growth rates. Van Ingen (van Ingen 1956) introduced the *e-to-the-N*-method, predicting transition by integrating disturbance amplification rates, with transition assumed when the integral reaches a critical threshold, typically corresponding to an amplification factor of $e^{N=9}$ in low-disturbance wind tunnels.

In both simulations and experiments, an initial disturbance is required to trigger the transition process. The nature and amplitude of this disturbance strongly influence the route the flow takes from laminar to turbulent. These various transition scenarios have been classified by Morkovin (1969), as illustrated in Fig. 1.3. Each path represents a distinct mechanism, depending primarily on the initial disturbance environment. Nonetheless, all scenarios share a common first step: receptivity, whereby external disturbances (e.g. free-stream vorticity, entropy fluctuations, or acoustic waves) are internalised into the boundary layer as instability modes, forming the foundation of any transition process.

When the initial disturbance level in the flow is relatively small, e.g. in real flight conditions or in a quiet wind tunnel, the transition follows Path A (black 'A' circle in Fig. 1.3), corresponding to the classical 'controlled' transition scenario. In this case, small-amplitude wave-like disturbances grow exponentially and their behaviour can be predicted by the Linear Stability Theory (LST). In zero-pressure-gradient flat-plate boundary layers, the primary modal instability is of the TS type, while at supercritical pressure under pseudo-boiling conditions, it can be associated with Mode II (see Chapter 3). Once the primary wave resulting from modal growth reaches finite amplitudes, secondary instabilities set in, which grow exponentially, as described by Secondary Instability Theory (SIT) (see Chapter 7). Secondary instabilities rapidly initiate the breakdown process, in which nonlinear interactions between primary modes, secondary modes, and higher harmonics take place, leading to the formation of complex three-dimensional flow structures, e.g. Λ-vortices. As the structures lose their spatial orientation and break up, transition onset occurs and the flow gradually transitions into a chaotic, turbulent state. This transition path (Path A), illustrated in Fig. 1.4 for a two-dimensional flat-plate boundary layer and first systematically observed in the experiments by Schubauer & Skramstad (1947), offers a controlled and reproducible framework ideally

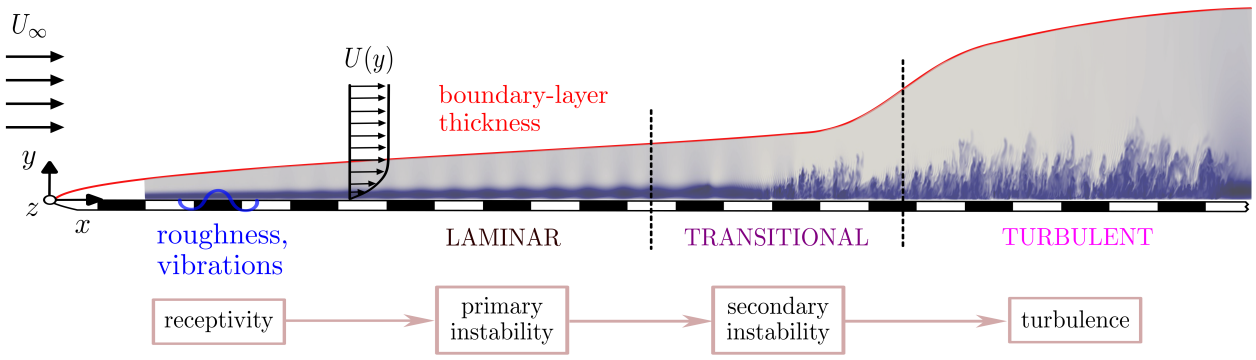

Figure 1.4: Path A, as classified by Morkovin (1969), illustrated for a two-dimensional flat-plate boundary-layer flow, following the experiments of Schubauer & Skramstad (1947).

suited for DNS-based investigations. Its predictable nature enables systematic parameter studies and reliable comparisons with theoretical predictions. Further details are provided in Chapter 6.

Paths B, C, and D in Fig. 1.3 initially involve transient, or non-modal, growth of disturbances. Unlike the exponential modal growth in Path A, this amplification mechanism is characterised by the short-term growth of disturbance energy arising from the non-orthogonality of linear stability modes, even when all eigenmodes are linearly stable. Transient growth has been proposed as a likely route to laminar-turbulent transition in scenarios such as Couette and pipe flow (Trefethen *et al.* 1993), where classical modal instabilities are absent; see Chapter 4. In flows with high levels of external noise or surface roughness, transition may occur via Path E, which entirely bypasses the classical amplification stages, immediately triggering nonlinear interactions and the rapid formation of turbulent spots. As Reshotko (2001) remarked, 'we often joked that bypass transition either bypassed the TS processes or bypassed our knowledge, or both.' Bypass transition is commonly observed in turbomachinery or on spherical forebodies, e.g. the 'blunt-body paradox' (Reshotko 2001). This thesis, however, focuses on flat-plate boundary layers under low-disturbance conditions and does not consider Path E.

1.4 Thesis objectives

This research aims to investigate flow instabilities and the transition to turbulence in fluids near the liquid-vapour critical point, where strong thermophysical property variations occur across the pseudo-boiling (Widom) line and the ideal-gas assumption breaks down. Operating under these thermodynamic conditions offers significant advantages for industrial applications, including enhanced thermal efficiency and reduced system size. However, the same property variations can also lead to heat transfer deterioration or enhancement and may either delay or promote the onset of turbulence. Accurate prediction of the laminar-to-turbulent transition is therefore essential for optimal system performance. Despite ongoing advances in transition research, the complex interplay among many influencing parameters makes a complete prediction of transition unfeasible. Meaningful progress can be achieved

only through the complementary use of theory, experiments, and numerical simulations, carried out with rigorous accuracy and applied to well-defined model problems with controlled disturbances. Given the experimental challenges associated with high-density and high-pressure flows in the supercritical-fluid region, this work adopts a multi-fidelity theoretical and numerical approach, bringing these tools together in a unified framework for the first time. This includes the use of modal and non-modal stability analysis to identify and analyse the exponential or algebraic growth of instabilities in the early stages of transition, secondary instability theory to characterise the subsequent destabilisation of finite-amplitude disturbances, and high-fidelity DNS to capture the nonlinear interactions and the eventual breakdown to turbulence. Within this framework, the main objectives of the research are to:

1. **extend the understanding of two-dimensional and three-dimensional linear unstable modes** in boundary layers at supercritical pressure, building on the work of Ren *et al.* (2019*b*), by examining their growth mechanisms and phase-speed characteristics across a wide range of flow conditions;

2. **provide a clear understanding of the additional inviscid mode** that emerges under pseudo-boiling conditions, clarifying its physical origin and its relation to the classical TS wave;

3. **determine the physical mechanisms governing short-time disturbance growth** and assess its relevance in boundary layers at supercritical pressure, where it may surpass the exponential amplification of unstable modes;

4. **develop a high-order, cost-effective, and energy-efficient solver** for simulating wall-bounded transitional and turbulent flows of compressible, single-phase, non-ideal fluids, enabling high-fidelity simulations targeting next generation Exascale supercomputers;

5. **investigate the secondary instability** of finite-amplitude primary waves in boundary layers at supercritical pressure, characterising the growth of secondary instability modes and their role in triggering breakdown;

6. **characterise the full transition scenario** by using DNS, from controlled disturbance excitation through primary and secondary instabilities to nonlinear breakdown.

7. **assess the fully turbulent boundary-layer regime** at supercritical pressure by evaluating variable-property scalings and the resulting predictions for skin friction and heat transfer.

1.5 Thesis outline

The thesis is organised as follows:

Chapter 2 introduces the governing equations, including a detailed description of non-ideal

equations of state and nonlinear transport-property models. Boundary-layer equations for a zero-pressure-gradient flat plate are also presented.

Chapter 3 investigates 2-D and 3-D viscous and inviscid modal instability, with particular focus on Mode II under pseudo-critical conditions and in the presence of a generalised inflection point. To examine the universality of the resulting inviscid instability, the stability of plane Couette flow with simple fluid models is then considered.

Chapter 4 addresses non-modal analysis. Optimal perturbation growth is characterised across different thermodynamic states, with emphasis on the effects of initial Reynolds number and wall temperature under pseudo-boiling conditions. Finally, a comparison between transient growth and exponential growth is provided by means of the N-factor.

Chapter 5 describes the CUBic Equation of state Navier–Stokes (CUBENS) solver used in the DNS investigations. The numerical discretisation and GPU implementation of CUBENS are discussed in detail. Validation against various benchmark cases is presented, followed by an assessment of the solver's performance on single- and multi-CPU/GPU architectures.

Chapter 6 presents fully compressible DNS results for (i) linear and nonlinear instabilities, (ii) the breakdown to turbulence, and (iii) the fully developed turbulent boundary layer. Two flow cases at supercritical pressure (reduced pressure of 1.10) are considered, each with a slightly heated wall – one entirely below the pseudo-critical temperature and one crossing it.

Chapter 7 focuses on secondary subharmonic resonance, with particular attention to the role of Mode II. Both Floquet-based secondary instability analysis and DNS of the complete breakdown to turbulence through subharmonic resonance are conducted.

Chapter 8 summarises the main findings of this research and provides recommendations for future investigations. Supplementary material is provided in the appendix at the end of the thesis.

Bibliography

Banuti, D. T. 2015 Crossing the Widom-line – Supercritical pseudo-boiling. *J. Supercrit. Fluids* **98**, 12–16.

Banuti, D. T., Raju, M. & Ihme, M. 2017 Similarity law for Widom lines and coexistence lines. *Phys. Rev. E* **95** (5), 052120.

Brunner, G. 2010 Applications of supercritical fluids. *Annu. Rev. Chem. Biomol. Eng.* **1**, 321–342.

Burke, M., Hsiang, S. M. & Miguel, E. 2015 Global non-linear effect of temperature on economic production. *Nature* **527**, 235–239.

Cinnella, P. & Gloerfelt, X. 2023 Insights into the turbulent flow of dense gases through high-fidelity simulations. *Comput. Fluids* **267**, 106067.

Crespi, F., Gavagnin, G., Sánchez, D. & Martínez, G. S. 2017 Supercritical carbon dioxide cycles for power generation: A review. *Appl. Energy* **195**, 152–183.

Davidson, P. A., Kaneda, Y., Moffatt, K. & Sreenivasan, K. R. 2011 *A Voyage Through Turbulence*. Cambridge University Press.

Garvin, J. B. & others 2022 Revealing the mysteries of Venus: The DAVINCI mission. *Planet. Sci. J.* **3**, 117.

Gaster, M. 1962 A note on a relation between temporally increasing and spatially increasing disturbances in hydrodynamic stability. *J. Fluid Mech.* **14**, 222–224.

Guardone, A., Colonna, P., Pini, M. & Spinelli, A. 2024 Nonideal compressible fluid dynamics of dense vapors and supercritical fluids. *Annu. Rev. Fluid Mech.* **56** (1), 241–269.

Heisenberg, W. 1924 Über Stabilität und Turbulenz von Flüssigkeitsströmen. *Ann. Phys.* **79**, 577–627.

van Ingen, J. L. 1956 A suggested semi-empirical method for the calculation of the boundary layer transition region. Technical Report VTH-74. Delft University of Technology, Department of Aerospace Engineering.

International Energy Agency 2023 World energy investment 2023. `https://www.iea.org/reports/world-energy-investment-2023` (accessed: 2025-07-04).

Iverson, B. D., Conboy, T. M., Pasch, J. J. & Kruizenga, A. M. 2013 Supercritical CO_2 Brayton cycles for solar-thermal energy. *Appl. Energy* **111**, 957–970.

Kotz, M., Levermann, A. & Wenz, L. 2024 The economic commitment of climate change. *Nature* **628**, 551–557.

Lamanna, G. 2024 *Supercritical fluids: properties and applications*. World Scientific.

Lebonnois, S. & Schubert, G. T. 2017 The deep atmosphere of Venus and the possible role of density-driven separation of CO_2 and N_2. *Nature Geosci.* **10**, 473–477.

Lees, L. & Lin, C. C. 1946 Investigation of the stability of the laminar boundary layer in a compressible fluid. *NACA Tech. Note* 1115.

MAN Energy Solutions 2024 Esbjerg heat pump. Press release, November 28, 2024, `https://www.man-es.com/discover/esbjerg-heat-pump` (accessed 2025-07-04).

Morkovin, M. V. 1969 On the many faces of transition. In *Viscous Drag Reduction* (ed. C. S. Wells), p. 1–31. Springer.

Orr, W. M. F. 1907 The stability or instability of the steady motions of a perfect liquid and of a viscous liquid. Part I: a perfect liquid. Part II: a viscous liquid. *Proc. R. Irish Acad. A* **27**, 9–138.

Porthos CO_2 Transport and Storage 2024 Porthos project – CO_2 transport and storage. `https://www.porthosco2.nl/en/project/` (accessed: 2025-07-04).

Prandtl, L. 1921 Bemerkungen über die Entstehung der Turbulenz. *ZAMM* **1**, 431–436.

Rayleigh, Lord 1880 On the stability, or instability, of certain fluid motions. *Proc. Lond. Math. Soc.* **9**, 57–70.

Rayleigh, Lord 1892 On the question of stability of the flow of fluids. *Phil. Mag.* **34**, 59–70.

Reinsch, T., Dobson, P. & Asanuma, H. 2017 Utilizing supercritical geothermal systems: a review of past ventures and ongoing research activities. *Geotherm. Energy* **5**.

Ren, J., Fu, S. & Pecnik, R. 2019*a* Linear instability of Poiseuille flows with highly non-ideal fluids. *J. Fluid Mech.* **859**, 89–125.

Ren, J., Marxen, O. & Pecnik, R. 2019*b* Boundary-layer stability of supercritical fluids in the vicinity of the Widom line. *J. Fluid Mech.* **871**, 831–864.

Reshotko, E. 2001 Transient growth: A factor in bypass transition. *Phys. Fluids* **5**, 1067–1075.

Reynolds, O. 1883 An experimental investigation of the circumstances which determine whether the motion of water shall be direct or sinuous, and of the law of resistance in parallel channels. *Phil. Trans. R. Soc.* **174**, 935–982.

Robinet, J.-C. & Gloerfelt, X. 2019 Instabilities in non-ideal fluids. *J. Fluid Mech.* **880**, 1–4.

Sayadi, T. 2012 Numerical simulation of controlled transition to developed turbulence in a zero-pressure-gradient flat-plate boundary layer. PhD thesis, Stanford University.

Schlichting, H. & Gersten, K. 2003 *Boundary Layer Theory*. Springer.

Schubauer, G. B. & Skramstad, H. K. 1947 Laminar boundary layer oscillations and transitions on a flat plate. *J. Aero. Sci.* **14**, 69–78.

Simeoni, G. G., Bryk, T., Gorelli, F. A., Krisch, M., Ruocco, G., Santoro, M. & Scopigno, T. 2010 The Widom line as the crossover between liquid-like and gas-like behaviour in supercritical fluids. *Nat. Phys.* **6** (7), 503–507.

Sommerfeld, A. 1908 Ein Beitrag zur hydrodynamischen Erklärung der turbulenten Flüssigkeitsbewegungen. In *Proceedings of the 4th International Congress of Mathematicians, III*, pp. 116–124.

Trefethen, L. N., Trefethen, A. E., Reddy, S. C. & Driscoll, T. A. 1993 Hydrodynamic stability without eigenvalues. *Science* **261**, 578–584.

Widom, B. 1965 Equation of state in the neighborhood of the critical point. *J. Chem. Phys.* **43**, 3898–3905.

aus der Wiesche, S. 2023 Experimental investigation techniques for non-ideal compressible fluid dynamics. *Int. J. Turbomach. Propuls. Power* **8**.

Xu, L., Kumar, P., Buldyrev, S. V., Chen, S.-H., Poole, P. H., Sciortino, F. & Stanley, H. E. 2005 Relation between the Widom line and the dynamic crossover in systems with a liquid–liquid phase transition. *Proc. Natl. Acad. Sci. USA* **102** (46), 16558–16562.

Yoo, J. Y. 2013 The turbulent flows of supercritical fluids with heat transfer. *Annu. Rev. Fluid Mech.* **45**, 495–525.

Zhang, X., Li, L.-F., Du, Z.-F., Hao, X.-L., Cao, L., Luan, Z.-D., Wang, B., Xi, S.-C., Lian, C., Yan, J. & Sun, W.-D. 2020 Discovery of supercritical carbon dioxide in a hydrothermal system. *Sci. Bull.* **65** (11), 958–964.

2

GOVERNING EQUATIONS

'I conceived the idea that there is no essential difference between the gaseous and the liquid state of matter. And so the idea of continuity occurred to me.'

J. D. van der Waals,
Nobel Lecture, 1910

Parts of the content of this chapter have been published under the title:

P. C. Boldini, R. Hirai, P. Costa, J. W. R. Peeters, and R. Pecnik,
CUBENS: A GPU-accelerated high-order solver for wall-bounded flows with non-ideal fluids.
Computer Physics Communications, Volume 309, 109507, 2025.

In the following, we present the fundamental governing equations and thermodynamic closures for a single-phase, non-reacting compressible fluid valid in the non-ideal thermodynamic region. The fluid is assumed to be Newtonian and in thermodynamic and chemical equilibrium.

2.1 Flow-conservation equations

The non-dimensional, fully-compressible Navier–Stokes (NS) equations are written as

$$\frac{\partial \mathbf{Q}}{\partial t} + \frac{\partial \left[\mathbf{F} + \mathbf{F}_{visc.}\right]}{\partial x} + \frac{\partial \left[\mathbf{G} + \mathbf{G}_{visc.}\right]}{\partial y} + \frac{\partial \left[\mathbf{H} + \mathbf{H}_{visc.}\right]}{\partial z} = \mathbf{S}, \tag{2.1}$$

where t is the time and $[x_1, x_2, x_3] = [x, y, z]$ are the Cartesian coordinates in the streamwise, wall-normal, and spanwise directions. The state vector $\mathbf{Q}$ in Eq. (2.1) is defined as

$$\mathbf{Q} = \left[\rho, \rho u, \rho v, \rho w, \rho e_0\right]^{\mathrm{T}}, \tag{2.2}$$

where ρ is the fluid density; ρu, ρv, ρw are the x-, y-, and z-momentum components with velocity $|\mathbf{u}| = [u, v, w]^{\mathrm{T}}$, respectively; $e_0 = e + |\mathbf{u}|^2/2$ is the specific total energy, where e is the specific internal energy (see Sec. 2.2). In Eq. (2.1), $\mathbf{F}$, $\mathbf{G}$, and $\mathbf{H}$ are the Euler fluxes, specified as

$$\mathbf{F} = \begin{pmatrix} \rho u \\ \rho u u + p \\ \rho u v \\ \rho u w \\ u(\rho e_0 + p) \end{pmatrix}, \quad \mathbf{G} = \begin{pmatrix} \rho v \\ \rho v u \\ \rho v v + p \\ \rho v w \\ v(\rho e_0 + p) \end{pmatrix}, \quad \mathbf{H} = \begin{pmatrix} \rho w \\ \rho w u \\ \rho w v \\ \rho w w + p \\ w(\rho e_0 + p) \end{pmatrix}, \tag{2.3a–c}$$

where p is the pressure, and the term $\rho e_0 + p$ is equal to ρh_0, with h_0 being the specific total enthalpy. Likewise, the viscous fluxes are expressed as:

$$\mathbf{F}_{\text{visc.}} = \begin{pmatrix} 0 \\ -\tau_{xx} \\ -\tau_{xy} \\ -\tau_{xz} \\ -u\tau_{xx} - v\tau_{xy} - w\tau_{xz} + q_x \end{pmatrix},$$

$$\mathbf{G}_{\text{visc.}} = \begin{pmatrix} 0 \\ -\tau_{xy} \\ -\tau_{yy} \\ -\tau_{yz} \\ -u\tau_{xy} - v\tau_{yy} - w\tau_{yz} + q_y \end{pmatrix}, \tag{2.4a–c}$$

$$\mathbf{H}_{\text{visc.}} = \begin{pmatrix} 0 \\ -\tau_{xz} \\ -\tau_{yz} \\ -\tau_{zz} \\ -u\tau_{xz} - v\tau_{yz} - w\tau_{zz} + q_z \end{pmatrix}.$$

The viscous stress tensor τ_{ij} and the heat flux vector q_j are given as

$$\tau_{ij} = \frac{\lambda}{Re}\delta_{ij}\frac{\partial u_k}{\partial x_k} + \frac{\mu}{Re}\left(\frac{\partial u_i}{\partial x_j} + \frac{\partial u_j}{\partial x_i}\right), \quad q_j = -\frac{\kappa}{ReEcPr}\frac{\partial T}{\partial x_j}, \tag{2.5a,b}$$

where μ is the dynamic viscosity, $\lambda = -2/3\mu$ is Lamé's constant with zero bulk viscosity (Stokes' hypothesis), δ_{ij} is the Kronecker delta, κ is the thermal conductivity, and T is the fluid temperature. The source term $\mathbf{S}$ in Eq. (2.1) includes: (i) the forcing term f_x to enforce constant mass-flow-rate in channel flows, and (ii) the buoyancy force, which may arise due to strong density variations along the wall-normal direction in supercritical fluids. Thus, $\mathbf{S}$ is expressed as:

$$\mathbf{S} = \begin{pmatrix} 0 \\ f_x \\ -Ri_{unit}(\rho - 1) \\ 0 \\ -Ri_{unit}(\rho - 1)v + uf_x \end{pmatrix}. \tag{2.6}$$

The non-dimensionalisation of Eq. (2.1) is based on the following reference values

$$t = \frac{t^* u^*_{ref}}{L^*_{ref}}, \quad x_i = \frac{x^*_i}{L^*_{ref}}, \quad u_i = \frac{u^*_i}{u^*_{ref}}, \quad \rho = \frac{\rho^*}{\rho^*_{ref}}, \quad p = \frac{p^*}{\rho^*_{ref} u^{*2}_{ref}},$$
$$T = \frac{T^*}{T^*_{ref}}, \quad e_0 = \frac{e^*_0}{u^{*2}_{ref}}, \quad \mu = \frac{\mu^*}{\mu^*_{ref}}, \quad \kappa = \frac{\kappa^*}{\kappa^*_{ref}}, \quad \nu = \frac{\nu^*}{\nu^*_{ref}}, \tag{2.7a–j}$$

where $(\cdot)^*$ denotes dimensional quantities, and $(\cdot)_{ref}$ corresponds to the reference state based on the considered flow configuration. As a result, the corresponding non-dimensional characteristic numbers are defined as

$$Re = \frac{\rho^*_{ref} u^*_{ref} L^*_{ref}}{\mu^*_{ref}}, \quad Ec = \frac{u^{*2}_{ref}}{c^*_{p,ref} T^*_{ref}}, \quad Pr = \frac{c^*_{p,ref}\,\mu^*_{ref}}{\kappa^*_{ref}}, \quad Ri_{unit} = \frac{1}{Fr^2} = \frac{L^*_{ref}\,g^*}{u^{*2}_{ref}}, \tag{2.8a–d}$$

where $c^*_{p,ref}$ is the specific heat capacity at constant pressure. The Reynolds number Re and the unit Richardson number Ri_{unit}, or the Froude number Fr, are based on a chosen reference length scale L^*_{ref}, and Ri_{unit} depends on the gravitational acceleration g^*. Accordingly, the buoyancy contribution is written relative to a reference hydrostatic state, so that it is proportional to the local density deviation, which appears as the factor $(\rho - 1)$ in Eq. (2.6). The hydrostatic background pressure p^*_h across the reference length scale (e.g. boundary-layer thickness or channel height) scales as $\Delta p^*_h \sim \Delta\rho^* g^* L^*_{ref} \sim Ri_{unit}\,\Delta\rho^* u^{*2}_{ref}$. Relative to the inertial pressure scale $\rho^*_{ref} u^{*2}_{ref}$, its variation is therefore of order $\mathcal{O}(Ri_{unit}\,\Delta\rho^*/\rho^*_{ref})$. For weakly and moderately stratified flows, where this quantity remains small, the corresponding hydrostatic pressure variation is negligible (see also Boldini *et al.* (2025)). The remaining parameters in Eq. (2.8*a–d*) are the Eckert number Ec and the Prandtl number Pr. The Mach number $M = u^*_{ref}/a^*_{ref}$, where a^*_{ref} is the speed of sound, can be obtained from Ec as a function of the selected equation of state.

2.2 Equations of state

In order to close the conservation equations in Eq. (2.1), thermal (i.e. $p = p(\rho, T)$) and caloric (i.e. $e = e(\rho, T)$) Equations of State (EoS) need to be defined by satisfying the compatibility condition, which is defined as

$$e = e_{ref} + \int_{T_{ref}}^{T} c_{v,\infty}(\check{T})\,\mathrm{d}\check{T} - \int_{\rho_{ref}}^{\rho} \left(T \left.\frac{\partial p}{\partial T}\right|_{\rho} - \frac{p}{\check{\rho}^2} \right) \mathrm{d}\check{\rho}, \tag{2.9}$$

where $c_{v,\infty} = \partial e/\partial T|_v$ is the specific heat capacity at constant volume in the ideal-gas limit, and $\check{(\cdot)}$ indicates an integration variable. The derivation of the compatibility equation relies on several fundamental thermodynamic identities, including the first law of thermodynamics, Maxwell relations, and total differentials. These identities ensure compatibility between the thermal and caloric EoS, as given in Eq. 2.9, and are provided in detail in Appendix A.2.

Two approaches can be considered for the definition of the thermal and caloric EoS. Thermodynamic libraries such as NIST REFPROP (Lemmon *et al.* 2013) and CoolProp (Bell *et al.* 2014) model well-known fluids efficiently and with high accuracy, but lack data for less-studied fluids and mixtures, often requiring experimental input. Moreover, they deliver exceptional accuracy near the vapour–liquid critical point, yet at a high computational cost. Crucially, they do not provide closed-form expressions for high-order thermodynamic derivatives – needed, for instance, in stability and sensitivity analyses. These derivatives must then be obtained numerically from tabulated data, which can introduce noise and spurious oscillations in higher-order terms (see Sec. 2.2.4). On the other hand, cubic EoS are simple and computationally efficient models that require only a small set of inputs (e.g. critical pressure and temperature, and the acentric factor), but are less accurate, especially near the critical point. One key advantage is their ability to be expressed in reduced form, satisfying the principle of corresponding states (Van der Waals 1873): at the same reduced conditions, indicated by the subscript $(\cdot)_r$, relative to the critical point, indicated by the subscript $(\cdot)_c^*$, different fluids exhibit similar thermodynamic behaviour.

From the EoS, additional thermodynamic response functions required throughout this work can be derived. The speed of sound a, specific isobaric heat capacity $c_p = \partial h/\partial T|_p$, where h is the specific enthalpy, and thermal expansion coefficient α_v are computed in a form valid for any EoS using the thermodynamic identities in Appendix A.2 as:

$$a^2 = \left.\frac{\partial p}{\partial \rho}\right|_e + \frac{p}{\rho^2}\left.\frac{\partial p}{\partial e}\right|_\rho, \quad c_p = c_v + \frac{T}{\rho^2}\left.\frac{\partial \rho}{\partial p}\right|_T \left.\frac{\partial p}{\partial T}\right|_\rho, \quad \alpha_v = \frac{1}{\rho}\left.\frac{\partial \rho}{\partial T}\right|_p. \tag{2.10a–c}$$

Besides entering the thermodynamic closure of the NS equations in Eq. 2.1 and the non-dimensional characteristic number in Eq. 2.8*a–d*, these quantities are also necessary for the implementation of the non-reflecting boundary conditions in the CUBENS solver, as discussed in Sec. 5.3.4.

In the following, we describe the different EoS employed in this work. The Ideal-Gas (IG) law is included for completeness, as it is also considered for validation against previous IG studies in the literature.

2.2.1 Ideal gas (calorically perfect)

The non-dimensional IG law $p = \rho R_g T$ holds, where the non-dimensional specific gas constant R_g is defined as $1/(\gamma M_\infty^2)$. The heat capacity ratio $\gamma = c_p/c_v$ is constant. Consequently, the caloric equation of state, given as $e = h - p/\rho = c_v T$, can be used to explicitly compute the temperature. Furthermore, the speed of sound a and thermal expansion coefficient α_v are determined as:

$$a = \sqrt{\gamma(\gamma-1)e}, \quad \alpha_v = \frac{1}{T}. \tag{2.11a,b}$$

2.2.2 Van der Waals

The reduced cubic Van der Waals (VdW) EoS is characterised by the compressibility factor at the critical point $Z_c = p_c^*/(\rho_c^* R_g^* T_c^*)$, which is equal to 3/8. The thermal and caloric equations are

$$p_r = \frac{8\rho_r T_r}{3-\rho_r} - 3\rho_r^2, \quad e_r = \frac{c_{v,r} T_r}{Z_c} - 3\rho_r, \quad c_{v,r} = \frac{c_v^*}{R_g^*} = \frac{f}{2}, \tag{2.12a–c}$$

where $p_r = p^*/p_c^*$ is the reduced pressure, $T_r = T^*/T_c^*$ is the reduced temperature, $\rho_r = \rho^*/\rho_c^*$ is the reduced density, $e_r = e^*\rho_c^*/p_c^*$ is the reduced internal energy, $c_{v,r} = c_v^*/R_g^*$ is the reduced specific isochoric heat capacity, and f is the number of active degrees of freedom of the fluid (Anderson 2006). For reference, the dimensional VdW parameters a^*, quantifying the intermolecular attractions, and b^*, representing the finite molecular size, are fixed by the thermodynamic critical point as $a^* = 27(R_g^* T_c^*)^2/(64 p_c^*)$ and $b^* = R_g^* T_c^*/(8 p_c^*)$. Additionally, the reduced specific isobaric heat capacity $c_{p,r} = c_p^*/R_g^*$ and speed of sound $a_r^2 = a^{*2}\rho_c^*/p_c^*$ are calculated as:

$$c_{p,r} = c_{v,r} + \left[1 - \frac{\rho_r(3-\rho_r)^2}{4T_r}\right]^{-1}, \quad a_r^2 = \left(\frac{c_{v,r}+1}{c_{v,r}^2}\right)(e_r + 3\rho_r)\left(\frac{3}{3-\rho_r}\right)^2 - 6\rho_r. \tag{2.13a,b}$$

The reduced thermal expansion coefficient $\alpha_{v,r} = \alpha_v^* T_c^*$ is expressed as

$$\alpha_{v,r} = \frac{1}{\rho_r}\frac{\partial p_r}{\partial T_r}\bigg|_{\rho_r} \Bigg/ \frac{\partial p_r}{\partial \rho_r}\bigg|_{T_r}, \tag{2.14}$$

with

$$\frac{\partial p_r}{\partial T_r}\bigg|_{\rho_r} = \frac{8\rho_r}{3-\rho_r}, \quad \frac{\partial p_r}{\partial \rho_r}\bigg|_{T_r} = \frac{24 T_r}{(3-\rho_r)^2} - 6\rho_r. \tag{2.15a,b}$$

Additional partial derivatives required for the stability analysis are given in Appendix A.3.1.

2.2.3 Peng–Robinson

For the reduced cubic Peng–Robinson (PR) EoS, the thermal equation is

$$p_r = \frac{Z_c^{-1}\rho_r T_r}{1 - b_r Z_c^{-1}\rho_r} - \frac{\alpha a_r Z_c^{-2}\rho_r^2}{1 + 2b_r Z_c^{-1}\rho_r - b_r^2 Z_c^{-2}\rho_r^2},$$
$$a_r = 0.45724, \quad b_r = 0.07780, \quad \alpha = \left[1 + K\left(1 - \sqrt{T_r}\right)\right]^2, \tag{2.16a–d}$$

where the constants a_r, b_r, and $Z_c = 0.3112$ are obtained by enforcing the critical-point conditions. The parameter α accounts for temperature-dependent intermolecular forces, and $K = 0.37464 + 1.54226\bar{\omega} - 0.26992\bar{\omega}^2$ is a function of the acentric factor $\bar{\omega}$. By enforcing thermodynamic consistency from the Maxwell relations in Appendix A.2, the caloric equation of state becomes

$$e_r = c_{v,r} T_r Z_c^{-1} + \frac{a_r Z_c^{-1}}{2 b_r \sqrt{2}} \sqrt{\alpha} (K+1) \ln\left(\frac{1 + b_r Z_c^{-1} \rho_r (1-\sqrt{2})}{1 + b_r Z_c^{-1} \rho_r (1+\sqrt{2})} \right),$$
$$c_{v,r} = \frac{f}{2} - \frac{a_r K (K+1)}{4 b_r \sqrt{2 T_r}} \ln\left(\frac{1 + b_r Z_c^{-1} \rho_r (1-\sqrt{2})}{1 + b_r Z_c^{-1} \rho_r (1+\sqrt{2})} \right), \tag{2.17a,b}$$

where f is the number of active degrees of freedom of the fluid. The reduced specific isobaric heat capacity $c_{p,r}$, speed of sound a_r^2, and thermal expansion coefficient $\alpha_{v,r}$ are calculated as:

$$c_{p,r} = c_{v,r} + \frac{Z_c T_r}{\rho_r^2} \left. \frac{\partial p_r}{\partial T_r} \right|_{\rho_r}^2 \left. \frac{\partial p_r}{\partial \rho_r} \right|_{T_r}, \quad a_r^2 = \frac{Z_c T_r}{c_{v,r} \rho_r^2} \left. \frac{\partial p_r}{\partial T_r} \right|_{\rho_r}^2 + \left. \frac{\partial p_r}{\partial \rho_r} \right|_{T_r},$$
$$\left. \frac{\partial p_r}{\partial T_r} \right|_{\rho_r} = K \sqrt{\frac{\alpha}{T_r}} \frac{a_r \rho_r^2 Z_c^{-2}}{1 + 2 b_r Z_c^{-1} \rho_r - b_r^2 Z_c^{-2} \rho_r^2} - \frac{\rho_r Z_c^{-1}}{b_r Z_c^{-1} \rho_r - 1},$$
$$\left. \frac{\partial p_r}{\partial \rho_r} \right|_{T_r} = \frac{Z_c^{-1} T_r}{(\rho_r b_r Z_c^{-1} - 1)^2} - \frac{a_r \alpha Z_c^{-2} (2\rho_r + 2 b_r Z_c^{-1} \rho_r^2)}{\left[1 + 2 b_r Z_c^{-1} \rho_r - \rho_r^2 b_r^2 Z_c^{-2}\right]^2},$$
$$\alpha_{v,r} = \frac{1}{\rho_r} \left. \frac{\partial p_r}{\partial T_r} \right|_{\rho_r} \Bigg/ \left. \frac{\partial p_r}{\partial \rho_r} \right|_{T_r}. \tag{2.18a–e}$$

Additional partial derivatives required for the stability analysis are given in Appendix A.3.2.

2.2.4 Multi-Parameter Equations of State

The state-of-the-art Multi-Parameter Equations of State (MPEoS) developed by Span & Wagner (2003) and Kunz & Wagner (2012) are empirical in nature and feature simultaneously optimised functional forms for both polar and non-polar fluids. In contrast to cubic EoS, the MPEoS use many empirically fitted terms to provide a thermodynamically consistent description over wide temperature and density ranges. The equations are expressed in terms of the Helmholtz energy as

$$\alpha(1/T_r, \rho_r) = \frac{a(1/T_r, \rho_r)}{R_g T} = \alpha^{id} + \alpha^r, \tag{2.19}$$

where α represents the reduced molar Helmholtz energy. The polynomial-like term α^{id} represents the ideal-gas contribution, while the exponential term α^r refers to the non-ideal fluid contribution. Such MPEoS are available through the NIST REFPROP library (Lemmon *et al.* 2013). Thermodynamic properties are typically retrieved using tabulated look-up tables as functions of two independent variables, e.g. ρ and T. Since REFPROP does not provide closed-form expressions for high-order derivatives, these are obtained numerically, e.g. via finite-difference approximations. For instance, the first and second derivatives of a

thermodynamic property, denoted generically by χ, can be determined using a second-order finite-difference method as:

$$\left.\frac{\partial \chi(\rho,T)}{\partial T}\right|_{\rho} = \frac{\chi(\rho,T+\epsilon_T)-\chi(\rho,T-\epsilon_T)}{2\epsilon_T}, \tag{2.20}$$

$$\left.\frac{\partial \chi(\rho,T)}{\partial \rho}\right|_{T} = \frac{\chi(\rho+\epsilon_\rho,T)-\chi(\rho-\epsilon_\rho,T)}{2\epsilon_\rho}, \tag{2.21}$$

$$\left.\frac{\partial^2 \chi(\rho,T)}{\partial T^2}\right|_{\rho} = \frac{\chi(\rho,T+\epsilon_T)-2\chi(\rho,T)+\chi(\rho,T-\epsilon_T)}{\epsilon_T^2}, \tag{2.22}$$

$$\left.\frac{\partial^2 \chi(\rho,T)}{\partial \rho^2}\right|_{T} = \frac{\chi(\rho+\epsilon_\rho,T)-2\chi(\rho,T)+\chi(\rho-\epsilon_\rho,T)}{\epsilon_\rho^2}, \tag{2.23}$$

$$\begin{aligned}\left.\frac{\partial}{\partial \rho}\right|_{T}\left(\left.\frac{\partial \chi(\rho,T)}{\partial T}\right|_{\rho}\right) &= \left.\frac{\partial}{\partial T}\right|_{\rho}\left(\left.\frac{\partial \chi(\rho,T)}{\partial \rho}\right|_{T}\right)\\ &= \frac{\chi(\rho+\epsilon_\rho,T+\epsilon_T)-\chi(\rho+\epsilon_\rho,T-\epsilon_T)}{4\epsilon_\rho\epsilon_T} - \frac{\chi(\rho-\epsilon_\rho,T+\epsilon_T)-\chi(\rho-\epsilon_\rho,T-\epsilon_T)}{4\epsilon_\rho\epsilon_T}.\end{aligned} \tag{2.24}$$

Here, ϵ_T and ϵ_ρ are the temperature and density step sizes, respectively. These derivatives are essential for the stability analysis in Chapters 3 and 4.

To assess the accuracy of the different thermal and caloric EoS, Fig. 2.1 displays the reduced density and the dimensional specific isobaric heat capacity c_p^* of supercritical CO_2 as a function of the reduced temperature for different reduced pressures p_r. The properties of supercritical CO_2 are summarised in Appendix A.1. The pentagrams indicate the pseudo-critical point, defined here as the locus of $\max\{c_p(T)\}$ predicted by the MPEoS as a function of p_r. As p_r increases, the c_p^* peak broadens and its maximum value decreases, while the pseudo-critical temperature shifts to higher T_r, reflecting a progressively weaker supercritical-state transition (across the Widom line). At $p_r = 1.10$, the VdW EoS (blue dotted line) reproduces the vapour-like state reasonably well, but shifts the pseudo-critical peak in c_p^* to a slightly higher temperature (blue circle), predicting $T_{pc}^* = 310.4\,\mathrm{K}$ instead of the MPEoS value $T_{pc}^* = 307.7\,\mathrm{K}$, and underestimates the peak value by about a factor of three. The PR EoS (dashed blue line) provides a better description of the liquid-like state and yields a more accurate pseudo-critical point (blue square), although discrepancies in the c_p^* peak remain. As expected, the IG EoS (black solid line) fails to predict any non-ideal behaviour near the critical point and in the liquid-like region.

2.3 Transport properties

To close the NS equations, the fluid's dynamic viscosity and thermal conductivity must be specified in addition to the equation of state.

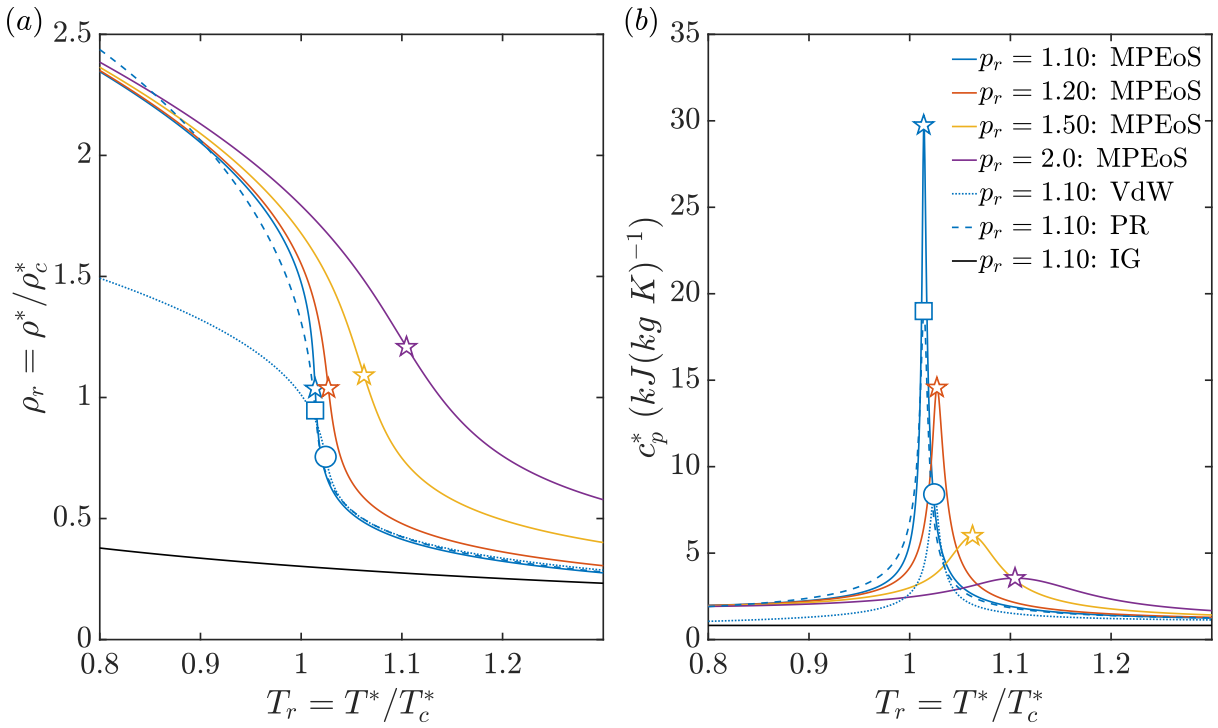

Figure 2.1: Supercritical CO_2: (a) reduced density $\rho_r = \rho^*/\rho_c^*$ and (b) specific heat at constant pressure c_p^* as functions of the reduced temperature $T_r = T^*/T_c^*$ for different reduced pressures $p_r = p^*/p_c^*$. Coloured solid lines correspond to MPEoS results. For $p_r = 1.10$, results for the VdW (···) and PR (– –) EoS are included, while the IG EoS is shown as a black solid line. The pentagrams, circles, and squares show the location of the pseudo-critical point, i.e. $T^* = T_{pc}^*$ for the MPEoS, VdW, and PR, respectively.

2.3.1 Power law and Sutherland's law (calorically perfect gas)

The non-dimensional dynamic viscosity $\mu = \mu^*/\mu_\infty^*$ is calculated as

$$\mu = T^n, \tag{2.25}$$

for the power law, where n is the power-law exponent, and as

$$\mu = T^{3/2}\frac{1 + T_{ref}^*/T_\infty^*}{T + T_{ref}^*/T_\infty^*}, \quad \text{with } T_{ref}^* = 110.4\,\text{K}, \tag{2.26}$$

for Sutherland's law (Marxen *et al.* 2007). The non-dimensional thermal conductivity is given by the relation $\kappa = \mu$.

2.3.2 Jossi, Stiel, and Thodos

Based on theoretical scaling and experimental findings, analytical expressions for dynamic viscosity and thermal conductivity for non-polar supercritical fluids were derived by Jossi *et al.* (1962) and Stiel & Thodos (1964), respectively, and are denoted as JST hereafter. The advantage of this model is its use of reduced quantities, providing a more universal and

general representation and enabling easier comparison across different species. The dynamic viscosity μ^* is defined implicitly as

$$\begin{aligned} F_\rho = \left[(\mu^* - \mu_0^*)\xi^* + 10^{-4}\right]^{1/4} = \\ + 0.10230 + 0.023364\rho_r + 0.058533\rho_r^2 \\ - 0.040758\rho_r^3 + 0.0093324\rho_r^4, \end{aligned} \tag{2.27}$$

where ρ_r is the reduced density, $\xi^* = 10^3 T_c^{*1/6}/(M^{*1/2} p_c^{*2/3})$ is the viscosity parameter, and μ_0^* is the viscosity at moderate pressures ($0.1\,\text{atm} < p^* < 5\,\text{atm}$), given as

$$\mu_0^* \xi^* = \begin{cases} 34 \times 10^{-5}\ T_r^{0.94}, & \text{for } T_r \leq 1.50, \\ 17.78 \times 10^{-5}\,(4.58 T_r - 1.67)^{5/8}, & \text{for } T_r > 1.50, \end{cases} \tag{2.28}$$

where T_r is the reduced temperature. The non-dimensional dynamic viscosity μ is then formulated as:

$$\mu = \frac{\mu^*}{\mu_\infty^*} = \frac{F_\rho^4 - 10^{-4} + \mu_0^* \xi^*}{F_{\rho,\infty}^4 - 10^{-4} + \mu_{0,\infty}^* \xi^*}, \tag{2.29}$$

where $(\cdot)_\infty$ denotes the reference (free-stream) state evaluated at $(\rho_\infty^*, T_\infty^*)$. The thermal conductivity κ^* is defined as

$$\begin{aligned} G_\rho = (\kappa^* - \kappa_0^*)\lambda^* Z_c^5 = 4.1868 \times 10^{-6} \\ \times \begin{cases} 14.0\,(\exp[0.535\rho_r] - 1), & \text{for } \rho_r < 0.50, \\ 13.1\,(\exp[0.67\rho_r] - 1.069), & \text{for } 0.50 \leq \rho_r \leq 2.0, \\ 2.976\,(\exp[1.155\rho_r] + 2.016), & \text{for } 2.0 < \rho_r \leq 2.80, \end{cases} \end{aligned} \tag{2.30}$$

where $\lambda^* = \xi^* M^*$ is the thermal conductivity parameter, and κ_0^* is the thermal conductivity of a polyatomic gas at atmospheric pressure (Hirschfelder *et al.* 1954), expressed as:

$$\kappa_0^* = \left(0.307 \frac{c_v^*}{R_g^*} + 0.539\right) \kappa_{0,\text{mon}}^*, \quad \kappa_{0,\text{mon}}^* = \frac{15}{4} \frac{R_g^*}{M^*} \mu_0^*. \tag{2.31a,b}$$

The non-dimensional thermal conductivity κ is then given by:

$$\kappa = \frac{\kappa^*}{\kappa_\infty^*} = \frac{G_\rho + Z_c^5 \kappa_0^* \lambda^*}{G_{\rho,\infty} + Z_c^5 \kappa_{0,\infty}^* \lambda^*}. \tag{2.32}$$

2.3.3 Chung

A more accurate representation of the liquid-like state is provided by the generalised correlations of Chung *et al.* (1988). Unlike JST, this model requires explicit specification of the considered fluid. The dynamic viscosity is written as

$$\mu^* = \mu_k^* + \mu_p^*, \tag{2.33}$$

where the modified dilute-gas viscosity, μ_k^*, and the correction term, μ_p^*, are defined as

$$\mu_k^* = \mu_0^* \left[\frac{1}{G_2} + A_6 Y \right],$$
$$\mu_p^* = 3.6344 \times 10^{-6} (M^* T_c^*)^{1/2} \rho_c^{*2/3} A_7 Y^2 G_2 \exp\left[A_8 + \frac{A_9}{T_\epsilon} + \frac{A_{10}}{T_\epsilon^2} \right], \tag{2.34a,b}$$

with

$$G_2 = \frac{A_1 \left[1 - \exp(-A_4 Y)\right] / Y + A_2 G_1 \exp(A_5 Y) + A_3 G_1}{A_1 A_4 + A_2 + A_3},$$
$$G_1 = \frac{1 - 0.5Y}{(1-Y)^3}, \tag{2.35a,b}$$

and with $Y = \rho_r/6$, $T_\epsilon = k_B^* T^*/\epsilon$, $k_B^* = 1.38064852 \times 10^{-23} J/K$, and $\epsilon = k_B^* T_c^*/1.2593$. The constants $A_{i=1,\dots,10}$ are linear functions of the form

$$A_i = a_0(i) + a_1(i)\bar{\omega} + a_2(i)\xi_r^4 + a_3(i)\varpi, \quad i \in \{1, \dots, 10\},$$
$$\varpi = 0.0682 + 4.704 \frac{[\text{number of -OH groups}]}{M^*}, \tag{2.36a,b}$$

where $\bar{\omega}$ is the acentric factor, $\xi_r = 131.3 \xi \rho_c^{*1/2} / T_c^{*1/2}$ is the reduced dipole moment (Reid *et al.* 2001), ϖ is an association parameter (Chung *et al.* 1988), and values for the coefficients a_0, a_1, a_2, and a_3 are given in Tab. 2.1. Note that for non-polar fluids, $\xi_r = 0$ and $\varpi = 0$. The dilute gas viscosity, μ_0^*, is obtained as

$$\mu_0^* = 4.0785 \times 10^{-6} \frac{(M^* T^*)^{1/2} \rho_c^{*2/3}}{\Omega_v} F_c,$$
$$F_c = 1 - 0.2756\bar{\omega} + 0.059035\xi_r^4 + \varpi, \tag{2.37a,b}$$

where Ω_v is the reduced collision integral, calculated as

$$\Omega_v = \frac{A_\Omega}{T_\epsilon^{B_\Omega}} + \frac{C_\Omega}{\exp(D_\Omega T_\epsilon)} + \frac{E_\Omega}{\exp(F_\Omega T_\epsilon)} + G_\Omega T_\epsilon^{B_\Omega} \sin(S_\Omega T_\epsilon^{W_\Omega} - H_\Omega), \tag{2.38}$$

i	a_0	a_1	a_2	a_3
1	6.32402	50.41190	-51.68010	1189.0200
2	0.0012102	-0.0011536	-0.0062571	0.037283
3	5.28346	254.20900	-168.48100	3898.27000
4	6.62263	38.09570	-8.46414	31.41780
5	19.74540	7.63034	-14.35440	31.52670
6	-1.89992	-12.53670	4.98529	-18.15070
7	24.27450	3.44945	-11.29130	69.34660
8	0.79716	1.11764	0.012348	-4.11661
9	-0.23816	0.067695	-0.81630	4.02528
10	0.068629	0.34793	0.59256	-0.72663

Table 2.1: Dynamic viscosity: a_i-coefficients (Duan *et al.* 2021).

j	b_0	b_1	b_2	b_3
1	2.41657	0.74824	-0.91858	121.72100
2	-0.50924	-1.50936	-49.99120	69.98340
3	6.61069	5.62073	64.75990	27.03890
4	14.54250	-8.91387	-5.63794	74.34350
5	0.79274	0.82019	-0.69369	6.31734
6	-5.86340	12.80050	9.58926	-65.52920
7	81.17100	114.15800	-60.84100	466.75500

Table 2.2: Thermal conductivity: b_j-coefficients (Duan *et al.* 2021).

with constants $A_\Omega = 1.16145$, $B_\Omega = 0.14874$, $C_\Omega = 0.52487$, $D_\Omega = 0.77320$, $E_\Omega = 2.16178$, $F_\Omega = 2.43787$, $G_\Omega = -6.435 \times 10^{-4}$, $H_\Omega = 7.27371$, $S_\Omega = 18.0323$, and $W_\Omega = -0.76830$.
The thermal conductivity is written as

$$\kappa^* = \kappa_k^* + \kappa_p^*, \tag{2.39}$$

where the modified dilute-gas thermal conductivity, κ_k^*, and the correction term, κ_p^*, are written as

$$\kappa_k^* = \kappa_0^* \left[\frac{1}{H_2} + B_6 Y \right],$$
$$\kappa_p^* = 3.586 \times 10^{-3} \frac{T_c^{*1/2} \rho_c^{*2/3}}{M^{*1/2}} B_7 Y^2 H_2 T_r^{1/2}, \tag{2.40a,b}$$

with the parameter $Y = \rho_r/6$, and

$$H_2 = \frac{B_1 \left[1 - \exp(-B_4 Y)\right]/Y + B_2 G_1 \exp(B_5 Y) + B_3 G_1}{B_1 B_4 + B_2 + B_3},$$
$$G_1 = \frac{1 - 0.5Y}{(1-Y)^3}. \tag{2.41a,b}$$

The constants $B_{j=1,\dots,7}$ are linear functions given by

$$B_j = b_0(j) + b_1(j)\bar{\omega} + b_2(j)\xi_r^4 + b_3(j)\varpi, \quad j \in \{1, \dots, 7\}, \tag{2.42}$$

with the aforementioned parameters $\bar{\omega}$, ξ_r, and ϖ. Values for the coefficients b_0, b_1, b_2, and b_3 are listed in Tab. 2.2. The dilute-gas conductivity κ_0^* is derived analogously to μ_0^* as

$$\kappa_0^* = 31.2 \frac{\mu_0^*}{M^*} \Psi,$$
$$\Psi = 1 + \alpha \frac{0.215 + 0.28288\alpha - 1.061\beta + 0.26665Z}{0.6366 + \beta Z + 1.061\alpha\beta}, \tag{2.43a,b}$$

with

$$\alpha = \frac{c_v^*}{R_g^*} - \frac{3}{2}, \quad \beta = 0.7862 - 0.7109\bar{\omega} + 1.3168\bar{\omega}^2,$$
$$Z = 2.0 + 10.5T_r^2. \tag{2.44a–c}$$

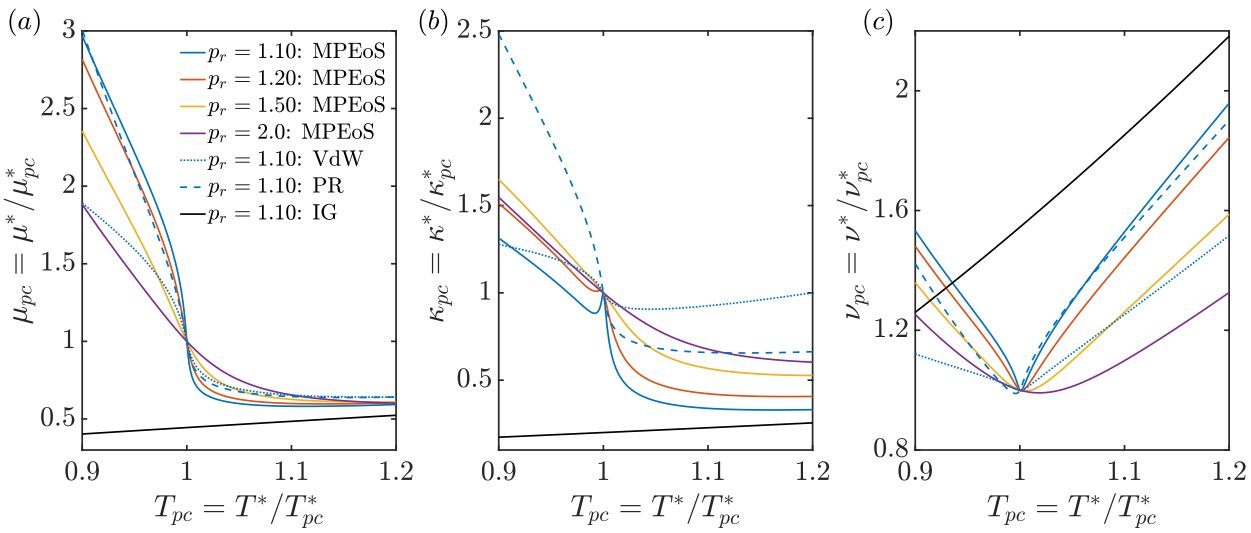

Figure 2.2: Supercritical CO_2: (a) dynamic viscosity $\mu_{pc} = \mu^*/\mu^*_{pc}$, (b) thermal conductivity $\kappa_{pc} = \kappa^*/\kappa^*_{pc}$, and (c) kinematic viscosity $\nu_{pc} = \nu^*/\nu^*_{pc}$ as functions of the pseudo-critical temperature $T_{pc} = T^*/T^*_{pc}$ for different reduced pressures $p_r = p^*/p^*_c$. Coloured solid lines correspond to MPEoS results. For $p_r = 1.10$, curves according to VdW (···) and PR (– –) EoS are included, while the IG EoS is shown as a black solid line.

2.3.4 Multi-Parameter Equations of State

As with the thermodynamic properties discussed above, Transport Properties (TP) are obtained from the NIST REFPROP library, which implements the transport models of Vesovic *et al.* (1990). For instance, the dynamic viscosity μ can be generally expressed as

$$\mu(\rho, T) = \mu_0(T) + \Delta\mu(\rho, T) + \Delta_c\mu(\rho, T), \tag{2.45}$$

where μ_0, $\Delta\mu$, $\Delta_c\mu$ are the contributions in the limit of zero density, at moderate density (e.g. many-body collisions, molecular-velocity correlations, and collisional transfer), and due to long-range fluctuations near the critical point, respectively. While μ_0 and $\Delta_c\mu$ can be determined analytically, the term $\Delta\mu$ relies on empirical correlations.

In Fig. 2.2, the dimensionless dynamic viscosity $\mu_{pc} = \mu^*/\mu^*_{pc}$, thermal conductivity $\kappa_{pc} = \kappa^*/\kappa^*_{pc}$, and kinematic viscosity $\nu_{pc} = \nu^*/\nu^*_{pc}$ of supercritical CO_2 are displayed as a function of T_{pc} for different reduced pressures p_r. All quantities are non-dimensionalised by their respective values at the pseudo-critical temperature T^*_{pc}. With increasing reduced pressure, the transport-property gradients become smoother as the fluid moves away from the critical point. The dynamic viscosity in Fig. 2.2(a) follows a similar trend to the density in Fig. 2.1(a), with the PR EoS providing better representation of the liquid-like state than the VdW EoS. For the thermal conductivity in Fig. 2.2(b), all considered analytical EoS fail to reproduce the κ peak at $T_{pc} = 1$ for $p_r = 1.10$. The kinematic viscosity in Fig. 2.2(c) exhibits a global minimum at the pseudo-critical point, arising from the slight temperature offset between density and dynamic viscosity. This well-known behaviour (Pioro *et al.* 2011; Bell *et al.* 2020; Saric *et al.* 2022) results from the sharp decrease in density significantly outpacing the more moderate reduction in dynamic viscosity across the pseudo-critical region. The IG

EoS fails to capture any non-ideal behaviour and, most importantly, the minimum of ν near T_{pc}.

2.4 Boundary-layer equations

The calculation of the laminar base-flow profiles is based on the compressible boundary-layer equations for self-similar flows (Ren *et al.* 2019; Boldini *et al.* 2023), combined with the respective EoS, under the assumption of a zero pressure gradient. The reference condition in Eq. (2.7*a–j*) is the free stream, denoted as $(\cdot)^*_\infty$. As a result, the corresponding non-dimensional characteristic parameters are

$$Re = \frac{\rho^*_\infty u^*_\infty L^*}{\mu^*_\infty}, \quad Ec_\infty = \frac{u^{*2}_\infty}{c^*_{p,\infty} T^*_\infty}, \quad Pr_\infty = \frac{c^*_{p,\infty}\mu^*_\infty}{\kappa^*_\infty}, \tag{2.46a–c}$$

where Re is the Reynolds number based on a chosen length scale L^*. Here, we adopt the local Blasius length scale δ^*, such that:

$$Re = \frac{\rho^*_\infty u^*_\infty \delta^*}{\mu^*_\infty} = \sqrt{Re_x}, \quad \delta^* = \sqrt{\frac{\mu^*_\infty x^*}{\rho^*_\infty u^*_\infty}}. \tag{2.47a,b}$$

After applying the boundary-layer assumptions (Schlichting & Gersten 2003) and an order-of-magnitude analysis to the NS equations (2.1), the dimensional boundary-layer equations become

$$\left.\begin{aligned} \frac{\partial(\rho^* u^*)}{\partial x^*} + \frac{\partial(\rho^* v^*)}{\partial y^*} &= 0, \\ \rho^* u^* \frac{\partial u^*}{\partial x^*} + \rho^* v^* \frac{\partial u^*}{\partial y^*} &= -\frac{\mathrm{d}p^*_\infty}{\mathrm{d}x^*} + \frac{\partial}{\partial y^*}\left(\mu^* \frac{\partial u^*}{\partial y^*}\right), \\ \frac{\partial p^*}{\partial y^*} &= 0, \\ \rho^*\left(u^* \frac{\partial h^*}{\partial x^*} + v^* \frac{\partial h^*}{\partial y^*}\right) &= -u^* \frac{\mathrm{d}p^*_\infty}{\mathrm{d}x^*} + \frac{\partial}{\partial y^*}\left(\kappa^* \frac{\partial T^*}{\partial y^*}\right) + \mu^* \left(\frac{\partial u^*}{\partial y^*}\right)^2, \end{aligned}\right\} \tag{2.48}$$

where h^* is the specific static enthalpy and p^*_∞ is the constant free-stream pressure throughout the flow field. The coordinate transformation based on the Lees–Dorodnitsyn variables (White 2006)

$$\xi = \int_0^x (\rho^*_\infty \mu^*_\infty u^*_\infty)\,\mathrm{d}x^*, \quad \eta = \int_0^y \left(\frac{\rho^* u^*_\infty}{\sqrt{2\xi}}\right)\mathrm{d}y^*, \tag{2.49a,b}$$

is applied. The transformed ordinary differential equations become

$$\left.\begin{aligned} (C f_{\eta\eta})_\eta + f f_{\eta\eta} &= 0, \\ f g_\eta + \left(\frac{C}{Pr} g_\eta\right)_\eta + C \frac{u^{*2}_\infty}{h^*_\infty} (f_{\eta\eta})^2 &= 0, \end{aligned}\right\} \tag{2.50}$$

where $(\cdot)_\eta$ denotes differentiation with respect to η and

$$f_\eta = \frac{u^*}{u^*_\infty}, \quad g = \frac{h^*}{h^*_\infty}, \quad C = \frac{\rho^*\mu^*}{\rho^*_\infty \mu^*_\infty} = \rho\mu, \quad Pr = \frac{c^*_p\,\mu^*}{\kappa^*}. \tag{2.51a–d}$$

In Eqs. (2.50) and (2.51*a–d*), f is related to the stream function and g is the dimensionless static specific enthalpy. The Chapman–Rubesin parameter C and local Prandtl number Pr are determined as functions of the enthalpy g from the respective EoS. Derivatives of the thermodynamic and transport properties are calculated either analytically or numerically (second-order finite differences as in Sec. 2.2.4) depending on the employed EoS and TP model (see Secs. 2.2 and 2.3). To close the system (2.50), Boundary Conditions (BCs) must be specified at the wall ($\eta = 0$) and in the free stream ($\eta \to \infty$) as

$$f(0) = 0, \quad f_\eta(0) = 0, \quad f_\eta(\eta \to \infty) = 1, \quad g(\eta \to \infty) = 1, \tag{2.52a–d}$$

while the wall condition for the enthalpy is either isothermal or adiabatic as

$$g(0) = g_w, \quad \text{or} \quad g_\eta(0) = 0, \tag{2.53a,b}$$

where $g_w(\rho_w, T_w)$ is the prescribed enthalpy at the wall. The system is solved numerically using a 4th-order Runge–Kutta scheme, together with the Newton–Raphson method to iteratively satisfy the boundary conditions at the wall.

Bibliography

Anderson, J. D. 2006 *Hypersonic and High-Temperature Gas Dynamics*. AIAA.

Bell, I. H., Galliero, G., Delage-Santacreu, S. & Costigliola, L. 2020 An entropy scaling demarcation of gas- and liquid-like fluid behaviors. *J. Chem. Phys.* **152** (19), 191102.

Bell, I. H., Wronski, J., Quoilin, S. & Lemort, V. 2014 Pure and pseudo-pure fluid thermophysical property evaluation and the open-source thermophysical property library CoolProp. *Industrial & Engineering Chemistry Research* **53** (6), 2498–2508.

Boldini, P. C., Gaspar, R., Bugeat, B., Costa, P., Peeters, J. W. R. & Pecnik, R. 2023 Direct numerical simulation of H-type transition in a flat-plate boundary layer with supercritical fluids. *14th International ERCOFTAC Symposium on Engineering Turbulence Modelling and Measurements (ETMM14), Barcelona, Spain, September 6-8* .

Boldini, P. C., Hirai, R., Costa, P., Peeters, J. W. R. & Pecnik, R. 2025 CUBENS: A GPU-accelerated high-order solver for wall-bounded flows with non-ideal fluids. *Comput. Phys. Commun.* **309**, 109507.

Chung, T. H., Ajlan, M., Lee, L. L. & Starling, K. E. 1988 Generalized multiparameter correlation for nonpolar and polar fluid transport properties. *Ind. Eng. Chem. Res.* **27**, 671–679.

Duan, L., Zheng, Q., Jiang, Z. & Wang, J. 2021 Dense gas effect on small-scale structures of compressible isotropic turbulence. *Phys. Fluids* **33**, 115113.

Hirschfelder, J., Curtiss, C. & Bird, R. 1954 *Molecular Theory of Gases and Liquids*. Wiley.

Jossi, A. J., Stiel, L. I. & Thodos, G. 1962 The viscosity of pure substances in the dense gaseous and liquid phases. *AIChE J.* **8**, 59–63.

Kunz, O. & Wagner, W. 2012 The GERG-2008 wide-range equation of state for natural gases and other mixtures: An expansion of GERG-2004. *J. Chem. Eng. Data* **57**, 30323091.

Lemmon, E. W., Huber, M. L. & Mclinden, M. O. 2013 NIST Standard Reference Database 23: Reference Fluid Thermodynamic and Transport Properties - REFPROP, Version 9.1. Available at: `http://www.nist.gov/srd/nist23.cfm`.

Marxen, O., Iaccarino, G. & Shaqfeh, E. S. G. 2007 Numerical simulation of hypersonic instability using different gas models. *Center Turbul. Res. Rep. CTR* pp. 15–27.

Pioro, I., Mokry, S. & Draper, S. 2011 Specifics of thermophysical properties and forced-convective heat transfer at critical and supercritical pressures. *Rev. Chem. Eng.* **27** (3-4), 191–214.

Reid, R. C., Prausnitz, J. M. & Sherwood, T. K. 2001 *The Properties of Gases and Liquids*, 5th edn. New York: McGraw-Hill Education.

Ren, J., Marxen, O. & Pecnik, R. 2019 Boundary-layer stability of supercritical fluids in the vicinity of the Widom line. *J. Fluid Mech.* **871**, 831–864.

Saric, D., Guevara-Carrion, G. & Vrabec, J. 2022 Thermodynamics of supercritical carbon dioxide mixtures across the Widom line. *Phys. Chem. Chem. Phys.* **24**, 28257–28270.

Schlichting, H. & Gersten, K. 2003 *Boundary Layer Theory*. Springer.

Span, R. & Wagner, W. 2003 Equations of state for technical applications. I. simultaneously optimized functional forms for nonpolar and polar fluids. *Intl. J. Thermophys.* **24**, 1–39.

Stiel, L. I. & Thodos, G. 1964 The thermal conductivity of nonpolar substances in the dense gaseous and liquid regions. *AIChE J.* **10**, 26–30.

Van der Waals, J. D. 1873 Over de continuïteit van den gas- en vloeistoftoestand. PhD thesis, Hoogeschool te Leiden.

Vesovic, V., Wakeham, W., Olchowy, G. A., Sengers, J. V., Watson, J. T. R. & Millat, J. 1990 The transport properties of carbon dioxide. *J. Phys. Chem. Ref. Data* **19**, 763–808.

White, F. M. 2006 *Viscous Fluid Flow, 3rd Edition*. Boston: McGraw-Hill.

3

MODAL STABILITY

Parts of the content of this chapter have been published under the titles:

- in Section 3.3.2: B. Bugeat, **P. C. Boldini**, and R. Pecnik,
  On the new unstable mode in the boundary layer flow of supercritical fluids.
  In Proceedings of the 12th International Symposium on Turbulence and Shear Flow Phenomena (TSFP-12), Osaka, Japan (Online), 2022.
- in Section 3.4.1: **P. C. Boldini**, B. Bugeat, J. W. R. Peeters, M. Kloker, and R. Pecnik,
  Transient growth in diabatic boundary layers with fluids at supercritical pressure.
  Physical Review Fluids 9, 083901, 2024.
- in Section 3.5: B. Bugeat, **P. C. Boldini**, A. M. Hasan, and R. Pecnik,
  Instability in strongly stratified plane Couette flow with application to supercritical fluids
  Journal of Fluid Mechanics, Volume 984, A31, 2024.

Linear stability studies traditionally assume ideal-gas behaviour, with Tollmien–Schlichting (TS) waves dominating incompressible boundary-layer flows and 'Mack modes' emerging at high Mach numbers. Supercritical fluids around the pseudo-critical point exhibit strong variations in thermophysical properties under pseudo-boiling conditions, generating a highly unstable Mode II distinct from classical TS waves. This chapter shows that the minimum of kinematic viscosity encountered near the pseudo-critical point produces a generalised inflection point, a necessary condition for inviscid instability in strongly stratified flows. By extending the compressible, ideal-gas inviscid theory of Lees & Lin (NACA Tech. Note 1115, 1946) to non-ideal fluid flows, we show that the Mach-dependent destabilisation and three-dimensional growth of Mode II are linked to the generalised inflection point that satisfies the generalised Fjørtoft criterion. Viscous and inviscid analyses of isothermal boundary layers confirm that Mode II persists without acoustic effects and remains predominantly two-dimensional at low Mach numbers. In addition, the appearance of Mode II with both cubic and multi-parameter equations of state highlights its universality in supercritical flows under pseudo-boiling conditions. A stratified plane Couette-flow model reveals the underlying mechanism behind Mode II: the combined action of shear and baroclinic effects.

3.1 Introduction

The majority of the transition studies employ the ideal-gas assumption, from incompressible flows to compressible shear-layer flows. Linear stability analyses of incompressible boundary layers show the formation of unstable Tollmien–Schlichting (TS) modes above the (hydrodynamic) critical Reynolds number (Schmid & Henningson 2001; Schlichting & Gersten 2003). Only in the case of a positive pressure gradient (Falkner–Skan flow) does the velocity exhibit an inflection point (inviscid instability), where viscosity destabilises the flow. As the Mach number increases, compressibility affects the characteristics of the TS mode (Mack 1984). In the subsonic regime, the TS mode is damped; for supersonic speeds, oblique Three-Dimensional (3-D) vorticity-type waves are (integrally) more amplified than Two-Dimensional (2-D) waves. For Mach numbers greater than approximately 3, see (Fedorov 2011; Zhong & Wang 2012), the density-weighted velocity profile becomes inflectional. As discovered by Lees & Lin (1946), a Generalised Inflection Point (GIP), analogous to the Rayleigh criterion for incompressible flows, is a necessary condition for inviscid instability. The location of the inflection point inside the boundary layer increases with increasing Mach number. In addition to these TS-like waves, an infinite number of acoustic higher modes emerge when the disturbance travels locally faster than the fast sound wave; the first of these modes is defined as the Mack second mode and becomes most dominant when the free-stream Mach number reaches a value of 4. The phenomenon is strongest for 2-D modes; wall cooling destabilises these modes but stabilises the first mode.

By increasing the Mach number even further, 'real-gas effects' become significant. This term is used in a broader, though strictly speaking incorrect, sense as the gas still behaves as a thermally perfect gas (Hirschel 2005). Instead, the correct expression should be high-temperature real-gas effects; these have been considered and examined in hypersonic flows for the development of re-entry or hypersonic vehicles. At such large Mach numbers, viscous dissipation within the boundary layer results in high temperatures at which the gas no longer behaves as an ideal gas. The effects of vibrational excitation, dissociation, radiation, ionisation, and surface ablation on the laminar-to-turbulent transition have been investigated since the 1990s. Malik & Anderson (1991) studied the influence of high-temperature effects on linear instabilities for Mach 10 and 15 boundary layers, showing stabilisation of the first-mode instability while the second Mack mode becomes more unstable. Further studies have considered chemical (Stuckert & Reed 1994) or thermal (Bertolotti 1998; Bitter & Shepherd 2015; Boldini 2018), thermo-chemical (Hudson *et al.* 1997; Chen *et al.* 2019 2021) non-equilibrium; different high-enthalpy models (Miró Miró *et al.* 2019); surface ablation (Mortensen 2018); surface-roughness effects (Stemmer *et al.* 2017), and porous walls (Fedorov *et al.* 2003).

3.1.1 Strongly stratified flows

Besides high-temperature gas effects, studies of transport-property variations, mainly density and viscosity stratification, have recently resumed for both incompressible and compressible flows. Density variations can play a significant role in flow dynamics through inertial effects.

Menkes (1959) was perhaps the first to tackle the stability of such flows, considering a hyperbolic tangent velocity profile with exponential density stratification, which was found to be stabilising in this particular configuration. Soteriou & Ghoniem (1995) more comprehensively studied an incompressible mixing layer of two fluids with different densities. Depending on the density ratio, the primary instability was shown to exhibit either weaker or larger growth rates, shifted phase speeds, and altered nonlinear development. This last point was subsequently examined via secondary stability analysis (Reinaud *et al.* 2000; Fontane & Joly 2008) and Direct Numerical Simulation (DNS) (Almagro *et al.* 2017). The mechanism responsible for the modified dynamics of this flow is the baroclinic torque, which generates vorticity from misalignments between pressure and density gradients (Soteriou & Ghoniem 1995; Reinaud *et al.* 1999; Dixit & Govindarajan 2010). It is also at play in compressible flows (Lesshafft & Huerre 2007) but is classically neglected in buoyant flows modelled via the Boussinesq approximation, which ignores density variations in inertial terms (Drazin 1958; Guha & Raj 2018).

Strong viscosity stratifications are central to our problem (see Sec. 2.3), greatly affecting the base flow profile. The instability of an immiscible flow separated by a discontinuous viscosity interface was firstly investigated by Yih (1967). A long-wave instability exists at low Reynolds numbers. This instability does not require density gradients or surface tension effects: the jump in viscosity at the interface is sufficient to destabilise the flow. Hooper & Boyd (1983), in a similar configuration, revealed that a short-wave instability also grows at low Reynolds numbers. Moreover, it was found that the less viscous fluid should be located in a thin layer close to the wall in order to stabilise long waves, whereas sufficient interfacial tension should be provided to stabilise short waves. The mechanisms of these instabilities were discussed by Hinch (1984) and Charru & Hinch (2000). The effect of an interface of finite thickness was studied by Ern *et al.* (2003). The authors recovered the presence of low-Reynolds-number instabilities and furthermore showed that certain thicknesses could induce larger growth rates than an infinitely small one. Finally, another viscous instability exists at larger but finite Reynolds numbers (Hooper & Boyd 1987). It is fundamentally different from the previous one, as its mechanism is not directly associated with the presence of the viscosity interface but, rather, of the wall.

The other limiting case of a stratified miscible flow, in which a mixing layer is totally merged inside the channel or boundary layer, was analysed by Herwig & Schäfer (1992); Wall & Wilson (1996 1997). The influence of temperature and viscosity perturbations on the hydrodynamic stability was investigated for both Poiseuille and boundary-layer flows by applying a temperature gradient in the base flow. Whilst for Poiseuille flow, a viscosity increase leads to stabilisation, for the boundary layer, a decrease/increase of viscosity towards the wall stabilises/destabilises the flow. Notably, instabilities driven by viscosity-stratification at low miscibility were found to be qualitatively similar to those observed in immiscible fluids. In further channel-flow studies, the effect of miscibility was studied by separating a two-fluid flow with a finite-thickness continuous mixed/viscosity-stratified layer (Ranganathan & Govindarajan 2001; Govindarajan 2001; Sahu & Govindarajan 2016). Ranganathan &

Govindarajan (2001) demonstrated that when the critical layer of the dominant disturbance overlaps the mixed layer, the flow can be significantly stabilised or destabilised, depending on whether the fluid in the channel centre is more or less viscous than the fluid close to the wall. In the former case, it has been shown that the strong stabilisation of a given mode is due to large negative production of disturbance kinetic energy under conditions of overlap. In contrast, Govindarajan (2001) showed that when the fluid at the wall is more viscous, a new overlap mode is generated in addition to an inviscid mode (inflectional velocity profile) and the classical TS mode. This occurs when the critical layer of the dominant disturbance extends into the mixed layer. A comprehensive review of these instabilities for different flow configurations can be found in Govindarajan & Sahu (2014).

3.1.2 Recent developments in the hydrodynamics of supercritical fluids

Little is known about the stability and transition to turbulence in fluids exhibiting non-ideal thermodynamic behaviour (Robinet & Gloerfelt 2019). Gloerfelt *et al.* (2020) examined the linear stability of dense gases at large Mach numbers. Due to the large heat capacity of these fluids, very weak temperature gradients were observed and nearly incompressible velocity profiles were recovered. The authors showed the stabilisation of the viscous mode and the existence of radiating supersonic instabilities. From a different perspective, Ren *et al.* (2019*a*) carried out a linear stability analysis of supercritical fluids in plane Poiseuille flow at finite Eckert numbers. Consequently, significant viscous heating was present at reduced but non-negligible Mach numbers, generating temperature gradients in the base-flow profile. The authors concluded that non-ideal gas effects may induce larger destabilisation of the flow in terms of growth-rate magnitude and critical Reynolds number.

In a seminal study, Ren *et al.* (2019*b*) explored the linear stability of supercritical CO_2 in an adiabatic flat-plate boundary layer flow. Exemplary stability diagrams are reported in Fig. 3.1. As viscous heating increases in the subcritical state ($T^*_\infty/T^*_{pc} < 1$, $T^*_w/T^*_{pc} < 1$), modal stabilisation is observed (Figs. 3.1a,b), in contrast to the modal destabilisation typically associated with wall heating under the ideal-gas assumption. When the temperature profile becomes transcritical ($T^*_\infty/T^*_{pc} < 1$, $T^*_w/T^*_{pc} > 1$; Fig. 3.1c), large density and viscosity variations occur in the base flow, i.e. the flow becomes strongly stratified. Consequently, a second unstable mode, referred to in this work as Mode II, emerges alongside the classical TS wave (Mode I). This mode exhibits growth rates more than one order of magnitude larger than those of TS waves, which could imply new rapid modal routes to transition to turbulence in these fluids. The authors rigorously show that this mode is inviscid, characterised by the GIP, and is not linked to Mack modes (Mack 1984) found in high-speed boundary layers. Importantly, Ren *et al.* (2019*b*) observe that the additional Mode II only appears when the temperature profile of the base flow crosses the pseudo-boiling point (Widom line). Recently, Ly & Ihme (2022) study a binary compressible mixing layer at supercritical pressures and also found evidence of this instability, pointing out that its strength decreases as the reduced

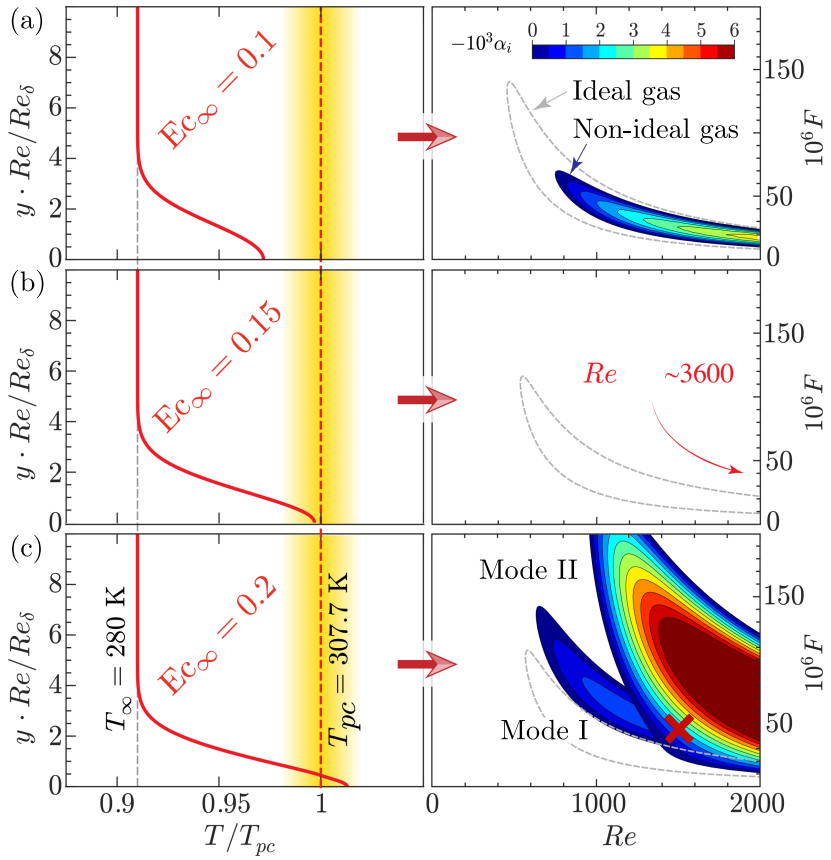

Figure 3.1: Boundary-layer temperature profiles (left column) and corresponding growth rates of perturbations in the F–Re stability diagram (right column) for increasing free-stream Eckert number: (a) $Ec_\infty = 0.1$, (b) $Ec_\infty = 0.15$, and (c) $Ec_\infty = 0.2$. In case (c), the temperature profile becomes transcritical, and two distinct unstable modes at the same F and Re, Mode I and Mode II, are observed (highlighted by the red marker in (c)). Stability results for an ideal gas are shown in grey. The red dashed line marks the pseudo-critical point, i.e. at the pseudo-critical temperature $T/T_{pc} = 1$.

pressure is increased away from the critical point. However, much remains to be understood about this instability, as the driving parameters and the physical mechanism remain unclear.

3.1.3 Objectives and assumptions

The main focus of this chapter is to investigate the role of Mode II in wall-bounded flows of supercritical fluids. The analysis begins with the linear stability of diabatic flat-plate boundary layers, where Mode II was first identified by Ren *et al.* (2019*b*). Specifically, we aim to demonstrate that Mode II is intrinsically linked to the presence of a minimum in kinematic viscosity at the Widom line. This connection is supported through inviscid stability analyses conducted within a non-ideal fluid framework. In addition, the influence of compressibility on Mode II is investigated to determine how Mach number affects the preferential amplification of 2-D versus 3-D waves. Finally, to isolate the underlying physical mechanisms, the base flow is simplified to a stratified plane Couette flow, using various forms

of stratification to mimic the strong variations in density and viscosity observed in boundary layers of supercritical fluids. This model simplification aims to highlight the central role of the kinematic viscosity minimum, regardless of other property variations, and to identify the driving mechanisms responsible for the onset of instability.

The assumptions regarding the flow regime considered in this chapter are summarised here. Buoyancy effects are neglected in the linearised stability equations presented in Sec. 3.2. Acoustic effects are also initially excluded to avoid potential ambiguities in the physical interpretation of the results related to acoustic instabilities; however, a fully compressible formulation is retained in accordance with Sec. 2.1. Both viscous and inviscid perturbations are analysed. As is common practice in the Linear Stability Theory (LST) framework (Mack 1984), the base flow is assumed to be locally parallel, which implies neglecting: (i) derivatives of the base-flow variables in the streamwise (x) and spanwise (z) directions, and (ii) the base-flow wall-normal velocity component $\bar{v}$.

The work is organised as follows. The governing equations for both viscous and inviscid modal stability analyses are introduced in Sec. 3.2, along with validation of the solvers. The 2-D stability of diabatic boundary layers with supercritical CO_2 is examined in Sec. 3.3, leading to a reformulation of the GIP criterion. The 3-D modal stability is addressed in Sec. 3.4, with particular focus on the destabilisation of inviscid neutral 2-D waves under pseudo-boiling conditions. Finally, Sec. 3.5 is dedicated to the study of stratified plane Couette flow, where the generation of disturbance vorticity is analysed and a comprehensive interpretation of the resulting instability is proposed. A summary and discussion of the results conclude this chapter in Sec. 3.6.

3.2 Methodology

The modal stability analysis is performed within the framework of LST. Thus, the flow field $\mathbf{q} = [p, u, v, w, T]^{\mathrm{T}}$ (differently from the conservative state vector in Eq. 2.2) is initially decomposed into a steady laminar part $\bar{\mathbf{q}}$, obtained from the boundary-layer equations in Sec. 2.4, and a fluctuating component $\mathbf{q}'$, infinitesimally small compared to $\bar{\mathbf{q}}$. This decomposition results in

$$\mathbf{q}(x, y, z, t) = \bar{\mathbf{q}}(y) + \epsilon \mathbf{q}'(x, y, z, t), \tag{3.1}$$

where $\epsilon \ll 1$. The base flow is assumed to be one-dimensional (1-D) and locally parallel in the streamwise direction. The fluctuating thermodynamic and transport properties (e.g. ρ', μ', κ') are determined as functions of the two independent thermodynamic properties p and T. For instance, the viscosity perturbation μ' is expressed as a first-order Taylor series in terms of the base-flow properties:

$$\mu' = \left.\frac{\partial \bar{\mu}}{\partial \bar{p}}\right|_{\bar{T}} p' + \left.\frac{\partial \bar{\mu}}{\partial \bar{T}}\right|_{\bar{p}} T'. \tag{3.2}$$

In the following, partial derivatives of a quantity with respect to $\bar{p}$ at constant $\bar{T}$ will be denoted as $\partial/\partial\bar{p}|_{\bar{T}} \equiv \partial/\partial\bar{p}$, and vice versa for $\partial/\partial\bar{T}\big|_{\bar{p}} \equiv \partial/\partial\bar{T}$. Mean-flow gradients of thermodynamic properties, e.g. $\partial\bar{p}/\partial\bar{T}$, are obtained either analytically or numerically, depending on

the equation of state and transport properties used (see Secs. 2.2 and 2.3). The perturbation $\mathbf{q}'$ is assumed to depend solely on the wall-normal direction and to be periodic in all other directions. Therefore, $\mathbf{q}'$ is written in the form of normal modes

$$\mathbf{q}'(x,y,z,t) = \hat{\mathbf{q}}(y)\exp[\mathrm{i}(\alpha x + \beta z - \omega t)] + \text{c.c.}, \tag{3.3}$$

where $\hat{\mathbf{q}}(y)$ is the perturbation eigenfunction, α is the non-dimensional streamwise wavenumber, $\beta \equiv \beta_r$ is the real spanwise wavenumber, $\omega \equiv \omega_r$ is the real angular frequency, and c.c. stands for the complex conjugate. In this work, the spatial problem is considered by prescribing β_r and ω_r. The streamwise wavenumber in Eq. (3.3) is set to be complex ($\alpha = \alpha_r + \mathrm{i}\alpha_i$), where α_i represents the local spatial growth rate. Hence, modal amplification occurs for $\alpha_i < 0$. Moreover, the wavenumber vector $\mathbf{k}$ is complex, with magnitude $\|\mathbf{k}\| = \sqrt{\alpha^2 + \beta_r^2}$, and the wave angle is $\Psi = \tan^{-1}(\beta_r/\alpha)$. The wavenumbers and the real angular frequency are non-dimensionalised by the local Blasius length scale (see Eqs. (2.47*a*,*b*)) and by δ^*/u^*_∞. Thus, the relation between ω and Re is a function of the non-dimensional frequency parameter F, as

$$F = \frac{2\pi f^* \mu^*_\infty}{\rho^*_\infty u^{*2}_\infty} = \frac{\omega^* \nu^*_\infty}{u^{*2}_\infty}, \quad F = \frac{\omega}{Re}, \tag{3.4a,b}$$

where f^* is the dimensional frequency in Hz and $\nu^*_\infty/u^{*2}_\infty$ is the viscous length scale.

3.2.1 Viscous instability

In the following, we focus on viscous analysis. According to LST, Eq. (3.1) is substituted into Eq. (2.1), and nonlinear terms of order $O(\epsilon^2)$ are neglected. In addition, buoyancy is ignored. Subsequently, after subtracting the steady base flow, the linearised stability equations can be expressed in a compact matrix form as follows:

$$\begin{aligned}
&\mathbf{L_t}\frac{\partial \mathbf{q}'}{\partial t} + \mathbf{L_x}\frac{\partial \mathbf{q}'}{\partial x} + \mathbf{L_y}\frac{\partial \mathbf{q}'}{\partial y} + \mathbf{L_z}\frac{\partial \mathbf{q}'}{\partial z} + \mathbf{L_{q'}}\,\mathbf{q}' \\
&+\mathbf{V_{xx}}\frac{\partial^2 \mathbf{q}'}{\partial x^2} + \mathbf{V_{yy}}\frac{\partial^2 \mathbf{q}'}{\partial y^2} + \mathbf{V_{zz}}\frac{\partial^2 \mathbf{q}'}{\partial z^2} \\
&+\mathbf{V_{xy}}\frac{\partial^2 \mathbf{q}'}{\partial x \partial y} + \mathbf{V_{xz}}\frac{\partial^2 \mathbf{q}'}{\partial x \partial z} + \mathbf{V_{yz}}\frac{\partial^2 \mathbf{q}'}{\partial y \partial z} = 0.
\end{aligned} \tag{3.5}$$

Here, $\mathbf{q}' = [p', u', v', w', T']^{\mathrm{T}}$ is the perturbation vector, and matrices $\mathbf{L_t}$, $\mathbf{L_x}$, $\mathbf{L_y}$, $\mathbf{L_z}$, $\mathbf{L_{q'}}$, $\mathbf{V_{xx}}$, $\mathbf{V_{yy}}$, $\mathbf{V_{zz}}$, $\mathbf{V_{xy}}$, $\mathbf{V_{xz}}$, and $\mathbf{V_{yz}}$ are functions of the base-flow properties and dimensionless parameters in Eqs. (2.46*a*–*c*). The expressions for these matrices are reported in Appendix A.4. The use of pressure, instead of density, is motivated by the low Mach numbers used in this work. When M_∞ approaches zero, the density perturbation ρ' is effectively decoupled from the pressure perturbation p', as the latter is only of hydrodynamic nature rather than of acoustic origin (Nemati *et al.* 2015). Consequently, we choose p' and T' as the two independent variables, as in Eq. (3.2). After substituting the normal mode ansatz in Eq. (3.3) into Eq. (3.5), the linearised stability equations can be recast as

$$\mathbf{R}\hat{\mathbf{q}} + \mathbf{S}\frac{\mathrm{d}\hat{\mathbf{q}}}{\mathrm{d}y} + \mathbf{T}\frac{\mathrm{d}^2\hat{\mathbf{q}}}{\mathrm{d}y^2} = \alpha\left(\mathbf{M}\hat{\mathbf{q}} + \mathbf{N}\frac{\mathrm{d}\hat{\mathbf{q}}}{\mathrm{d}y}\right) + \alpha^2\mathbf{P}\hat{\mathbf{q}}, \tag{3.6}$$

where

$$\left.\begin{aligned} \mathbf{R} &= -\mathrm{i}\omega\mathbf{L_t} + \mathrm{i}\beta\mathbf{L_z} + \mathbf{L_{q'}} - \beta^2\mathbf{V_{zz}}, \\ \mathbf{S} &= \mathbf{L_y} + \mathrm{i}\beta\mathbf{V_{yz}}, \\ \mathbf{T} &= \mathbf{V_{yy}}, \\ \mathbf{M} &= -\mathrm{i}\mathbf{L_x} + \beta\mathbf{V_{xz}}, \\ \mathbf{N} &= -\mathrm{i}\mathbf{V_{xy}}, \\ \mathbf{P} &= \mathbf{V_{xx}}. \end{aligned}\right\} \tag{3.7}$$

A pseudo-spectral collocation method based on N Chebyshev collocation points, $\hat{y}_j = \cos(j\pi/N)$ with $j = 1, 2, ..., N.$, is employed. Thus, the partial derivatives with respect to the wall-normal direction y are replaced by the corresponding differentiation matrices $\mathbf{D}$ as:

$$\frac{\mathrm{d}\hat{\mathbf{q}}}{\mathrm{d}y} = \mathbf{D}\hat{\mathbf{q}}, \quad \frac{\mathrm{d}^2\hat{\mathbf{q}}}{\mathrm{d}y^2} = \mathbf{D}^2\hat{\mathbf{q}}. \tag{3.8a,b}$$

For the considered boundary-layer problem, near-wall grid clustering is applied in accordance with Schmid & Henningson (2001). One half of the grid points $\hat{y}_j$ are mapped onto the interval $[0, y_{mid}]$, whilst a wider grid spacing is preferred for the far-field region up to $y = y_{max}$. The transformation has the form

$$y = a\frac{1+\hat{y}}{b-\hat{y}}, \tag{3.9}$$

with parameters $a = y_{mid}\, y_{max}/(y_{max} - 2y_{mid})$ and $b = 1 + 2a/y_{max}$. The boundary conditions for $\hat{\mathbf{q}}$ are given as:

$$\left.\begin{aligned} \hat{u} = \hat{v} = \hat{w} = 0, \quad \text{at} \quad y = 0, \\ \hat{u} = \hat{v} = \hat{w} = \hat{T} = 0, \quad \text{at} \quad y = y_{max}. \end{aligned}\right\} \tag{3.10}$$

Although the pressure eigenfunction $\hat{p}$ is not prescribed at the wall, the temperature eigenfunction at the wall depends on the wall boundary condition of the base-flow solution in Eqs. (2.53a,b). Thus, the boundary condition for T' reads:

$$\left.\begin{aligned} T'(0) = 0, \quad \text{for } \bar{g}(0) = g_w \\ \frac{\mathrm{d}T'(0)}{\mathrm{d}y} = 0, \quad \text{for } \frac{\mathrm{d}\bar{g}(0)}{\mathrm{d}\eta} = 0. \end{aligned}\right\} \tag{3.11}$$

Finally, the non-linear system in Eq. (3.6) is written as

$$\mathbb{A}_0\hat{\mathbf{q}} = \alpha\mathbb{A}_\alpha\hat{\mathbf{q}} + \alpha^2\mathbb{A}_{\alpha^2}\hat{\mathbf{q}}, \tag{3.12}$$

where $\mathbb{A}_0$, $\mathbb{A}_\alpha$, $\mathbb{A}_{\alpha^2}$ are $5N \times 5N$ matrices, and $\hat{\mathbf{q}} = (\hat{\mathbf{q}}_1, \ldots, \hat{\mathbf{q}}_N)^{\mathrm{T}}$ is a $5N$-dimensional column vector containing all discretised perturbations. Equation (3.12) is a quadratic eigenvalue problem, which is recast as a linear eigenvalue problem (see Malik (1990)), as

$$\begin{bmatrix} \mathbb{A}_0 & \mathbf{0} \\ \mathbf{0} & \mathbf{I} \end{bmatrix}\begin{bmatrix} \hat{\mathbf{q}} \\ \alpha\hat{\mathbf{q}} \end{bmatrix} = \alpha\begin{bmatrix} \mathbb{A}_\alpha & \mathbb{A}_{\alpha^2} \\ \mathbf{I} & \mathbf{0} \end{bmatrix}\begin{bmatrix} \hat{\mathbf{q}} \\ \alpha\hat{\mathbf{q}} \end{bmatrix}, \tag{3.13}$$

where $\mathbf{I}$ is the identity matrix. In this procedure, the size of the state vector (and hence the size of the system) is increased. The eigenvalue problem is solved using the LAPACK implementation of the QZ algorithm (also called the generalised Schur decomposition).

3.2.2 Inviscid instability

We consider 3-D perturbations as in Eq. (3.3) in the limit of infinite Reynolds number ($Re \to \infty$). Lees & Lin (1946) showed that if the inviscid solutions are regarded as the infinite Reynolds number limit of viscous solutions, a consistent inviscid theory can be constructed (Mack 1984). In supersonic boundary layers, inviscid stability analysis of a viscous base flow has been abundantly used in the literature, as Mack modes originate from an inviscid mechanism. For instance, the work of Tunney *et al.* (2015), who investigated the self-similar compressible boundary layers with a velocity overshoot, provided a successful comparison between viscous and inviscid stability analyses. Given the inviscid nature of Mode II (Ren *et al.* 2019*b*), it is relevant to extend the analysis to the inviscid regime. Thus, the linearised stability equations in Eq. (3.5) can be simplified to:

$$\mathbf{L_t}\frac{\partial \mathbf{q}'}{\partial t} + \mathbf{L_x}\frac{\partial \mathbf{q}'}{\partial x} + \mathbf{L_y}\frac{\partial \mathbf{q}'}{\partial y} + \mathbf{L_z}\frac{\partial \mathbf{q}'}{\partial z} + \mathbf{L_{q'}}\,\mathbf{q}' = 0. \tag{3.14}$$

By inserting Eq. (3.3) into Eq. (3.14) and introducing the relative Mach number M_r for non-ideal fluid flows as

$$M_r = \frac{(\alpha\bar{u} - \omega)}{(\alpha^2 + \beta_r^2)^{1/2}\,\bar{a}} = \frac{\bar{u}\cos(\Psi) - c}{\bar{a}}, \tag{3.15}$$

where $\bar{a}$ is the base-flow speed of sound and $c = \omega/\|\mathbf{k}\| = \omega/(\alpha^2 + \beta_r^2)^{1/2}$ is the complex phase velocity, we obtain the coupled system

$$\left.\begin{aligned} \hat{v}_y &= \frac{\alpha\bar{u}_y}{\alpha\bar{u} - \omega}\hat{v} + \frac{\mathrm{i}\,(\alpha^2 + \beta_r^2)}{\bar{\rho}\,(\alpha\bar{u} - \omega)}\,(1 - M_r^2)\,\hat{p}, \\ \hat{p}_y &= -\bar{\rho}\mathrm{i}\,(\alpha\bar{u} - \omega)\,\hat{v}, \end{aligned}\right\} \tag{3.16}$$

where $\hat{v}$ and $\hat{p}$ are the wall-normal velocity and pressure perturbation eigenfunctions, respectively. For simplicity, all first- and second-order derivatives in the wall-normal direction, $\mathrm{d}(\cdot)/\mathrm{d}y$ and $\mathrm{d}^2(\cdot)/\mathrm{d}y^2$, are hereafter denoted as $(\cdot)_y$ and $(\cdot)_{yy}$, respectively. The system in Eq. (3.16) can be written as a single second-order equation for $\hat{p}$:

$$\hat{p}_{yy} - \left(\frac{2\alpha\bar{u}_y}{\alpha\bar{u} - \omega} + \frac{\bar{\rho}_y}{\bar{\rho}}\right)\hat{p}_y - \left(\alpha^2 + \beta_r^2\right)\left(1 - M_r^2\right)\hat{p} = 0, \tag{3.17}$$

or for $\hat{v}$:

$$\left(\alpha^2 + \beta_r^2 + \theta\right)\hat{v} - \xi\hat{v}_y - \eta\hat{v}_{yy} = 0, \tag{3.18}$$

where the functions θ, ξ, and η are equal to:

$$\left.\begin{aligned} \theta &= \frac{\alpha\left(\bar{\rho}\bar{u}_y\right)_y}{\bar{\rho}\,(1 - M_r^2)\,(\alpha\bar{u} - \omega)} + \frac{2\alpha M_r M_{r,y}\bar{u}_y}{(\alpha\bar{u} - \omega)\,(1 - M_r^2)^2}, \\ \xi &= \frac{\bar{\rho}_y}{\bar{\rho}\,(1 - M_r^2)} + \frac{2M_r M_{r,y}}{(1 - M_r^2)^2}, \\ \eta &= \frac{1}{1 - M_r^2}. \end{aligned}\right\} \tag{3.19}$$

The inviscid stability equations in Eq. (3.17) and Eq. (3.18) can also be referred to as the compressible counterpart of the Rayleigh equation for non-ideal fluid flows. To close the equations, the following inviscid boundary conditions are prescribed:

$$\left.\begin{aligned} \hat{p}_y = \hat{v} = 0, \quad \text{at } y = 0, \\ \hat{p} \to 0, \quad \text{and} \quad \hat{v} \to 0, \quad \text{at } y \to \infty. \end{aligned}\right\} \tag{3.20}$$

As explained in Mack (1984), Eqs. (3.17) and (3.18) change their nature from elliptic to hyperbolic when M_r^2 becomes greater than unity, and multiple solutions are present. Ren *et al.* (2019*b*) demonstrated that M_r^2 is always below unity in the transcritical state (pseudo-boiling conditions), ruling out an acoustic origin of the transcritical Mode II. Moreover, since Eq. (3.18) is singular at the critical layer, i.e. $y = y_{cr}$, where $\bar{u} = c$ (not to be confused with the thermodynamic critical point), the term

$$\frac{\mathrm{d}}{\mathrm{d}y}\left(\bar{\rho}\frac{\mathrm{d}\bar{u}}{\mathrm{d}y}\right) \tag{3.21}$$

must vanish at $y = y_s$ (inflection point) such that $y = y_c$ is a regular singular point (Ren *et al.* 2019*b*). If there is a point in the boundary layer at $y = y_s$ where the term in Eq. (3.21) vanishes, then the base flow possesses a GIP. The condition $\left(\bar{\rho}\bar{u}_y\right)_y = 0$ corresponds to the GIP criterion for non-ideal fluid flows, consistent with the original formulation of the GIP criterion, $\left(\bar{u}_y/\bar{T}\right)_y$, proposed by Lees & Lin (1946) under the ideal-gas assumption. In the context of inviscid stability, Eq. (3.21) represents the generalisation of Rayleigh's condition for incompressible flows, i.e. $\bar{u}_{yy} = 0$ (Rayleigh 1880). For a subsonic perturbation, that is $M_r^2 < 1$, Lees & Lin (1946) showed that the existence of a GIP is a sufficient and necessary condition for the presence of an inviscid neutral instability at $y_s > y_o$, where y_o is the point at which $\bar{u} = 1 - 1/M_\infty$. The phase velocity of this neutral wave is $c = \bar{u}_s = \bar{u}(y_s)$.

Assuming now the inviscid disturbance state vector as $\hat{\mathbf{q}}_{\mathbf{inv.}} = [\hat{p}, \hat{v}]^{\mathrm{T}}$, the system in Eq. (3.16) can be solved in two different ways. First, Eq. (3.16) is written in a compact matrix form, similarly to the viscous instability problem in Eq. (3.6). Hence, the new form reads

$$\mathbf{R}_{\mathbf{inv.}}\hat{\mathbf{q}}_{\mathbf{inv.}} + \mathbf{S}_{\mathbf{inv.}}\frac{\partial\hat{\mathbf{q}}_{\mathbf{inv.}}}{\partial y} = \alpha\left(\mathbf{M}_{\mathbf{inv.}}\hat{\mathbf{q}}_{\mathbf{inv.}} + \mathbf{N}_{\mathbf{inv.}}\frac{\partial\hat{\mathbf{q}}_{\mathbf{inv.}}}{\partial y}\right) + \alpha^2\mathbf{P}_{\mathbf{inv.}}\hat{\mathbf{q}}_{\mathbf{inv.}}, \tag{3.22}$$

where matrices $\mathbf{R}_{\mathbf{inv.}}$, $\mathbf{S}_{\mathbf{inv.}}$, $\mathbf{M}_{\mathbf{inv.}}$, $\mathbf{N}_{\mathbf{inv.}}$, and $\mathbf{P}_{\mathbf{inv.}}$ are functions of the base-flow properties and stability parameters. The expressions for these matrices can be found in Appendix A.4. The final discretised nonlinear system is similar to Eq. (3.12) and is solved with boundary conditions in Eq. (3.20) using the LAPACK implementation of the QZ algorithm. The advantage of this formulation is the numerical avoidance of resolving the critical layer, i.e. $y = y_{cr}$. At this location, the inviscid system becomes singular for neutral disturbances, i.e. $\mathfrak{I}(c) = 0$, where c is the complex phase speed (see Eq. 3.15). Conversely, the second procedure to solve Eq. (3.16) avoids the singularity at the critical layer by considering only unstable perturbations, i.e. $\mathfrak{I}(c) > 0$, and integrates the first-order system given as

$$\frac{\mathrm{d}\hat{\mathbf{q}}_{\mathbf{inv.}}}{\mathrm{d}y} = \mathbf{A}_{\mathbf{inv.}}\hat{\mathbf{q}}_{\mathbf{inv.}}, \tag{3.23}$$

Fluid	EoS	T^*_∞ (K)	T^*_∞/T^*_{pc}	Ec_∞	Case	Pr_∞	M_∞	T^*_w/T^*_{pc}
CO_2 at $p^*_\infty = 80\,\text{bar}$	MPEoS (Sec. 2.2.4)	280	0.910	0.05	T280Ec005	2.133	0.329	0.942
				0.10	T280Ec010		0.465	0.972
				0.15	T280Ec015		0.570	0.997
				0.20	T280Ec020		0.658	1.013

Table 3.1: Base-flow parameters of the validation cases at a supercritical pressure of $p^*_\infty = 80\,\text{bar}$. All cases assume an adiabatic wall with temperature T^*_w. The transcritical case, highlighted in red, features $T^*_w/T^*_{pc} > 1$, indicating a temperature profile crossing the Widom line. The pseudo-critical temperature T^*_{pc} for CO_2 at $p^*_\infty = 80\,\text{bar}$ is $T^*_{pc} = 307.7\,\text{K}$.

along the wall-normal direction y (real axis) using a 4th-order Runge–Kutta scheme, analogously to the solution of the boundary-layer equations in Sec. 2.4, from the free stream to the wall (Tunney *et al.* 2015). Matrix $\mathbf{A_{inv}}$ is a function of the base-flow properties and stability parameters and is reported in Appendix A.4. In the free stream, i.e. $y \to \infty$, the initial condition for $\hat{\mathbf{q}}_{\mathbf{inv}.}$ is approximated by:

$$\left.\begin{aligned} \hat{p}_{inv.} &\sim \exp\left(-y\sqrt{(\alpha^2+\beta_r^2)(1-M_r^2)}\right), \\ \hat{v}_{inv.} &\sim \frac{-\mathrm{i}\sqrt{(\alpha^2+\beta_r^2)(1-M_r^2)}}{\alpha-\omega}\hat{p}. \end{aligned}\right\} \tag{3.24}$$

At the wall, $y = 0$, the Newton–Raphson iteration method is employed for the local eigenvalue search in accordance with the boundary conditions in Eq. (3.20). For the initial value of α, the corresponding viscous solution according to Eq. (3.12) is first calculated.

3.2.3 Validation

To validate the boundary-layer and stability solvers employed in this study, and to introduce the relevant terminology, we briefly compare base-flow and stability results for selected adiabatic cases previously examined in detail by Ren *et al.* (2019*b*). The flow conditions correspond to CO_2 at a supercritical pressure of $p^*_\infty = 80\,\text{bar}$ and are summarised in Tab. 3.1. In the first three cases, the base-flow temperature remains in the subcritical state ($T^*/T^*_{pc} < 1$), resulting in only weakly non-ideal gas effects. In contrast, case 'T280Ec020' exhibits a transcritical temperature profile crossing the Widom line, with vapour-like behaviour near the wall ($T^*_w/T^*_{pc} > 1$).

Laminar base flow

The laminar base-flow profiles of the four cases listed in Tab. 3.1 are shown in Fig. 3.2. Temperature, streamwise velocity, density, and dynamic viscosity are plotted as functions of the self-similar wall-normal coordinate $\mathrm{d}\eta = (\rho^* u^*_\infty/\sqrt{2\xi})\,\mathrm{d}y^*$, as defined in Sec. 2.4. Below the pseudo-critical temperature $T^*_{pc} = 307.7\,\text{K}$, the boundary layer with supercritical CO_2 exhibits liquid-like behaviour; above it, the flow becomes vapour-like. As viscous dissipation increases

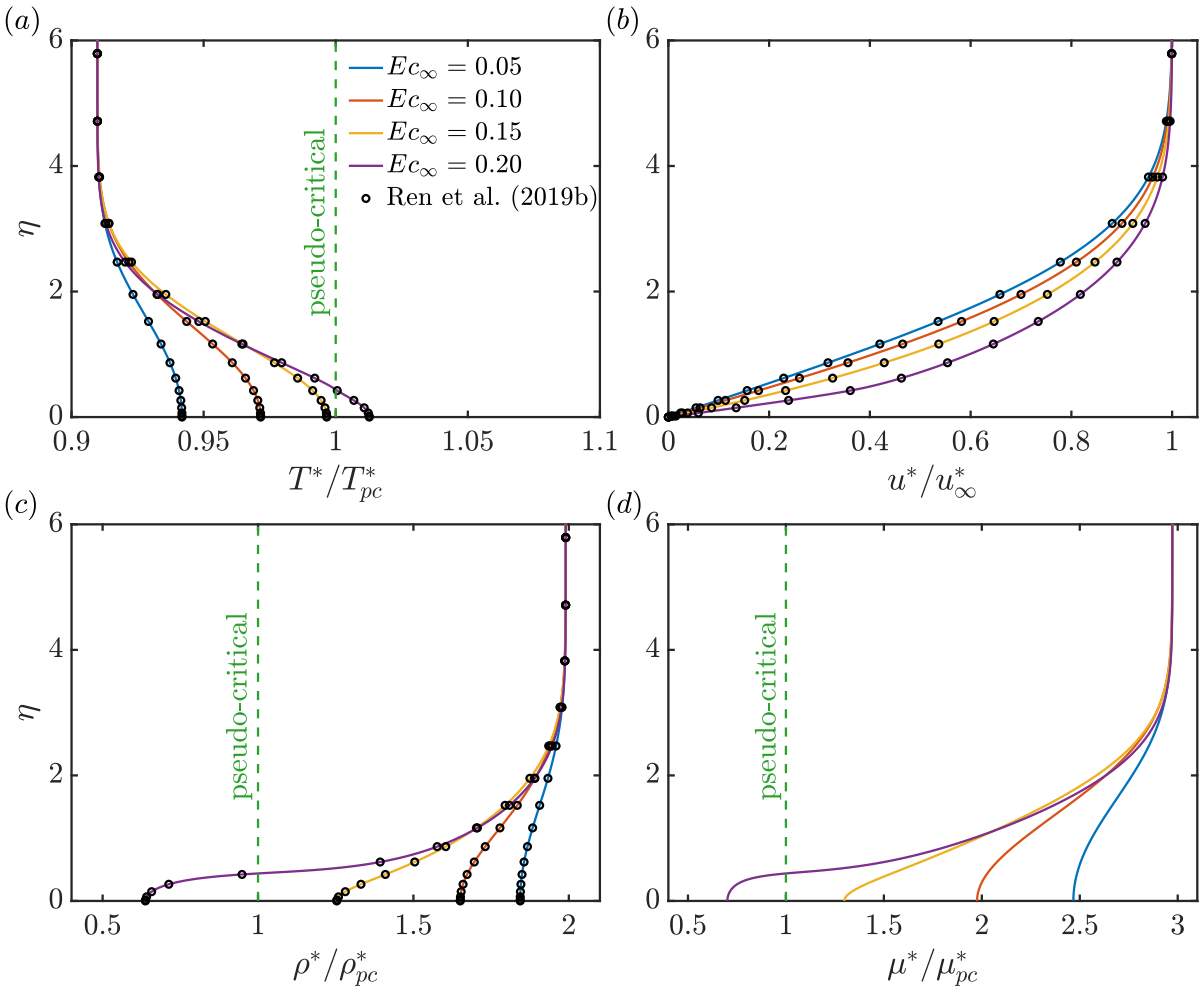

Figure 3.2: Base-flow profiles of the 'T280' adiabatic case (Ren *et al.* 2019*b*) at four different Eckert numbers: (a) temperature T^*/T^*_{pc}, (b) streamwise velocity u^*/u^*_∞, (c) density ρ^*/ρ^*_{pc}, and (d) dynamic viscosity μ^*/μ^*_{pc} plotted against the self-similar wall-normal coordinate η. The green dashed line (– –) marks the pseudo-critical point, with pseudo-critical temperature $T^* = T^*_{pc}$. All profiles are computed with at least 20 000 wall-normal points.

with the Eckert number, the wall temperature rises, and the temperature profile in Fig. 3.2(a) may cross the pseudo-critical point, marking a transcritical-temperature configuration. This continuous phase transition generates pronounced stratification in density (Fig. 3.2c) and viscosity (Fig. 3.2d) close to the wall, with steep gradients in thermodynamic and transport properties near the Widom line. Unlike ideal gas, viscosity decreases with increasing temperature in the subcritical-temperature region, while in the supercritical-temperature region it only increases far from the pseudo-critical point. Another non-ideal effect is visible in the velocity profiles (Fig. 3.2b): as the Eckert number increases, the near-wall velocity profile becomes fuller and the boundary-layer thickness decreases. Overall, the results obtained with the in-house boundary-layer solver show very good agreement with those reported by Ren *et al.* (2019*b*).

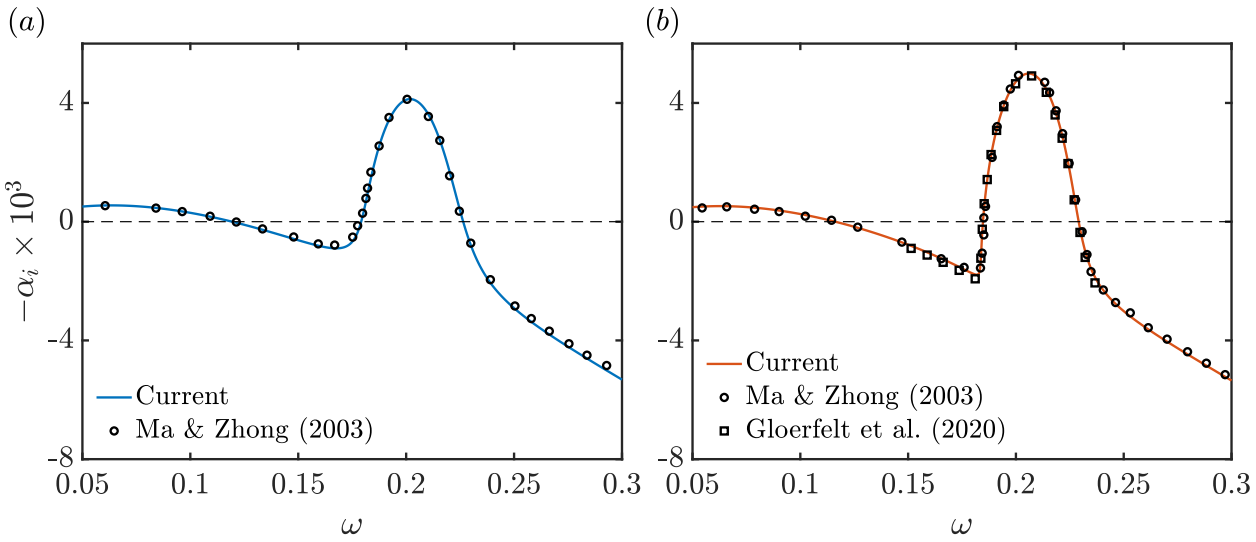

Figure 3.3: Evolution of the growth rate $-\alpha_i$ versus the dimensionless circular frequency ω under the ideal-gas assumption: (a) $T'_w = 0$ (isothermal wall), (b) $\mathrm{d}T'/\mathrm{d}y|_w = 0$ (adiabatic). Solid lines denote the in-house solver; black circle (∘) and square (□) symbols denote the results of Ma & Zhong (2003) and Gloerfelt *et al.* (2020), respectively.

Viscous stability analysis

To verify the in-house linear stability solver, we first compare its results with those of Ma & Zhong (2003) and Gloerfelt *et al.* (2020) for an ideal gas, and with those of Ren *et al.* (2019*b*) for a fluid at supercritical pressure. In the ideal-gas cases, the free-stream Mach number is 4.5, the Prandtl number is 0.72, the free-stream temperature is 65.15 K, the wall is adiabatic, and LST is performed at a Reynolds number of $Re = 2000$. Figure 3.3 shows excellent agreement in growth rates under two wall boundary conditions: $T'_w = 0$ (isotherm) in Fig. 3.3(a), and $\mathrm{d}T'/\mathrm{d}y|_w = 0$ (adiabatic) in Fig. 3.3(b).

For the second validation, we consider the transcritical case 'T280Ec020'. For brevity, the subcritical cases in Tab. 3.1 are not shown. Figure 3.4(a) displays the spatial eigenvalue spectrum at $Re = 1500$ and $F = 45 \times 10^{-6}$, revealing the co-existence of the two unstable modes characteristic of the transcritical state (Modes I and II), in agreement with the results of Ren *et al.* (2019*b*) (black circle (∘) symbols). While such dual-mode instability is known in viscosity-stratified channel flows (Govindarajan & Sahu 2014), it was not reported in boundary-layer flows prior to the study of Ren *et al.* (2019*b*). Figures 3.4(b,c) present the eigenfunctions of Modes I and II, compared with those of Ren *et al.* (2019*b*). All amplitudes are normalised by $\max\{|\hat{u}|\}$ and plotted against the self-similar wall-normal coordinate η, scaled by the boundary-layer thickness δ_{99}. Both modes are shown near their maximum amplification location in the stability diagram: Mode I at $Re \approx 1265$ and Mode II at $Re \approx 1895$ (each at $F = 75{\times}10^{-6}$). In both cases, density fluctuations peak near the Widom line, although amplitudes are significantly higher for Mode II. The remaining perturbations exhibit similar shapes for the two modes. Notably, the critical layer η_{cr} for Mode II lies below the pseudo-critical point η_{pc} due to its lower phase speed ($c_r \approx 0.30 - 0.35$) compared with Mode I

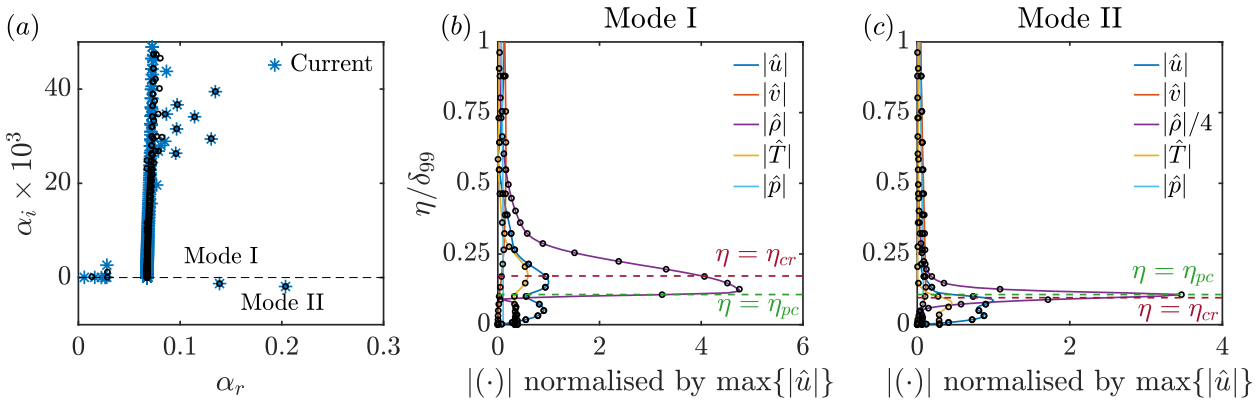

Figure 3.4: Transcritical case 'T280Ec020': (a) eigenvalue spectrum at $Re = 1500$ and $F = 45 \times 10^{-6}$ (Modes I and II visible), (b,c) wall-normal eigenfunctions of u', v', T', ρ', and p' normalised by $\max\{|\hat{u}|\}$. Mode I is shown at $Re \approx 1265, F = 75 \times 10^{-6}$ in panel (b); Mode II at $Re \approx 1895, F = 75 \times 10^{-6}$ in panel (c). Black circle ($\circ$) symbols indicate the results of Ren *et al.* (2019*b*). In (b,c), the critical layer and pseudo-critical point are denoted by η_{cr} and η_{pc}, respectively.

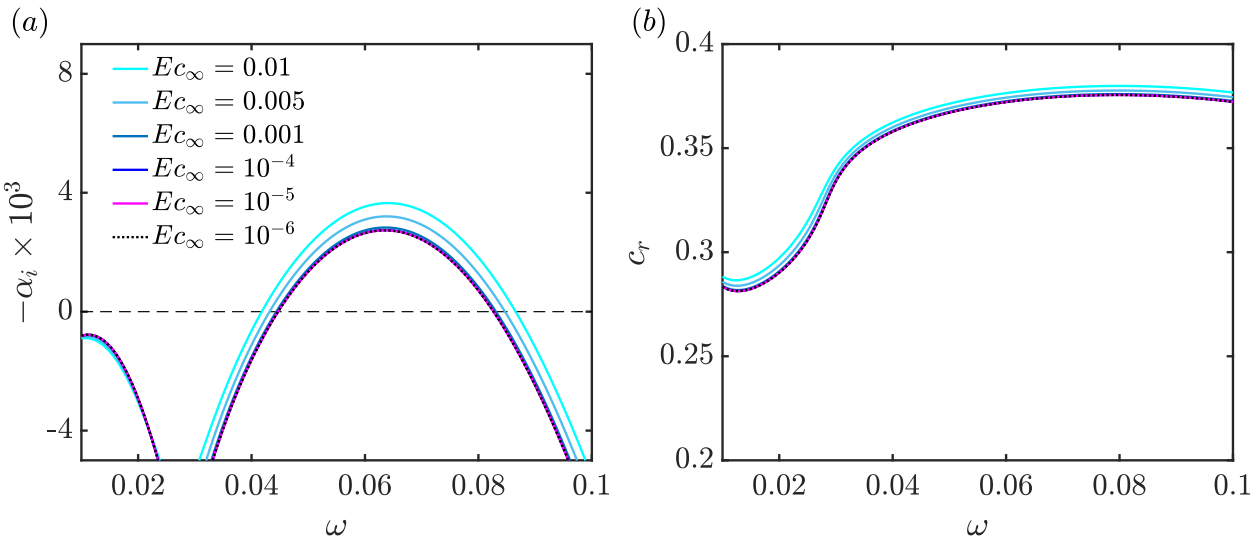

Figure 3.5: Influence of the free-stream Eckert number at $Re = 1500$ for the transcritical case 'T280Ec020' with an isothermal wall ($T_w^*/T_\infty^* = 1.113$): (a) growth rate $-\alpha_i$ and (b) real phase speed c_r as functions of the dimensionless frequency ω.

($c_r \approx 0.40$–0.50), which shifts the critical layer closer to the wall (Fig. 3.4c).

To further assess linear stability under isothermal wall conditions in the zero-Eckert limit (see Sec. 3.3), we validate the in-house stability solver using the transcritical case 'T280Ec020' from Fig. 3.2, imposing a fixed wall-to-free-stream temperature ratio of $T_w^*/T_\infty^* = 1.113$. To minimise compressibility effects, the free-stream Eckert number Ec_∞ is progressively reduced towards zero. Note that, under isothermal wall conditions, the wall temperature perturbation satisfies $T_w' = 0$ (Ma & Zhong 2003). Figure 3.5 shows the resulting evolution of the growth rate $-\alpha_i$ and the real part of the phase speed c_r as functions of the dimensionless frequency ω. Starting from $Ec_\infty = 0.2$, the growth rate of the unstable Mode II, whose maximum is

Fluid	EoS	T^*_∞/T^*_{pc}	T^*_w/T^*_{pc}	Case	Pr_∞
CO_2 at $p^*_\infty = 80\,\text{bar}$	MPEoS (Sec. 2.2.4)	0.90	0.85	T09w085	2.11
			0.90	T09w090	
			0.95	T09w095	
			1.05	T09w105	
		1.10	1.20	T11w120	1.22
			1.10	T11w110	
			1.05	T11w105	
			0.95	T11w095	

Table 3.2: Base-flow parameters of the investigated isothermal cases at a supercritical pressure of $p^*_\infty = 80\,\text{bar}$. All cases assume an isothermal wall, with T^*_w as the wall temperature, and are in the zero-Eckert limit. The transcritical cases, highlighted in red, feature either $T^*_w/T^*_{pc} > 1$ for $T^*_\infty/T^*_{pc} < 1$ or $T^*_w/T^*_{pc} < 1$ for $T^*_\infty/T^*_{pc} > 1$, indicating temperature profiles that cross the Widom line. The pseudo-critical temperature for CO_2 at $p^*_\infty = 80\,\text{bar}$ is $T^*_{pc} = 307.7\,\text{K}$.

$\max\{-\alpha_i \times 10^3\} \approx 5$, decreases gradually as the Eckert number is reduced, reaching $\max\{-\alpha_i \times 10^3\} \approx 2.7$ in the limit $Ec_\infty \to 0$. The trends in Figs. 3.5(a,b) demonstrate good convergence of the in-house stability solver as compressibility effects vanish.

3.3 Isothermal boundary layers

In this section, we investigate the linear stability of isothermal boundary-layer flows at supercritical pressure in the limit of zero Eckert number. By employing the new isothermal boundary condition in Eqs. (2.53*a*,*b*), the parameter space can be extended to cover a broader range of non-ideal flow conditions. In addition to assessing the non-ideal gas effects by varying T^*_∞ and compressibility effects by varying Ec_∞, we also consider variations in wall temperature T^*_w. This enables a systematic analysis of the influence of wall cooling and heating on the stability of supercritical boundary layers across different thermodynamic states. Furthermore, as the Eckert number approaches zero, corresponding to a vanishing Mach number, the physical complexity is reduced by eliminating acoustic effects from the stability problem, which were retained in the analysis of Ren *et al.* (2019*b*).

We examine two distinct free-stream conditions: one in the liquid-like state ($T^*_\infty < T^*_{pc}$), hereafter 'T09', and one in the vapour-like state ($T^*_\infty > T^*_{pc}$), hereafter 'T11'. The degree of wall heating or cooling is controlled through the prescribed wall temperature. The supercritical pressure is fixed at $p^*_\infty = 80\,\text{bar}$, consistent with Ren *et al.* (2019*b*). An overview of the cases is given in Tab. 3.2. All cases remain either subcritical or supercritical with respect to temperature, except for the transcritical cases 'T09w105' (heating across the Widom line) and 'T11w095' (cooling across the Widom line), which exhibit the strongest non-ideal-gas effects.

The base-flow profiles for the liquid-like ('T09') and vapour-like ('T11') free-stream condition are shown in Fig. 3.6 and Fig. 3.7, respectively. Four different wall temperatures are selected for each free-stream condition as listed in Tab. 3.2. Cases 'T09w090' and 'T11w110' correspond to the incompressible Blasius profile. Both wall cooling and heating are examined for each free-stream condition, together with a transcritical case in which thermodynamic and transport properties develop large gradients near the Widom line. In the 'T09' cases (Fig. 3.6), the boundary-layer thickness δ_{99}, evaluated at $\bar{u}^*/u^*_\infty = 0.99$, decreases with increasing wall temperature. This trend mirrors the increase in Eckert number in the adiabatic profiles of Fig. 3.2. In contrast, the 'T11' cases (Fig. 3.7) exhibit markedly different behaviour. Wall cooling leads to an increase in density (Fig. 3.7c) and viscosity (Fig. 3.7d) near the wall, particularly in the transcritical case 'T11w095', where the temperature drops into the liquid-like state near the wall. As shown in Fig. 3.7(b), the velocity profile of 'T11w095' exhibits an Inflection Point (IP), indicated by a black star, which is absent in the transcritical case 'T09w105'. Because $\bar{u}_{yy} = 0$ occurs within the boundary layer, the classical inflection-point criterion of Rayleigh (1880) is satisfied, providing the necessary condition for an inviscid instability.

3.3.1 Viscous analysis

In the following, a viscous stability analysis of the isothermal base-flow profiles, as outlined in Sec. 3.2.1, is conducted. The primary objective is to identify the flow conditions that promote the appearance of Mode II and to extend the adiabatic results of Ren *et al.* (2019*b*).

Figure 3.8 shows the growth rate $-\alpha_i$ in the Re–F stability diagram, where $Re = \sqrt{Re_x}$, for the 'T09' cases (liquid-like free stream). A comparison of Figs. 3.8(a–c) shows that, in the subcritical state ($T^*/T^*_{pc} < 1$), the flow becomes more stable as the wall temperature approaches the Widom line. This trend is consistent with the findings of Ren *et al.* (2019*b*), who reported increased stabilisation in the subcritical state as the Eckert number increases, given a fixed free-stream temperature. Conversely, wall cooling in the subcritical state leads to flow destabilisation. One and only one unstable mode is found in this state, the TS-wave, closely resembling the incompressible case in the absence of a temperature gradient. As the wall temperature is increased and the Widom line is crossed (Figs. 3.8d–f), the transcritical Mode II emerges alongside Mode I (the TS wave). At $T^*_w/T^*_{pc} = 1.02$ (Fig. 3.8d), Mode I is the only unstable mode for $Re < 2000$. Although this temperature ratio is comparable to that in Fig. 3.2, the present analysis is conducted in the zero-Eckert limit, meaning compressibility effects that would otherwise destabilise Mode II are absent. With further wall heating, dual-mode behaviour becomes evident: the critical Reynolds number Re_{crit} for the onset of Mode II decreases significantly, and its growth rate becomes larger. Consequently, even small changes in wall temperature induce abrupt shifts in the linear stability characteristics of Mode II. At $T^*_w/T^*_{pc} = 1.03$, the growth rate of Mode II is already three times higher than that of Mode I. In Fig. 3.8(f), both modes are simultaneously unstable at the same values of Re and F. Notably, as the wall temperature increases further into the transcritical state, Mode II expands across a broader frequency range, while Mode I experiences only minor

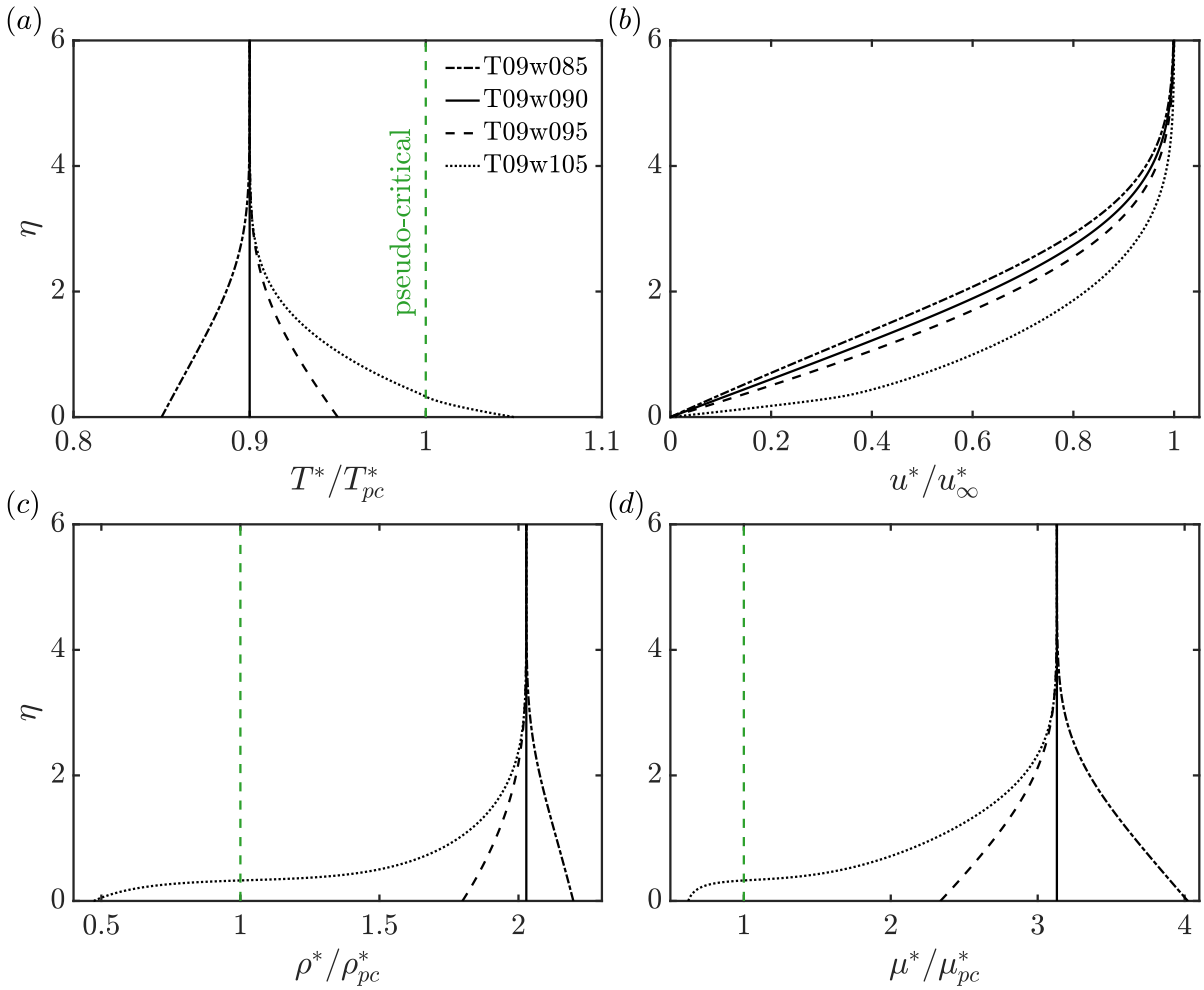

Figure 3.6: Base-flow profiles of the 'T09' zero-Eckert cases at four wall temperatures: (a) temperature T^*/T^*_{pc}, (b) streamwise velocity u^*/u^*_∞, (c) density ρ^*/ρ^*_{pc}, and (d) dynamic viscosity μ^*/μ^*_{pc} plotted against η. The green dashed line (– –) denotes the pseudo-critical point, i.e. at the pseudo-critical temperature $T^* = T^*_{pc}$. All profiles are computed with at least 20 000 wall-normal points.

changes: a slight increase in growth rate and a monotonic reduction in its critical Reynolds number. These results demonstrate that the two co-existing modes persist even in the zero-Eckert-number limit, confirming that Mode II is not linked to acoustic effects. Furthermore, as shown by Bugeat *et al.* (2022), Mode II also appears under transcritical conditions when using the cubic Van der Waals (VdW) Equation of State (EoS) (Sec. 2.2.2) together with analytical diffusion laws (Sec. 2.3.2). This highlights the robustness of the transcritical Mode II and suggests that such simplified thermodynamic models still capture the essential physical mechanism responsible for its growth, providing a useful framework for a more fundamental analysis of the instability.

Turning to the real phase velocity ($c_r = \omega/\alpha_r$), we find that c_r within the neutral stability curves generally ranges between 0.2 and 0.6. In the transcritical state, Mode I exhibits higher phase velocities ($c_r \approx 0.4$ to 0.6) than Mode II ($c_r \approx 0.2$ to 0.3), consistent with the finite-Eckert results of Ren *et al.* (2019*b*). Further insight into the phase velocity at constant $Re =$

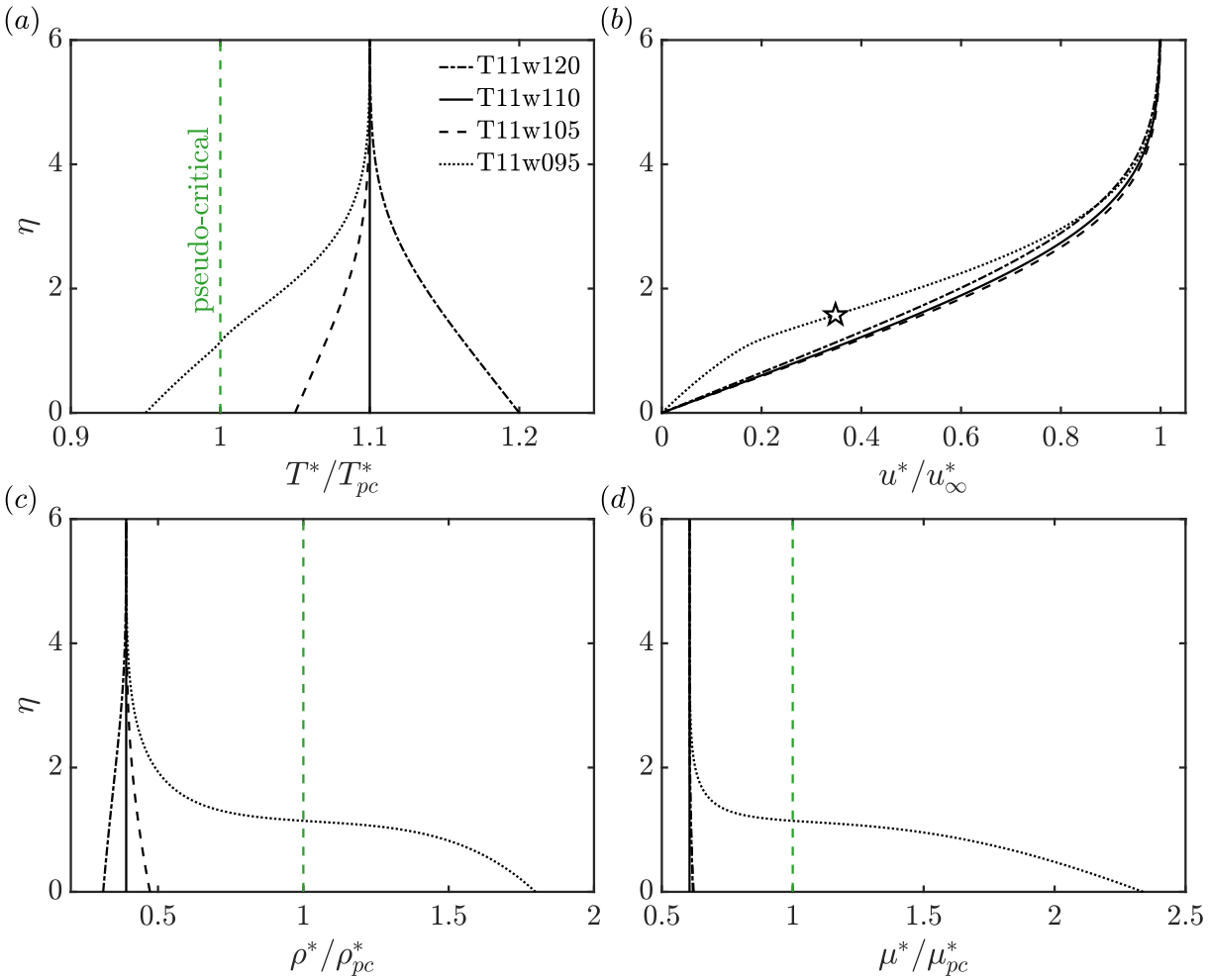

Figure 3.7: Base-flow profiles of the 'T11' zero-Eckert cases at four wall temperatures: (a) temperature T^*/T^*_{pc}, (b) streamwise velocity u^*/u^*_∞, (c) density ρ^*/ρ^*_{pc}, and (d) dynamic viscosity μ^*/μ^*_{pc} plotted against η. The green dashed line (– –) denotes the pseudo-critical point, i.e. at the pseudo-critical temperature $T^* = T^*_{pc}$. In (c), the IP is marked by a black star (⋆) symbol. All profiles are computed with at least 20 000 wall-normal points.

2000 is provided in Fig. 3.9. In Fig. 3.9(a), the evolution of c_r for Mode I is shown as a function of the dimensionless frequency ω, with black and red curves representing subcritical and transcritical cases, respectively. In Ren *et al.* (2019*b*), Mode I under transcritical conditions (at finite Eckert number) was hypothesised to be a continuation of the viscous mode present in the subcritical state, based on (i) the qualitative similarity of the neutral stability curves in the Re–F diagram and (ii) the close agreement in phase velocity. This interpretation is further demonstrated by Fig. 3.9(b), which shows that the phase velocity corresponding to the maximum growth rate evolves smoothly across the pseudo-critical point at $T^*_w/T^*_{pc} = 1$, with no signs of discontinuity. This continuous behaviour of c_r suggests that Mode I undergoes a gradual transformation rather than a sharp modal bifurcation as the flow is heated from subcritical to transcritical conditions (supercritical-state transition). Hence, Mode I remains fundamentally a viscous, shear-driven instability, even though non-ideal gas effects may subtly alter its modal behaviour. Figures 3.9(c,d) display the corresponding behaviour for Mode II.

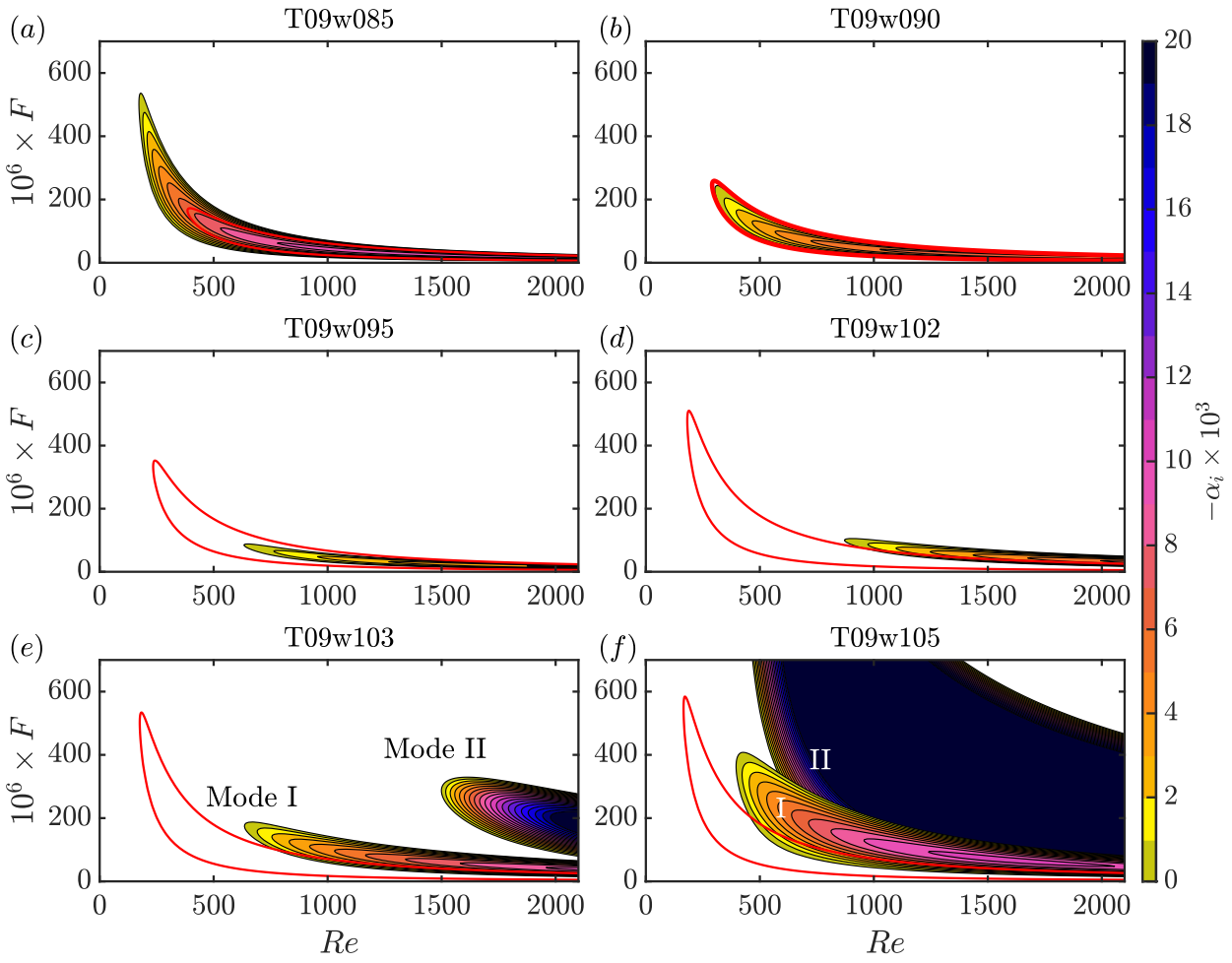

Figure 3.8: Growth-rate ($-\alpha_i$) contours in the Re–F stability diagram of 'T09' cases: (a) T09w085, (b) T09w090 (incompressible boundary layer), (c) T09w095, (d) T09w102 (transcritical case with $T_w^*/T_{pc}^* = 1.02$), (e) T09w103 (transcritical case with $T_w^*/T_{pc}^* = 1.03$), and (f) T09w105. In (e,f), Modes I and II are indicated. The red solid lines represent the ideal-gas neutral stability ($\alpha_i = 0$) at equal T_w^*/T_∞^* ratios.

Once this mode appears, below $Re_{crit} = 2000$, its phase velocity is initially lower than that of Mode I for the same T_w^*/T_{pc}^*, but increases steadily with rising wall temperature. Note that the maximum growth rate $-\alpha_{i,max}$ also increases abruptly. This concurrent rise suggests that Mode II is driven purely by non-ideal-gas effects, which become strongly pronounced in the transcritical state, and that it arises from an inviscid instability mechanism fundamentally distinct from that of Mode I.

We now examine the 'T11' cases, characterised by vapour-like free-stream conditions. The corresponding growth-rate contours are shown in Fig. 3.10. Similar to the trends in Fig. 3.8, stabilisation occurs as the wall temperature approaches the Widom line, provided it is not crossed. Wall heating in the vapour-like state (Fig. 3.10a) produces a destabilising effect, even in the zero-Eckert-number limit, in contrast to the behaviour under the ideal-gas assumption. The unstable mode in the supercritical-temperature state corresponds to the classical TS-wave. However, unlike the transcritical heating scenario displayed in

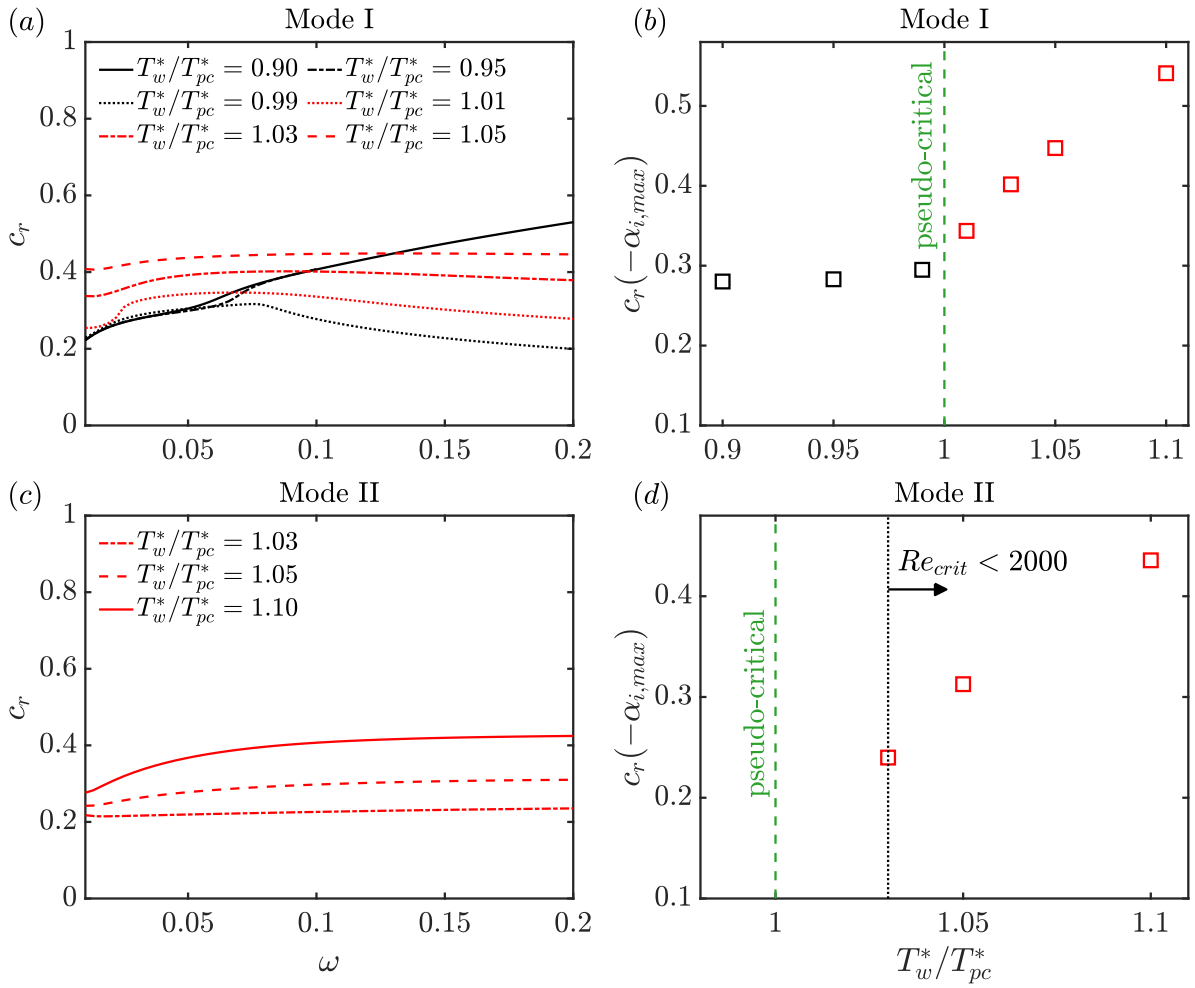

Figure 3.9: Real phase velocity c_r for the 'T09' cases at $Re = 2000$: evolution of (a) Mode I and (c) Mode II as a function of the dimensionless frequency ω; c_r corresponding to the maximum growth rate $(-\alpha_{i,max})$ of (b) Mode I and (d) Mode II, plotted against the reduced wall temperature T_w^*/T_{pc}^*. The green dashed line (– –) indicates the pseudo-critical temperature $T^* = T_{pc}^*$. The critical Reynolds number below which subcritical growth appears is denoted by Re_{crit}.

Figs. 3.10(d–f), only a single unstable mode is found when the supercritical-state transition occurs from vapour-like to liquid-like conditions. As discussed later in Sec. 3.3.3, this mode is inviscid in character and is Mode-II like. Thus, any supercritical-state transition leads to the appearance of a highly unstable inviscid mode. Its onset is abrupt: even at $T_w^*/T_{pc}^* = 0.98$, the critical Reynolds number drops sharply to $Re_{crit} \approx 400$. Further wall cooling amplifies the instability and extends the unstable region upstream towards lower Reynolds numbers. In this region, however, the base-flow solution may become inaccurate due to the classical singular behaviour of the wall-normal velocity at the flat-plate leading edge ($v \to \infty$ as $Re \to 0$). With additional wall cooling, the maximum growth rate in the Re–F stability diagram shifts towards lower Reynolds numbers (see Figs. 3.10e,f), suggesting a destabilising role of viscosity at moderate Reynolds numbers under transcritical-cooling conditions.

As Fig. 3.9, we analyse the phase velocity of the 'T11' cases. All supercritical-

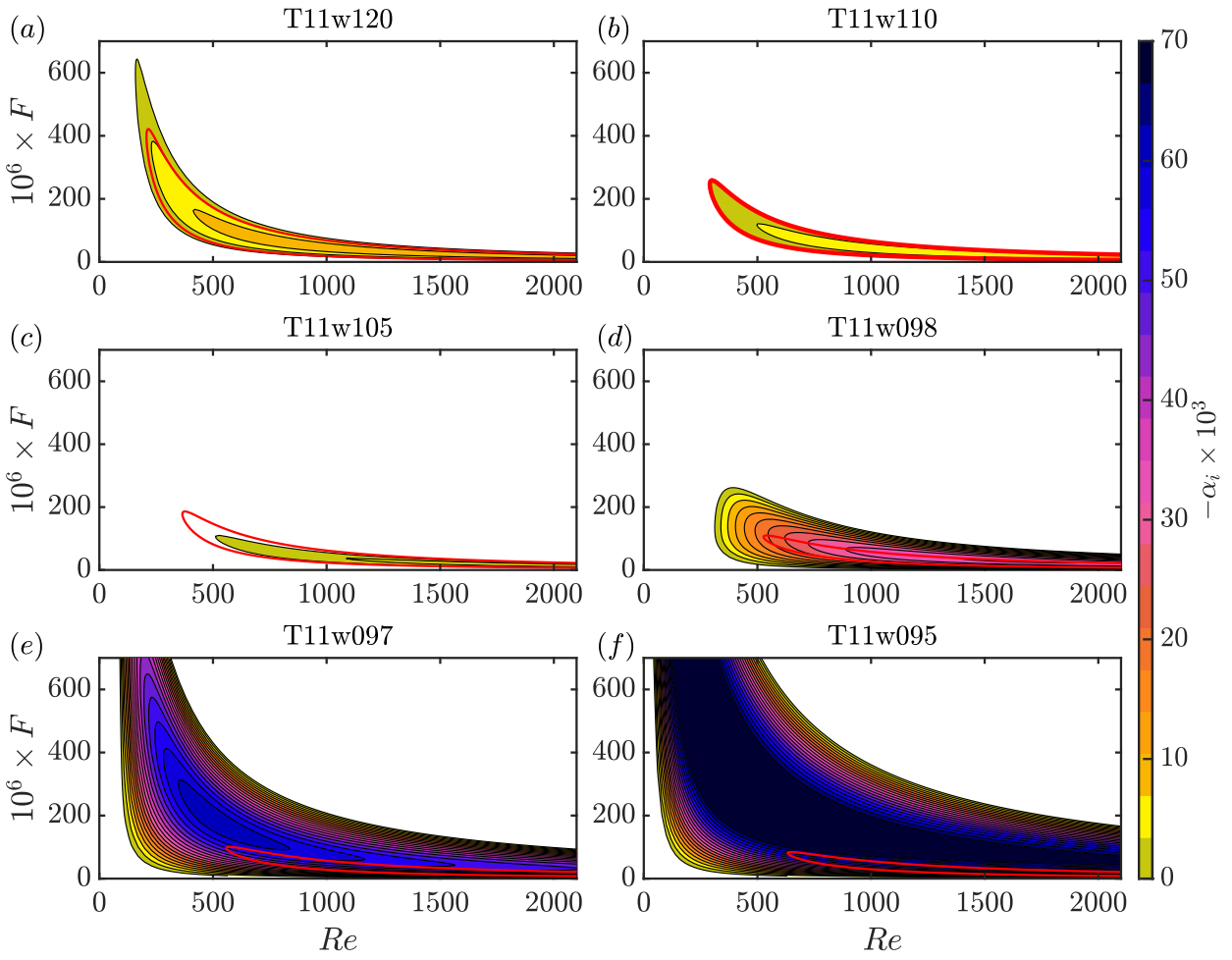

Figure 3.10: Growth-rate ($-\alpha_i$) contours in the Re–F stability diagram of 'T11' cases: (a) T11w120, (b) T11w110 (incompressible boundary layer), (c) T11w105, (d) T11w098 (transcritical case with T_w^*/T_{pc}^* = 0.98), (e) T11w097 (transcritical case with T_w^*/T_{pc}^* = 0.97), and (f) T11w095. The red solid lines represent the ideal-gas neutral stability (α_i = 0) at equal T_w^*/T_∞^* ratios.

temperature cases exhibit a comparable values in the range $c_r \approx 0.2$ to 0.5. In stark contrast, the transcritical-cooling cases display significantly lower and nearly constant values ($c_r \approx 0.1$ to 0.2) across the entire stability diagram. This behaviour is evident in Fig. 3.11(a), where black and red lines represent supercritical and transcritical cases, respectively. When c_r at the maximum growth rate is plotted against T_w^*/T_{pc}^* (Fig. 3.11b), a clear discontinuity appears, with an abrupt jump around the pseudo-critical point. This discontinuity strongly indicates that the mode arising under transcritical-cooling conditions, being inviscid in nature, is not a continuation of the viscous mode that exists under supercritical-temperature conditions. In other words, the viscous mode ceases to exist as the flow is cooled below the pseudo-critical point. Coexistence of the two modes occurs only for heating across the Widom line, in agreement with Figs. 3.8(d–f). From a practical standpoint, this abrupt and asymmetrical modal transition under pseudo-boiling conditions implies that even small thermal changes around the pseudo-critical point can produce dramatic shifts in the flow

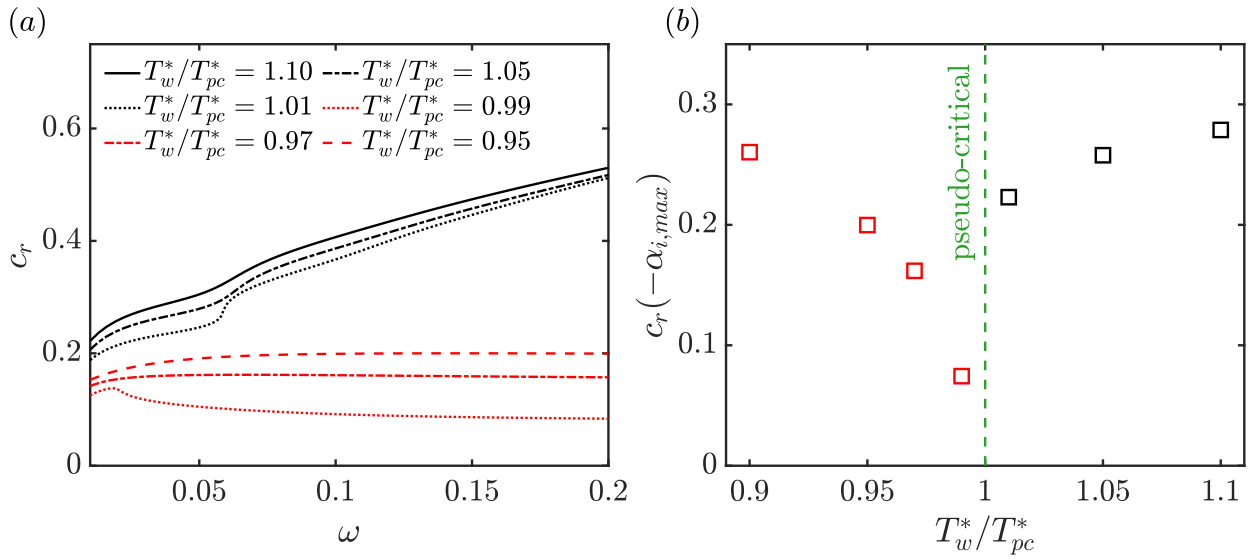

Figure 3.11: Real phase velocity c_r for the 'T11' cases at $Re = 2000$: (a) evolution as a function of the dimensionless frequency ω; (b) c_r at the maximum growth rate ($-\alpha_{i,max}$), plotted against the reduced wall temperature T_w^*/T_{pc}^*. The green dashed line (– –) denotes the pseudo-critical temperature $T^* = T_{pc}^*$.

stability.

Figure 3.12 displays typical eigenfunction profiles for the transcritical cases 'T09w105' and 'T11w095'. For 'T09w105', the wall-normal distributions of Mode I and II at $Re = 1000$ and $F = 200 \times 10^{-6}$ closely resemble the corresponding profiles under adiabatic-wall conditions (Fig. 3.4). In contrast, the eigenfunctions for the transcritical wall-cooling case (Fig. 3.12c), extracted at $Re = 300$ and $F = 200 \times 10^{-6}$, exhibit notable differences. The density perturbation $\hat{\rho}$ shows a significantly stronger peak at the pseudo-critical point, while the pressure perturbation attains substantially larger amplitudes than those of Mode II in the transcritical wall-heating case in Fig. 3.12(b). Moreover, the critical layer, $\eta = \eta_{cr}$, lies above the pseudo-critical point, in a region where the fluid is in the liquid-like state – a feature that becomes relevant in Sec. 3.4.

3.3.2 Inviscid analysis

To elucidate the inviscid nature of Mode II and isolate its behaviour from viscous effects, inviscid stability calculations (see Sec. 3.2.2) are performed in the limit of $Re \to \infty$.

The analysis begins with the adiabatic transcritical case 'T280Ec020' from Tab. 3.1, using the corresponding laminar base-flow profile shown in Fig. 3.2. The inviscid growth rate $-\alpha_i$ and the real phase velocity c_r of Mode II are plotted against the dimensionless frequency ω in Fig. 3.13. The inviscid results are obtained using both the quadratic eigenvalue problem Eq. (3.22) (hereafter EVP) and the iterative shooting method Eq. (3.23) (hereafter IT) with excellent agreement between the two methods. Note that the inviscid eigenvalue analysis is limited to unstable perturbations to avoid the singularity at the critical layer. In addition, Fig. 3.13 includes results from the viscous stability analysis at different Reynolds numbers.

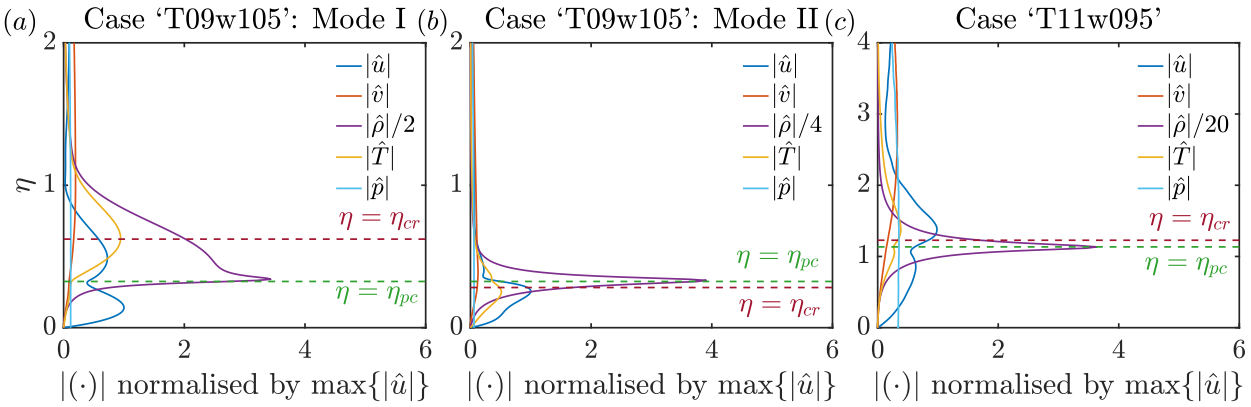

Figure 3.12: Wall-normal eigenfunctions of u', v', T', ρ', and p', normalised by $\max\{|\hat{u}|\}$, for the transcritical cases 'T09w105' and 'T11w095'. In (a,b), Mode I and Mode II of 'T09w105' are shown at $Re \approx 1000, F = 200 \times 10^{-6}$; panel (c) corresponds to 'T11w095' at $Re \approx 300, F = 200 \times 10^{-6}$. The critical layer and pseudo-critical point are denoted by η_{cr} and η_{pc}, respectively. Note that the normalisation of $\hat{\rho}$ differs between the three panels.

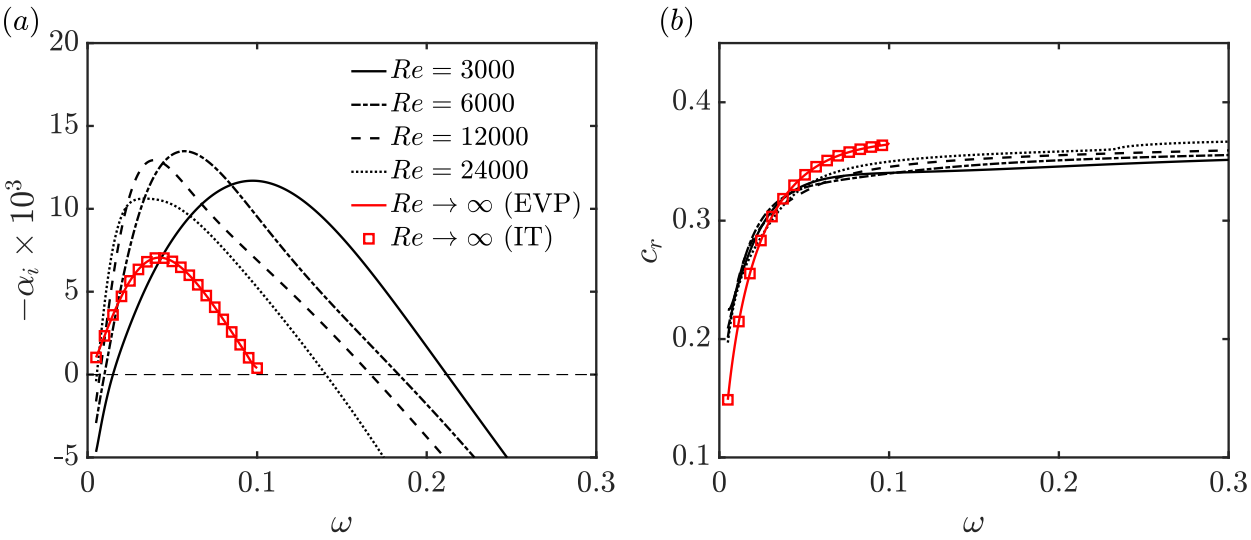

Figure 3.13: Effect of the Reynolds number on the stability of Mode II for case 'T280Ec020': (a) growth rate $-\alpha_i$ and (b) real phase speed c_r as functions of the dimensionless frequency ω. The inviscid results are shown in red, with 'EVP' denoting the quadratic eigenvalue problem and 'IT' the iterative shooting method.

Notably, the largest growth rates are obtained at moderate Reynolds numbers compared to the inviscid limit ($Re \to \infty$), indicating a destabilising effect of viscosity, with a $-\alpha_i$-peak between $Re = 6000$ and 12000. At even lower Reynolds numbers (e.g. $Re = 3000$), viscous effects become stabilising again for Mode II.

The inviscid analysis is now extended to boundary-layer profiles with wall heating in the zero-Eckert-number limit. For this investigation, the cubic VdW EoS (Sec. 2.2.2) is employed in combination with analytical diffusion laws (Sec. 2.3.2). The reduced pressure p^*/p_c^* is set to 1.08, and the pseudo-critical temperature corresponds to $T_{pc}^* = 1.11 T_\infty^*$. Figure 3.14(a) shows the inviscid growth rate of Mode II for different wall temperatures. When

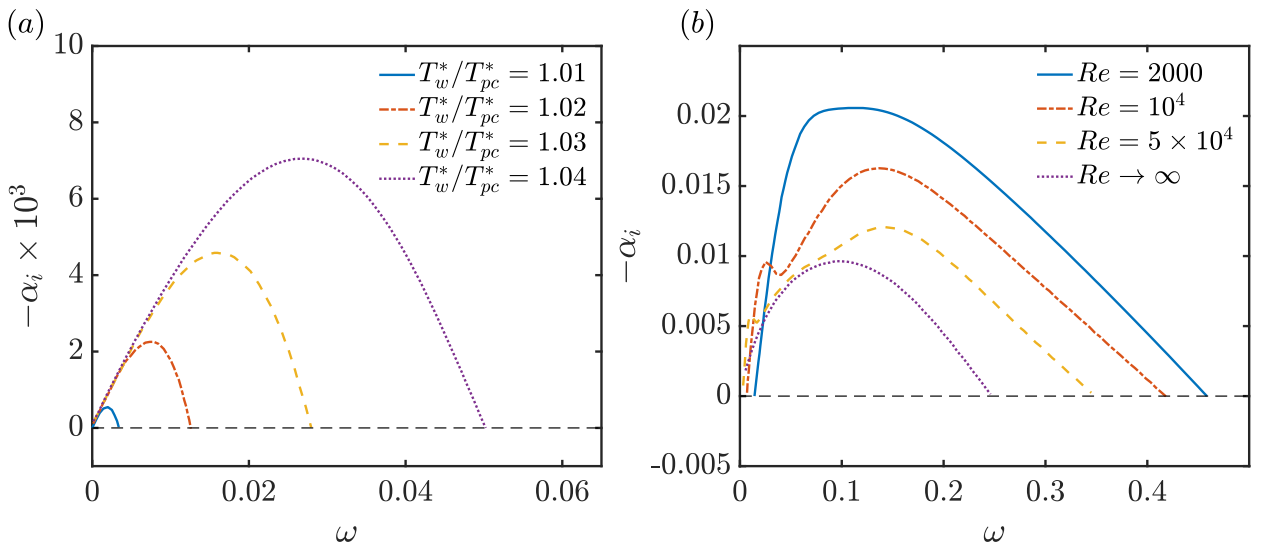

Figure 3.14: Inviscid linear stability analysis ($Re \to \infty$): (a) growth rate $-\alpha_i$ of Mode II for different wall temperatures; (b) effect of the Reynolds number on the growth rate of Mode II at $T_w^*/T_{pc}^* = 1.08$.

the wall temperature is below the pseudo-critical value ($T_w^*/T_{pc}^* < 1$), no unstable inviscid mode is found. However, as soon as $T_w^*/T_{pc}^* > 1$, Mode II shows a positive growth rate, which increases with further wall heating under pseudo-boiling conditions. The wall temperatures considered in Fig. 3.14(a) lie just above the pseudo-critical temperature, with $T_w^*/T_{pc}^* = 1.01$ corresponding to $T_w^*/T_\infty^* = 1.12$. In addition, the cut-off frequency of the instability, at which the perturbation becomes neutral, also shifts to higher values with increasing T_w^*/T_{pc}^*, thereby extending the range of unstable frequencies. These findings provide strong evidence that Mode II is intrinsically linked to the supercritical-state transition (crossing the Widom line) of the base-flow profile and is sensitive to the associated rapid changes in thermophysical properties.

The inviscid analysis in Fig. 3.14(a) reveals that the closer T_w^*/T_{pc}^* is to unity, the lower the corresponding inviscid growth rate – provided that $T_w^*/T_{pc}^* > 1$. In viscous stability calculations, this implies that Mode II may be entirely suppressed by viscous damping at Reynolds numbers relevant to boundary-layer flows. This is consistent with the results in Figs. 3.8(e,f), where only a small portion of the boundary layer is unstable at $T_w^*/T_{pc}^* = 1.03$, while a significantly larger unstable region emerges at $T_w^*/T_{pc}^* = 1.05$. This behaviour is characteristic of an inviscid instability: the larger the inviscid growth rate, the more viscous damping is required to stabilise it, and therefore the lower the critical Reynolds number Re_{crit} must be. However, in this case, viscous damping is not the only effect influencing Mode II. As shown in Fig. 3.14(b), the growth rate of Mode II is plotted for various Reynolds numbers and compared to the inviscid result ($Re \to \infty$), analogous to the comparison in Fig. 3.13(a). Interestingly, higher growth rates are observed at moderate Reynolds numbers than in the inviscid case, indicating a destabilising contribution from viscosity. For sufficiently small Reynolds numbers ($Re < 2000$), viscous damping becomes dominant and eventually stabilises the flow – consistent with the trend already observed in Fig. 3.11(a) for an adiabatic boundary

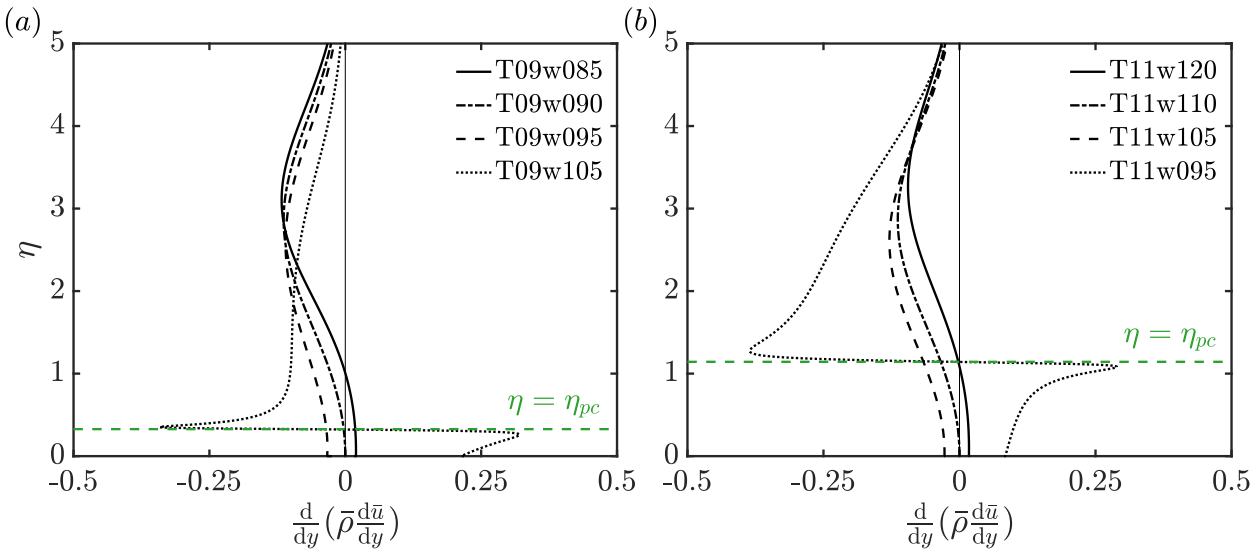

Figure 3.15: Distribution of $\mathrm{d}/\mathrm{d}y(\bar{\rho}\,\mathrm{d}\bar{u}/\mathrm{d}y)$ associated with the GIP at four different wall temperatures for cases (a) 'T09' and (b) 'T11'. A GIP is present where this quantity equals zero. The green dashed line (– –) marks the pseudo-critical point at $T^* = T^*_{pc}$.

layer.

Investigating why Mode II exhibits larger growth rates at finite Reynolds numbers than in the inviscid limit would be a valuable direction for future investigations. This phenomenon is not unusual – it also occurs for the first mode in supersonic boundary layers, which, in addition to being inviscidly unstable, is further destabilised by the viscous TS mechanism typical of incompressible flows; see Mack (1984). A similar TS-like viscous destabilisation has already been observed for Mode I under pseudo-boiling conditions; see Sec. 3.2.1. This raises fundamental questions about the nature of the destabilisation mechanism governing Mode II at finite Reynolds numbers, which would merit dedicated investigation. Given the physical similarities between supercritical fluids and miscible fluid systems (see e.g. Sec. 3.3.3), one possible approach could involve examining whether the low-Reynolds-number instability observed in miscible fluids may, to some extent and in a way that remains to be understood, provide insight into the behaviour of Mode II under transcritical conditions.

3.3.3 Origin of the unstable inviscid mode

Discarding viscous effects, the inviscid linearised stability equations reduce to Eq. (3.18), the compressible counterpart of the Rayleigh equation (Rayleigh 1880; Mack 1984). In the presence of density gradients, a necessary condition for instability is the existence of a GIP in the base-flow profile (Ren *et al.* 2019*b*), defined by:

$$\left(\bar{\rho}\bar{u}_y\right)_y = 0. \tag{3.25}$$

Figure 3.15 shows the quantity in Eq. (3.25) for the 'T09' and 'T11' cases listed in Tab. 3.2. Notably, a GIP is identified at three different thermodynamic states: (i) the subcritical state with wall cooling (case 'T09w085'), (ii) the supercritical state with wall heating

(case 'T11w120'), and (iii) the transcritical state with both wall heating and cooling (cases 'T09w105' and 'T11w095'). In the non-transcritical cases, the GIP criterion closely resembles the classical inflection condition of ideal-gas boundary layers, associated with a shear-driven instability. In contrast, in the transcritical state, Eq. (3.25) is satisfied precisely at the Widom line. This suggests that a GIP emerges systematically whenever the supercritical-state transition (Banuti 2015) takes place.

In the following, the appearance of a GIP in both non-transcritical and transcritical boundary layers is further analysed by revisiting the governing equations. To determine the conditions under which Eq. (3.25) becomes positive at the wall (indicating the presence of a GIP), we examine the x-momentum equation under the assumption of zero streamwise pressure gradient ($\mathrm{d}p/\mathrm{d}x = 0$) reads at the wall:

$$\left.\frac{\mathrm{d}^2\bar{u}}{\mathrm{d}y^2}\right|_w = -\left(\frac{1}{\bar{\mu}}\frac{\mathrm{d}\bar{\mu}}{\mathrm{d}y}\frac{\mathrm{d}\bar{u}}{\mathrm{d}y}\right)_w . \tag{3.26}$$

The viscosity gradient at the wall can be decomposed as

$$\left.\frac{\mathrm{d}\bar{\mu}}{\mathrm{d}y}\right|_w = \underbrace{\left(\left.\frac{\partial\bar{\mu}}{\partial\bar{T}}\right|_{\bar{\rho}}\frac{\partial\bar{T}}{\partial y}\right)_w}_{T\text{ term}} + \underbrace{\left(\left.\frac{\partial\bar{\mu}}{\partial\bar{\rho}}\right|_{\bar{T}}\frac{\partial\bar{\rho}}{\partial y}\right)_w}_{\rho\text{ term}}, \tag{3.27}$$

which controls the sign of the IP in Eq. (3.26) as follows:

$$\left.\frac{\mathrm{d}\bar{\mu}}{\mathrm{d}y}\right|_w = \begin{cases} > 0, & \text{IP shifts towards the wall,} \\ < 0, & \text{IP shifts away from the wall.} \end{cases} \tag{3.28}$$

The thermodynamic derivatives of viscosity with respect to T and ρ, i.e. $\partial\bar{\mu}/\partial\bar{T}|_{\bar{\rho}}$ and $\partial\bar{\mu}/\partial\bar{\rho}|_{\bar{T}}$, are properties of the fluid rather than of the flow. Their behaviour is illustrated in Fig. A.1.2 (Appendix A.1) for the considered supercritical CO_2. Notably, the term $\partial\bar{\mu}/\partial\bar{\rho}|_{\bar{T}}$ remains always negative near the Widom line, while the term $\partial\bar{\mu}/\partial\bar{T}|_{\bar{\rho}}$ changes sign in the subcritical state, below the pseudo-critical point. To better understand how wall heating and cooling influence the sign and position of the IP, the terms in Eq. (3.27) are analysed in Fig. 3.16. In the subcritical 'T09' cases with liquid-like free stream (Figs. 3.16a–f), the ρ term in Eq. (3.27) dominates, irrespective of the wall condition. This is due to the large magnitude of $\partial\bar{\mu}/\partial\bar{\rho}|_{\bar{T}}$, which far exceeds that of $\partial\bar{\mu}/\partial\bar{T}|_{\bar{\rho}}$. In case 'T09w085', wall cooling leads to $\mathrm{d}\bar{\mu}/\mathrm{d}y|_w < 0$, resulting in the appearance of an IP and a fuller velocity profile compared to the incompressible ('T09w090') or wall-heated case ('T09w095') shown in Fig. 3.6(b). In the supercritical 'T11' cases with vapour-like free stream (Figs. 3.16j–o), although $\partial\bar{\mu}/\partial\bar{T}|_{\bar{\rho}}$ is larger in magnitude than $\partial\bar{\mu}/\partial\bar{\rho}|_{\bar{T}}$, the wall-normal density gradient dominates over the temperature gradient. As a result, the T and ρ contributions in Eq. (3.27) nearly cancel out, with a slightly dominant ρ term yielding $\mathrm{d}\bar{\mu}/\mathrm{d}y|_w < 0$. In the transcritical state (Figs. 3.16g–i and 3.16p–r), the dominance of the ρ terms becomes even more pronounced, with a clear peak at the Widom line. In case 'T09w105' (transcritical wall heating), the positive $\bar{\mu}$ gradient at the wall, $\mathrm{d}\bar{\mu}/\mathrm{d}y|_w > 0$, leads to a fuller velocity profile, as seen in Fig. 3.6(b). Conversely,

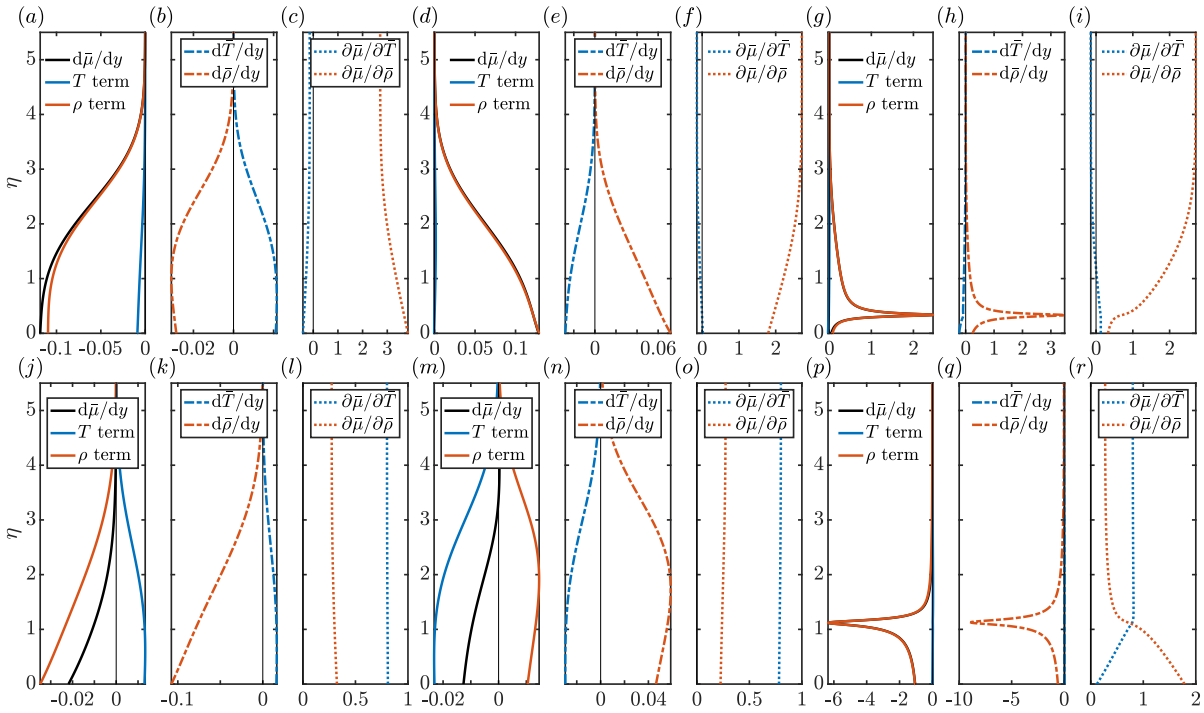

Figure 3.16: Wall-normal viscosity gradient from Eq. (3.27), its individual contributions (term T and term ρ), and their components: (a–c) T09w085, (d–f) T09w095, (g–i) T09w105, (j–l) T11w105, (m–o) T11w120, and (p–r) T11w095.

transcritical wall cooling (case 'T11w095') inverts the sign of the wall viscosity gradient, $\mathrm{d}\bar{\mu}/\mathrm{d}y|_w < 0$, causing a pronounced shift of the IP away from the wall and resulting in a thinner velocity profile, as highlighted in Fig. 3.7(b). Comparable trends for the subcritical and transcritical states were reported by Ren & Kloker (2022), who also noted the prevailing influence of the ρ contribution in Eq. (3.27). However, their analysis of the supercritical-temperature state was based on different flow conditions, which led to partially diverging observations for this state.

Following the analysis of the x-momentum equation at the wall, Eq. (3.26) is substituted into Eq. (3.25), evaluated at the wall, yielding:

$$\left.\frac{\mathrm{d}\bar{u}}{\mathrm{d}y}\right|_w \left(\left.\frac{\mathrm{d}\bar{\rho}}{\mathrm{d}y}\right|_w - \frac{\bar{\rho}_w}{\bar{\mu}_w}\left.\frac{\mathrm{d}\bar{\mu}}{\mathrm{d}y}\right|_w\right) = \bar{\rho}_w \left.\frac{\mathrm{d}\bar{T}}{\mathrm{d}y}\right|_w \left.\frac{\mathrm{d}\bar{u}}{\mathrm{d}y}\right|_w \left(\frac{1}{\bar{\rho}_w}\left.\frac{\partial\bar{\rho}}{\partial\bar{T}}\right|_{\bar{p},w} - \frac{1}{\bar{\mu}_w}\left.\frac{\partial\bar{\mu}}{\partial\bar{T}}\right|_{\bar{p},w}\right). \tag{3.29}$$

It is important to note that Eq. (3.29) holds under the boundary-layer assumption of $\partial\bar{p}/\partial y = 0$, which allows the use of the chain rule to express the wall-normal derivatives of $\bar{\mu}$ as:

$$\frac{\mathrm{d}\bar{\mu}}{\mathrm{d}y} = \frac{\mathrm{d}\bar{T}}{\mathrm{d}y}\left.\frac{\partial\bar{\mu}}{\partial\bar{T}}\right|_{\bar{p}}, \qquad \frac{\mathrm{d}\bar{\rho}}{\mathrm{d}y} = \frac{\mathrm{d}\bar{T}}{\mathrm{d}y}\left.\frac{\partial\bar{\rho}}{\partial\bar{T}}\right|_{\bar{p}}. \tag{3.30a,b}$$

The term in parentheses in Eq. (3.29) simplifies to

$$\left(\frac{1}{\bar{\rho}_w}\left.\frac{\partial\bar{\rho}}{\partial\bar{T}}\right|_{\bar{p},w} - \frac{1}{\bar{\mu}_w}\left.\frac{\partial\bar{\mu}}{\partial\bar{T}}\right|_{\bar{p},w}\right) = -\frac{1}{\bar{\nu}_w}\left.\frac{\partial\bar{\nu}}{\partial\bar{T}}\right|_{\bar{p},w}, \tag{3.31}$$

where $\bar{\nu} = \bar{\mu}/\bar{\rho}$ is the base-flow kinematic viscosity, shown in Fig. 2.2(c). As a result, the GIP

State	Case	T^*_∞/T^*_{pc}	T^*_w/T^*_{pc}	$\partial\bar{\nu}/\partial\bar{T}\vert_{\bar{p},w}$	$\mathrm{d}\bar{T}/\mathrm{d}y\vert_w$	$\mathrm{d}/\mathrm{d}y(\bar{\rho}\,\mathrm{d}\bar{u}/\mathrm{d}y)\vert_w$	GIP
Subcritical cooling	T09w085	0.90	0.95	-	+	+	✓
Supercritical heating	T11w120	1.10	1.20	+	-	+	✓
Transcritical heating	T09w105	0.90	1.05	+	-	+	✓
Transcritical cooling	T11w095	1.10	0.95	-	+	+	✓

Table 3.3: Summary of the flow conditions under which the GIP criterion, $\mathrm{d}/\mathrm{d}y(\bar{\rho}\,\mathrm{d}\bar{u}/\mathrm{d}y) = 0$, is satisfied, in agreement with Fig. 3.15.

criterion at the wall becomes:

$$\left.\frac{\mathrm{d}}{\mathrm{d}y}\left(\bar{\rho}\frac{\mathrm{d}\bar{u}}{\mathrm{d}y}\right)\right|_w = -\underbrace{\frac{\bar{\rho}_w}{\bar{\nu}_w}\left.\frac{\mathrm{d}\bar{u}}{\mathrm{d}y}\right|_w}_{>0}\left.\frac{\mathrm{d}\bar{T}}{\mathrm{d}y}\right|_w\left.\frac{\partial\bar{\nu}}{\partial\bar{T}}\right|_{\bar{p},w}. \tag{3.32}$$

Since $\bar{\rho}_w$, $\bar{\nu}_w$, and $\mathrm{d}\bar{u}/\mathrm{d}y|_w$ are always positive at the wall, the sign of Eq. (3.32) depends solely on the product of $\mathrm{d}\bar{T}/\mathrm{d}y|_w$ and $(\partial\bar{\nu}/\partial\bar{T})_{\bar{p},w}$, the latter being purely a fluid-dependent quantity. It follows that

$$\left.\frac{\partial\bar{\nu}}{\partial\bar{T}}\right|_{\bar{p},w} = \begin{cases} < 0, & \text{as } T^* < T^*_{pc}, \\ > 0, & \text{as } T^* > T^*_{pc}, \end{cases} \tag{3.33}$$

and

$$\left.\frac{\mathrm{d}\bar{T}}{\mathrm{d}y}\right|_w = \begin{cases} < 0, & \text{heating}, \\ > 0, & \text{cooling}, \end{cases} \tag{3.34}$$

assuming negligible viscous dissipation. Moreover, since $\mathrm{d}/\mathrm{d}y(\bar{\rho}\,\mathrm{d}\bar{u}/\mathrm{d}y)$ is always negative at the boundary-layer edge, a GIP within the boundary layer, i.e. a change in the sign of Eq. (3.25), can only occur when the right-hand side of Eq. (3.32) becomes positive. The flow conditions for which the criterion is satisfied are summarised in Tab. 3.3, confirming the results shown in Fig. 3.15.

Recalling Eq. (3.32), we observe the direct dependence of the GIP on the kinematic viscosity. Figure 2.2 revealed that $\bar{\nu}$ exhibits an extremum at the Widom line. This raises the question: does the presence of an extremum in $\bar{\nu}$ necessarily indicate a GIP, and consequently, the emergence of the inviscid Mode-II instability? To explore this, we examine the base flow in the vicinity of the pseudo-critical point, where strong local gradients in dynamic viscosity are expected. In a boundary-layer flow over a flat plate, viscous stresses are typically balanced by advection. However, this balance changes near the wall, where advection weakens and eventually vanishes due to the no-slip condition. If viscosity varies, an additional term involving its gradient appears, see Eq. (3.26), and may locally dominate the momentum balance – especially for fluids exhibiting large viscosity variations. The streamwise momentum

equation in the boundary layer can be written as:

$$\frac{\partial}{\partial y}\left(\bar{\mu}\frac{\partial \bar{u}}{\partial y}\right) = \bar{\rho}\bar{u}\frac{\partial \bar{u}}{\partial x} + \bar{\rho}\bar{v}\frac{\partial \bar{u}}{\partial y}. \tag{3.35}$$

When viscosity effects dominate

$$\frac{\partial}{\partial y}\left(\bar{\mu}\frac{\partial \bar{u}}{\partial y}\right) \gg \bar{\rho}\bar{u}\frac{\partial \bar{u}}{\partial x} + \bar{\rho}\bar{v}\frac{\partial \bar{u}}{\partial y}, \tag{3.36}$$

this balance simplifies to:

$$\bar{\mu}\frac{\mathrm{d}^2\bar{u}}{\mathrm{d}y^2} + \frac{\mathrm{d}\bar{\mu}}{\mathrm{d}y}\frac{\mathrm{d}\bar{u}}{\mathrm{d}y} \simeq 0. \tag{3.37}$$

To verify the validity of this approximation, we apply the Lees–Dorodnitsyn transformation introduced in Sec. 2.4, yielding the transformed streamwise momentum equation as

$$\frac{1}{\bar{C}}\frac{\mathrm{d}\bar{u}}{\mathrm{d}\eta}\frac{\mathrm{d}\bar{C}}{\mathrm{d}\eta} + \frac{\mathrm{d}^2\bar{u}}{\mathrm{d}\eta^2} + \frac{\bar{f}}{\bar{C}}\frac{\mathrm{d}\bar{u}}{\mathrm{d}\eta} = 0, \quad \frac{\mathrm{d}^2\bar{u}}{\mathrm{d}\eta^2} = -\frac{1}{\bar{C}}\frac{\mathrm{d}\bar{u}}{\mathrm{d}\eta}\left(\underbrace{\frac{\mathrm{d}\bar{C}}{\mathrm{d}\eta}}_{\text{viscous}} + \underbrace{\bar{f}}_{\text{advection}}\right), \tag{3.38a,b}$$

where $\bar{f} = \int_0^\eta \bar{u}\,\mathrm{d}\eta$ is the dimensionless streamfunction. Equations (3.38a,b) resemble Eq. (3.26), being governed primarily by the 'viscous' term near the wall, since the 'advection' term vanishes there. The balance of 'viscous' and 'advection' terms in Eqs. (3.38a,b) is plotted in Figs. 3.17(a,b) for the transcritical cases 'T09w105' and 'T11w095'. Note that, in the non-transcritical cases, the 'advection' and 'viscous' terms are of comparable magnitude near the wall, causing Eq. (3.37) to break down. Conversely, in the transcritical state, the near-wall supercritical-state transition causes the 'viscous' term to significantly prevail over the 'advection' term. Up to the pseudo-critical point, $\eta = \eta_{pc}$, viscous effects dominate, and the assumption in Eq. (3.37) holds. Consequently, we assume that the GIP criterion at the wall, Eq. (3.32), based only on viscous effects, can be extended approximately across the boundary layer as:

$$\frac{\mathrm{d}}{\mathrm{d}y}\left(\bar{\rho}\frac{\mathrm{d}\bar{u}}{\mathrm{d}y}\right) \simeq -\frac{\bar{\rho}}{\bar{\nu}}\frac{\mathrm{d}\bar{u}}{\mathrm{d}y}\frac{\mathrm{d}\bar{T}}{\mathrm{d}y}\left.\frac{\partial \bar{\nu}}{\partial \bar{T}}\right|_{\bar{p}}. \tag{3.39}$$

The validity of Eq. (3.39) compared to the exact GIP criterion in Eq. (3.25) is assessed in Figs. 3.17(c,d) for the transcritical cases 'T09w105' and 'T11w095'. Regardless of whether wall heating or cooling is applied, the approximation holds very well near the wall, where viscosity effects dominate. Excellent agreement is also observed in the immediate vicinity of the pseudo-critical point, where the strongest gradients in viscosity are found. Importantly, this is also the location where the GIP is observed. Therefore, Eq. (3.39) offers a meaningful interpretation: the GIP arises from the extremum of kinematic viscosity located at the Widom line, which is a necessary condition for the existence of the inviscid instability (Mode-II instability). Farther from the wall, where advection becomes dominant again, Eq. (3.39) no longer holds. Nevertheless, these findings suggest that a boundary layer with a supercritical fluid, whose temperature profile crosses the Widom line, exhibits an inviscid

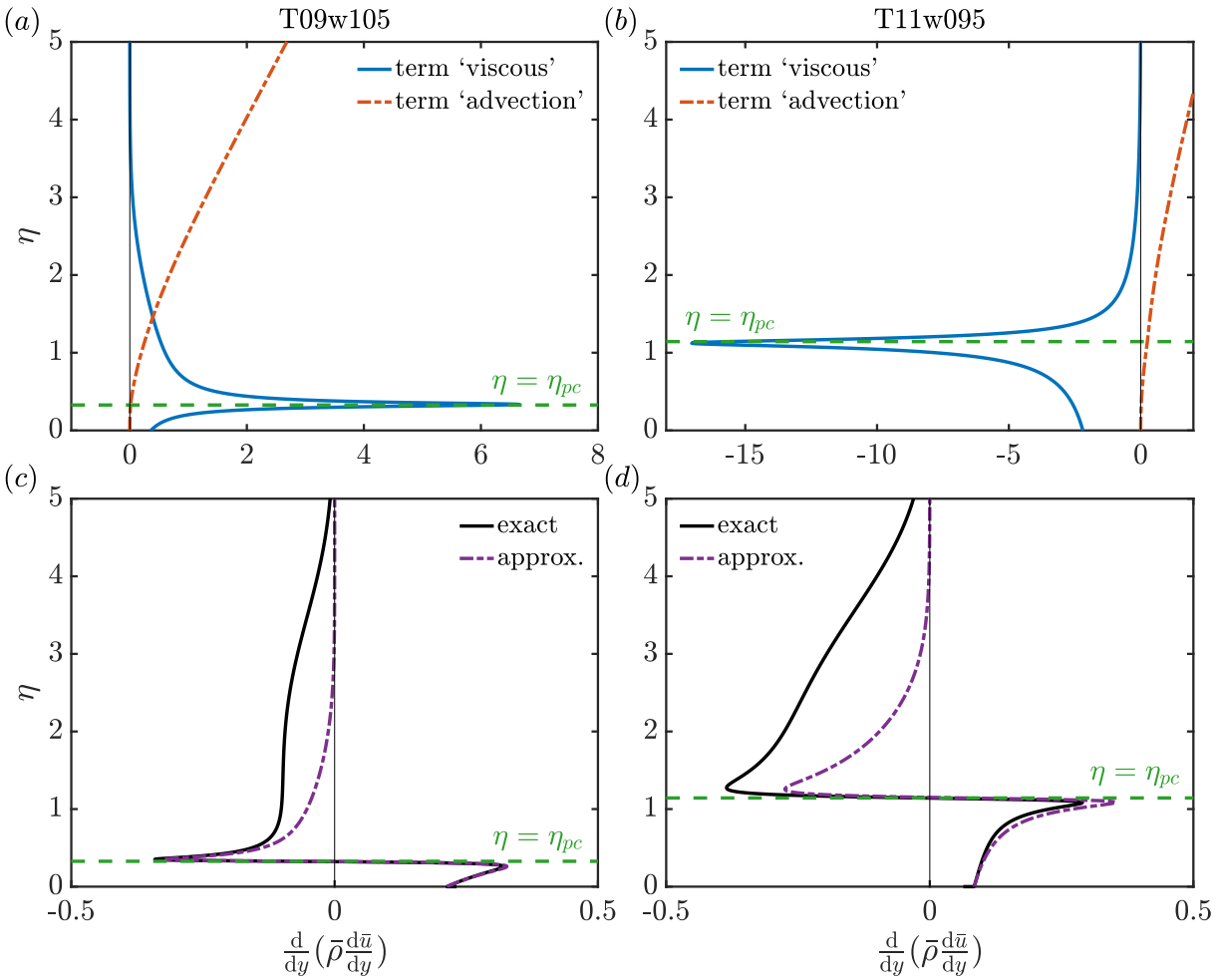

Figure 3.17: Transcritical cases 'T09w105' (a,c) and 'T11w095' (b,d): (a,b) comparison of the 'viscous' term ($\mathrm{d}\bar{C}/\mathrm{d}\eta$) and the 'advection' term ($\bar{f}$) from Eq. (3.38a,b); (c,d) comparison between the exact GIP criterion in Eq. (3.25) and its approximation in Eq. (3.39). A GIP is present where the respective quantity equals zero. The green dashed line (– –) marks the pseudo-critical point at $T^* = T^*_{pc}$.

instability associated with a GIP located near the Widom line. This behaviour does not occur under the ideal-gas assumption, as the fluid-dependent property $\partial\bar{\nu}/\partial\bar{T}|_{\bar{p}}$, given by

$$\bar{\nu}\left(\frac{1}{\bar{\mu}}\frac{\partial\bar{\mu}}{\partial\bar{T}}\bigg|_{\bar{p}} - \frac{1}{\bar{\rho}}\frac{\partial\bar{\rho}}{\partial\bar{T}}\bigg|_{\bar{p}}\right), \tag{3.40}$$

is always positive. This results from:

$$\frac{\partial\bar{\mu}}{\partial\bar{T}}\bigg|_{\bar{p}} = \frac{(1+\bar{S})\sqrt{\bar{T}}(0.5\bar{T}+1.5\bar{S})}{(\bar{T}+\bar{S})^2} > 0, \quad \frac{\partial\bar{\rho}}{\partial\bar{T}}\bigg|_{\bar{p}} = -\frac{\bar{\rho}}{\bar{T}} < 0, \tag{3.41a,b}$$

with $\bar{S} = T^*_{ref}/T^*_\infty$ denoting the dimensionless temperature parameter in Sutherland's law (see Sec. 2.3.1). Figure 3.18 confirms this trend, along with the results obtained using the VdW EoS (see Sec. 2.2.2).

The current study focused on supercritical CO_2 at a reduced pressure of $p_r = p^*/p^*_c = 1.084$, but it is relevant to investigate whether a minimum of kinematic viscosity also occurs in other supercritical fluids. In Fig. 3.19, the kinematic viscosity, normalised by its

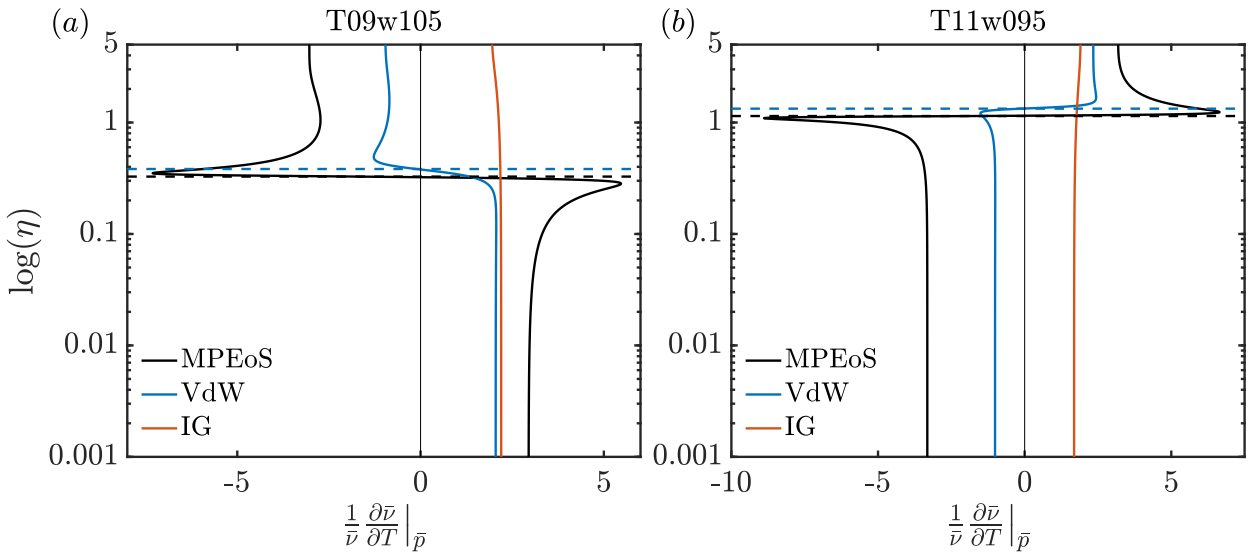

Figure 3.18: Wall-normal profiles of the kinematic viscosity gradient $\partial\bar{\nu}/\partial\bar{T}\big|_{\bar{p}}$ in logarithmic scale: transcritical cases (a) 'T09w105' and (b) 'T11w095' are shown with black solid lines. Results for the same wall-to-free-stream temperature ratio, $T_w^*/T_\infty^* = 1.167$, obtained using the VdW EoS and the ideal-gas (IG) assumption are plotted with solid blue and red lines, respectively. The location of the pseudo-critical point, $\eta = \eta_{pc}$, where $T^* = T_{pc}^*$, is marked by a dashed line.

corresponding value at the pseudo-critical point, is plotted as a function of the reduced temperature T^*/T_{pc}^* for four different reduced supercritical pressures. Note that the pseudo-critical temperature differs between fluids and also varies with pressure (see Appendix A.1 for supercritical CO_2). Supercritical CO_2, toluene, and O_2 all exhibit a distinct minimum in ν, suggesting that the approximation of the GIP criterion in Eq. (3.39) can be extended to other non-polar supercritical fluids. Note that non-polar fluids are characterised by weak intermolecular forces and lack permanent dipole moments, in contrast to polar fluids, which exhibit strong hydrogen bonding. As the reduced pressure increases, the minimum shifts slightly away from the pseudo-critical point, and the ν gradient becomes smoother. In contrast, H_2O behaves significantly differently in the liquid-like state, likely due to its strong polarity. This observation for non-polar supercritical fluids may motivate further investigation of other flows exhibiting similar viscosity extrema. Certain fluid mixtures, such as methanol–toluene, are known to feature a minimum in kinematic viscosity at intermediate mole fractions (McAllister 1960). The stability of shear flows involving viscosity-stratified layers was first studied by Yih (1967) who demonstrated that viscosity gradients can cause instability at low Reynolds numbers. Ern *et al.* (2003) later extended this analysis to include the effect of a finite interface between fluids. Such work could be revisited in the context of fluid mixtures featuring a minimum in kinematic viscosity, where inviscid instability mechanisms may enrich the system dynamics. In this case, it can be noted that the viscosity profile is driven by the concentration of a fluid species – a scalar that follows a transport–diffusion equation analogous to the enthalpy (non-ideal gas) considered in the present study. From

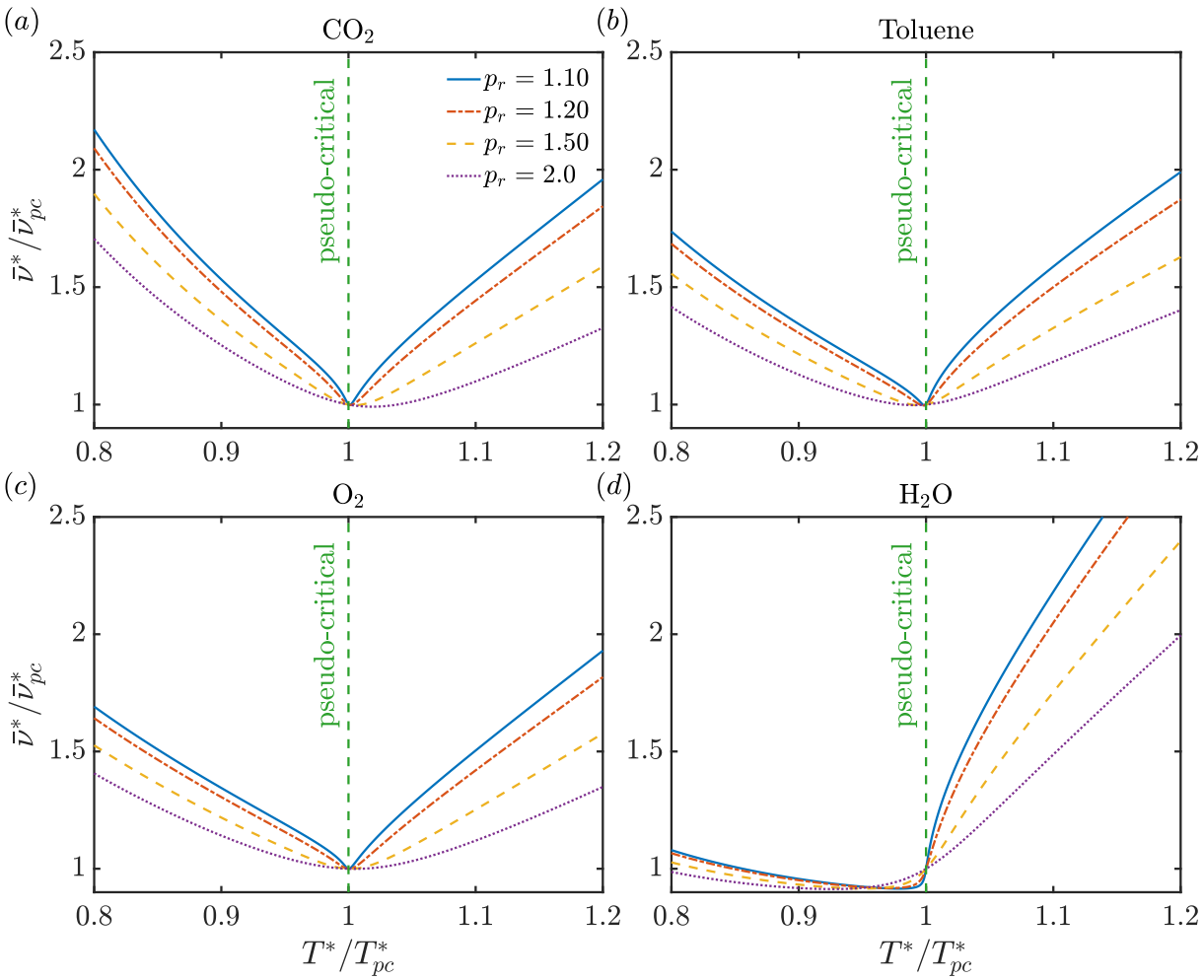

Figure 3.19: Dimensionless kinematic viscosity, normalised by its value at the pseudo-critical point, as a function of reduced temperature T^*/T^*_{pc}, for four different reduced pressures $p_r = p^*/p^*_c = (1.10, 1.20, 1.50, 2.0)$: (a) CO_2, (b) toluene, (c) O_2, and (d) H_2O. The green dashed line (– –) marks the pseudo-critical point at $T^*/T^*_{pc} = 1$.

a theoretical standpoint, the two cases are thus closely related. A comprehensive review of viscosity-stratified flows is provided by Govindarajan & Sahu (2014).

3.4 Three-dimensional disturbances

In Ren *et al.* (2019*b*), the influence of 3-D perturbations on the local growth rate was studied for an adiabatic wall at finite Eckert numbers. In order to measure the oblique-wave effect, the maximum local growth ratio was investigated, which is defined as:

$$r_\beta = \max_{\forall \omega, Re} \{\alpha_{i,\beta=\beta_{max}}/\alpha_{i,\beta=0}\}. \tag{3.42}$$

2-D perturbations were found to be most unstable in the subcritical state, whereas a maximum local-growth ratio larger than one was obtained for oblique disturbances in the supercritical state. In the transcritical state, Mode I and Mode II were most locally amplified in 3-D and 2-D, respectively.

In this section, a similar investigation is undertaken with a special focus on the integral amplification rather than the local one. The base-flow profiles initially follow those of Sec. 3.3 with an isothermal wall. Three supercritical states at a supercritical pressure of $p^* = 80\,\text{bar}$ ($p_r = 1.084$) are considered: subcritical, supercritical, and transcritical. Viscous modal stability analysis is performed with spanwise wavenumber $\beta > 0$. Stability diagrams are first obtained in the Re–ω–β space up to $Re = 2000$. Cuts of Re–ω are then considered at different β with iso-contours of the largest N-factor (see Sec. 4.5 for the calculation of the N-factor) over all spanwise wavenumbers. Furthermore, the effect of increasing Mach number (compressibility) on the growth rate and phase speed is investigated. Finally, in Sec. 3.4.2, the inviscid formulation is considered with $Re \to \infty$. In this case, only Mode II is present in the transcritical state. In this scenario, the effect of Mach number in the amplification of 3-D waves is analysed.

3.4.1 Viscous analysis

For the non-transcritical cases, either in the subcritical or in the supercritical state, the two exemplary cases 'T09w085' and 'T11w105' are illustrated in Figs. 3.20(a,c) and 3.20(b,d), respectively. Their largest growth rate in the stability diagram and their largest integral amplification are detected at $\beta = \beta_{max} = 0$, with larger values for the subcritical cooling state. For instance, the largest eigenvalues correspond to $(c_r, -\alpha_i, Re, \beta) = (0.301, 0.010, 1400, 0)$ and $(c_r, -\alpha_i, Re, \beta) = (0.252, 0.0053, 2200, 0)$ for cases 'T09w085' and 'T11w105', respectively. The real part of the phase velocity c_r is computed as ω/α_r. Note that, as illustrated in Figs. 3.20(c,d), there are spanwise wavenumbers at which 3-D modes are locally more amplified than 2-D modes. Unlike at finite Eckert numbers (Ren *et al.* 2019*b*), all non-transcritical cases in the zero-Eckert-number limit have their maximum local-growth ratio and largest integral amplification for 2-D perturbations.

The effect of an increasing spanwise wavenumber is displayed in Fig. 3.21 for the transcritical case 'T09w105'. Mode II exhibits its largest growth rate over all frequencies at $\beta = \beta_{max} = 0$, while Mode I can also be most unstable for 3-D disturbances. The largest eigenvalues are found at $(c_r, -\alpha_i, Re, \beta) = (0.457, 0.011, 2000, 0)$ and $(c_r, -\alpha_i, Re, \beta) = (0.312, 0.072, 2060, 0)$ for Mode I and Mode II, respectively. Nevertheless, Mode II is almost unaffected by a β-increase, being extremely unstable in the considered parameter space. Hence, N-factors up to 90 are achieved at $Re = 2000$. For Mode I, an increase in β leads to a stabilisation analogous to the non-transcritical cases.

For case 'T11w095', in Fig. 3.22, similar to Mode II in the transcritical wall-heating case, the highly unstable inviscid mode is largely unaffected by a β-increase. Yet, the instability extends up to the flat-plate leading edge and to relatively high frequencies. Interestingly, the largest growth rate, i.e. $-\alpha_{i,max} = 0.0946$, is found at a very low local Reynolds number of $Re = 220$ with a phase speed of $c_r = 0.217$. With respect to the integral amplification, we observe an N-factor of 15 already at $Re = 200$. We can conclude that, for all investigated cases, the current modal analysis has revealed the 'dominance' of 2-D disturbances in the zero-Eckert-number limit. Both the local amplification (over most of the frequency spectrum)

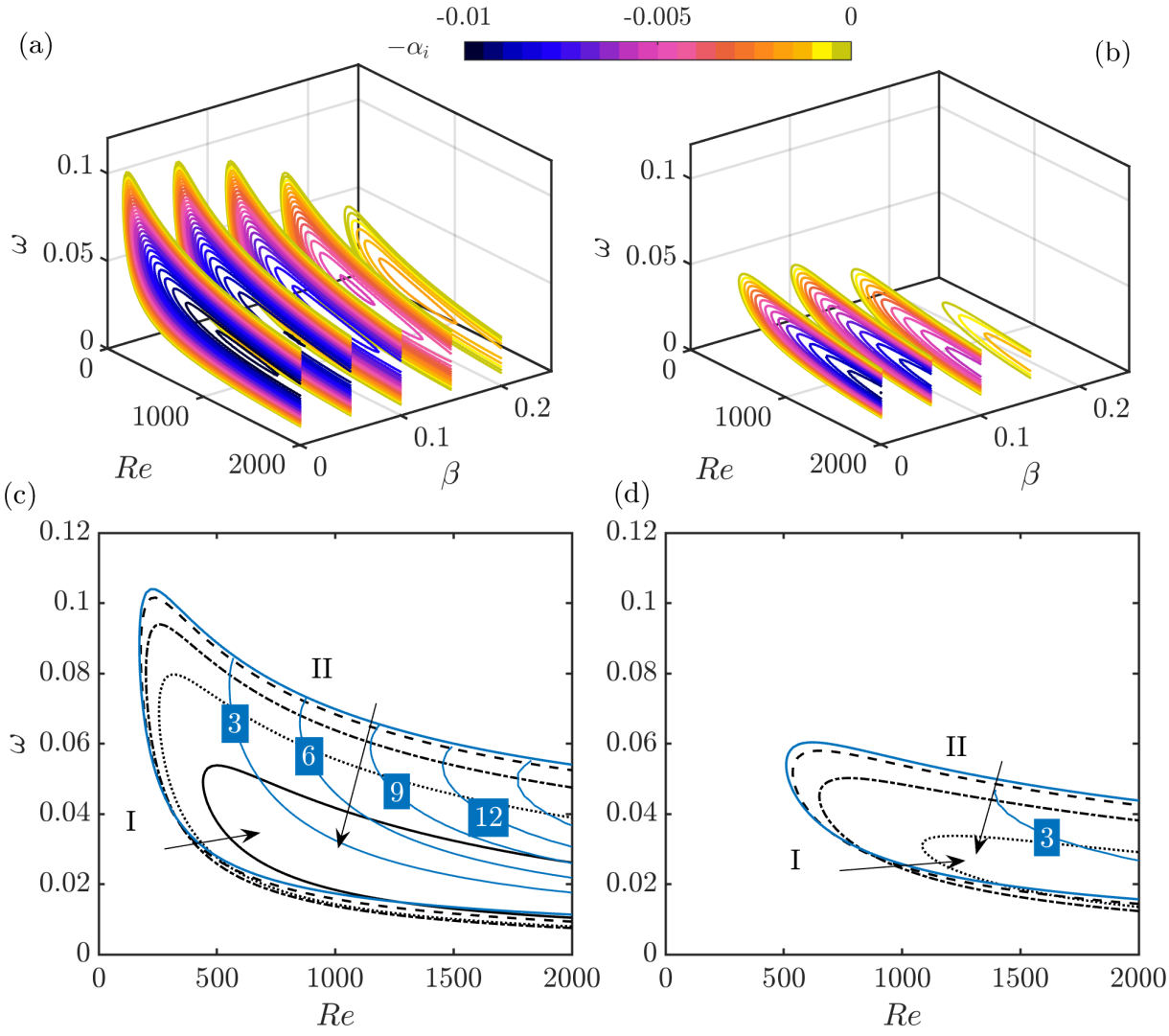

Figure 3.20: Slices of $-\alpha_i$-contours in the Re–ω–β (a,b) and neutral stability curves in the Re–ω (c,d) space: (a,c) case 'T09w085', (b,d) case 'T11w105'. In (c,d), maximum N-factors are indicated in blue and are located always at $\beta = \beta_{max} = 0$. Arrows in (c,d) indicate a β-increase with $\Delta\beta = 0.05$ of the neutral stability curve with branch I and II (from blue solid line at $\beta = 0$ to black solid line at $\beta = 0.2$).

as well as the maximum local-growth ratio, and the N-factor are found largest for 2-D modes.

These results indicate that reducing the Mach number may have the effect of shifting the maximum (local and integral) amplification from a 3-D to a 2-D mode independently of the considered thermodynamic state at supercritical pressure. In the following, we investigate this behaviour by increasing the Mach number M_∞ within the subsonic regime, i.e. $M_\infty < 1$, while prescribing the same wall temperature. With regard to the base-flow profiles (not shown), an increase in Mach number results in a comparatively small change in the temperature and density profiles. Viscous dissipation in the supercritical state is reduced when compared to the subcritical state, also indicated by the lower free-stream Eckert number Ec_∞ for the same M_∞. In the subcritical state, the Mach number increase is limited to avoid crossing the

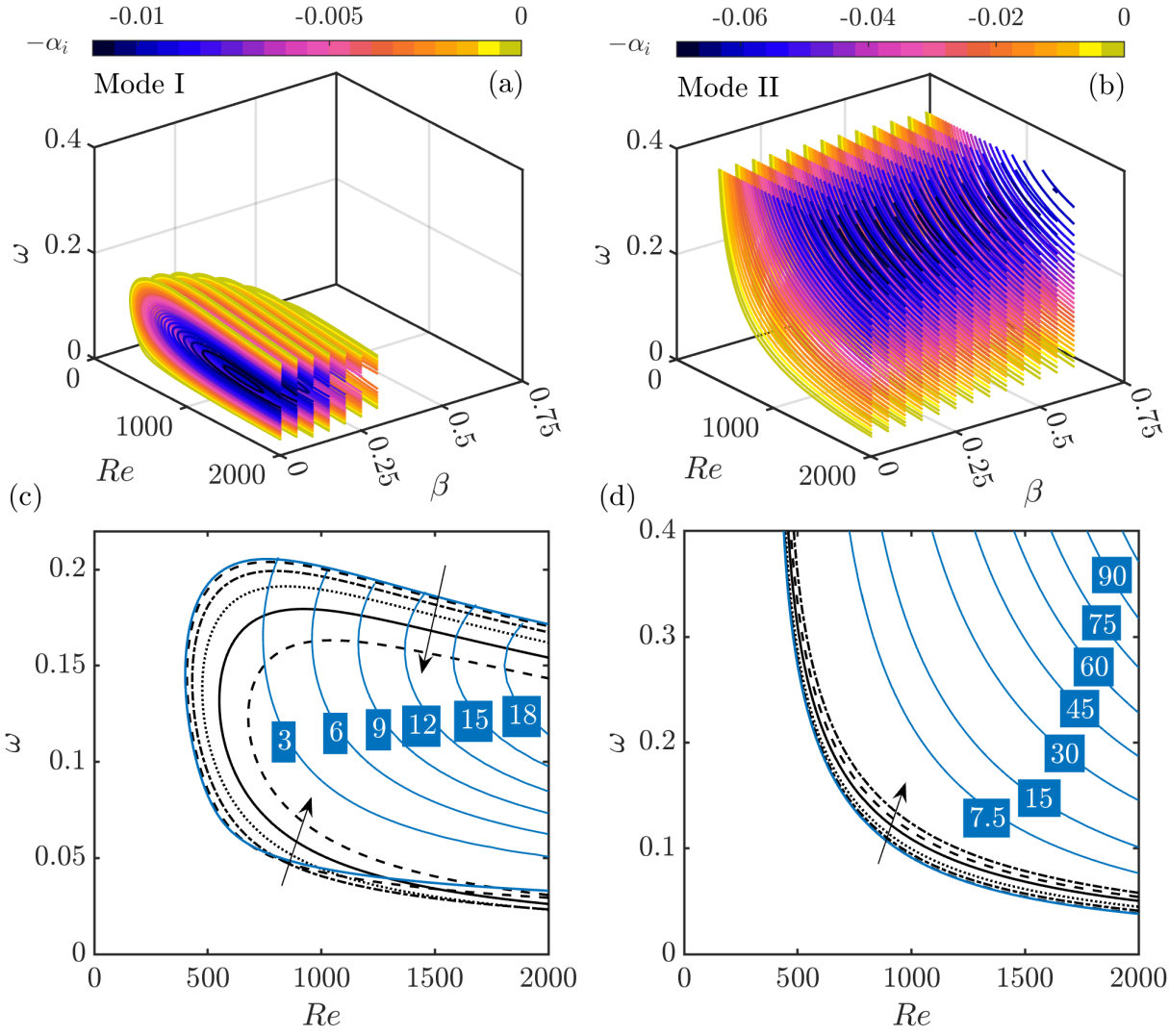

Figure 3.21: Case T09w105. Slices of $-\alpha_i$-contours in the Re–ω–β (a,b) and neutral stability curves in the Re–ω (c,d) space: (a,c) Mode I, (b,d) Mode II. In (c,d), maximum N-factors are indicated in blue and are located always at $\beta = \beta_{max} = 0$. Arrows in (c,d) indicate a β-increase with $\Delta\beta = 0.05$ of the neutral stability curve (from blue solid line at $\beta = 0$ to black dashed line at $\beta = 0.25$).

Widom line and thereby entering the transcritical state. In the latter state, with wall heating, increasing the Mach number leads to a noticeable rise in the height of the Widom-line crossing, which corresponds to the location of the GIP. In contrast, the height of supercritical-state transition is not varied with increasing Mach number under transcritical wall cooling.

In the non-transcritical cases (not shown), sufficiently high Mach numbers favour the amplification of 3-D disturbances, with supercritical cases exhibiting higher values of r_β than subcritical ones. Increasing the Mach number reduces the growth rate of the most amplified 2-D mode and narrows the unstable range of β in the subcritical state, while the opposite occurs in the subcritical state. Consequently, the modal symmetry observed at zero Eckert number between supercritical heating/subcritical cooling and supercritical cooling/subcritical heating breaks down at finite Mach numbers due to base-flow asymmetry

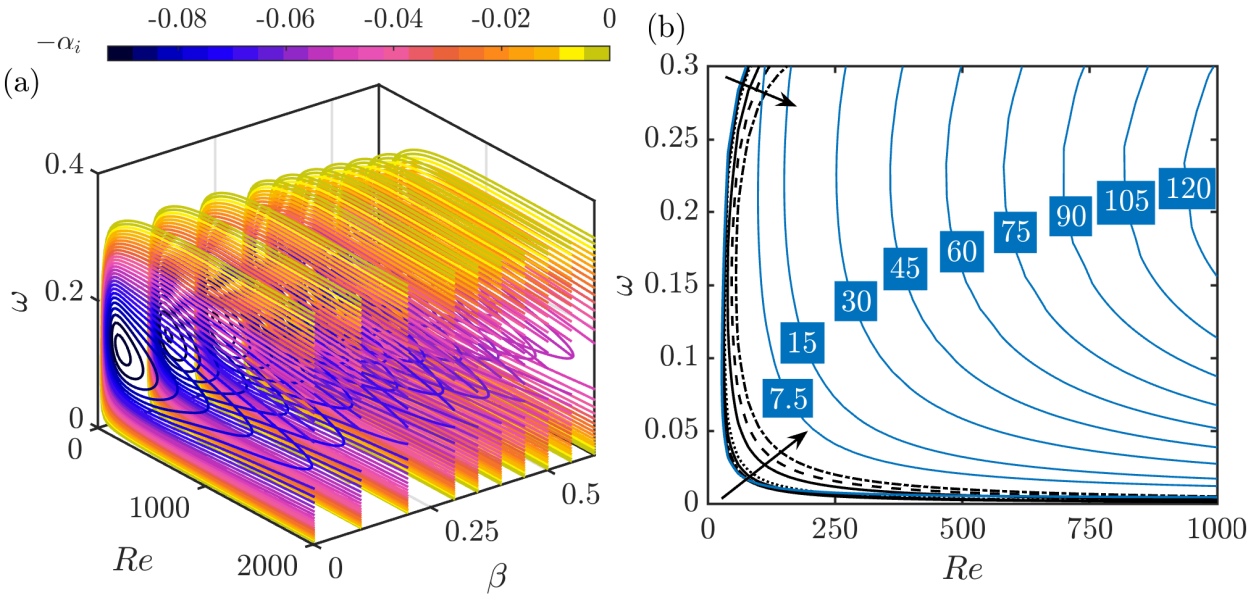

Figure 3.22: Case 'T11w095'. Slices of $-\alpha_i$-contours in the Re–ω–β (a) and neutral stability curves in the Re–ω (b) space. In (b), maximum N-factors are indicated in blue and are located always at $\beta = \beta_{max} = 0$. Arrows in (b) indicate a β-increase with $\Delta\beta = 0.05$ of the neutral stability curve (from blue solid line at $\beta = 0$ to black dashed line at $\beta = 0.25$).

induced by compressibility effects. In the following, we analyse the transcritical cases in more detail. Unlike the cases listed in Tab. 3.2, the free-stream temperature is $T^*_\infty/T^*_{pc} = 0.95$ with $Pr_\infty = 2.39$ for transcritical wall heating, referred to hereafter as case 'T095w105', while for transcritical wall cooling, the free-stream temperature is equal to $T^*_\infty/T^*_{pc} = 1.05$ with $Pr_\infty = 1.59$, referred to hereafter as case 'T105w095'. As shown in Fig. 3.23(a), in case 'T095w105', due to the fuller velocity profile (see Sec. 3.3.3) and the minimum of the speed of sound $\bar{a}$ at the Widom line, the flow becomes supersonic at that location for $M_\infty \gtrsim 0.75$. This effect does not occur in Fig. 3.23(b) for transcritical wall cooling since the velocity profile exhibits significantly lower momentum in the near-wall region (see Sec. 3.3.3).

The growth-rate ratio r_β is shown in Figs. 3.24(a–c) for both transcritical cases as the free-stream Mach number increases. It is relevant to note that, for both cases, the growth rate of the most amplified 2-D mode, either Mode I or II, decreases with increasing Mach number. In Fig. 3.24(a), r_β of Mode I is shown only up to $M_\infty = 0.63$, because the Mode-I (TS-type) instability becomes stable for $M_\infty \gtrsim 0.77$ at this wall-to-free-stream temperature ratio T^*_w/T^*_∞. In fact, with increasing β and M_∞, the growth rate of Mode I decreases, indicating an overall stabilising influence of compressibility and the largest growth rates occurring for 2-D modes, in contrast to the results of Ren *et al.* (2019*b*). For the inviscid Mode II in Fig. 3.24(b), 3-D perturbations are more unstable than 2-D ones only from the transonic regime onwards ($M_\infty \gtrsim 0.77$), once a supersonic region appears around the Widom line as shown in Fig. 3.23(a). From $M_\infty \geq 0.63$, two local maxima of r_β emerge in the stability diagram: one at small β and low Reynolds number, which vanishes at large β, and another at large β and moderate Reynolds number, which becomes the global maximum for large β. In the transcritical wall-cooling case in Fig. 3.24(c), only a supersonic free stream can produce

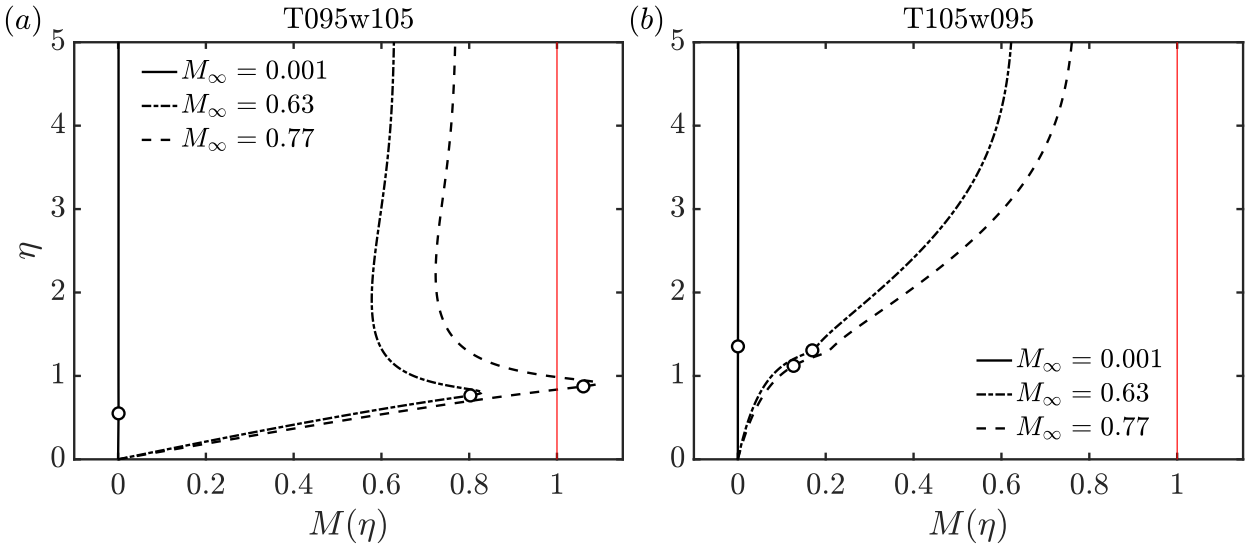

Figure 3.23: Wall-normal profile of the local Mach number $M(\eta)$ at three different free-stream Mach numbers $M_\infty = [0.001, 0.63, 0.77]$: (a) case 'T095w105', and (b) case 'T105w095'. The sonic line is marked in red.

a growth-rate ratio larger than unity. For subsonic boundary-layer flows, 2-D perturbations remain more unstable.

Figures 3.24(d–e) show the phase-speed ratio $\tilde{c}/\bar{u}_s$ of the corresponding unstable mode, where $\tilde{c} = c/\cos(\Psi)$ is the 3-D phase speed (Mack 1987) and $\bar{u}_s$ is the base-flow velocity at the GIP (index s). Note that $\tilde{c}$ coincides with $c_x = \omega/\alpha$, and is therefore independent of the wave orientation (Mack 1984). This is relevant for the later investigation in Sec. 3.4.2 in the inviscid limit ($Re \to \infty$), where the inviscid neutral wave has a phase speed of $\tilde{c} = c_x = \bar{u}_s$, with $\bar{u}_s = \bar{u}(y_s)$ (Mack 1984). Following the analysis in Sec. 3.3.3, the location of the GIP approximately corresponds to the location of the pseudo-critical point, i.e. the Widom line, and thus $y_s \approx y_{GIP} \approx y_{pc}$. In other words, the inviscid neutral wave with $c_x = \bar{u}_s \approx \bar{u}_{pc}$ has its critical layer at (or very close to) the GIP, in the immediate vicinity of the Widom line.

For transcritical heating in 'T095w105', the phase speed of Mode I in Fig. 3.24(d) exhibits a similar evolution to that observed for subcritical heating. Conversely, for Mode II in Fig. 3.24(e) as the spanwise wavenumber β increases, $\tilde{c}$ decreases initially, and then increases again. Moreover, the ratio $\tilde{c}/\bar{u}_s$ remains below unity, as the critical layer always lies below the GIP. For case 'T105w095', by contrast, the critical layer lies above the GIP and $\tilde{c}/\bar{u}_s$ is always greater than unity. Furthermore, the phase speed at large β is always lower than that of the most amplified 2-D wave at every subsonic M_∞. In both transcritical cases, the trend of $\tilde{c}/\bar{u}_s$ with increasing β, i.e. increasing Re, confirms that the phase-speed ratio of the amplified wave will eventually approach a value between $1 - 1/M_\infty$ and unity in the inviscid limit at $Re \to \infty$ (Mack 1984). Interestingly, as compressibility effects become significant ($M_\infty \geq 0.63$), the evolution of $\tilde{c}/\bar{u}_s$ appears to be linked to the growth-rate ratio and depends on whether the wall is heated or cooled. In the former, when $r_\beta < 1$, $\tilde{c}/\bar{u}_s$ increases with increasing β, whereas for $r_\beta > 1$, $\tilde{c}/\bar{u}_s$ decreases. In the latter, the opposite behaviour is observed.

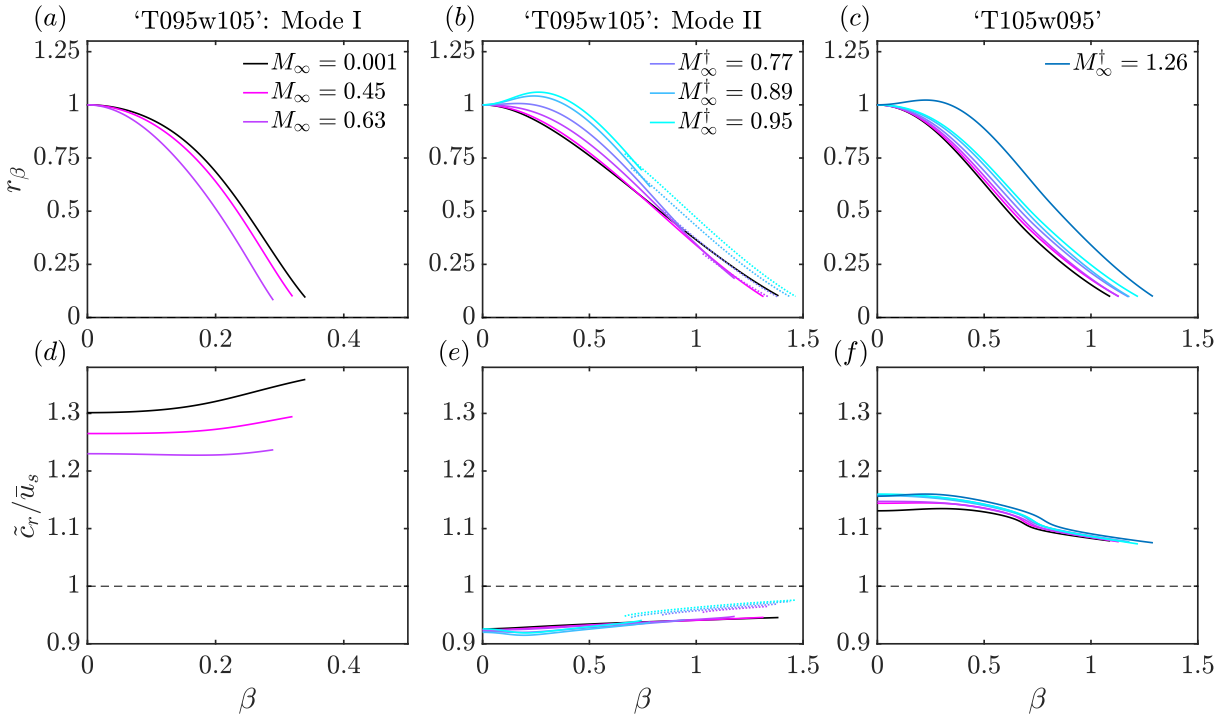

Figure 3.24: Evolution of the (a–c) growth-rate ratio r_β and (d–f) reduced 3-D phase speed $\tilde{c}/\bar{u}_s$, with $\bar{u}_s$ being the velocity at the GIP, as a function of the spanwise wavenumber β: (a,d) Mode I for transcritical heating 'T095w105', (b,e) Mode II for transcritical heating 'T095w105', and (c,f) transcritical cooling 'T105w095'. In (b), the dotted lines indicate the corresponding r_β of a second local maximum in the stability diagram. The superscript (†) indicates base-flow profiles with the local Mach number larger than unity (see Fig. 3.23). In (d–f), the dashed line indicates the inviscid neutral wave.

3.4.2 Inviscid analysis

In the limit of $Re \to \infty$, similarly to Sec. 3.3.2, we investigate the three-dimensionality of the inviscid mode in the transcritical state. The inviscid instability framework introduced in Sec. 3.2.2 is applied here with $\beta > 0$. At different free-stream Mach numbers, Figs. 3.25(a,b) present the growth-rate ratio r_β for cases 'T095w105' and 'T105w095', respectively, while Figs. 3.25(c,d) display the corresponding phase-speed ratio $\tilde{c}/\bar{u}_s$. The results confirm that increasing compressibility preferentially promotes 3-D waves, accompanied by a decrease in the 3-D phase speed once r_β increases. Viscous effects damp this behaviour, especially for case 'T105w095' which features a liquid-like, highly viscous near-wall region. For this case, the inviscid 3-D phase speed of the amplified wave lies below $\bar{u}_s$, in contrast to the viscous solution in Fig. 3.24(f), while the inviscid neutral wave retains $\tilde{c} = c_x = \bar{u}_s$. In other words, in the transcritical state, the inviscid amplified wave travels at $y < y_s$ with a phase speed smaller than the phase speed of the GIP, i.e. in the vicinity of the pseudo-critical point.

In the following, we further investigate the destabilisation of the inviscid neutral 2-D wave for finite spanwise wavenumbers as the Mach number increases. In the inviscid limit,

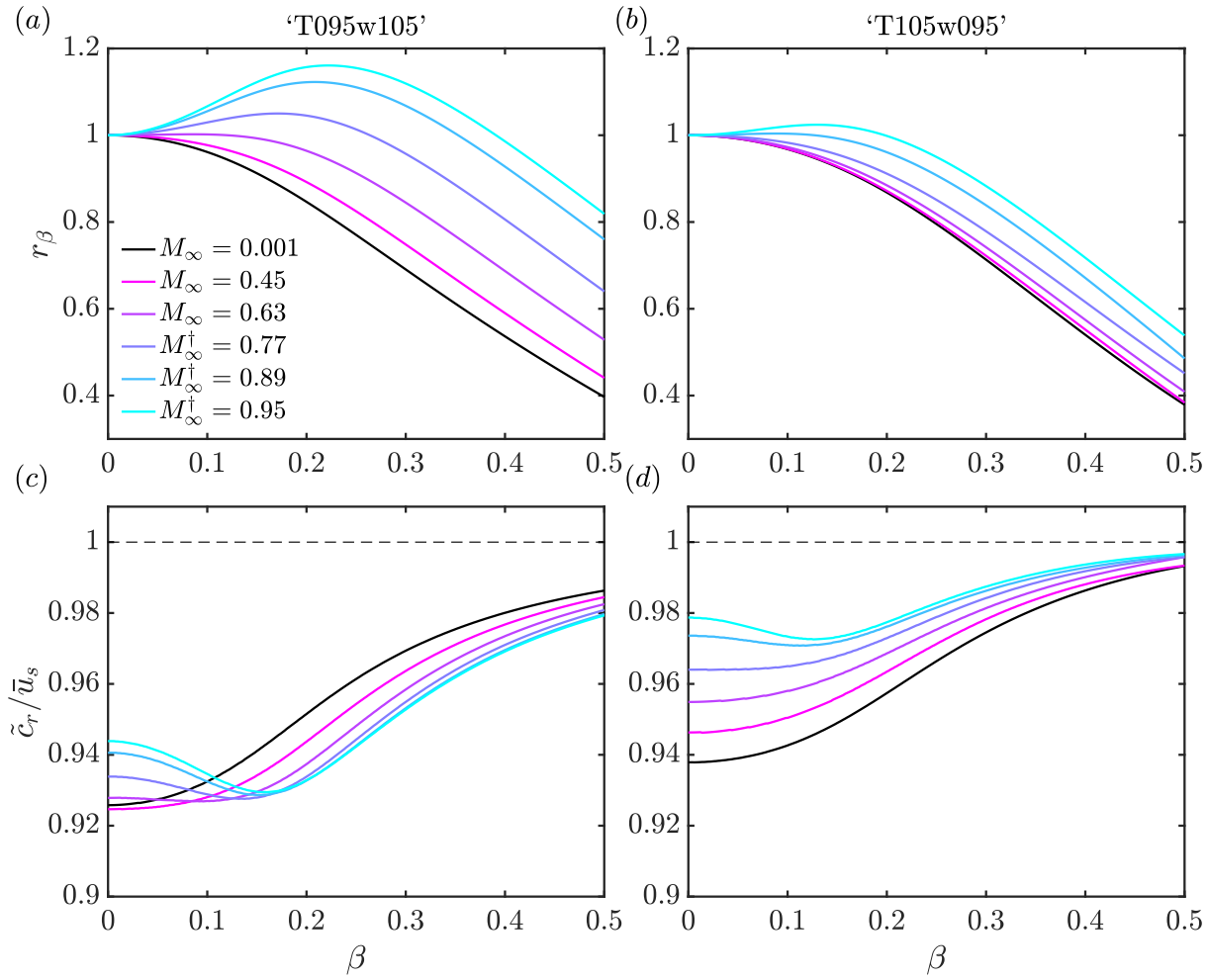

Figure 3.25: Evolution of the (a,b) growth-rate ratio r_β and (c,d) reduced 3-D phase speed $\tilde{c}/\bar{u}_s$, with $\bar{u}_s$ being the velocity at the GIP, as a function of the spanwise wavenumber β for different free-stream Mach numbers: (a,c) transcritical case 'T095w105', and (b,d) transcritical case 'T105w095'. The superscript (†) indicates base-flow profiles with the local Mach number larger than unity (see Fig. 3.23). In (d–f), the dashed line indicates the inviscid neutral wave.

the governing equation (Eq. (3.17)) can be written as

$$\hat{v}_{yy} + \frac{\zeta_{1,y}}{\zeta_1}\hat{v}_y - \left(\zeta_2 + \frac{\zeta_3}{\zeta_1}\right)\hat{v} = 0, \tag{3.43}$$

with

$$\zeta_1 = \frac{\bar{\rho}}{1 - M_r^2}, \quad \zeta_2 = (\alpha^2 + \beta^2)(1 - M_r^2), \quad \zeta_3 = \frac{(\zeta_1 \bar{u}_y)_y}{\bar{u} - c_x}. \tag{3.44a–c}$$

We adopt a temporal stability framework by prescribing the real streamwise and spanwise wavenumbers α_r and β_r, while treating the phase velocity c_x as a complex eigenvalue. This approach is consistent with the inviscid analysis of Lees & Lin (1946), who showed that a GIP is a necessary condition for the existence of amplified 2-D disturbances, provided that a neutral 2-D wave with wavenumber $\alpha = \alpha_s$ and $c_x = \bar{u}_s$ exists. Extending this approach

to 3-D instabilities, we consider a fixed streamwise wavenumber $\alpha_r > 0$, and treat c_x as an analytic function of β^2. Denoting $\lambda = \beta^2$, we expand $c_x(\beta^2)$ in a Taylor series around $\lambda = 0$:

$$c_x(\lambda) = c_x|_{\lambda=0,\alpha_r} + \lambda \left.\frac{\mathrm{d}c_x}{\mathrm{d}\lambda}\right|_{\lambda=0,\alpha_r} + \frac{\lambda^2}{2} \left.\frac{\mathrm{d}^2 c_x}{\mathrm{d}\lambda^2}\right|_{\lambda=0,\alpha_r} + \dots \tag{3.45}$$

If $\mathfrak{I}\{\mathrm{d}c_x/\mathrm{d}\lambda|_{\lambda=0,\alpha_r}\} \neq 0$, where $\mathfrak{I}\{\}$ denotes the imaginary part, then at first order in λ the growth rate increases or decreases depending on the sign of this quantity. This indicates that the neutral 2-D wave is destabilised by finite but small β^2. To evaluate this derivative, we differentiate Eq. (3.43) with respect to λ, obtaining

$$\begin{aligned}&\frac{\mathrm{d}}{\mathrm{d}y}\left(\zeta_1\hat{v}\frac{\mathrm{d}\hat{v}_\lambda}{\mathrm{d}y} - \zeta_1\hat{v}_\lambda\hat{v}_y\right) + \zeta_1\frac{\partial}{\partial\lambda}\left(\frac{\zeta_{1,y}}{\zeta_1}\right)\hat{v}\hat{v}_y - \zeta_1\frac{\partial}{\partial\lambda}\left(\zeta_2 + \frac{\zeta_3}{\zeta_1}\right)\hat{v}^2 \\ &= \left[-\zeta_1\frac{\partial}{\partial c_x}\left(\frac{\zeta_{1,y}}{\zeta_1}\right)\hat{v}\hat{v}_y - \zeta_1\frac{\partial}{\partial c_x}\left(\zeta_2 + \frac{\zeta_3}{\zeta_1}\right)\hat{v}^2\right]\frac{\mathrm{d}c_x}{\mathrm{d}\lambda},\end{aligned} \tag{3.46}$$

where the subscript $(\cdot)_\lambda$ denotes the total derivative with respect to λ, with $c_x = c_x(\lambda)$, as follows:

$$\frac{\mathrm{d}(\cdot)}{\mathrm{d}\lambda} = \frac{\partial(\cdot)}{\partial\lambda} + \frac{\mathrm{d}c_x}{\mathrm{d}\lambda}\frac{\partial(\cdot)}{\partial c_x}. \tag{3.47}$$

Integrating Eq. (3.46) from the wall up to $y_2 \to \infty$ and rearranging, the derivative $\mathrm{d}c_x/\mathrm{d}\lambda$ can be written as:

$$\frac{\mathrm{d}c_x}{\mathrm{d}\lambda} = \frac{\displaystyle\int_0^{y_2}\frac{\mathrm{d}}{\mathrm{d}y}\left(\zeta_1\hat{v}\frac{\mathrm{d}\hat{v}_\lambda}{\mathrm{d}y} - \zeta_1\hat{v}_\lambda\hat{v}_y\right)\mathrm{d}y + \int_0^{y_2}\zeta_1\frac{\partial}{\partial\lambda}\left(\frac{\zeta_{1,y}}{\zeta_1}\right)\hat{v}\hat{v}_y\mathrm{d}y - \int_0^{y_2}\zeta_1\frac{\partial}{\partial\lambda}\left(\zeta_2 + \frac{\zeta_3}{\zeta_1}\right)\hat{v}^2\,\mathrm{d}y}{\displaystyle\int_0^{y_2} -\zeta_1\frac{\partial}{\partial c_x}\left(\frac{\zeta_{1,y}}{\zeta_1}\right)\hat{v}\hat{v}_y\,\mathrm{d}y + \int_0^{y_2}\zeta_1\frac{\partial}{\partial c_x}\left(\zeta_2 + \frac{\zeta_3}{\zeta_1}\right)\hat{v}^2\,\mathrm{d}y}. \tag{3.48}$$

The first integral in the numerator of Eq. (3.48) simplifies to

$$\int_0^{y_2}\frac{\mathrm{d}}{\mathrm{d}y}\left(\zeta_1\hat{v}\frac{\mathrm{d}\hat{v}_\lambda}{\mathrm{d}y} - \zeta_1\hat{v}_\lambda\hat{v}_y\right)\mathrm{d}y = \left[\zeta_1\hat{v}\frac{\mathrm{d}\hat{v}_\lambda}{\mathrm{d}y} - \zeta_1\hat{v}_\lambda\hat{v}_y\right]_0^{y_2} = -\left[\zeta_1\hat{v}\frac{\mathrm{d}\hat{v}_\lambda}{\mathrm{d}y} + \zeta_1\hat{v}_\lambda\hat{v}_y\right]_{y_2}, \tag{3.49}$$

using the boundary conditions $\hat{v} = \hat{v}_\lambda = 0$ at $y = 0$ and as $y_2 \to \infty$. As $y_2 \to \infty$, the asymptotic behaviour of $\hat{v}_y$ and $\mathrm{d}\hat{v}_\lambda/\mathrm{d}y$ is

$$\hat{v}_y|_{y\to\infty} = -\sqrt{(\alpha^2+\beta^2)(1-M_r^2)}\,\hat{v}_\infty, \tag{3.50}$$

$$\left.\frac{\mathrm{d}\hat{v}_\lambda}{\mathrm{d}y}\right|_{y\to\infty} = -\sqrt{(\alpha^2+\beta^2)(1-M_r^2)}\,(\hat{v}_\lambda)_\infty - \frac{\mathrm{d}}{\mathrm{d}\lambda}\left(\sqrt{(\alpha^2+\beta^2)(1-M_r^2)}\right)\hat{v}_\infty. \tag{3.51}$$

Since $\hat{v}|_{y_2\to\infty} = 0$, the contribution in the first integral (Eq. (3.49)) vanishes. The remaining partial derivatives in the expression for $\mathrm{d}c_x/\mathrm{d}\lambda$ are given by

$$\frac{\partial}{\partial\lambda}\left(\frac{\zeta_{1,y}}{\zeta_1}\right) = \frac{-(M_r^2)_y}{(\alpha^2+\beta^2)(1-M_r^2)^2}, \tag{3.52}$$

$$\frac{\partial}{\partial\lambda}\left(\zeta_2 + \frac{\zeta_3}{\zeta_1}\right) = 1 - \frac{2\alpha^2 M_\infty^2}{\bar{a}(\alpha^2+\beta^2)^2(1-M_r^2)^2}\left(\frac{\bar{u}-c_x}{\bar{a}}\right)_y\bar{u}_y, \tag{3.53}$$

$$\frac{\partial}{\partial c_x}\left(\frac{\zeta_{1,y}}{\zeta_1}\right) = \frac{-2\alpha^2 M_\infty^2}{\bar{a}(\alpha^2+\beta^2)(1-M_r^2)}\left[\left(\frac{\bar{u}-c_x}{\bar{a}}\right)_y\left(1 + \frac{2M_r^2}{1-M_r^2}\right) - (\bar{u}-c_x)\frac{\bar{a}_y}{\bar{a}^2}\right], \tag{3.54}$$

$$\frac{\partial}{\partial c_x}\left(\zeta_2 + \frac{\zeta_3}{\zeta_1}\right) = \frac{(\bar{\rho}\bar{u}_y)_y}{\bar{\rho}(\bar{u}-c_x)^2} + \frac{2\alpha^2 M_\infty^2}{\bar{a}^2}\left[(\bar{u}-c_x) + \frac{\bar{u}_y}{(\alpha^2+\beta^2)(1-M_r^2)}\left(\frac{\bar{a}_y}{\bar{a}} - \frac{(M_r^2)_y}{1-M_r^2}\right)\right]. \tag{3.55}$$

The term

$$\frac{(\bar{\rho}\bar{u}_y)_y}{\bar{\rho}(\bar{u}-c_x)^2}, \tag{3.56}$$

is the only singular contribution in the expression for $\mathrm{d}c_x/\mathrm{d}\lambda$, and appears in the denominator. All other terms are real and finite when evaluating the integrals in Eq. (3.48) for the neutral wave with $c_x = \bar{u}_s$. As shown by Lees & Lin (1946), the point where $M_r^2 = 1$ is only an apparent singularity in Eq. (3.43); the genuine singularity arises when $\bar{u} = c_x$. Hence, for the neutral wave with $c_x = \bar{u}_s$ (corresponding to $\alpha = \alpha_s$), the sign of the imaginary part of $\mathrm{d}c_x/\mathrm{d}\lambda$ is controlled by

$$\mathrm{sign}\left\{-\mathcal{N} \times \Im\{\mathcal{D}\}\right\}, \tag{3.57}$$

where $\mathcal{N}$ and $\mathcal{D}$ denote the numerator and denominator of the expression for $\mathrm{d}c_x/\mathrm{d}\lambda$, respectively. Lees & Lin (1946) further expanded the singular term in Eq. (3.56), showing that its imaginary part in Eq. (3.48) can be written as

$$\Im\left\{\int_0^{y_2}\left[\frac{\zeta_1}{\bar{\rho}(\bar{u}-c_x)^2}(\bar{\rho}\bar{u}_y)_y\right]\hat{v}^2\,\mathrm{d}y\right\} = \pi|\hat{v}_{cr}|^2\left[\frac{(\bar{\rho}\bar{u}_y)_{yy}|_{cr}}{(\bar{u}_{cr})_y^2}\right], \tag{3.58}$$

where the subscript $(\cdot)_{cr}$ indicates that the function is evaluated at the critical layer, $y = y_{cr} = y_s \approx y_{pc}$. At this location, following the analysis in Sec. 3.3.3, one finds $(\bar{\rho}\bar{u}_y)_y \approx -\bar{\rho}\bar{u}_y\bar{\nu}_y/\bar{\nu}$. Moreover, under pseudo-boiling, the kinematic viscosity $\bar{\nu}$ attains a minimum at the GIP. Thus, it holds that $(\bar{\rho}\bar{u}_y)_{yy}|_{cr} \approx -\bar{\rho}\bar{u}_y\bar{\nu}_{yy}/\bar{\nu}|_{cr}$. Since $\bar{u}_y|_{cr} > 0$ and $\bar{\nu}_{yy}|_{cr} > 0$, the right-hand-side of Eq. (3.58) is negative. This satisfies the Fjørtoft's theorem extended to variable-density flows (see Sec. 3.5.2 and Bugeat *et al.* (2024)), which can be written as

$$(\bar{\rho}\bar{u}_y)_{yy}|_{cr} < 0, \tag{3.59}$$

and is equivalent to observing a maximum of $\bar{\rho}\bar{u}_y$ at the GIP in the base-flow profile. Consequently, the inequality in Eq. (3.58) implies:

$$\Im\{\mathcal{D}\} < 0, \quad \text{for} \quad \alpha = \alpha_s. \tag{3.60}$$

Note that, since M_r^2 is everywhere below unity in the boundary layers considered, there is a unique wavenumber α_s corresponding to $\bar{u}_s$ for the neutral subsonic wave (Mack 1984). Recalling the sign relation in Eq. (3.57), an inviscid neutral 2-D wave is amplified for $\beta > 0$ if the numerator is positive. The numerator of Eq. (3.48) can be written as:

$$\mathcal{N} = \underbrace{\int_0^{y_2} -\zeta_1\hat{v}^2\,\mathrm{d}y}_{a_1} + \underbrace{\int_0^{y_2}\frac{\zeta_1(M_r^2)_y}{(\alpha^2+\beta^2)(1-M_r^2)^2}\left(\frac{\bar{u}_y}{\bar{u}-c_x}\hat{v}^2 - \hat{v}\hat{v}_y\right)\mathrm{d}y}_{a_2+a_3}. \tag{3.61}$$

In the incompressible limit $M_\infty \to 0$, the relative Mach number M_r vanishes. The leftmost integral a_1 in Eq. (3.61) is then the only non-zero term, with $\zeta_1 = \bar{\rho}$. Since its integrand is negative for all y, it follows that $a_1 < 0$, and therefore $\Im\{\mathrm{d}c_x/\mathrm{d}\lambda\} < 0$. Hence, in the incompressible limit $M_\infty \to 0$, the neutral inviscid wave with $\alpha = \alpha_s$ is most amplified for

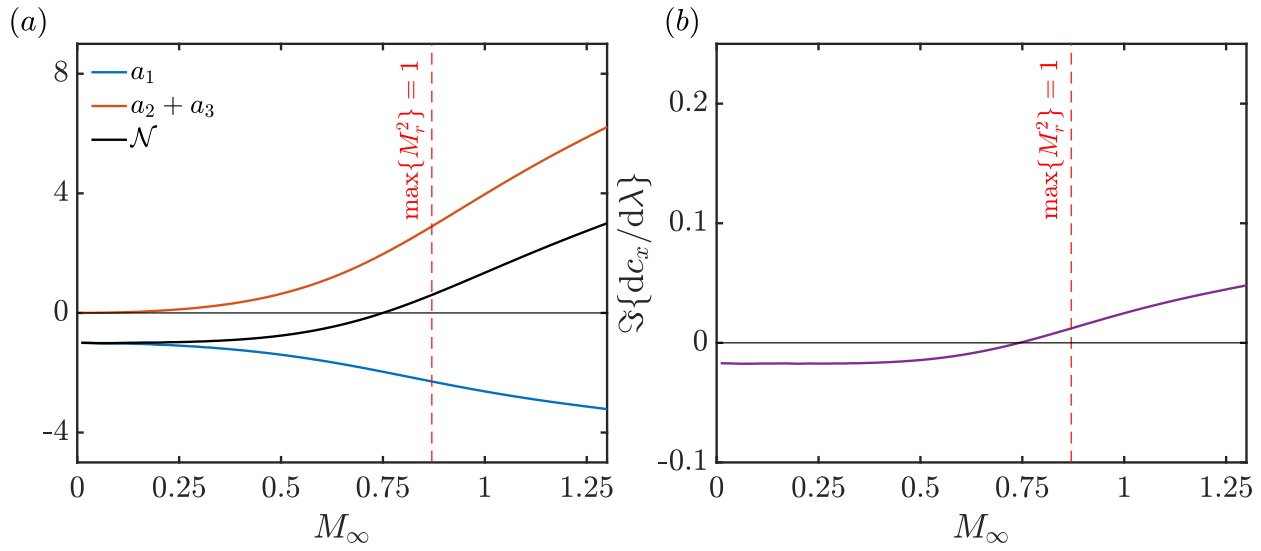

Figure 3.26: Analysis of the inviscid neutral 2-D wave with $\alpha = \alpha_s$ and $c_x = \bar{u}_s$ for the transcritical case 'T095w105': evolution of (a) the numerator terms a_1, $a_2 + a_3$, and the numerator $\mathcal{N}$ in Eq. (3.61), and (b) the imaginary part of $\mathrm{d}c_x/\mathrm{d}\lambda$ in Eq. (3.48) as a function of the free-stream Mach number. The red dashed line indicates the sonic line of the neutral wave, for which the maximum relative Mach number $\max\{M_r^2\}$ is equal to unity.

$\beta = 0$, i.e. for purely 2-D perturbations. For $M_r \neq 0$, the remaining terms in the numerator in Eq. (3.61), namely $a_2 + a_3$, can be written as:

$$\underbrace{\int_0^{y_2} \zeta_1 \frac{-(M_r^2)_y}{(\alpha^2+\beta^2)(1-M_r^2)^2} \hat{v}\hat{v}_y \,\mathrm{d}y}_{a_2} + \underbrace{\int_0^{y_2} \zeta_1 \frac{2\alpha^2 M_\infty^2}{\bar{a}(\alpha^2+\beta^2)^2(1-M_r^2)^2} \left(\frac{\bar{u}-c_x}{\bar{a}}\right) \bar{u}_y \hat{v}^2 \,\mathrm{d}y}_{a_3}. \tag{3.62}$$

Now consider a subsonic wave, i.e. $|M_r| < 1$, such that $\zeta_1 > 0$, and assume that M_r increases monotonically with the wall-normal coordinate y, i.e. $[(\bar{u}-c_x)/\bar{a}]_y \geq 0$. Under this assumption, the integrand of a_1 in Eq. (3.61) remains negative for all y, so $a_1 < 0$. Regarding a_2 in Eq. (3.62), the quantity M_r^2 decreases for $y < y_c$ and increases for $y > y_c$, while the perturbation $\hat{v}$ typically increases for $y < y_c$ and decreases for $y > y_c$. Since all other factors in the integrand of a_2 are positive, the overall integral a_2 is expected to be positive ($a_2 > 0$). Similarly, the integrand of a_3 is positive for all y, and therefore $a_3 > 0$. While both a_2 and a_3 vanish when $M_\infty = 0$, they are expected to be positive as soon as $M_\infty > 0$. Thus, increasing Mach number contributes positively to the amplification of the neutral wave with $\alpha = \alpha_s$ for $\beta^2 > 0$.

Figure 3.26 illustrates this effect for the transcritical-heating case 'T095w105' in the temporal framework. The 2-D neutral wave with $c_x = \bar{u}_s$ is considered, where both $\bar{u}_s$ and the corresponding wavenumber α_s vary with the Mach number. The wall-normal velocity perturbation $\hat{v}$ is normalised by its maximum absolute value, i.e. $\max\{|\hat{v}|\}$. The derivative $\mathrm{d}c_x/\mathrm{d}\lambda$ is computed using the integral expression in Eq. (3.48) and validated against solutions of the inviscid eigenvalue problem in Eq. (3.16) for increasing values of β^2. In Fig. 3.26(a), the combined contribution of $a_2 + a_3$ in the numerator $\mathcal{N}$ of Eq. (3.61) confirms that these terms contribute positively to the growth of $\mathrm{d}c_x/\mathrm{d}\lambda$. In the limit $M_\infty \to 0$, however, the negative term a_1 dominates the numerator. In Fig. 3.26(b), the neutral wave with $\alpha = \alpha_s$

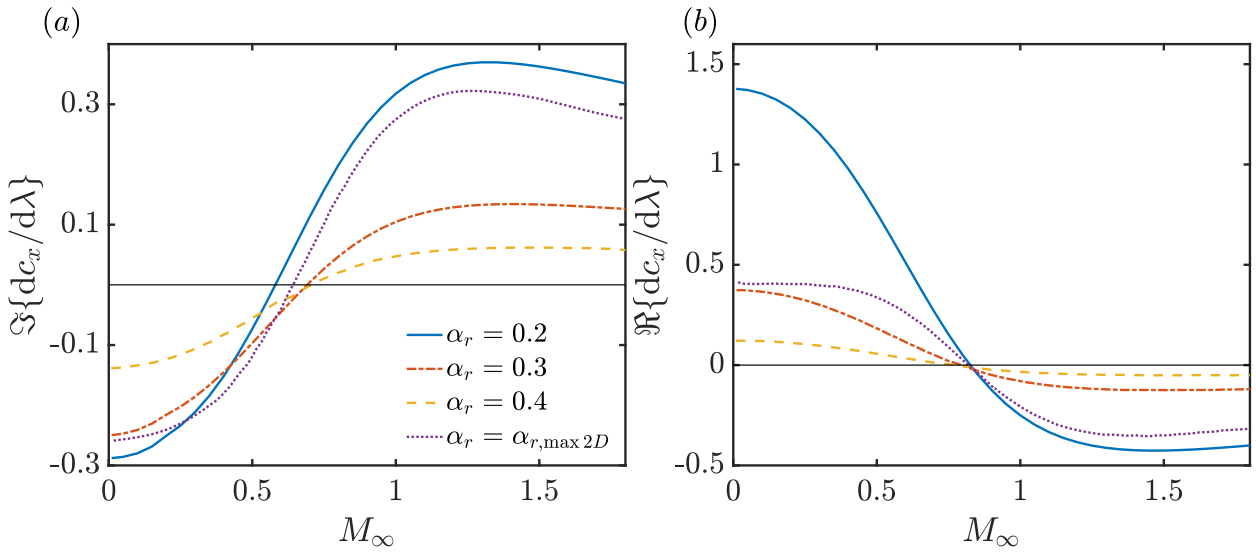

Figure 3.27: Evolution of $\mathrm{d}c_x/\mathrm{d}\lambda$ for amplified inviscid waves with different α_r for the transcritical case 'T095w105': (a) the imaginary part (growth-rate ratio) and (b) the real part (phase speed), both as functions of the free-stream Mach number. The neutral wave with maximum 2-D amplification is indicated by $\alpha_r = \alpha_{r,max2\mathrm{D}}$.

exhibits increasing amplification for $\beta^2 > 0$ even within the subsonic regime, where 'subsonic' refers to the relative Mach number M_r satisfying $M_r^2 < 1$. Moreover, the imaginary part of $\mathrm{d}c_x/\mathrm{d}\lambda$ continues to rise into the supersonic regime, indicating sustained amplification of 3-D disturbances.

We now consider amplified waves adjacent to the neutral wave at $(\alpha_s, \bar{u}_s)$. Figure 3.27 shows both the imaginary and real parts of $\mathrm{d}c_x/\mathrm{d}\lambda$ for three selected values of α_r, as well as for $\alpha_r = \alpha_{r,\max 2D}$, which maximises the amplification of the 2-D wave for each free-stream Mach number. As M_∞ increases, the imaginary part of $\mathrm{d}c_x/\mathrm{d}\lambda$ becomes positive, while the real part becomes negative. This trend mirrors the behaviour observed in Fig. 3.25: an increase in the growth-rate ratio (corresponding to $\Im(\mathrm{d}c_x/\mathrm{d}\lambda) > 0$) and a decrease in the phase speed c_x (corresponding to $\Re(\mathrm{d}c_x/\mathrm{d}\lambda) < 0$ for small values of β^2. Finally, for large Mach numbers, e.g. $M_\infty \gtrsim 1.5$, both the real and imaginary parts of $\mathrm{d}c_x/\mathrm{d}\lambda$ tend to decrease in magnitude. This is consistent with the asymptotic limit $M_\infty \to \infty$, in which all terms in the numerator of the expression for $\mathrm{d}c_x/\mathrm{d}\lambda$ in Eq. (3.48) vanish. In this limit, the three-dimensionality of the neutral 2-D wave depends on higher-order terms in the Taylor expansion of $c_x(\lambda)$ in Eq. (3.45), which are neglected in the present analysis.

3.5 Model: strongly-stratified plane Couette flow

The inviscid stability of a strongly density- and viscosity-stratified plane Couette flow is examined by considering a differentially heated configuration. Three fluid models are first investigated, with different density and dynamic viscosity laws that vary strongly with temperature. Different types of stratification are then observed in the flow; however, the three

fluid models are designed to all feature a minimum of kinematic viscosity. In doing so, we aim to demonstrate the central role played by this minimum in the stability of the systems, regardless of the other property variations in the flow. Using piecewise linear base-flow approximations, analytical results are derived by solving the Rayleigh equation in the presence of strong density gradients, which governs the inviscid linear stability of these flows. A more realistic fluid model based on the VdW EoS (Sec. 2.2.2) and diffusion laws (Sec. 2.3.2) at supercritical pressure is used to ultimately discuss the instability in supercritical fluids. Buoyancy is ignored, but density variations are retained in the inertial terms. Acoustics are not taken into account in order to remove potential ambiguities in the physical interpretation of the results with acoustic instabilities. The low-Mach approximation is used. As a result, no viscous heating is at play; temperature gradients are generated in the flow by boundary conditions. Finally, only inviscid perturbations are considered.

The goal of this section is to demonstrate that inviscid instabilities in strongly stratified shear flows can arise from the presence of a minimum in kinematic viscosity. In particular, we seek to provide evidence that the recently observed unstable Mode II in supercritical fluids is linked to the minimum of kinematic viscosity occurring at the Widom line, as shown in Sec. 3.3.3. We further aim to identify the underlying physical mechanisms driving these instabilities.

3.5.1 Theoretical and numerical framework

Fluid models

Four fluids are considered throughout this section, each of them being associated with a different EoS and viscosity law. However, they all share the common property of assuming an extremum of kinematic viscosity ν at a given temperature. Recalling that $\nu = \mu/\rho$, different ways to generate a minimum of ν can be imagined. Three theoretical fluid models are used to control and study a restricted number of parameters. A fourth more realistic model for supercritical fluids, based on the VdW EoS, is considered. A summary of the different fluids is provided in Fig. 3.28, while a detailed description is given in the following:

- Fluid VB (bump of dynamic viscosity with constant density): in this model, density is assumed constant, while the viscosity is chosen to locally exhibit a bump at a temperature T_m^*, using a Gaussian function (in this section, all dimensional quantities are denoted by the superscript $(\cdot)^*$). Note that, in this case, the non-dimensional kinematic viscosity is equal to the non-dimensional dynamic viscosity, both reading

$$\mu = \nu = 1 + A_v \exp\left(-\left(\frac{T-1}{\delta T_v}\right)^2\right), \tag{3.63}$$

  using T_m^* as the reference temperature. The reference viscosities are μ_∞^* and ν_∞^*, which are the asymptotic values away from the bump. The parameter A_ν controls the amplitude of the bump, and its sign determines whether the kinematic viscosity admits a minimum ($A_\nu < 0$) or a maximum ($A_\nu > 0$). The characteristic width of the bump is

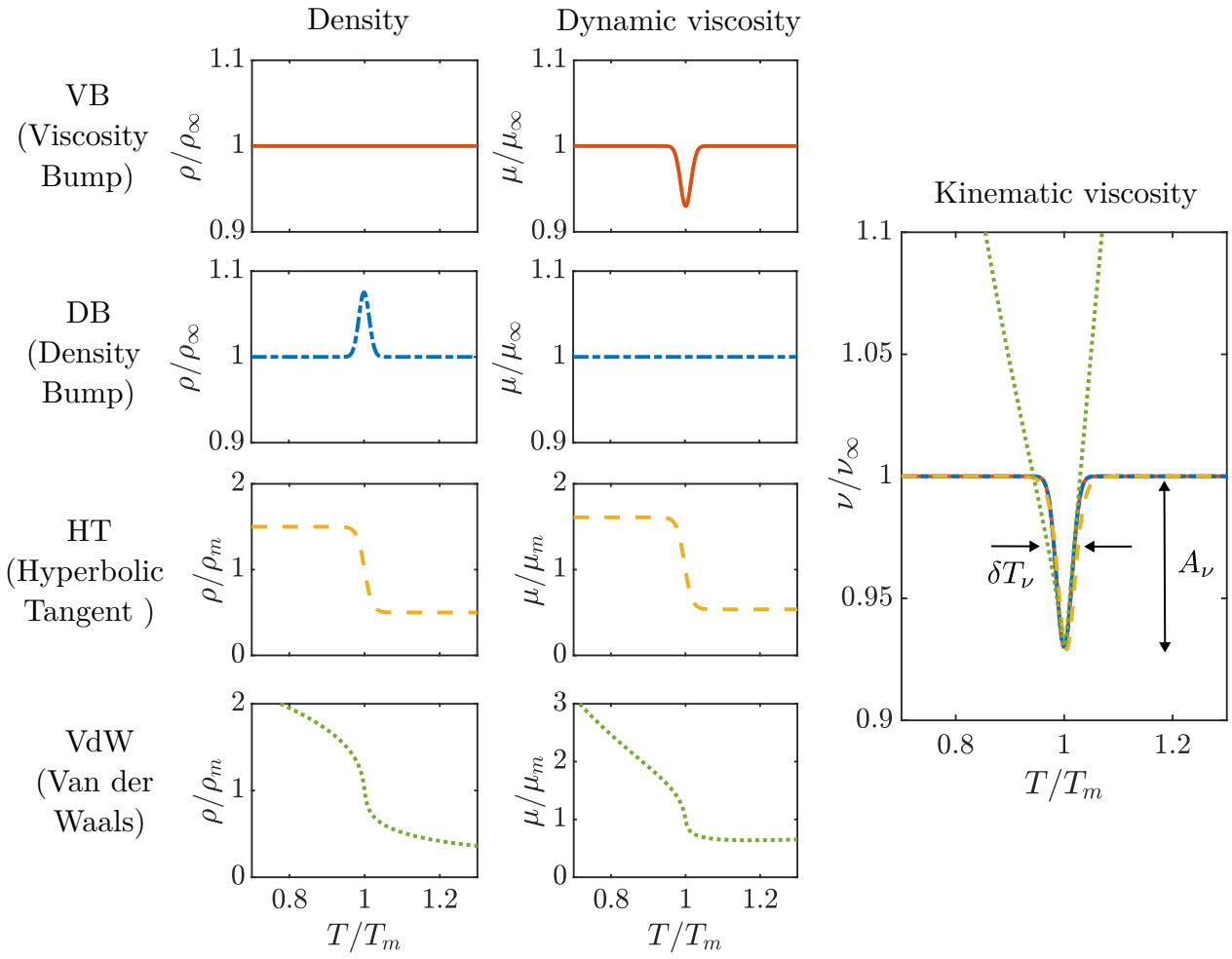

Figure 3.28: The four fluid models considered in this section.

set through δT_ν, which is again made non-dimensional using T_m^*. Finally, the thermal conductivity κ is assumed to be constant.

- Fluid DB (bump of density with constant dynamic viscosity): inversely to fluid VB, μ is kept constant in fluid DB while a bump is introduced in the density profile. This bump is chosen such that the resulting kinematic viscosity has the same expression as in Eq. (3.63). Hence, the density law simply reads

$$\rho = \frac{1}{1 + A_\nu \exp\left(-\left(\dfrac{T-1}{\delta T_\nu}\right)^2\right)}, \tag{3.64}$$

  and since, in this case, $\nu = 1/\rho$, ν is the same as in fluid VB. The conductivity κ is again chosen to be constant.

- Fluid HT (hyperbolic tangent laws): thermal conductivity is also kept constant, while dynamic viscosity and density are now both allowed to vary according to hyperbolic tangent laws. In order to generate an extremum of kinematic viscosity, a small shift is introduced between the two hyperbolic tangents, controlled by the non-dimensional parameter ϵ_T . This choice is inspired by supercritical fluids and represents an attempt

to mimic some of their features in the vicinity of the pseudo-boiling region. The non-dimensional governing laws for fluid HT are formally written as

$$\rho = 1 - \gamma \tanh\left[\frac{T-1}{\delta T_{\mu,\rho}}\right], \tag{3.65}$$

$$\mu = 1 - \gamma \tanh\left[\frac{T-(1+\varepsilon_T)}{\delta T_{\mu,\rho}}\right]. \tag{3.66}$$

The reference temperature $T_m^\star$ is here defined as the point of anti-symmetry of the density profile. The density at $T = 1$ and the viscosity at $T = 1 + \epsilon_T$ are used as the reference scales. The parameter γ controls the jump of density and dynamic viscosity while $\delta T_{\mu,\rho}$ sets the temperature range over which this jump takes place. The fluid properties are shown in Fig. 3.28, where it is verified that the kinematic viscosity admits a minimum around $T = 1$. By analogy with fluids VB and DB, it is possible to estimate the amplitude A_ν of this minimum, as well as the characteristic width δT_ν of the temperature range over which it occurs. The following relations will be used in this analysis:

$$A_\nu = \frac{\gamma \varepsilon_T}{\delta T_{\mu,\rho}}, \tag{3.67}$$

$$\delta T_\nu = 1.2 \delta T_{\mu,\rho}. \tag{3.68}$$

The derivation and verification of these expressions are detailed in Bugeat *et al.* (2024).

- Fluid VdW (a model for supercritical fluids): the reduced VdW EoS is used and can be found in Eqs. (2.12*a–c*). For the diffusion laws, the JST models in Sec. 2.3.2 are used for the dynamic viscosity and the thermal conductivity. Note that the reference temperature, here again noted $T_m^\star$ to maintain consistency with the previous fluids, is usually termed pseudo-boiling or pseudo-critical temperature in supercritical fluids. Density and dynamic viscosity are strongly correlated, and both exhibit strong gradients in the pseudo-boiling region. This motivated the choice of fluid HT, where density and viscosity are both defined using a hyperbolic tangent function, aiming to capture these gradients while neglecting variations elsewhere. The kinematic viscosity admits a minimum around the pseudo-critical temperature but is not localised, as opposed to the other fluids. The relatively simple model of fluid HT is found to reproduce this minimum reasonably well as a result of the shift ϵ_T introduced between the hyperbolic tangent laws, but differs away from this point since ν remains strictly constant in fluid HT. In analogy to the previous fluids, the characteristic scales δT_ν and A_ν are extracted from the kinematic viscosity law as

$$\delta T_\nu = T_2 - T_1, \tag{3.69}$$

$$A_\nu = \frac{\nu_e}{\nu_e + 2(\nu_{av} - \nu_e)} - 1, \tag{3.70}$$

where T_1 and T_2 ($T_1 < T_m < T_2$) are the temperatures at the two inflection points of $\nu(T)$, and $\nu_e + 2(\nu_{av} - \nu_e)$ is the reference viscosity, with $\nu_{av} = (\nu_1 + \nu_2)/2$. Finally, note

that the reduced pressure is the control parameter of the kinematic viscosity seen as a function of the temperature. Consequently, $\nu(T)$ differs for each reduced pressure p_r and, therefore, so do δT_ν and A_ν.

Base flow

Plane Couette flow occurs between two plates and is driven by the upper plate moving at speed u_1^*, which is used as the reference velocity scale. The streamwise and wall-normal directions are denoted by x and y, respectively. The flow is assumed to be parallel: the streamwise velocity u does not depend on x, and the wall-normal and spanwise components of the velocity v and w, respectively, are zero. The lower plate is fixed and, given the no-slip conditions, the non-dimensional streamwise velocity at the boundaries verifies $u(0) = 0$ and $u(1) = 1$. The distance h^* between the two plates is used as the reference length scale. The lower plate is kept at temperature T_0^*, chosen as the reference temperature. We choose to consider the non-dimensional temperature gradient τ between the two plates as an input parameter, which in turn sets the temperature of the upper plate. The boundary conditions for the temperature are then $T(0) = 1$ and $T(1) = 1 + \tau$. Under the assumption of a steady flow without pressure gradient, the flow is driven by the top wall, the non-dimensional NS equations (see Eq. 2.1) reduce to a system of ordinary differential equations:

$$\left(\bar{\mu}\bar{u}_y\right)_y = 0, \tag{3.71}$$

$$\left(\bar{\kappa}\bar{T}_y\right)_y = 0. \tag{3.72}$$

The inertial terms are zero given the parallel flow assumption, and the problem does not depend on the Reynolds and Prandtl numbers. Besides, the temperature is decoupled from the velocity field. When κ is constant, as it is supposed to be in fluids VB, DB and HT, the temperature profile is readily obtained as $\bar{T}(y) = 1 + \tau y$. As for fluid VdW, Eq. (3.72) is solved using Newton's method by setting the initial guess as the aforementioned linear profile. Once $\bar{T}$ is obtained, the density profile is also known via the EoS. The velocity profile is finally obtained by integration of Eq. (3.71) with the knowledge of the dynamic viscosity profile as a function of T and ρ. Finally, note that we make the arbitrary choice to locate the extremum of kinematic viscosity at the centre line of the flow, $y = 1/2$. This is achieved by accordingly setting $T_m^*/T_0^* = 1 + \tau/2$ under the assumption that the temperature profile is linear - which is indeed the case for fluids VB, DB and HT.

The base flows associated with the three fluid models VB, DB and HT are presented in Figs. 3.29(a–c). The density and dynamic viscosity profiles have the same behaviour as those presented in Sec. 3.5.1 – the constant temperature gradient of the base flow providing a linear mapping from T to y. Different velocity profiles are observed. In fluid VB, stronger gradients are present in the centre, where dynamic viscosity decreases. This is a result of the conservation of $\bar{\mu}\bar{u}_y$ across the flow, yielding $\bar{u}_y \propto 1/\bar{\mu}$. While almost imperceptible in Fig. 3.29(a), the presence of these stronger gradients is clearly visible in Fig. 3.29(d), where the profile of $|\Phi|$ with $\Phi = -\bar{\rho}\bar{u}_y$, i.e. the density-weighted vorticity (see Sec. 3.5.2), is shown.

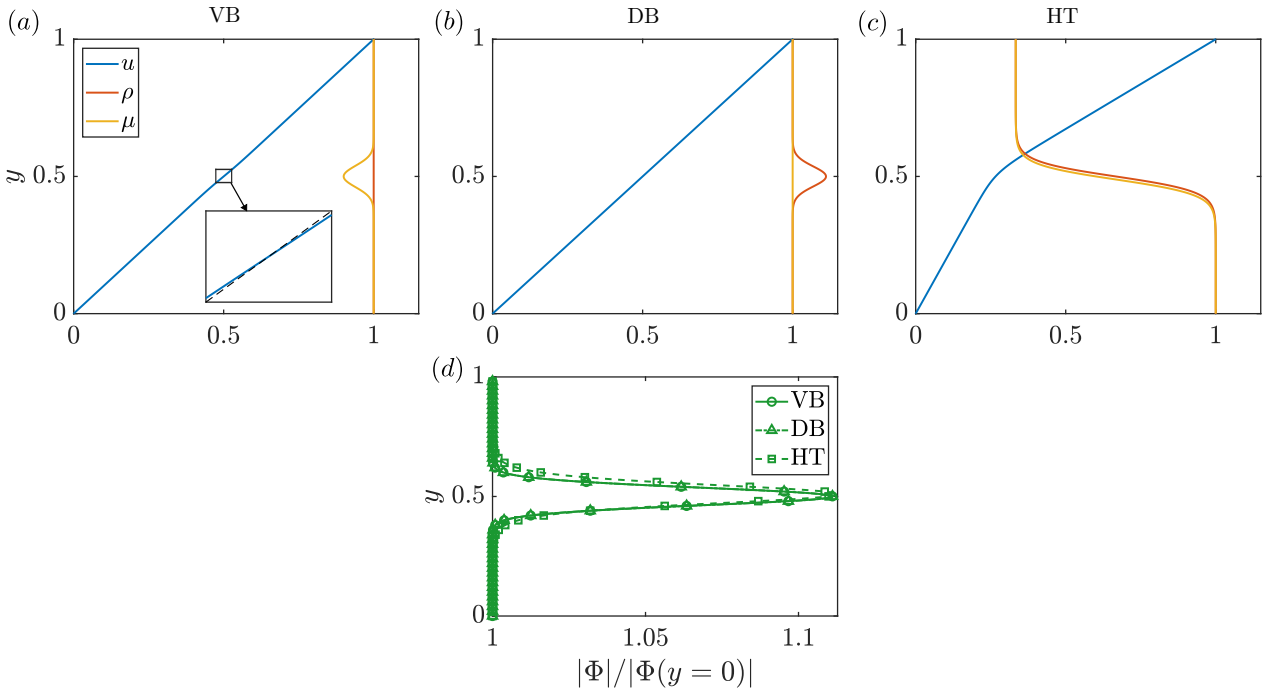

Figure 3.29: (a–c) Base-flow profiles of fluids VB, DB and HT, for $\delta T_\nu = 10^{-2}$, $A_\nu = -10^{-1}$, and $\tau = 0.2$. The inset in (a) is a close-up of the velocity profile in the central region, with a comparison with the linear function $f(y) = y$ shown by the black dashed line. (d) Resulting profile of $|\Phi|$ for each fluid.

Indeed, in the case of fluid VB, density is constant and $|\Phi|$ reduces to $|\Omega = -\bar{u}_y|$. As for fluid DB, the velocity profile is linear (Fig. 3.29b) since the viscosity is constant. Vorticity is therefore constant, but $|\Phi|$ still assumes a maximum at the centre as it now follows the density profile. Turning to fluid HT, the velocity profile features two regions of distinct gradient, which are, again, a consequence of the viscosity distribution (Fig. 3.29c). The resulting profile of $|\Phi|$, exhibiting a maximum in the central region as in the two previous fluids, is here a combination of the variations of density and vorticity. In summary, all fluids feature an excess of $|\Phi|$ in the central region. The normalised profiles of $|\Phi|$ all collapse (Fig. 3.29d) since identical parameters δT_ν and A_ν are chosen for each fluid. Note that we will only consider $A_\nu < 0$ in order to generate a maximum of $|\Phi|$, since no instability can occur otherwise according to the generalised Fjørtoft criterion (see Sec. 3.5.2).

A typical base flow of fluid VdW is shown in Fig. 3.30. The general behaviour is similar to that observed for fluid HT in Fig. 3.29(c), the latter being, indeed, an attempt to model some important features of the former. Two regions of markedly different shear rate can be identified. The density and dynamic viscosity profiles are not as simple as in fluid HT: strong gradients are present in the central region, but properties also exhibit weaker variations away from it. The resulting profile of $|\Phi|$ in Fig. 3.30(b) follows that of the kinematic viscosity profile, presented in Fig. 3.28. Note that, in contrast to the previous fluids, the minimum of $\bar{\nu}$ is not exactly reached at $y = 1/2$ but is shifted upwards. This is linked to the procedure used to set the location of the minimum through the reference temperature at the wall and based on the assumption of a constant temperature gradient. This assumption is not exact

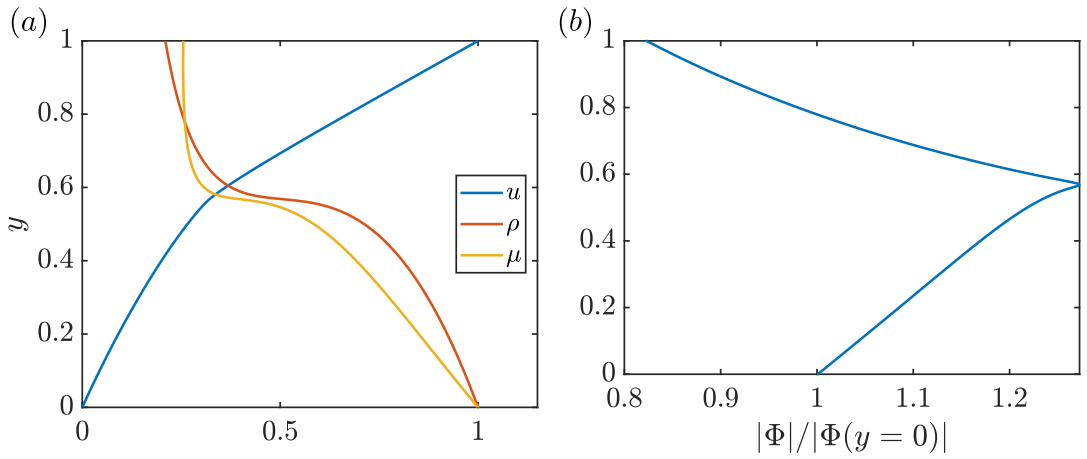

Figure 3.30: Base-flow profile of fluid VdW at $p_r = 1.06$ and $\tau = 0.5$. (a) Velocity, density and dynamic viscosity profiles. (b) Normalised density-weighted vorticity profile.

for fluid VdW as thermal conductivity varies, causing the observed shift.

Rayleigh equation for strong density gradients

Perturbations of the form $\mathbf{q}'(x,y,t) = \Re\{\hat{\mathbf{q}}(y)\exp(\mathrm{i}(\alpha x - \omega t))\}$ are now considered, where $\mathbf{q}' = [u', v', T']^{\mathrm{T}}$ is the state vector of the perturbations. Given $M_r = 0$ and $\beta = 0$, the inviscid linearised stability equation in Eq. (3.18) can then be recast into the Rayleigh equation governing the linear dynamics of incompressible flows with strong density gradients (see also Fontane & Joly (2008)) as

$$\bar{\rho}(\bar{u} - c)\left[\hat{v}_{yy} + \frac{\bar{\rho}_y}{\bar{\rho}}\hat{v}_y - \alpha^2\hat{v}\right] - \left(\bar{\rho}\bar{u}_y\right)_y\hat{v} = 0, \tag{3.73}$$

where $c = \omega/\alpha$ is the complex phase velocity. Note that the disturbance temperature does not appear in Eq. (3.73) since the linearised mass and momentum equations are decoupled from the energy equation (low-Mach approximation; see **?**). Temperature disturbances are deduced from the hydrodynamic disturbances, which can be calculated independently. Thermal effects are, however, at play in the velocity and density profiles of base flow, which the momentum equations, and ultimately the Rayleigh equation in Eq. (3.73), depend on. A temporal framework is adopted.

In order to interpret some results, it can be useful to consider an alternative formulation of the problem in terms of the disturbance vorticity $\xi' = \partial v'/\partial x - \partial u'/\partial y$. For a parallel base flow without pressure gradients, ξ' is governed, in the physical space, by the linear equation

$$\frac{\partial \xi'}{\partial t} + \bar{u}\frac{\partial \xi'}{\partial x} = \underbrace{-\Omega_y v'}_{S_\xi} \underbrace{-\frac{\bar{\rho}_y}{\bar{\rho}^2}\frac{\partial p'}{\partial x}}_{B_\xi}, \tag{3.74}$$

where $\Omega = -\bar{u}_y$ is the vorticity of the base flow. The left-hand side represents the material derivative of ξ' by the base flow. The right-hand side corresponds to vorticity sources, which may induce an instability. The term S_ξ is the production of vorticity responsible for shear

flow instabilities. The second term, B_ξ, is the baroclinic torque, which may generate vorticity when the density and pressure gradients are not aligned. In the absence of density gradients, this term is evidently zero.

3.5.2 Criterion of instability based on the kinematic viscosity profile

The necessary IP condition for inviscid instability, i.e. $\bar{u}_{yy} = 0$, was established by Rayleigh (1880) for constant-density flows. In the presence of a density gradient, the GIP criterion in Eq. (3.25) holds. Introducing now the density weighted vorticity $\Phi = \bar{\rho}\bar{u}_y$, shown in Fig. 3.29(d) and Fig. 3.30(b), a necessary condition of inviscid instability is that $\Phi_y = 0$ somewhere in the base-flow profile. The location where this condition is verified is termed GIP. In the presence of a GIP as in the considered base flows in Sec. 3.5.1, an additional, more restrictive necessary condition of instability was given by Fjørtoft (1950). This criterion can be generalised to varying-density flows, stating that a region where

$$\Phi_y(\bar{u} - \bar{u}_s) > 0, \tag{3.75}$$

is required in the base-flow profile in order to observe an inviscid instability, where $\bar{u}_s = \bar{u}(y_s)$ denotes the velocity at the wall-normal position y_s associated with the GIP. In the present base flows, y_s coincides with the GIP location. The proofs of these two results, stated in the case where density gradients are non-zero, straightforwardly follow those given in Schmid & Henningson (2001) for constant-density flows by considering Eq. (3.73). Furthermore, we can show that verifying Eq. (3.73) throughout the base flow, except where $\Phi_y(\bar{u} - \bar{u}_s) = 0$, leads to the presence of a maximum of $|\Phi|$. A Taylor expansion of Eq. (3.75) can be performed about y_s, leading to:

$$\Phi_{yy,s}\,(y - y_s)\,(\bar{u}_s + \bar{u}_{y,s}\,(y - y_s) - \bar{u}_s) > 0. \tag{3.76}$$

Simplifying Eq. (3.76) and multiplying by $\bar{\rho}_s$ yields:

$$-\Phi_{yy,s}\Phi_s\,(y - y_s)^2 > 0. \tag{3.77}$$

If $\Phi_s > 0$, Eq. (3.77) requires that $\Phi_{yy,s} < 0$, meaning that a maximum of Φ must exist at y_s given that $\Phi_{y,s} = 0$. Doing an analogous reasoning if $\Phi_s < 0$, we then conclude that the necessary condition for an inviscid instability to exist, given by the generalised Fjørtoft criterion, is equivalent to the presence of a maximum of $|\Phi|$ at the GIP. This extends the well-known interpretation of a maximum of absolute vorticity in constant-density flows. Indeed, noting that, under the parallel flow assumption, the vorticity of the base flow Ω is simply $\Omega = -\bar{u}_y$, the quantity Φ can be interpreted as the density-weighted vorticity. For constant-density flows, the usual interpretation of the Fjørtoft criterion is then recovered, since $|\Phi| = |\Omega|$ in this case. However, in the presence of density variations, a maximum of Ω is no longer a necessary condition of instability, and the existence of a maximum of $|\Phi|$ should instead be examined.

Plane Couette flow

Combining $\rho = \mu/\nu$ and the streamwise momentum equation in Eq. (3.71), it follows that

$$(\bar{\nu}\Phi)_y = 0, \tag{3.78}$$

which, after distributing the wall-normal derivative, can be recast as:

$$\frac{\Phi_y}{\Phi} = -\frac{\bar{\nu}_y}{\bar{\nu}}. \tag{3.79}$$

The important result follows: in stratified plane Couette flow, the existence of a maximum of $|\Phi|$ is equivalent to the existence of a minimum of $\bar{\nu}$. Because of the generalised Fjørtoft criterion, a minimum of kinematic viscosity in the base-flow profile is then a necessary condition of inviscid instability. This motivated the choice of the fluid models considered in this work (Sec. 3.5.1), which all feature a minimum of $\bar{\nu}$ and, therefore, potentially exhibit an instability.

Poiseuille flow

In contrast, Poiseuille flow is driven by a constant pressure gradient $\partial p^*/\partial x^*$ in the streamwise direction. The velocity scale $u_r^* = h^{*2}/\mu_0^* \, \partial p^*/\partial x^*$ can be introduced since the flow results from a balance between friction forces and the pressure gradient. The parameter h^* is the distance between the two fixed plates and μ_0^* is a reference dynamic viscosity, for example at the lower plate. The non-dimensional streamwise momentum equation then reads:

$$(\bar{\mu}\bar{u}_y)_y = 1. \tag{3.80}$$

Proceeding similarly to Eq. (3.78), it follows that

$$(\bar{\nu}\Phi)_y = -1. \tag{3.81}$$

The right-hand side is equal to 1 whereas it was zero in plane Couette flow. This is due to the pressure gradient driving Poiseuille flow, and this difference will modify the criterion of instability. To show this, let us first integrate Eq. (3.81), yielding

$$\Phi = \frac{y_0 - y}{\bar{\nu}}, \tag{3.82}$$

with $y \in [-1/2, 1/2]$, using h^* as the reference length scale. The location, where $\Phi = 0$, i.e. $\bar{u}_y = 0$, is y_0, which is usually at the centre of the velocity profile at $y_0 = 0$. The existence of such a point inside the domain is guaranteed given the boundary conditions on the velocity profile $\bar{u}(-1/2) = \bar{u}(1/2) = 0$. Differentiating Eq. (3.82) leads to:

$$\Phi_y = -\frac{1}{\bar{\nu}}\left(1 + \frac{(y_0 - y)\bar{\nu}_y}{\bar{\nu}}\right). \tag{3.83}$$

The GIP criterion of instability, $\Phi_y = 0$, eventually reduces to

$$\frac{\bar{\nu}_y}{\bar{\nu}} = \frac{1}{y - y_0}, \tag{3.84}$$

where we ignore the point $y = y_0$ at which no GIP can exist, since $\Phi_y(y_0) = 1/\bar{\nu}(y_0) > 0$. Besides, because $1/(y - y_0)$ is strictly non-zero, a minimum of kinematic viscosity is not a condition for the existence of a GIP in plane Poiseuille flow, contrary to plane Couette flow. In other words, not every flow profile in the transcritical state, i.e. crossing the Widom line, meets Eq. 3.84.

Equation (3.84) can be further examined. Unlike non-heated, constant viscosity Poiseuille flow, the viscosity profile may here break the central symmetry of the velocity profile, which may prevent y_0 from necessarily being zero. As a result, the inequality $|y - y_0| < 1$ holds. Therefore, the condition in Eq. (3.84) can only be satisfied if strong enough gradients of viscosity are present in the flow, verifying:

$$\left|\frac{\bar{\nu}_y}{\bar{\nu}}\right| > 1. \tag{3.85}$$

We can further write that

$$\bar{\nu}_y = \left.\frac{\partial \bar{\nu}}{\partial y}\right|_{\bar{p}} \frac{\mathrm{d}\bar{T}}{\mathrm{d}y}, \tag{3.86}$$

which, estimating the non-dimensional temperature gradient as $\mathrm{d}\bar{T}/\mathrm{d}y \sim \Delta T$, gives a necessary condition for the existence of a GIP in plane Poiseuille flow:

$$\left|\frac{1}{\bar{\nu}} \left.\frac{\partial \bar{\nu}}{\partial \bar{T}}\right|_{\bar{p}}\right| > \frac{1}{\Delta T}. \tag{3.87}$$

This can be interpreted as the need for the kinematic viscosity law of the fluid to contain a temperature scale, defined as $\Delta T_\nu = \bar{\nu}/(\partial\bar{\nu}/\partial\bar{T})|_{\bar{p}}$, that is smaller than the temperature scale ΔT of the flow.

3.5.3 Stability results

The different sources of vorticity production

The generation of disturbance vorticity can be examined from the structure of the unstable modes in the physical space. The wall-normal velocity perturbations are made of a plane progressive wave along x (Fig. 3.31). A peak is observed in the central region of the flow, consistent with the linear increase from zero at the wall predicted in the outer regions. The associated pressure field is a plane progressive wave with a phase shift of $\pi/2$ with respect to v'. Note that results are here presented for fluid HT, but nearly identical fields are obtained for fluids VB and DB.

In fluid VB, vorticity production only results from the shear term S_ξ in Eq. (3.74), given that $\bar{\rho}_y = 0$. Given its mathematical expression, S_ξ follows the same wave structure as v', multiplied by the factor $-\Omega_y$. The vorticity profile $|\Omega|$ of the base flow, which is equal to $|\Phi|$ for this fluid, is only non-zero around the central layer. It features strong positive and negative gradients around the lower and upper interfaces, respectively (Fig. 3.29d). As a result, the structure of S_ξ contains two out-of-phase waves that are localised around each interface of the central layer, as seen in Fig. 3.32(a). The field of total vorticity production, $S_\xi + B_\xi$, has the same structure as S_ξ since $B_\xi = 0$.

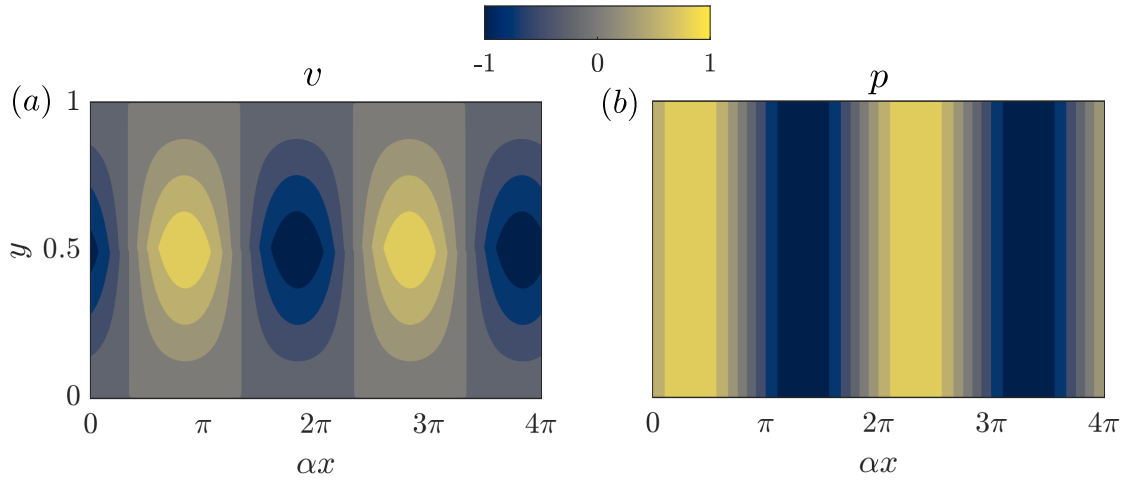

Figure 3.31: Wall-normal velocity $v = v'$ (a) and pressure $p = p'$ (b) of the unstable mode in fluid HT at $\alpha = 10^{-2}$ and $A_\nu = -0.05$, plotted in the physical space (x, y) at an arbitrary time t.

A similar reasoning can be applied to fluid DB, in which only baroclinic effects are at play given that the base-flow vorticity is constant. The structure of the baroclinic term B_ξ (Eq. (3.74)) is deduced from that of p' and the profile of $-\bar{\rho}_y/\bar{\rho}^2$. Given that $\bar{\rho} = \Phi$ for this fluid, the B_ξ field presented in Fig. 3.32(e) is found to be similar to that of S_ξ observed for fluid VB (Fig. 3.32a). As $S_\xi = 0$, it follows that the total vorticity production $S_\xi + B_\xi$ also resembles that of fluid VB (Figs. 3.32g,h).

As for fluid HT, both S_ξ and B_ξ are active in the generation of disturbance vorticity, and their structure (Figs. 3.32c,f) is markedly different from that of the two previous fluids. Both feature a peak around the central region. This is again a result of the profiles of $-\Omega$ and $-\bar{\rho}_y/\bar{\rho}^2$. Moreover, S_ξ and B_ξ exhibit a phase difference of π. This is readily understood from the phase difference of $\pi/2$ between v' and p', another phase shift of $\pi/2$ being added to B_ξ as it contains $\partial p'/\partial x$ (Eq. (3.74)). Despite being out of phase and having a similar structure, the sum of S_ξ and B_ξ is not zero. Instead, $S_\xi + B_\xi$ is composed of two out-of-phase waves around each interface (Fig. 3.32i), similar to what was observed for fluids DB and VB. This behaviour can be linked to the profile of Φ with the following arguments. Around the central region, the x-momentum equation can be approximated to $\Phi v' \simeq \partial p'/\partial x$. This results from $\partial u'/\partial t + \bar{u}\,\partial u'/\partial x$ being much smaller than $\Phi v'$ in this region, given that the phase velocity of u' is here close to $\bar{u}$, and that the growth rate ω_i is small (this is more evident in the spectral space, where this term is simply $\mathrm{i}\alpha(\bar{u} - c)\hat{u}$). Under this approximation, the linearised vorticity equation (Eq. (3.74)) can be recast as

$$\frac{\partial \xi'}{\partial t} + \bar{u}\frac{\partial \xi'}{\partial x} \simeq -\frac{\Phi_y}{\bar{\rho}}v', \tag{3.88}$$

where the right-hand side corresponds to $S_\xi + B_\xi$; this shows how the quantity Φ encapsulates both shear and baroclinic effects. The profile of Φ_y and the structure of v' ultimately explain the structure of $S_\xi + B_\xi$ in fluid HT (Fig. 3.32i). Note that the denominator $\bar{\rho}$ attached to Φ_y in Eq. (3.88), modulates the amplitude of the minimum and maximum of Φ_y; it can be seen,

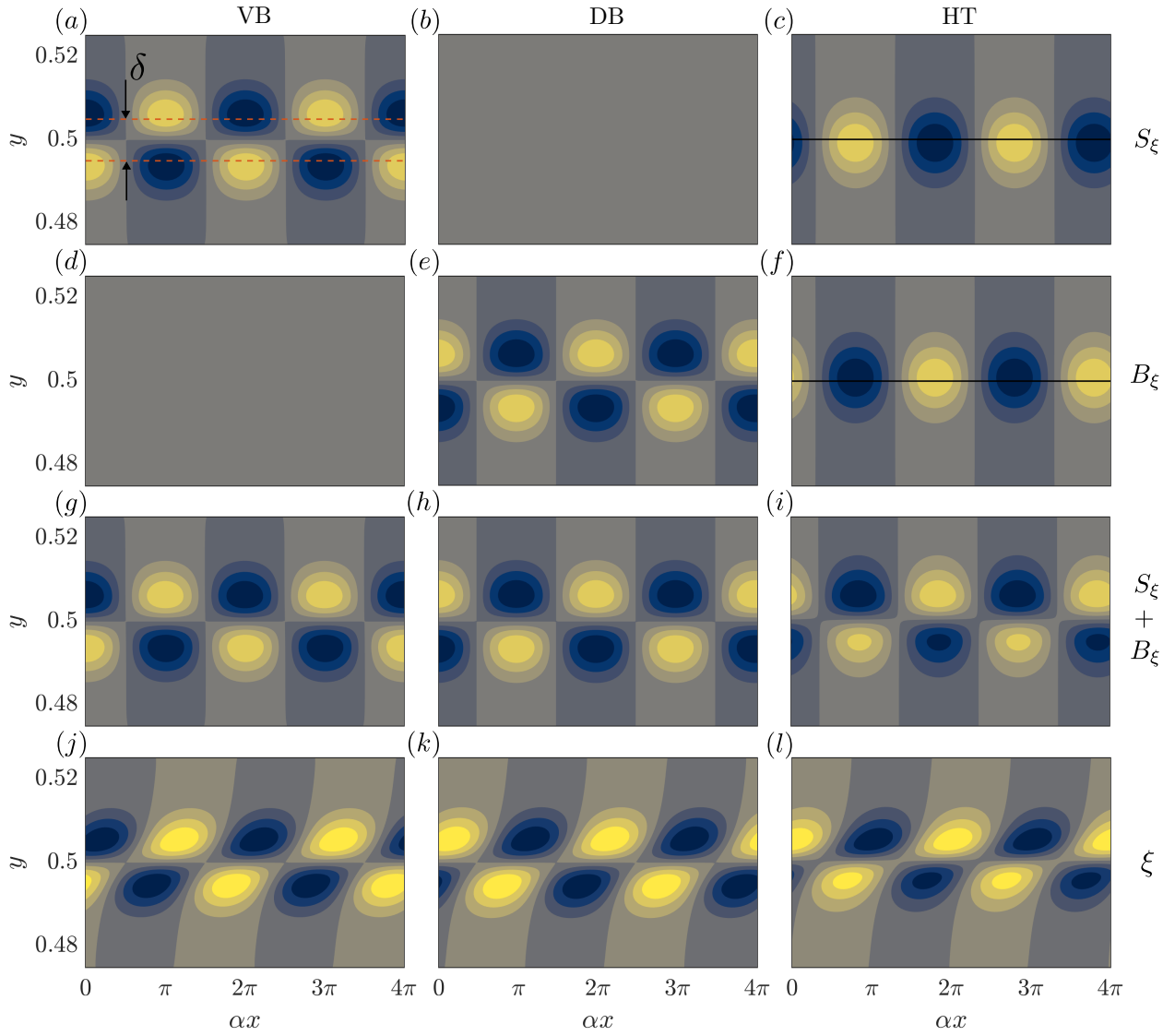

Figure 3.32: Terms of the vorticity equation (Eq. (3.74)) plotted in the physical space (x, y) at an arbitrary time t, for the unstable modes presented in Fig. 3.31. The shear term, the baroclinic term, their sum and the resulting vorticity are shown from top to bottom, in that order. Each column corresponds to one fluid. In each panel, fields are normalised by their maximum absolute value, and colour bars are the same as in Fig. 3.31. The central layer of thickness δ with a maximum of $|\Phi|$ is shown in (a) by the red dashed line; its location is identical in each figure, albeit not reproduced to ease visualisation. The location $y = 1/2$ is indicated by the black solid line in (c,f), revealing an offset of the wave below and above this line, respectively.

in Fig. 3.32(i), that larger peaks are observed around the upper interface than those around the lower interface, given that $\bar{\rho}$ is smaller in the upper region.

Overall, the structure of the total vorticity production $S_\xi + B_\xi$ is similar for each fluid, regardless of the fluid stratification. The associated vorticity fields are finally displayed in Figs. 3.32(j–l). Their structure follows that of $S_\xi + B_\xi$, with an alteration resulting from advection effects (left-hand side of the vorticity equation, Eq. (3.74)). The final picture is

two vorticity waves travelling along each interface, with a phase difference of π minus a phase shift induced by advection. It can also be noted that these waves are generated around the critical layer y_{cr}, defined as $\bar{u}(y_{cr}) = c_\phi$ (not to be confused with the thermodynamic critical point). In fluids VB and DB, $c_\phi = 1/2$ which, by symmetry of the base flow, leads to $y_{cr} = 1/2$. In fluid HT, the phase speed of the mode presented in Fig. 3.32 is $c_\phi = 0.45$; we have verified that $\bar{u}(1/2) = 0.45$.

The relative amplitudes of the terms plotted in Fig. 3.32 are hidden by the normalisation of each field. The maximum absolute value that each field reaches within the physical space (x, y) is used in the normalisation procedure. While the relative maximum amplitudes are 1 for fluids VB and DB, for fluid HT, it is shown that the shear and baroclinic effects act with similar strengths. Furthermore, the total source of vorticity $(S_\xi + B_\xi)$ is approximately six times weaker than these effects as it proceeds from the interference of the two waves, cancelling out a large part of their amplitude.

The different terms of the vorticity equation (Eq. (3.74)), for the unstable mode in fluid VdW are now examined. The shear term S_ξ (Fig. 3.33a) and the baroclinic term B_ξ (Fig. 3.33b) are each composed of a unique wave, which reaches a maximum in the central region around the minimum of kinematic viscosity. This is similar to the observations made for fluid HT in Figs. 3.32(c,f). But because non-zero gradients of $\bar{\mu}$ and $\bar{\rho}$ persist away from the central region in fluid VdW (Fig. 3.30a), these terms are not as localised in the centre as in fluid HT. This is particularly noticeable for B_ξ, which extends further in the upper region, as $\bar{\rho}_y$ is non-zero and $\bar{\rho}$ is much smaller than in the lower region. The sum $S_\xi + B_\xi$ contains two out-of-phase waves (Fig. 3.33c) as S_ξ and B_ξ are themselves out of phase and are slightly shifted from each other in the wall-normal direction. However, because of the aforementioned asymmetrical structure of B_ξ, the upper wave is not localised around the upper interface of the central layer. This constitutes a significant difference with fluid HT (Fig. 3.32i). Nevertheless, the final picture is essentially identical: after advection is accounted for, the vorticity field contains two waves localised around each interface, with an additional phase shift leading to a phase difference smaller than π between them (Fig. 3.33d). The role played by advection in the localisation of $S_\xi + B_\xi$ in the central region can be understood from the vorticity equation (Eq. (3.74)), which can be recast, in the spectral space, as:

$$|\xi'| = \frac{|S_\xi + B_\xi|}{\alpha|\bar{u} - c|}. \tag{3.89}$$

Therefore, $|\xi'|$ increases as the phase velocity of the disturbance approaches that of the base flow – which occurs in the central region, as will be shown in the next subsection. Overall, the theoretical stability model developed for fluid HT predicts important features of the stability of fluid VdW. This indicates that the main ingredients of the inviscid instability developing in supercritical fluids are indeed contained in fluid HT. These ingredients are the presence of strong, localised gradients of density and viscosity and the associated existence of a localised minimum of kinematic viscosity.

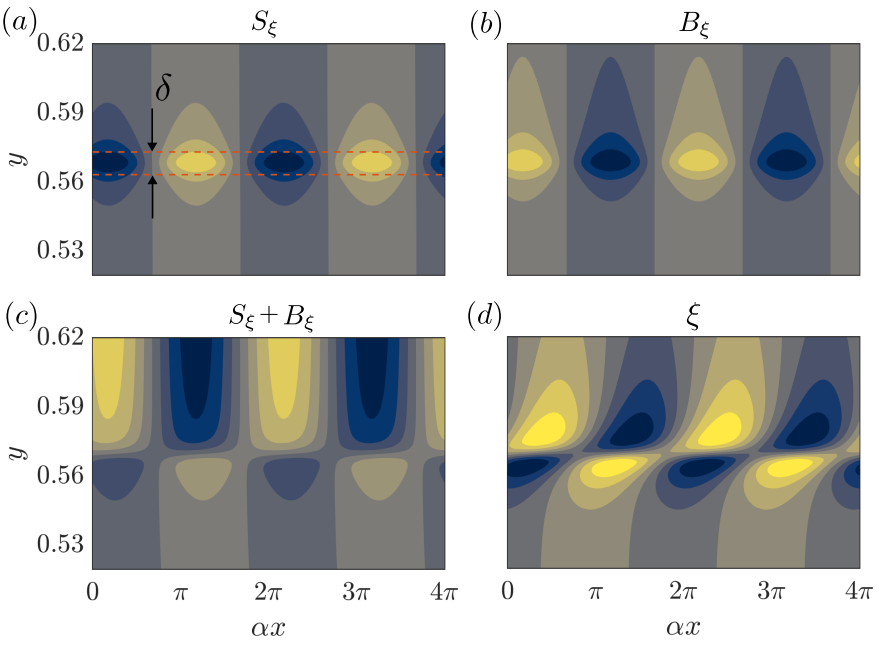

Figure 3.33: Terms of the vorticity equation (Eq. (3.74)) for the unstable mode in fluid VdW at $\alpha = 10^{-2}$, $p_r = 1.06$ and $\tau = 0.5$. Normalisation, colour bars and annotations are identical to those detailed in Fig. 3.32. Note that, in fluid VdW, the central region is defined as being centred around the minimum of kinematic viscosity. (a) Shear production term. (b) Baroclinic production term. (c) Sum of the shear and baroclinic production terms. (d) Vorticity disturbance $\xi = \xi'$.

Physical interpretation

These results can be interpreted within the wave-interaction theory as reviewed by Carpenter *et al.* (2011). In this framework, instabilities are seen as a result of vorticity waves developing along two interfaces that are located close enough so that each wave modifies the velocity field of the other. The modified velocity field further deforms each interface, which yields additional vorticity production. This forms a positive feedback loop in which the two vorticity waves are amplified, constituting an instability. In order to achieve amplification, these waves have to be phase-locked, which was indeed observed for the three fluids in Figs. 3.32(j–l). The appearance of vorticity waves along each interface has been shown to be driven by the structure of Φ in Eq. (3.88). The physical mechanisms giving rise to these vorticity waves are now further examined.

In fluid VB, the instability arises from an excess of vorticity in a localised layer. This is the essential ingredient of the Kelvin–Helmholtz instability, which is well known and will not be further discussed. The mechanism of this instability has indeed been given following either kinematic (Batchelor 2000) or dynamic (Charru & Hinch 2000) arguments. Carpenter *et al.* (2011) also examined this instability from a wave-interaction perspective.

In fluid DB, only baroclinic effects produce vorticity disturbance. This originates from misalignments between gradients of density and pressure (Soteriou & Ghoniem 1995). More precisely, given the flow assumptions, this misalignment can only be generated via the density

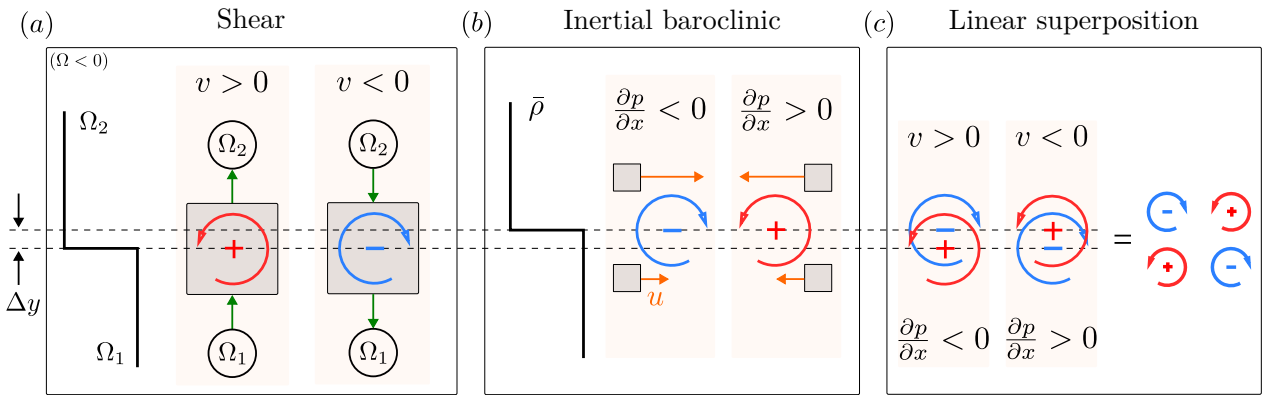

Figure 3.34: Sketch illustrating the mechanism generating the two vorticity waves in fluid HT. Red and blue vortices indicate positive and negative values of the vorticity disturbance $\xi = \xi'$, respectively. These disturbances are generated by shear (a) and baroclinic (b) mechanisms. Solid black lines represent the vorticity (a) and density (b) profiles of the base flow, Ω and $\bar{\rho}$, respectively. Note that $\Omega < 0$ and that a shift Δy exists between the interfaces of Ω and $\bar{\rho}$. Vertical green arrows in (a) represent the transport of Ω by the disturbance $v = v'$ in and out of a control volume centred around the interface. Horizontal orange arrows in (b) show the disturbance streamwise velocity of a fluid parcel that is induced by a streamwise gradient of disturbance pressure. The magnitude of this velocity depends on $\bar{\rho}$, which modifies the inertia of the fluid parcel whether it is located in the lower or upper region. The linear superposition of the waves generated in (a) and (b) is shown in (c).

stratification of the base flow and the gradient of pressure perturbations in the streamwise direction. Physically, two parcels of fluid at different wall-normal locations, having two different densities (that of the base flow), do not have the same streamwise acceleration when submitted to a streamwise perturbation of pressure (Reinaud *et al.* 1999). This induces a wall-normal gradient of streamwise velocity, i.e. vorticity. In fluid DB, the central region has an excess of density. The above mechanism of vorticity production, therefore, occurs between the lower and central layer, as well as between the upper and central layer. This results in the two vorticity waves that have been observed in Fig. 3.32(h).

As for fluid HT, the generation of the two vorticity waves is not as straightforward. A sketch of the mechanism is shown in Figs. 3.34(a–c). On the one hand, disturbance vorticity is generated following the inertial baroclinic mechanism described in the previous paragraph. However, contrary to fluid DB, this occurs only between two regions of the flow, the lower and the upper ones, which have different densities (Fig. 3.29c) – the central layer playing the role of an interface between them. This idealised representation is illustrated in figure Fig. 3.34(b). Therefore, only one interface is felt by the baroclinic perturbations, instead of two as in fluid DB. This results in only one vorticity wave, which is generated in the central region, as previously observed in Fig. 3.32(f). On the other hand, disturbance vorticity is also produced by a shear mechanism, which consists in the wall-normal transport of base-flow vorticity by the perturbations. The base flow can also be divided into two regions of vorticity – smaller and larger magnitudes of the shear rate are indeed observed in the lower and

upper part of the flow, respectively (Fig. 3.29c). The central layer again plays the role of an interface between these two regions, and only one interface is felt by the shear perturbations, as sketched in Fig. 3.34(a). As a result, only one wave is generated by the shear mechanism, as previously observed in Fig. 3.32(c). This is a consequence of the plane wave structure of v, which, as it takes positive and negative values along x, alternatively transports parcels of fluid that contain smaller and larger magnitudes of Ω towards the central region. At this point, each mechanism generates one wave that is localised in the central layer. These two waves are out of phase, as discussed in the previous section. Moreover, because of the existing shift between the viscosity and density profiles in fluid HT (Fig. 3.29c), a small shift $y \sim \epsilon T/\tau$ also exists between the interface at play in each mechanism (Fig. 3.34). As a result, the two central waves are slightly shifted relative to each other, and their superposition gives rise to two waves localised on either side of the central layer (Fig. 3.34c). These phase-locked, interacting vorticity waves are the source of the instability in fluid HT, according to the interpretation of wave-interaction theory. Similarly, the inviscid instability in fluid VdW can be understood as the result of combined shear and baroclinic mechanisms, which generate two interacting waves centred around the central layer. Our study further shows that the minimum in kinematic viscosity, reached at the Widom line, is the leading cause of this instability.

Other types of flow may develop a localised minimum of viscosity and thus potentially support a similar instability. In this study, temperature governs the distribution of kinematic viscosity, but other scalar fields, such as the stress profile in non-Newtonian fluids, may play a similar role (see also Sec. 3.3.3). In plane Couette flow, the uniform stress leads to linear stability, but stress variations, due to shear thinning or thickening, induced by viscous heating (Eldabe *et al.* 2007) or a pressure gradient, as in Couette–Poiseuille flow (Nouar & Frigaard 2009), can create a viscosity minimum. However, because of the pressure gradient, the instability criterion derived here does not apply, and such isothermal non-Newtonian flows may therefore remain stable.

3.6 Conclusions

In this chapter, we perform linear stability analysis of diabatic flat-plate boundary layers at supercritical pressure. Supercritical carbon dioxide (CO_2) at a constant pressure of 80 bar (above its critical pressure of 73.9 bar) is chosen as a representative non-ideal fluid near the Widom line. The classical framework of Linear Stability Theory (LST), including both viscous and inviscid perturbations, is extended to account for non-ideal gas effects. Validation against the results of Ren *et al.* (2019*b*) confirms the accuracy of the solvers under adiabatic wall conditions.

Section 3.3 focuses on the viscous and inviscid modal stability of isothermal boundary layers at supercritical pressure in the zero-Eckert-number limit. Subcritical, supercritical, and transcritical states are examined relative to the pseudo-critical temperature of CO_2 (T^*_{pc} = 307.7 K) by prescribing free-stream and wall temperatures at a fixed free-stream Mach number

of 10^{-3}. In both subcritical (liquid-like, $T^*_\infty/T^*_{pc} = 0.90$, with $T^*_w < T^*_{pc}$) and supercritical (vapour-like, $T^*_\infty/T^*_{pc} = 1.10$, with $T^*_w > T^*_{pc}$) cases, approaching T^*_{pc} stabilises the flow.

In transcritical conditions, either with wall heating ($T^*_\infty/T^*_{pc} < 1$, $T^*_w > T^*_{pc}$) or cooling ($T^*_\infty/T^*_{pc} > 1$, $T^*_w < T^*_{pc}$), the wall-normal gradient of the base-flow viscosity

$$\frac{\mathrm{d}\bar{\mu}}{\mathrm{d}y} = \underbrace{\left(\left.\frac{\partial\bar{\mu}}{\partial\bar{T}}\right|_{\bar{\rho}}\frac{\partial\bar{T}}{\partial y}\right)}_{T\text{ term}} + \underbrace{\left(\left.\frac{\partial\bar{\mu}}{\partial\bar{\rho}}\right|_{\bar{T}}\frac{\partial\bar{\rho}}{\partial y}\right)}_{\rho\text{ term}}, \tag{3.90}$$

with $\bar{\mu} = f(\bar{\rho}, \bar{T})$, is dominated by the density-dependent term, which is negligible under non-transcritical conditions. A positive μ gradient at the wall leads to a fuller velocity profile, while the negative μ gradient at the wall due to wall cooling shifts the Inflection Point (IP) away from the wall, yielding a thinner velocity profile.

With regard to modal stability, the transcritical heating case confirms the dual-mode appearance reported by Ren *et al.* (2019*b*), featuring a strongly unstable transcritical Mode II appearing alongside the viscous Mode I (Tollmien–Schlichting (TS) wave). Mode II, which persists even in the absence of acoustic effects, shifts significantly upstream with only a slight increase in wall temperature and exhibits a broader unstable frequency range. Phase velocity analysis shows that the shear-driven Mode I represents a continuation of the TS mode in the subcritical state, whereas Mode II, associated with the strongest non-ideal gas effects across the Widom line, exhibits a much lower phase speed. In the transcritical cooling case, no viscous Mode I is found, regardless of wall temperature. Instead, the flow is destabilised up to the leading edge by the sudden appearance of an inviscid mode with characteristics similar to Mode II in the transcritical heating case. The evolution of the phase speed highlights this asymmetric modal behaviour: the viscous mode is entirely suppressed once the wall temperature enters the vapour-like state, while the inviscid mode emerges with very low phase speed. These trends are further confirmed using the cubic Van der Waals (VdW) Equation of State (EoS) in place of property look-up tables, demonstrating that this simpler and more universal thermodynamic model captures the essential physical mechanisms driving the linear growth of instabilities in supercritical fluids.

A linear inviscid stability analysis is conducted to investigate the nature of Mode II. Its growth rate increases with wall temperature in the transcritical state, confirming that, in the viscous limit, the critical Reynolds number shifts upstream as the wall temperature rises. Interestingly, larger growth rates are observed at moderate Reynolds numbers than at infinitely large ones, indicating a destabilising effect of viscosity, before viscous damping dominates at low Reynolds numbers.

The origin of the unstable inviscid Mode II is further investigated. Building on the findings of Ren *et al.* (2019*b*), who linked the appearance of the Generalised Inflection Point (GIP), i.e. $(\bar{\rho}\bar{u}_y)_y = 0$, we perform a theoretical analysis by approximating the streamwise momentum equation. At the pseudo-critical point, where viscous effects dominate, inertial effects can be reasonably neglected. This approximation still yields an accurate prediction of the GIP within the boundary layer. Under these conditions, the GIP criterion can be

reformulated in terms of an extremum of the kinematic viscosity, $\bar{\nu} = \bar{\mu}/\bar{\rho}$, as:

$$\frac{\mathrm{d}}{\mathrm{d}y}\left(\bar{\rho}\frac{\mathrm{d}\bar{u}}{\mathrm{d}y}\right) \simeq -\frac{\bar{\rho}}{\bar{\nu}}\frac{\mathrm{d}\bar{u}}{\mathrm{d}y}\frac{\mathrm{d}\bar{T}}{\mathrm{d}y}\left.\frac{\partial\bar{\nu}}{\partial\bar{T}}\right|_{\bar{p}}. \tag{3.91}$$

A minimum in $\bar{\nu}$ is found at the Widom line, not only for supercritical CO_2, but also for other non-polar supercritical fluids and fluids described by the VdW EoS. These results suggest that any supercritical fluid with a temperature profile crossing the Widom line will exhibit an inviscid instability associated with a GIP located in its vicinity.

The modal instability of oblique perturbations is examined for both non-transcritical and transcritical cases in Sec. 3.4. At a low free-stream Mach number of 10^{-3}, 2-D modes exhibit the highest amplification, both locally (across most of the frequency spectrum) and integrally. This suggests that, as shown in the oblique modal stability analysis at finite Mach numbers by Ren *et al.* (2019*b*), decreasing the Mach number (i.e. reducing compressibility effects) may shift the largest possible local and integral amplification from a 3-D to a 2-D mode – regardless of the thermodynamic state at supercritical pressure. This behaviour is further investigated in the following.

In the non-transcritical states, Mode I becomes preferentially 3-D for sufficiently high Mach numbers, around $M_\infty \gtrsim 0.8$. In the transcritical heating case, Mode I, whose critical layer lies above the Widom line, is instead found to be preferentially 2-D. Conversely, Mode II, whose critical layer is located below the Widom line, is preferentially 3-D when the Mach number exceeds approximately $M_\infty \gtrsim 0.7$. In the transcritical cooling case, the critical layer of the highly unstable inviscid mode is initially located above the Widom line for small β, but shifts towards it as β increases, with a concurrent decrease in phase speed. Regardless of whether wall heating or cooling is applied, viscous effects stabilise the oblique inviscid mode, while its phase speed, $c_x = \omega/\alpha$, remains below that of the GIP in the inviscid limit. To elucidate this behaviour, we extend the ideal-gas inviscid framework of Lees & Lin (1946) to non-ideal-gas boundary layers and analyse the evolution of the complex phase speed c_x for a neutral inviscid 2-D wave when β^2 departs from zero. It is found that the amplification of 3-D waves is driven by a sign change of the numerator $\mathcal{N}$ of $\mathrm{d}c_x/\mathrm{d}\beta^2$, which reads:

$$\mathcal{N} = \int_0^{y_2} -\zeta_1\hat{v}^2\,\mathrm{d}y + \int_0^{y_2} \frac{\zeta_1(M_r^2)_y}{(\alpha^2+\beta^2)(1-M_r^2)^2}\left(\frac{\bar{u}_y}{\bar{u}-c_x}\hat{v}^2 - \hat{v}\hat{v}_y\right)\mathrm{d}y. \tag{3.92}$$

The first (leftmost) integral is always negative for a subsonic wave, i.e. $|M_r| < 1$, while the second (rightmost) is positive. In the limit of zero Mach number, the rightmost integral vanishes, resulting in $\mathcal{N} < 0$ and, thus, damping of the inviscid wave for $\beta^2 > 0$. For sufficiently high Mach numbers, however, $\mathcal{N}$ becomes positive, leading to amplification of 3-D waves. This Mach-dependent sign change, arising from the same critical-layer singularity identified by Lees & Lin (1946), satisfies the generalised Fjørtoft condition at the GIP: once the base flow develops such a GIP near the pseudo-critical point, the resulting mode is predisposed to three-dimensionalisation, consistent with the behaviour of Mode II observed in the viscous 3-D computations.

The aforementioned link between the existence of a GIP and a minimum of kinematic viscosity in boundary layers with supercritical fluids motivates the study of Mode II in a

more canonical setting to seek a universal interpretation, as detailed in Sec. 3.5. A strongly density- and viscosity-stratified plane Couette flow is considered, as it strictly satisfies the streamwise momentum of the boundary-layer equations, i.e. $\bar{\mu}\,\bar{u}_{yy} + \bar{\mu}_y\bar{u}_y \equiv 0$.

In this framework, we show that a minimum of kinematic viscosity in the base flow leads to the appearance of a GIP, which additionally satisfies the generalised Fjørtoft criterion. This implies that, in flows with strong density variations, a maximum of vorticity is no longer a necessary condition for instability; instead, one must examine the existence of a maximum in the density-weighted vorticity, $|\Phi|$ with $\Phi = -\bar{\rho}\bar{u}_y$. Upon reformulation, the presence of a maximum in $|\Phi|$ is shown to be equivalent to the existence of a minimum in $\bar{\nu}$. As a result, a minimum of kinematic viscosity becomes a necessary condition for inviscid instability in plane Couette flow due to the generalised Fjørtoft criterion. Conversely, in plane Poiseuille flow, the inclusion of a streamwise pressure gradient driving the base flow violates the aforementioned streamwise momentum equation, thereby invalidating the minimum kinematic-viscosity criterion for the GIP – unless viscosity gradients in the flow are sufficiently strong.

This motivated the choice of three fluid models, termed VB (viscosity bump), DB (density bump), and HT (hyperbolic tangent), which are all designed to exhibit a minimum of ν, while featuring different stratifications of density and dynamic viscosity. In all cases, two phase-locked vorticity waves travelling along the interfaces of the central layer are found. The growth of the instability is ultimately interpreted as the result of the interaction between these two waves. These waves are generated by either shear effects in fluid VB or by baroclinic effects in fluid DB. In fluid HT, which features strong stratifications of both density and viscosity, the two waves are shown to result from a combination of shear and baroclinic mechanisms. The stability of a supercritical fluid governed by the VdW EoS is finally examined. The stability model is found to quantitatively predict the neutral curve of this more realistic fluid. The combined action of shear and baroclinic effects in vorticity production gives rise to two vorticity waves around the central layer, suggesting that the physical interpretation proposed for fluid HT also captures the essential mechanism of instability in supercritical fluids. Ultimately, the stability models developed for these simplified fluids shed light on the transcritical Mode II in boundary layers, providing a quantitative prediction of the stability diagram and identifying the dominant mechanisms at play.

Bibliography

Almagro, A., García-Villalba, M. & Flores, O. 2017 A numerical study of a variable-density low-speed turbulent mixing layer. *J. Fluid Mech.* **830**, 569–601.

Banuti, D. T. 2015 Crossing the Widom-line – Supercritical pseudo-boiling. *J. Supercrit. Fluids* **98**, 12–16.

Batchelor, G. K. 2000 *An Introduction to Fluid Dynamics*. Cambridge University Press.

Bertolotti, F. B. 1998 The influence of rotational and vibrational energy relaxation on boundary-layer stability. *J. Fluid Mech.* **372**, 93–118.

Bitter, N. P. & Shepherd, J. E. 2015 Stability of highly cooled hypervelocity boundary layers. *J. Fluid Mech.* **778**, 586–620.

Boldini, P. C. 2018 Effects of thermal non-equilibrium on hypersonic boundary-layer transition. Master's thesis, University of Stuttgart, conducted at the Laboratory for Advanced Simulation of Turbulence (Tsinghua University).

Bugeat, B., Boldini, P. C., Hasan, A. M. & Pecnik, R. 2024 Instability in strongly stratified plane Couette flow with application to supercritical fluids. *J. Fluid Mech.* **984**, A31.

Bugeat, B., Boldini, P. C. & Pecnik, R. 2022 On the new unstable mode in the boundary layer flow of supercritical fluids. In *Proceedings of the 12th International Symposium on Turbulence and Shear Flow Phenomena (TSFP-12)*.

Carpenter, J. R., Tedford, E. W., Heifetz, E. & Lawrence, G. A. 2011 Instability in stratified shear flow: review of a physical interpretation based on interacting waves. *Appl. Mech. Rev.* **64**, 060801.

Charru, F. & Hinch, E. J. 2000 'Phase diagram' of interfacial instabilities in a two-layer Couette flow and mechanism of the long-wave instability. *J. Fluid Mech.* **414**, 195–223.

Chen, X., Boldini, P. C. & Song, F. 2019 Research on hypersonic boundary-layer stability with high-temperature effects. In *Proceedings of the 2018 Asia-Pacific International Symposium on Aerospace Technology (APISAT 2018)*, pp. 499–512. Springer Nature.

Chen, X., Wang, L. & Fu, S. 2021 Parabolized stability analysis of hypersonic thermal-chemical nonequilibrium boundary-layer flows. *AIAA J.* **59**, 2382–2395.

Dixit, H. N. & Govindarajan, R. 2010 Vortex-induced instabilities and accelerated collapse due to inertial effects of density stratification. *J. Fluid Mech.* **646**, 415–439.

Drazin, P. G. 1958 The stability of a shear layer in an unbounded heterogeneous inviscid fluid. *J. Fluid Mech.* **4** (2), 214–224.

Eldabe, N. T. M., El-Sabbagh, M. F. & El-Sayed, M. A.-S. 2007 The stability of plane Couette flow of a power-law fluid with viscous heating. *Phys. Fluids* **19**, 094107.

Ern, P., Charru, F. & Luchini, P. 2003 Stability analysis of a shear flow with strongly stratified viscosity. *J. Fluid Mech.* **496**, 295–312.

Fedorov, A. 2011 Transition and stability for high-speed boundary layers. *Ann. Rev. Fluid Mech.* **43**, 79–95.

Fedorov, A., Shiplyuk, A., Maslov, A., Burov, E. & Malmuth, N. 2003 Stabilization of a hypersonic boundary layer using an ultrasonically absorptive coating. *J. Fluid Mech.* **479**, 99–124.

Fjørtoft, R. 1950 Application of integral theorems in deriving criteria of stability for laminar flows and for the baroclinic circular vortex. *Geofys. Publ. Oslo* **17**, 1–52.

Fontane, J. & Joly, L. 2008 The stability of the variable-density Kelvin–Helmholtz billow. *J. Fluid Mech.* **612**, 237–260.

Gloerfelt, X., Robinet, J.-C., Sciacovelli, L., Cinnella, P. & Grasso, F. 2020 Dense-gas effects on compressible boundary-layer stability. *J. Fluid Mech.* **893**, A19.

Govindarajan, R. 2001 Effect of miscibility on the linear instability of two-fluid channel flow. *Int. J. Multiph. Flow* **30**, 1177–1192.

Govindarajan, R. & Sahu, K. C. 2014 Instabilities in viscosity-stratified flow. *Ann. Rev. Fluid Mech.* **46**, 331–353.

Guha, A. & Raj, R. 2018 On the inertial effects of density variation in stratified shear flows. *Phys. Fluids* **30** (12), 126603.

Herwig, H. & Schäfer, P. 1992 Influence of variable properties on the stability of two-dimensional boundary layers. *J. Fluid Mech.* **243**, 1–14.

Hinch, E. J. 1984 A note on the mechanism of the instability at the interface between two shearing fluids. *J. Fluid Mech.* **144**, 463–465.

Hirschel, E. H. 2005 *Basics of Aerothermodynamics*. Springer-Verlag.

Hooper, A. P. & Boyd, W. G. C. 1983 Shear-flow instability at the interface between two viscous fluids. *J. Fluid Mech.* **128**, 507–528.

Hooper, A. P. & Boyd, W. G. C. 1987 Shear-flow instability due to a wall and a viscosity discontinuity at the interface. *J. Fluid Mech.* **179**, 201–225.

Hudson, M. L., Chokani, N. & Candler, G. V. 1997 Linear stability of hypersonic flow in thermo-chemical nonequilibrium. *AIAA J.* **35**, 958–964.

Lees, L. & Lin, C. C. 1946 Investigation of the stability of the laminar boundary layer in a compressible fluid. *NACA Tech. Note* 1115.

Lesshafft, L. & Huerre, P. 2007 Linear impulse response in hot round jets. *Phys. Fluids* **19** (2), 024102.

Ly, N. & Ihme, M. 2022 Destabilization of binary mixing layer in supercritical conditions. *J. Fluid Mech.* **945**, R2.

Ma, Y. & Zhong, X. 2003 Receptivity of a supersonic boundary layer over a flat plate. Part 1. Wave structures and interactions. *J. Fluid Mech.* **488**, 31–78.

Mack, L. M. 1984 Boundary-layer linear stability theory. *AGARD Report No. 709: Special Course on Stability and Transition of Laminar Flow.* AGARD.

Mack, L. M. 1987 Review of linear compressible stability theory. In *In Stability of Time Dependent and Spatially Varying Flows* (ed. D. L. Dwoyer & M. Y. Hussaini), p. 164–187. Springer.

Malik, M. R. 1990 Numerical methods for hypersonic boundary layer stability. *J. Comput. Phys.* **86**, 376–413.

Malik, M. R. & Anderson, E. C. 1991 Real gas effects on hypersonic boundary-layer stability. *Phys. Fluids A* **3**, 803–821.

McAllister, R. A. 1960 The viscosity of liquid mixtures. *AIChE J.* **6**, 427—-431.

Menkes, J. 1959 On the stability of a shear layer. *J. Fluid Mech.* **6** (4), 518–522.

Miró Miró, F., Beyak, E. S., Pinna, F. & Reed, H. L. 2019 High-enthalpy models for boundary-layer stability and transition. *Phys. Fluids* **31**, 044101.

Mortensen, C. H. 2018 Toward and understanding of supersonic modes in boundary-layer transition for hypersonic flow over blunt cones. *J. Fluid Mech.* **846**, 789–814.

Nemati, H., Patel, A., Boersma, B. J. & Pecnik, R. 2015 Mean statistics of a heated turbulent pipe flow at supercritical pressure. *Int. J. Heat Mass Transf.* **83**, 741–752.

Nouar, C. & Frigaard, I. 2009 Stability of plane Couette–Poiseuille flow of shear-thinning fluid. *Phys. Fluids* **21**, 064104.

Ranganathan, B. T. & Govindarajan, R. 2001 Stabilisation and destabilisation of channel flow by location of viscosity-stratified fluid layer. *Phys. Fluids* **13**, 1–3.

Rayleigh, Lord 1880 On the stability, or instability, of certain fluid motions. *Proc. Lond. Math. Soc.* **9**, 57–70.

Reinaud, J., Joly, L. & Chassaing, P. 1999 Numerical simulation of a variable-density mixing-layer. *ESAIM: Proc.* **7**, 359–368.

Reinaud, J., Joly, L. & Chassaing, P. 2000 The baroclinic secondary instability of the two-dimensional shear layer. *Phys. Fluids* **12** (10), 2489–2505.

Ren, J., Fu, S. & Pecnik, R. 2019*a* Linear instability of Poiseuille flows with highly non-ideal fluids. *J. Fluid Mech.* **859**, 89–125.

Ren, J. & Kloker, M. 2022 Instabilities in three-dimensional boundary-layer flows with a highly non-ideal fluid. *J. Fluid Mech.* **951**, A9.

Ren, J., Marxen, O. & Pecnik, R. 2019*b* Boundary-layer stability of supercritical fluids in the vicinity of the Widom line. *J. Fluid Mech.* **871**, 831–864.

Robinet, J.-C. & Gloerfelt, X. 2019 Instabilities in non-ideal fluids. *J. Fluid Mech.* **880**, 1–4.

Sahu, K. C. & Govindarajan, R. 2016 Linear stability analysis and direct numerical simulation of two-layer channel flow. *J. Fluid Mech.* **798**, 889–909.

Schlichting, H. & Gersten, K. 2003 *Boundary Layer Theory*. Springer.

Schmid, P. J. & Henningson, D. S. 2001 *Stability and transition in shear flows*. Springer.

Soteriou, M. C. & Ghoniem, A. F. 1995 Effects of the free-stream density ratio on free and forced spatially developing shear layers. *Phys. Fluids* **7** (8), 2036–2051.

Stemmer, C., Birrer, M. & Adams, N. A. 2017 Hypersonic boundary-layer flow with an obstacle in thermochemical equilibrium and nonequilibrium. *J. Spacecr. Rockets* **54**, 899–915.

Stuckert, G. & Reed, H. L. 1994 Linear disturbances in hypersonic, chemically reacting shock layers. *AIAA J.* **32**, 1384–1393.

Tunney, A. P., Denier, J. P., Mattner, T. W. & Cater, J. E. 2015 A new inviscid mode of instability in compressible boundary-layer flows. *J. Fluid Mech.* **785**, 301–323.

Wall, D. P. & Wilson, S. K. 1996 The linear stability of channel flow of fluid with temperature-dependent viscosity. *J. Fluid Mech.* **323**, 107–132.

Wall, D. P. & Wilson, S. K. 1997 The linear stability of flat-plate boundary-layer flow of fluid with temperature-dependent viscosity. *Phys. Fluids* **9**, 2885–2898.

Yih, C.-S. 1967 Instability due to viscosity stratification. *J. Fluid Mech.* **27** (2), 337–352.

Zhong, X. & Wang, X. 2012 Direct numerical simulation of receptivity, instability and transition of hypersonic boundary layers. *Ann. Rev. Fluid Mech.* **44**, 527–561.

4

NON-MODAL STABILITY

The content of this chapter has been published under the title:

P. C. Boldini, B. Bugeat, J. W. R. Peeters, M. Kloker, and R. Pecnik,
Transient growth in diabatic boundary layers with fluids at supercritical pressure.
Physical Review Fluids 9, 083901, 2024.

We study non-modal disturbances in the spatial framework using an eigenvector decomposition of the linearised Navier–Stokes equations under the assumption of locally parallel flow. To account for non-ideality, a new energy norm is derived. Several heat transfer scenarios at supercritical pressure are investigated, which are of practical relevance in technical applications. The boundary layers with the fluid at supercritical pressure are heated or cooled by prescribing the wall and free-stream temperatures so that the temperature profile is either entirely subcritical (liquid-like), supercritical (vapour-like), or transcritical (crossing the Widom line). In the non-transcritical states, the resulting streamwise-independent streaks originate from the lift-up effect. Wall cooling enhances the energy amplification for both subcritical and supercritical states. When the temperature is increased beyond the Widom line, a strong sub-optimal growth is observed over very short streamwise distances due to the Orr mechanism. Due to the additional presence of transcritical Mode II, the optimal energy growth at large distances is found to arise from an interplay between lift-up and Orr mechanisms. As a result, optimal disturbances are streamwise-modulated streaks with strong thermal components and with a wave angle inversely proportional to the local Reynolds number. The non-modal growth is put in perspective with modal growth by means of an N-factor comparison. In the non-transcritical states, modal stability dominates regardless of wall-temperature variations. In contrast, in the transcritical state, non-modal N-factors are found to resemble the imposition of an adverse pressure gradient in the ideal-gas state. When cooling beyond the Widom line, optimal growth is greatly enhanced, yet strong inviscid instability prevails. When heating beyond the Widom line, optimal growth could be sufficiently large to favour transition, particularly with a high free-stream-turbulence level.

4.1 Introduction

In the case of compressible boundary-layer flows under the ideal-gas assumption, it is well-known that various transition scenarios involve instabilities preceding or bypassing the aforementioned exponential modal growth (Schmid 2007). Non-modal growth, also known as transient growth, has emerged as a potential mechanism for explaining transition scenarios over a wide range of parameter values, such as in the 'blunt-body paradox' (Reshotko 2001; Reshotko & Tumin 2000). Hanifi *et al.* (1996) conducted the first transient growth analysis in compressible boundary layers in a temporal formulation. Similar to incompressible flows (Andersson *et al.* 1999), initial optimal perturbations took the form of local streamwise vorticity disks, which evolve into linearly growing streamwise streaks driven by the lift-up effect (Landahl 1980; Luchini 2000). Simultaneously, for compressible flows, density and temperature fluctuations also increase linearly with time (Hanifi & Henningson 1998). Analogous conclusions were drawn in a spatial framework (Tumin & Reshotko 2001). Optimal output perturbations, in the form of streamwise velocity streaks, were found in supersonic and hypersonic flows under the ideal-gas assumption (Bitter 2015; Paredes *et al.* 2016). Here, wall cooling below the adiabatic temperature reduces the level of non-modal energy amplification. Conversely, at low Mach numbers (e.g. $M_\infty = 0.5$) and with highly cooled walls (e.g. $T_w/T_\infty = 0.3$, where T_w is the wall temperature), no modal instabilities are found, and thus, transition to turbulence is likely to be driven only by transient growth (Bitter 2015).

Another example, where large thermodynamic and transport property gradients play a major role in flow instability, is in stratified flows (Govindarajan & Sahu 2014). The impact of viscosity stratification on transient growth has been studied for both incompressible and compressible Couette (Malik *et al.* 2008; Saikia *et al.* 2017) and channel (Chikkadi *et al.* 2005; Sameen & Govindarajan 2007; Sameen *et al.* 2011) flows. In the latter, it was discovered that any viscosity stratification does not significantly affect transient growth, whereas an increase in Prandtl number can lead to a total-energy amplification rise by over an order of magnitude. Recently, Jose *et al.* (2020) studied the role of buoyancy on stratified viscosity profiles in water and air. When the bottom layer is denser than the top one, transient-growth stabilisation occurs, and vice versa. The optimal perturbation energy is found to be constantly localised in low-viscosity regions, leading to the formation of strong localised streaks. As the Richardson number is increased, these optimal perturbations are no longer streamwise independent. A similar behaviour was found in stably stratified boundary layers (Parente *et al.* 2020) under the Boussinesq assumption, where the optimal energy growth is a combination of the lift-up and the Orr mechanism. Furthermore, as buoyancy effects become larger than shear production, the optimal energy gain and optimal time decrease, while the optimal streamwise wavenumber increases, confirming the existence of oblique optimal perturbations. The first study on non-modal growth with supercritical carbon dioxide at $p = 80\,\mathrm{bar}$ was performed in a Poiseuille flow (Ren *et al.* 2019*a*). Regardless of the temperature flow state (subcritical, supercritical, or transcritical with respect to the pseudo-boiling temperature), non-ideality always promoted transient growth at a constant T_w/T_{center}, where T_{center} is the centreline

temperature. The same behaviour was discovered when the level of viscous heating, controlled by the product of the Prandtl Pr_∞ and Eckert Ec_∞ number, was increased in contrast to the ideal-gas assumption. Optimal initial perturbations were found to be streamwise-independent vortices, while optimal output perturbations were represented by velocity streaks. In the transcritical temperature case, either when $Pr_\infty Ec_\infty$ is sufficiently large or when the Widom line is crossed, the most non-modally unstable condition appears, leading to the additional formation of large thermal streaks in the dense near-wall region close to the Widom line.

The main focus of this work is to investigate the non-modal growth of Two-Dimensional (2-D) Zero-Pressure-Gradient (ZPG) flat-plate boundary layers with fluids close to the critical point. Specifically, we aim to elucidate the role of Mode II in transient growth, as first discussed by Robinet & Gloerfelt (2019). In order to include non-ideal-gas effects in the non-modal stability analysis, a new energy norm has been derived, differently from Ren *et al.* (2019*a*). The transient growth calculations reported in this work are conducted in the spatial framework, enabling the comparison with the spatial exponential amplification of unstable modes. The competition between modal and non-modal growth mechanisms remains a fundamental research question, independently of the gas behaviour. For instance, N-factor correlations provide valuable insights into the classical e^N method for transition prediction (see Levin & Henningson (2003); Tempelmann *et al.* (2012)). Moreover, understanding the conditions under which the increased level of transient growth could be critical allows for a shift from transition models based solely on linear growth towards amplitude-based transition prediction. This methodology is applied for the first time to fluids at supercritical pressure, opening new perspectives in the study of instability and transition mechanisms in non-ideal fluids.

The work is organised as follows: in Sec. 4.2, the governing equations for non-modal stability analysis are presented. The derivation of the new energy norm is then undertaken. Subsequently (Sec. 4.3), base-flow properties of eight flow cases at a constant supercritical pressure of 80 bar for carbon dioxide ($p^*/p_c^* = 1.084$, with p_c^* being the critical pressure) are introduced. Given a diabatic wall, different temperature profiles are considered, namely below, above, and crossing the Widom line. These states are defined as subcritical, supercritical, and transcritical (pseudo-boiling, (Banuti 2015)) with respect to the pseudo-critical temperature. Note that critical here refers to the thermodynamic critical point, not to be confused with subcritical growth below critical Reynolds numbers in hydrodynamic stability theory (Schmid & Henningson 2001). Non-modal stability analysis results are then reported in Sec. 4.4. Optimal amplifications and perturbations are investigated for all states. Effects of initial Reynolds number and wall temperature, with a special focus on the transcritical wall-heating and -cooling cases, are considered. The final section, Sec. 4.5, is dedicated to the comparison between transient growth of perturbation energy and exponential growth of unstable discrete eigenvalues by means of N-factors. Finally, conclusions are presented in Sec. 4.6.

4.2 Methodology

4.2.1 Flow-conservation equations

The fundamental flow-conservation equations for a single-phase, non-reacting compressible fluid suitable for the non-ideal thermodynamic region are presented in Sec. 2.1, with reference values being the free-stream flow conditions. Nevertheless, in this chapter, a Mach number of 10^{-3} is chosen to reduce the complexity of the physical problem, ruling out strong acoustic effects on the flow stability. Therefore, the non-dimensionalisation is adjusted, as the pressure is only of hydrodynamic nature in this case (Nemati *et al.* 2016). The dimensionless specific internal energy e is non-dimensionalised with $c^*_{p,\infty}T^*_\infty$, leading to the following primitive momentum and internal-energy equations:

$$\rho\frac{Du_i}{Dt} = -\frac{\partial p}{\partial x_i} + \frac{1}{Re}\frac{\partial \tau_{ij}}{\partial x_j}, \tag{4.1a}$$

$$\rho\frac{De}{Dt} = -Ec_\infty p\frac{\partial u_j}{\partial x_j} + \frac{Ec_\infty}{Re}\frac{\partial\left(u_i\tau_{ij}\right)}{\partial x_j} - \frac{1}{RePr_\infty}\frac{\partial q_j}{\partial x_j}. \tag{4.1b}$$

Similarly to Chapter 2, the second viscosity coefficient λ is equal to $-2/3\mu$. The bulk viscosity μ_b has proven to have a very limited influence on the stability of Poiseuille flows at supercritical pressure (see Ren *et al.* (2019*a*)), and therefore it is set to 0 in agreement with Ren *et al.* (2019*b*). An additional assumption is that buoyancy effects are not considered here. The corresponding non-dimensional characteristic parameters are defined according to Eqs. (2.8*a–d*) with free-stream flow conditions denoted with $(\cdot)_\infty$ and where L^* is the chosen length scale. We opt for the local Blasius length scale δ^* as in Eqs. (2.47*a*,*b*). The Mach number $M_\infty = u^*_\infty/a^*_\infty$, with a^*_∞ as the speed of sound, can be obtained from Ec_∞. In order to close the conservation equations, an Equation of State (EoS) and transport properties need to be defined. We choose 80 bar as the reference pressure of supercritical CO_2 based on previous studies (see, for instance, Ren *et al.* (2019*b*)). Its properties are summarised in Appendix A.1. Both thermodynamic and transport properties are obtained from the NIST REFPROP library (Lemmon *et al.* 2013), which is transformed into 2-D look-up tables as functions of p and T. These properties are needed both for the laminar base-flow calculation and the stability analysis.

4.2.2 Base-flow calculation

The calculation of the base-flow profiles is performed according to Sec. 2.4. Grid-independent results are achieved with a wall-normal resolution of at least 10 000 points to accurately capture the strong property gradients around the Widom line, and a domain size approximately equal to 10 times the boundary-layer thickness.

4.2.3 Stability calculation

The stability analysis is performed under the framework of Linear Stability Theory (LST) according to Sec. 3.2. The modification of the Navier–Stokes equations in Sec. 4.2.1 results in new base-flow matrices, detailed in Appendix B.1.

Energy norm

Before addressing transient growth analysis, it is necessary to define an inner product and an associated energy norm. In Ren *et al.* (2019*a*), the energy norm for non-ideal-gas flows was chosen to ensure convergence with respect to energy amplification. Nevertheless, pressure-related energy terms persisted. Their contribution to the total disturbance energy must vanish, as compression work is conservative (Hanifi *et al.* 1996). Thus, following Mack's norm for ideal gas as in Hanifi *et al.* (1996), a rigorous definition of the norm for non-ideal-gas flows must be formulated. This norm will allow us to consider the characteristic non-orthogonality of the eigenfunctions and to quantify the magnitude of transient-growth energy amplification. First, a scalar product based on the energy density, as proposed by Tumin & Reshotko (2001), is defined as

$$(\hat{\mathbf{q}}_k, \hat{\mathbf{q}}_l)_E = \int_0^\infty \hat{\mathbf{q}}_k^H \mathbf{M} \hat{\mathbf{q}}_l \, \mathrm{d}y, \tag{4.2}$$

where the superscript H denotes the complex conjugate transpose, and the matrix $\mathbf{M}$ is the energy matrix. The associated norm is expressed as:

$$2E = \|\hat{\mathbf{q}}\|_E^2 = (\hat{\mathbf{q}}, \hat{\mathbf{q}})_E. \tag{4.3}$$

For compressible flows under the ideal-gas assumption (Chu 1965; Mack 1984; Hanifi *et al.* 1996), Eq. (4.3) results in

$$2E = \int_\Omega \left[m_{u_i} u_i' u_i'^\dagger + m_\rho \rho' \rho'^\dagger + m_T T' T'^\dagger \right] \mathrm{d}\Omega, \tag{4.4}$$

where $(\cdot)^\dagger$ and Ω denote the complex conjugate and the spatial domain, respectively. The coefficients $m_{u_{1,2,3}}$, m_ρ, and m_T of the symmetric positive-definite matrix $\mathbf{M}$ were derived by Hanifi *et al.* (1996) and take the form of

$$m_\rho = \frac{R_g \bar{T}}{\bar{\rho}}, \quad m_u = \bar{\rho}, \quad m_v = \bar{\rho}, \quad m_w = \bar{\rho}, \quad m_T = \frac{\bar{\rho} c_v}{E c_\infty \bar{T}}, \tag{4.5a–e}$$

with R_g and c_v being the gas constant and the specific heat at constant volume, respectively. However, for non-ideal-gas conditions in Ren *et al.* (2019*a*), the coefficients m_ρ and m_T were assumed to be unity, revealing a robust convergence behaviour for energy amplification. Here, instead, we follow the same procedure as outlined in Hanifi *et al.* (1996). As will be shown below, the coefficients in Eq. (4.4) are modified so that the pressure-related term, appearing in the form $\nabla \cdot (p' \mathbf{u}')$, can be eliminated after spatial integration. By multiplying

each disturbance equation in Eq. (3.5) with $m_\rho\rho'$, $m_{u_i}u_i'$, $m_T T'$, respectively, and summing the equations, the following result is obtained

$$\frac{1}{2}\frac{\partial}{\partial t}\left[m_\rho\rho'^2 + m_{u_i}u_i'^2 + m_T\left.\frac{\partial\bar{e}}{\partial\bar{T}}\right|_{\bar{\rho}}T'^2 + 2m_T\left.\frac{\partial\bar{e}}{\partial\bar{\rho}}\right|_{\bar{T}}\rho'T'\right] = \\ -m_\rho\bar{\rho}\rho'\frac{\partial u_i'}{\partial x_i} - \frac{m_{u_i}}{\bar{\rho}}u_i'\frac{\partial p'}{\partial x_i} - m_T\frac{Ec_\infty\bar{p}}{\bar{\rho}}T'\frac{\partial u_i'}{\partial x_i} - m_T\left.\frac{\partial\bar{e}}{\partial\bar{\rho}}\right|_{\bar{T}}\rho'\frac{\partial T'}{\partial t} + \text{visc.} \tag{4.6}$$

where visc. represents the viscous terms. When integrating over the spatial domain Ω, the pressure-work term in the right-hand side (RHS) of Eq. (4.6) disappears, as both of the following properties are satisfied (Bitter 2015; Chen *et al.* 2022): (1) the disturbances are periodic in space, and (2) the wall-normal velocity is zero. Consequently, using integration by parts yields:

$$\int_\Omega \nabla\cdot(p'\mathbf{u}')\,d\Omega = \int_\Omega m_\rho\bar{\rho}\rho'\frac{\partial u_i'}{\partial x_i}\mathrm{d}\Omega - \int_\Omega m_{u_i}\frac{1}{\bar{\rho}}p'\frac{\partial u_i'}{\partial x_i}\mathrm{d}\Omega + \int_\Omega m_T\frac{Ec_\infty\bar{p}}{\bar{\rho}}T'\frac{\partial u_i'}{\partial x_i}\,\mathrm{d}\Omega. \tag{4.7}$$

The left-hand side (LHS) of Eq. (4.6) represents the time rate of change of the disturbance energy as:

$$\frac{\partial E}{\partial t} = \frac{1}{2}\frac{\partial}{\partial t}\int_\Omega\left[m_\rho\rho'^2 + m_{u_i}u_i'^2 + m_T\left.\frac{\partial\bar{e}}{\partial\bar{T}}\right|_{\bar{\rho}}T'^2 + 2m_T\left.\frac{\partial\bar{e}}{\partial\bar{\rho}}\right|_{\bar{T}}\rho'T'\right]\mathrm{d}\Omega. \tag{4.8}$$

By choosing $m_{u_i} = \bar{\rho}$ similar to the ideal-gas norm (Hanifi *et al.* 1996), and

$$m_\rho = \frac{1}{\bar{\rho}}\left.\frac{\partial\bar{p}}{\partial\bar{\rho}}\right|_{\bar{T}}, \quad m_T = \frac{\bar{\rho}}{Ec_\infty\bar{p}}\left.\frac{\partial\bar{p}}{\partial\bar{T}}\right|_{\bar{\rho}}, \tag{4.9a,b}$$

the pressure-work term is eliminated. Thus, the resulting energy norm for non-ideal gas is written as:

$$2E = \int_\Omega\left[\frac{1}{\bar{\rho}}\left.\frac{\partial\bar{p}}{\partial\bar{\rho}}\right|_{\bar{T}}\rho'^2 + \bar{\rho}u_i'^2 + \frac{\bar{\rho}}{Ec_\infty\bar{p}}\left.\frac{\partial\bar{p}}{\partial\bar{T}}\right|_{\bar{\rho}}\left.\frac{\partial\bar{e}}{\partial\bar{T}}\right|_{\bar{\rho}}T'^2 + 2\frac{\bar{\rho}}{Ec_\infty\bar{p}}\left.\frac{\partial\bar{p}}{\partial\bar{T}}\right|_{\bar{\rho}}\left.\frac{\partial\bar{e}}{\partial\bar{\rho}}\right|_{\bar{T}}\rho'T'\right]\mathrm{d}\Omega. \tag{4.10}$$

The kinetic energy of a perturbation is therefore

$$2E_{kin.} = \int_\Omega \bar{\rho}u_i'^2\mathrm{d}\Omega, \tag{4.11}$$

whereas its internal energy is given as:

$$2E_{\text{int.}} = 2\left(E_{\rho'} + E_{T'} + E_{\rho'T'}\right) = \\ \int_\Omega\left[\frac{1}{\bar{\rho}}\left.\frac{\partial\bar{p}}{\partial\bar{\rho}}\right|_{\bar{T}}\rho'^2 + \frac{\bar{\rho}}{Ec_\infty\bar{p}}\left.\frac{\partial\bar{p}}{\partial\bar{T}}\right|_{\bar{\rho}}\left.\frac{\partial\bar{e}}{\partial\bar{T}}\right|_{\bar{\rho}}T'^2 + 2\frac{\bar{\rho}}{Ec_\infty\bar{p}}\left.\frac{\partial\bar{p}}{\partial\bar{T}}\right|_{\bar{\rho}}\left.\frac{\partial\bar{e}}{\partial\bar{\rho}}\right|_{\bar{T}}\rho'T'\right]\mathrm{d}\Omega. \tag{4.12}$$

The inner product and the associated norm can then be expressed in symbolic form as in Eqs. (4.2) and (4.3), respectively. The newly proposed energy matrix $\mathbf{M}$ for a non-ideal gas is then:

$$\mathbf{M} = \begin{bmatrix} \frac{1}{\bar{\rho}}\left.\frac{\partial\bar{p}}{\partial\bar{\rho}}\right|_{\bar{T}} & 0 & 0 & 0 & \frac{\bar{\rho}}{Ec_\infty\bar{p}}\left.\frac{\partial\bar{p}}{\partial\bar{T}}\right|_{\bar{\rho}}\left.\frac{\partial\bar{e}}{\partial\bar{\rho}}\right|_{\bar{T}} \\ 0 & \bar{\rho} & 0 & 0 & 0 \\ 0 & 0 & \bar{\rho} & 0 & 0 \\ 0 & 0 & 0 & \bar{\rho} & 0 \\ \frac{\bar{\rho}}{Ec_\infty\bar{p}}\left.\frac{\partial\bar{p}}{\partial\bar{T}}\right|_{\bar{\rho}}\left.\frac{\partial\bar{e}}{\partial\bar{\rho}}\right|_{\bar{T}} & 0 & 0 & 0 & \frac{\bar{\rho}}{Ec_\infty\bar{p}}\left.\frac{\partial\bar{p}}{\partial\bar{T}}\right|_{\bar{\rho}}\left.\frac{\partial\bar{e}}{\partial\bar{T}}\right|_{\bar{\rho}} \end{bmatrix}. \tag{4.13}$$

The matrix $\mathbf{M}$ is positive definite, meeting the requirement of the energy-norm definition (Chu 1965). For an ideal gas, Eq. (4.13) simplifies to

$$\mathbf{M} = \mathrm{diag}\left(\frac{R_g\bar{T}}{\bar{\rho}}, \bar{\rho}, \bar{\rho}, \bar{\rho}, \frac{\bar{\rho}\, c_v}{Ec_\infty\bar{T}}\right), \tag{4.14}$$

recovering Chu's (Chu 1965) and Mack's norm (Hanifi *et al.* 1996).

Non-modal analysis

Once the eigenmode spectrum is obtained, the spatial optimisation method of Tumin & Reshotko (2001) is applied. The disturbance vector $\mathbf{q}'$ is projected onto the truncated eigenvector space spanned by the first K spatial eigenvalues α_k and eigenfunctions $\hat{\mathbf{q}}_k$. Consequently, the optimal transient growth, or optimal energy amplification, at the specific downstream coordinate is then calculated as

$$G = G(\omega, \beta, Re, x) = \max_{\hat{\mathbf{q}}(0)} \frac{E(\hat{\mathbf{q}}(x))}{E(\hat{\mathbf{q}}(0))} = \max_{\hat{\mathbf{q}}(0)} \frac{\|\hat{\mathbf{q}}(x)\|_E^2}{\|\hat{\mathbf{q}}(0)\|_E^2}, \tag{4.15}$$

where $E(\hat{\mathbf{q}}(x))$ is the total perturbation energy defined in Eq. (4.10), and $E(\hat{\mathbf{q}}(0))$ is its value at the initial location $x = 0$. The optimal transient growth can be expressed in terms of the L_2-(Euclidean)-norm as

$$G = \|\mathbf{F}\boldsymbol{\Lambda}\mathbf{F}^{-1}\|_2^2, \tag{4.16}$$

with

$$\boldsymbol{\Lambda} = \mathrm{diag}(\exp(\mathrm{i}\alpha_1 x), ..., \exp(\mathrm{i}\alpha_K x)), \quad \mathbf{A} = \mathbf{F}^H\mathbf{F}, \quad \mathbf{A}_{kl} = (\hat{\mathbf{q}}_k, \hat{\mathbf{q}}_l) = \int_0^\infty \hat{\mathbf{q}}_k^H \mathbf{M}\hat{\mathbf{q}}_l \,\mathrm{d}y, \tag{4.17a–c}$$

and $\mathbf{M}$ as in Eq. (4.13). The L_2-norm of matrix $\mathbf{F}\boldsymbol{\Lambda}\mathbf{F}^{-1}$ can be computed by means of singular value decomposition (SVD). The value of G is obtained by the square of the largest singular value, whereas its optimal conditions, i.e. optimal perturbations, can be computed via the right singular vector (Schmid & Henningson 2001). Following the notation in Hanifi *et al.* (1996), the maximum value of G over all x is denoted as G_{max}, and its maximum over all β and ω, is referred to as G_{opt}, with the optimal spanwise wavenumber β_{opt}, optimal frequency ω_{opt}, and optimal location x_{opt}, respectively. For the purpose of code validation, transient-growth results in Tumin & Reshotko (2001) are reproduced and reported in Appendix B.2. Additionally, under non-ideal-gas conditions, a grid-independence study is performed for a highly non-ideal reference case.

4.3 Flow cases

Before conducting the non-modal stability analysis, base-flow profiles must be known first. A constant pressure of $p^* = 80\,\mathrm{bar}$, which is for CO_2 1.084 times larger than the critical pressure p_c^*, is selected. Note that the closer the ratio p^*/p_c^* to unity, the stronger the thermodynamic non-ideality. To better assess the thermodynamic states considered in this study, a T_r–p_r

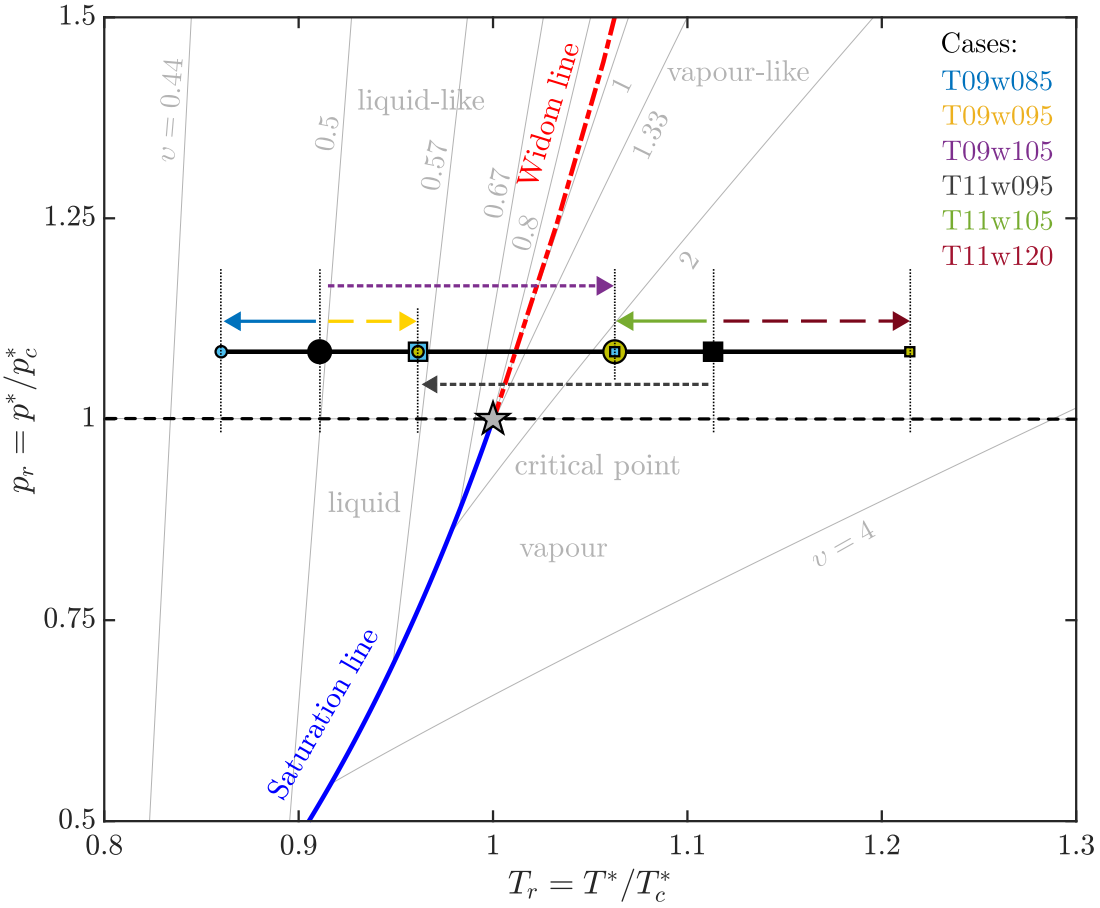

Figure 4.1: Reduced temperature-pressure (T_r–p_r) diagram with isolines of reduced specific volume (υ_r): isobar at $p^* = 80\,\text{bar}$ for CO_2 with the corresponding cases (lines) of Tab. 4.1. Note that the lines are offset for a better representation.

diagram is shown in Fig. 4.1 together with isolines of reduced specific volume ($\upsilon_r^* = 1/\rho_r^* = \upsilon^*/\upsilon_c^*$). Along the isobar (thick black line), two different configurations are considered: four cases have a subcritical temperature with respect to the free-stream temperature of $T_\infty^*/T_{pc}^* = 0.90$ (marked by a black circle (●) in Fig. 4.1), and four have a supercritical free-stream temperature of $T_\infty^*/T_{pc}^* = 1.10$ (marked by a black square (■) in Fig. 4.1). Here, T_{pc}^* denotes the pseudo-critical temperature, which is defined as the temperature at which the specific heat at constant pressure peaks along an isobar. At $p^* = 80\,\text{bar}$, this corresponds to $T_{pc}^*/T_c^* = 1.012$, which defines the pseudo-critical point on the Widom line. Note that while the pressure is always supercritical, cases that are subcritical in temperature are referred to as subcritical hereafter, and the same applies to supercritical. By varying the wall temperature per case, one can control the non-ideal-gas effects, which are maximal in the proximity of the Widom line. Therefore, for both free-stream configurations, one case is considered in which the temperature within the boundary layer crosses the Widom line (defined as transcritical hereafter). All cases are listed in Tab. 4.1 and represented in Fig. 4.1.

In all configurations, a Mach number of 10^{-3} is chosen to reduce the complexity of the

State	T^*_∞/T^*_{pc}	T^*_w/T^*_{pc}	T^*_w/T^*_∞	Wall	θ	Case	Line style
Subcrit. temp.	0.90	0.85	0.944	cooling	0.7080	T09w085	—
		0.90	1.0	isotherm	0.6641	T09w090	- - -
		0.95	1.056	heating	0.6178	T09w095	- - -
Transcrit. temp.	0.90	1.05	1.167	heating	0.4608	T09w105	- - - -
	1.10	0.95	0.864	cooling	0.9779	T11w095	- - - -
Supercrit. temp.	1.10	1.05	0.955	cooling	0.6931	T11w105	—
		1.10	1.0	isotherm	0.6641	T11w110	- - -
		1.20	1.091	heating	0.6290	T11w120	- - -

Table 4.1: Flow parameters at $p^* = 80\,\text{bar}$ for CO_2 and $M_\infty = 10^{-3}$. T^*_w is the wall temperature, and θ is the non-dimensional compressible momentum thickness, as defined in White (2006). Cases can be found in Fig. 4.1.

physical problem, ruling out strong acoustic effects on the flow stability. In the upper third of Tab. 4.1, cases with $T^*_\infty/T^*_{pc} = 0.90$ (liquid-like free stream) are presented. The temperature profiles for these cases remain subcritical, except for case T09w105, which becomes transcritical, i.e. $T^*_\infty/T^*_{pc} < 1$ and $T^*_w/T^*_{pc} > 1$. Furthermore, it holds: $Ec_\infty = 5.27 \times 10^{-7}$, $Pr_\infty = 2.11$, and a unit Reynolds number of $Re_u = 5.317 \times 10^6\,\text{m}^{-1}$. Cases with $T^*_\infty/T^*_{pc} = 1.10$ (vapour-like free stream) are shown in the lower third of Tab. 4.1. By mirroring case T09w105 on the Widom line, while maintaining the same ΔT, case T11w095 results in the transcritical case for a vapour-like free stream. Furthermore, it is: $Ec_\infty = 9.92 \times 10^{-8}$, $Pr_\infty = 1.22$, and a unit Reynolds number of $Re_u = 2.209 \times 10^6\,\text{m}^{-1}$.

The base-flow profiles for all cases in Tab. 4.1 are shown in Fig. 4.2. Dimensional quantities are made dimensionless by the corresponding quantities at the pseudo-critical point, except for the streamwise velocity u and kinematic viscosity ν (see Eqs. (2.7*a*–*j*)). Temperature, streamwise velocity, density, and kinematic viscosity are plotted over the wall-normal coordinate y, which is made dimensionless by the local Blasius length scale δ^* (see Eqs. (2.47*a*,*b*)). As the temperature profile crosses the Widom line (see Fig. 4.2a), regardless of the free-stream temperature, large variations in thermodynamic and transport properties are noticeable (e.g. density in Fig. 4.2d). As a result, both transcritical cases T09w105 and T11w095 exhibit inflectional base-flow profiles according to the definition of the Generalised Inflection Point (GIP), i.e. $\mathrm{d}/\mathrm{d}y(\bar{\rho}\,\mathrm{d}\bar{u}/\mathrm{d}y) = 0$. This GIP is located in the proximity of the Widom line, as indicated in Figs. 4.2(b–d) with a black circle ($\circ$) symbol. This leads to a minimum of kinematic viscosity ν near the pseudo-critical point (see Figs. 4.2e,f), as already observed in Bugeat *et al.* (2022). Moreover, for case T11w095, an inflectional $\bar{u}(y)$-profile, i.e. $\mathrm{d}^2\bar{u}/\mathrm{d}y^2 = 0$ (marked by a black star ($\star$) symbol), is found above the pseudo-critical point, due to a strong wall cooling similar to Ren & Kloker (2022) (see Sec. 3.3.3).

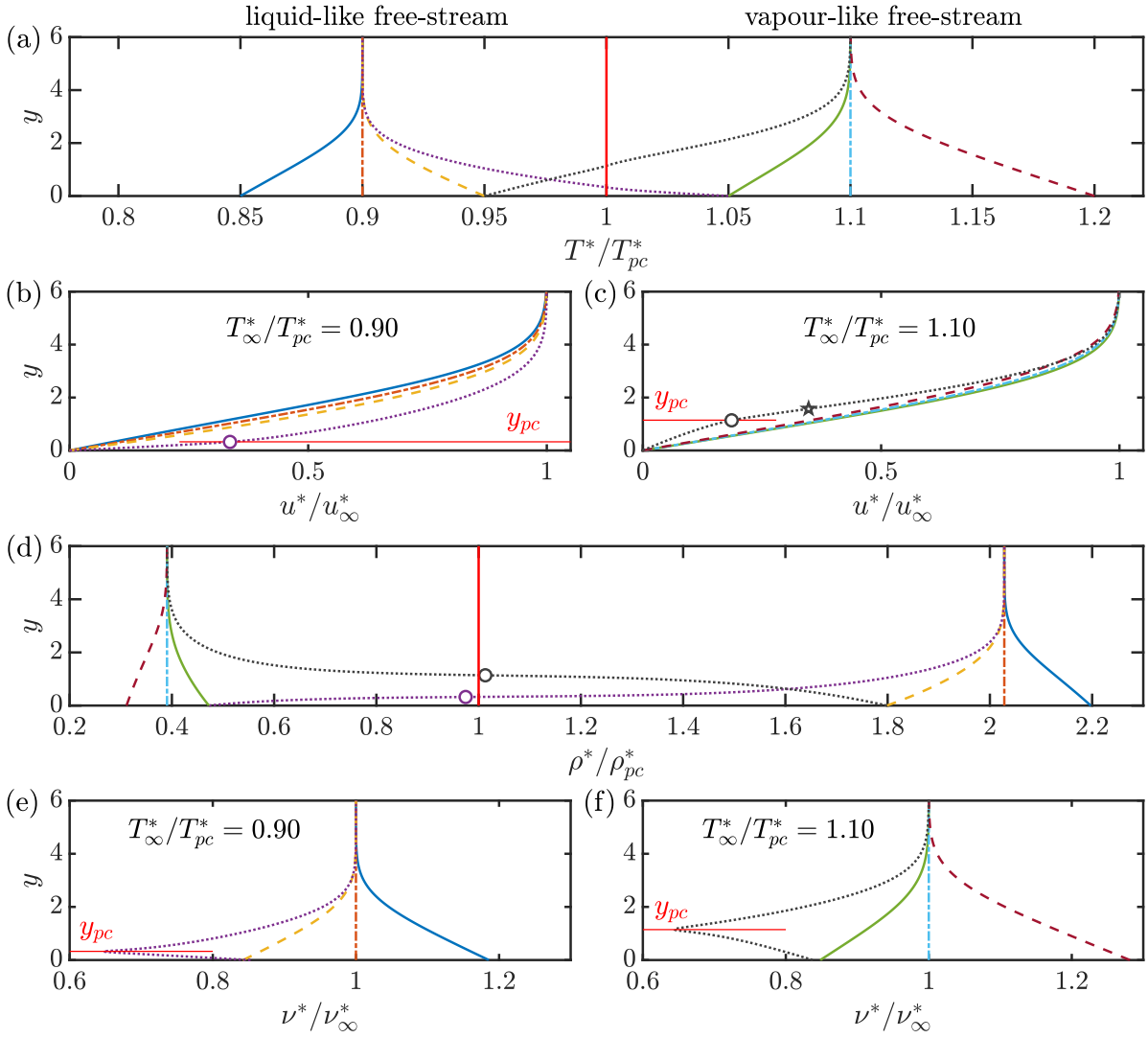

Figure 4.2: Base-flow profiles for the considered cases: (a) temperature, (b,c) streamwise velocity, (d) density and (e,f) kinematic viscosity over the dimensionless wall-normal coordinate y. See Tab. 4.1 for line legend. The red solid line (–) in (a,d) indicates the pseudo-critical point, i.e. at the pseudo-critical temperature $T^* = T^*_{pc}$. The location of the GIP is marked by a black circle (∘) symbol in (b–d). In (c), the location of the inflection point is marked by a black star (⋆) symbol. The location of the pseudo-critical point is indicated with y_{pc} in panels (b,c) and (e,f).

4.4 Non-modal analysis

In this section, we present the non-modal and modal stability analyses of the boundary-layer flows. After calculating the maximum and optimal energy amplifications in Sec. 4.4.1, Section 4.4.2 provides profiles of the optimal disturbances for selected cases, with special focus on the transcritical state. Subsequently, the influence of Reynolds number and wall temperature on transient growth is investigated. Finally, in Sec. 4.5, a comparison between non-modal and modal growth is provided.

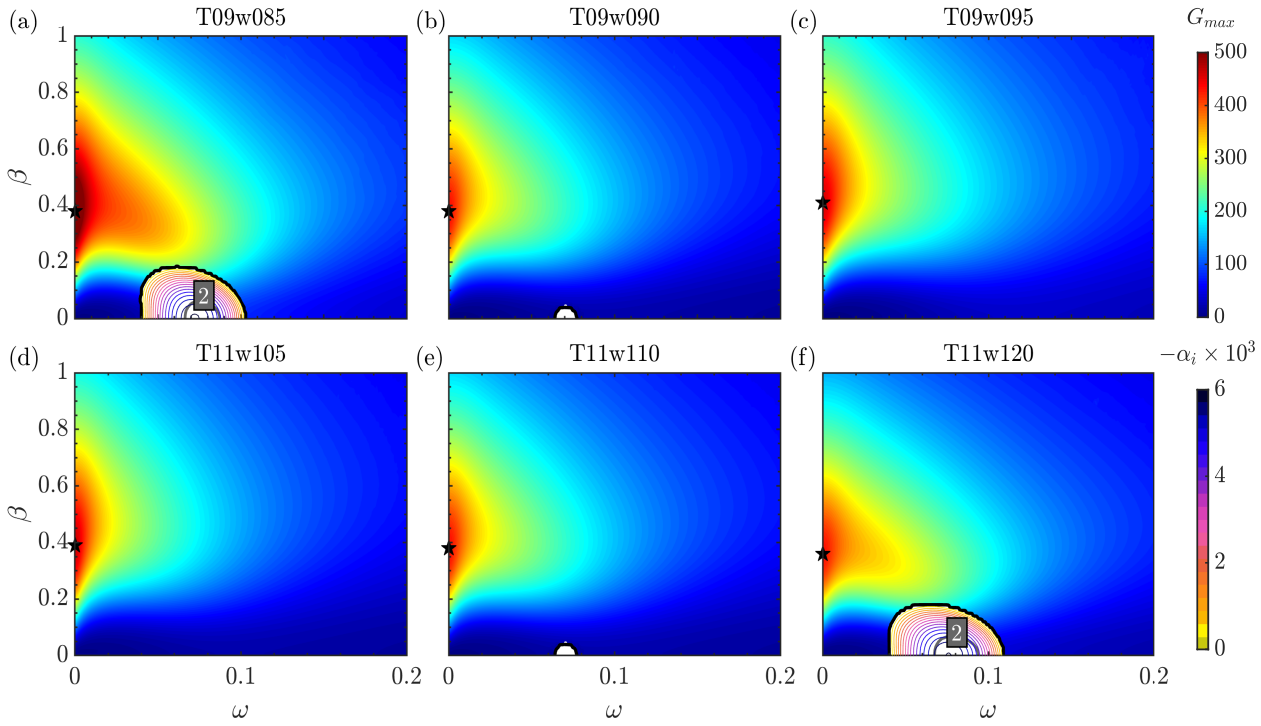

Figure 4.3: Contour plot of G_{max} and growth rate $-\alpha_i$ (modally unstable regions) against the angular frequency ω and spanwise wavenumber β at $Re = 300$ for the subcritical and supercritical cases: (a) T09w085, (b) T09w090, (c) T09w095, (d) T11w105, (e) T11w110, and (f) T11w120. G_{opt}, i.e. $\max\{G_{max}\}$, is denoted with a black star ($\star$) symbol. N-factor iso-contours are indicated in grey (see panels a and f).

4.4.1 Optimal amplifications

Optimal growth has been studied for the subcritical (T09w090, T09w095, T09w085), supercritical (T11w110, T11w105, T11w120), and transcritical (T09w105, T11w095) cases. An initial local Reynolds number of $Re = 300$ is chosen, and the optimisation process is conducted up to $x = 3000$ until the maximum value of $G(x)$, i.e. G_{max}, is found. Each contour plot in Figs. 4.3 and 4.4 has been computed on a grid of $\Delta\omega = 0.001 \times \Delta\beta = 0.01$. The coloured contour represents $G_{max}(\omega, \beta)$, and the largest G_{max}, or rather G_{opt}, is marked with a black star ($\star$). Secondary contour regions display an unstable mode of spatial growth rate $-\alpha_i$ with contour lines equally spaced between 0 and $\max\{-\alpha_i\}$. Here, the optimisation process is stopped. Furthermore, the integral amplification, e.g. N-factor, contours are indicated. For their calculation, the local growth rate has been integrated from $Re = 300$ to the optimal transient location at Re_{opt}, given by x_{opt}. A more comprehensive comparison between non-modal and modal N-factors is later performed in Sec. 4.5. In the non-transcritical cases, as the wall temperature increases towards the Widom line, either through an increase in T_w (subcritical state) or a reduction in T_w (supercritical state), modal amplification is completely damped. The unstable regions in Fig. 4.3(a) and Fig. 4.3(f) correspond to the only modal instability present in the subcritical and supercritical states, according to Ren *et al.* (2019*b*). They are of Tollmien–Schlichting-wave type. Overall, wall cooling in the liquid-like

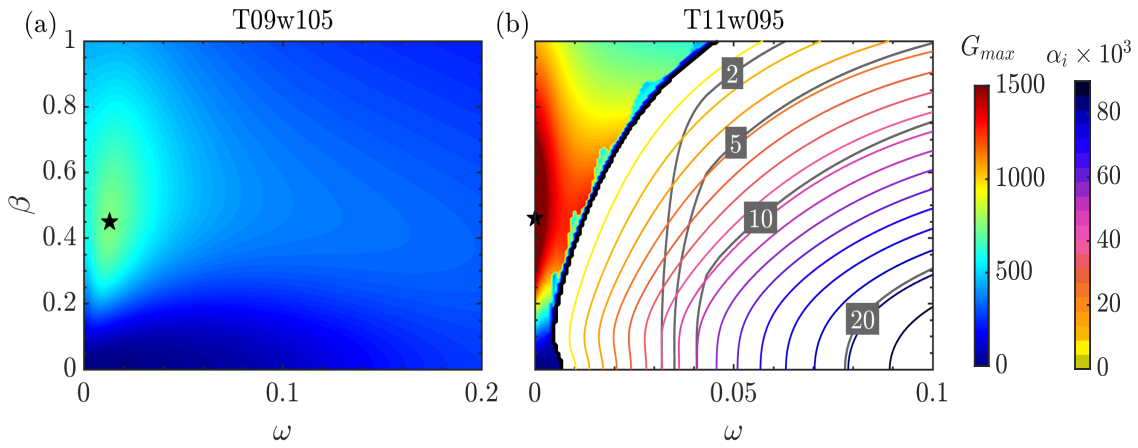

Figure 4.4: Contour plot of G_{max} and growth rate $-\alpha_i$ (modally unstable regions) against the angular frequency ω and spanwise wavenumber β at $Re = 300$ for the transcritical cases: (a) T09w105, and (b) T11w095. G_{opt}, i.e. $\max\{G_{max}\}$, is denoted with a black star ($\star$) symbol. N-factor iso-contours are indicated in grey.

region (see T09w085 in Fig. 4.3a) shows a similar transient-growth behaviour as wall cooling in the vapour-like region (see T11w105 in Fig. 4.3d). Cases T09w090 and T11w110 retain an identical energy amplification, reproducing the isothermal incompressible limit, which is independent of the considered gas law.

With respect to the transcritical cases in Fig. 4.4, G_{opt} significantly increases compared to the non-transcritical cases, especially in the case of cooling across the Widom line (T11w095) with $G_{opt} = 1750$. Note that, while for case T09w105 modal instabilities are not present at $Re = 300 < Re_{crit}$ (with Re_{crit} being the critical Reynolds number), case T11w095 is highly modally unstable (only one single mode) already at $Re = 300$. In contrast to the non-transcritical cases and case T11w095, wall heating across the Widom line (case T09w105) causes a shift of ω_{opt} from 0 to finite values. For instance, in Fig. 4.4(b), it is $\omega_{opt} = 0.013$. A similar shift is observed when a temporal analysis is performed in Appendix B.3. The physical mechanism responsible for the shift is explained in Sec. 4.4.2. Differently than in the non-transcritical cases, case T09w105 unveils a weakly decaying behaviour of G_{max} for large angular frequency ω around β_{opt}. It is interesting to note that at $\beta = 0$, there is a distinct increase in G_{max} along the ω-axis with a sub-optimal amplification peak of $G_{max} \approx 282$ at $\omega \approx 0.23$. A further analysis of the sub-optimal energy amplification is performed in Sec. 4.4.2.

Contours of the maximum location x_{max} are displayed in Figs. 4.5 and 4.6 for the same $\Delta\omega \times \Delta\beta$ grid as in Figs. 4.3 and 4.4. The optimum transient growth is always located at large streamwise locations (long-distance amplification) in agreement with the observations of Corbett & Bottaro (2000) and Bitter & Shepherd (2015) for incompressible and compressible boundary layers. Similarly, for small x (short-distance amplification), G_{opt} is always detected at large ω-values before shifting to $\omega = 0$ as x increases. This phenomenon is observed for all non-transcritical cases and case T11w095, except for the non-trivial case T09w105 in Fig. 4.5(g) where ω_{opt} is finite.

A summary of transient growth for the subcritical, transcritical, and supercritical states

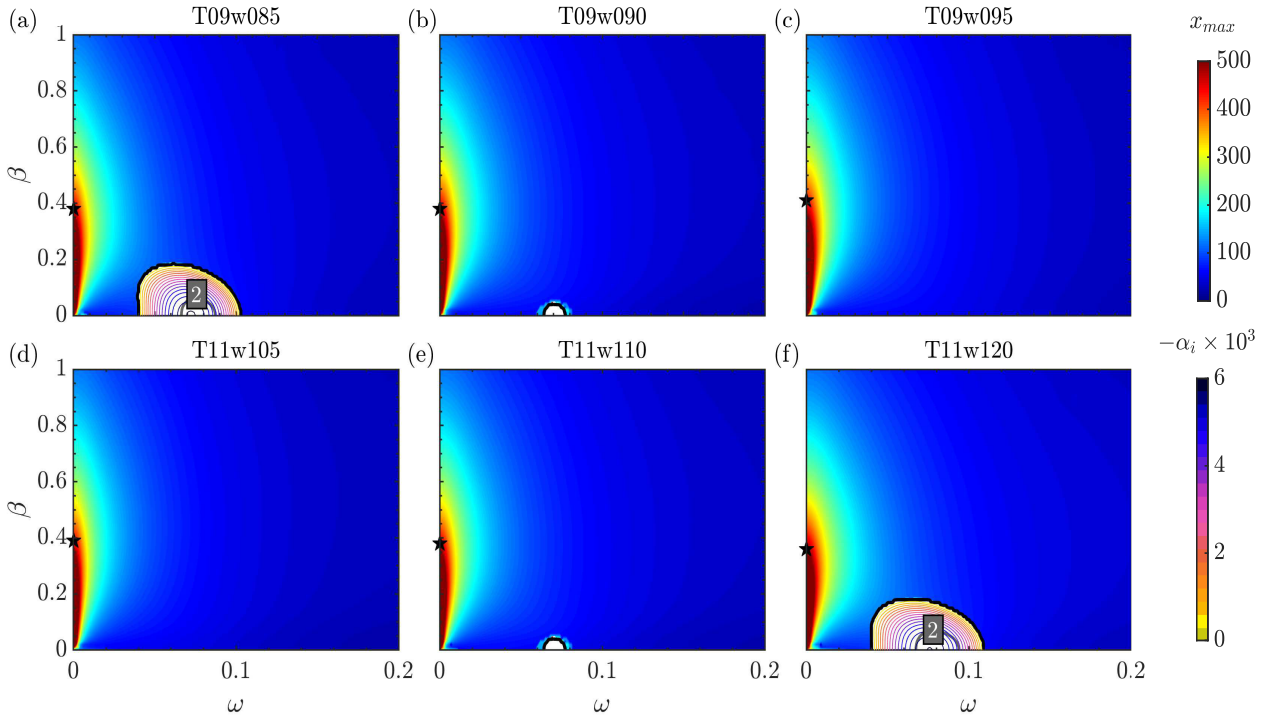

Figure 4.5: Contour plot of x_{max} and growth rate $-\alpha_i$ (modally unstable regions) against the angular frequency ω and spanwise wavenumber β at $Re = 300$ for the subcritical and supercritical cases: (a) T09w085, (b) T09w090, (c) T09w095, (d) T11w105, (e) T11w110, and (f) T11w120. The black star ($\star$) symbol refers to G_{opt}, i.e. $\max\{G_{max}\}$, according to Fig. 4.3. N-factor iso-contours are indicated in grey.

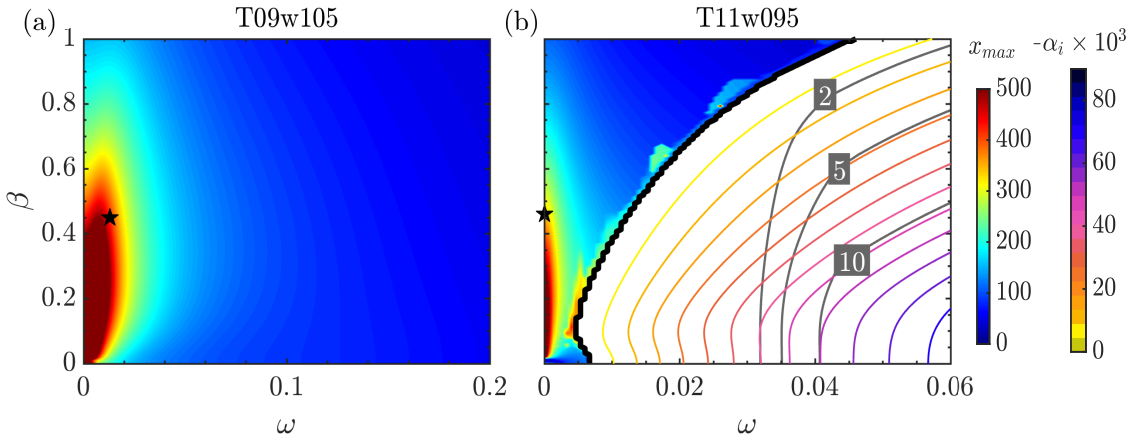

Figure 4.6: Contour plot of x_{max} and growth rate $-\alpha_i$ (modally unstable regions) against the angular frequency ω and spanwise wavenumber β at $Re = 300$ for the transcritical cases: (a) T09w105, and (b) T11w095. The black star ($\star$) symbol refers to G_{opt}, i.e. $\max\{G_{max}\}$, according to Fig. 4.4. N-factor iso-contours are indicated in grey.

is reported in Tab. 4.2. Note that the value of $G_{kin.opt}$ is calculated using the kinetic part and a frozen internal energy of $\mathbf{M}$ in Eq. (4.13), with $\mathbf{M} = \mathrm{diag}\,(1, \bar{\rho}, \bar{\rho}, \bar{\rho}, 1)$ (see Appendix B.4). Furthermore, the effect of the energy norm on the optimal growth is analysed. From Tab. 4.2, it is evident that, given the same temperature ratio T_w^*/T_∞^*, the optimal energy amplification

Case	G_{opt}	$G_{kin.opt}$	x_{opt}	Re_{opt}	ω_{opt}	β_{opt}	$\max\{-\alpha_i\}$
T09w085	540	476	464	478.7		0.377	0.569×10^{-2}
T09w090	437	437	462	478.1	0	0.381	0.238×10^{-3}
T09w095	460	397	434	469.2		0.408	-
T09w105	758	490	422	465.4	0.013	0.45	-
T11w095	1750	1.6704×10^4	346	440.2	0	0.46	0.089
T11w105	466	457	447	473.4		0.391	-
T11w110	437	437	462	478.1	0	0.381	0.238×10^{-3}
T11w120	434	414	490	486.8		0.364	0.566×10^{-2}

Table 4.2: Summary of spatial transient growth characteristics at $Re = 300$: subcritical, transcritical and supercritical cases.

increases more when the wall is cooled compared to the incompressible reference case, as density increases for both states. In fact, the largest G_{opt} is found for case T09w085, with the largest density ratio, i.e. $\rho^*_w/\rho^*_\infty = 1.0834$, among all non-transcritical cases of Tab. 4.1. This confirms the trend encountered in the ideal-gas results of Tumin & Reshotko (2001) at $M_\infty = 0.5$. Regarding the optimal energy amplification with frozen internal energy $G_{kin.opt}$, its greater impact is noticed in the subcritical state, where G_{opt} drops by more than 10%. For case T09w105, G_{opt} significantly increases due to non-ideal-gas effects, whereas $G_{kin.opt}$ consistently drops (density ratio at the wall: $\rho^*_w/\rho^*_\infty \approx 0.23$). When the vapour-like free stream is cooled down at the wall to a liquid-like state (case T11w095 with $\rho^*_w/\rho^*_\infty \approx 4.61$), the optimal energy amplification is strongly dampened by the non-ideal-gas effects, i.e. $G_{opt} \ll G_{kin.opt}$, while ω_{opt} is found at $\omega = 0$. Concerning the ratio between kinetic $\hat{E}_{kin.}$ and total energy $\hat{E}$, obtained by evaluating Eqs. (4.11) and (4.10), respectively, for $\hat{\mathbf{q}} = \hat{\mathbf{q}}_{opt}$, a value of 32% is found for case T09w105, whereas a value of 47% is found for case T11w095. This demonstrates how optimal thermal fluctuations become relevant whenever the Widom line is crossed, i.e. for large property variations. An analysis of the optimal energy amplification and spanwise wavenumber as a function of the wall temperature is performed in Sec. 4.4.4.

4.4.2 Optimal perturbations

Subcritical and supercritical states

For all subcritical and supercritical cases in Fig. 4.3 and Tab. 4.2, G_{opt} occurs at $\omega = 0$, indicating an input streamwise vortex typical of the ideal-gas assumption (Hanifi *et al.* 1996; Tumin & Reshotko 2001; Bitter 2015), as shown for case T09w095 in Fig. 4.7(a). Similar profiles are found for the other non-transcritical cases of Tab. 4.2 (not shown for brevity), as the initial perturbation energy, i.e. Eq. (4.10), is entirely of kinetic nature.

Figure 4.7(b) illustrates the flow response to the streamwise vortex at $x = x_{opt}$ for case T09w095. The output optimal disturbance mainly consists of streamwise velocity, taking the form of streamwise (high-low velocity) streaks, with negligible temperature and density

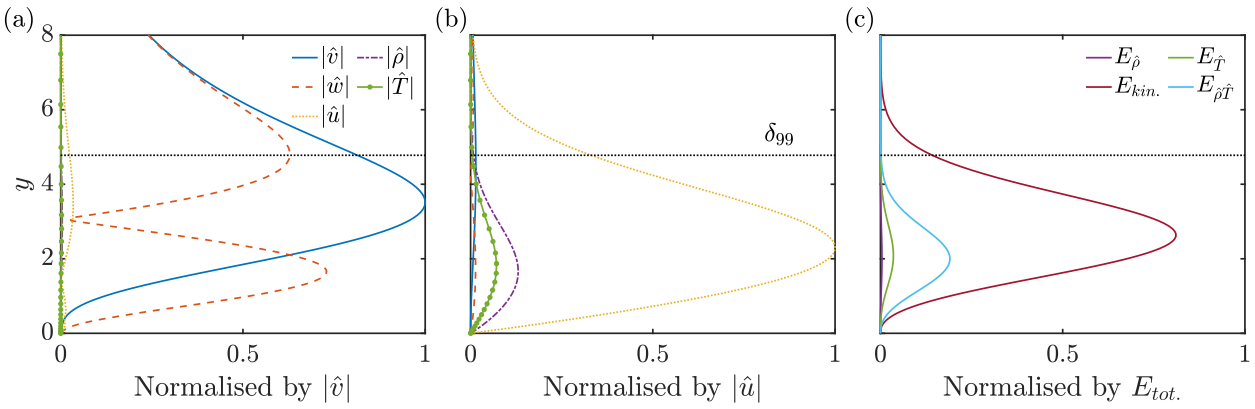

Figure 4.7: Absolute value of the optimal disturbances at $Re = 300$ over wall-normal distance y for T09w095 of Tab. 4.2: (a) initial, (b) output, and (c) output energy amplitude obtained by Eqs. (4.11) and (4.12) with respect to the total energy. The boundary-layer thickness is indicated by δ_{99}.

disturbances due to small corresponding mean-flow gradients. Similar streamwise velocity streaks are recovered for all subcritical and supercritical cases in Tab. 4.2 (only T09w095 displayed for brevity). The formation of velocity streaks has been explained by the lift-up effect (Landahl 1980). Note that, for case T09w095, the kinetic-energy fraction $\hat{E}_{kin.}/\hat{E}$ decreases from 99.9% to 86% after amplification, whereas for the subcritical cases, this drop is only up to 5%. Fig. 4.3(c) exhibits that the total energy amplitude is predominantly kinetic (large $\hat{E}_{kin.}/\hat{E}$), while the non-diagonal terms $\hat{E}_{\rho'T'}$ in matrix $\mathbf{M}$ of Eq. (4.13) contribute less than 20% due to small base-flow thermodynamic derivatives. This indicates a weak influence of non-ideality on the transient growth in the subcritical and supercritical states, with optimal perturbations resembling those in the incompressible ideal-gas state (Andersson *et al.* 1999; Tumin & Reshotko 2001).

Transcritical state

Figs. 4.8(a,b) present the optimal initial and output perturbations for the transcritical case T09w105, respectively. The initial disturbance at $x = 0$ takes the form of counter-rotating vortices, similar to the other two states. The resulting velocity streaks at maximum amplification have strong thermal $\hat{\rho}$ and $\hat{T}$ components. A notably strong density disturbance, absent in the non-transcritical cases (see e.g. Fig. 4.7b), peaks at the pseudo-critical point due to the abrupt mean-density gradient observed in Fig. 4.2(d). In Fig. 4.7(c) the energy amplitude of the disturbance components, normalised by the total energy indicates that $\hat{E}_{\hat{\rho}\hat{T}}$ reaches almost unity at the pseudo-critical point (largest non-ideal-gas effects), with negligible kinetic-energy contribution. By contrast, the kinetic-energy peak occurs in the liquid-like state (high-viscosity region) around $y \approx 0.35$, alongside the maximum temperature disturbance and a secondary peak of $\hat{E}_{\hat{\rho}\hat{T}}$. Similar to the non-transcritical cases in Fig. 4.7, the resulting optimal streaks are regions of excess and defect of streamwise momentum in the streamwise direction.

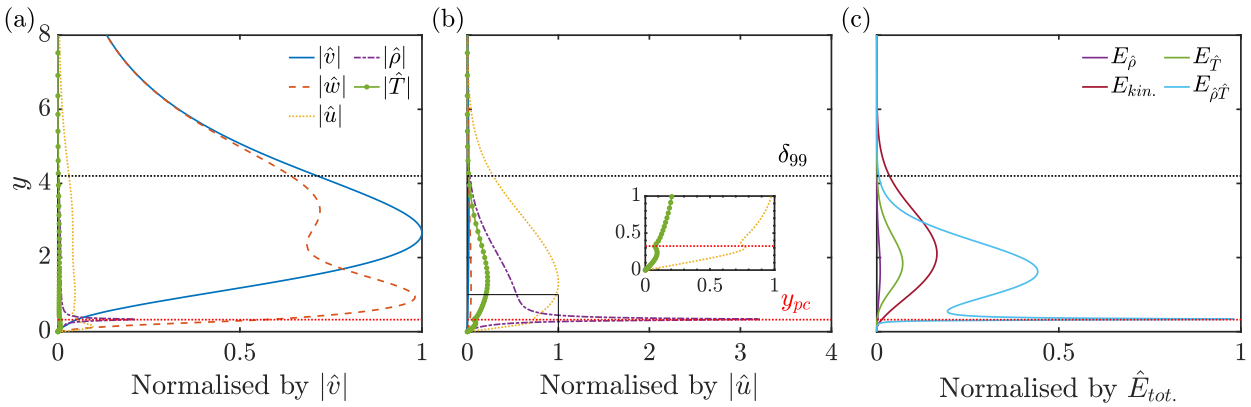

Figure 4.8: Absolute value of the optimal disturbances at $Re = 300$ over wall-normal distance y for T09w105 of Tab. 4.2: (a) initial, (b) output, (c) output energy amplitude obtained by Eqs. (4.11) and (4.12) with respect to the total energy amplitude. The boundary-layer thickness and the location of the pseudo-critical point, i.e. at the pseudo-critical temperature $T^* = T^*_{pc}$, are indicated by δ_{99} and y_{pc}, respectively.

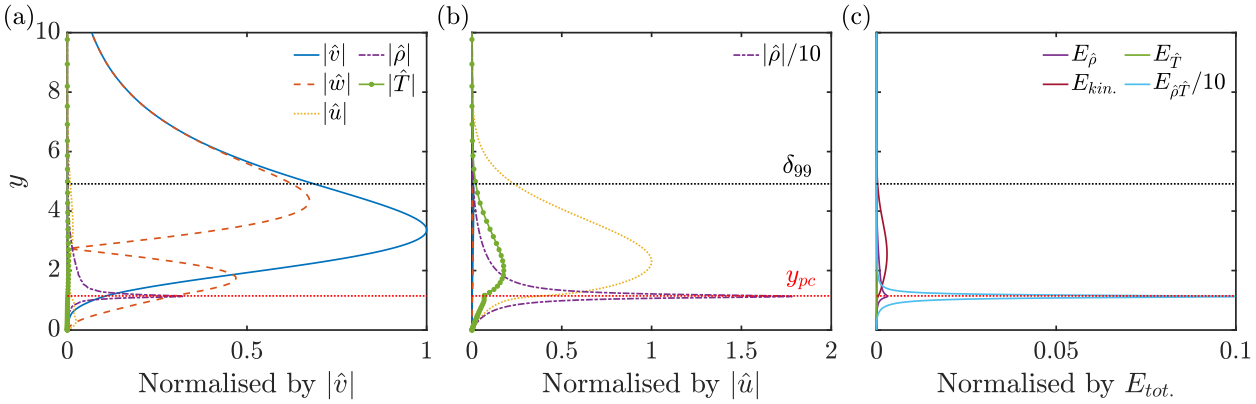

Figure 4.9: Absolute value of the optimal disturbances at $Re = 300$ over wall-normal distance y for T11w095 of Tab. 4.2: (a) initial, (b) output, (c) output energy amplitude obtained by Eqs. (4.11) and (4.12) with respect to the total energy amplitude. The boundary-layer thickness and the location of the pseudo-critical point, i.e. at the pseudo-critical temperature $T^* = T^*_{pc}$, are indicated by δ_{99} and y_{pc}, respectively.

The optimal perturbations for the transcritical case T11w095, where the temperature profile is cooled over the Widom line, are examined hereafter. Fig. 4.4(b) reveals that streamwise-independent streaks ($\omega_{opt} = 0$, $\beta_{opt} = 0.46$) are the optimal disturbances, differing from case T09w105. This is confirmed by the wall-normal profiles of optimal perturbations in Figs. 4.9(a) and 4.9(b), driven by the lift-up effect. Unlike the other cases, thermal streaks, i.e. $\hat{\rho}$ and $\hat{T}$, are even more significant, with the density disturbance reaching a factor 18 at the pseudo-critical point due to a larger mean density gradient than in case T09w105. Fig. 4.9(c) displays the disturbance energy amplitude, showing the maximum total energy amount at the pseudo-critical point, attributed to the abrupt gradients of the thermophysical properties (see Fig. 4.2). Here, non-ideality is greatest, while the kinetic-energy content is almost negligible throughout the boundary layer.

Transcritical state: vortex tilting

The mechanism of streak generation is best explained by the lift-up effect or vortex tilting (Butler & Farrell 1992; Brandt 2014). For a more accurate physical interpretation of the Widom line's effect on the optimal perturbation profiles, we consider the inviscid compressible vorticity equation, denoted as ω_i, as

$$\frac{\partial \omega_i}{\partial t} + u_j \frac{\partial \omega_i}{\partial x_j} = -\omega_i \frac{\partial u_j}{\partial x_j} + \frac{\epsilon_{ijk}}{\rho^2} \frac{\partial \rho}{\partial x_j} \frac{\partial p}{\partial x_k}, \tag{4.18}$$

where ϵ_{ijk} is the Levi–Civita symbol, and the second term on the RHS is the baroclinic term. After superposition and linearisation of Eq. (4.18) (see Appendix B.5), the wall-normal vorticity perturbation component, ω'_y, component becomes

$$\frac{\partial \omega'_y}{\partial t} + \bar{u} \frac{\partial \omega'_y}{\partial x} = -\frac{\partial v'}{\partial z} \frac{\partial \bar{u}}{\partial y}, \tag{4.19}$$

where the baroclinic term is zero, $\partial \bar{u}/\partial y$ is the spanwise mean-flow vorticity, and $\partial v'/\partial z$ is the perturbation strain rate of the initial vortex (Farrell & Ioannou 1993). The latter tilts the mean-flow vorticity into the wall-normal y direction, increasing ω'_y. Thus, the vortex-tilting mechanism depends on the initial disturbance strain rate $\partial v'_{in}/\partial z$, which can be assessed via the initial streamwise vorticity $\omega'_{x,in} = \partial w'_{in}/\partial y - \partial v'_{in}/\partial z$.

Figures 4.10(a,b) illustrate the initial streamwise vorticity, perturbation strain rate, and base-flow streamwise momentum for subcritical case T09w095 and transcritical case T09w105, respectively. The streamwise vorticity $|\hat{\omega}_{x,in}|$ exhibits two peaks: a lower one due to wall boundary conditions ($\hat{v}$ and $\hat{w}$ are zero at the wall), which does not correspond to a streamwise vortex, and an upper peak, far from the wall, corresponding to the vortex structure responsible for the largest amount of wall-normal redistribution (where $\partial \hat{v}_{in}/\partial z$ is largest). Here, $\hat{\omega}_{y,out}$ (black line) peaks, consistent across all the non-transcritical cases of Tab. 4.1.

In the transcritical case T09w105, as shown in Fig. 4.10(b), the Widom line affects the streamwise vorticity $\hat{\omega}_{x,in}$, peaking due to the large y-gradient of spanwise perturbation velocity $\hat{w}_{in}$ (not displayed). However, in this region, the low wall-normal displacement (see $\hat{v}_{in}$ in Fig. 4.8a) of a larger streamwise momentum (see the blue dotted line at $y = y_{pc}$ in comparison to case T09w095) reduces the contribution of the $\hat{w}_{in}$-peak to the lift-up effect. Additionally, the perturbation strain rate resembles the subcritical case shown in Fig. 4.10(a), but the Widom line significantly enhances the base-flow shear near the wall (see red dash-dotted line in Fig. 4.10b), considerably affecting, in turn, the vortex-tilting term ($|\partial \bar{u}/\partial y \cdot \partial \hat{v}_{in}/\partial z|$). As a result, $\hat{\omega}_{y,out}$ is substantially altered at the pseudo-critical point, exhibiting a secondary peak (inset of Fig. 4.10b), which corresponds to the $\hat{u}_{out}$-peak in Fig. 4.8(b). Thus, the streamwise-velocity streaks have two distinct peaks, the larger near the maximum perturbation strain rate and a smaller one at the pseudo-critical point. On the other hand, it is important to note that the $\hat{u}_{out}$-peak at the pseudo-critical point in Fig. 4.8(b) minimally affects the energy amplification, as internal energy, rather than kinetic energy, dominates the G-increase in this transcritical case (see G_{opt} vs. $G_{kin.opt}$ in Tab. 4.2).

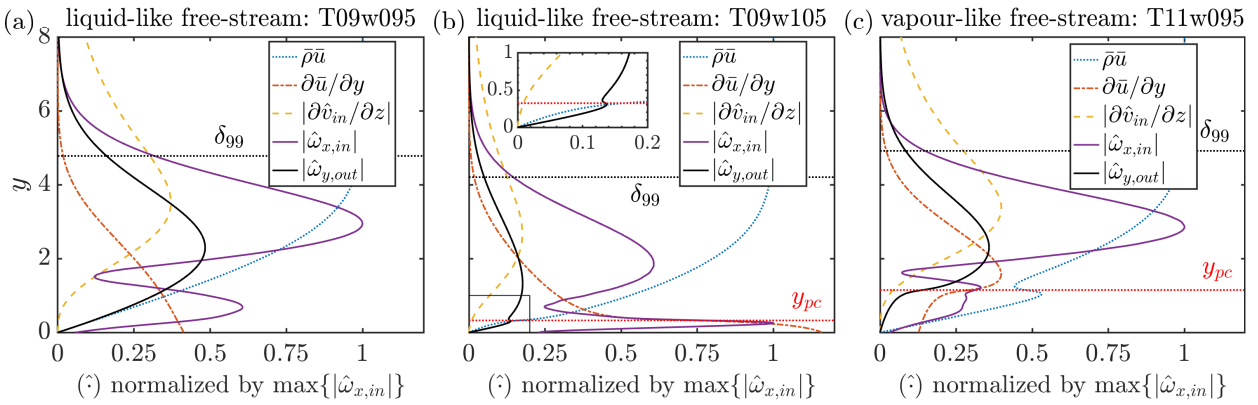

Figure 4.10: Vortex tilting: (a) case T09w095, (b) case T09w105, (c) case T11w095. All disturbance terms (·̂) are normalised by max{$|\hat{\omega}_x|$}. The boundary-layer thickness and the location of the pseudo-critical point, i.e. at the pseudo-critical temperature $T^* = T^*_{pc}$, are indicated by δ_{99} and y_{pc}, respectively.

Similar to the transcritical wall-heating case depicted in Fig. 4.10(b), the vortex tilting in the transcritical wall-cooling case is examined in Fig. 4.10(c). As with case T09w105, the perturbation strain rate $\partial\hat{v}_{in}/\partial z$ (Fig. 4.10c) remains unaffected by the Widom line. Instead, its influence is evident in $\hat{\omega}_{x,in}$, causing a substantial reduction in the lower peak near the wall. Below the pseudo-critical point, in the liquid-like state (see the large $\bar{\rho}_w$ in Fig. 4.2d), we observe a considerable increase in the horizontal momentum near $y = y_{pc}$ (blue dotted line, Fig. 4.10c). This suggests a stronger lift-up in this region. Indeed, the resulting peak in $\hat{\omega}_{y,out}$ occurs just above the pseudo-critical point, where the vortex-tilting term $|\partial\bar{u}/\partial y \cdot \partial\hat{v}_{in}/\partial z|$ is largest. Unlike Fig. 4.10(b), there is no secondary $\hat{u}_{out}$-peak at the pseudo-critical point in this case, as the mean-flow vorticity $\partial\bar{u}/\partial y$ near the wall is small. These observations suggest that the resulting streaks have a higher amplitude than those in case T09w105, attributed to a stronger vortex-tilting term $|\partial\bar{u}/\partial y \cdot \partial\hat{v}_{in}/\partial z|$. This behaviour is supported by the greater optimal energy amplification of case T11w095 compared to case T09w105: from Tab. 4.2, $G_{opt,\mathrm{T11w095}} > G_{opt,\mathrm{T09w105}}$.

Following the analysis in Sec. 3.3.3, in the vicinity of the pseudo-critical point, viscous effects dominate the streamwise momentum over advection. In this region, the approximation of the GIP, $\mathrm{d}/\mathrm{d}y(\bar{\rho}\,\mathrm{d}\bar{u}/\mathrm{d}y) \approx 0$, holds. This condition can be rewritten as

$$\left.\frac{\mathrm{d}\ln(\bar{\Omega})}{\mathrm{d}y}\right|_{y_{pc}} \simeq -\left.\frac{\mathrm{d}\bar{\mu}}{\mathrm{d}y}\right|_{y_{pc}}, \tag{4.20}$$

where $\bar{\Omega} = -\mathrm{d}\bar{u}/\mathrm{d}y$ is the mean-flow vorticity. From Eq. (4.20), it follows that:

$$\left.\frac{\mathrm{d}\ln(\bar{\Omega})}{\mathrm{d}y}\right|_{y_{pc}} \simeq \left(-\frac{1}{\bar{\mu}}\frac{\mathrm{d}\bar{T}}{\mathrm{d}y}\left.\frac{\partial\bar{\mu}}{\partial\bar{T}}\right|_{\bar{p}}\right)_{y_{pc}}. \tag{4.21}$$

The quantity $\partial\bar{\mu}/\partial\bar{T}|_{\bar{p}}$ is negative and large near the pseudo-critical point. In the case of wall heating with $\mathrm{d}\bar{T}/\mathrm{d}y < 0$, the right-hand side of Eq. (4.21) is negative, leading to a large decrease in $\bar{\Omega}$ at the pseudo-critical point. In contrast, for wall cooling with $\mathrm{d}\bar{T}/\mathrm{d}y > 0$, $\bar{\Omega}$

increases. In this latter case, since $\bar{\Omega}$ is always negative at the boundary-layer edge, there must exist a location with $y > y_{pc}$ where the LHS of Eq. (4.21) vanishes. This corresponds to the maximum in $|\bar{\Omega}|$ observed in Fig. 4.10(c), and leads to a peak in $\hat{\omega}_{y,out}$ above the pseudo-critical point.

Transcritical state: lift-up effect and Orr mechanism

For both transcritical cases, a detailed analysis of the spatial evolution of the optimal amplification is conducted to comprehend its structure. Beginning with case T09w105, Fig. 4.11(a) presents the transient growth $G(x)$ at ω_{opt} and β_{opt}, obtained from Eq. (4.16). This represents the optimal gain envelope over all possible initial conditions. To calculate the disturbance profiles over the streamwise distance x, we assume the same initial condition at $x = 0$ for the optimal perturbation and perform space marching up to $x = x_{opt}$, following $g(x)$ (red dashed line). At this location, the energy amplification $g(x)$ is equal to the maximum value of the G-envelope (solid blue line), while remaining lower for $x \neq x_{opt}$. For the calculation of $g(x)$, Eq. (4.16) utilises $\mathbf{F}$ associated with the right singular eigenvector at $x = x_{opt}$. Fig. 4.11(b) provides a Three-Dimensional (3-D) snapshot of the streamwise velocity perturbations, revealing oblique elongated structures. These results are computed based on the optimal perturbation chosen from $g(x)$ of Fig. 4.11(a). The physical mechanism of the lift-up effect is evident in the cross-stream slices (yz-plane) of Figs. 4.12(a–c), where contours of the output streamwise velocity perturbation u'_{out} are superimposed over the velocity vectors of the cross-stream perturbation velocity $|\vec{V'_{out}}| = \sqrt{v'^2_{out} + w'^2_{out}}$ at three different streamwise locations. Resulting high-velocity streaks ($\Re(u'_{out}) > 0$) form where counter-rotating vortices pull high-momentum fluid downward, and vice versa for low-velocity streaks ($\Re(u'_{out}) < 0$). This behaviour extends to the density and temperature streaks, where streamwise vortices act with the mean-density and against the mean-temperature profile, respectively. At $x = x_{opt} = 425$, the lift-up mechanism maximises streak amplification. The crossing of the Widom line introduces secondary u'_{out}-peaks, notably in the near-wall region, especially at early x, as demonstrated by the vortex-tilting mechanism in Fig. 4.10(b). Despite the 2-D parallel-flow assumption, vortices in Figs. 4.12(a–c) are not symmetrical with respect to the wall-normal axis but inclined in the spanwise direction. Within a very short distance ($x \approx 50$), they are first erected before being tilted in the other direction farther downstream. This observation suggests the presence of another mechanism contributing to additional energy amplification in the cross-plane spanwise component (Hack & Moin 2017). Notably, the shift of the optimal amplification G_{opt} to finite frequencies, visible in Fig. 4.4(a), implies that the Orr mechanism (Orr 1907) enhances the optimal amplification.

Examining a wall-normal slice (xy-plane) in Figs. 4.12(d,e) reveals the presence of this additional mechanism. Initially misaligned with the mean shear, the output streamwise velocity perturbations in Fig. 4.12(d) gradually incline in the direction of shear as they move downstream. During this process, the disturbance extracts energy from the mean-shear energy through the action of the Reynolds stress $u'_{out}v'_{out}$ (Fig. 4.12e), which increases due to conservation of circulation in an xy-plane (Parente *et al.* 2020). Subsequently, disturbance

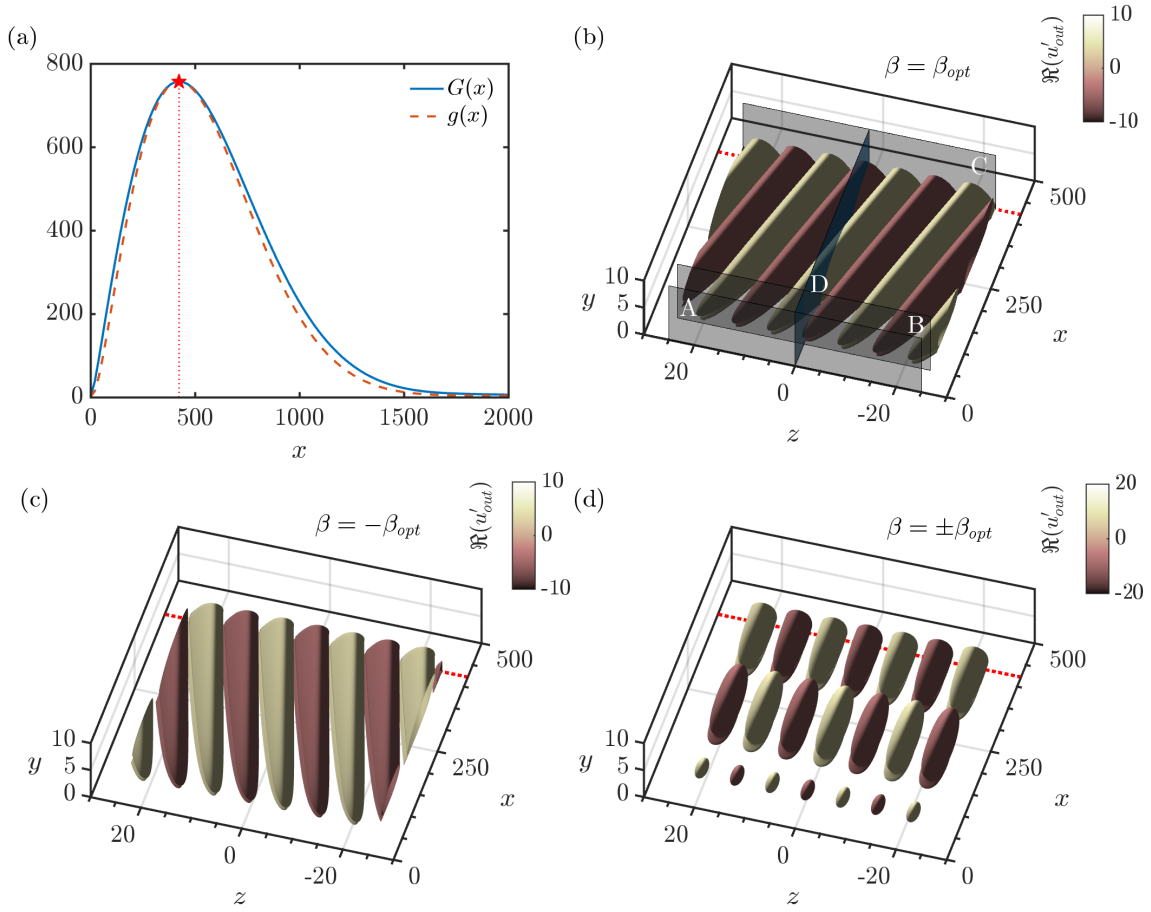

Figure 4.11: Case T09w105 ($Re = 300$, $\omega_{opt} = 0.013$, $\beta_{opt} = 0.45$): (a) envelope of the optimal transient growth $G(x)$ (—) and transient growth $g(x)$ of the optimal perturbation (- -) over the streamwise direction x, the red dotted line indicates the location of the optimal perturbation ($g(x_{opt}) = G(x_{opt})$); (b) iso-contours of the streamwise velocity perturbations ($\Re(u'_{out}) = \pm 4.0$) for $\beta = \beta_{opt}$ corresponding to their transient growth g; (c) iso-contours of the streamwise velocity perturbations ($\Re(u'_{out}) = \pm 4.0$) for $\beta = -\beta_{opt}$; (d) superposition of iso-contours ($\Re(u'_{out}) = \pm 8.0$) with $\pm\beta_{opt}$. The red dashed line indicates the optimal growth location ($x = x_{opt}$). Planes: A, B, C and D of Fig. 4.12.

energy is returned to the mean flow, with viscosity effects becoming relevant at large x. The largest absolute value of $u'_{out}v'_{out}$ occurs at $x \approx 240$, farther upstream than $x_{opt} = 425$. The Orr mechanism enhances cross-stream velocity, leading to an additional increase of the streamwise velocity perturbations (Farrell & Ioannou 1993), which peak at $x = x_{opt}$. This positive interplay between Orr mechanism, originally located at $\beta = 0$ and $\omega > 0$, and the lift-up effect, originally located at $\beta > 0$ and $\omega = 0$, results in optimal transient growth at finite frequencies and spanwise wavenumbers, e.g. $\omega_{opt} > 0, \beta_{opt} > 0$. Such interaction was previously discovered in constant-shear flows (Butler & Farrell 1992; Farrell & Ioannou 1993) and more recently in strongly stratified flows (Saikia *et al.* 2017) under the Boussinesq assumption (Parente *et al.* 2020).

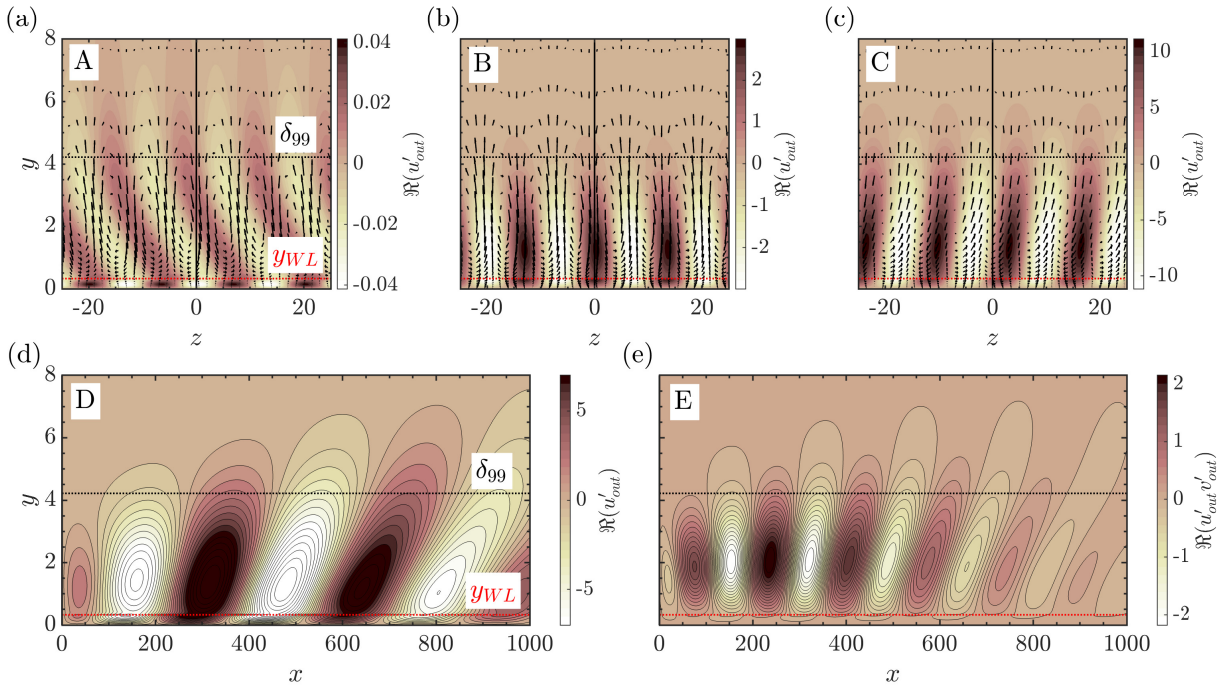

Figure 4.12: Case T09w105. Contours of the optimal streamwise velocity perturbation u'_{out} and velocity vectors of the resulting cross-stream perturbation velocity $|\vec{V'_{out}}| = \sqrt{v'^2_{out} + w'^2_{out}}$ on a zy-plane: (a) $x = 0$, (b) $x = 50$, (c) $x = x_{opt} = 425$. Contours of the optimal perturbation on an xy-plane at $z = 0$: (d) streamwise velocity u'_{out}, (e) Reynolds stress $u'_{out}v'_{out}$. Note that δ_{99} and y_{pc} are constant due to the parallel mean-flow assumption used in the transient-growth analysis. Capital A, B, C, D correspond to planes in Fig. 4.11.

When observing the oblique perturbations in Fig. 4.11(b), one may question why the optimal streaks exhibit such an orientation with a wave angle Ψ, with $\tan(\Psi) = \beta/\alpha$. In the context of the 2-D spanwise-periodic underlying base flow, achieving the same optimal growth is possible with a spanwise wavenumber β as well as with $-\beta$ (see Butler & Farrell (1992)). This implies that identical 3-D structures are obtained with opposite inclination to the wall-normal axis (Fig. 4.11c). In addition, the Reynolds-stress mechanism observed in Figs. 4.12(d–e) is exactly replicated. Since we are considering eigenvalues and eigenvectors of a linear amplification problem (Luchini 2000), a superposition of the two oblique waves can be calculated. As depicted in Fig. 4.11(d), this results in a chequered wave pattern, arising from multiple standing waves in the spanwise direction with a resultant zero propagation angle. These streamwise and spanwise alternating structures resemble the initial stage of an oblique transition (see, for instance, Berlin *et al.* (1994)). In fact, the (nonlinear) generation of a streamwise vortex by two least-damped Orr–Sommerfeld (OS) oblique waves with $(\omega, \pm\beta)$ is followed by the transient growth of vortex-generated streaks. An analysis of the superposed cross-stream slices in Figs. 4.12(a–c) unveils symmetrical structures in the spanwise direction, featuring zero cross-stream velocity.

Oblique elongated structures are evident not only for the dynamic streaks but also for the thermal streaks, as previously observed in Fig. 4.8. Thus, slices of 3-D density

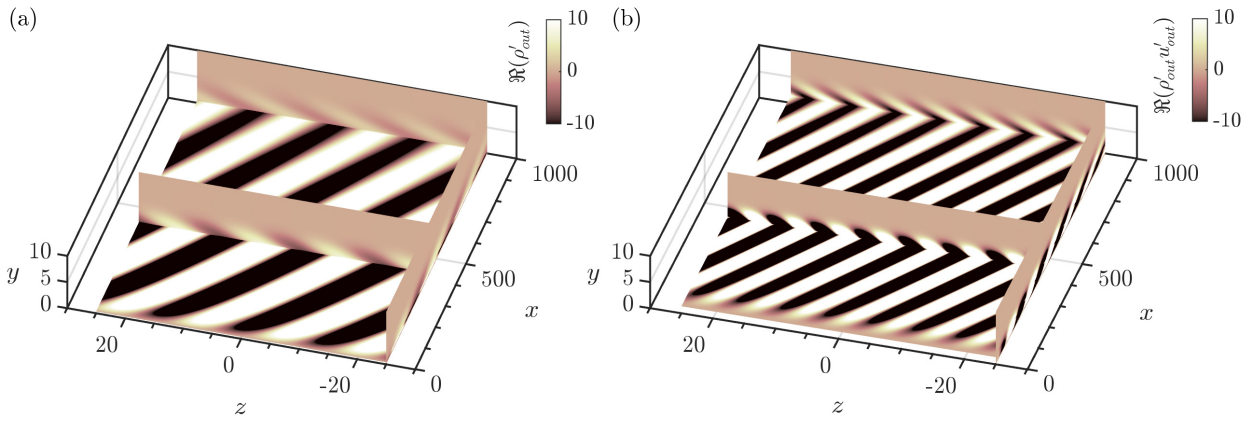

Figure 4.13: Case T09w105 (Re = 300, ω_{opt} = 0.013, β_{opt} = 0.45). Slices of 3-D contours of optimal disturbances: (a) density, (b) x-momentum.

perturbations are shown in Fig. 4.13(a). Note that a phase difference of π exists between high- and low-density and -temperature streaks, akin to observations in 3-D compressible ideal-gas boundary layers (Tempelmann *et al.* 2012). Similar perturbation shapes are observed for the x-momentum in Fig. 4.13(b), where regions of high and low density correspond to regions of low and high streamwise velocity, respectively.

In the transcritical wall-cooling case T11w095, optimal perturbations correspond to velocity streaks, alongside strong density and temperature streaks, which are streamwise-independent as indicated by G_{opt} at ω_{opt} = 0 and β_{opt} = 0 in Fig. 4.4(b). These structures resemble those in the subcritical and supercritical states, albeit with significantly larger thermal streaks amplitudes.

Sub-optimal growth

As previously pointed out, optimal transient growth is found at $x_{opt} \gg 1$ due to a combined Orr and lift-up mechanism. However, in case T09w105, as shown in Fig. 4.4(a), strong sub-optimal growth is evident at short distances from the initial location. This non-trivial phenomenon is further investigated hereafter.

In Figs. 4.14 and 4.15, we reconsider the maximum energy amplification G_{max} in the ω–β space for the wall-heating cases T09w090 (isothermal incompressible limit), T09w095, and T09w105, with black isolines denoting G_{max}/G_{opt} = 2/3 (dash-dotted) and G_{max}/G_{opt} = 1/3 (dashed). Notably, the region between G_{max}/G_{opt} = 1/3 and 2/3 is significantly larger when the base-flow temperature crosses the Widom line, as seen in case T09w105 (Fig. 4.15). Energy amplifications exceeding $G_{opt}/3$ are observed along the ω-axis for spanwise-uniform disturbances, demonstrating the Orr mechanism's substantial contribution to the energy amplification for the transcritical wall-heating case. In fact, $\max\{G_{max}(\omega, \beta = 0)\}$ (black square (■) symbol) in case T09w105 exceeds those of cases T09w095 and T09w090 by a factor of 7.8 and 12.3, respectively. Simultaneously, in Fig. 4.15, the non-negligible sub-optimal growth peaks much earlier in space than the global optimal (black star (★) symbol) at large ω and low β. Grey dashed isolines indicate a ratio of x_{max} to x_{opt} of about 1/8, with

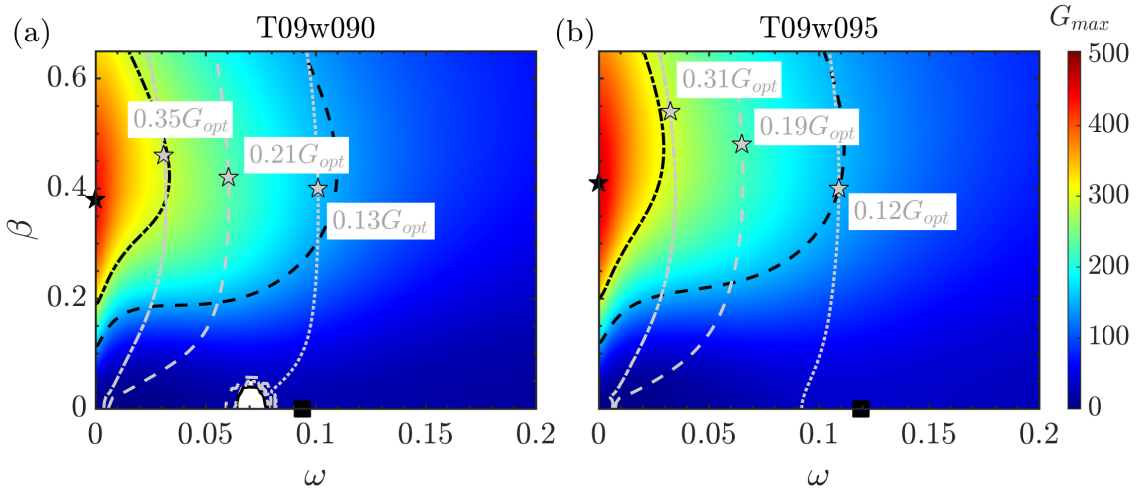

Figure 4.14: Contour plot of G_{max} in the ω–β space at $Re = 300$ for cases: (a) T09w090, and (b) T09w095. The optimal gain, G_{opt}, i.e. $\max\{G_{max}\}$, is denoted with a black star ($\star$) symbol. Black lines represent $G_{max}/G_{opt} = 2/3$ (dash-dotted) and $G_{max}/G_{opt} = 1/3$ (dashed), respectively, while grey lines represent $x_{max}/x_{opt} = 1/3$ (dash-dotted), $x_{max}/x_{opt} = 1/5$ (dashed), and $x_{max}/x_{opt} = 1/8$ (dotted). Black square ($\blacksquare$) symbols denote $\max\{G_{max}(\omega, \beta = 0)\}$, whereas grey star ($\star$) symbols denote $\max\{G_{max}(x_{max}/x_{opt} = 1/3) = 0.35G_{opt}\}$, $\max\{G_{max}(x_{max}/x_{opt} = 1/5)\}$, and $\max\{G_{max}(x_{max}/x_{opt} = 1/8)\}$, from left to right with increasing ω.

$x_{opt} = 422$ according to Tab. 4.2. This confirms the observations of Corbett & Bottaro (2000) and Butler & Farrell (1992) in the temporal framework, where sub-optimal disturbances, associated with short time scales, are no longer streamwise uniform but reach their maximum amplitude more rapidly. Moreover, tracking the streamwise evolution of G_{max} (grey stars) in Fig. 4.15 reveals highly oblique disturbances at small x given the large ω_{max}, with the initial disturbance no longer resembling a streamwise vortex. At large x, similar disturbance shapes to those in Fig. 4.8 are recovered. This behaviour aligns with previous findings for ideal gas at $M_\infty = 5.0$ (Bitter 2015).

In Fig. 4.16(a), a comparison of optimal and sub-optimal energy amplification over the streamwise distance is presented. The global optimal transient growth, marked by a black star symbol in Fig. 4.14(c), is considered, alongside the largest sub-optimal transient growths peaking at $x = [x_{opt}/3, x_{opt}/5, x_{opt}/8]$ (grey star symbols in Fig. 4.14c). Notably, at $x \approx 52$ from the initial location, the local maximum energy amplification $G_{max}(x_{max}/x_{opt} = 1/8)$ exceeds the optimal energy amplification to a significant extent. This signifies a near-optimal amplification of $G_{max}/G_{opt} \approx 0.43$ at a distance eight times shorter than x_{opt}, highlighting the relevance of sub-optimal energy growth. Recalling the analysis of the oblique perturbations in Sec. 4.4.2, an analysis of the initial condition yielding maximum sub-optimal gain at $x_{max}/x_{opt} = 1/8$, denoted as $g(x_{max}/x_{opt} = 1/8)$ in Fig. 4.16(a), is performed. At this location, the sub-optimal spanwise wavenumber and frequency are $\beta = 0.38$ and $\omega = 0.204$, respectively. In Fig. 4.16(b), a strong tilting of the flow structures characteristic of the Orr mechanism is noticeable, resulting in larger spanwise velocity components compared to those in Fig. 4.12.

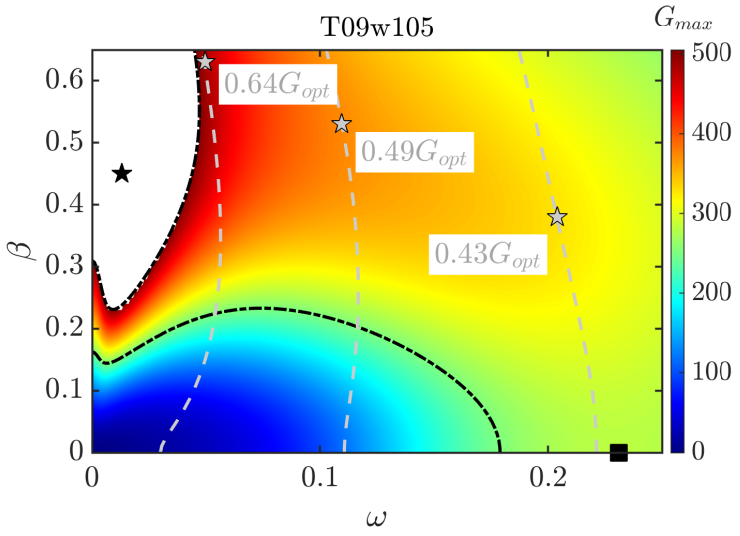

Figure 4.15: Contour plot of G_{max} in the ω–β space at $Re = 300$ for case T09w105. The optimal gain, G_{opt}, i.e. $\max\{G_{max}\}$, is denoted with a black star ($\star$) symbol. Black lines represent $G_{max}/G_{opt} = 2/3$ (dash-dotted) and $G_{max}/G_{opt} = 1/3$ (dashed), respectively, while grey lines represent $x_{max}/x_{opt} = 1/3$ (dash-dotted), $x_{max}/x_{opt} = 1/5$ (dashed), and $x_{max}/x_{opt} = 1/8$ (dotted). Black square ($\blacksquare$) symbols denote $\max\{G_{max}(\omega, \beta = 0)\}$, whereas grey star ($\star$) symbols denote $\max\{G_{max}(x_{max}/x_{opt} = 1/3) = 0.35G_{opt}\}$, $\max\{G_{max}(x_{max}/x_{opt} = 1/5)\}$, and $\max\{G_{max}(x_{max}/x_{opt} = 1/8)\}$, from left to right with increasing ω.

This leads to oblique structures with a wave angle Ψ of approximately 42°, in contrast to the nearly streamwise-independent global optimal structures in Figs. 4.11(b,c) with $\Psi \approx 2°$. This result confirms the observation of Corbett & Bottaro (2000), where larger local optima can be achieved at $x \ll x_{opt}$ via efficient energy extraction from the mean flow through the Orr mechanism. As x increases and $\omega_{opt} \to 0$, the lift-up mechanism becomes dominant, and (nearly) streamwise-independent structures are recovered.

4.4.3 Effect of the initial Reynolds number

In Sec. 4.4.2, all investigations were performed at a constant initial Reynolds number of $Re = 300$. For both incompressible and compressible boundary-layer flows under the ideal-gas assumption, streamwise-independent modes scale according to Gustavsson (1991); Hanifi & Henningson (1998); Tumin & Reshotko (2001): for the spatial theory, G varies quadratically with the local Reynolds number, and x scales linearly with Re. Thus, a similar analysis is performed for the non-ideal-gas cases in Tab. 4.1. The optimal energy amplification is calculated for initial Reynolds numbers $Re = 300, 1000$, and 3000, using the same β_{opt} at $Re = 300$ and $\omega = 0$. Figs. 4.17(a) and 4.17(b) illustrate the scaling relations for cases with wall heating from a liquid-like free stream and wall cooling from a vapour-like free stream, respectively. Curves at different Re collapse for the same temperature difference, confirming the scaling law's validity not only at subcritical and supercritical temperatures, but also in

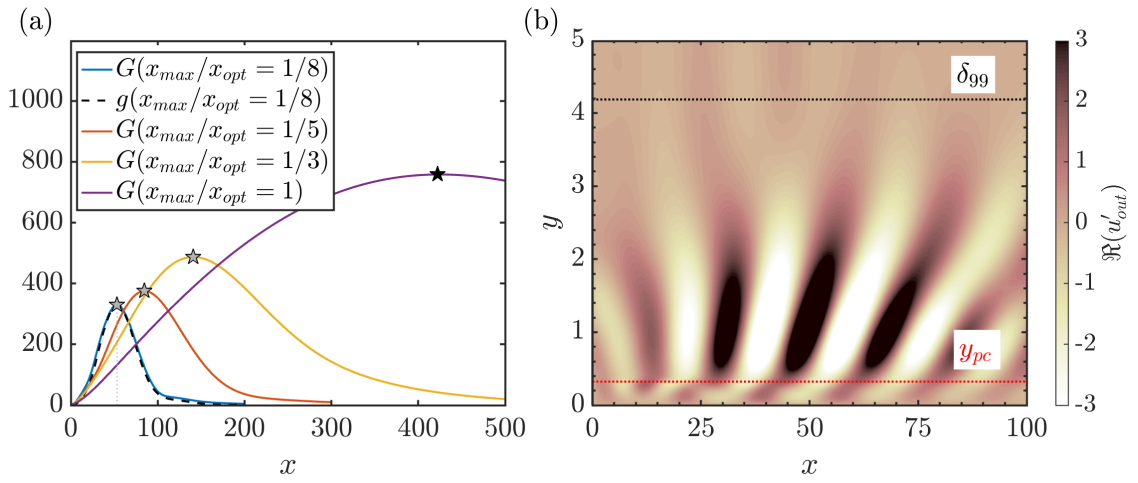

Figure 4.16: Case T09w105. (a) Over the streamwise direction x: envelope of the largest sub-optimal transient growth at $x_{max}/x_{opt} = 1/8$ (—), $x_{max}/x_{opt} = 1/5$ (—), $x_{max}/x_{opt} = 1/3$ (—), sub-optimal transient growth $g(x_{max}/x_{opt} = 1/8)$ of the optimal perturbation (- -), and envelope of the (global) optimal transient growth at $\omega_{opt} = 0.013$ and $\beta = 0.45$ (—, black star indicates the global maximum as in Fig. 4.14c); the grey dotted line indicates the location of the maximum energy growth (grey star as in Fig. 4.14c). (b) Contours of the output streamwise velocity perturbations corresponding to the black dotted line $g(x_{max}/x_{opt} = 1/8)$ (xy-plane at $z = 0$).

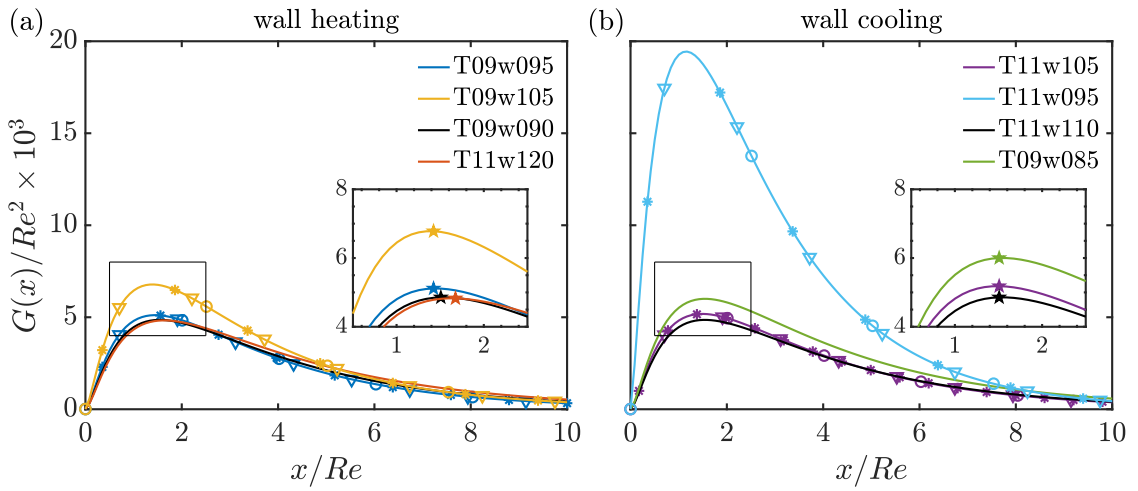

Figure 4.17: Streamwise-independent disturbances. Energy amplification $G(x)/Re^2$ over the streamwise distance x/Re at $\beta = \beta_{opt}(Re = 300)$ and $\omega = 0$. Lines in (a): T09w095, T09w105, T09w090, and T11w120. Lines in (b): T11w105, T11w095, T11w110, and T09w085. Symbols: circle ($\circ$) ($Re = 300$), asterisk ($*$) ($Re = 1000$), triangle ($\triangledown$) ($Re = 3000$). Cases T09w090, T11w120, T11w110, and T09w085 are displayed without symbols for better representation, but they also obey the scaling. In the insets, G_{max}/Re^2 is marked by a coloured star ($\star$) symbol.

the presence of strong non-ideality across the Widom line.

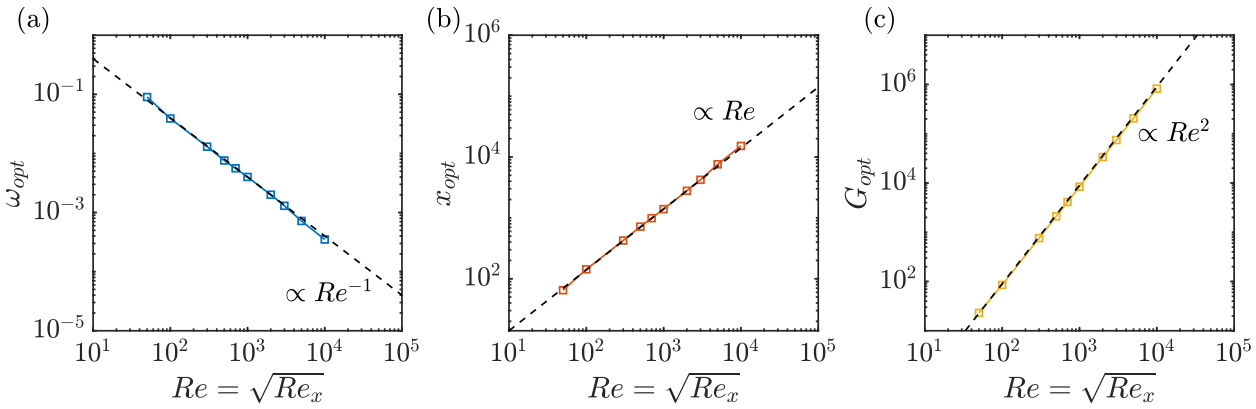

Figure 4.18: Case T09w105: (a) optimal frequency, (b) optimal location, and (c) optimal energy amplification. The dashed black lines indicate the power-law approximations with corresponding exponent n.

Transcritical wall heating: scaling laws

The transcritical case T09w105, previously identified with streamwise-modulated streaks at Re = 300, is examined further. In Figs. 4.18(a,b), the optimal frequency ω_{opt} and optimal location x_{opt} are plotted against the initial Reynolds number for the optimal amplification G_{opt} shown in Fig. 4.18(c). As Re increases, the optimal energy amplification shifts to lower frequencies, while the spanwise wavenumber remains nearly unaltered (not displayed here for the sake of brevity). This shift can be interpreted as a reduction in the Orr mechanism, with the mere lift-up effect becoming dominant as $\omega \to 0$. The decrease in ω_{opt} can be well approximated by $\omega_{opt} \propto Re^n$, with $n = -1$, similar to the relation $\omega_{opt} \propto Re^{-0.8}$ obtained by Hack & Moin (2017) when including non-parallel effects. This trend suggests that optimal perturbations have zero frequency in the inviscid limit of $Re \to \infty$ (Hack & Moin 2017). Moreover, power laws for G_{opt} and x_{opt}, akin to those for streamwise-independent perturbations (see Fig. 4.17), hold even when the Orr mechanism is at play. Hence, the relations $x_{opt} \propto Re$ and $G_{opt} \propto Re^2$ are valid regardless of the underlying physical mechanism. At Re = 50 and 1000, the optimal perturbations are presented in Figs. 4.19(a,b) and 4.19(c,d), respectively. As expected, the spanwise and wall-normal velocity components are most pronounced initially. However, a notable input streamwise velocity amplitude at Re = 50, especially near the pseudo-critical point, highlights the influence of the Orr mechanism at low Reynolds numbers. In contrast, at Re = 1000, the lift-up effect predominates, with $\hat{u}_{in} \approx 0$. Additionally, examining the output spanwise velocity perturbation $\hat{w}_{out}$ reveals that at Re = 50 with $\omega_{opt} \gg 0$, the Orr mechanism significantly amplifies the spanwise velocity, consistent with Jiao *et al.* (2021).

Recalling the streaks' shape in Fig. 4.13 and the evolution of the optimal frequency in Fig. 4.18, the wave angle of the oblique streaks likely depends on the initial Reynolds number. To explore this, snapshots of the resulting optimal streak tangential velocity $|\vec{V}'_{res}| = \sqrt{u'^2 + w'^2}$ on an xz-plane are illustrated in Figs. 4.20(a,e,h), Figs. 4.20(b,f,i), and Figs. 4.20(c,g,j) at Re = 50, 300, and 1000, respectively. Optimal perturbations are obtained with $\beta = \beta_{opt}$ in

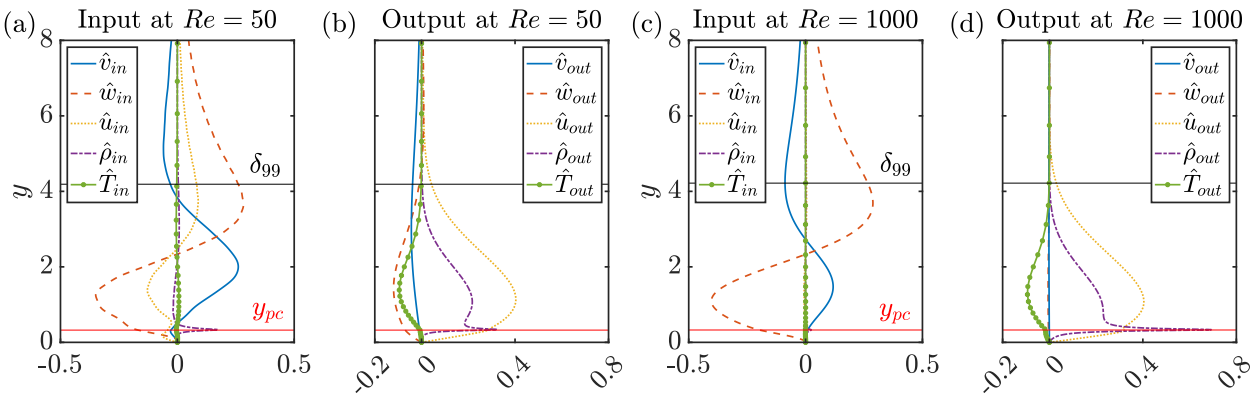

Figure 4.19: Case T09w105. Wall-normal profiles of optimal input (a,c) and output (b,d) disturbances (real part) at two different initial Reynolds numbers: (a,b) $Re = 50$, and (c,d) $Re = 1000$. The boundary-layer thickness and the location of the pseudo-critical point, i.e. at the pseudo-critical temperature $T^* = T^*_{pc}$, are indicated by δ_{99} and y_{pc}, respectively.

Figs. 4.20(a–c), with $\beta = -\beta_{opt}$ in Figs. 4.20(e–g), and with $\beta = \pm\beta_{opt}$ in Figs. 4.20(i–k). To calculate the streaks' wave angle $\tan(\Psi) = \beta_{opt}/\alpha$, the optimal spanwise wavenumber is derived from $G_{opt}(\beta_{opt}, \omega_{opt})$. The streamwise wavenumber α is extracted as follows: the spatial evolution of the wall-normal maximum of the streamwise perturbation velocity is evaluated at $z = 0$ (see plane D in Fig. 4.11b), determining the streamwise wavelength λ_x from the wave period of the oscillating streamwise velocity, and thus $\alpha = 2\pi/\lambda_x$. This method achieves a good agreement between the calculated Ψ and the actual streaks' orientation. Repeating the procedure at different Re, the dependence of Ψ on the Reynolds number is displayed on a logarithmic axis in Fig. 4.20(d). As the optimisation proceeds downstream, streaks progressively evolve into 2-D structures due to the frequency shift of their optimal transient growth. Since β_{opt} remains nearly unchanged while ω_{opt} scales as Re^{-1}, the wave angle Ψ follows the same power law, approaching zero as $Re \to \infty$. Note that this analysis uses a locally-parallel spatial optimisation procedure, so generalising the actual streak structure to the entire flat-plate distance requires advanced non-local methods, such as a PSE-based formulation (Tempelmann *et al.* 2012; Paredes *et al.* 2016). As highlighted in Fig. 4.11(c), oblique streaks can have both positive and negative wave angles, having the same patterns, with their superposition in Figs. 4.20(i–k) depending on the initial Reynolds number. When moving downstream, the chequerboard wave pattern stretches due to a larger streamwise wavenumber.

Transcritical wall heating: role of Mode II

To understand the frequency shift in the optimal energy amplification for the transcritical wall-heating case T09w105, we analyse the underlying eigenspectrum, forming the eigenvector basis for the matrix $\mathbf{F}$ (see Sec. 4.2.3), used in calculating the energy growth G in Eq. (4.16). Figs. 4.21(a–c) show the eigenspectra at $Re = 50$, 300, and 10^4 with the corresponding $\omega = \omega_{opt}$, obtained by solving the eigenvalue problem in Eq. (3.12). As identified by Ren *et al.* (2019*b*), two discrete modes (Mode I and II), here damped, appear when the base-

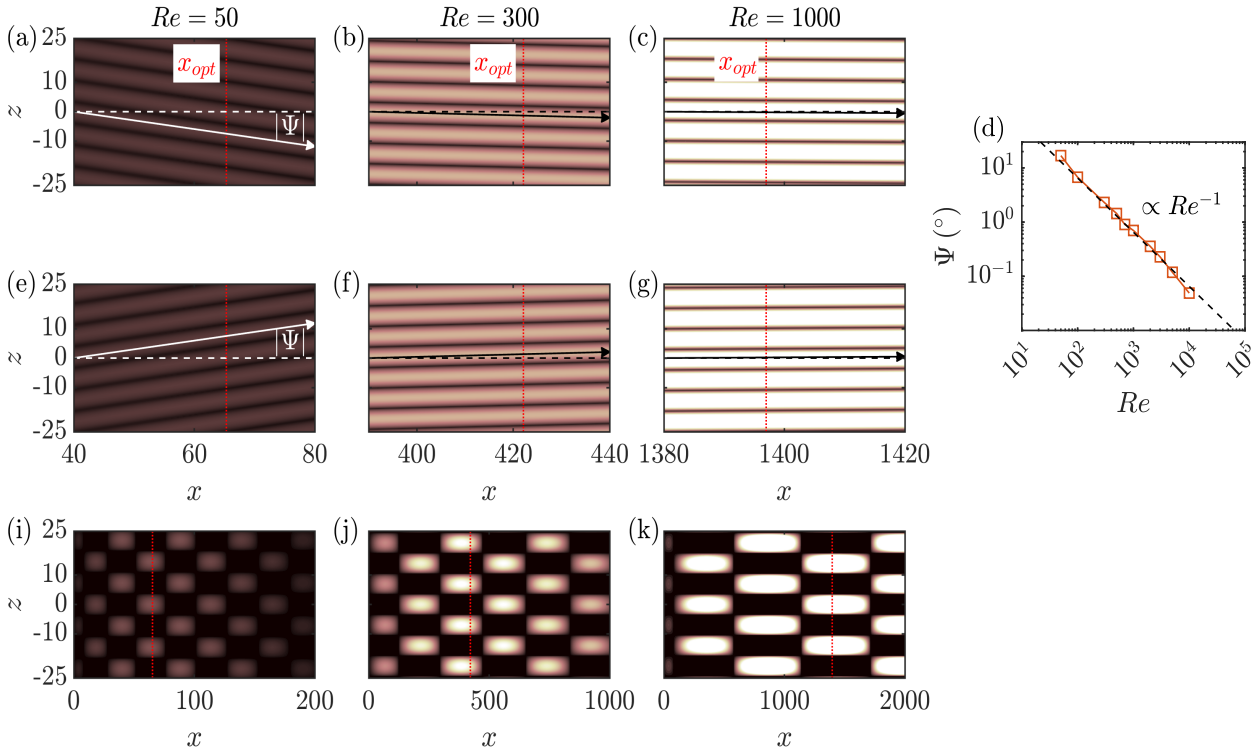

Figure 4.20: Case T09w105. In (a–c) and (e–j), contour plots in the xz-plane ($y = 0.77$) of the resulting streaks' tangential velocity $|\vec{V}'_{res}|$: (a,e,h) $Re = 50$, (b,f,i) $Re = 300$, and (c,g,j) $Re = 1000$; (a–c) $\beta = \beta_{opt}$, (e–g) $\beta = -\beta_{opt}$, and (h–j) $\beta = \pm\beta_{opt}$. The arrow represents the velocity vector with wave angle Ψ. In (d), development of the streaks' wave angle Ψ as a function of the initial Reynolds number. The dashed black line indicates the power-law approximation with exponent $n = -1$.

flow temperature crosses the Widom line from a liquid-like free-stream to a vapour-like wall. Mode I, resembling the Tollmien–Schlichting mode, always exists, regardless of the thermodynamic state. In Figs. 4.21(a–c), the only continuous branches at $M_\infty = 10^{-3}$ belong to the vorticity and entropy modes (indicated by the vertical dash-dotted line with $\alpha = \omega$). For 3-D disturbances, i.e. $\beta = \beta_{opt} > 0$, two vorticity modes and one entropy mode are found, in agreement with Tumin (2007). When moving downstream, the continuous branches become more distinct, and the two discrete modes approach the vorticity/entropy modes. At $Re = 10^4$, in fact, both Mode I and II nearly synchronise with the continuous spectrum at a phase velocity of $c_r \approx 1$. As synchronisation progresses from $Re = 50$ to 10^4, the two eigenmodes contributing to the largest optimal amplification are tracked (see purple circles in Figs. 4.21a–c), which are computed via the right singular eigenvector associated with the largest singular value of $\mathbf{F\Lambda F}^{-1}$ in Eq. (4.16). The modes with the highest transient-growth contribution are consistently Mode I and II, indicating that, regardless of the initial Reynolds number, these two slowly-decaying modes are the main contributors to energy amplification, while the other modes in the continuous spectrum decay rapidly and play a minor role. For ideal gas at $M_\infty = 5.0$, a similar process for discrete modes was witnessed by Bitter (2015), where optimal disturbances were oblique for $x < x_{opt}$, unlike the continuous-spectrum interaction in Schmid

(2007). However, in Bitter (2015), the least-damped discrete mode corresponds to the Mack second mode, which differs from the current Mode II in supercritical fluids (Ren *et al.* 2019*b*).

Since transient growth is mathematically linked to the non-orthogonality of the eigenvectors in the initial value problem, analysing the underlying eigenspectrum is essential for our study (Corbett & Bottaro 2000). Gustavsson (1991) notes that the individual and least-damped OS mode can interfere with the continuous branches, leading to the largest energy amplification. Therefore, we investigate how the two discrete least-damped modes contribute to transient growth and energy amplification in a spatial framework. First, G_{opt} at finite β_{opt} and ω_{opt}, based on the full spectrum of Figs. 4.21(a–c), is shown by a blue line in Fig. 4.21(d), coinciding with Fig. 4.18(c). Next, Mode II is excluded from the optimisation, producing a modified eigenspectrum similar to the non-transcritical cases. With the same optimal frequency and spanwise wavenumber, the modified optimal amplification $G_{\text{w.o.II}}$ (red line in Fig. 4.21d) is calculated. Excluding Mode II results in a significant drop in G, with $G_{opt}/G_{\text{w.o.II}} \approx 5$. Discarding both Mode I and II yields the energy amplification $G_{\text{w.o.I+II}}$ (yellow line in Fig. 4.21d), which experiences a slight decrease compared to $G_{\text{w.o.II}}$. Hence, the substantial drop in G is primarily due to the increase in non-ideality when crossing the Widom line, and consequently, the presence of Mode II. Fig. 4.21(e) displays the maximum energy amplification over the frequency at a constant spanwise wavenumber of $\beta = \beta_{opt}$. Omitting Mode II from the initial value problem shifts the peak optimal growth (blue star (★) symbol) from finite frequency values (blue line) to $\omega = 0$ (red line), resembling non-transcritical cases in Fig. 4.3, where streamwise-independent disturbances were found. Comparing $G_{opt,\text{w.o.II}}$ at $\omega = 0$ with G_{opt} of case T09w095 (black (▼) symbol) reveals similar values, reflecting the spectra similarity.

Physically, considering the results from Sec. 4.4.1 and 4.4.2 in relation to Mode II, one might infer that the Orr mechanism disappears once Mode II is omitted from the eigenspectrum. Nevertheless, even in the non-transcritical cases where G_{opt} is at $\omega = 0$, the Orr mechanism is present at $\omega > 0$ (Farrell & Ioannou 1993), though it results in sub-optimal energy growth (see Fig. 4.14). This is typical of wall-bounded shear flows, where the dominant energy growth is associated with 2-D streaks (Butler & Farrell 1992). In unbounded infinite-shear flows, the combination of Orr and lift-up mechanisms has been revealed to be optimal, as transient growth is inherently 3-D relying on the interplay of these two mechanisms (Kaminski *et al.* 2014). In terms of modal analysis, with the appearance of Mode II and its high contribution to transient growth, an additional degree of non-orthogonality is introduced (Schmid 2007), enhancing the interaction, already for sub-optimal energy growth (see Fig. 4.14), between the lift-up effect and Orr mechanism. The latter significantly amplifies the spanwise velocity (Jiao *et al.* 2021), as observed in Figs. 4.12(a–c) with inclined structures in the spanwise direction and in Figs. 4.19(b,d) with larger $\hat{w}_{out}$ at lower Reynolds numbers. This behaviour is supported by the cases in Tab. 4.2, where only one discrete least-damped mode is present, and the interplay of lift-up and Orr mechanism only produces sub-optimal energy growth (see Fig. 4.14).

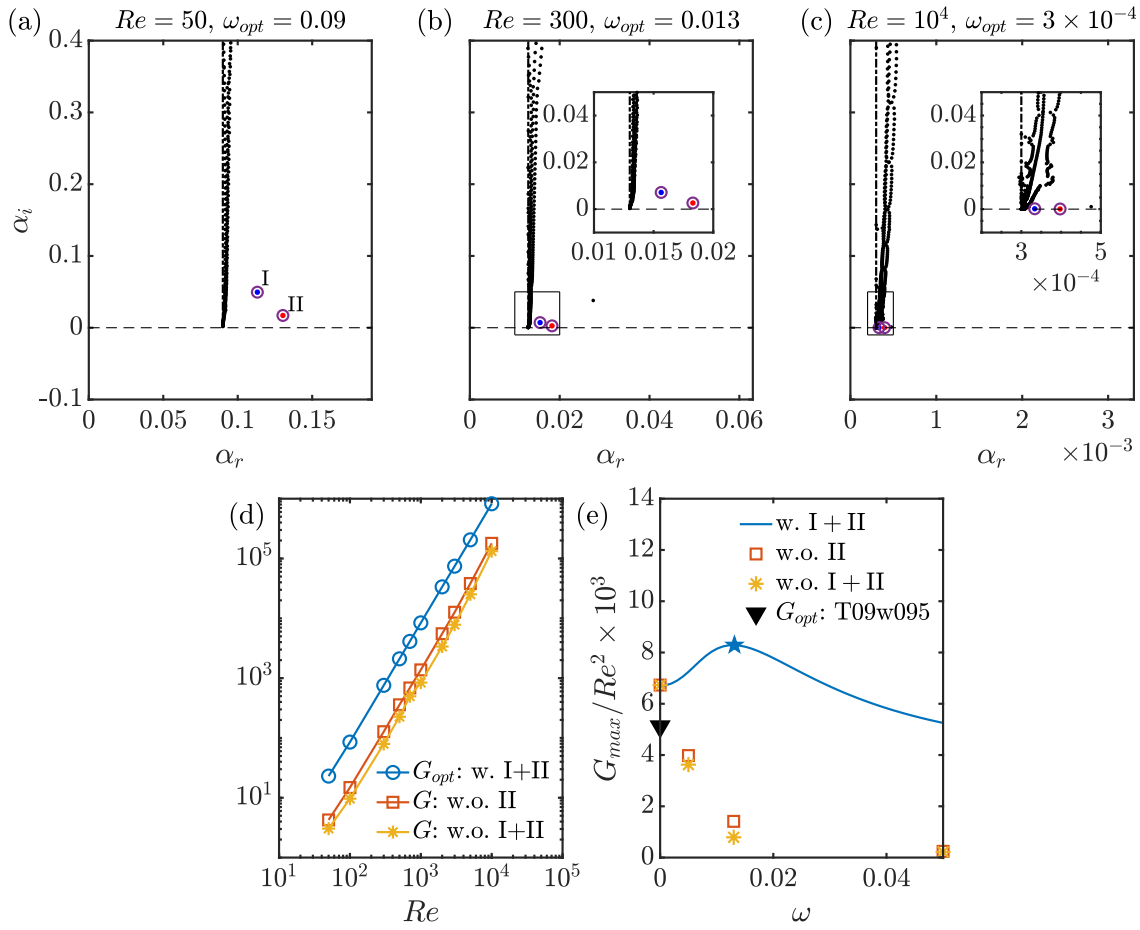

Figure 4.21: Case T09w105. Eigenspectrum at (a) $Re = 50$, (b) $Re = 300$, and (c) $Re = 10^4$ (higher mesh resolution needed), $\omega = \omega_{opt}$. Blue and red dots represent Mode I and II, respectively. The two modes with the largest contribution to the optimal growth are circled in purple. The black dash-dotted line refers to the continuous spectra according to Tumin (2007). In (d), the optimal energy amplification is plotted over the local Reynolds number for the full spectrum (blue line); note that G for the full spectrum without Mode II (red line) and full spectrum without Mode I and II (yellow line) is no longer G_{opt} for these cases. In (e), the maximum energy amplification is plotted over the frequency for the full spectrum (blue line with G_{opt} marked by a blue (★) symbol), full spectrum w.o. Mode II (red line), and full spectrum w.o. Mode I and II (yellow line). G_{opt} of case T09w095 (marked by a black (▼) symbol).

4.4.4 Effect of wall temperature

The influence of wall temperature on transient growth is examined. For the non-transcritical cases in Tab. 4.2, a preliminary trend was evident in Fig. 4.3. In the subcritical and supercritical states, wall cooling exhibits higher amplification rates than wall heating. Here, consistent with Corbett & Bottaro (2000), the influence of the non-dimensional compressible momentum thickness $\theta = \int_0^\infty \rho u(1-u)\,\mathrm{d}y$ (see White (2006)) is considered, with its value given in Tab. 4.1. Figs. 4.22(a,c) and Figs. 4.22(b,d) plot the maximum energy amplification G_{max}/Re_θ^2 and its distance x_{max}/Re_θ over the rescaled spanwise wavenumber $\beta_\theta = \beta\theta$, re-

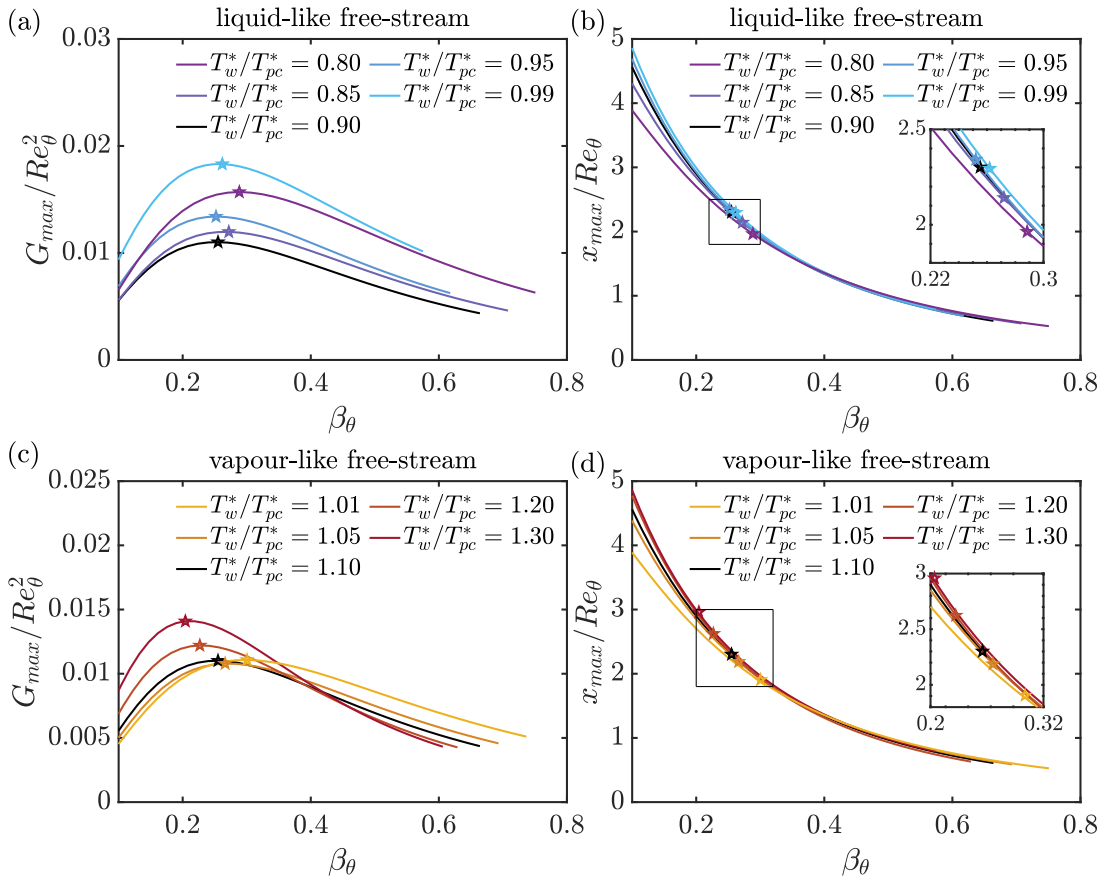

Figure 4.22: Subcritical and supercritical states. Maximum energy amplification G_{max}/Re_θ^2 and its distance x_{max}/Re_θ at different T_w^*/T_{pc}^*: (a,b) $T_\infty^*/T_{pc}^* = 0.90$, and (c,d) $T_\infty^*/T_{pc}^* = 1.10$. The optimal amplification G_{opt} is indicated with a coloured star ($\star$) symbol.

spectively. Streamwise-independent modes are considered, as they are the most non-modally amplified perturbations in Fig. 4.3. The wall temperature is varied for subcritical free-stream conditions with $T_\infty^*/T_{pc}^* = 0.90$, as shown in Fig. 4.3(a), and for supercritical free-stream conditions with $T_\infty^*/T_{pc}^* = 1.10$, as shown in Fig. 4.3(b). The impact of a diabatic wall is more pronounced in the subcritical state (Fig. 4.22a), where both wall cooling and wall heating cause a greater increase in G than in the supercritical state of Fig. 4.22(c). As θ decreases with increasing T_w^*/T_∞^* in both states, the highest G_{max}/Re_θ^2 occurs with wall heating. Notably, in the supercritical state, the lowest G_{opt}/Re_θ^2 is found not with $T_w^*/T_\infty^* = 1.0$ but with a slightly negative wall-temperature gradient. Corbett & Bottaro (2000) noted the universal behaviour of the momentum thickness scaling for a Falkner–Skan boundary layer. In fact, with a θ-scaling, the optimal spanwise wavenumber $\beta_{\theta,opt}$ was independent of the mean-flow pressure gradient, a behaviour nearly replicated in Fig. 4.22(a) for a liquid-like free-stream, where $\beta_{\theta,opt}$ ranges from 0.25 to 0.29. Even more noteworthy, x_{max}/Re_θ exhibits nearly exact scaling with β_θ in both states (Figs. 4.22b,d).

A similar investigation is conducted for the transcritical wall-heating case T09w105, previously shown in Fig. 4.4(a). Here, the free-stream temperature is constant at $T_\infty^*/T_{pc}^* = 0.90$, while the wall temperature increases from $T_w^*/T_{pc}^* = 1.01$ to $T_w^*/T_{pc}^* = 1.10$ in the vapour-

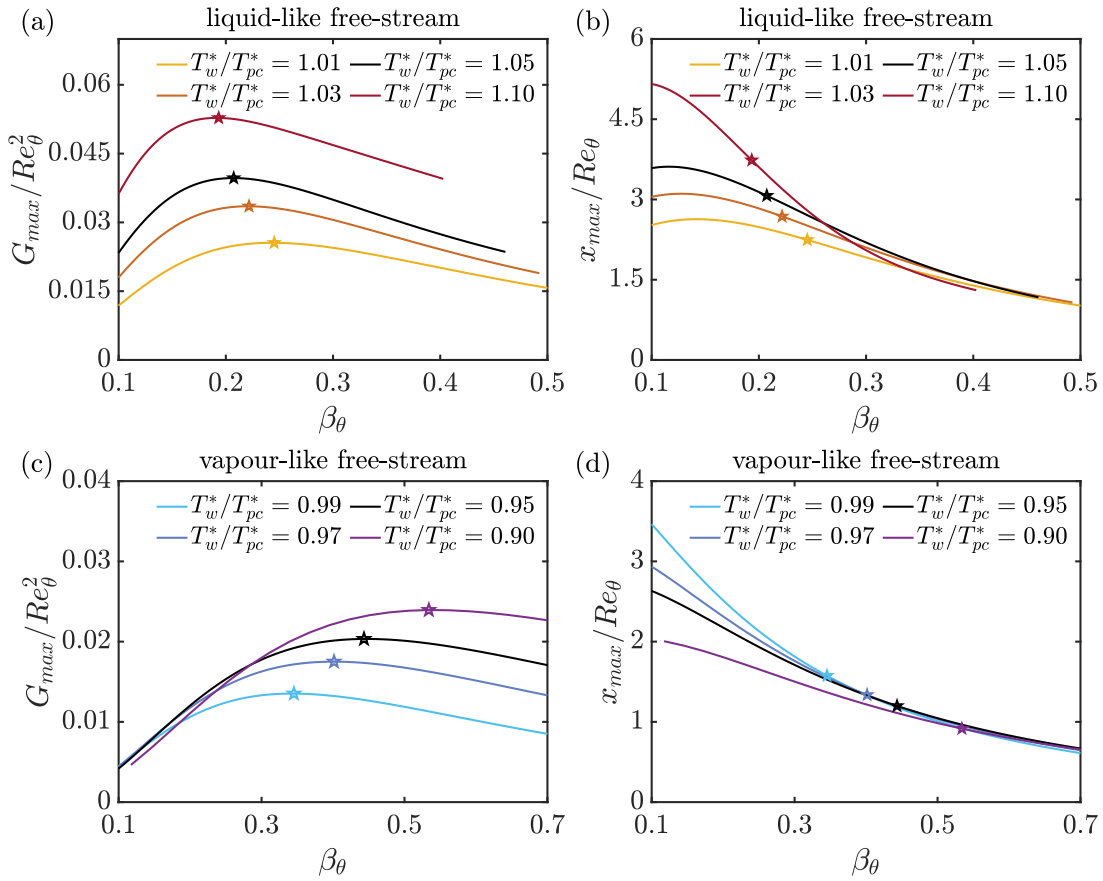

Figure 4.23: Transcritical state. Maximum energy amplification G_{max}/Re_θ^2 and its distance x_{max}/Re_θ at different T_w^*/T_{pc}^*: (a,b) $T_\infty^*/T_{pc}^* = 0.90$, and (c,d) $T_\infty^*/T_{pc}^* = 1.10$. The optimal amplification G_{opt} is indicated with a coloured star ($\star$) symbol.

like state. Consequently, the momentum thickness θ decreases from 0.533 to 0.403, and the height of the pseudo-critical point relative to the boundary-layer thickness, i.e. y_{pc}/δ_{99}, rises. Figs. 4.23(a,b) present results at four different wall temperatures. Note that optimal growth shifts to finite frequencies just after the Widom is crossed, with streamwise-modulated streaks observed up to $T_w^*/T_{pc}^* = 1.10$. Beyond this ratio, energy amplification at very low frequencies dominates before G_{opt} is found at $\omega = 0$. Hence, optimal streamwise-independent streaks with $\Psi = 0°$ occur for a wall-heating factor T_w^*/T_∞^* greater than 1.22. In Figs. 4.23(a,b), a wall-temperature increase above T_{pc}^* no longer follows the θ scaling as in Figs. 4.22(a,b). An even larger shift of $\beta_{\theta,opt}$ is observed in Figs. 4.23(c,d), despite good overlap in x_{max}/Re_θ for large β_θ. Here, the free-stream temperature is constant at $T_\infty^*/T_{pc}^* = 1.10$, while the wall temperature varies from $T_w^*/T_{pc}^* = 0.99$ to $T_w^*/T_{pc}^* = 0.90$ in the liquid-like state. The momentum thickness θ increases from 0.803 to 1.173, with the height of the pseudo-critical point increasing due to wall cooling. Note also that the boundary-layer thickness grows with stronger transcritical wall cooling, achieving a similar growth of the pseudo-critical point with the same $\Delta T = |T_\infty^* - T_w^*|$ for both transcritical wall heating and cooling. However, wall-normal gradients of base-flow properties at the Widom line, e.g. $|\partial\bar{\rho}/\partial y|_{pc}$, are larger for the transcritical wall-cooling case for the same ΔT (see Sec. 4.4.2), leading to larger G_{opt}, scaled

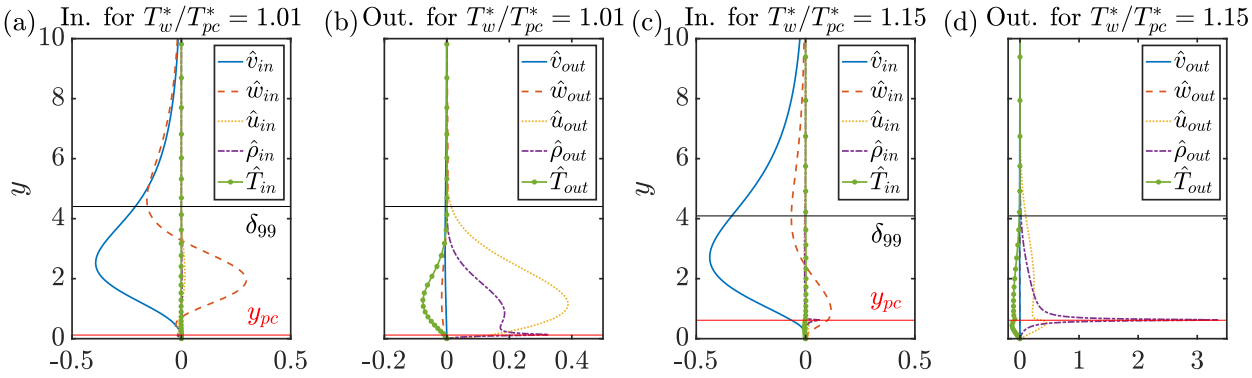

Figure 4.24: Transcritical wall heating at $Re = 300$. Wall-normal profiles of optimal input (a,c) and output (b,d) disturbance at two different wall temperatures: (a,b) $T_w^*/T_{pc}^* = 1.01$, and (c,d) $T_w^*/T_{pc}^* = 1.15$. The boundary-layer thickness and the location of the pseudo-critical point, i.e. at the pseudo-critical temperature $T^* = T_{pc}^*$, are indicated by δ_{99} and y_{pc}, respectively.

with Re^2. Overall, it is evident that, with strong non-ideality, the momentum thickness is no longer the universal scaling parameter in transient growth.

To highlight the influence of transcritical wall heating on the optimal perturbations, the wall-normal profiles of optimal input and output disturbances at $T_w^*/T_{pc}^* = 1.01$ and $T_w^*/T_{pc}^* = 1.15$ are displayed in Figs. 4.24(a,b) and Figs. 4.24(c,d), respectively. The Reynolds number is $Re = 300$. At $T_w^*/T_{pc}^* = 1.01$, with G_{opt} at $\omega_{opt} \approx 0.01$, the Orr mechanism results in small but non-zero streamwise velocity and larger spanwise velocity for the input perturbations, causing cross-stream inclination of the perturbation structures (Figs. 4.12a–c). At $T_w^*/T_{pc}^* = 1.15$, optimal amplifications are found at zero frequency with $\hat{u}_{in} = 0$ and a smaller $\hat{w}_{in}$ than in Fig. 4.24(a). Despite the Widom line moving away from the wall, the shapes of the input disturbances remains nearly identical, as seen in Tumin & Reshotko (2003) for compressible ideal-gas boundary layers. On the other hand, the output profiles are greatly affected by different transcritical wall heating. The amplitude of the density perturbation (purple dash-dotted line) at the Widom line increases with its local base-flow gradient, with $\mathrm{d}\bar{\rho}/\mathrm{d}y|_{pc}$ at $T_w^*/T_{pc}^* = 1.15$ being 1.5 times larger than at $T_w^*/T_{pc}^* = 1.01$, resulting in stronger density streaks. Regarding the output streamwise velocity perturbation (yellow dotted line), its peak shifts from the middle of the boundary layer in Fig. 4.24(b) to the pseudo-critical point in Fig. 4.24(d), due to a stronger vortex-tilting term ($|\partial\bar{u}/\partial y \cdot \partial\hat{v}_{in}/\partial z|$) around the pseudo-critical point, driven by larger perturbation strain rate away from the wall. Thus, the highest increase in $\hat{\omega}_y$ occurs around the pseudo-critical point, with the secondary peak of $\hat{u}_{out}$ in the boundary layer's centre being less amplified compared to the case with $T_w^*/T_{pc}^* = 1.01$. For the transcritical wall-cooling cases (Figs. 4.23c,d), similar features to the transcritical wall-heating cases are found (not shown here for the sake of brevity). However, due to a larger $\partial\bar{\rho}/\partial y|_{pc}$, the output density perturbations exhibit significantly larger amplitudes than the output velocity perturbations. The vortex-tilting term $|\partial\bar{u}/\partial y \cdot \partial\hat{v}_{in}/\partial z|$ is greatly enhanced by wall cooling, increasing both mean-flow vorticity and perturbation strain rate. This term

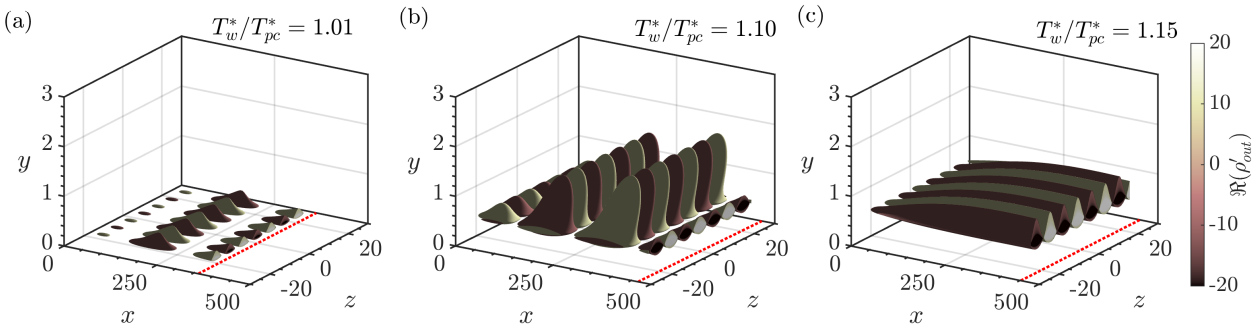

Figure 4.25: Transcritical wall heating at $Re = 300$. Iso-contours of the optimal density perturbations ($\Re(\rho'_{out}) = \pm 8.0$): (a) $T_w^*/T_{pc}^* = 1.01$ (superposition), (b) $T_w^*/T_{pc}^* = 1.10$ (superposition), and (c) $T_w^*/T_{pc}^* = 1.15$. The red dashed line indicates the optimal growth location ($x = x_{opt}$).

peaks above y_{pc}, which rises as T_w^*/T_{pc}^* decreases. As a result, the wall-normal vorticity perturbation component $\hat{\omega}_{y,out}$ shows a similar profile to Fig. 4.10(c), but more pronounced around the pseudo-critical point.

Figure 4.25 visualises the 3-D optimal density perturbation structures for $T_w^*/T_{pc}^* = (1.01, 1.10, 1.15)$. For the first two cases, perturbations with $\beta = \pm\beta_{opt}$ are superimposed, while for $T_w^*/T_{pc}^* = 1.15$ optimal disturbances are streamwise-independent. As T_w^*/T_{pc}^* increases to 1.10, ω_{opt} also increases, causing oblique structures to have a larger wave angle and a shorter streamwise wavelength, resulting in a strong alternating chequered wave pattern. Additionally, at $T_w^*/T_{pc}^* = 1.01$, the largest density structures are confined to the pseudo-critical region. As the wall temperature increases to $T_w^*/T_{pc}^* = 1.10$, these structures extend into the mid-section of the boundary layer, exhibiting significant amplitudes. At $T_w^*/T_{pc}^* = 1.15$ (Fig. 4.25c), even stronger density perturbations are present, yet they remain predominantly located around the pseudo-critical region.

4.5 Modal growth versus non-modal growth

In this study, energy amplification has been maximised at x_{opt}, yet these locations may be too large to justify the locally parallel assumption, as x is non-dimensionalised by the Blasius length scale δ. For every case in Tab. 4.1 x_{opt} is proportional to Re_0, the initial local Reynolds number. This suggests that the optimal disturbance requires $O(Re_0 \cdot \delta)$ to grow from the initial location x_0. As $\delta \propto \sqrt{x} \propto Re$, the growth of the boundary-layer thickness, which is proportional to the Blasius length scale (White 2006), corresponds to a factor $\sqrt{x_{opt}}/\sqrt{x_0}$ or Re_{opt}/Re_0 from x_0 to x_{opt}. Consequently, a shorter x near the leading edge is required for the same increase in δ, where the locally parallel and boundary-layer assumptions are more likely to fail. Yet, previous studies on the non-parallel effects (Andersson *et al.* 1999; Tumin & Reshotko 2003) have revealed similar optimal distances to those found here, to those of Butler & Farrell (1992) for incompressible flows, and to those of Bitter (2015) for hypersonic flows. For this reason, further investigations are not pursued.

With large x_{opt}, transient growth might be irrelevant for transition to turbulence due to an earlier exponential growth of modal instabilities. Thus, it is necessary to assess which mechanism is more likely to lead to nonlinear breakdown. To properly compare non-modal with modal calculations, the integral amplification N is evaluated, as G in Eq. (4.16) is optimised over a prescribed space interval (Schmid 2007). Hence, the integral spatial amplification rate, namely the N-factor, is used. The N-factor for modal instabilities (Smith & Gamberoni 1956; van Ingen 1956) is calculated as

$$N = \int_{x_0}^{x} -\alpha_i(\omega/Re, \beta)dx, \quad N_{modal}(x) = \max_{\omega/Re,\beta}\{N(x, \omega/Re, \beta)\}, \tag{4.22a,b}$$

where x_0 is the streamwise location for neutral instability (branch I), and $N_{modal}(x)$ represents the envelope of all possible modal N-factors over all frequencies and spanwise wavenumbers. An analysis of the modal growth of 3-D disturbances for cases in Tab. 4.1 is reported in Sec. 3.4. In summary, for all cases, the maximum growth rate at a constant frequency, i.e. $\max_{\omega=\text{const.}}\{-\alpha_i\}$, is dependent on β, and thus 2-D modes are not always the most unstable. Yet, the maximum integral amplification N is always found for 2-D modes, i.e. $N_{modal}(x) = \max_{\forall\omega}\{N(\beta = 0)\}$.

Contrary to modal growth, the N-factor for non-modal (optimal) growth follows Bitter (2015); Tempelmann *et al.* (2012); Levin & Henningson (2003) and is expressed as

$$N_{opt}(x, Re_0) = 0.5 \ln(G), \tag{4.23}$$

where N_{opt} depends on the initial Reynolds number Re_0 and G is chosen as the optimal amplification G_{opt}. Note that, while short-distance energy amplification can be larger than $G_{opt}(Re_0)$ at $x \ll x_{opt}$, G_{opt} is the global maximum for each value of Re_0. In both non-transcritical and transcritical wall-cooling cases, ω_{opt} is zero. However, in the transcritical wall-heating case, ω_{opt} varies with Re_0 due to a non-constant wave angle of the streaks (see Fig. 4.18a), so G must be adapted in the streamwise direction. Moreover, β_{opt} remains almost constant with respect to the chosen Re_0 and is initially selected as the optimal one at $Re_0 = 300$ (see Tab. 4.2) before performing the optimisation at different $Re_{0,N}$ (initial optimal location). For a strict comparison with integral amplifications, the calculation of N_{opt} excludes modal growth, ensuring that only finite G_{opt} from stable eigenmodes are considered. The envelope of N_{opt}, $N_{opt,env.}$, represents the maximum transient growth at each streamwise location. Despite the boundary-layer growth, non-modal calculations are performed under the locally parallel assumption. Non-parallel results of Tumin & Reshotko (2003) indicate a difference in N_{opt} of only 0.4–0.5 (Bitter 2015), which is deemed acceptable for comparing to modal growth.

Table 4.3 summarises the comparison between non-modal and modal growth for the non-transcritical cases. Transient growth, present in the subcritical flow region below the critical Reynolds number, achieves a maximum N-factor of 4.6 up to $Re = 2000$, corresponding to energy amplifications of about 10^4, ($G = \exp(N)^2$). This occurs only when the wall is heated in the liquid-like state or cooled in the vapour-like state towards the Widom line. Conversely, modal growth dominates the transition to turbulence once the wall is cooled

Case	$Re_{0,N}$	Re_N	β_N	$N(Re_N)$	$G_{opt}(Re_N)$
T09w085	440	605	0.45	3.4	947
T09w090	760	1040	0.46	3.9	2314
T09w095	1470	2010	0.49	4.6	9725
T11w105	1240	1705	0.47	4.4	6966
T11w120	425	595	0.44	3.3	739

Table 4.3: Summary of the N-factor comparison between modal and non-modal growth for subcritical and supercritical cases. $Re_{0,N}$, Re_N, and β_N indicate the initial optimal Reynolds number, the local Reynolds number at which N_{modal} exceeds N_{opt}, and the optimal spanwise wavenumber at Re_N, respectively. $N(Re_N)$ is the N-factor at this position, with its corresponding energy amplification $G_{opt}(Re_N) = \exp\{N(Re_N)\}^2$. Cases T09w090 and T11w110 are identical.

in the subcritical state or heated in the supercritical state. Accurate transition predictions require knowledge of the initial disturbance energy and the underlying receptivity process. The N-values for nonlinear breakdown or transition to turbulence depend on various factors, such as disturbance sources (Bitter 2015). For instance, transient growth can be significant in noisy environments with high free-stream turbulence levels Tu (Levin & Henningson 2003) or discrete wall roughness elements (Reshotko & Tumin 2004). While the disturbance structures here are similar to those in ideal-gas studies, accurate analogies are limited due to a lack of transition experiments and unknown receptivity mechanisms in boundary layers at supercritical pressure. Hence, it remains uncertain whether transient growth is critical for the cases in this study.

The analysis in Tab. 4.3 is also applied to the transcritical cases in Fig. 4.26. For case T09w105, N_{opt}-calculations involve modifying ω_{opt} as a function of Re_0, as illustrated in Fig. 4.18(a). Overall, the transcritical cases exhibit significantly stronger modal growth than the non-transcritical cases. With transcritical wall heating (case T09w105), the highly unstable Mode II, resulting from inviscid instability (see GIP in Fig. 4.2(b), even though the velocity profile is fuller), is present (yellow line). Mode I (red line) is also more unstable than its counterpart in the liquid-like state, given the same wall-to-free-stream temperature ratio $T_w^*/T_\infty^* = 1.167$. For case T09w105, larger growth rates of Mode II compared to Mode I and the low non-modal energy amplification let the modal instability dominate further downstream around $Re \approx 590$. This suggests that at these thermodynamic transcritical conditions, growth occurs below the critical Reynolds number (also called subcritical growth in hydrodynamic stability theory), but with modest amplification rates. As noted for the non-transcritical cases, transient growth might be critical only if a simple analogy is drawn with the other ideal-gas transient-growth studies.

When the wall temperature is cooled over the Widom line (case T11w095), an even stronger modal instability, also of inviscid nature, is found. In this transcritical wall-cooling case, only one mode is unstable regardless of frequency and Reynolds number. The GIP

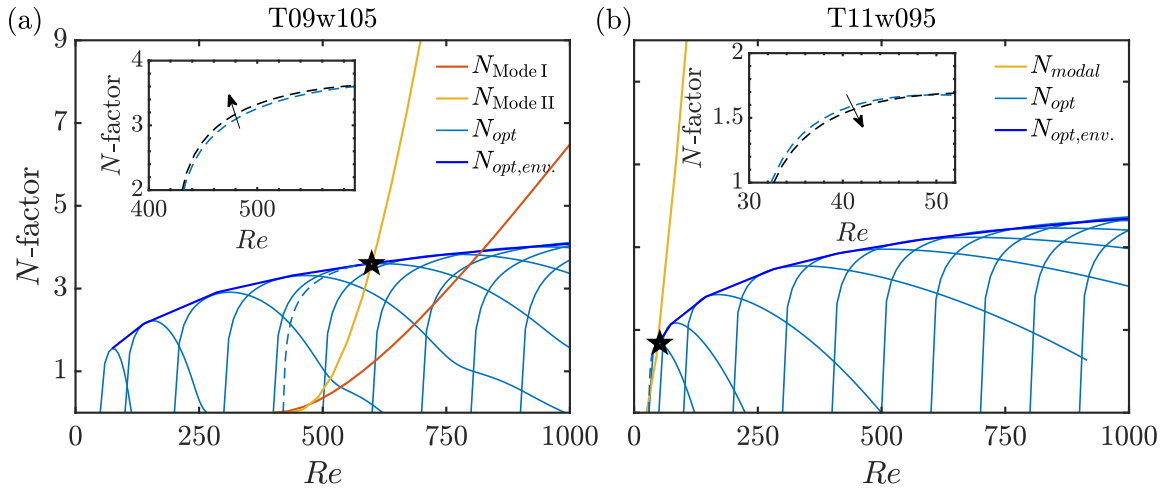

Figure 4.26: N-factor calculation: N_{modal} (—) and (—) are the N-factors obtained from Mode I and II, respectively, according to the modal stability analysis; N_{opt} (—) is the N-factor corresponding to transient growth, and $N_{opt,env.}$ (—) is the envelope of N_{opt}. (a) T09w105, and (b) T11w095. The optimal growth originating from the optimal initial position $x_{0,N}$ is indicated with a dashed blue line. The location x_N at which $N_{modal} = N_{opt}$ is denoted with a black star (⋆). In the inset, the optimal growth is varied over the spanwise wavenumber (black arrow); black dashed line illustrates the maximum optimal growth at β_N.

Case	$Re_{0,N}$	Re_N	β_N	$N(Re_N)$	$G_{opt}(Re_N)$
T09w105	420	590	0.53	3.5	1097
T11w095	30	52	0.40	1.7	30

Table 4.4: Summary of the N-factor comparison between modal and non-modal growth for transcritical cases. $Re_{0,N}$, Re_N, and β_N indicate the initial optimal Reynolds number, the local Reynolds number at which N_{modal} exceeds N_{opt}, and the optimal spanwise wavenumber at Re_N, respectively. $N(Re_N)$ is the N-factor at this position, with its corresponding energy amplification $G_{opt}(Re_N) = \exp\{N(Re_N)\}^2$.

moves away from the wall, due to the immense viscosity gradient at the wall (Ren & Kloker 2022), while the $\bar{u}(y)$-profile becomes inflectional above the Widom line, leading to a strong inviscid instability. As shown in Fig. 4.26(b), the exponential growth (yellow line) surpasses the algebraic growth near the flat-plate leading edge due to this inviscid instability. Thus, subcritical disturbance growth is irrelevant here. Note that the boundary-layer assumption may be inadequate here due to leading-edge effects. Regarding the optimal spanwise wavenumber in the insets of Fig. 4.26, one can recognise that the optimal N-factor is not affected by a change in β. A summary of the N-factor analysis is provided in Tab. 4.4.

Fig. 4.27 presents a final comparison of all supercritical cases, with Fig. 4.27(a) for a liquid-like free stream (cases T09w090, T09w085, T09w095, and T09w105) and Fig. 4.27(b) for a vapour-like free stream (cases T11w110, T11w105, T11w120, and T11w095). Non-modal

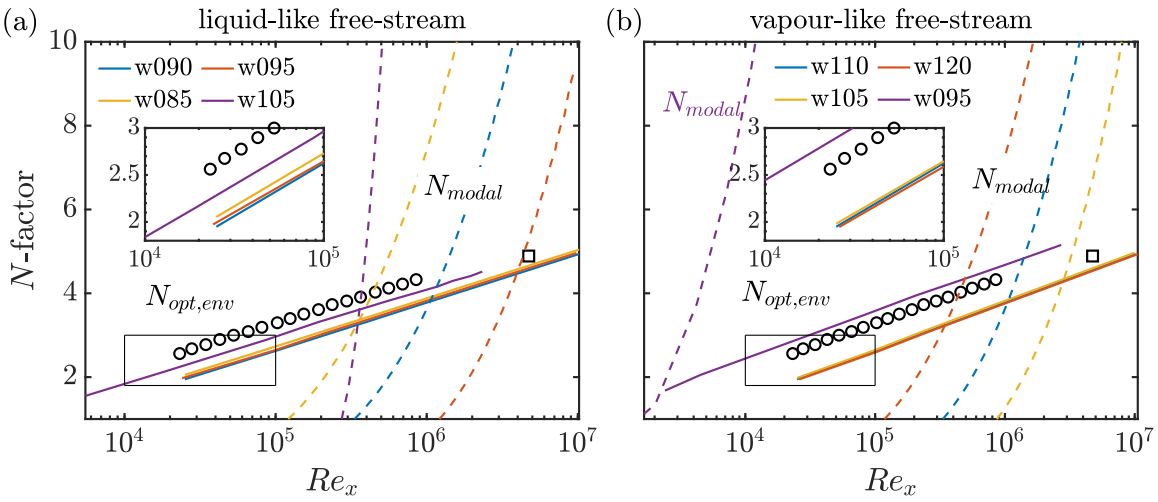

Figure 4.27: Envelope curves of optimal non-modal and modal growth: (a) liquid-like free-stream cases with $T^*_\infty/T^*_{pc} = 0.90$, (b) vapour-like free-stream cases with $T^*_\infty/T^*_{pc} = 1.10$. $N_{opt,env.}$: continuous line, N_{modal}: dashed line. For case T09w105, one common modal N-factor is calculated for Mode I and II. The black circle (∘) and square (□) symbols refer to the adverse and zero pressure gradient cases of Levin & Henningson (2003), respectively.

4

growth is represented as a straight line on a logarithmic scale. Non-transcritical cases exhibit $N_{opt,env.}$-factors that are unaffected by minor wall-to-free-stream temperature variation near the Widom line. For the transcritical cases, cooling over the Widom line in Fig. 4.27(b) significantly increases $N_{opt,env.}$, with $N_{opt,env.,\mathrm{T11w095}}/N_{opt,env.,\mathrm{T11w110}} \approx 1.34$. Nevertheless, this rise is even more pronounced for modal growth (see dashed lines). When examining the N-factors in Fig. 4.27 for a Falkner–Skan boundary layer with Adverse (APG, Hartree parameter $\beta_H = -0.1$) and Zero Pressure Gradient as in Levin & Henningson (2003), three main conclusions arise. First, an increase in the APG has a similar effect on transient growth as heating or cooling over the Widom line in a ZPG boundary layer at supercritical pressure, with transcritical wall cooling revealing a larger amplification. In case T11w095, exponential growth with a strong inviscid instability dominates from the leading edge. Secondly, Levin & Henningson (2003) predicts that with increased APG, the required level of free-stream turbulence for bypass transition decreases. In fact, when Tu > 3, $Re_{x,tr}$ was seen to shift to values below 10^5. If confirmed for a non-ideal boundary-layer flow at supercritical pressure, transient growth could be critical for transition in case T09w105, as non-modal growth in Fig. 4.27(a) dominates over modal growth below $Re_x \approx 3 \times 10^5$. Lastly, comparing the ZPG case from Levin & Henningson (2003) with case T09w090 reveals a difference of $N \approx 0.4$–0.5, demonstrating the robustness of the locally parallel assumption used in this study for non-modal optimisation against an adjoint-based optimisation algorithm with parabolised stability equations.

4.6 Conclusions

Transient growth of diabatic flat-plate boundary layers is examined at supercritical pressure. Supercritical carbon dioxide (CO_2) at a constant pressure of 80 bar (with a critical pressure of 73.9 bar) is selected as a representative non-ideal fluid in the proximity of the Widom line. Optimal energy amplifications and disturbances are calculated in the spatial framework by means of a singular value decomposition of the locally-parallel, linearised compressible Navier–Stokes equations. To account for non-ideality and strong thermophysical property variations around the Widom line, a novel non-ideal energy norm is derived in Sec. 4.2 such that pressure work is eliminated. The new norm is equal to Chu's (Chu 1965) and Mack's (Hanifi *et al.* 1996) norms under the ideal-gas assumption.

This study explores the subcritical, supercritical, and transcritical states (relative to the pseudo-boiling temperature of CO_2, T^*_{pc} = 307.7 K), determined by prescribing free-stream and wall temperatures at a fixed Mach number of 10^{-3} (see Sec. 4.3). In the subcritical (liquid-like: T^*_∞/T^*_{pc} = 0.90 with $T^*_w < T^*_{pc}$) and supercritical (vapour-like: T^*_∞/T^*_{pc} = 1.10 with $T^*_w > T^*_{pc}$) states, wall cooling enhances transient growth. For the subcritical cases, the optimal streamwise distance x_{opt} decreases, while the optimal spanwise wavenumber β_{opt} increases as the wall temperature approaches the Widom line. Conversely, in the supercritical state, the opposite trend is observed. In these two weakly non-ideal states, the maximal energy amplification and its distance scale best with the compressible momentum thickness, in agreement with the Falkner–Skan boundary layer of Corbett & Bottaro (2000) under the ideal-gas assumption. The optimal energy amplification is detected at finite spanwise wavenumbers, yet the optimal frequency is zero, indicating that the optimal disturbances correspond to counter-rotating vortices, which evolve into streamwise-independent streaks. This corresponds to the well-known lift-up mechanism, in agreement with ideal-gas results. Moreover, scaling laws, e.g. $G \propto Re^2$ and $x_{max} \propto Re$, consistently hold.

When the wall temperature crosses the Widom line (transcritical wall-heating: T^*_∞/T^*_{pc} = 0.90 with $T^*_w > T^*_{pc}$; transcritical wall-cooling: T^*_∞/T^*_{pc} = 1.10 with $T^*_w < T^*_{pc}$), optimal structures are no longer exclusively streamwise independent. In the transcritical wall-heating state, a finite optimal frequency suggests the involvement of the Orr mechanism. In fact, analysis of the Reynolds stress reveals that optimal disturbance structures are initially tilted against the mean shear before being re-oriented to it. A strong contribution of the Orr mechanism is observed for sub-optimal transient growth, where larger local energy-amplification peaks than the global optimal one can be achieved for $x \ll x_{opt}$. This leads to highly-oblique sub-optimal disturbance structures, which do not originate from a streamwise vortex. The Orr mechanism exists also for perturbations with a negative spanwise wavenumber. Thus, the resulting superposition forms a chequerboard pattern, analogous to the oblique-transition mechanism in Berlin *et al.* (1994). Moreover, streamwise-modulated streaks in the transcritical wall-heating state exhibit significant streamwise velocity disturbances and strong thermal components ($\hat{\rho}$ and $\hat{T}$) around the pseudo-critical point. While similar large density streaks are also observed in the transcritical wall-cooling state, they are not oblique. Despite com-

parable $|T_w^* - T_\infty^*|$, transcritical wall cooling yields higher optimal energy amplification rates G_{opt}/Re^2. This increase can be explained by the vortex-tilting mechanism, which highlights the alignment of the output wall-normal vorticity with the highest wall-normal displacement above the pseudo-critical point. Conversely, a misalignment between the two in the transcritical wall-heating state results in a smaller G, albeit with a secondary peak of the optimal streamwise velocity at the pseudo-critical point.

When considering the effect of initial Reynolds number, scaling laws hold for both optimal streamwise-independent and -modulated disturbances. Particularly, in the case of optimal oblique streaks in transcritical wall-heating, we observe a dependence of the optimal frequency ω_{opt} on Re^{-1}, while the optimal energy G_{opt} scales with Re^2. This implies that as $Re \to \infty$, the Orr mechanism is not active, leading to the recovery of streamwise-independent structures. Consequently, the streaks' wave angle Ψ becomes proportional to Re^{-1}. Investigating the underlying eigenspectrum in the transcritical wall-heating state reveals the influence of the non-orthogonal eigenfunctions on optimal growth. Specifically, the stable transcritical Mode II is found to actively participate in the interplay between lift-up and the Orr mechanism. If this mode is intentionally excluded from the optimisation procedure, both mechanisms yield only significantly reduced sub-optimal growth, resulting in modified optimal transient growth solely associated with streamwise-independent disturbances, growing via the lift-up mechanism.

In relation to the effect of wall temperature on transient growth, we note that the momentum-thickness scaling is ineffective in the transcritical state, in contrast to the non-transcritical states. In the transcritical wall-heating state, increasing the wall temperature initially shifts optimal frequencies to higher values. However, once the pseudo-critical point moves away from the near-wall layer, optimal energy growth is found at $\omega = 0$. Stronger wall heating leads to a rise in the density perturbation amplitudes around the pseudo-critical point due to greater mean-flow density gradients. In contrast, in the transcritical wall-cooling state, G_{opt} remains at $\omega_{opt} = 0$, while β_{opt} slightly increases. Notably, an increase of only 5% in wall temperature can result in a 30% to 70% gain in G_{opt}. Furthermore, similar optimal disturbance structures are detected when, in the transcritical state, the optimal perturbations are streamwise independent.

A comparison between modal and non-modal growth across all states is presented in Sec. 4.5. Initially, the modal instability of oblique perturbations is studied for both non-transcritical and transcritical cases. At the low Mach number of 10^{-3} employed in this study, 2-D modes exhibit the highest amplifications, both locally (across most of the frequency spectrum) and integrally. This suggests that, as shown in the oblique modal stability analysis at finite Mach numbers in Ren *et al.* (2019*b*), decreasing the Mach number (compressibility effects) shifts the largest possible local and integral amplification from a 3-D to a 2-D mode, regardless of the considered thermodynamic state at supercritical pressure. Notably, no critical N-factors of transition have been experimentally measured for flows at supercritical pressure so far, hence transition-prediction analogies can only be drawn in relation to ideal-gas transient-growth results. In the non-transcritical states, transient growth is marginally

affected by the non-ideal thermodynamic state. Within their best-case scenarios (subcritical wall-heating and supercritical wall-cooling), modal growth prevails over transient growth at amplification levels around $N \approx 4$. On the other hand, in the transcritical state, characterised by a highly inflectional base flow (inviscid instability), modal instability dominates, especially for transcritical wall-cooling, where no subcritical transition below the critical Reynolds number is likely to occur. In this scenario, the increase in the non-modal N-factor, i.e. N_{opt}, is significant compared to the non-transcritical wall-cooling cases, similar to the effect of an adverse pressure gradient in ideal-gas transient-growth calculations. A similar analogy applies to transcritical wall-heating, albeit with lower transient-growth amplifications, reaching up to $N \approx 3.5$ before a strong modal amplification emerges. Nevertheless, a critical Reynolds number of approximately 3×10^5 could be sufficiently large to favour transition via transient growth, particularly when the level of free-stream turbulence is high.

Discussions on the influence of an increasing reduced pressure on the N-factor comparison indicate that, for transcritical wall-heating, transient growth is likely to be the prevailing route to turbulence. Conversely, for transcritical wall-cooling, modal growth consistently dominates.

Bibliography

Andersson, P., Berggren, M. & Henningson, D. S. 1999 Optimal disturbances and bypass transition in boundary layers. *J. Fluid Mech.* **11**, 134–150.

Banuti, D. T. 2015 Crossing the Widom-line – Supercritical pseudo-boiling. *J. Supercrit. Fluids* **98**, 12–16.

Berlin, S., Lundbladh, A. & Henningson, D. 1994 Spatial simulations of oblique transition in a boundary layer. *Phys. Fluids* **6**, 1949–1951.

Bitter, N. P. 2015 Stability of Hypervelocity Boundary Layers. PhD thesis, California Institute of Technology.

Bitter, N. P. & Shepherd, J. E. 2015 Stability of highly cooled hypervelocity boundary layers. *J. Fluid Mech.* **778**, 586–620.

Brandt, L. 2014 The lift-up effect: the linear mechanism behind transition and turbulence in shear flows. *Eur. J. Mech. (B/Fluids)* **47**, 80–96.

Bugeat, B., Boldini, P. C. & Pecnik, R. 2022 On the new unstable mode in the boundary layer flow of supercritical fluids. In *Proceedings of the 12th International Symposium on Turbulence and Shear Flow Phenomena (TSFP-12)*.

Butler, K. M. & Farrell, B. F. 1992 Three-dimensional optimal perturbations in viscous shear flow. *Phys. Fluids A* **4**, 1637–1650.

Chen, X., Wang, L. & Fu, S. 2022 Energy transfer of hypersonic and high-enthalpy boundary layer instabilities and transition. *Phys. Rev. Fluids* **7**, 033901.

Chikkadi, V., Sameen, A. & Govindarajan, R. 2005 Preventing transition to turbulence: a viscosity stratification does not always help. *Phys. Rev. Lett.* **95**, 264504.

Chu, T. B. 1965 On the energy transfer to small disturbances in fluid flow (part I). *Acta Mech.* **1**, 215–234.

Corbett, P. & Bottaro, A. 2000 Optimal perturbations for boundary layers subject to stream-wise pressure gradient. *Phys. Fluids* **12**, 120–130.

Farrell, B. F. & Ioannou, P. J. 1993 Optimal excitation of three-dimensional perturbations in viscous constant shear flow. *Phys. Fluids A* **5**, 1390–1400.

Govindarajan, R. & Sahu, K. C. 2014 Instabilities in viscosity-stratified flow. *Ann. Rev. Fluid Mech.* **46**, 331–353.

Gustavsson, L. H. 1991 Energy growth of three-dimensional disturbances in plane Poiseuille flow. *J. Fluid Mech.* **224**, 241–260.

Hack, M. J. P. & Moin, P. 2017 Algebraic disturbance growth by interaction of Orr and lift-up mechanisms. *J. Fluid Mech.* **829**, 112–126.

Hanifi, A. & Henningson, D. S. 1998 The compressible inviscid algebraic instability for streamwise independent disturbances. *Phys. Fluids* **10**.

Hanifi, A., Schmid, P. J. & Henningson, D. S. 1996 Transient growth in compressible boundary layer flow. *Phys. Fluids* **8**, 826–837.

van Ingen, J. L. 1956 A suggested semi-empirical method for the calculation of the boundary layer transition region. Technical Report VTH-74. Delft University of Technology, Department of Aerospace Engineering.

Jiao, Y., Hwang, Y. & Chernyshenko, S. I. 2021 Orr mechanism in transition of parallel shear flow. *Phys. Rev. Fluids* **6**, 023902.

Jose, S., Brandt, L. & Govindarajan, R. 2020 Localisation of optimal perturbations in variable viscosity channel flow. *Int. J. Heat Fluid Flow* **85**, 108588.

Kaminski, A. K., Caulfield, C. P. & Taylor, J. R. 2014 Transient growth in strongly stratified shear layers. *J. Fluid Mech.* **758**, R4.

Landahl, M. T. 1980 A note on an algebraic instability of inviscid parallel shear flows. *J. Fluid Mech.* **98**, 243–251.

Lemmon, E. W., Huber, M. L. & Mclinden, M. O. 2013 NIST Standard Reference Database 23: Reference Fluid Thermodynamic and Transport Properties - REFPROP, Version 9.1. Available at: `http://www.nist.gov/srd/nist23.cfm`.

Levin, O. & Henningson, D. S. 2003 Exponential vs algebraic growth and transition prediction in boundary layer flow. *Flow Turbul. Combust.* **70**, 183–210.

Luchini, P. 2000 Reynolds number independent instability of the boundary layer over a flat surface: optimal perturbations. *J. Fluid Mech.* **404**, 289–309.

Mack, L. M. 1984 Boundary-layer linear stability theory. *AGARD Report No. 709: Special Course on Stability and Transition of Laminar Flow.* AGARD.

Malik, M., Dey, J. & Alam, M. 2008 Linear stability, transient energy growth, and the role of viscosity stratification in compressible plane Couette flow. *Phys. Rev. E* **77**, 036322.

Nemati, H., Patel, A., Boersma, B. J. & Pecnik, R. 2016 The effect of thermal boundary conditions on forced convection heat transfer to fluids at supercritical pressure. *J. Fluid Mech.* **800**, 531–556.

Orr, W. M. F. 1907 The stability or instability of the steady motions of a perfect liquid and of a viscous liquid. Part I: a perfect liquid. Part II: a viscous liquid. *Proc. R. Irish Acad. A* **27**, 9–138.

Paredes, P., Choudhari, M. M., Li, F. & Chang, C. L. 2016 Optimal growth in hypersonic boundary layers. *AIAA J.* **54**, 3050–3061.

Parente, E., Robinet, J. C., De Palma, P. & Cherubini, S. 2020 Modal and non-modal stability of a stably stratified boundary layer flow. *Phys. Rev. Fluids* **5**, 113901.

Ren, J., Fu, S. & Pecnik, R. 2019*a* Linear instability of Poiseuille flows with highly non-ideal fluids. *J. Fluid Mech.* **859**, 89–125.

Ren, J. & Kloker, M. 2022 Instabilities in three-dimensional boundary-layer flows with a highly non-ideal fluid. *J. Fluid Mech.* **951**, A9.

Ren, J., Marxen, O. & Pecnik, R. 2019*b* Boundary-layer stability of supercritical fluids in the vicinity of the Widom line. *J. Fluid Mech.* **871**, 831–864.

Reshotko, E. 2001 Transient growth: A factor in bypass transition. *Phys. Fluids* **5**, 1067–1075.

Reshotko, E. & Tumin, A. 2000 The blunt body paradox – a case for transient growth. In *Laminar-Turbulent Transition*, p. 403–408. Berlin: Springer.

Reshotko, E. & Tumin, A. 2004 Role of transient growth in roughness-induced transition. *AIAA J.* **42 (4)**, 766–770.

Robinet, J.-C. & Gloerfelt, X. 2019 Instabilities in non-ideal fluids. *J. Fluid Mech.* **880**, 1–4.

Saikia, B., Ramachandran, A., Sinha, K. & Govindarajan, R. 2017 Effects of viscosity and conductivity stratification on the linear stability and transient growth within compressible Couette flow. *Phys. Fluids* **29**, 1–20.

Sameen, A., Bale, R. & Govindarajan, R. 2011 The effect of wall heating on instability of channel flow – CORRIGENDUM. *J. Fluid Mech.* **673**, 603–605.

Sameen, A. & Govindarajan, R. 2007 The effect of wall heating on instability of channel flow. *J. Fluid Mech.* **577**, 417–442.

Schmid, P. J. 2007 Nonmodal stability theory. *Annu. Rev. Fluid Mech.* **39**, 129–162.

Schmid, P. J. & Henningson, D. S. 2001 *Stability and transition in shear flows*. Springer.

Smith, A. M. O. & Gamberoni, N. 1956 Transition, pressure gradient, and stability theory. Technical Report ES 26388. Douglas Aircraft Co.

Tempelmann, D., Hanifi, A. & Henningson, D. S. 2012 Spatial optimal growth in three-dimensional compressible boundary layers. *J. Fluid Mech.* **704**, 251–279.

Tumin, A. 2007 Three-dimensional spatial normal modes in compressible boundary layers. *J. Fluid Mech.* **586**, 295–322.

Tumin, A. & Reshotko, E. 2001 Spatial theory of optimal disturbances in boundary layers. *Phys. Fluids* **13**, 2097–2104.

Tumin, A. & Reshotko, E. 2003 Optimal disturbances in compressible boundary layers. *AIAA J.* **41**, 2357–2363.

White, F. M. 2006 *Viscous Fluid Flow, 3rd Edition*. Boston: McGraw-Hill.

5

CUBENS: HIGH-FIDELITY SOLVER

The content of this chapter has been published under the title:

P. C. Boldini, R. Hirai, P. Costa, J. W. R. Peeters, and R. Pecnik,
CUBENS: A GPU-accelerated high-order solver for wall-bounded flows with non-ideal fluids.
Computer Physics Communications, Volume 309, 109507, 2025.

We present a massively parallel GPU-accelerated solver for direct numerical simulations of transitional and turbulent flat-plate boundary layers and channel flows involving fluids in non-ideal thermodynamic states. While several high-fidelity open-source solvers exist, all are restricted to the ideal-gas region. In contrast, the CUBic Equation of state Navier–Stokes solver (CUBENS) can accurately model and simulate the non-ideal thermodynamics of single-phase compressible fluids in the vicinity of the vapour–liquid saturation line or the critical point. By employing high-order finite-difference schemes and convective terms in split, kinetic-energy-, and entropy-preserving form, the solver is numerically stable and robust with minimal numerical dissipation, enabling it to capture the steep variations of non-ideal thermodynamic properties. For cost-effective high-fidelity simulations, in addition to MPI parallelization, CUBENS is GPU-accelerated using OpenACC directives for computation offloading, and asynchronous GPU-aware MPI for efficient GPU-GPU communication. Moreover, CUBENS is compatible with both NVIDIA and AMD GPU architectures, achieving significant performance results while ensuring energy-efficient simulations. For instance, using 64 NVIDIA A100 GPUs compared to 8192 CPUs at the same computational cost results in a speed-up of approximately 130×. In multi-node and multi-GPU configurations ranging from 2 to 128 compute nodes (8 to 512 GPUs), a strong scaling efficiency of around 52% and a weak scaling efficiency of 0.88 with 1024^3 points per GPU, corresponding to approximately 5 billion degrees of freedom, are achieved. The solver is validated against selected literature cases, covering transitional to turbulent ideal and non-ideal flows up to the transonic regime. In particular, we demonstrate the solver's suitability and applicability for direct numerical simulations of transitional boundary layers with supercritical fluids and with buoyancy effects.

5.1 Introduction

The application of single-phase fluids in non-ideal thermodynamic states has rapidly expanded the relevance of a new branch of fluid mechanics called non-ideal compressible fluid dynamics (aus der Wiesche 2023). Given the increasing number of industrial applications operating under non-ideal-gas conditions, such as turbomachinery and heat exchangers (White *et al.* 2021), the development of more accurate theoretical, experimental, and numerical tools is essential (Guardone *et al.* 2024). A major challenge, however, is the lack of knowledge regarding transitional and turbulent boundary layers due to the difficulty in conducting experiments at high density and temperature conditions (Cinnella & Gloerfelt 2023). In contrast, high-fidelity simulations can significantly enhance and accelerate the design of new engineering systems that operate under non-ideal-gas conditions. Fluids above their vapour–liquid critical point, i.e. in the supercritical-fluid region, play a key role in future energy conversion systems, see e.g. Zhao *et al.* (2024).

In this region, if a high-pressure liquid-like or vapour-like fluid is isobarically heated or cooled across the pseudo-critical (Widom) line, defined as $\max\{c_p(T)\}$, a continuous phase transition with significant variations in thermophysical properties occurs. This transition can lead to either heat-transfer deterioration or enhancement (Yoo 2013), and may delay or promote the onset of turbulence (Ren *et al.* 2019; Boldini *et al.* 2024). Due to the non-ideal-fluid behaviour close to the thermodynamic vapour–liquid critical point, the ideal-gas (IG) Equation of State (EoS) $p = \rho R_g T$ (with p as pressure, ρ as density, R_g as specific gas constant, and T as temperature) is not applicable, requiring more complex EoS. It is important to clarify that the term 'complex' does not refer to the complexity of fluid molecules themselves, e.g. fluids with High Molecular Complexity (HMC). Instead, non-ideal-gas dynamic phenomena affect the flow of all fluids whose thermodynamic states fall within the non-ideal thermodynamic region, including those with simpler molecular structures, such as Low Molecular Complexity (LMC) fluids (Guardone *et al.* 2024).

The first high-fidelity simulations of non-ideal-fluid flows have been conducted for only a limited number of specific configurations. For example, Kawai (2019) investigated turbulent boundary layers with the LMC fluid parahydrogen at supercritical pressure and transcritical temperatures. Due to the abrupt density variation across the Widom lime, large density fluctuations were observed, which significantly altered the near-wall turbulence. In the case of a dense vapour of an HMC fluid, Sciacovelli *et al.* (2017a) performed the first Direct Numerical Simulation (DNS) of a supersonic turbulent channel configuration. The high isobaric heat capacity of HMC fluids results in negligible temperature variations, despite observing pressure fluctuations similar to those in IG cases. Conversely, supersonic flows of an HMC fluid are found to exhibit both a 'vapour-like' (e.g. speed of sound) and 'liquid-like' (e.g. viscosity) behaviour (Sciacovelli *et al.* 2017a). With the semi-local scaling (see Patel *et al.* (2015)), turbulence statistics for variable-property flows show remarkable agreement with incompressible-gas cases. In Patel *et al.* (2016); Pecnik & Patel (2017), turbulence modulation by non-ideal viscosity laws was investigated. Once again, the semi-local Reynolds

number proved to best quantify turbulence in variable-property flows. Ma *et al.* (2018) found that while semi-local scaling worked well for the bottom cooled wall, it was less suitable for the top-heated wall, where density fluctuations were significant. Following Patel *et al.* (2016), an improved near-wall mean temperature formulation was proposed by Guo *et al.* (2022) to better collapse the slope of the logarithmic region. Studies by Nemati *et al.* (2016); Peeters *et al.* (2016); Kim *et al.* (2019) on turbulent flows with LMC fluids at supercritical pressure revealed that the thermal wall-boundary condition greatly influences heat transfer in supercritical fluids, and that property fluctuations considerably impact turbulent streak evolution. He *et al.* (2021) and Cao *et al.* (2021) demonstrated that supercritical CO_2 (LMC fluid) turbulent pipe flows are prone to laminarisation, primarily due to the alternating dominance of buoyancy and inertia mechanisms.

Only in recent times have selected transition routes to turbulence in wall-bounded flows with non-ideal fluids been explored. The first DNS of a spatially developing Boundary Layer (BL) with HMC fluids was conducted by Sciacovelli *et al.* (2020) for PP11 and by Gloerfelt *et al.* (2023) for Novec649, two HMC fluids. Dense-vapour BLs revealed large fluctuations in Mach number and dilatation compared to light-gas BLs at high Mach numbers. Additionally, by means of DNS, Boldini *et al.* (2023) investigated the first controlled laminar-to-turbulent transition of a transcritical BL with an LMC fluid at supercritical pressure. The H-type breakdown unveiled a combination of strong vortical structures, resembling Λ-vortices, as well as high- and low-speed and density streaks. Overall, the transition to turbulence was found to be much more abrupt than in the case at supercritical pressure with subcritical temperature.

All the aforementioned studies can be classified as high-fidelity simulations, where all temporal and spatial flow scales are fully resolved. A key requirement for conducting these simulations is the minimisation of dispersion and dissipation errors in the calculation of convective terms (Kuya *et al.* 2018). Numerical dispersion at large wave numbers can be reduced by employing high-order finite-difference schemes (Kok 2009), which, in turn, enhance spatial resolution (Cinnella & Gloerfelt 2023). To minimise numerical dissipation, it is essential to preserve not only the primary variables (mass, momentum, and total energy) but also the secondary ones (energy and entropy). This approach also improves the numerical stability of the proposed scheme (Coppola *et al.* 2019).

A first attempt to conserve kinetic energy was proposed by Kennedy & Gruber (2008) using a cubic-split form of the convective terms. This approach, later rewritten by Pirozzoli (2010) for computational efficiency, is now commonly known as the Kennedy-Gruber–Pirozzoli (KGP) scheme. An improvement of this Kinetic-Energy Preserving (KEP) scheme was made by Kuya *et al.* (2018) and Kuya & Kawai (2021), who developed a high-order accurate Kinetic-Energy-and-Entropy-Preserving (KEEP) scheme that provides improved numerical robustness compared to the existing KEP scheme. Importantly, while the KEEP scheme enhances the entropy preservation of the KEP scheme, resulting in greater numerical robustness, it does not ensure a conservative calculation of the entropy convection term, meaning that entropy is not conserved to machine precision (Tamaki *et al.* 2022). In a new study,

Aiello *et al.* (2025) developed a spatial discretisation to achieve exact entropy-conservative numerical fluxes for an arbitrary EoS.

Nonetheless, these classical preserving schemes are unable to maintain the Pressure-Equilibrium-Preserving (PEP) property, which refers to the discrete scheme's ability to reproduce a travelling density wave with an initially constant velocity and pressure distribution. To suppress spurious pressure oscillations, several strategies have emerged. De Michele & Coppola (2024) proposed Asymptotically Entropy Conservative (AEC) schemes under the IG assumption, based on the harmonic mean for internal energy, which exhibit both PEP and KEP properties. In the KEEP-PEP version presented by Shima *et al.* (2021), a variation of the split-form discretisation for the internal-energy convective term (logarithmic mean) was derived, albeit under the assumption of an IG. In fact, due to the linear relationship between pressure and internal energy in this case, the PEP condition was ensured. Yet, when non-ideal-gas dynamic phenomena affect the flow, the strongly nonlinear dependencies of the EoS affect the relationship between pressure and internal energy, making the formulation of the internal-energy flux non-trivial. Although the IG PEP condition of Shima *et al.* (2021) provides a first-order approximation of pressure equilibrium for any EoS, spurious, non-physical pressure and velocity oscillations can occur in abrupt flow variations (e.g. under pseudo-boiling conditions close to the vapour–liquid critical point) (Kawai *et al.* 2015; Hickey *et al.* 2013). These oscillations persist as grid-to-grid variations, even with mesh refinement or additional filtering, potentially leading to numerical instabilities (Kawai 2019). A first attempt to specifically address this issue was made by Bernades *et al.* (2023) with the 'KGP-Pt' scheme, where the term 'Pt' refers to the time derivative of pressure. In this approach, the pressure evolution equation is discretised directly instead of the total energy equation, resulting in better preservation of pressure equilibrium; however, this comes at the cost of conserving total energy and entropy. Despite these advancements, no numerical method currently exists that is capable of discretely preserving both primary and secondary variables while simultaneously enforcing pressure equilibrium for non-ideal fluids. Consequently, performing DNS of supercritical flows near the thermodynamic critical point remains highly challenging from a numerical standpoint.

To summarise, the following numerical requirements are essential for high-fidelity simulations of transitional and turbulent wall-bounded flows of compressible single-phase non-ideal fluids: (i) a high-order scheme to achieve greater accuracy, (ii) appropriate modeling of nonlinear thermodynamic and transport properties, (iii) accurate resolution of the strong property variations near the Widom line, and (iv) high-spatial resolution to resolve the smallest coherent thermal structures. Note that, in the proximity of the critical point and across the Widom line, the Prandtl number becomes $O(Pr) \gg 1$. This necessitates high-spatial resolution to resolve the smallest scale of the temperature field, such as the Batchelor length scale η_B, defined as $\eta_B = \eta_k/\sqrt{Pr}$, where η_k is the Kolmogorov scale. Consequently, substantial computational resources are necessary to perform stable and accurate scale-resolving simulations.

In the past, high-fidelity solvers relied on Central Processing Unit (CPU) execution

and Message Passing Interface (MPI) parallelisation. Yet, the advent of Graphics Processing Units (GPUs) has significantly advanced the progress towards Exascale computing (Alowayyed *et al.* 2017). As a result, High-Performance-Computing (HPC) architectures are progressively adopting heterogeneous nodes that combine CPUs with GPUs as accelerators. For instance, approximately 40% of the current TOP500 (TOP500.org 2024*b*) list's computing power comes from GPU-accelerated systems, a profound contrast to over a decade ago when such systems were absent from the list. Furthermore, among the most efficient supercomputers in the current GREEN500 list (TOP500.org 2024*a*), all of the top 30 employ GPU-accelerated energy-efficient computing units. Notably, these systems are powered exclusively by either NVIDIA or AMD GPUs, although Intel has recently entered the competition with the Aurora supercomputer at Argonne National Laboratory, which currently ranks as the second-fastest in the world and is number 42 on the GREEN500 list. This paradigm shift has recently led to many incompressible and compressible DNS solvers being GPU-accelerated or entirely developed for GPU-based architectures, yielding remarkable speed-ups of 10 to 20 times compared to CPU-only architectures (Kim *et al.* 2023).

Among them, we summarise a selection of open-source direct numerical simulation solvers. Two of the most common academic incompressible Navier–Stokes solvers are AFiD (Zhu *et al.* 2018) and CaNS (Costa *et al.* 2021), which utilise CUDA Fortran and OpenACC GPU-acceleration, respectively. Conversely, in the compressible-flow community, high-order solvers such as STREAmS (Bernardini *et al.* 2023) for the IG state and HTR (Di Renzo 2022) for hypersonic reacting flows employ CUDA Fortran and task-based Legion for GPU-based architectures, respectively. Another example is URANOS (De Vanna *et al.* 2023), which leverages the advantageous OpenACC paradigms for GPU acceleration. As a directive-based method, OpenACC is fully independent of the computing architecture and more user-friendly than CUDA Fortran, requiring minimal code adaptations. Significant performance improvements have recently been achieved for both STREAmS and URANOS, as outlined in Salvadore *et al.* (2024) and De Vanna & Baldan (2024), respectively. In the case of STREAmS, a comprehensive performance analysis on Intel GPUs demonstrated a 40% increase in performance compared to other available GPUs. Meanwhile, URANOS has been enhanced for portability to AMD GPUs and includes the implementation of a chunking strategy for flux calculations.

In the community of wall-bounded flows with compressible single-phase non-ideal fluids, the development of new high-fidelity GPU-accelerated solvers has only recently begun. Regarding high-fidelity numerical solvers for non-ideal compressible fluid dynamics, four in-house codes are reported here: (i) MUSICAA (Sciacovelli *et al.* 2017a), which employs high-order central finite-difference schemes and MPI parallelisation for transitional and turbulent BLs of HMC fluids; (ii) 3DNS (Wheeler 2024), which utilises high-order compact finite-difference schemes and multi-block parallelisation for turbomachinery studies; (iii) PadeLibs (Song *et al.* 2023), which implements high-order compact finite-difference methods and GPU-acceleration for turbulent boundary flows with LMC fluids at supercritical pressure; and (iv) RHEA (Jofre *et al.* 2023), which uses low-order central-difference schemes and GPU-

acceleration via OpenACC for turbulent flows with LMC fluids at supercritical pressure. However, no publicly available GPU-accelerated high-order solver exists for simulating wall-bounded transitional and turbulent flows with compressible single-phase non-ideal fluids in canonical geometries. Therefore, we present a state-of-the-art solver featuring high-order energy-preserving schemes, achieving excellent numerical robustness with minimal numerical dissipation for the simulation of single-phase non-reacting flows involving highly non-ideal fluids.

Given the reasons outlined above, the open-source CUBic Equation of state Navier–Stokes (CUBENS) solver has been developed for Direct Numerical Simulations of transitional and turbulent wall-bounded flows with compressible non-ideal fluids. The CUBENS solver efficiently operates on the latest generations of GPU-accelerated clusters (TOP500.org 2024*b*), such as Snellius (SURF, the Netherlands) and LUMI (CSC, Finland), and is fully compatible with the two leading and most powerful GPU architectures, NVIDIA and AMD, through the OpenACC standard (OpenACC Architecture Review Board 2021). With respect to the spatial discretisation, high-order central finite-difference schemes are employed alongside the KEEP-PEP scheme for the convective fluxes and pressure-equilibrium conservation. The solver accounts for the strongly nonlinear nature of thermodynamics and fluid properties by combining cubic EoS with non-ideal transport-property (TP) models.

This manuscript provides a comprehensive description of the CUBENS solver, detailing its governing equations, validation, and performance. The paper is structured as follows: Section 5.2 introduces the conservation equations, non-ideal EoS, and nonlinear TP models. Section 5.3 discusses the numerical discretisation of CUBENS, followed by its GPU implementation in Section 5.4. In Section 5.5, the solver is validated against various benchmark cases. For additional transitional BL flows, see Section 5 of (). Section 5.6 presents the code performance on both single and multi-CPU and -GPU architectures. Finally, conclusions are drawn in Section 5.7.

5.2 Governing equations

The fundamental governing equations and thermodynamic models for a single-phase, non-reacting compressible fluid suitable for the non-ideal thermodynamic region are presented in Chapter 2.

5.3 Numerical methods

A summary of the numerical techniques employed to solve Eq. (2.1) is discussed hereafter. For more details, see the corresponding references.

5.3.1 Spatial discretisation

A high-order explicit central finite-difference method is combined with split convective derivatives for local kinetic energy and entropy conservation. Here, the high-order KEEP scheme in Cartesian coordinates (Kuya & Kawai 2021) is combined with the variation of Shima *et al.* (2021) for PEP conditions. By using this scheme, both primary (mass, momentum, and total energy) and secondary (kinetic energy and entropy) conservative quantities are conserved while maintaining numerical stability. Thus, aliasing errors are minimised, and the whole range of turbulence scales can be captured without any stabilisation scheme, such as artificial diffusivity or filtering (Coppola *et al.* 2019). Note that the PEP discretisation of internal energy exactly holds under the IG assumption. However, for non-ideal fluids, no current numerical scheme can fully conserve this property. Therefore, a compromise is made, with the IG PEP condition serving as a first approximation to satisfy pressure equilibrium for arbitrary EoS (see 'PEP-IG' scheme in Bernades *et al.* (2023)).

By defining the numerical flux $\tilde{F}_\phi|_{(i\pm1/2)}$ for a scalar ϕ at the cell interfaces $(i \pm 1/2)$, we can write the spatial derivative of the convective term as

$$\frac{\partial \rho\phi u}{\partial x} \simeq \frac{\tilde{F}_\phi|_{(i+1/2)} - \tilde{F}_\phi|_{(i-1/2)}}{\Delta x}, \tag{5.1}$$

considering a second-order discretisation. Thus, Eq. (2.1) in differential and inviscid form is discretised by the numerical fluxes at cell index i as:

$$\left.\frac{\partial \rho}{\partial t}\right|_i + \frac{\tilde{C}|_{(i+1/2)} - \tilde{C}|_{(i-1/2)}}{\Delta x_j} = 0, \tag{5.2}$$

$$\left.\frac{\partial \rho u_k}{\partial t}\right|_i + \frac{\tilde{M}_{u_k}|_{(i+1/2)} - \tilde{M}_{u_k}|_{(i-1/2)}}{\Delta x_j} + \frac{\tilde{\Pi}|_{(i+1/2)} - \tilde{\Pi}|_{(i-1/2)}}{\Delta x_j} = 0, \tag{5.3}$$

where $\tilde{C}$, $\tilde{M}_{u_k}$, $\tilde{\Pi}$ are the mass, momentum, and pressure-gradient ($k = 1, 2, 3$) numerical fluxes, respectively, and:

$$\begin{aligned}\left.\frac{\partial \rho E}{\partial t}\right|_i + \frac{\tilde{K}|_{(i+1/2)} - \tilde{K}|_{(i-1/2)}}{\Delta x_j} + \frac{\tilde{I}|_{(i+1/2)} - \tilde{I}|_{(i-1/2)}}{\Delta x_j} \\ + \frac{\tilde{P}|_{(i+1/2)} - \tilde{P}|_{(i-1/2)}}{\Delta x_j} = 0.\end{aligned} \tag{5.4}$$

where $\tilde{K}$, $\tilde{I}$, and $\tilde{P}$ are the kinetic energy, internal energy, and pressure-diffusion numerical fluxes, respectively. Their expressions can be found in Shima *et al.* (2021), where a new internal energy numerical flux that maintains velocity and pressure equilibrium at the contact interface is defined. Note that, in the context of non-ideal fluids, a diffuse interface occurs along the Widom line when the flow is at supercritical pressure and under transcritical conditions. This scenario is characterised by a continuous transcritical contact surface (Kawai *et al.* 2015) between the high-density liquid-like and the low-density vapour-like state. In CUBENS, we focus on fully resolving the diffuse interface and selecting the appropriate flow

q	$a_{q,1}$	$a_{q,2}$	$a_{q,3}$
2	1/2	-	-
4	2/3	-1/12	-
6	3/4	-3/20	1/60

Table 5.1: Coefficients a_{q,i_s} for the central difference approximation of first derivative. q is the order of accuracy, and i_s is the stencil size.

regime to minimise spurious oscillations, as the PEP condition of Shima *et al.* (2021) strictly applies only under IG conditions.

The high-order extension is achieved by following the approach proposed in Pirozzoli (2011) for KEP schemes. Hence, the convective numerical flux $\tilde{F}_\phi|_{(i\pm1/2)}$ is extended to an arbitrary order of accuracy as

$$\tilde{F}_\phi|_{(i\pm1/2)} = 2\sum_{i_s=1}^{q/2} a_{q,i_s} \times \sum_{j=0}^{i_s-1} \frac{\rho_{(i\mp j)} + \rho_{(i\mp j\pm i_s)}}{2} \frac{\phi_{(i\mp j)} + \phi_{(i\mp j\pm i_s)}}{2} \frac{u_{(i\mp j)} + u_{(i\mp j\pm i_s)}}{2}, \tag{5.5}$$

where a_{q,i_s} are the coefficients used for the central difference approximations of the first derivative, with an order of accuracy q and stencil size i_s (see Tab. 5.1 for up to 6th-order). In CUBENS, the order of accuracy of the convective terms ($q = 2, 4, 6$) can be explicitly selected by the user. The diffusion fluxes in Eqs. (2.4) are discretised using a central finite-difference approximation both for first- and second-order derivatives, with CUBENS supporting 2nd- and 4th-order finite differences.

5.3.2 Time discretisation

After spatial discretisation, the system in Eq. (2.1) can be explicitly advanced in time. This results in

$$\frac{\partial \mathbf{Q}}{\partial t} = \mathbf{R}(\mathbf{Q}, t), \tag{5.6}$$

where $\mathbf{R}$ is the nonlinear spatial differential operator and $\mathbf{Q}$ is the state vector as in Eq. (2.2). Subsequently, a third-order Total Variation Diminishing (TVD) low-storage Runge–Kutta scheme (Gottlieb & Shu 1998) is applied to advance $\mathbf{Q}^n$ from time t^n to $\mathbf{Q}^{n+1}$ at t^{n+1}, with time step $\Delta t = t^{n+1} - t^n$. This yields:

$$\begin{aligned} \mathbf{Q}^{(1)} &= \mathbf{Q}^n + \Delta t \mathbf{R}\left(\mathbf{Q}^n\right), \\ \mathbf{Q}^{(2)} &= \frac{3}{4}\mathbf{Q}^n + \frac{1}{4}\left[\mathbf{Q}^{(1)} + \Delta t \mathbf{R}\left(\mathbf{Q}^{(1)}\right)\right], \\ \mathbf{Q}^{(n+1)} &= \frac{1}{3}\mathbf{Q}^n + \frac{2}{3}\left[\mathbf{Q}^{(2)} + \Delta t \mathbf{R}\left(\mathbf{Q}^{(2)}\right)\right]. \end{aligned} \tag{5.7a–c}$$

To ensure numerical stability (Coleman & Sandberg 2010), the Courant–Friedrichs–Lewy (CFL) and Fourier criteria need to hold according to

$$\Delta t_{\mathrm{CFL}} \propto \left(\frac{\Delta x_j}{|\mathbf{u}_j + a|}\right), \quad \Delta t_{\mu} \propto \left(\frac{\Delta x_j^2}{\mu}\right), \quad \Delta t_{\kappa} \propto \left(\frac{\Delta x_j^2}{\kappa}\right), \tag{5.8a–c}$$

where Δx_j is the grid size in the corresponding j-direction, and a is the speed of sound (see Sec. 2.2). The global time step Δt to advance $\mathbf{Q}^n$ is then calculated from Eq. (5.6) as a minimum condition from:

$$\Delta t = \mathrm{CFL} \cdot \min(\Delta t_{\mathrm{CFL}}, \Delta t_{\mu}, \Delta t_{\kappa}). \tag{5.9}$$

For CFL < 1, the 3rd-order Runge–Kutta method is numerically stable (Gottlieb & Shu 1998). Thus, the CFL number in all directions can be set arbitrarily by the user, typically between 0.5 and 0.8.

In numerical simulations of controlled transitional BLs (Ren *et al.* 2019; Marxen *et al.* 2013 2014), it is also common practice to specify the time step Δt based on the frequency of the primary disturbance ω_0 as follows

$$\Delta t = \frac{2\pi}{\omega_0}\frac{1}{LP}, \tag{5.10}$$

where LP is a multiple of the number of samples saved during each forcing period. The parameter LP can be adjusted by the user by, for instance, constraining CFL to values not larger than 0.8.

5.3.3 Computational domains

Two canonical geometries can be considered in CUBENS: channel flow and flat-plate BL. While the former configuration can be utilised in alignment with DNS studies under supercritical pressure conditions (Ma *et al.* 2018; Kim *et al.* 2019), the canonical flat-plate geometry remains largely unexplored for transitional and turbulent BLs with LMC fluids, particularly under the influence of density stratification.

Channel

The channel configuration has a wall-normal height L_y of $2H^*$, where H^* is the half channel height and represents the reference length. For the non-dimensionalisation of Eq. (2.1), the following reference values are used

$$\begin{gathered} t = \frac{t^* u^*_{ref}}{H^*}, \quad x_i = \frac{x_i^*}{H^*}, \quad u_i = \frac{u_i^*}{u^*_{ref}}, \quad \rho = \frac{\rho^*}{\rho^*_w}, \quad p = \frac{p^*}{\rho^*_w u^{*2}_{ref}}, \\ T = \frac{T^*}{T^*_w}, \quad e_0 = \frac{e_0^*}{u^{*2}_{ref}}, \quad \mu = \frac{\mu^*}{\mu^*_w}, \quad \kappa = \frac{\kappa^*}{\kappa^*_w}, \end{gathered} \tag{5.11a–i}$$

where $(\cdot)_w$ indicates the selected reference wall values (note that non-isothermal conditions can be also considered in CUBENS by imposing a temperature difference between top and

bottom wall), and u^*_{ref} is the reference velocity, e.g. centerline velocity. In streamwise and spanwise directions, the mesh is uniform, while in the wall-normal direction, it follows a hyperbolic tangent function given by

$$y = y_e \left[1 + \frac{\tanh(0.5\sigma(\eta - 1)}{\tanh(0.5\sigma)} \right], \tag{5.12}$$

where the wall-normal coordinate η extends from 0 to 2.

Transitional boundary layer

The computational domain for a laminar BL transitioning to turbulence is illustrated in Fig. 5.1(a). The inflow is located at x_0 and the outflow at x_e. The domain height is given by y_e, and the spanwise domain extends from 0 to z_e. To achieve laminar-to-turbulent transition, disturbances are triggered by a wall-normal blowing and suction strip ($x_1 < x < x_2$), see Sec. 5.3.4. The reference length L^*_{ref} in Eqs. (2.7*a*–*j*) and (2.8*a*–*d*) is chosen as the BL thickness at the start of the computational domain, $\delta^*_{99,0}(u = 0.99)$. The other reference quantities in Eqs. (2.7*a*–*j*) and (2.8*a*–*d*) correspond to free-stream flow conditions and are denoted with $(\cdot)_\infty$. After the re-scaling of all dimensions, the dimensionless BL thickness $\delta_{99,0}$ at the domain inlet Re_0 is equal to unity. The corresponding local Reynolds number Re, based on the Blasius length scale δ^*, and Reynolds number Re_x, based on the streamwise coordinate x^*, are dependent on $\delta^*_{99,0}$ and can be written as:

$$Re = \frac{\rho^*_\infty u^*_\infty \delta^*}{\mu^*_\infty} = \sqrt{Re_x} = Re_0 \frac{\delta^*}{\delta^*_{99,0}}, \quad \delta^* = \sqrt{\frac{\mu^*_\infty x^*}{\rho^*_\infty u^*_\infty}}. \tag{5.13a,b}$$

In the spanwise z-direction, an equidistant mesh is applied with constant grid spacing Δz. The same applies for the streamwise x-direction, although streamwise stretching with $\Delta x \propto \tanh(x)$ is available. In the wall-normal y-direction, a grid stretching towards the wall is applied. The wall-normal distribution y with N_y grid points is then expressed as

$$\begin{aligned} y &= y_e \left[K_1 \eta + (1 - K_1) \left(1 + \frac{\tanh(0.5\sigma(\eta - 1)}{\tanh(0.5\sigma)} \right) \right], \\ \eta &= 0, ..., 1, \quad K_1 = \frac{0.6}{Re_{\tau,0}} \frac{N_y - 1}{y_e}, \end{aligned} \tag{5.14a,b}$$

where $Re_{\tau,0} = \delta^*_{99,0}/\delta^*_{99,v}$ is the prescribed friction Reynolds number at the domain inlet, with $\delta_{99,v} = \overline{\mu}^*_w/(\overline{\rho}^*_w u^*_\tau)$, and σ is the stretching factor for near-wall region refinement.

Turbulent boundary layer

The computational domain in CUBENS for a turbulent BL is illustrated in Fig. 5.1(b). The same numerical setup and reference quantities are chosen as for a transitional BL in Fig. 5.1(a). However, the following differences need to be taken into account. The reference length is selected as the mean turbulent BL thickness at the inlet, defined as $\delta^*_{99,0}$, which remains constant by fixing the mean inflow profiles. Inflow turbulence fluctuations are generated using the recycling-rescaling (RR) method of Urbin & Knight (2001). First, the mean

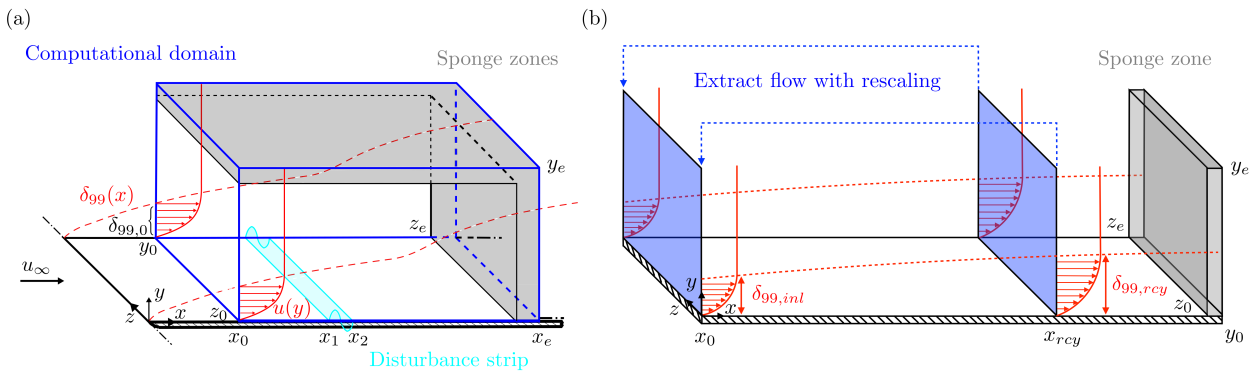

Figure 5.1: DNS computational domain for (a) transitional BL and (b) turbulent BL. All the reference values are explained in Sec. 5.3.3.

velocity and temperature profiles, either known a priori or obtained from a transitional BL simulation, are extracted at the streamwise recycling position, x^*_{rcy}. The rescaling parameter β, which is the ratio of the inlet and recycling friction velocities, is estimated from the ratio of the mean turbulent BL thicknesses as

$$\beta \equiv \frac{u^*_{\tau,0}}{u^*_{\tau,rcy}} \approx \left(\frac{\delta^*_{99,rcy}}{\delta^*_{99,0}}\right)^{0.1}, \tag{5.15}$$

where $\delta_{99,rcy}$ is the mean turbulent BL thickness at the recycling position. The recycled velocity profiles are then decomposed into a (Reynolds) average, denoted as $\overline{(\cdot)}$, and fluctuating component, denoted as $(\cdot)'$. The log- and defect-laws are applied to the inner- and outer-layer scaling of the velocity, respectively (Urbin & Knight 2001). Note that this method can be further improved, particularly for strongly cooled or heated BLs and high Mach number flows, by applying the approach proposed by Hasan *et al.* (2024). This yields the following relationships between the mean velocity profiles at the inlet and the recycling position as

$$\begin{aligned} \overline{u}^{inn}_{vD,0} &= \beta \overline{u}^{inn}_{vD,rcy}, \\ \overline{u}^{out}_{vD,0} &= u_{\infty,vD} - \beta\left(u_{\infty,vD} - \overline{u}^{out}_{vD,rcy}\right), \end{aligned} \tag{5.16a,b}$$

where superscripts *inn* and *out* denote the inner- and outer-layer scaled quantities, respectively, and the subscript vD refers to the van Driest transformation (van Driest 1951), which is defined as

$$\overline{u}_{vD} = \frac{u_\infty}{A}\sin^{-1}\left(A\frac{\overline{u}}{u_\infty}\right), \quad A = \sqrt{\frac{M^2_\infty Pr_t\,(\gamma-1)/2}{1+M^2_\infty Pr_t\,(\gamma-1)/2}}, \tag{5.17a,b}$$

where the turbulent Prandtl number Pr_t is constant and equal to 0.89 (IG). The inner- and outer-layer fluctuating components are rescaled using the same parameter β. Finally, the mean and fluctuating components are combined using a weighted average (Lund *et al.* 1998) to determine the new inflow profile as

$$u_0 = \left(\overline{u}^{inn}_0 + u'^{inn}_0\right)(1-W(y)) + \left(\overline{u}^{out}_0 + u'^{out}_0\right)W(y), \tag{5.18}$$

Case	Inlet	Top	Outlet	Bottom
BL	subsonic	$\mathcal{L}_1 = K(p - p_\infty)$	$\mathcal{L}_1 = 0$	no-slip
Channel	periodic	no-slip	periodic	no-slip

Table 5.2: Summary of the non-reflecting BCs for flat-plate BL and channel configurations. $\mathcal{L}_1$ is the amplitude of the incoming wave with constant K according to Rudy & Strikwerda (1980).

where the weighting function $W(y)$ is:

$$W(y) = \frac{1}{2}\left(1 + \left\{\tanh\left[\frac{4\,(y-B)}{(1-2B)\,y + B}\right] \Big/ \tanh(4)\right\}\right), \quad B = 0.2. \tag{5.19}$$

This same weighting procedure is applied consistently to all other flow variables.

5.3.4 Boundary conditions

Based on the computational domain described in Sec. 5.3.3, non-reflecting Boundary Conditions (BCs) are applied at the domain boundaries according to the inviscid characteristic wave analysis of Thompson (1987) and Poinsot & Lele (1992). To account for gas non-ideality, the extension of Okong'o & Bellan (2002) for single-phase flow is implemented. While the Local One-Dimensional Inviscid (LODI) problem is not affected by gas non-ideality, the speed of sound a, thermal expansion coefficient α_v, and isobaric heat capacity c_p are modified according to the corresponding EoS in Sec. 2.2. Additionally, the inclusion of a wall-normal buoyant force, as indicated by the source term in Eq. (2.6), should be considered due to the large wall-normal density gradients that may arise within the BL, particularly at supercritical pressure under transcritical conditions. Thus, an inhomogeneous term, i.e. $\mathbf{C}$ in Eq. (5.20*a–d*), appears on the right-hand side of the characteristic equations (Thompson 1987). The one-dimensional characteristic form of the Euler equations reads:

$$\begin{aligned} &\frac{\partial \mathbf{Q}^*}{\partial t} + \mathbf{A}\frac{\partial \mathbf{Q}^*}{\partial x} + \mathbf{C} = 0, \quad \text{with} \\ &\mathbf{Q}^* = \begin{pmatrix} \rho \\ u \\ p \end{pmatrix}, \quad \mathbf{A} = \begin{pmatrix} u & \rho & 0 \\ 0 & u & 1/\rho \\ 0 & \rho a^2 & u \end{pmatrix}, \quad \mathbf{C} = \begin{pmatrix} 0 \\ Ri_{unit}(\rho - 1)/\rho \\ 0 \end{pmatrix}. \end{aligned} \tag{5.20a–d}$$

Both wave speeds λ_i and wave amplitudes $\mathcal{L}_i$ are identical to those in (Okong'o & Bellan 2002), except for $\mathcal{L}_5$ at the wall, which is modified due to the buoyancy force:

$$\mathcal{L}_{5,new} = \mathcal{L}_5 - 2aRi_{unit}(\rho - 1). \tag{5.21}$$

A summary of the non-reflecting BCs for the aforementioned computational domains is presented in Tab. 5.2. For the BC at the bottom (and at the top in the case of channel flow), CUBENS can switch between an adiabatic and an isothermal no-slip, non-reflecting wall-BC. Regardless of the geometry considered, periodic BCs are employed in the spanwise direction.

For BL calculations, numerical sponge zones can additionally be applied to the boundaries to minimise acoustic reflections (Mani 2012). The reference solution inside the sponge region is the similarity solution of the compressible laminar BL (White 2006), combined with the chosen EoS (see Ren *et al.* (2019); Boldini *et al.* (2024) for more details).

To simulate a transitional BL and to achieve a controlled laminar-to-turbulent transition, disturbances are triggered by a wall-normal blowing and suction strip. This approach represents a vibrating ribbon, in agreement with the controlled experimental studies of Kachanov *et al.* (1977). Two different disturbance strips between x_1 and x_2, with $x_{mid} = 0.5(x_1 + x_2)$, can be selected by the user. Both are dependent on the non-dimensional frequency ω, given as

$$\omega = FRe, \quad \text{with} \quad F = \frac{2\pi f^* \mu^*_\infty}{\rho^*_\infty u^{*2}_\infty}, \tag{5.22}$$

where f^* is the dimensional frequency. In Huai *et al.* (1997); Rist & Fasel (1995); Fasel *et al.* (1990); Sayadi *et al.* (2013), the Three-Dimensional (3-D) wall-normal velocity distribution is prescribed as

$$v(y = 0) = f(x)\left[A_{2\text{-D}} \sin(\omega_{2\text{-D}} t) + A_{3\text{-D}} \sin(\omega_{3\text{-D}} t)\cos(\beta z)\right], \tag{5.23}$$

where $A_{2\text{-D}}$ is the amplitude of the primary Two-Dimensional (2-D) and $A_{3\text{-D}}$ of the 3-D wave, with $\beta = 2\pi/z_e$ being the spanwise wavenumber. The variation of the disturbance strip in the x-direction is equal to:

$$\begin{aligned} f(x) &= 15.1875\xi^5 - 35.4375\xi^4 + 20.25\xi^3, \\ \xi &= \begin{cases} \dfrac{x - x_1}{x_{mid} - x_1}, & x_1 < x < x_{mid}, \\ \dfrac{x_2 - x}{x_2 - x_{mid}}, & x_{mid} < x < x_2. \end{cases} \end{aligned} \tag{5.24a,b}$$

Conversely, in agreement with Sciacovelli *et al.* (2020); Franko & Lele (2013), additional N_{mod} modes can be excited via the 3-D blowing and suction of the form

$$\begin{aligned} v(y = 0) &= f(x)g(z) \sum_{i=1}^{N_{mod}} A_i \sin(\omega_i t - \beta_i z), \\ f(x) &= \exp\left[\frac{-(x - x_{mid})^2}{\sigma^2}\right], \end{aligned} \tag{5.25a,b}$$

where A_i and β_i are the wave amplitude and spanwise wavenumber of mode i, respectively. The spanwise variation of the disturbance strip is given by

$$\begin{aligned} g(z) = 1 &+ 0.1\exp\left[-\left(\frac{z - z_{mid} - z_w}{z_w}\right)^2\right] \\ &- 0.1\exp\left[-\left(\frac{z - z_{mid} + z_w}{z_w}\right)^2\right], \end{aligned} \tag{5.26}$$

where z_{mid} and z_w are the mid-point and width of the disturbance strip, respectively.

5.4 Solver implementation

Given the current transformation of HPC systems towards Exascale supercomputing, it is desirable to develop a solver that can run on different modern architectures, with performance portability. CUBENS is written in modern Fortran and currently consists of roughly 18 000 lines of source code, organised in modular components, which greatly facilitates code readability, maintenance, and further development. In this context, two different supercomputing architectures are chosen: the Dutch national supercomputer Snellius, based at SURF (165th and 240th in the TOP500 list for CPU and GPU cores, respectively (TOP500.org 2024*b*)) with NVIDIA A100 GPUs, and the pre-exascale EuroHPC JU LUMI supercomputer, based at CSC in Finland (5th in the TOP500 (TOP500.org 2024*b*)), with AMD MI250X GPUs. Portability to Intel GPUs is currently not supported due to limited access to this architecture.

At the coarse-grained level, MPI is adopted for parallel computations in distributed memory. The geometry is divided into several computational subdomains using the 2DECOMP&FFT library (Li & Laizet 2010). Specifically, the domain decomposition is performed in the streamwise and spanwise direction, with ghost cells at the domain boundaries. Thus, stencils for finite-difference schemes can be calculated with the support of data exchange to adjacent subdomains. When migrating to a system with different computing units, such as multicore processors and accelerators, the two main requisites are to have a low-cost code development that is easy to maintain for domain experts. The use of directives is desirable here, as they are naturally masked by the compiler and treated as comments for the standard CPU implementation. The OpenACC (OpenACC Architecture Review Board 2021) standard is adopted to accelerate the solver at the fine-grained (thread-level) parallelisation on GPUs and to manage host-device data movement. As a directive-based programming model designed for GPU computations, OpenACC uses directives to instruct the compiler on how to offload computations to the GPU, or on how to perform data transfer. Note that the two different architectures used in this work required different compilers that support OpenACC. On Snellius, we use the NVIDIA compiler shipped in the NVIDIA HPC SDK (NVIDIA 2023), whereas, for LUMI – and specifically its GPU partition, LUMI-G – we use the Cray compiler from the Cray Compiler Environment (CCE). For the compilation of CUBENS on the two architectures, the solver uses a standard build system based on GNU make, tailored to easily switch from one architecture to the other. With the flag `ARCH` in the CUBENS makefile, the user can choose between the NVHPC and Cray compilers. For CPU partitions, CUBENS supports GNU, Cray, and Intel compilers.

5.4.1 GPU-porting

Before presenting the details of the GPU porting, Algorithm 5.1 shows the simplified code structure of CUBENS. CUBENS runs its GPU-accelerated cases in a so-called GPU-resident fashion. After the initialisation of the main variables on the host (CPU), the data associated with variables required on the device (GPU) are copied using the `!$acc enter data copyin(list)` directive. Note that any Host-to-Device (H2D) or Device-to-Host (D2H) oper-

```
program main_CUBENS
...
call init() ! Subroutines initialisation
!$acc enter data copyin (variables)
call init_solution() ! Initial solution initialisation
!$acc update device (variables)
do istep=istart+1,istart+nsteps ! Time loop
    ...
    call calc_timestep() ! Calculation of the time-step
    do RK_step=1,RK_order ! Loop over Runge-Kutta substeps
        call MPI_comm() ! ghost cells communication
        call set_BC() ! Boundary conditions
        call calc_Euler_flux() ! Euler fluxes
        call calc_Visc_flux() ! Viscous fluxes
        call calc_Update_variables() ! Update primary variables
        call calc_RK_step() ! Runge-Kutta step
    enddo
    !$acc update host(variables) async(n)
    !$acc wait
    call output()! Write output/restart files
enddo
...
!$acc end data
...
end program
```

Algorithm 5.1: Simplified code structure of the main operations in CUBENS.

ation is associated with a performance loss due to limited host-device communication bandwidth and should therefore be minimised. Afterward, the initial solution is prescribed on the host before the values on the device are updated using `!$acc update device(list)`. At this point, we identify the most time-consuming part of the code: the `nsteps` time loop, which contains Runge–Kutta substeps at each `istep`, and especially the calculation of the Navier–Stokes Right-Hand Side (RHS). The RHS consists of (a) inviscid Euler fluxes in `calc_Euler_flux()` (see Eqs. (2.3*a*–*c*)), (b) viscous diffusive fluxes in `calc_Visc_flux()` (see Eqs. (2.4)), (c) the source term (see Eq. (2.6)), and (d) boundary conditions or `set_BC()` in Section 5.3.4.

Next, we discuss the acceleration of operations performed within each Runge–Kutta substep, specifically contained in `calc_RK_step()`, as shown in Algorithm 5.1. In this regard, the OpenACC acceleration of the temporal advancement of the density variable in the first Runge–Kutta step (`RK_step=1`) is illustrated in Algorithm 5.2. The `parallel` construct of OpenACC is used for a prescriptive approach to the compiler. Within a parallel region of the code, the `parallel loop` construct can be applied to specifically parallelise a nested loop, as displayed.

OpenACC supports up to three levels of parallelism, ranging from coarse to fine: `gang`,

```
program calc_RK_step
...
!$acc parallel default(present)
!$acc loop gang, vector collapse(3)
do k=1,k_max ! Loop over the streamwise direction
    do j=1,j_max ! Loop over the spanwise direction
        do i=1,i_max ! Loop over the wall-normal direction
            rho(i,j,k) =  rho_Old(i,j,k) + dt*0.5_rp*RHS_rho1(i,j,k) !
   rho_Old: density at         former time step (istep-1)
            ... ! other non-conservative variables
        enddo
    enddo
enddo
!$acc end parallel loop
...
end program
```

Algorithm 5.2: Calculation of the first Runge-Kutta step (RK_step = 1) for the density variable. Values at the former time step (at istep-1) are indicated with index _Old.

`worker`, and `vector` (see OpenACC Architecture Review Board (2021)). In Algorithm 5.2, the OpenACC directive parallelises three nested loops by distributing iterations across multiple gangs and vectorizing them for efficient parallel execution. If the level of parallelism is not specified, the compiler independently schedules the loop iterations on the target accelerator device. Furthermore, another level of parallelism can be added using the `collapse` clause, which exposes the three nested loops to thread-level parallelisation. This transforms the nested loops over $k_{\max}$, $j_{\max}$, and $i_{\max}$ into a single loop of size $k_{\max} \times j_{\max} \times i_{\max}$, to be distributed among parallel threads.

Once the Runge–Kutta substeps are completed, the solution on the device can be transferred to the host with the `update host` clause. This D2H data movement is again associated with efficiency loss. However, the generation of output and restart files can be controlled by the user by specifying the frequency of data writing. Another way to mitigate the problem is to exploit asynchrony between operations using OpenACC's `async(n)` clause, where `n` represents the so-called OpenACC *queue* number, similar to concurrent, independent streams in CUDA Fortran. This technique has been applied to treat the inviscid fluxes in Section 5.4.2.

An essential task in porting the code to GPU is profiling to assess performance. To address this, we use either (a) the NVIDIA Nsight Systems performance tool together with the NVIDIA Tools Extension (NVTX) library, which is a C-based library previously used for optimizing other GPU-based codes, see e.g. Costa *et al.* (2021); De Vanna *et al.* (2023), or (b) the ROCm open-source stack for AMD GPUs (AMD 2024). Both libraries are linked to a dedicated profiling module in CUBENS, i.e. `timer.f90`. The timing module reports the average time per task for each tagged region, and it also supports more detailed reporting, including minimum and maximum times per call and per task. An example of the tagged Runge–Kutta substep calculation in CUBENS is presented in Algorithm 5.3.

```
...
call timer_tic("start calc_RK_step",1)
call calc_RK_step()
call timer_toc("end calc_RK_step",1)
...
```

Algorithm 5.3: Profiling example of calc_RK_step with timer module.

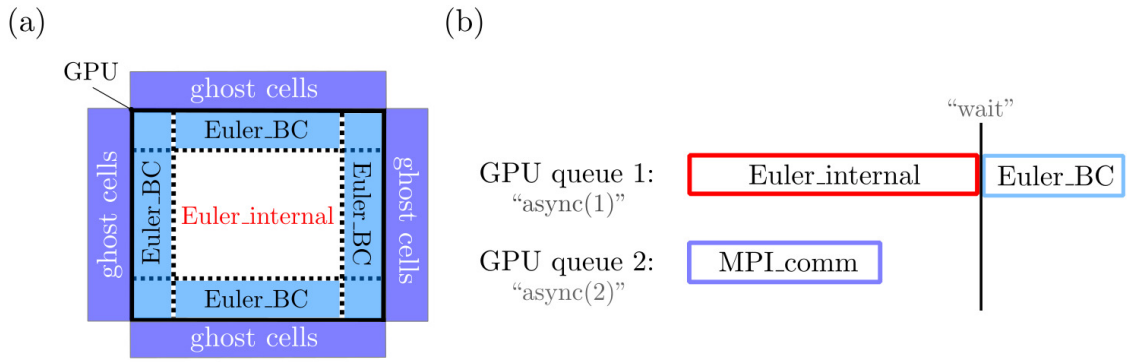

Figure 5.2: CUBENS asynchronous operations: (a) GPU domain with fluxes at the internal cells and boundary cells, and ghost cells; (b) sketch of `async` clauses for `Euler_internal` and `MPI_comm` before `wait` clause.

5

5.4.2 Treatment of the inviscid fluxes

Since the host and device have physically distinct memories, which are accessible simultaneously, one can leverage both memories by performing data movement while executing parallel operations on the device. With the `async(n)` clause, independent asynchronous operations can be executed in parallel before the `wait` clause ensures the completion of all parallel operations. We employ this technique in CUBENS to speed up the calculation of the RHS. Specifically in Algorithm 5.1, the modules `MPI_comm`, `set_BC`, and `Euler_flux` can be effectively parallelised. In fact, the `MPI_comm` module is only responsible for updating the ghost cells at the domain boundaries as a function of the finite-difference stencils. On the other hand, as displayed in Fig. 5.2(a), the calculation of the `Euler_flux` section can be split into two parts: the fluxes at the interior nodes, i.e. `Euler_internal`, and those at the boundaries `Euler_BC`. Consequently, the execution of `Euler_internal` is independent of the operations at the domain boundaries, and thus can be run in parallel with `MPI_comm`. Simultaneously, the execution of `Euler_BC` can only be performed after the ghost cells have been updated. As illustrated in Fig. 5.2(b), a `wait` clause ensures the correct evaluation of the BCs in time, and thus of the fluxes at the boundaries. With this strategy, the workload distribution of `MPI_comm` is overlapped with `Euler_internal`.

```
...
#if defined(_GPU_DIRECT)
!$acc host_data use_device(buff_send9_k,buff_send9_j,buff_recv9_j,
   buff_recv9_k)
call MPI_SENDRECV(buff_send9_k(:,:,:,1:nHalo),xs(1)*xs(2)*9*nHalo, &
                  real_type,neigh%kp,0, &
                  buff_recv9_k(:,:,:,1:nHalo),xs(1)*xs(2)*9*nHalo, &
                  real_type,neigh%km,0, &
                  MPI_COMM_WORLD,istat,ierr)
...
!$acc end host_data
#endif
...
```

Algorithm 5.4: Code snippet from the `MPI_comm` module for GPU-aware MPI data transfer. `-D_GPU_DIRECT` is a pre-processing flag.

5.4.3 Multi-GPU implementation

For high-fidelity simulations, multiple processing units need to be exploited. In a multi-GPU implementation, two communication approaches can be identified. While in the traditional approach, accelerators are connected via host-based MPI, leading to inefficient H2D and D2H data transfer, a GPU-aware MPI implementation can be extremely beneficial. With Unified Virtual Addressing (UVA), the host and all devices' memory are unified into a large (virtual) address space, improving communication efficiency (De Vanna *et al.* 2023). In CUBENS, the MPI initialisation is conducted in accordance with Costa *et al.* (2021); De Vanna *et al.* (2023). Each GPU is assigned an MPI rank (`rank`) along with a device identification number (`dev_id`). GPU-aware MPI can then be activated by using the `-D_GPU_DIRECT` compiler option. In Algorithm 5.4, an example of GPU-to-GPU data transfer is shown. The `host_data` clause is used to share the address of the device data to the host. The list of arrays, e.g. `use_device(variables_list)`, which are already present in the device memory, are directly passed to the traditional MPI routine `MPI_SENDRECV`. Note that in CUBENS, the transfer data – both sending (see `buff_send9_k`) and receiving (see `buff_recv9_k`) – contain a four-dimensional array, where 9 is the number of transferred variables and `k` is the streamwise direction with `nHalo` ghost cells.

5.5 Validation

In this section, the CUBENS solver is first validated using a set of benchmark cases. These include: (a) the laminar-to-turbulent transition of an IG decaying vortex, (b) the IG flat-plate H-type breakdown, (c) a turbulent BL using the recycling-rescaling method, and (d) the linear small-amplitude disturbance evolution in a laminar BL with an LMC fluid at supercritical pressure.

Case	TPs	M_∞	Ec_∞	Pr_∞	$Ri_{w,0}$	γ	T_w^*/T_∞^*
Sec. 5.5.1	Power law	[0.1, 0.5, 1.0]	[0.004, 0.1, 0.4]	0.75	-	1.4	-
Sec. 5.5.2	Sutherland's law	0.2	0.016	0.75	-		adiabatic
Sec. 5.5.3	Sutherland's law	0.2	0.016	0.75	-		adiabatic
Sec. 5.5.4	Sutherland's law	0.2	0.016	0.72	[-0.01,0,0.01]		1.05

Table 5.3: Base-flow properties for IG cases of Section 5.5. The inlet Richardson number at the wall is defined as $Ri_{w,0} = Ri_{unit,0}(\rho_w - 1)$.

Case	EoS	TPs	p_r	$T_{r,\infty}$	M_∞	Ec_∞	Pr_∞	Z_∞	c_v^*/R^*	T_w^*/T_∞^*
Section 5.5.5	Peng–Robinson	Chung	1.084	0.92	0.2	0.01	2.39	0.165	9/2	1.125

Table 5.4: Base-flow properties for non-ideal-gas cases of Section 5.5. The free-stream compressibility factor is defined as $Z_\infty = p_r/(\rho_{r,\infty} R_g T_{r,\infty})$.

Subsequently, this section showcases the CUBENS solver's capability for the direct numerical simulations of strongly-stratified wall-bounded flows with compressible, single-phase, non-ideal fluids. An additional transitional flat-plate BL at zero pressure gradient with stable and unstable stratification (see Sec. 5.5.4) is considered. It is important to note that all flow cases in this section employ 6th-order accuracy for the convective fluxes and 4th-order accuracy for the diffusive fluxes. Overall, these simulations pave the way for future investigations with the CUBENS solver, with detailed analyses planned. The flow parameters for the ideal gas and non-ideal-gas cases presented in this section are shown in Tab. 5.3 and Tab. 5.4, respectively.

5.5.1 Compressible Taylor–Green Vortex

The accuracy of the numerical scheme is assessed using the canonical Taylor–Green Vortex (TGV) problem. Originally formulated for incompressible flows by DeBonis (2013), the TGV problem has recently been extended to strongly compressible regimes (Peng & Yang 2018; Sciacovelli *et al.* 2021; Lusher & Sandham 2021). The flow is initialised in a triply periodic cubic domain with a side length of 2π as

$$\begin{cases} \rho(x,y,z,t=0) = \rho_{init}, \\ u(x,y,z,t=0) = u_{init}\sin(x)\cos(y)\cos(z), \\ v(x,y,z,t=0) = -u_{init}\cos(x)\sin(y)\cos(z), \\ w(x,y,z,t=0) = 0, \\ p(x,y,z,t=0) = p_{init} + \dfrac{\rho_{init}u_{init}^2}{16}\left[\cos(2x)+\cos(2y)\right]\left[2+\cos(2z)\right], \end{cases} \tag{5.27}$$

where p_{init} is computed using the non-dimensional IG law as $1/(\gamma M_{init}^2)$, and ρ_{init} and u_{init} are set to unity. The initial temperature field is derived from the IG law using p and ρ. The

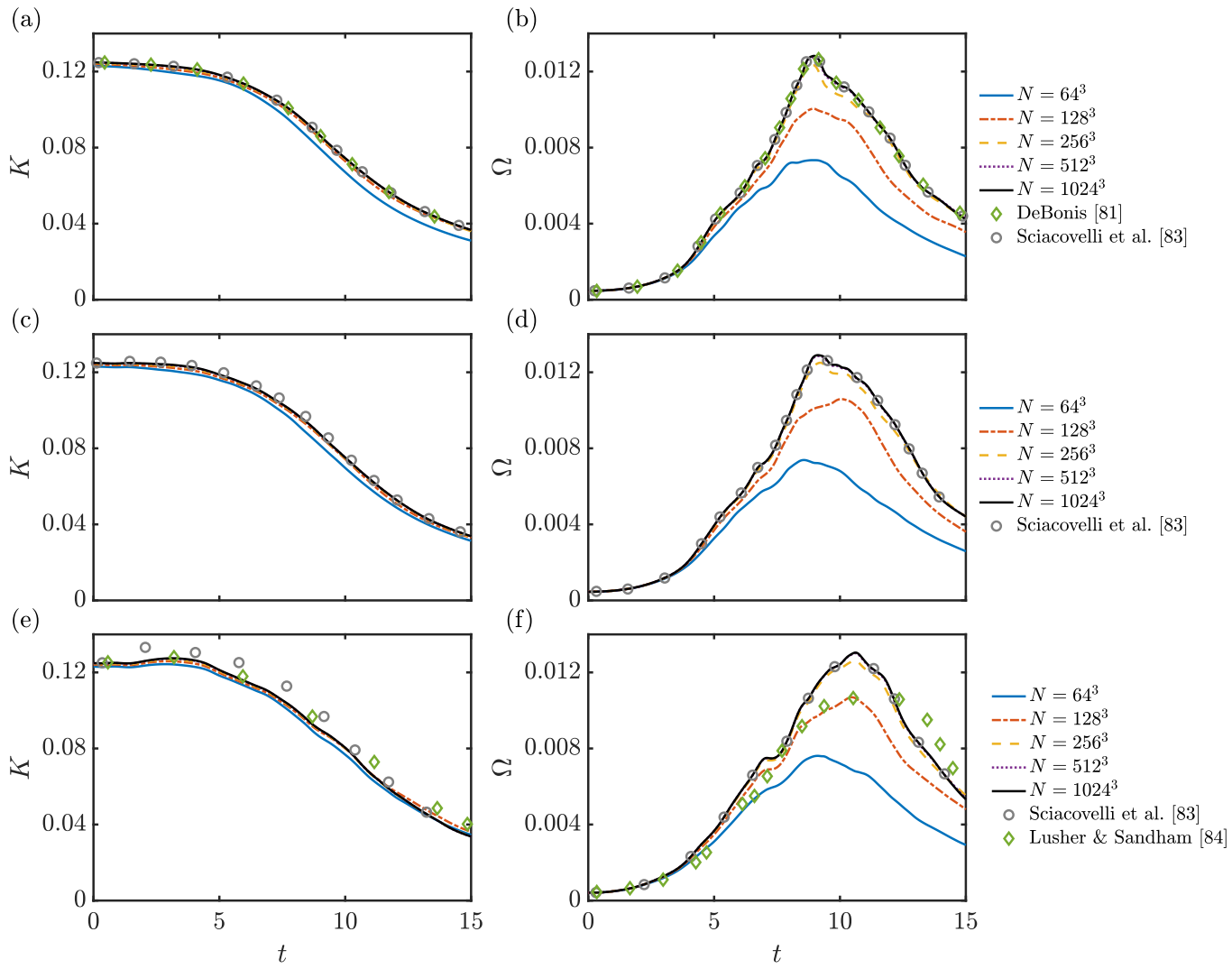

Figure 5.3: Influence of grid resolution on the Taylor–Green Vortex problem: (a,c,e) kinetic energy K and (b,d,f) enstrophy Ω as a function of dimensionless time t. The reference Mach numbers are as follows: (a,b) $M_{init} = 0.1$, (c,d) $M_{init} = 0.5$, and (e,f) $M_{init} = 1.0$. Grey circles represent the results from Sciacovelli *et al.* (2021). In (a,b), green diamonds correspond to the spectral results from DeBonis (2013), and in (e,f) to Lusher & Sandham (2021).

Reynolds number Re_L is set to 1600, and additional flow parameters are listed in Tab. 5.3. Simulations are conducted on grids ranging from 64^3 to 1024^3 grid points, with a constant CFL number of 0.5, up to a dimensionless time of $t = 15$. For validation purposes, the kinetic energy K and enstrophy Ω are calculated as

$$K = \frac{1}{\mathcal{V}} \int_{\mathcal{V}} \rho u_i u_i \, d\mathcal{V}, \quad \Omega = \frac{1}{Re} \int_{\mathcal{V}} \mu \omega_i \omega_i \, d\mathcal{V}, \quad i = 1, 2, 3 \tag{5.28a,b}$$

where $\omega_i = \epsilon_{ijk} \partial u_k / \partial x_j$ is the vorticity, and $\mathcal{V}$ is the computational domain.

Figure 5.3 shows K and Ω as a function of dimensionless time for three different Mach numbers. Results are compared with those from Sciacovelli *et al.* (2021) on a $N = 1024^3$ mesh for all Mach numbers, with the reference solution (spectral method) reported in DeBonis (2013) for $M_{init} = 0.1$, and with Lusher & Sandham (2021) on a $N = 512^3$ mesh for $M_{init} = 1.0$.

Note that for M_{init} = 1.0, the results shown in Figs. 5.3(e,f) are obtained exclusively using the KEEP scheme, as the KEEP-PEP scheme leads to numerical instability. In contrast, for all other subsonic cases, both the KEEP and KEEP-PEP schemes produce identical results.

First, for M_{init} = 0.1, the kinetic energy agrees very well with Sciacovelli *et al.* (2021) and DeBonis (2013), except on the coarsest grid of 64^3 mesh points. Enstrophy, however, exhibits a stronger dependency on the grid resolution, showing remarkable convergence to the literature for meshes of $N = 512^3$ points and larger. Second, at higher Mach numbers ($M_{init} >$ 0.5), the effect of increasing pressure work becomes evident at early stages. While kinetic energy shows a slight increase in Figs. 5.3(c,e) due to internal-energy conversion, the growth of enstrophy in Figs. 5.3(d,f) is slower compared to Fig. 5.3(b) at M_{init} = 0.1. For M_{init} = 1.0, the peak Mach number reaches up to 1.95, leading to the formation of shocklets and supersonic flow regions (not shown here). It is worth noting that the KEEP and KEEP-PEP schemes implemented in the CUBENS solver were designed for shock-free compressible flows. To robustly and accurately resolve discontinuities, shock-capturing methods employing shock sensors and localised artificial diffusivity would be necessary (Kuya *et al.* 2018). However, this approach would compromise energy and pressure-equilibrium conservation, necessitating a balance between shock-free and shock-capturing methods.

In this regard, for M_{init} = 1.0, the enstrophy computed by CUBENS matches well with Sciacovelli *et al.* (2021), who used a high-order upwind scheme with high-order artificial dissipation, while the kinetic energy computed by CUBENS aligns with Lusher & Sandham (2021), who applied a hybrid central non-oscillatory high-order scheme. However, discrepancies arise in the comparison of K against Sciacovelli *et al.* (2021) and Ω against Lusher & Sandham (2021), especially at later times when the latter appears to be more dissipative than CUBENS. The variations in the value of K may originate from the significant contribution of the pressure-work term in the kinetic-energy equation at higher Mach numbers. This non-conservative term, along with the pressure-dilatation term in the internal-energy equation, ensures consistency in the pressure-diffusion term of the total-energy equation, as outlined by Kuya *et al.* (2018). However, their discretisation in non-conservative form results in significantly reduced numerical robustness compared to the KEEP scheme employed in CUBENS (Kuya & Kawai 2021). Concerning the conservation of total entropy, inviscid TGV simulations from Kuya & Kawai (2021) at a lower reference Mach number of 0.4 show that this quantity is well preserved and the density fluctuations converge to constant values, regardless of the pressure-work contribution. Ultimately, achieving stable solutions requires a trade-off between enforcing primary and secondary conservation properties, depending on the flow regime and flow physics (Bernades *et al.* 2023).

5.5.2 Transitional boundary layer of an ideal gas

Here, CUBENS is tested for a 3-D flat-plate BL with the classical subharmonic H-type breakdown investigated by Sayadi *et al.* (2013). To provide a visual representation of the results obtained with CUBENS, the instantaneous flow structures are displayed using isocontours of the Q-criterion in Fig. 5.4.

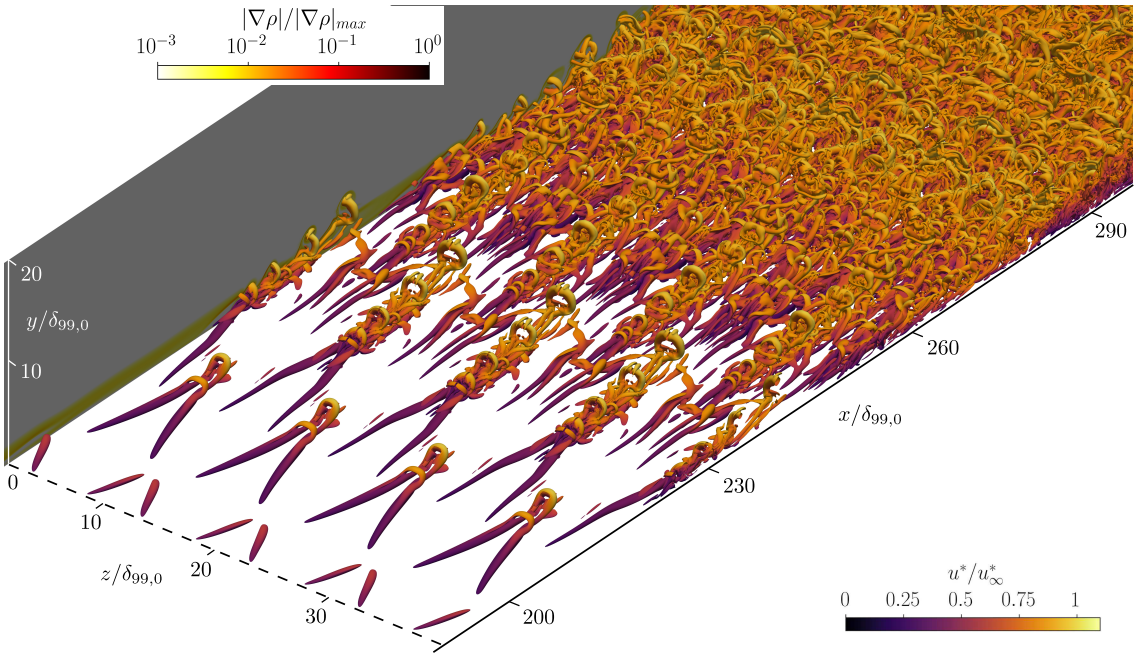

Figure 5.4: Flat-plate BL H-type breakdown with CUBENS. Visualisation of the instantaneous flow structures using isosurfaces of the Q-criterion ($Q = 0.015$), coloured by the streamwise velocity. The side plane is coloured by the normalised density gradient. Note that the domain is copied four times in the spanwise direction for better visualisation.

5

The dimensions of the computational domain are $0 \leq x/\delta_{99,0} \leq 515$ in the streamwise direction, $0 \leq y/\delta_{99,0} \leq 20$ in the wall-normal direction, and $0 \leq z/\delta_{99,0} \leq 9.63$ in the periodic spanwise direction. The inlet BL thickness $\delta_{99,0}$ is based on the inlet Reynolds number of $Re_0 = \sqrt{10^5}$. Non-reflecting BCs, along with numerical sponge zones, are applied at the inlet, top, and outflow boundaries, whereas the domain is periodic in the spanwise direction. At the wall, the no-slip and fully-reflective conditions are applied. In order to trigger transition, 'controlled' disturbances are introduced at the disturbance strip between $x_1/\delta_{99,0} = 41.8$ and $x_2/\delta_{99,0} = 51.8$. The wall-normal velocity distribution in Eq. (5.23) is selected. It induces a Tollmien–Schlichting (TS) wave ($A_{2\text{-D}} = 7.5 \times 10^{-3}$) at a reduced frequency of $F_{2\text{-D}} = F_0 = 124 \times 10^{-6}$, along with a pair of oblique waves ($A_{3\text{-D}} = 8.5 \times 10^{-5}$ with $\beta = \beta_0 = 0.65$) at half the frequency of the primary wave, i.e. $F_{3\text{-D}} = 62 \times 10^{-6}$. The computational domain is discretised with $N_x \times N_y \times N_z = 4000 \times 600 \times 150$ grid points. While an equidistant grid-point distribution is prescribed in the streamwise and spanwise directions, stretching in the wall-normal direction is applied using Eqs. (5.14a,b). The stretching factor σ is selected such that a Δy^+ (superscript $(\cdot)^+$ for wall units) of 0.59 in the first grid cell is obtained, normalised in wall units at $\max\{C_f\}$. For the other directions, the grid spacing in wall units is $\Delta x^+ = 10.0$ and $\Delta z^+ = 4.9$.

Once the DNS has reached a time-periodic solution, flow snapshots are extracted within two forcing periods and Fast-Fourier Transformed (FFT) in time and spanwise direction. Note that the spanwise FFT uses the FFTW package (Frigo & Johnson 2005), and it is fully MPI-parallelised in the CUBENS solver. The Fourier components are denoted with (h, k),

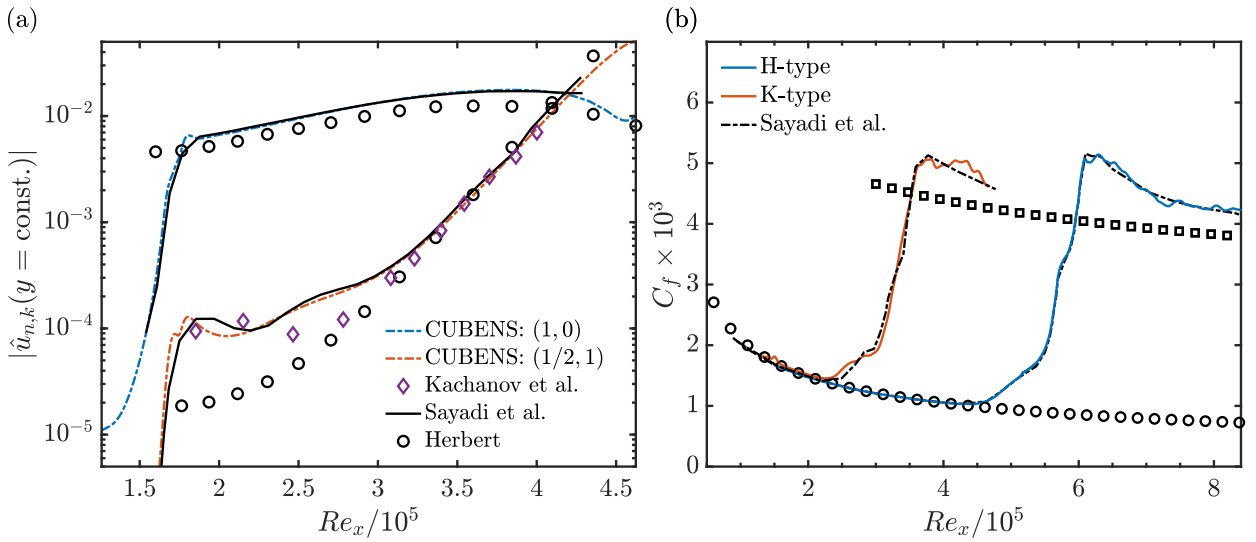

Figure 5.5: H-type breakdown with CUBENS. (a) downstream development of the streamwise disturbance amplitude at constant $y/\delta_{99,0} = 0.26$ (purple diamonds from Kachanov *et al.* (1977), black lines from Sayadi *et al.* (2013), black circles from Herbert (1988)); (b) time- and spanwise-averaged skin-friction coefficient (black dash-dotted line from Sayadi *et al.* (2013), black circles from the laminar self-similar solution, black squares from turbulent correlation of White (2006)). In (b), red line refers to the K-type breakdown of Sayadi *et al.* (2013) simulated in CUBENS.

where h indicates a wave with frequency $h \cdot F_0$ and k denotes the spanwise wavenumber $k \cdot \beta_0$. In Fig. 5.5(a), the spatial development of the FFT streamwise velocity disturbance $|\hat{u}|$ at constant $y/\delta_{99,0} = 0.26$ is displayed. Excellent agreement between the CUBENS simulation and Sayadi *et al.* (2013) is observed for both the primary and subharmonic growth at later stages. Only in the proximity of the disturbance strip, small quantitative differences are found for the oblique modes. This can be attributed to a slight variation in the receptivity mechanism at the disturbance strip caused by the different numerical scheme and setup. For the subharmonic disturbances, very good agreement is also achieved with the experiments of Kachanov *et al.* (1977). For $Re_x < 3 \times 10^5$, the values obtained from secondary-instability theory (see Herbert (1988)) diverge because the receptivity mechanism of the oblique waves is still active, and the primary-wave amplitude is not large enough to trigger the onset of secondary instability. For a more complete comparison of the H-type breakdown, the time- and spanwise-averaged distribution of the skin-friction coefficient is plotted over the Reynolds number Re_x in Fig. 5.5(b). We observe good agreement with the results of Sayadi *et al.* (2013), including for the K-type breakdown. While the transition location and the increase in C_f are very well matched, small misalignments are visible in the C_f-peak (overshoot). This could be due to a different time-averaging procedure. Note that transition to turbulence is an extremely nonlinear process and is very sensitive to the numerical setup.

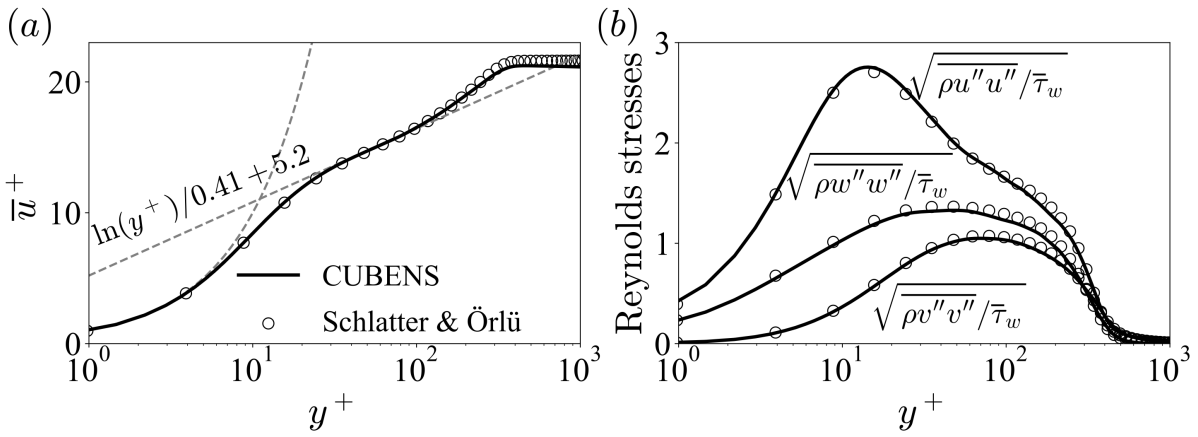

Figure 5.6: Validation of the incompressible turbulent BL simulations by Schlatter & Örlü (2010) (black circles) with CUBENS. Over the dimensionless wall-normal coordinate y^+, (a) mean streamwise velocity profile $\bar{u}^+$ and (b) the three components of the Reynolds normal stress.

5.5.3 Turbulent boundary layer of an ideal gas

To validate the recycling-rescaling method in Sec. 5.3.3, we compare the incompressible turbulent BL of Schlatter & Örlü (2010) at $M_\infty = 0.2$. The flow parameters are listed in Tab. 5.3. The inlet friction Reynolds number and momentum-thickness Reynolds number are $Re_{\tau,0} = 112.9$ and $Re_{\theta,0} = 234.0$, respectively. The grid spacings in wall units are $\Delta x^+ = \Delta z^+ = 4.4$ and $\Delta y^+ = 0.73$, which are comparable to those in (Schlatter & Örlü 2010). The computational domain dimensions are $L_x = 144.0\,\delta_{99,0}$, $L_y = 14.5\,\delta_{99,0}$, and $L_z = 7.0\,\delta_{99,0}$ in the streamwise, wall-normal, and spanwise directions, respectively. A sponge region of $14.5\,\delta_{99,0}$ is placed at the outlet. The recycling position is set to $x_{rcy} = 112.3\,\delta_{99,0}$. Note that $\delta_{99,0}$ is the mean turbulent BL thickness at the inlet.

Figure 5.6 illustrates the profiles of the time- and spanwise-averaged turbulent statistics obtained at $x = 123.9\,\delta_{99,0}$ over the dimensionless wall-normal coordinate $y^+ = y/\delta_v$, with $\delta_v = \overline{\nu}_w/u_\tau$ and $u_\tau = \sqrt{\overline{\tau}_w/\overline{\rho}_w}$. The CUBENS solver successfully replicates the mean streamwise velocity profile and Reynolds stresses in agreement with Schlatter & Örlü (2010).

It is worth mentioning that the current recycling-rescaling method fails when applied to a turbulent BL of a non-ideal compressible fluid with heat transfer. Employing the classical Van Driest's velocity transformation in Eqs. (5.17*a*,*b*) can lead to an inaccurate prediction of the velocity profile under strong property variations near the wall, and particularly when crossing the Widom line ('pseudo-boiling phenomenon'), as noted by Bai *et al.* (2022). A recent successful attempt to go beyond Van Driest's approach in non-ideal-fluid flows was proposed by Hasan *et al.* (2023) in channel flow at supercritical pressure. However, in transcritical (pseudo-boiling) BLs, large mean-density ratios and density fluctuations can induce a near-wall convective flux in the stress-balance equation, making the new scaling law transformation inaccurate. Overall, the generation of inflow turbulent profiles for strongly non-ideal flows remains an open research question.

5.5.4 Stably and unstably stratified boundary layer of an ideal gas

This section validates the wall-normal buoyancy force in the source term of Eq. (2.6) and in the BCs of Eq. (5.21). As a test case, we consider the controlled laminar-to-turbulent transition of a flat-plate BL with positive (unstably stratified) and negative (stably stratified) buoyancy force. As in Sec. 5.5.2, the H-type breakdown is selected.

To exclusively investigate the buoyancy effect on the transition to turbulence, we opt for the IG assumption. While the temperature at the wall is fixed, the sign of the gravitational acceleration g^* is modified to obtain a positive or negative Richardson number in Eqs. (2.8*a–d*). In this way, the buoyancy force is either directed against (unstable stratification, positive gravity) or aligned with the temperature gradient (stable stratification, negative gravity). The flow parameters are shown in Tab. 5.3, which also include a reference neutrally buoyant case, i.e. $Ri_{w,0} = 0$. Similar BCs to those in Sec. 5.5.2 are applied. The dimensions of the computational domain are $0 \leq x/\delta_{99,0} \leq 541$, $0 \leq y/\delta_{99,0} \leq 20$, and $0 \leq z/\delta_{99,0} \leq 9.63$. The disturbance strip, as described in Eq. (5.23), is located between $x_1/\delta_{99,0} = 21.4$ and $x_2/\delta_{99,0} = 31.4$. For this comparison, we choose the perturbation frequency and amplitude of the fundamental mode $(1, 0)$ to match the growth of the primary instability across all three cases. Note that before activating the disturbance strip, a converged laminar solution is obtained, as the BL departs from self-similarity when a buoyancy force is present. The computational domain is discretised with $N_x \times N_y \times N_z = 7420 \times 390 \times 150$ grid points, along with wall-normal stretching ($\Delta y^+ = 0.44$ at the wall). For the other directions, the grid spacing in wall units is $\Delta x^+ = \Delta z^+ = 4.9$.

In Fig. 5.7(a), the spatial development of the FFT streamwise velocity disturbance $|\hat{u}|$ at constant $y/\delta_{99,0} = 0.26$ is displayed. Note that, recalling Eqs. (2.8*a–d*), the unit Richardson number is proportional to the local Blasius length scale δ^*. This implies that when moving downstream, the Ri_{unit} increases according to

$$Ri_{unit} = Ri_{unit,0} \frac{Re}{Re_0}, \tag{5.29}$$

where $Ri_{unit,0}$ is the inlet Richardson number based on the BL thickness $\delta_{99,0}$. The same scaling applies to the wall Richardson number, defined as $Ri_w = Ri_{unit}(\rho_w - 1)$, where ρ_w is the density at the wall. Additionally, the growth rate according to the in-house LST solver is included to validate the linear growth of the fundamental mode. In all three scenarios, a good quantitative agreement between DNS and LST is observed for the primary growth. With regard to the subharmonic mode $(1/2, 1)$, the unstable stratification enhances the secondary instability, shifting the transition location farther upstream; see Fig. 5.8. Here, snapshots of the streamwise velocity inside the BL, i.e. xz-plane at a constant wall-normal height of $y/\delta_{99,0} = 0.4$, are presented. Staggered patterns of Λ-vortices, characteristic of the H-type transition, are visible. The transition location shifts considerably downstream as $Ri_w > 0$ (negative gravity).

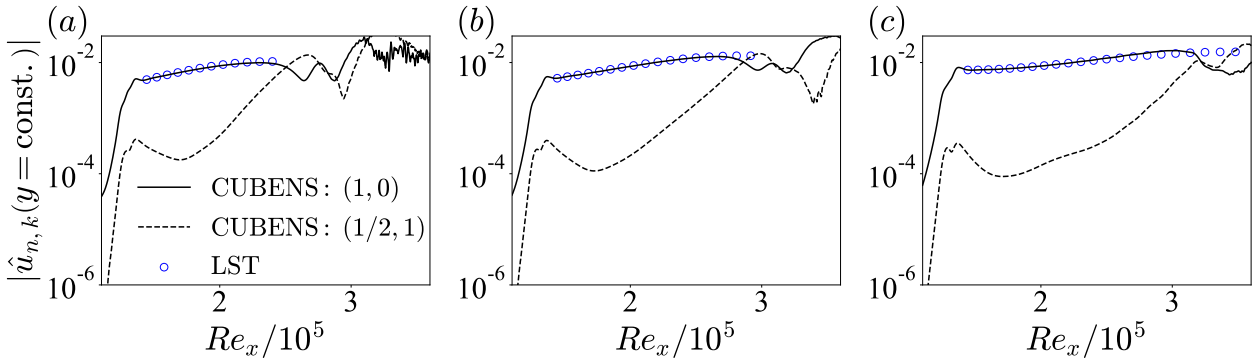

Figure 5.7: Downstream development of the $|u'|$-disturbance amplitude at constant $y/\delta_{99,0} = 0.26$ for modes (1,0) and (1/2,1) in (a) unstably-stratified ($Ri_{w,0} = -0.01$), (b) neutrally-buoyant ($Ri_{w,0} = 0$), and (c) stably-stratified ($Ri_{w,0} = 0.01$) BL. The wall Richardson number is defined as $Ri_w = Ri_{unit}(\rho_w - 1)$. The LST solution is represented by blue circles.

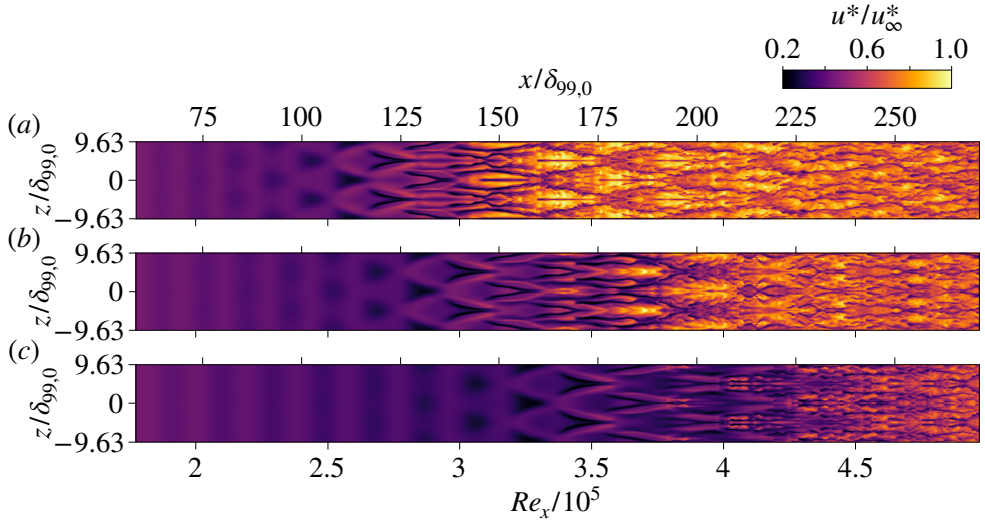

Figure 5.8: Contours of instantaneous streamwise velocity (xz-plane at $y/\delta_{99,0} = 0.4$) of (a) unstably-stratified ($Ri_{w,0} = -0.01$), (b) neutrally-buoyant ($Ri_{w,0} = 0$), and (c) stably-stratified ($Ri_{w,0} = 0.01$), BL. The wall Richardson number is defined as $Ri_w = Ri_{unit}(\rho_w - 1)$. Note that the results are copied once in the spanwise direction for better visualisation.

5.5.5 Boundary-layer instability of a fluid at supercritical pressure

The influence of strongly nonlinear thermodynamics on the stability of a 2-D zero pressure gradient flat-plate BL is investigated. To achieve the strongest departure from the IG behaviour, we consider an LMC fluid at supercritical pressure that is heated such that the BL crosses the Widom line (transcritical state). The Peng–Robinson (PR) EoS with Chung's model for the TPs is selected.

The flow parameters are reported in Tab. 5.4. This setup corresponds to supercritical CO_2 at $T^*_\infty = 280\,\text{K}$ (liquid-like free stream) and pressure $p^* = 80\,\text{bar}$, while the wall is heated

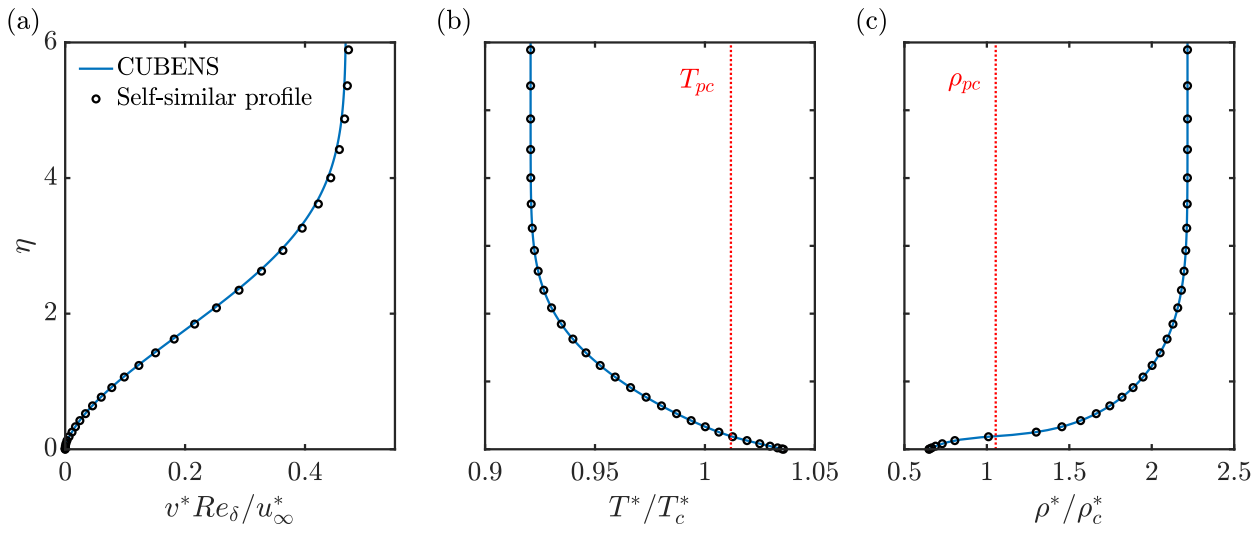

Figure 5.9: Laminar solution with CUBENS (blue lines) for (a) wall-normal velocity, (b) temperature, and (c) density profile. The self-similar solution is marked with black circles. In (b,c), the pseudo-critical temperature and density are indicated in red, respectively.

into the vapour-like state. The inflow Reynolds number is $Re_0 = 700$, with a streamwise domain extension of $x/\delta_{99,0} = 575$. Comparisons between the fully developed DNS solution and the self-similar solution of the compressible BL equations (see Ren *et al.* (2019); Boldini *et al.* (2024)) are provided in Fig. 5.9. Significant consistency with the self-similar profiles is observed, especially for the temperature, density, and streamwise velocity (not shown here). However, a minimal deviation of about 1% in the wall-normal velocity is noted, as the assumption of a perfectly constant pressure in the wall-normal direction is not valid in the supercritical fluid region near the critical point (not shown here). Therefore, we conclude that a minor non-zero wall-normal pressure gradient, which is neglected in the canonical self-similar approximation, remains in the numerical integration of the conservation equations, resulting in a minimal deviation in the wall-normal velocity profile.

In order to compare the linear disturbance evolution with the in-house linear-stability theory (LST) solver (see Ren *et al.* (2019); Boldini *et al.* (2024)), the 2-D disturbance strip in Eq. (5.23) is activated at $x_{mid}/\delta_{99,0} = 38$ with $\beta = 0$ and a small linear forcing amplitude of about $A_{2\text{-D}} = 10^{-5} M_\infty$. A non-dimensional frequency of $F = 80 \times 10^{-6}$ is selected according to the LST results. Once the simulation has reached a time-periodic solution, a similar procedure as in Sec. 5.5.2 is performed. The results are Fourier transformed in time with the fundamental frequency of $\Omega = \omega_{2\text{-D}}/2$, yielding complex Fourier coefficients $\hat{q}_j$ for a given harmonic j and flow variable q. For the sake of comparison with the LST reference solution, the normalised disturbance growth rate and phase speed of the first harmonic are calculated as

$$\alpha_i(x) = -\frac{Re}{Re_0}\frac{1}{\hat{q}_1^{max}}\frac{\partial \hat{q}_1^{max}}{\partial x}, \quad c_r(x) = \frac{\omega Re_0}{Re}\left(\frac{\partial \hat{\phi}_1}{\partial x}\right)^{-1}, \tag{5.30}$$

with $\hat{q}_1^{max}(x) = \max\{|\hat{q}_1(x = \text{const.}, y)|\}$ being the wall-normal maximum amplitude of the fundamental harmonic $\hat{q}_1$ and $\hat{\phi}_1 = \arg(\hat{q}_1)$ being the phase angle. Given the transcritical BL

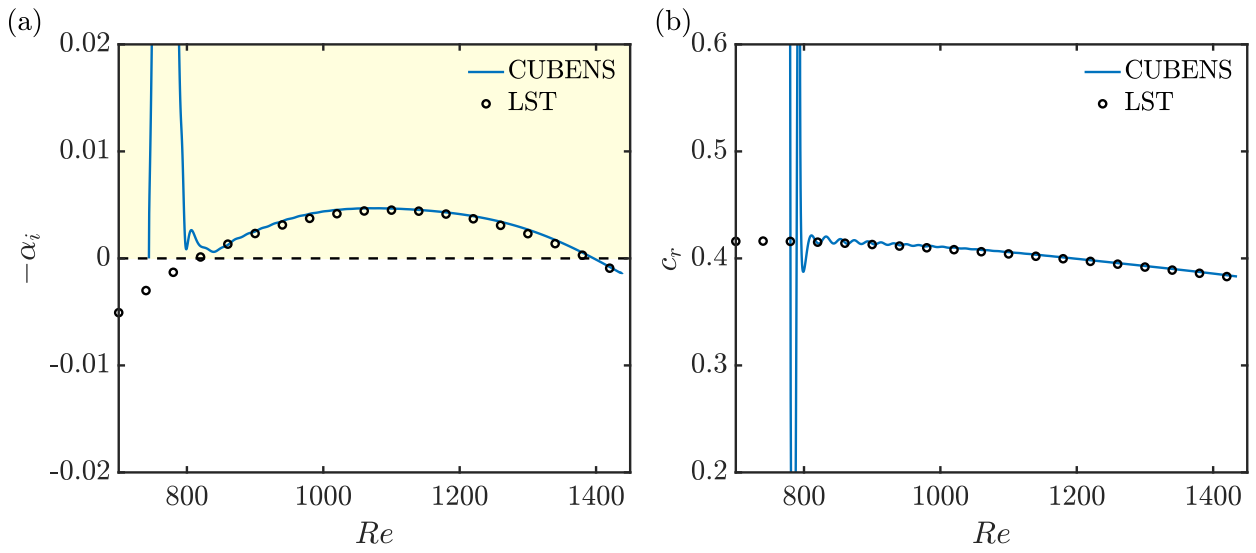

Figure 5.10: BL instability in the transcritical state with CUBENS (blue lines): (a) growth rate $-\alpha_i$, and (b) phase speed c_r as a function of the local Reynolds number Re. The LST solution is marked with black circles.

profiles in Fig. 5.9, the streamwise evolutions of the growth rate and phase speed are displayed in Fig. 5.10. In this case, Mode I, of TS-type, is the primary unstable mode. Conversely, if the wall temperature is further increased, as presented in Boldini *et al.* (2023), the only modal instability present in the BL is caused by the transcritical Mode II (see e.g. Ren *et al.* (2019) for more information on Mode II). Overall, good agreement with the reference results is observed for both considered quantities. The minimal deviations in the growth rate are attributed to non-parallel effects, which are not included in the LST framework.

5.6 Solver performance

In this section, the performance of the CUBENS solver is assessed by conducting strong and weak scaling tests for the Taylor–Green Vortex presented in Sec. 5.5.1. The tests are carried out on both Snellius and LUMI. On Snellius, a single CPU node is equipped with 128 AMD EPYC 7H12 CPUs, while a GPU node consists of 4 NVIDIA A100 GPUs paired with 72 Intel Xeon Platinum 8360Y 36C 2.4GHz processors. On LUMI, a single CPU node contains 128 AMD EPYC 7763 CPUs, while a GPU node consists of 4 AMD MI250X GPUs, each featuring two Graphics Compute Dies (GCDs), along with a 64-core AMD EPYC 7A53 CPU. All tests run a warm-up of 100 time steps on both computing units for each architecture, before calculating an average wall time per step (every 10 steps). Data input/output (I/O) to disk is discarded.

In the following, we analyse the performance of a single CPU and a GPU. This choice is motivated by: (a) the memory limits of the graphics cards employed in these supercomputing architectures, and (b) the need to understand the relationship between memory occupancy and performance speed-up for both partition units. These results serve as the baseline for

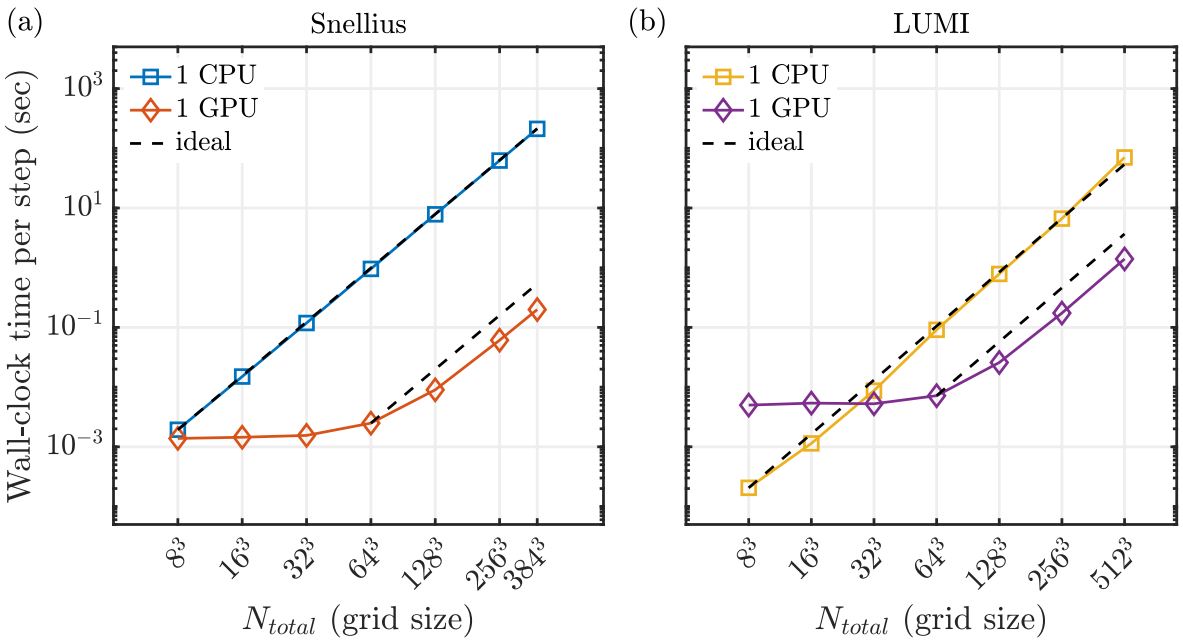

Figure 5.11: Performance of CUBENS on a single CPU and GPU. Wall-clock time per step in seconds over the grid size N_{total} for the TGV problem: (a) Snellius, (b) LUMI. The dashed black lines refer to the ideal solutions.

extending the computational approach to a multi-GPU setup.

5.6.1 Single CPU and single GPU performance

In this analysis, we examine the wall-clock time per step of a single CPU core (Snellius: 1 AMD EPYC 7H12, LUMI: 1 AMD EPYC 7763) and a single GPU (Snellius: 1 NVIDIA A100, LUMI: 1 AMD MI250X GPU), as the grid size increases by a factor of 8. The performance results in Fig. 5.11 are presented without intra- and inter-node communication, as MPI communication between multiple computing units and nodes could bias the results. On both systems, the increase in CPU wall-clock time is proportional to the increase in grid size, whereas, up to $N = 64^3$, the GPU remains underutilised, resulting in only a slight increase in execution time per time step. However, once the GPU is sufficiently utilised ($N > 64^3$), the wall-clock time increases proportionally to the eightfold increase in grid size. The calculations are constrained by the available memory, which is 40 GB for the NVIDIA A100 GPUs and 64 GB for AMD MI250X. Therefore, CUBENS can run on a single GPU up to a grid size of $N = 384^3$ on Snellius and up to $N = 512^3$ on LUMI. Notably, one LUMI CPU is approximately 10 times faster than one Snellius CPU (33.2M vs. 3.8M transistors). Simultaneously, we observe a performance drop for CUBENS on one AMD MI250X compared to one NVIDIA A100 GPU, with a slowdown factor of 2.9× for the benchmark simulation scenario with 50 million grid points presented in Sec. 5.5.1.

Given these results, it is crucial to understand which parts of the code consume the most time in order to optimise the multi-GPU implementation.

The workload distribution is shown in percentage for a single EPYC 7H12 CPU in

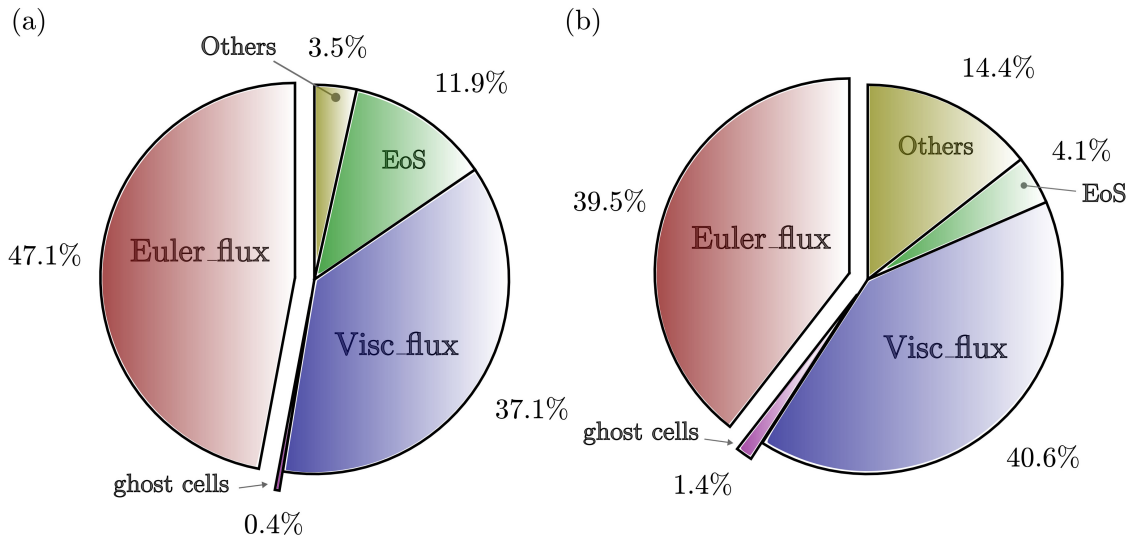

Figure 5.12: Code profiling on Snellius for (a) single CPU and (b) single GPU with $N = 256^3$ grid points. Workload distribution of: Euler fluxes (`Euler_flux`, Eqs. (2.3*a*–*c*)), viscous fluxes (`Visc_flux`, Eq. (2.4)), updating ghost cells (included in `MPI_comm` module), EoS and TP models (`EoS`), and other calculations (`Others`).

Fig. 5.12(a) and for a single A100 NVIDIA GPU in Fig. 5.12(b). Note that a similar code profiling result is observed for the corresponding partitions on the LUMI cluster. The case considered is the TGV problem at $M_{init} = 0.1$ with $N = 256^3$ grid points, and the main relevant sections inside the time loop are tracked using the `MPI_WTIME` function on the CPU and the `-D_USE_NVTX` flag on the GPU. Note that the wall-clock time per step for a single CPU is $t = 62.3\,\text{s}$, while for a single GPU it is $t = 0.06\,\text{s}$.

For both computing units, the calculation of the inviscid (Euler) fluxes (see Eqs. (2.3*a*–*c*)) and viscous fluxes (see Eqs. (2.4)) are the most time-consuming operations, accounting for over 70% of the total workload across the three Runge–Kutta substeps. Copying data into the ghost cells, which corresponds to exchanging data at the periodic BCs in the TGV problem, is negligible for a single partition, regardless of the hardware architecture (module `set_BC` in Algorithm 5.1 does not apply here).

The computational time required to calculate both caloric and thermal EoS, along with TPs, as shown in Fig. 5.12, is relatively small, accounting for approximately 12% of the total time on a single CPU. Notably, the impact of thermodynamics calculations on the total workload decreases when using a single GPU.

With respect to the GPU architecture used in Fig. 5.12(b), we further investigate the kernel-level performance of the two most computationally expensive kernels – Euler and viscous fluxes – through a roofline analysis (not shown here). This preliminary performance analysis revealed that both kernels are compute-bound, indicating high computational efficiency relative to data movement. Moreover, the Euler- and viscous-fluxes kernels achieve 62.5% and 64.7% of the GPU's FP64 FLOPS peak performance, respectively.

As the previous profiling was performed using the most computationally efficient IG EoS, i.e. power law, it is relevant to assess how a more complex thermodynamics affect the compu-

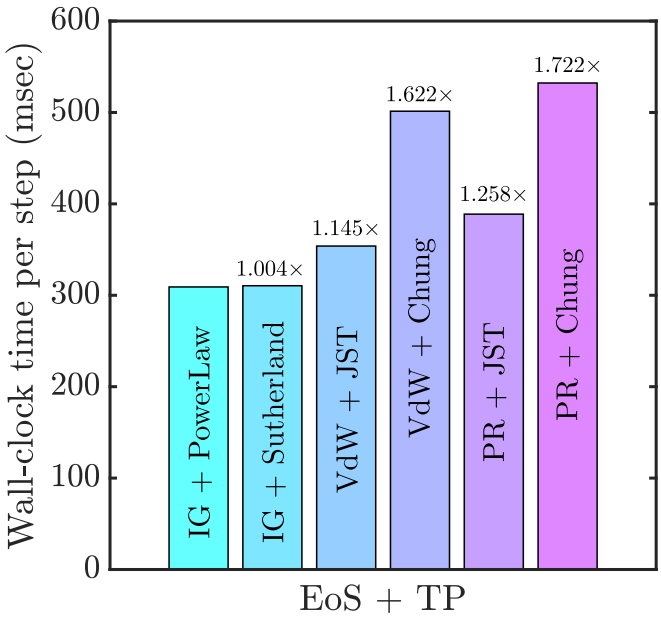

Figure 5.13: Impact of Equation of State (EoS) and Transport Property (TP) models on the wall-clock time per step for the TGV problem with $N = 256^3$ grid points. The different EoS and TP models are reported in Secs. 2.2 and 2.3.

tational time. Therefore, an investigation into the effect of different EoS and TP models on the wall-clock time per step is conducted using the Taylor–Green Vortex benchmark case as in Fig. 5.12, while varying the EoS and TP models and adjusting thermodynamic conditions accordingly (e.g. reduced temperature and pressure are $T_r = 1.50$ and $p_r = 1.50$, respectively, for non-ideal thermodynamic states). The total number of grid points is $N = 256^3$. The results are reported in Fig. 5.13, with the reference case being the IG EoS and a power law for viscosity. As expected, the largest slowdown of 1.72× is attributed to the most detailed combination of EoS and TP, i.e. the PR EoS with Chung's model. The latter is slower than the PR EoS with the JST model for TP by approximately 40%.

5.6.2 Multi-GPU performance on different GPU architectures

The parallel performance of CUBENS is assessed through strong- and weak-scaling tests. As the number of GPU partitions increases, the communication-to-computation ratio rises from 9% (4 GPUs) to 70% (16 GPUs). This ratio further increases to 79% when using the traditional Host-based MPI, due to greater latency and overhead with larger datasets. Thus, the use of GPU-aware MPI (see Sec. 5.4.3), combined with the asynchronous treatment of the Euler fluxes (see Sec. 5.4.2), is preferred for the strong- and weak-scaling analysis. Figure 5.14(a) reports the strong scaling of CUBENS. It is important to note that the GPU architecture available on the Snellius cluster limits usage to a maximum of 64 GPUs. While the number of GPUs is doubled in each step, two different grid sizes are selected for each supercomputing architecture. The first corresponds to the grid size required for full memory occupancy ($N = 384^3$ on Snellius and $N = 512^3$ on LUMI), and the second targets high-

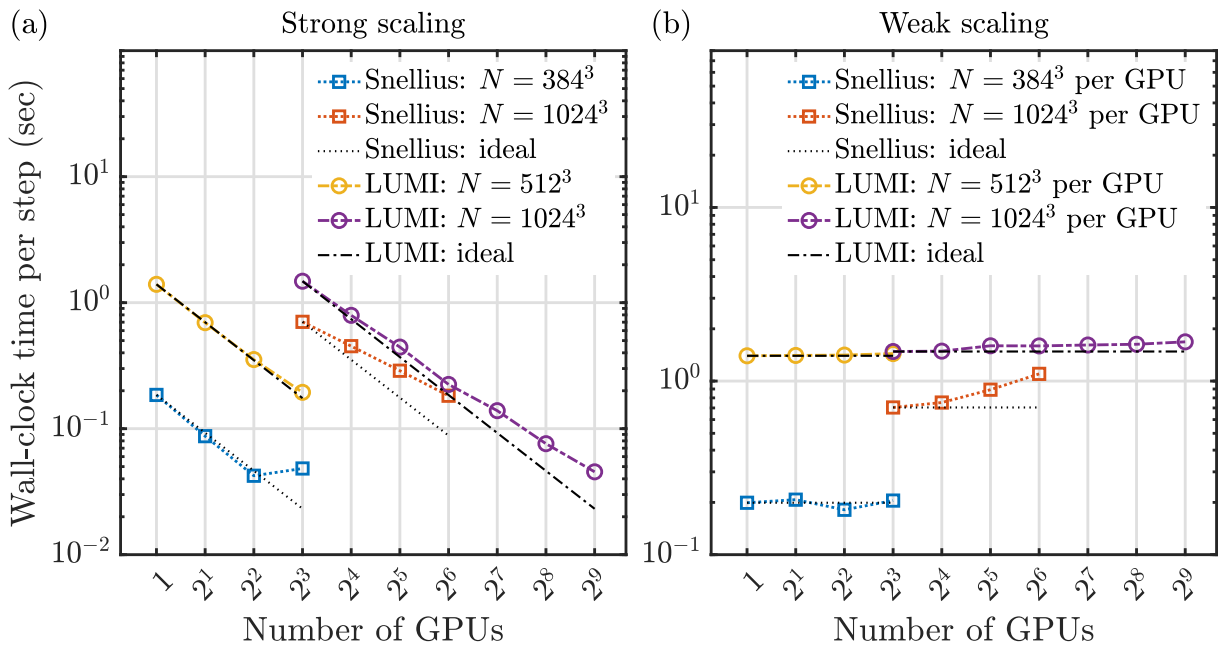

Figure 5.14: Wall-clock time per step in seconds for (a) strong scaling and (b) weak scaling using NVIDIA A100 GPUs on Snellius and AMD MI250X GPUs on LUMI. The dashed black line represents the ideal scaling. Note the different y-axis range between (a) and (b).

5

fidelity simulations that resolve both the Kolmogorov and Batchelor scales ($N = 1024^3$, or approximately 5 billion degrees of freedom).

For the Snellius cluster, excellent scaling is achieved with $N = 384^3$ points up to 4 GPUs. However, when 8 GPUs are used, a considerable performance slowdown occurs, resulting in approximately the same wall-clock time per step as with 4 GPUs. This slowdown corresponds to the transition from a single-node to a multi-node configuration. In the Snellius cluster's inter-node communication, the InfiniBand HDR100 bandwidth is limited by the Peripheral Component Interconnect Express (PCIe), with approximately 12.5 GB/s bandwidth per GPU. This inevitable performance drop is not unique to the current supercomputer architecture, but can be even more severe for algorithms with more complex (i.e. collective) communication patterns; see Romero *et al.* (2022). In contrast, no slowdown is observed on LUMI's GPU partitions, thanks to the high memory bandwidth of the Slingshot-11 network, providing 50 GB/s bidirectional bandwidth per GPU, along with double the intra-node communication (Infinity Fabric) compared to the Snellius cluster. As a result, a speed-up of 7.2× is achieved for $N = 512^3$ grid points, scaling from 1 to 8 LUMI GPUs.

With 8 GPUs (2 nodes) on Snellius and 16 GPUs (2 nodes) on LUMI, full memory occupancy per GPU is reached with a larger grid size of $N = 1024^3$. On Snellius, increasing the compute nodes eightfold, from 2 to 16, results in a strong-scaling speed-up of about 3.9. On LUMI, increasing the compute nodes by a factor 64, from 2 to 128, yields a strong-scaling speed-up of about 33. Similar strong-scaling efficiencies, around 50%, were also observed in other open-source DNS solvers for wall-bounded flows (Bernardini *et al.* 2023; Di Renzo 2022; De Vanna *et al.* 2023). Comparing Host-based MPI data transfer to GPU-aware MPI, the

latter reveals a speed-up on Snellius between 2× (2 GPUs with 384^3 grid points) and 2.5× (64 GPUs with 1024^3 grid points), respectively. On LUMI, the speed-up ranges from 1.1× (2 GPUs with 512^3 grid points) to 1.7× (64 GPUs with 1024^3 grid points). The asynchronous treatment of the inviscid fluxes becomes more advantageous as the number of nodes increases, e.g. a speed-up of 1.1× with 2 nodes compared to 1.3× with 16 nodes on both architectures.

If we only consider a CPU-based approach, we can compare the performance drop to the GPU-accelerated version of CUBENS, given the same computational cost in Standard Billing Units (SBUs). For example, on the Snellius cluster, with a total of 8192 CPUs (64 CPU nodes), the wall-clock time per step is $\Delta t = 24.18\,\mathrm{s}$ for $N = 1024^3$ grid points. Compared to the value of 0.183 s achieved with 16 GPU nodes, the computational speed-up of the GPU-accelerated system over the CPU-based system is approximately 130×.

Figure 5.14(b) shows the weak scaling wall-clock time per step, calculated by fixing the grid points per GPU to 384^3 and 1024^3 on Snellius, and to 512^3 and 1024^3 on LUMI. The number of GPU domains is progressively doubled in the respective grid direction, ensuring that the ratio between grid points in one direction and GPU partitions remains constant. A stable weak-scaling efficiency of around 1 is observed for the smaller number of grid points per GPU ($N = 384^3$ and $N = 512^3$), regardless of the computing architecture. However, for larger grid sizes ($N = 1024^3$), increasing inter-node communication significantly impacts weak scaling on the Snellius architecture, with the efficiency dropping to 0.64 from 8 to 64 GPUs. On LUMI, the weak-scaling analysis for $N = 1024^3$ grid points per GPU yields impressive results, achieving an efficiency of 0.88 from 8 to 512 GPUs. This result is comparable to the weak-scaling efficiencies reported in Bernardini *et al.* (2023); De Vanna *et al.* (2023), but with more than 30 times the number of grid points per GPU. Notably, with 2^3 GPUs, LUMI achieves the same performance for $N = 512^3$ and $N = 1024^3$ grid points, once again highlighting LUMI's superior memory capacity and bandwidth compared to the Snellius cluster.

5.6.3 Energy consumption of CUBENS

Finally, we relate the performance improvements of the GPU-accelerated version of CUBENS, discussed in Secs. 5.6.1 and 5.6.2, to the power consumption of the simulations. In fact, greater emphasis is needed on enhancing the energy efficiency of high-fidelity simulations to reduce their carbon footprint (Horwitz 2024). To investigate this, the TGV problem from Sec. 5.5.1 with $N = 256^3$ is simulated on the Snellius architecture using both CPUs and GPUs until $t = 15$. For a fair comparison, we consider the same computational price of 1 SBU, i.e. 128 CPUs vs. 1 GPU. Energy management and consumption are monitored by the Energy Aware Runtime (EAR) library. By enabling the flag `--ear=on`, power usage of the active computing cores is tracked throughout the runtime. The results are summarised in Tab. 5.5. The reported power output accounts for all power usage by the motherboard (computing unit, memory, network, etc.), but GPU cooling processes, which typically exceed those of CPUs, are not captured by the EAR library. Regarding energy usage, CUBENS consumed 1.51 kWh to advance the solution on 128 CPUs, compared to only 0.019 kWh on

CU	Number of cores	Snellius AWF	Wall-clock time per step	Power per core	Energy
CPU	128	1	0.71 s	4.46 W	5.43 MJ (1.51 kWh)
GPU	1	128	0.013 s	98.3 W	68 kJ (0.019 kWh)

Table 5.5: Energy consumption on Snellius for CPU-based and GPU-accelerated architectures with $N = 256^3$ grid points. The acronyms CU and AWF stand for computing unit and accounting weight factor, respectively.

a single GPU. In other words, the energy consumption on a single graphics processing unit is 80× more energy efficient than on traditional processors, for the same computational cost. Note that if I/O operations were active, the GPU energy consumption would likely be higher due to the continuous, time-consuming, D2H data transfer.

5.7 Conclusions

We have introduced the open-source DNS code, CUBic Equation of state Navier–Stokes (CUBENS). The solver is GPU-accelerated for pre-exascale supercomputing architectures, employs high-order central finite-difference schemes, ensures kinetic energy and entropy conservation, and accounts for the strongly nonlinear behaviour of thermodynamic and fluid properties. CUBENS is designed to address both fundamental research and industrial applications operating under non-ideal-gas conditions.

In addition to the canonical single-phase, non-reacting compressible Navier–Stokes equations, the solver incorporates a wall-normal buoyant force relevant in strongly stratified wall-bounded flows. Special attention is given to the implementation of non-ideal thermodynamic laws, including cubic equations of state and modified transport-property models. CUBENS utilises high-order explicit central finite-difference schemes for both convective and diffusive fluxes. In particular, its KEEP split convective form discretisation is non-dissipative, enhances numerical stability with minimised aliasing errors, and conserves kinetic energy and entropy. This approach enables stable direct numerical simulations of shock-free, high-Re flows with strong density variations. Additionally, the pressure-equilibrium-preserving (PEP) property is ensured under linear approximation for non-ideal fluids, providing further robustness under transcritical conditions.

CUBENS offers flexibility in simulating different canonical flow geometries, such as (a) transitional boundary layers with controlled disturbance excitation, (b) turbulent boundary layers using the recycling and rescaling method, and (c) channel flows. Non-reflecting inviscid boundary conditions with viscous numerical sponges are adapted for non-ideal flow conditions, also accounting for a wall-normal buoyant force. The solver has been successfully tested against various benchmark cases, including the compressible Taylor–Green Vortex, H-type transition to turbulence in a compressible boundary layer, IG turbulent boundary layer, stable and unstable stratified transitional boundary layer, and a laminar boundary layer with a non-ideal fluid at supercritical pressure and its linear instability.

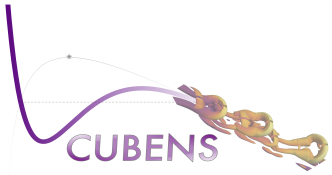

Figure 5.15: CUBENS logo

Considerable attention is dedicated to accelerating the solver for massively parallel simulations, targeting the next generation of Exascale supercomputers. CUBENS supports both NVIDIA and AMD GPU architectures, with the OpenACC directive-based method chosen for architecture interoperability and ease of code extension. Further speed-up is achieved when using multiple GPUs by (a) overlapping inviscid flux calculations at interior cells with MPI communication at boundary cells, and (b) employing GPU-aware MPI communication to avoid data transfer to the host CPU. For example, with 64 NVIDIA A100 GPUs compared to 8192 CPUs at the same computational price, a speed-up of approximately 130× is achieved. Notably, the strong and weak scaling performance has been outstanding, especially on AMD-based supercomputing architectures. For instance, in a multi-GPU-node configuration ranging from 8 to 512 GPUs, the strong scaling speed-up reaches a factor of 33, while a weak scaling efficiency of 0.88 is achieved for $N = 1024^3$ grid points per GPU.

The capability of CUBENS to simulate computationally expensive transitional and turbulent boundary layers in non-ideal-fluid flows under stratified conditions has been thoroughly investigated and successfully demonstrated in Sec. 5.5. This represents a significant advancement in understanding the impact of complex thermodynamic effects on the dynamics of wall-bounded flows.

Significant improvements and expansions of CUBENS are currently in progress. Key areas of development include: (a) addressing the supersonic and hypersonic flow regime with appropriate shock-capturing techniques, (b) implementing curvilinear coordinates to handle more realistic geometries found in turbomachinery, and (c) developing a new recycling and rescaling method for diabatic boundary layers with strongly non-ideal fluids. Additionally, achieving exact discrete conservation of the PEP property for arbitrary equations of state would allow for the extension of CUBENS to high-fidelity simulations at the critical point and within the two-phase region.

The open-source version of CUBENS (see Fig. 5.15) is available at the following link: `https://github.com/pcboldini/CUBENS`.

Bibliography

Aiello, A., De Michele, C. & Coppola, G. 2025 Entropy conservative discretization of compressible Euler equations with an arbitrary equation of state. *J. Comput. Phys.* **528**, 113836.

Alowayyed, S., Groen, D., Coveney, P. V. & Hoekstra, A. G. 2017 Multiscale computing in the Exascale era. *J. Comput. Sci.* **22**, 15–25.

AMD 2024 *ROCm™ Software 6.1.2.*.

Bai, T., Griffin, K. P. & Fu, L. 2022 Compressible velocity transformations for various noncanonical wall-bounded turbulent flows. *AIAA J.* **60**, 4325.

Bernades, M., Jofre, L. & Capuano, F. 2023 Kinetic-energy- and pressure-equilibrium-preserving schemes for real-gas turbulence in the transcritical regime. *J. Comput. Phys.* **493**, 112477.

Bernardini, M., Modesti, D., Salvadore, F. & Pirozzoli, S. 2023 STREAmS 2.0: supersonic turbulent accelerated Navier-Stokes solver version 2.0. *Comput. Phys. Commun.* **285**, 108644.

Boldini, P. C., Bugeat, B., Peeters, J. W. R., Kloker, M. & Pecnik, R. 2024 Transient growth in diabatic boundary layers with fluids at supercritical pressure. *Phys. Rev. Fluids* **9**, 083901.

Boldini, P. C., Gaspar, R., Bugeat, B., Costa, P., Peeters, J. W. R. & Pecnik, R. 2023 Direct numerical simulation of H-type transition in a flat-plate boundary layer with supercritical fluids. *14th International ERCOFTAC Symposium on Engineering Turbulence Modelling and Measurements (ETMM14), Barcelona, Spain, September 6-8* .

Cao, L. Y., Xu, R. N., Yan, J. J., He, S. & Jiang, X. P. 2021 Direct numerical simulation of convective heat transfer of supercritical pressure CO2 in a vertical tube with buoyancy and thermal acceleration effect. *J. Fluid Mech.* **927**, A29.

Cinnella, P. & Gloerfelt, X. 2023 Insights into the turbulent flow of dense gases through high-fidelity simulations. *Comput. Fluids* **267**, 106067.

Coleman, G. N. & Sandberg, R. D. 2010 A primer on direct numerical simulation of turbulence – methods, procedures and guidelines. *Tech. Rep.*. University of Southampton.

Coppola, G., Capuano, F., Pirozzoli, S. & De Luca, L. 2019 Numerically stable formulations of convective terms for turbulent compressible flows. *J. Comput. Phys.* **382**, 86–104.

Costa, P., Phillips, E., Brandt, L. & Fatica, M. 2021 GPU acceleration of CaNS for massively-parallel direct numerical simulations of canonical fluid flows. *Comput. Math. Appl.* **81**, 502–511.

De Michele, C. & Coppola, G. 2024 Novel pressure-equilibrium and kinetic-energy preserving fluxes for compressible flows based on the harmonic mean. *J. Comput. Phys.* **518**, 113338.

De Vanna, F., Avanzi, F., Cogo, M., Sandrin, S., Bettencourt, M., Picano, F. & Benini, E. 2023 URANOS: a GPU accelerated Navier-Stokes solver for compressible wall-bounded flows. *Comput. Phys. Commun.* **287**, 108717.

De Vanna, F. & Baldan, G. 2024 URANOS-2.0: improved performance, enhanced portability, and model extension towards exascale computing of high-speed engineering flows. *Comput. Phys. Commun.* **303**, 109285.

DeBonis, J. R. 2013 Solutions of the Taylor-Green vortex problem using high-resolution explicit finite difference methods. *in 51st AIAA Aerospace Sciences Meeting: The New Horizons Forum and Aerospace Exposition (AIAA, 2013)* pp. 2013–0382.

Di Renzo, M. 2022 HTR-1.3 solver: Predicting electrified combustion using the hypersonic task-based research solver. *Comput. Phys. Commun.* **272**, 108247.

van Driest, E. R. 1951 Turbulent boundary layer in compressible fluids. *J. Aeronaut. Sci.* **18**, 145–160.

Fasel, H. F., Rist, U. & Konzelmann, U. 1990 Numerical investigation of the three-dimensional development in boundary-layer transition. *AIAA J.* **28**, 29–37.

Franko, K. J. & Lele, S. K. 2013 Breakdown mechanisms and heat transfer overshoot in hypersonic zero pressure gradient boundary layers. *J. Fluid Mech.* **730**, 491–532.

Frigo, M. & Johnson, S. G. 2005 The design and implementation of FFTW3. *Proc. IEEE* **93**, 216–231.

Gloerfelt, X., Bienner, A. & Cinnella, P. 2023 High-subsonic boundary-layer flows of an organic vapour. *J. Fluid Mech.* **971**, A8.

Gottlieb, S. & Shu, C. W. 1998 Total variation diminishing Runge–Kutta schemes. *Math. Comput.* **67**, 73–85.

Guardone, A., Colonna, P., Pini, M. & Spinelli, A. 2024 Nonideal compressible fluid dynamics of dense vapors and supercritical fluids. *Annu. Rev. Fluid Mech.* **56** (1), 241–269.

Guo, J., Yang, X. I. A. & Ihme, M. 2022 Structure of the thermal boundary layer in turbulent channel flows at transcritical conditions. *J. Fluid Mech.* **934**, A45.

Hasan, A. M., Larsson, J., Pirozzoli, S. & Pecnik, R. 2023 Incorporating intrinsic compressibility effects in velocity transformations for wall-bounded turbulent flows. *Phys. Rev. Fluids* **8**, L112601.

Hasan, A. M., Larsson, J., Pirozzoli, S. & Pecnik, R. 2024 Estimating mean profiles and fluxes in high-speed turbulent boundary layers using inner/outer-layer scalings. *AIAA J.* **62** (2), 848–853.

He, J., Tian, R., Jiang, P. X. & He, S. 2021 Turbulence in a heated pipe at supercritical pressure. *J. Fluid Mech.* **920**, A45.

Herbert, T. 1988 Secondary instability of boundary layers. *Annu. Rev. Fluid Mech.* **20**, 487–526.

Hickey, J.-P., Ma, P. C., Ihme, M. & Thakur, S. 2013 Large eddy simulation of shear coaxial rocket injector: real fluid effects. In *49th AIAA/ASME/SAE/ASEE Joint Propulsion Conference*. AIAA Paper 2013-4071.

Horwitz, J. A. K. 2024 Estimating the carbon footprint of computational fluid dynamics. *Phys. Fluids* **36**, 045109.

Huai, X., Joslin, R. D. & Piomelli, U. 1997 Large-eddy simulation of transition to turbulence in boundary layers. *Theor. Comput. Fluid Dyn.* **9**, 149–163.

Jofre, L., Abdellatif, A. & Oyarzun, G. 2023 RHEA: an open-source reproducible hybrid-architecture flow solver engineered for academia. *J. Open Source Softw.* **8**, 4637.

Kachanov, Y. S., Kozlov, V. V. & Levchenko, V. Y. 1977 Nonlinear development of a wave in a boundary layer. *Fluid Dyn.* **12**, 383–390.

Kawai, S. 2019 Heated transcritical and unheated non-transcritical turbulent boundary layers at supercritical pressures. *J. Fluid Mech.* **865**, 563–601.

Kawai, S., Terashima, H. & Negishi, H. 2015 A robust and accurate numerical method for transcritical turbulent flows at supercritical pressure with an arbitrary equation of state. *J. Comput. Phys.* **300**, 116–135.

Kennedy, C. A. & Gruber, A. 2008 Reduced aliasing formulations of the convective terms within the Navier–Stokes equations for a compressible fluid. *J. Comput. Phys.* **227**, 1676–1700.

Kim, K., Hickey, J.-P. & Scalo, C. 2019 Pseudophase change effects in turbulent channel flow under transcritical temperature conditions. *J. Fluid Mech.* **871**, 52–91.

Kim, Y., Ghosh, D., Constantinescu, E. M. & Balakrishnan, R. 2023 GPU-accelerated DNS of compressible turbulent flows. *Comput. Fluids* **251**, 105744.

Kok, C. 2009 A high-order low-dispersion symmetry-preserving finite-volume method for compressible flow on curvilinear grids. *J. Comput. Phys.* **228**, 6811–6832.

Kuya, Y. & Kawai, S. 2021 High-order accurate kinetic-energy and entropy preserving (KEEP) schemes on curvilinear grids. *J. Comput. Phys.* **442**, 110482.

Kuya, Y., Totani, K. & Kawai, S. 2018 Kinetic energy and entropy preserving schemes for compressible flows by split convective forms. *J. Comput. Phys.* **375**, 823–853.

Li, N. & Laizet, S. 2010 2DECOMP&FFT – a highly scalable 2D decomposition library and FFT interface. *Cray User Group 2010 Conference* pp. 1–13.

Lund, T. S., Wu, X. & Squires, K. D. 1998 Generation of turbulent inflow data for spatially-developing boundary layer simulations. *J. Comput. Phys.* **140**, 233–258.

Lusher, D. J. & Sandham, N. D. 2021 Assessment of low-dissipative shock-capturing schemes for the compressible Taylor–Green vortex. *AIAA J.* **59**, 533–545.

Ma, P. C., Yang, X. I. A. & Ihme, M. 2018 Structure of wall-bounded flows at transcritical conditions. *Phys. Rev. Fluids* **3**, 034609.

Mani, A. 2012 Analysis and optimization of numerical sponge layers as a nonreflective boundary treatment. *J. Comput. Phys.* **231**, 704–716.

Marxen, O., Iaccarino, G. & Magin, T. E. 2014 Direct numerical simulations of hypersonic boundary-layer transition with finite-rate chemistry. *J. Fluid Mech.* **755**, 35–49.

Marxen, O., Magin, T. E., Shaqfeh, E. S. G. & Iaccarino, G. 2013 A method for the direct numerical simulation of hypersonic boundary-layer instability with finite-rate chemistry. *J. Comput. Phys.* **255**, 572–589.

Nemati, H., Patel, A., Boersma, B. J. & Pecnik, R. 2016 The effect of thermal boundary conditions on forced convection heat transfer to fluids at supercritical pressure. *J. Fluid Mech.* **800**, 531–556.

NVIDIA 2023 *NVIDIA HPC SDK Version 23.1 Documentation*.

Okong'o, N. & Bellan, J. 2002 Consistent boundary conditions for multicomponent real gas mixtures based on characteristic waves. *J. Comput. Phys.* **176**, 330–344.

OpenACC Architecture Review Board 2021 *OpenACC application program interface version 3.2*.

Patel, A., Boersma, B. J. & Pecnik, R. 2016 The influence of near-wall density and viscosity gradients on turbulence in channel flows. *J. Fluid Mech.* **809**, 793–820.

Patel, A., Peeters, J. W. R., Boersma, B. J. & Pecnik, R. 2015 Semi-local scaling and turbulence modulation in variable property turbulent channel flows. *Phys. Fluids* **27**, 095101.

Pecnik, R. & Patel, A. 2017 Scaling and modelling of turbulence in variable property channel flows. *J. Fluid Mech.* **823**, R1.

Peeters, J. W. R., Pecnik, R., Rohde, M., van der Hagen, T. H. J. J. & Boersma, B. J. 2016 Turbulence attenuation in simultaneously heated and cooled annular flows at supercritical pressure. *J. Fluid Mech.* **799**, 505–540.

Peng, N. & Yang, Y. 2018 Effects of the Mach number on the evolution of vortex-surface fields in compressible Taylor-Green flows. *Phys. Rev. Fluids* **3**, 013401.

Pirozzoli, S. 2010 Generalized conservative approximations of split convective derivative operators. *J. Comput. Phys.* **229**, 7180–7190.

Pirozzoli, S. 2011 Stabilized non-dissipative approximations of Euler equations in generalized curvilinear coordinates. *J. Comput. Phys.* **230**, 2997–3014.

Poinsot, T. J. & Lele, S. K. 1992 Time dependent boundary conditions for hyperbolic systems. *J. Comput. Phys.* **101**, 104–129.

Ren, J., Marxen, O. & Pecnik, R. 2019 Boundary-layer stability of supercritical fluids in the vicinity of the Widom line. *J. Fluid Mech.* **871**, 831–864.

Rist, U. & Fasel, H. 1995 Direct numerical simulation of controlled transition in a flat-plate boundary layer. *J. Fluid Mech.* **298**, 211–248.

Romero, J., Costa, P. & Fatica, M. 2022 Distributed-memory simulations of turbulent flows on modern GPU systems using an adaptive pencil decomposition library. *in Proceedings of the Platform for Advanced Scientific Computing Conference, ACM, June 2022* .

Rudy, D. H. & Strikwerda, J. C. 1980 A nonreflecting outflow boundary condition for subsonic Navier-Stokes calculations. *J. Comput. Phys.* **36**, 55–70.

Salvadore, F., Rossi, G., Sathyanarayana, S. & Bernardini, M. 2024 OpenMP offload toward the exascale using Intel® GPU Max 1550: evaluation of STREAmS compressible solver. *J. Supercomput.* **80**, 21094–21127.

Sayadi, T., Hamman, C. W. & Moin, P. 2013 Direct numerical simulation of complete H-type and K-type transitions with implications for the dynamics of turbulent boundary layers. *J. Fluid Mech.* **724**, 480–509.

Schlatter, P. & Örlü, R. 2010 Assessment of direct numerical simulation data of turbulent boundary layers. *J. Fluid Mech.* **659**, 116–126.

Sciacovelli, L., Cinnella, P. & Gloerfelt, X. 2017a Direct numerical simulations of supersonic turbulent channel flows of dense gases. *J. Fluid Mech.* **821**, 153–199.

Sciacovelli, L., Gloerfelt, X., Passiatore, D., Cinnella, P. & Grasso, F. 2020 Numerical investigation of high-speed turbulent boundary layers of dense gases. *Flow Turbul. Combust.* **105**, 555–579.

Sciacovelli, L., Passiatore, D., Cinnella, P. & Pascazio, G. 2021 Assessment of a high-order shock-capturing central-difference scheme for hypersonic turbulent flow simulations. *Comput. Fluids* **230**, 105134.

Shima, N., Kuya, Y., Tamaki, Y. & Kawai, S. 2021 Preventing spurious pressure oscillations in split convective form discretization for compressible flows. *J. Comput. Phys.* **427**, 110060.

Song, H., Ghate, A. S., Dai, S., Chandra, A. & Lele, S. K. 2023 Conservative and robust compact finite difference approach for simulations of dense gas flows. *AIAA AVIATION 2023 Forum* .

Tamaki, Y., Kuya, Y. & Kawai, S. 2022 Comprehensive analysis of entropy conservation property of non-dissipative schemes for compressible flows: KEEP scheme redefined. *J. Comput. Phys.* **468**, 111494.

Thompson, K. W. 1987 Time dependent boundary conditions for hyperbolic systems. *J. Comput. Phys.* **68**, 1–24.

TOP500.org 2024*a* GREEN500 the list. `https://top500.org/lists/green500/2024/06/`, accessed: 2024-10-18.

TOP500.org 2024*b* TOP500 the list. `https://top500.org/lists/top500/list/2024/06/`, accessed: 2024-10-18.

Urbin, G. & Knight, D. 2001 Large-eddy simulation of a supersonic boundary layer using an unstructured grid. *AIAA J.* **39**, 1288–1295.

Wheeler, A. P. S. 2024 High fidelity simulation of dense vapours with thermodynamic consistent modelling. *Comput. Fluids* **268**, 106088.

White, F. M. 2006 *Viscous Fluid Flow, 3rd Edition*. Boston: McGraw-Hill.

White, T. M., Bianchi, G., Chai, L., Tassou, S. A. & Sayma, A. I. 2021 Review of supercritical CO2 technologies and systems for power generation. *Appl. Therm. Eng.* **185**, 116447.

aus der Wiesche, S. 2023 Experimental investigation techniques for non-ideal compressible fluid dynamics. *Int. J. Turbomach. Propuls. Power* **8**.

Yoo, J. Y. 2013 The turbulent flows of supercritical fluids with heat transfer. *Annu. Rev. Fluid Mech.* **45**, 495–525.

Zhao, A., Pecnik, R. & Peeters, J. W. R. 2024 Thermodynamic analysis and heat exchanger calculations of transcritical high-temperature heat pumps. *Energy Convers. Manag.* **303**, 118172.

Zhu, X., Phillips, E., Spandan, V., Donners, J., Ruetsch, G., Romero, J., Ostilla-Mónico, R., Yang, Y., Lohse, D., Verzicco, R., Fatica, M. & Stevens, R. 2018 AFiD-GPU: a versatile Navier–Stokes solver for wall-bounded turbulent flows on GPU clusters. *Comput. Phys. Commun.* **229**, 199–210.

6

COMPLETE TRANSITION

The content of this chapter has been published under the title:

P. C. Boldini, B. Bugeat, J. W. R. Peeters, M. Kloker, and R. Pecnik,
Direct numerical simulation of complete transition to turbulence with a fluid at supercritical pressure.
Journal of Fluid Mechanics, Volume 1025, A59, 2025.

The objective of this chapter is to investigate the unexplored laminar-to-turbulent transition of a heated flat-plate boundary layer with a fluid at supercritical pressure. Two temperature ranges are considered: a subcritical case, where the fluid remains entirely in the liquid-like state, and a transcritical case, where the pseudo-critical (Widom) line is crossed and pseudo-boiling occurs. Fully compressible direct numerical simulations are used to study (i) the linear and nonlinear instabilities, (ii) the breakdown to turbulence, and (iii) the fully developed turbulent boundary layer. In the transcritical state, two-dimensional forcing generates not only a train of billow-like structures around the Widom line, resembling Kelvin–Helmholtz instability, but also near-wall travelling regions of flow reversal. These spanwise-oriented billows dominate the early nonlinear stage. When high-amplitude subharmonic three-dimensional forcing is applied, staggered Λ-vortices emerge more abruptly than in the subcritical case. However, unlike the classic H-type breakdown under zero pressure gradient observed in ideal-gas and subcritical states, the H-type breakdown is triggered by strong shear layers caused by flow reversals – similar to that observed in adverse-pressure-gradient boundary layers. Without oblique-wave forcing, transition is only slightly delayed and follows a naturally selected fundamental breakdown (K-type) scenario. Hence, in the transcritical state, it is possible to trigger nonlinearities and achieve transition to turbulence relatively early using only a single two-dimensional wave that strongly amplifies background noise. In the fully turbulent region, we demonstrate that variable-property scaling accurately predicts turbulent skin-friction and heat-transfer coefficients.

6.1 Introduction

Fluids at supercritical pressure have enabled the development of more efficient, compact industrial processes and continue to offer promising opportunities for future energy-conversion technologies (Guardone *et al.* 2024). Among different fluids, carbon dioxide (CO_2) has emerged as a promising working medium for power cycles in geothermal and concentrated solar energy systems, as well as for heat pumps in industrial heating applications. In the aerospace sector, supercritical fuel injection improves mixing and combustion efficiency in both air-breathing and liquid rocket engines (Wang & Yang 2017). Supercritical fluids also occur in nature, e.g. the CO_2/N_2 mixture in the lower atmosphere of Venus (Morellina *et al.* 2020).

At supercritical conditions, i.e. above the thermodynamic critical point, the liquid–vapour boundary vanishes and strong variations in thermophysical properties occur within a narrow temperature range around the pseudo-critical temperature T_{pc}, also referred to as pseudo-boiling (Banuti 2015), at which the isobaric heat capacity reaches its maximum. In this non-ideal, single-phase thermodynamic region, the ideal-gas assumption fails.

Supercritical fluids have been extensively investigated in fully developed turbulent flows. Yoo (2013) highlighted the complexity of supercritical heat-transfer measurements, in which thermophysical property variations may either enhance or deteriorate heat transfer. Early computational studies on turbulent flows at supercritical pressure mainly focused on open flow configurations, such as shear layers Okong'o & Bellan (2002), mixing layers (Okong'o & Bellan 2010), and jets (Sharan & Bellan 2021), as well as on closed flow configurations such as pipes (Bae *et al.* 2005; Nemati *et al.* 2016; He *et al.* 2021; Cao *et al.* 2021), channels (Patel *et al.* 2016; Ma *et al.* 2018; Kim *et al.* 2019; Guo *et al.* 2022; Li *et al.* 2023 2024), and annular flows (Peeters *et al.* 2016). These studies underlined the significant impact of local property variations on large-scale structures, and the presence of relaminarisation mechanisms. Semi-local scaling has been demonstrated to best characterise turbulence in variable-property flows, assuming weak density and viscosity fluctuations. However, in turbulent boundary layers with parahydrogen at supercritical pressure and transcritical temperature conditions, large density fluctuations of order $\sqrt{\overline{\rho'\rho'}}/\overline{\rho} \approx 0.4-1.0$ significantly alter near-wall turbulence and its statistics (Kawai 2019). As a result, semi-local scaling was found not to collapse the velocity transformation.

Conversely, many industrial applications operating at supercritical conditions frequently involve flows that have not yet reached a fully turbulent state. Even under the ideal-gas assumption, transition to turbulence remains of fundamental importance across subsonic, supersonic, and high-Mach-number flows (Saric *et al.* 2002; Fedorov 2011). In high-speed flows, real-gas effects have been studied extensively (Candler 2019), yet they are often erroneously linked to non-ideal-gas effects (Guardone *et al.* 2024). Unlike real-gas effects, non-ideal-gas effects near the thermodynamic critical point are characterised by strong stratification (Govindarajan & Sahu 2014) and abrupt variations in thermophysical properties.

Transition to turbulence can follow different routes depending on the type of flow dis-

turbances present in the flow (Morkovin 1969). In this work, we focus on the transitional sequence typically observed under low levels of free-stream turbulence: (i) receptivity to external disturbances, (ii) primary modal or non-modal disturbance growth, (iii) secondary instability and nonlinear interactions, and (iv) eventual breakdown to turbulence. Only recently, Linear Stability Theory (LST) of boundary layers with fluids at supercritical pressure has been investigated (Robinet & Gloerfelt 2019). The first such analysis by Ren *et al.* (2019) for an adiabatic Zero-Pressure-Gradient (ZPG) flat-plate boundary layer with supercritical CO_2 revealed strong sensitivity to the temperature profile relative to the pseudo-critical temperature. As the flow crosses the pseudo-critical (Widom) line, i.e. under transcritical temperature conditions, a new inviscid mode (Mode II) emerges, exhibiting growth rates an order of magnitude greater than those of Mode I, which corresponds to the Tollmien–Schlichting (TS) instability. It is worth noting that this dual-mode instability occurs only when heating from a liquid-like free stream. Unlike Mack's second mode in hypersonics, Mode II is not of acoustic nature. Moreover, the Mode-II instability is largest for Two-Dimensional (2-D) perturbations, as also confirmed for low-Mach, diabatic boundary layers by Boldini *et al.* (2024). Bugeat *et al.* (2022) further showed that Mode II is associated with a minimum of kinematic viscosity at the Widom line – a feature common to all non-polar supercritical fluids at transcritical temperature conditions. Thus, according to the Generalised-Inflection-Point (GIP) criterion, such boundary layers are inviscidly unstable. In plane Couette flow, Bugeat *et al.* (2024) demonstrated that this inviscid instability arises from a localised maximum of density-weighted vorticity and consists of two phase-locked-vorticity waves induced by shear and baroclinic effects around the kinematic-viscosity minimum.

Alongside previous modal stability analyses, Boldini *et al.* (2024) investigated transient growth with fluids at supercritical pressure. When heating beyond the Widom line, where Mode II is unstable, optimal energy growth arises from an interplay between lift-up and Orr mechanisms. Conversely, wall cooling was found to resemble the effect of an Adverse Pressure Gradient (APG) under the ideal-gas assumption. A similar trend appeared in Cross-Flow (CF) dominated Three-Dimensional (3-D) boundary layers (Ren & Kloker 2022), where the inviscid TS mode can be amplified far more than classical CF modes, effectively suppressing them, akin to imposing strong deceleration under the ideal-gas assumption.

In controlled transition, a linearly amplified 2-D wave grows to finite amplitude, triggering secondary instabilities and nonlinear interactions that lead to the growth of 3-D waves with subsequent breakdown. These mechanisms remain unexplored for supercritical fluids, despite their importance for accurate transition prediction. Under the ideal-gas assumption, two canonical breakdown paths, K-type and H-type, have been studied extensively via experiments (Klebanoff *et al.* 1962; Kachanov & Levchenko 1984) and Direct Numerical Simulations (DNS) (Fasel *et al.* 1990; Rist & Fasel 1995; Bake *et al.* 2002; Sayadi *et al.* 2013) in incompressible boundary layers. These scenarios depend on the choice of initial disturbance wavelengths and spanwise wavenumbers. In K-type fundamental resonance, a primary 2-D TS wave and a steady longitudinal vortex mode, often forced, as in Klebanoff's experiment, nonlinearly generate a symmetric pair of oblique modes at the same TS frequency. Alter-

natively, these oblique modes can be introduced directly, inducing the steady vortex mode. Their 3-D development leads to aligned Λ-shaped vortices, each consisting of two elongated legs of streamwise vorticity and a tip of spanwise vorticity. In contrast, H-type subharmonic resonance, following Craik's model (Craik 1971), involves forcing oblique modes at half the TS frequency, forming staggered Λ-vortices without a steady vortex mode. In both scenarios, Λ-vortices develop into hairpin structures with a localised high-shear layer atop their heads, eventually evolving into Ω- or ring-like vortices that mark the onset of turbulence. The DNS studies of K- and H-type breakdown have since been extended to APG flows (Kloker 1993; Kloker & Fasel 1995) and to supersonic and hypersonic regimes in various geometries (Fezer & Kloker 1999; Franko & Lele 2013; Sivasubramanian & Fasel 2015; Hader & Fasel 2019; Unnikrishnan & Gaitonde 2020).

The DNS remains the most effective tool for isolating specific perturbation waves and their effects on the transition routes (Zhong 1998). In the context of non-ideal-fluid flows, high-order DNS have recently been employed to study the O-type breakdown in boundary layers with dense vapours, such as PP11-vapour at $M_\infty = 2.25$ and 6 (Sciacovelli *et al.* 2020), and Novec649-vapour at $M_\infty = 0.9$ (Gloerfelt *et al.* 2023), which exhibit negligible dissipation and heat conduction. In these studies, density fluctuations remain small relative to the mean value. In contrast, under supercritical conditions near the Widom line, the abrupt variation of thermodynamic properties induces large density fluctuations and poses major numerical challenges for accurate and robust DNS analysis (Kawai 2019).

The main objective of this work is to investigate the nonlinear interactions and transition to turbulence in a boundary layer with a supercritical fluid, aiming to improve transition prediction under non-ideal-gas conditions. Specifically, we focus on elucidating the role of Mode-II instability in the nonlinear regime, examining the subsequent stages beyond the linear stability analysis of Ren *et al.* (2019). The strongly nonlinear thermodynamics and abrupt fluid-property variations are accounted for by combining (i) the Van der Waals (VdW) cubic Equation of State (EoS) in reduced form, based on the principle of corresponding states to retain generality, and (ii) non-ideal transport-property models for a generic supercritical fluid. To numerically investigate supercritical fluids and tackle the related computational challenges, we employ the open-source solver CUBic Equation of state Navier–Stokes (CUBENS) (Boldini *et al.* 2025). We perform DNS with controlled transition scenarios using harmonic disturbance forcing to isolate the most critical nonlinear mechanisms and limit modal interactions. To study the nonlinear regime, only a single fundamental 2-D wave is excited in a 2-D DNS set-up, as Mode-II instability is most unstable for 2-D perturbations. For the breakdown to turbulence, 3-D DNS are performed with 3-D forcing, in line with the aforementioned ideal-gas transitional boundary layer simulations. Building upon the 2-D nonlinear analysis, a pair of subharmonic oblique waves is introduced alongside the large amplitude 2-D wave. The amplitude of the oblique waves is set to either finitely large or infinitesimally small. Finally, the fully turbulent regime is analysed to evaluate the accuracy of mean velocity and enthalpy scaling laws. A predictive tool for the turbulent skin friction and heat transfer in non-ideal fluids is developed.

The work is organised as follows. Section 6.2 outlines the governing equations, with a focus on non-ideal thermodynamic models and numerical methods. Sec. 6.3 presents two flow cases at supercritical pressure (reduced pressure of 1.10) and describes their respective DNS set-ups. Two temperature profiles for a slightly heated wall are considered, one below and one crossing the pseudo-critical temperature T_{pc}. Sec. 6.4 examines the 2-D linear and nonlinear evolution of Mode-II instability. Selected 3-D transitional cases are then presented and analysed in Sec. 6.5, followed by an assessment of the resulting turbulent boundary layers in Sec. 6.6. Finally, the study is concluded in Sec. 6.7.

6.2 Methodology

We consider single-phase, non-reacting flows of supercritical fluids, governed by the fully compressible Navier–Stokes (NS) equations, expressed in both differential and dimensionless form as in Eq. (2.1). For its non-dimensionalisation and reference quantities based on free-stream conditions, we refer to Sec. 5.11. In the present study, the VdW cubic EoS (see Sec. 2.2.2) in reduced form is chosen to balance accuracy and computational efficiency (Boldini *et al.* 2025). This choice is motivated by the principle of corresponding states (Van der Waals 1873), which renders the reduced formulation independent of the specific fluid. Notably, Bugeat *et al.* (2022) found that the modal behaviour with the VdW EoS qualitatively resembles that obtained using the NIST REFPROP library (Lemmon *et al.* 2013). The analytical expressions of Jossi *et al.* (1962) and Stiel & Thodos (1964), denoted as JST hereafter, for the dynamic viscosity and thermal conductivity of non-polar supercritical fluids, respectively, are employed for the transport-property models (see Sec. 2.3.2). These correlations, which depend on reduced quantities, are applicable to non-polar fluids at supercritical conditions and provide a general representation of thermodynamics near the critical point. They are detailed in Boldini *et al.* (2025).

The linear stability analysis is performed within the framework of LST for non-ideal fluids (Ren *et al.* 2019; Boldini *et al.* 2024) (see Chapter 3).

The DNS are performed using the CUBENS solver (see Chapter 5). The time step Δt is defined based on the frequency of the primary-wave disturbance, $\omega_{2\text{-D}}$, as $\Delta t = 2\pi/(\omega_{2\text{-D}} LP)$, where LP is a multiple of the number of samples saved per forcing period (Ren *et al.* 2019). The parameter LP is chosen such that the maximum Courant–Friedrichs–Lewy number remains below 0.8 in all directions. Non-reflecting boundary conditions for single-phase, non-ideal fluid flows (Okong'o & Bellan 2002), along with numerical sponge zones (Mani 2012), are applied at the domain boundaries. At the isothermal or adiabatic wall, no-slip and no-penetration conditions are imposed, while periodic boundary conditions are applied in the spanwise (z) direction. For post-processing, spectral analysis is performed in time and in the z-direction (for 3-D simulations), with Fourier components denoted as $(\omega/\omega_{2\text{-D}}, \beta/\beta_0)$, where $\omega_{2\text{-D}}$ and β_0 are the fundamental frequency and spanwise wavenumber of the disturbance strip, respectively. In the streamwise direction, the wall-normal maximum amplitudes of the mass-flux perturbation $(\rho u)' = \bar{\rho}u' + \bar{u}\rho' + \rho' u'$, with $\bar{\rho}$ and $\bar{u}$ from the steady base-flow solu-

tion in Sec. 6.3.1, are used for quantification. For a quantitative analysis of the transitional (Sec. 6.5.3) and turbulent (Sec. 6.6) boundary layers, time- and spanwise-averaged quantities are sampled every 50 time steps over approximately ten periods of the primary 2-D wave.

6.3 Flow cases and computational set-up

The flow and computational parameters for the ZPG transitional boundary-layer flows in this study are presented below. A Mach number of 0.2, following Sayadi *et al.* (2013), and a free-stream reduced pressure of $p_{r,\infty} = 1.10$ for the cases at supercritical pressure are selected. To illustrate the considered thermodynamic states, Fig. 6.1 shows the reduced temperature–pressure (T_r–p_r) diagram with selected isolines of reduced density $\rho_r = \rho^*/\rho_c^*$. Two thermodynamic states at supercritical pressure are considered, relative to the reduced pseudo-critical temperature of $T_{r,pc} = 1.024$, both with a free-stream reduced temperature of $T_{r,\infty} = 0.90$ and a weakly heated isothermal wall (subscript $(\cdot)_w$). In the subcritical (liquid-like) temperature case (denoted hereafter as Tw095), the wall temperature is $T_{r,w} = 0.95$, such that the boundary-layer temperature remains below $T_{r,pc}$. It is important to note that the term 'subcritical' here refers solely to the thermodynamic state and should not be confused with subcritical growth below the critical Reynolds number in hydrodynamic stability theory (Schmid & Henningson 2001). In the transcritical temperature case (denoted hereafter as Tw110), i.e. under pseudo-boiling conditions (Banuti 2015), the wall temperature reaches $T_{r,w} = 1.10$, causing the boundary-layer temperature to cross the Widom line near the wall, which in turn triggers Mode-II instability. Note that, while the Widom line is formally defined in the temperature–pressure phase diagram (as shown in Fig. 6.1), it is used hereafter as a convenient reference in spatial coordinates, where it corresponds to the local pseudo-critical point at a given supercritical pressure. In both cases, the free-stream compressibility factor $Z_\infty = Z_c p_{r,\infty}/(\rho_{r,\infty} T_{r,\infty})$ is equal to 0.254. For the ideal-gas reference case of Sayadi *et al.* (2013) (hereafter denoted as TadIG), a free-stream temperature of $T_\infty^* = 300\,\mathrm{K}$ with $Z_\infty = 1.0$ (ideal-gas assumption) and an adiabatic wall are considered. All relevant flow parameters are listed in Tab. 6.1. For cases Tw095 and Tw110, the free-stream parameters are set as follows: Eckert number $Ec_\infty = 0.0159$, Prandtl number $Pr_\infty = 1.0$, reduced speed of sound $a_{r,\infty} = \sqrt{a_\infty^{*2}/(p_c^* v_c^*)} = 2.766$ ($v^* = 1/\rho^*$, specific volume), reduced specific heat at constant pressure $c_{p,r,\infty} = 8.024$, and reduced specific heat at constant volume $c_{v,r,\infty} = 9/2$. In contrast, for case TadIG, the free-stream Eckert number, Prandtl number, and heat capacity ratio are $Ec_\infty = 0.016$, $Pr_\infty = 0.75$, and $c_p^*/c_v^* = 1.4$, respectively.

The computational domain is a rectangular box on top of the flat plate. The inlet boundary-layer thickness $\delta_{99,0}$ is used as the reference length scale and is set to unity at the inlet location, $x_0 = x_0^*/\delta_{99,0}^*$. The inlet Reynolds number is defined based on the distance from the leading edge, $Re_{x,0}$. The domain extends to x_e and is initialised with the self-similar boundary-layer laminar solution described in Sec. 6.3.1. The spanwise domain size corresponds to the disturbance spanwise wavelength λ_z, with $0 < z/\delta_{99,0} < \lambda_z$. Further details on the DNS set-up, including a sensitivity analysis of the grid resolution, are provided in

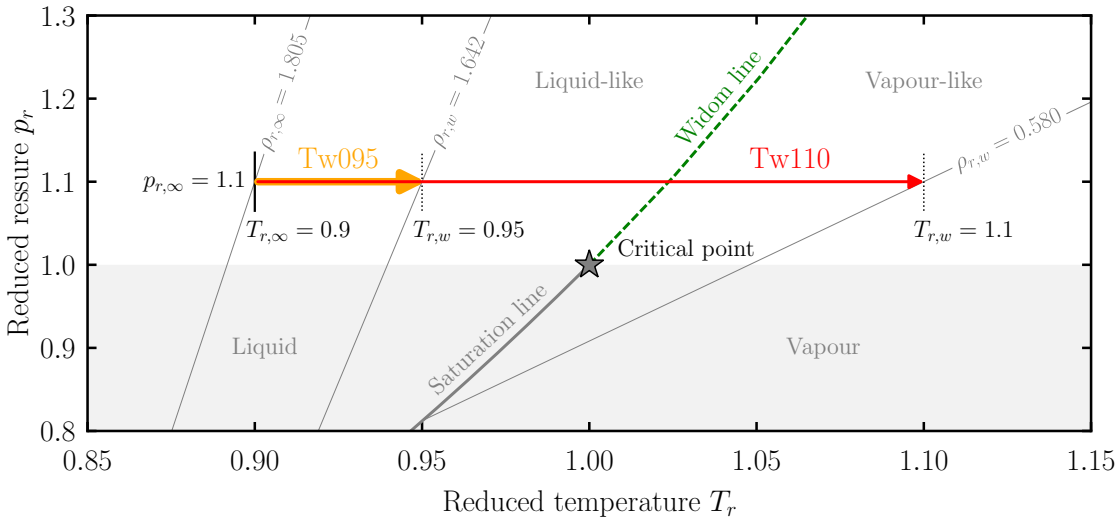

Figure 6.1: Reduced temperature–pressure (T_r–p_r) diagram with isolines of reduced density ρ_r: isobar at $p_{r,\infty} = 1.10$ with cases at supercritical pressure of Tab. 6.1, i.e. Tw095 (→) and Tw110 (→). The saturation line and pseudo-critical (Widom) line, i.e. locus of the maxima of the isobaric specific heat capacity, follow the approximate generalised equation $p_r = \exp\{(T_r - 1)A_{VdW}/\min(T_r, 1)\}$, with $A_{VdW} = 4$ (Banuti 2015).

	Non-ideal fluid at supercritical pressure		Ideal gas
Case	Tw095	Tw110	TadIG
State	subcrit. temp.	transcrit. temp.	-
Wall	isotherm	isotherm	adiabatic
T_w^*/T_c^*	0.95	1.10	-
T_w^*/T_∞^*	1.056	1.222	1.007
Line style			

Table 6.1: Thermodynamic conditions for the three flow cases. For the supercritical pressure cases, the common flow parameters are the free-stream reduced pressure $p_\infty^*/p_c^* = 1.10$ and reduced temperature $T_\infty^*/T_c^* = 0.90$. For all cases, the Mach number is $M_\infty = 0.2$. The wall temperature is denoted by T_w^*. The non-ideal fluid flow cases at supercritical pressure are represented in the reduced temperature-pressure (T_r–p_r) diagram in Fig. 6.1.

Appendix C.1.

6.3.1 Initial conditions

The computational domain is initialised using the self-similar boundary-layer profiles based on Lees–Dorodnitsyn variables (Ren *et al.* 2019; Boldini *et al.* 2024). The initial flow profiles for all cases listed in Tab. 6.1 are plotted over the wall-normal coordinate $\partial\eta = (\rho^* u_\infty^*/\sqrt{2\xi})\,\partial y^*$

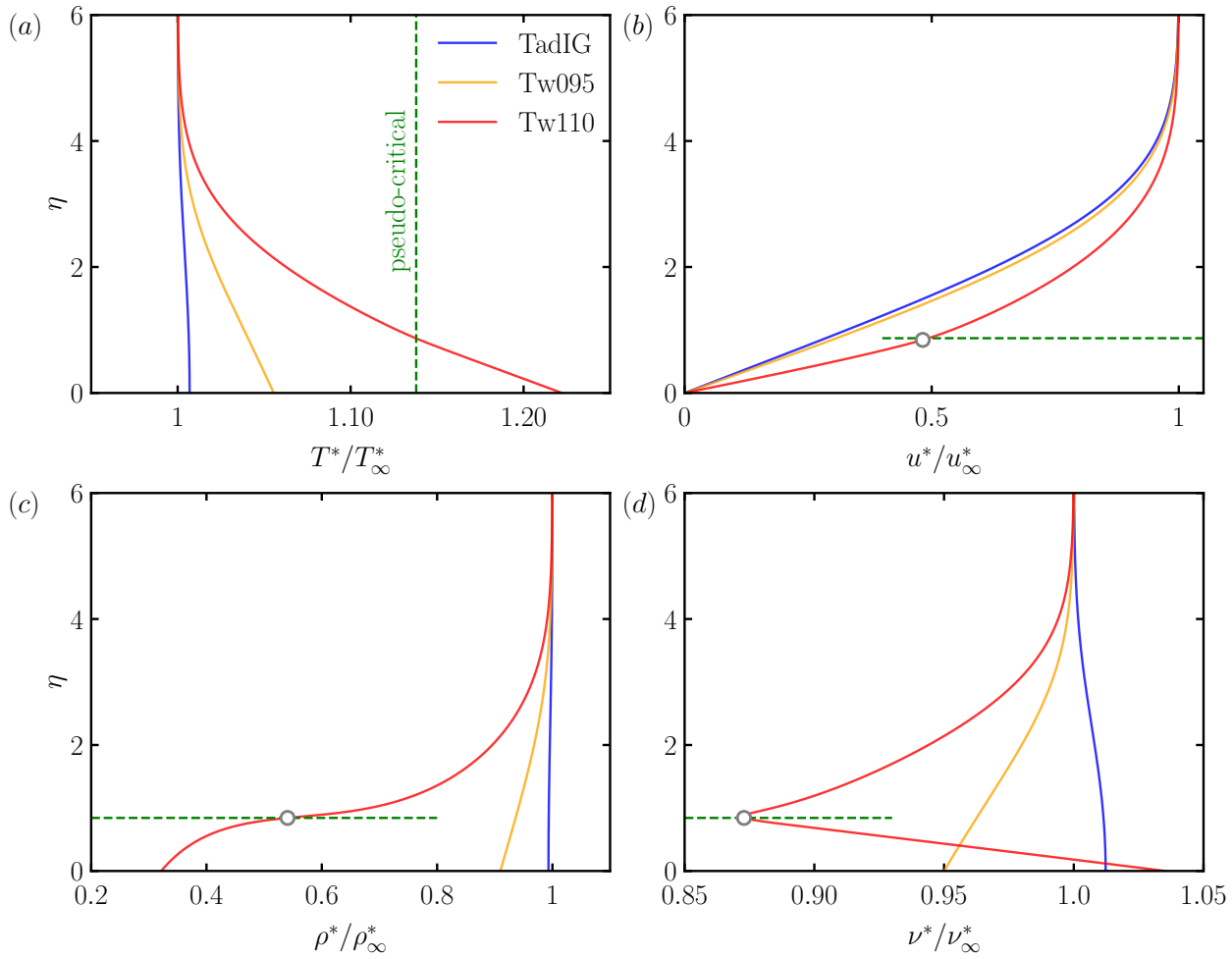

Figure 6.2: Laminar profiles for the considered cases: (a) temperature T^*/T^*_∞, (b) streamwise velocity u^*/u^*_∞, (c) density ρ^*/ρ^*_∞, and (d) kinematic viscosity ν^*/ν^*_∞ as a function of the self-similar wall-normal coordinate η. The line legend is in agreement with Tab. 6.1 for cases TadIG, Tw095, and Tw110. The dashed green line (– –) indicates the pseudo-critical point, i.e. at the pseudo-critical temperature $T^* = T^*_{pc}$. The location of the GIP for the transcritical case Tw110 is marked by the circle (○) symbol in (b–d).

in Fig. 6.2. As temperature increases from liquid-like to vapour-like conditions (Fig. 6.2a), the largest gradients in thermodynamic and transport properties, particularly in density (Fig. 6.2c), occur at the pseudo-critical point (green dashed line). This gives rise to an inflectional base-flow profile in case Tw110, as defined by the GIP criterion, i.e. $\mathrm{d}(\bar{\rho}\,\mathrm{d}\bar{u}/\mathrm{d}y)/\mathrm{d}y = 0$. As shown in Fig. 6.2(d), the GIP coincides with the minimum of kinematic viscosity near the pseudo-critical point, and occurs for non-polar fluids at supercritical pressure and transcritical temperature (Bugeat *et al.* 2022 2024). The streamwise velocity (Fig. 6.2b) highlights the more pronounced profile of case Tw110, which resembles that of a transitional boundary-layer profile. Appendix C.2 presents a comparison between the unperturbed 2-D DNS solutions, which have reached a steady-state solution, and the initial self-similar solutions for both cases Tw095 and Tw110.

Parameter	TadIG	Tw095-LA	Tw095-IA	Tw110-LA	Tw110-IA
$A_{3\text{-D}}$	8.5×10^{-5}	8.5×10^{-5}	1.0×10^{-8}	8.5×10^{-5}	1.0×10^{-8}

Table 6.2: Forcing set-up: 'LA' and 'IA' denote finite 3-D amplitude forcing and infinitesimally small 3-D amplitude forcing, respectively. Other parameters are fixed: $A_{2\text{-D}} = 7.5\times10^{-3}$ at $F_{2\text{-D}} = 124\times10^{-6}$, z-symmetric 3-D wave at $F_{3\text{-D}} = 62\times10^{-6}$, with $Re_{x,mid} = 1.72\times10^{5}$ (cases TadIG and Tw095) or $Re_{x,mid} = 9.61\times10^{4}$ (cases Tw110).

6.3.2 Disturbance strip

Disturbances are introduced via a blowing-and-suction disturbance strip on the flat-plate surface. Once the laminar base flow reaches a steady-state solution, the localised 3-D disturbance (Sayadi *et al.* 2013) is activated as

$$v(x, y = 0, z, t) = f(x)\left[A_{2\text{-D}}\sin(\omega_{2\text{-D}}t) + A_{3\text{-D}}\sin(\omega_{3\text{-D}}t)\cos(\beta_0 z)\right], \tag{6.3}$$

where $A_{2\text{-D}} = A^*_{2\text{-D}}/u^*_\infty$ and $A_{3\text{-D}} = A^*_{3\text{-D}}/u^*_\infty$ are the wave amplitudes for the primary 2-D and z-symmetric 3-D waves, respectively, and $\omega_{2\text{-D}} = \omega^*_{2\text{-D}}\delta^*_{99,0}/u^*_\infty$ and $\omega_{3\text{-D}} = \omega^*_{3\text{-D}}\delta^*_{99,0}/u^*_\infty$ are the corresponding angular frequencies. The spanwise wavenumber $\beta_0 = \beta^*_0\delta^*_{99,0} = 2\pi/\lambda_z$ equals the spanwise size z_e of the computational domain (see Tab. C.1.1). The streamwise variation in Eq. (6.3) is governed by the function $f(x) = 15.1875\xi^5 - 35.4375\xi^4 + 20.25\xi^3$, with $\xi = (x - x_1)/(x_{mid} - x_1)$ for $x_1 < x < x_{mid}$, and $\xi = (x_2 - x)/(x_2 - x_{mid})$ for $x_{mid} < x < x_2$, where $x_{mid} = (x_1 + x_2)/2$ corresponds to $Re_{x,mid}$ (see Tab. 6.2). The disturbance strip is positioned upstream of branch I (see Fig. 6.3). Since no experimental studies on controlled transition with supercritical fluids are currently available, the ideal-gas H-type breakdown scenario from Sayadi *et al.* (2013), validated by Boldini *et al.* (2025), is used as a reference, with $F_{2\text{-D}} = 124\times10^{-6}$ and $\lambda_z = 9.63$. In Sec. 6.4 and Sec. 6.5, 2-D and 3-D simulations are performed, respectively. In the 2-D simulations, a 2-D wave ($\beta_r = 0$) with frequency $F_{2\text{-D}}$ is forced, with amplitude $A_{2\text{-D}} = 1.0\times10^{-8}$ in the linear regime, and increased to either 7.5×10^{-4} or 7.5×10^{-3} in the nonlinear regime. The latter corresponds to the amplitude used in the ideal-gas H-type breakdown reference simulation from Boldini *et al.* (2025). For the 3-D simulations, $A_{2\text{-D}}$ is set to 7.5×10^{-3}, while two amplitude levels for the z-symmetric 3-D wave with $F_{3\text{-D}} = 62\times10^{-6}$ are considered: infinitesimally small (denoted as 'IA') or finite (denoted as 'LA'). The differences in forcing parameters for all simulations are summarised in Tab. 6.2. The non-dimensional angular frequency ω and the frequency parameter F are related by $\omega = FRe_0$, with $F = \omega^*\mu^*_\infty/(\rho^*_\infty u^{*2}_\infty)$ and local Reynolds number $Re_0 = \sqrt{Re_{x,0}}$.

6.4 2-D analysis: linear and nonlinear regimes

This section focuses on the behaviour of Mode-II instability and its evolution from the linear regime (Sec. 6.4.1) to the nonlinear regime (Sec. 6.4.2), highlighting the role of the Widom

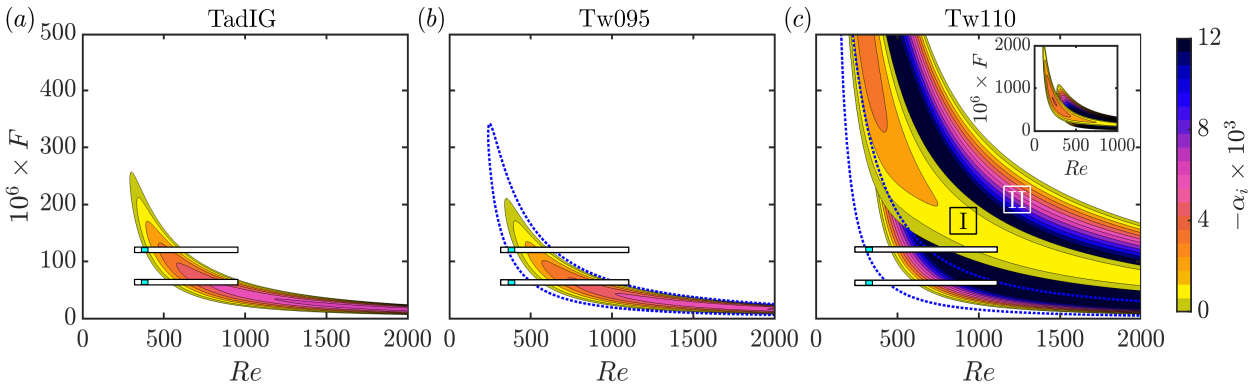

Figure 6.3: Growth-rate ($-\alpha_i$) contours in the Re–F stability diagram: (a) TadIG, (b) Tw095, and (c) Tw110 (Mode I and II). The dotted blue lines in (b,c) represent the ideal-gas neutral stability at equal T_w^*/T_∞^*-ratios. In the inset of (c), the wide frequency band of Mode I and II is displayed. The location of the DNS domain and perturbation strip for subharmonic breakdown, i.e. $F_{3\text{-D}} = 0.5F_{2\text{-D}} = 62 \times 10^{-6}$, are marked by white and cyan bars, respectively, as described in Sec. 6.3.2.

line (pseudo-boiling). This 2-D investigation serves as a precursor to the fully 3-D breakdown scenarios in Sec. 6.5.

6.4.1 Linear evolution

Starting from the base-flow profiles in Sec. 6.3.1, linear stability analysis is performed for the cases listed in Tab. 6.1. Fig. 6.3 displays the growth rate $-\alpha_i$ in the Re–F stability diagram, where $Re = \sqrt{Re_x}$. In Fig. 6.3(b), increasing the wall temperature towards $T_{r,pc}$ stabilises the flow. This trend is reversed under ideal-gas conditions, where a higher T_w^*/T_∞^*-ratio leads to destabilisation (dotted blue line). In Fig. 6.3(c), upon crossing the pseudo-critical point from the liquid-like free stream, Mode II appears (Ren *et al.* 2019), becoming highly unstable even at low Reynolds numbers. Simultaneously, Mode I, exhibiting growth rates an order of magnitude lower, becomes unstable over a much broader frequency band, extending up to $F \approx 2 \times 10^{-3}$. This modal behaviour shifts the critical Reynolds number Re_{crit}, i.e. $\alpha_i = 0$, towards lower values. The DNS domain, indicated by rectangular bars in Fig. 6.3, is placed inside the linearly unstable region, with the disturbance strip (coloured in cyan) positioned somewhat upstream of, or close to, Re_{cr} at the selected frequency F. As shown in Fig. 6.3(c) for case Tw110, the DNS domain spans nearly the entire linearly unstable region of Mode II at $F_{2\text{-D}} = 124 \times 10^{-6}$, consistent with our aim of investigating transition to turbulence triggered by Mode-II instability.

In the context of the 2-D DNS, a steady laminar solution is first obtained (see Sec. 6.3.1) and LST-DNS comparisons of growth rate and phase speed are provided in Appendix C.3. The eigenfunctions, normalised by $\max\{|\hat{u}|\}$, are successfully compared in Figs. 6.4(a,c) at $Re = 500$ for case Tw095 and at $Re = 650$ for case Tw110. In the subcritical state, u' shows a phase jump near $y/\delta_{99,0} \approx 1$, and ρ' is confined near the wall around the critical layer $y = y_{cr}$, defined by $\bar{u}(y_{cr}) = c_r$ (not to be confused with the thermodynamic critical point),

resembling the ideal-gas case TadIG (not shown here). For Tw110, Mode II is affected by the pseudo-critical point (green dashed line at $y = y_{pc}$ in Fig. 6.4c), with $\max\{|\hat{u}|\}$ located in the vapour-like state. Figures 6.4(b,d) provide an overview of the modal instability in Tw095 and Tw110 via contours of ρ'. In the latter case, the density fluctuations form 'rope-shaped' patterns around the pseudo-critical point, where gradients in transport and thermodynamic properties are largest (see Fig. 6.2), near the GIP (horizontal grey line), in agreement with Ren *et al.* (2019). While similar density patterns occur for the second-mode instability in a hypersonic boundary layer (Unnikrishnan & Gaitonde 2020), two key distinctions apply here: (i) transcritical Mode II is not linked to Mack second mode (Ren *et al.* 2019), and (ii) at $M_\infty = 0.2$, pressure perturbations are predominantly of hydrodynamic nature. Note that, contrary to Ren *et al.* (2019), the wall-normal distribution of the pressure eigenfunction $\hat{p}$ peaks at the wall rather than at the pseudo-critical point (see Fig. 6.4c).

A key question concerning Mode-II instability, as it manifests under transcritical heating conditions, concerns its physical linear mechanism. Bugeat *et al.* (2024) demonstrated in a plane Couette flow that shear and baroclinic effects interact to generate two vorticity waves around the central layer, coinciding with the location of the minimum of kinematic viscosity and the critical layer. Similarly, the present 2-D boundary-layer flow is analysed using the linearised vorticity equation, where $\bar{\Omega} = \partial\bar{v}/\partial x - \partial\bar{u}/\partial y$ is the base-flow vorticity, for the disturbance vorticity $\xi = \partial v'/\partial x - \partial u'/\partial y$ as:

$$\underbrace{\frac{D\xi}{Dt}}_{LHS} \approx \underbrace{v'\frac{\partial^2\bar{u}}{\partial y^2}}_{S_\xi} + \underbrace{\frac{\partial\bar{u}}{\partial y}\left(\frac{\partial u'}{\partial x} + \frac{\partial v'}{\partial y}\right)}_{C_\xi} \underbrace{-\frac{1}{\bar{\rho}^2}\frac{\partial\bar{\rho}}{\partial y}\frac{\partial p'}{\partial x}}_{B_\xi} + O(\mu). \tag{6.4}$$

Here, S_ξ, C_ξ, and B_ξ denote the shear, compressible stretching, and baroclinic terms, respectively. The viscous term is represented by $O(\mu)$. The term $1/\bar{\rho}^2\,\partial\rho'/\partial x\,\partial\bar{p}/\partial y$, which belongs to B_ξ, is negligible (see Appendix C.2). Figure 6.5 evaluates Eq. (6.4) for case Tw110. For case Tw095, the only significant term of Eq. (6.4) far from the wall is the shear contribution S_ξ, where $|\partial^2\bar{u}/\partial y^2|$ is maximal. In the spectral domain at $Re = 650$, Fig. 6.5(a) confirms that both S_ξ and B_ξ reach a maximum near the pseudo-critical point, where the minimum of $\bar{\nu}$ is located. At the GIP, where the density-weighted vorticity $\Phi = \bar{\rho}\bar{\Omega}$ is maximal (Fig. 6.5b), the compressible stretching term C_ξ also peaks and remains large in the vapour-like region. The viscous term $O(\mu)$ exhibits a local maximum at the pseudo-critical point due to its direct dependence on $|\partial^2\bar{u}/\partial y^2|$, which is largest at y_{pc}. In Fig. 6.5(c), the sum of S_ξ and B_ξ exhibits two out-of-phase waves with a phase difference of π (not shown), located around y_{pc} and exhibiting asymmetry due to the structure of B_ξ. When the out-of-phase C_ξ-term is included, as shown in Fig. 6.5(e), the two vorticity waves shift around the critical layer at $y = y_c$. This behaviour is consistent with Bugeat *et al.* (2024), where C_ξ was absent and the critical layer coincided with the GIP, i.e. the centerline of the plane Couette flow under the parallel flow assumption. In other words, the misalignment between the critical layer and the GIP in the boundary layer results in a corresponding shift of the two vorticity waves. With the addition of the viscous $O(\mu)$-term, the vorticity perturbation ξ in Fig. 6.5(f) is further amplified near the wall, tilting the near-wall vorticity wave in the upstream direction.

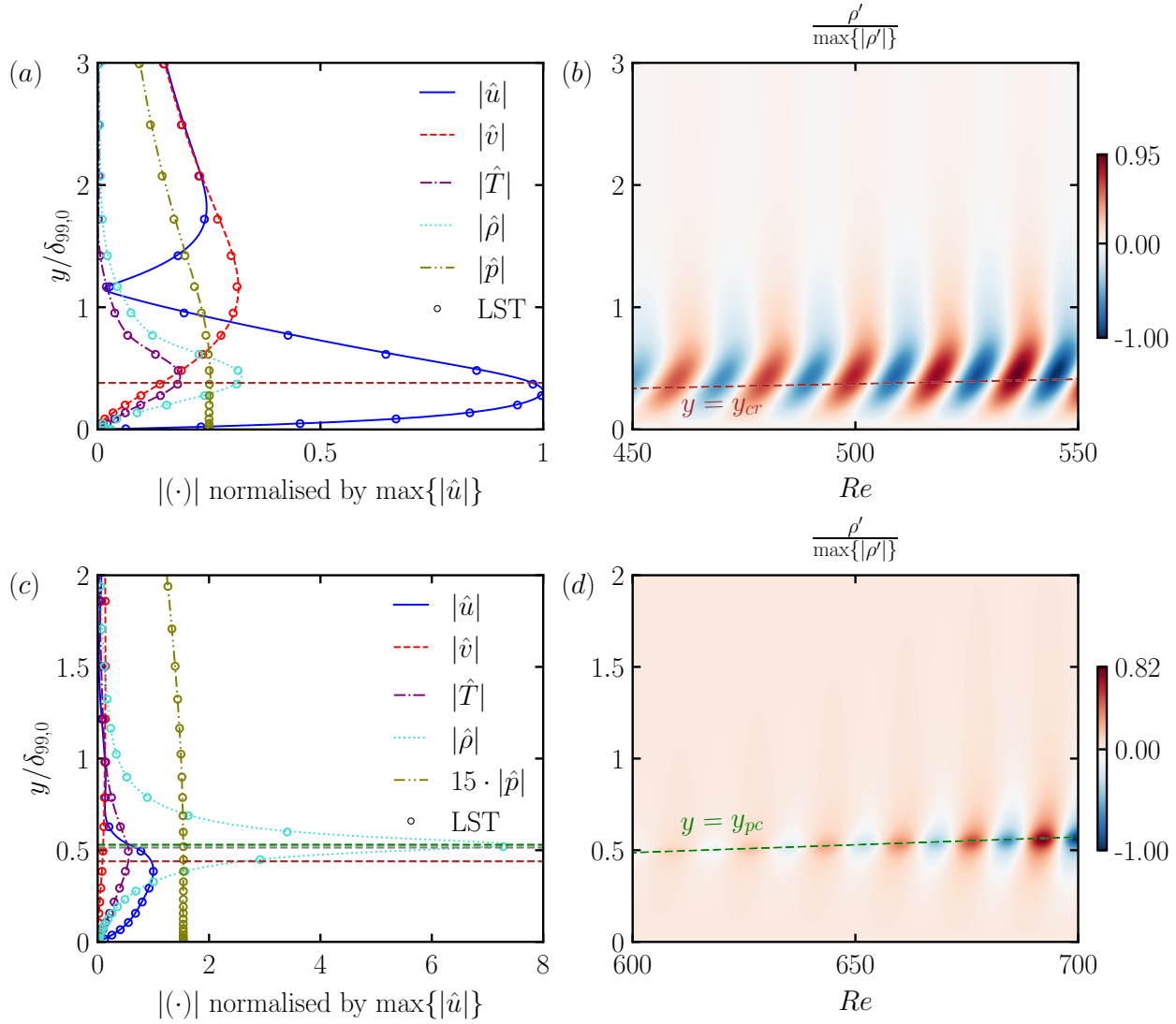

Figure 6.4: Cases Tw095 (a,b) and Tw110 (c,d): (a,c) wall-normal eigenfunctions (lines DNS data, circles LST) of u', v', T', ρ', and p' normalised by $\max\{|\hat{u}|\}$ at $Re = 500$ (Tw095) and $Re = 650$ (Tw110); contours ρ' (b,d) normalised by their respective maximum. The locations of the pseudo-critical point $y = y_{pc}$, i.e. where $\bar{T}^* = T^*_{pc}$, the GIP $y = y_{GIP}$, and the critical layer $y = y_{cr}$ are indicated in green (- -), grey (- -), and brown (- -), respectively.

6.4.2 Nonlinear evolution

We now focus on the nonlinear response of the boundary layer to a finite-amplitude perturbation, with the blowing–suction amplitude increased to $A_{2\text{-D}} = 7.5 \times 10^{-3}$, compared to the infinitesimal amplitude used in Sec. 6.4.1. Fourier modes are denoted using the double-spectral notation $(\omega/\omega_{2\text{-D}}, 0)$, where $\omega_{2\text{-D}}$ is the fundamental frequency.

Figure 6.6(a) shows the downstream modal evolution for case Tw095. Once the 1%-threshold is crossed at $Re \approx 600$, the primary (1,0) mode decays. Higher harmonics (2,0), (3,0), and beyond are slaved to the primary wave through weakly nonlinear effects in the receptivity region. Despite being linearly stable, they follow the streamwise growth, and subsequent stabilisation, of the forced (1,0), with amplitudes approximately two orders of

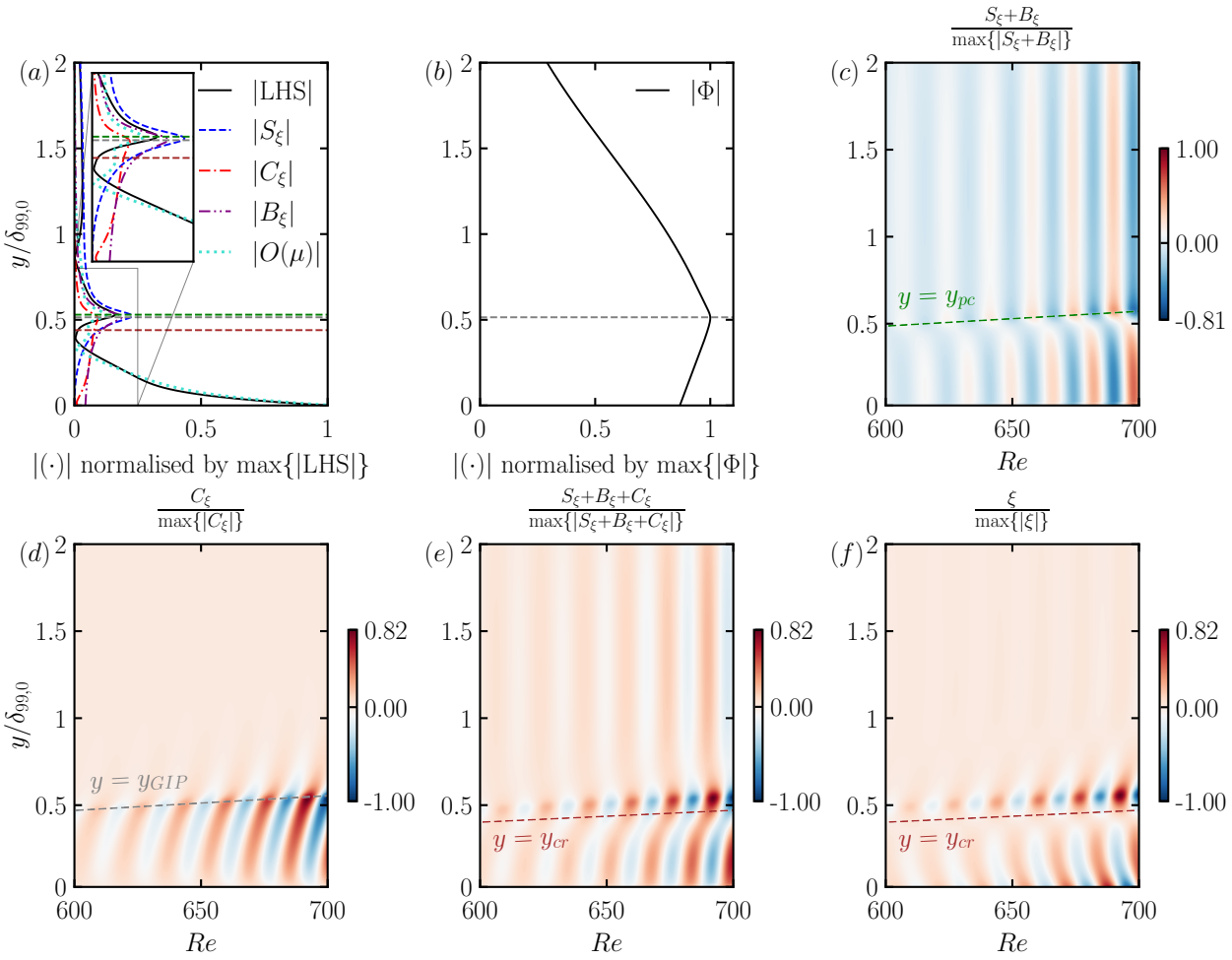

Figure 6.5: Case Tw110. Terms of the vorticity perturbation equation in Eq. (6.4): (a) spectral domain at $Re = 650$ (all terms are normalised by $\max\{|D\xi/Dt|\}$); (b) normalised density-weighted vorticity $|\Phi| = |\bar{\rho}\bar{\Omega}|$; (c) $S_\xi + B_\xi$; (d) C_ξ; (e) $S_\xi + B_\xi + C_\xi$; and (f) ξ. The locations of the pseudo-critical point $y = y_{pc}$, i.e. where $\bar{T}^* = T^*_{pc}$, the GIP $y = y_{GIP}$, and the critical layer $y = y_{cr}$ are indicated in green (- -), grey (- -), and brown (- -), respectively.

magnitude lower. Wall-normal profiles of streamwise velocity and density at $Re = 500$ and 700 (Figs. 6.6b,c) reveal only minor nonlinear effects, with the boundary-layer receptivity resembling the incompressible TadIG case.

In contrast to the subcritical state, nonlinearity significantly influences the 2-D modal evolution in case Tw110. To highlight this, $A_{2\text{-D}}$ is increased from 7.5×10^{-4} in Fig. 6.7(a) to 7.5×10^{-3} in Fig. 6.7(b). In the low-amplitude case, modes $(1,0)$ and $(2,0)$ follow the LST prediction up to $Re \approx 700$, and, as shown in Fig. 6.3(c), linear instability also arises at $2F_{2\text{-D}}$, with a larger growth rate than that of $(1,0)$. Higher harmonics ($\omega/\omega_{2\text{-D}} \geq 3$) deviate from their linear evolution, growing rapidly to high amplitudes, unlike in the subcritical state (Fig. 6.6a). This behaviour resembles the Kelvin–Helmholtz (KH) instability in a mixing layer (Babucke *et al.* 2007). In the high-amplitude case in Fig. 6.7(b), higher harmonics exceed the 0.1% amplitude threshold at lower values of Re. Mode $(2,0)$, which is more unstable than mode $(1,0)$ in the linear regime, surpasses $(1,0)$ at $Re \approx 600$, before

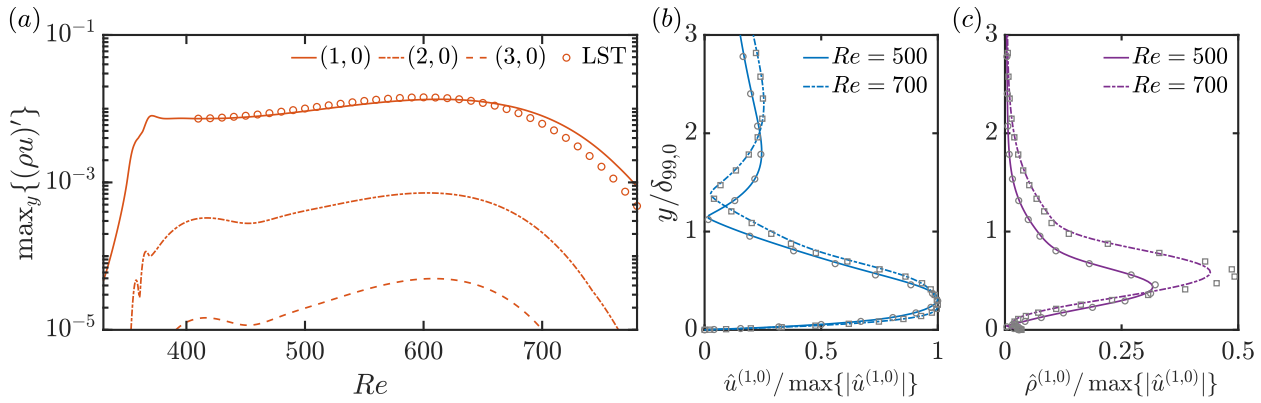

Figure 6.6: Case Tw095 with $A^{(1,0)}_{\text{2-D}} = 7.5 \times 10^{-3}$: (a) maximum wall-normal mass-flux amplitude for mode (1,0) (solid line), (2,0) (dash-dotted line), and (3,0) (dashed line); streamwise velocity (b) and density (c) perturbations as functions of the wall-normal coordinate $y/\delta_{99,0}$ at $Re = 500$ (solid line) and $Re = 700$ (dash-dotted line), normalised by their respective $\max\{|\hat{u}^{(1,0)}|\}$. In (b,c), the scaled LST solution is represented with circle (○) symbols at $Re = 500$, and with square (▫) symbols at $Re = 700$.

nonlinearly saturating after reaching the 2%-amplitude threshold. As it peaks at $Re \approx 700$, a subharmonic resonance mechanism with its subharmonic mode $(1,0)$, typically observed as vortex pairing in mixing layers (Monkewitz 1988), emerges, destabilising the latter. Thus, mode $(1,0)$ undergoes strong destabilisation and becomes the most dominant mode again further downstream. At this streamwise location, the Mean-Flow Distortion (MFD), i.e. mode $(0,0)$, reaches up to 5%, and all higher harmonics are fully nonlinear. It is worth noting that, contrary to the conclusions of Kachanov (1994) – who reported that a threshold amplitude of the 2-D fundamental TS wave of the order of 29% of the mean flow was required to amplify 2-D subharmonics – the amplitude of mode $(2,0)$ reaches only 5% in the present case under transcritical conditions. The resonant interaction between modes $(1,0)$ and $(2,0)$ is further evidenced by their phase speeds c_r in Figs. 6.7(c,d). For the low-amplitude case ($A^{(1,0)}_{\text{2-D}} = 7.5 \times 10^{-4}$), the phase speeds are sufficiently close near $Re \approx 800$. In contrast, for the high-amplitude case, $c_r^{(1,0)}$ and $c_r^{(2,0)}$ remain nearly identical across the entire computational domain, triggering subharmonic resonance at $Re \approx 700$. Notably, at $Re \approx 730$, $c_r^{(2,0)}$ increases sharply, deviating from its linear evolution (in grey) and indicating strong nonlinear stabilisation (Fig. 6.7b). The results presented here are based on $F_{\text{2-D}} = 124 \times 10^{-6}$. However, we also examine higher fundamental frequencies, as detailed in Appendix C.4.

To qualitatively assess the nonlinear evolution of Mode II, selected perturbation contours for $A^{(1,0)}_{\text{2-D}} = 7.5 \times 10^{-3}$ are shown in Figs. 6.8(a,b). The region corresponding to highest specific heat at constant pressure, between $98\% \max\{c_p\}$ and $\max\{c_p\}$, is shaded in green. At this high disturbance level, the constant-pressure assumption for a laminar boundary layer breaks down, and $\max\{c_p\}$ depends on both reduced pressure and temperature. It is estimated using the analytical Widom-line relation $T_{r,pc} = 1/A_{\text{VdW}} \ln(p_r) + 1$, where the Widom line, defined as the locus of pseudo-critical points at supercritical pressure (Fig. 6.1), is characterised by the critical slope $A_{\text{VdW}} = T_c/p_c(\mathrm{d}p/\mathrm{d}T)_c = 4$ (Banuti 2015). Unlike in

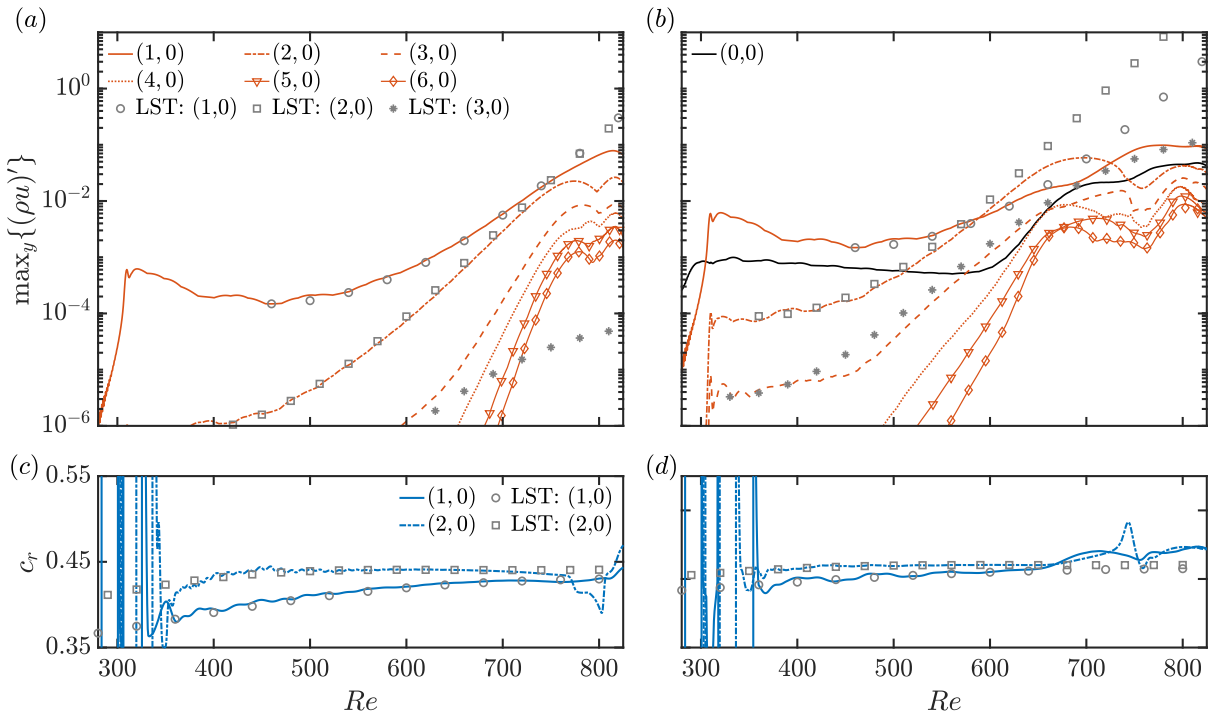

Figure 6.7: Case Tw110, with (a,c) $A^{(1,0)}_{\text{2-D}} = 7.5 \times 10^{-4}$ and (b,d) $A^{(1,0)}_{\text{2-D}} = 7.5 \times 10^{-3}$, for: (a,b) maximum wall-normal mass-flux amplitude for mode $(1,0)$ (solid line), $(2,0)$ (dash-dotted line), $(3,0)$ (dashed line), $(4,0)$ (dotted line), $(5,0)$ (solid line with ▽), and $(6,0)$ (solid line with ◇); (c,d) phase speed c_r for modes $(1,0)$ (solid line) and $(2,0)$ (dash-dotted line). In (b), the MFD $(0,0)$ is indicated with a black solid line. The LST solution is represented with circle (○) symbols for mode $(1,0)$, square (▫) symbols for mode $(2,0)$, and asterisk (∗) symbols for mode $(3,0)$.

the linear regime (Figs. 6.4c,d), where the pseudo-critical point height grows with $\sqrt{x}$, the nonlinear disturbance wave propagation leads to increasing distortion of the Widom line, proportional to the perturbation magnitude (Figs. 6.8a,b). The large harmonic mode $(2,0)$, prominent between $Re \approx 600$ and 720, halves the streamwise wavelength of the perturbation wave ($(1,0)$ as the fundamental), thereby doubling the oscillation frequency of the Widom line. As shown in the inset of Fig. 6.8(a), the crests and troughs of the Widom line align with regions of positive and negative wall-normal velocity perturbation v'. Since v' and the pressure perturbation p' are out of phase (Luhar *et al.* 2014; Bugeat *et al.* 2024), the upward and downward displacements of the Widom line correspond to local pressure decreases and increases, respectively. Density perturbations in Fig. 6.8(b), initially confined near the Widom line in the linear regime (Fig. 6.4d), now reach up to 20% of the free-stream value in regions where p'_r is negative, i.e. closer to the critical point. These perturbations mirror the billowing behaviour of the Widom line, with $\rho' < 0$ around the Widom-line crests, and $\rho' > 0$ around the troughs.

The term 'billowing' is used by analogy with classical shear-layer flows, where a periodic train of large, rolling wave-like structures forms as the KH instability evolves nonlinearly (Klaassen & Peltier 1985; Liu *et al.* 2023). Here, a train of streamwise-growing density billows

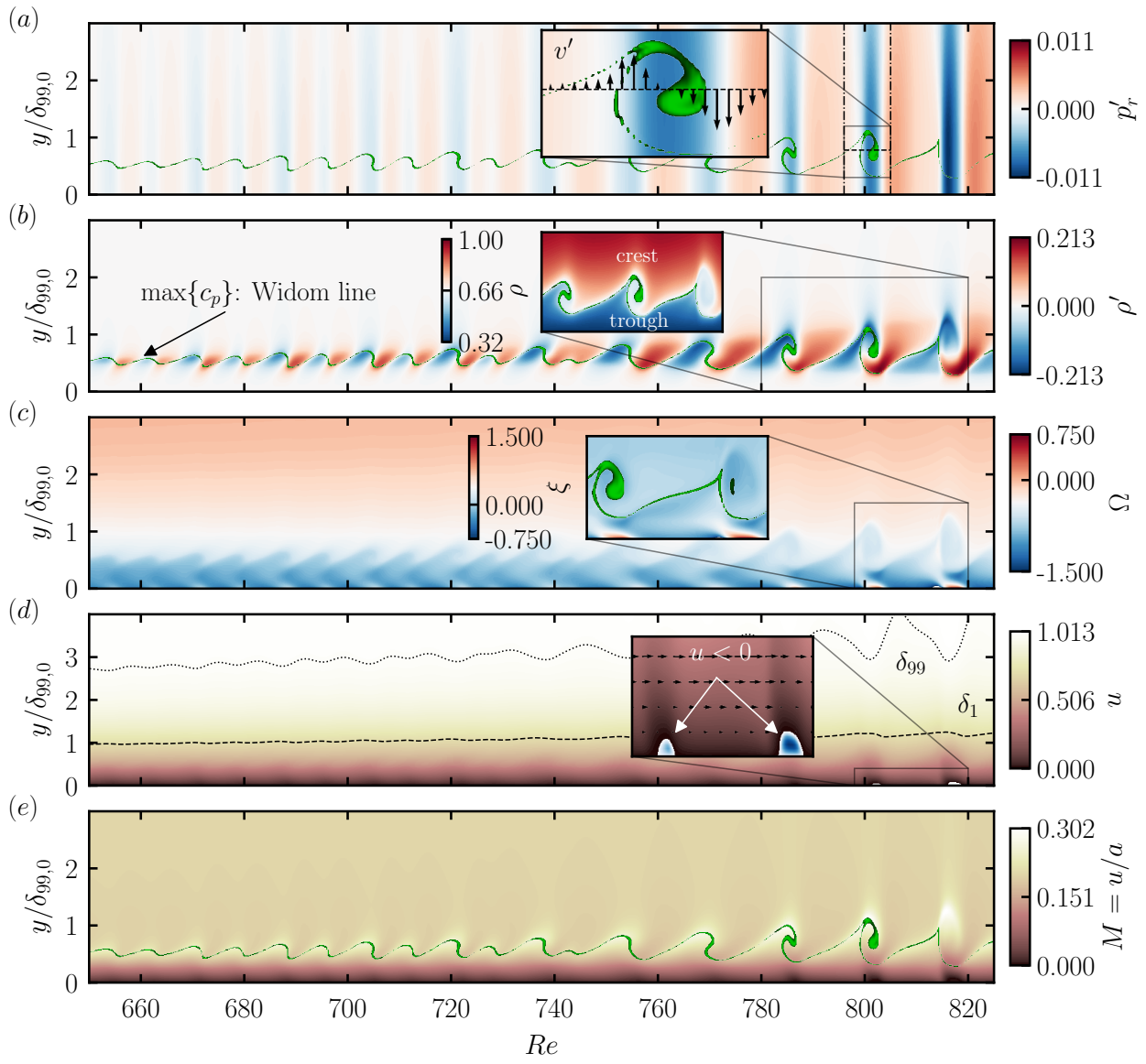

Figure 6.8: Case Tw110. Instantaneous contours at $T/T_0 = 0$, where $T_0 = 2\pi/\omega_0$ (fundamental frequency ω_0), with $A^{(1,0)}_{\text{2-D}} = 7.5\times10^{-3}$: (a) reduced pressure fluctuation $p'_r = p^{*\prime}/p^*_c$, (b) density fluctuation ρ', (c) vorticity Ω, (d) streamwise velocity u, with boundary-layer thickness δ_{99} and displacement thickness δ_1 indicated by dotted and dashed lines, respectively, and (e) Mach number $M = u/a$. The Widom line $y = y_{WL}$ lies within the green region, i.e. between 98% max{c_p} and max{c_p}. Note that the Widom line is used here as a spatial reference for the local pseudo-critical point at supercritical pressure. Insets in panels (a–c) show the wall-normal velocity fluctuation v', density ρ, and vorticity fluctuation ξ, respectively. The inset in (d) highlights separation zones ($u < 0$) in blue and includes velocity vectors $|\vec{V}| = \sqrt{u^2 + v^2}$. A supplementary movie of the billow roll-ups is available at `https://github.com/pcboldini/DNSvisualisation`.

arises (see inset of Fig. 6.8b). In both shear layers and the present case, billowing arises from an excess of vorticity concentrated in a localised flow region (see Fig. 6.5b). Although the train of billowing flow patterns is caused by the transcritical Mode-II instability rather than

by the KH instability, Bugeat *et al.* (2024) proved that the resulting vorticity fields are identical in the linear regime. Thus, it is not surprising that, in the nonlinear regime, the billowing patterns observed here resemble those seen in classical KH-type roll-ups, despite the absence of a true shear-layer mechanism.

Figures 6.8(b,c) highlight the nonlinear evolution of these billows via contours of ρ' and vorticity $\Omega = \partial v/\partial x - \partial u/\partial y$. Their deformation and streamwise growth progressively narrow the near-wall vapour-like region, which shifts significantly closer to the wall at $Re \approx 800$ compared to the linear regime. Simultaneously, the upper liquid-like fluid is lifted up by the rolling billows. Peaks in Ω, which were previously aligned with the Widom line in the laminar regime, now appear below the Widom-line troughs in the near-wall region and at the wall. Starting from $Re \approx 780$, and recurring periodically downstream, the Ω-peaks strengthen (high-shear regions), and their magnitude scales with their fluctuation ξ (inset of Fig. 6.8c). The contours of streamwise velocity in Fig. 6.8(d) reveal the emergence of near-wall flow-reversal regions ($u < 0$), located just beneath the near-wall Ω-peaks at the Widom-line troughs, indicating the formation of a developing shear layer near the wall. In the vicinity of these flow reversal zones, a region of low streamwise velocity forms, leading to the reduction of the boundary-layer thickness δ_{99} by approximately 10% relative to the unperturbed profile. At $Re \approx 800$, the near-wall separation zone reaches a height of approximately 2% of δ_{99}, while the billow crest extends beyond $y/\delta_{99,0} = 1$. Here, the local Mach number reaches its maximum, as shown in Fig. 6.8(e). This behaviour results from both the boundary-layer displacement effect and the reduction in the local speed of sound at the Widom line. Downstream of the crest, the Mach number rapidly returns to its laminar value.

To further investigate the near-wall high-shear region during billow roll-up, wall-normal profiles are extracted at $Re = 802$, corresponding to the first flow reversal found in Fig. 6.8(d). Figures 6.9(a,b) show the streamwise velocity u and the reduced specific heat at constant pressure $c_{p,r}/c_{p,r,\infty}$, respectively, at four time instants within one forcing period $T_0 = 2\pi/\omega_0$. Between $t/T_0 = 0.95$ and $t/T_0 = 0$, the billow roll-up induces two distinct kinks in the u-profile: one at the billow crest at $y/\delta_{99,0} \approx 1.0$, and another at the trough near $y/\delta_{99,0} \approx 0.3$. These locations coincide with sharp peaks in c_p (Fig. 6.9b), with the highest values occurring at $t/T_0 = 0$, linked to a local pressure drop $p'_r < 0$ (see Fig. 6.8a). Beneath the near-wall kink in the vapour-like region, flow reversal at the wall is observed (inset of Fig. 6.9a), along with a GIP, where the density-weighted vorticity $\Phi = \rho\Omega$ is maximal (grey circle). Here, the vorticity experiences a maximum, with an inviscid instability found according to the generalised Fjørtoft criterion (Bugeat *et al.* 2024). By $t/T_0 = 0.25$, no further GIP or flow reversal is observed, confirming the periodic nature of the billow generation. At $t/T_0 = 0.50$, the profiles resemble those of the unperturbed boundary layer (Fig. 6.2). The large near-wall shift in the instantaneous u observed over one T_0 is caused by strong near-wall velocity fluctuations, reaching up to 5% of the root mean square (r.m.s.) value, (Fig. 6.9c), sustained by both the primary mode $(1,0)$ and its first harmonic $(2,0)$. A secondary peak in u'_{rms} at $y/\delta_{99,0} \approx 0.7$ is primarily attributed to mode $(1,0)$. Density fluctuations (Fig. 6.9d) are dominant in the high-c_p region, with the ρ'_{rms}-peak located at the height of the far-wall

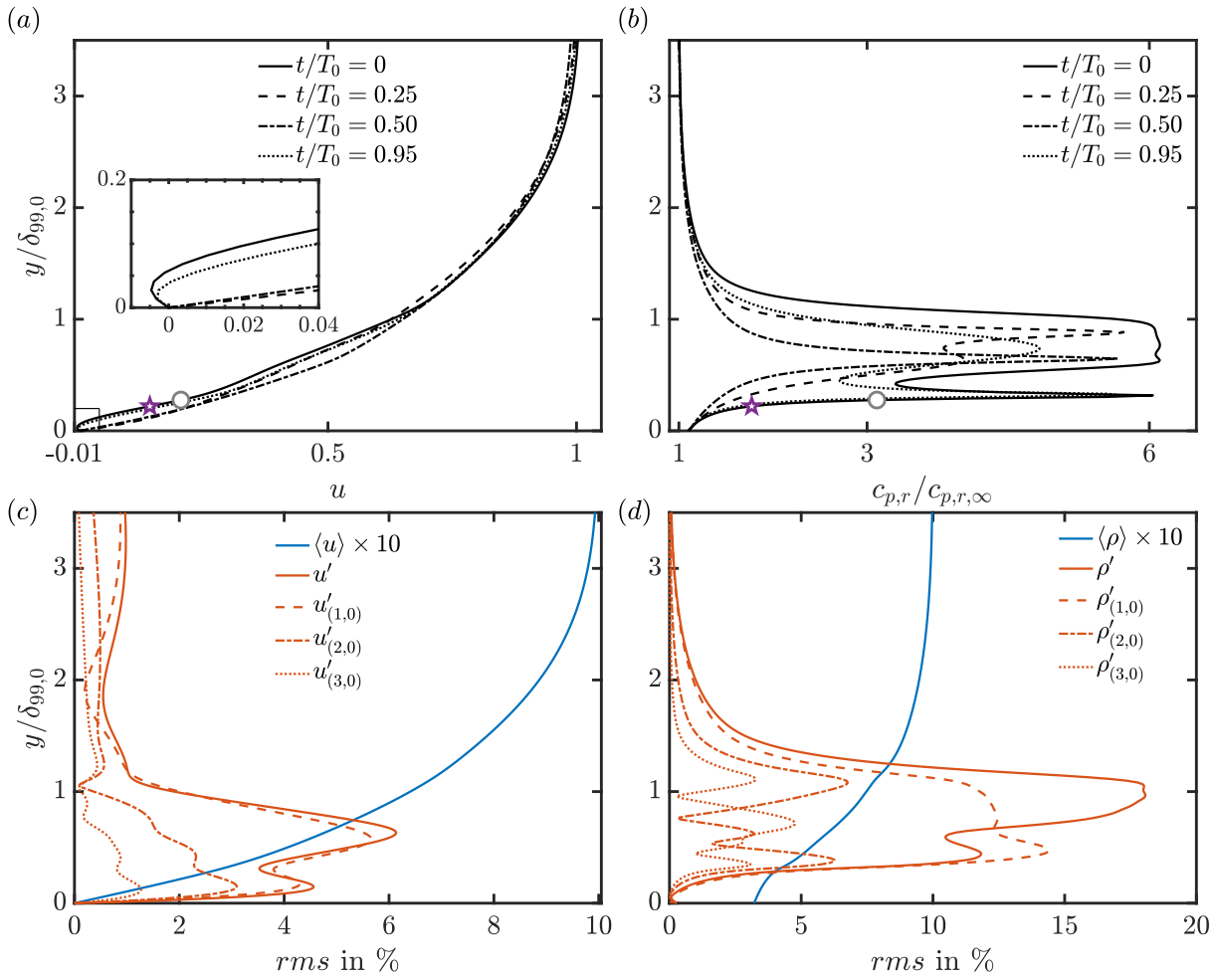

Figure 6.9: Case Tw110 for $A^{(1,0)}_{\text{2-D}} = 7.5 \times 10^{-3}$. Wall-normal slice at $Re = 802$ showing: (a,b) instantaneous streamwise velocity u and reduced specific heat at constant pressure $c_{p,r}/c_{p,r,\infty}$ at time periods $t/T_0 = [0, 0.25, 0.5, 0.95]$, where $T_0 = 2\pi/\omega_0$ is the fundamental forcing period; (c,d) time-averaged streamwise velocity $\langle u \rangle$ and density $\langle \rho \rangle$ profiles. In (c,d), the r.m.s. of u' and ρ', respectively, and higher harmonics (modes $(1,0)$, $(2,0)$, and $(3,0)$) are shown. The locations of the GIP and IP at $t/T_0 = 0$ are marked in insets (a,b) by circle (○) and star (☆) symbols, respectively.

6

u-kink.

In conclusion, under transcritical conditions, we observe localised flow reversal beneath the billow roll-up at $Re = 802$, along with the formation of a shear layer just above it. This behaviour is linked to the sharp near-wall increase in c_p, which amplifies near-wall u-disturbances and destabilises the local mean flow. In other words, this effect is tied to the upward and downward displacements of the Widom line, which correspond to decreases and increases in reduced pressure p_r, respectively. As p_r decreases, steep gradients in thermodynamic properties intensify. Ultimately, the initial assumption of a ZPG laminar boundary layer breaks down. When the billow rolls up, a net $\mathrm{d}p/\mathrm{d}x > 0$ (APG) forms. Simultaneously, the MFD is insufficient to counteract the large near-wall (Mode-II) u-fluctuations, leading to a travelling region of flow reversal. While Taylor (1936) attributed transition in

incompressible flows to unsteady pressure gradients caused by 'external' disturbances leading to separation (see note by Kloker (2024)), similar localised separation zones, such as those in Fig. 6.8(d), were found under strong APG in the K-type breakdown of an ideal-gas boundary layer (Kloker 1993; Kloker & Fasel 1995) and in the laminar-to-turbulent transition experiments of Kosorygin (1994). In the current study, however, the disturbance is 'internal', originating from the displacement of the Widom line, and is absent under weakly non-ideal-gas conditions at the same forcing amplitude.

6.5 3-D breakdown to turbulence

Building on the 2-D nonlinear analysis of the Mode-II instability, we perform 3-D DNS to assess the complete breakdown to turbulence. A z-symmetric oblique wave with spanwise wavenumber β_0 and half the frequency of the primary wave is introduced alongside the 2-D wave. The oblique wave is imposed with either an infinitesimal amplitude ('IA') or a finite amplitude ('LA'). The 2-D wave amplitude, $A_{2\text{-D}} = 7.5 \times 10^{-3}$, is consistent with Sec. 6.4.2. In the subcritical state, case Tw095-IA is reported in Sec. 6.5.1 for comparison but ultimately excluded from further analysis, as it does not trigger transition.

6.5.1 Modal analysis

Figure 6.10 presents the relevant modes for the subcritical cases with infinitesimal and finite amplitude, Tw095-IA and Tw095-LA, and the transcritical cases with infinitesimal and finite amplitude, Tw110-LA and Tw110-IA. All share the same fundamental frequency and spanwise wavenumber; the 'LA'-cases in Figs. 6.10(b,c) use the same 2-D and 3-D forcing amplitudes, while the 'IA'-cases in Figs. 6.10(a,d) have an infinitesimal 3-D forcing amplitude of $A_{3\text{-D}} = 1.33 \times 10^{-6} A_{2\text{-D}}$ (see Tab. 6.2).

In case Tw095-IA (Fig. 6.10a), no transition occurs. Although the oblique mode $(1/2, 1)$ undergoes secondary subharmonic growth starting at $Re_x/10^5 \approx 3$, its amplitude remains insufficient to trigger nonlinear interactions. The primary 2-D mode $(1, 0)$ decays in line with Fig. 6.6(a), while mode $(0, 2)$ continues to grow due to transient growth (Boldini *et al.* 2024).

In contrast, case Tw095-LA (Fig. 6.10b) transitions to turbulence via the subharmonic instability, which rapidly induces three-dimensionality. Its modal evolution closely resembles that of case TadIG (not shown). At the disturbance strip, higher harmonics such as $(2, 0)$ and $(3/2, 1)$ are also triggered but remain only moderately amplified. When the primary wave $(1, 0)$ reaches $\sim 1\%$ at $Re_x/10^5 \approx 2.9$, subharmonic resonance sets in, and the forced subharmonic oblique mode $(1/2, 1)$, absent in the 2-D DNS set-up in Fig. 6.6(a), grows rapidly, surpassing $(1, 0)$ near $Re_x/10^5 \approx 4$. Compared to TadIG, this process is delayed due to the slower destabilisation of $(1, 0)$ as the wall temperature is increased towards the Widom line. During the secondary-instability growth, higher modes experience strong nonlinear amplification, contributing to the increase of the MFD $(0, 0)$ near $C_{f,min} = \min\{C_f\}$. Later, all

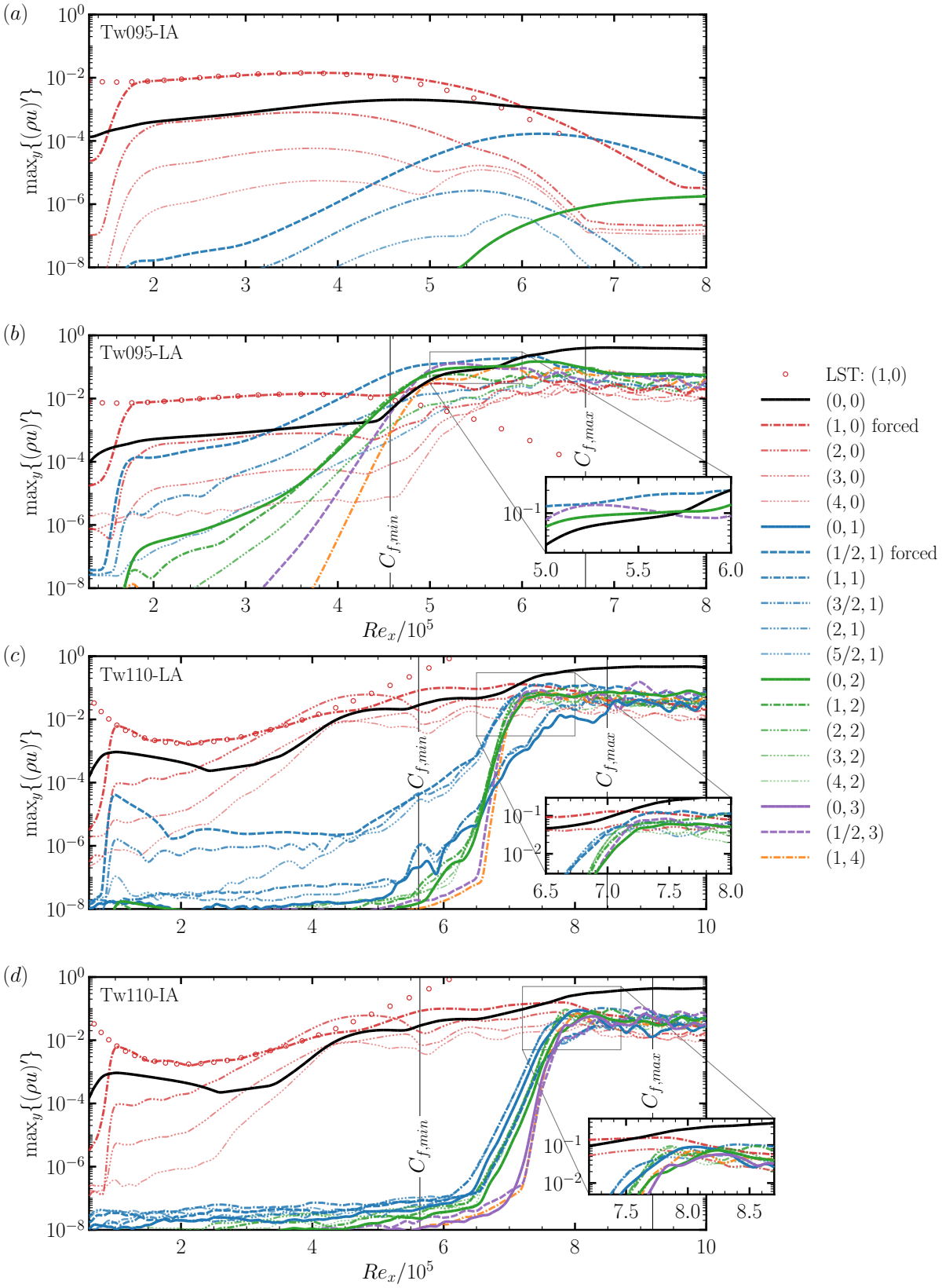

Figure 6.10: Streamwise evolution of the y-maximum of $(\rho u)'$ for the most relevant modes $(\omega/\omega_{2\text{-D}}, \beta/\beta_0)$ for case: (a) Tw095-IA, (b) Tw095-LA, (c) Tw110-LA, and (d) Tw110-IA. The minimum and maximum values of the time- and spanwise-averaged skin-friction coefficient are indicated as $C_{f,min} = \min\{C_f\}$ and $C_{f,max} = \max\{C_f\}$, respectively. Insets in (c) and (d) highlight the relevant modes in the breakdown region. Note the different Re_x-axis limits between the subcritical (a,b) and (c,d) transcritical cases.

modes saturate except for $(1/2,3)$, which matches the amplitude of $(1/2,1)$ at $Re_x/10^5 \approx 5.3$. Hereafter, a wave–vortex triad typical of the oblique breakdown (Chang & Malik 1994) forms between the strongly nonlinear $(1/2,3)$ and steady vortex mode $(0,2)$, further destabilising $(1/2,1)$ (see inset of Fig. 6.10b). Further downstream where nonlinear saturation sets in, mode $(0,0)$ reaches its maximum, marking the onset of turbulence at $C_{f,max} = \max\{C_f\}$.

For case Tw110-LA in Fig. 6.10(c), although the evolution of the fundamental wave and its higher harmonics closely follows the 2-D development in Fig. 6.7(b) up to $Re_x/10^5 \approx 6.5$, the subharmonic resonance is significantly delayed due to the strong 2-D nonlinearity of the higher harmonics. The oblique mode $(1/2,1)$ is initially strongly damped between $Re_x/10^5 \approx 1.0$ and 2.0, and maintains a low amplitude level, along with $(3/2,1)$, up to $Re_x/10^5 \approx 4.7$. Before mode $(1,0)$ undergoes subharmonic resonance with $(2,0)$ (see Sec. 6.4.2), it saturates and a phase-speed-locking process (cf. Hader & Fasel (2019)) occurs between mode $(1,0)$ and its secondary wave $(1/2,1)$, triggering the growth of $(1/2,1)$ via the secondary-instability mechanism (Herbert 1988). Mode $(1/2,1)$ and its higher harmonics grow to nonlinear amplitude levels and saturate at $Re_x/10^5 \approx 6.0$. On the contrary, modes with spanwise-wavenumber parameter $\beta/\beta_0 = 1$ briefly grow near $C_{f,min}$ due to nonlinear interaction, but do not contribute to the later breakdown stage. When the amplitudes of subharmonic modes ($\omega/\omega_0 = 1/2$) approach those of the primary wave and higher harmonics, additional higher modes with $\beta/\beta_0 \geq 2$ are nonlinearly amplified, rapidly growing downstream and enhancing both the destabilisation of $(1,0)$ and the MFD. In the early breakdown stage, following the saturation of mode $(1,0)$ at $Re_x/10^5 \approx 7.1$, mode $(1/2,1)$ grows nonlinearly, surpassing mode $(1,0)$ at $Re_x/10^5 \approx 7.35$, while the MFD $(0,0)$ exceeds the 20%-amplitude threshold. In the late transitional stage, before $C_{f,max}$ at $Re_x/10^5 \approx 8.5$, mode $(1/2,1)$ remains dominant, eventually followed by the abrupt growth of $(1/2,3)$ at $Re_x/10^5 \approx 9.0$.

Figure 6.10(d) illustrates the modal evolution of case Tw110 with infinitesimal 3-D forcing ('IA'). As expected, up to $\min\{C_f\}$, the evolution of modes $(h,0)$, with $h \geq 0$, matches that of case Tw110-LA in Fig. 6.10(c). No subharmonic resonance of $(1/2,1)$ occurs further downstream in this case, as no phase-speed locking mechanism between the primary wave and its subharmonic is present. In contrast, fundamental resonance with $(1,1)$ sets in at $Re_x/10^5 \approx 6.2$, along with the amplification of 3-D harmonic modes with spanwise-wavenumber parameter $\beta/\beta_0 = 2$, before mode $(1/2,1)$ grows nonlinearly only from $Re_x/10^5 \approx 6.5$ onwards. Around $Re_x/10^5 \approx 7.2$, the spectrum rapidly fills up with all other nonlinearly amplified 3-D modes, contributing to a significant increase in the MFD $(0,0)$. Note that mode $(1,1)$ arises initially due to numerical background noise, and the forcing of $(1/2,1)$ remains likewise at the noise level; therefore, both are insignificant and not representative of classical boundary-layer modes in the early nonlinear stage. Further downstream around $Re_x/10^5 \approx 6.0$, both modes $(1,1)$ and $(0,1)$ (forming a wave–vortex triad with $(1,0)$) begin to behave as discrete boundary-layer wave modes, whereas $(1/2,1)$ continues to be a continuous, non-resonant mode. Under such numerical background-noise conditions, and in the absence of primary instability of the investigated 3-D modes, the fundamental-resonance mechanism proves to be more robust than the subharmonic one. Eventually, the steady mode

$(0,1)$, which dominates the transitional stage in the K-type breakdown (Boldini *et al.* 2026), reaches the amplitude level of $(1,0)$. In the final breakdown stage, $(1,1)$ and $(1/2,3)$ alternate as the dominant modes before $C_{f,max}$ is reached. Compared to Tw110-LA, the transition is more gradual, but follows a K-type breakdown scenario. Notably, despite the infinitesimal 3-D forcing, breakdown to turbulence is triggered solely by the 2-D fundamental wave and numerical background noise, a behaviour not observed in case Tw095-IA under weakly non-ideal-gas conditions.

6.5.2 Flow structures

To investigate the mechanisms driving the breakdown in both thermodynamic states, Fig. 6.11 displays the streamwise evolution of the relevant transitional flow structures using isocontours of the Q-criterion.

The subcritical case Tw095-LA (Fig. 6.11a) exhibits the classical H-type breakdown, similar to the ideal-gas case TadIG, with staggered Λ-vortices and high-shear layers (Bake *et al.* 2002) above the vortices' tips, characterised by peaks in $\omega_z \propto \partial u/\partial y$. Conversely, no vortices are present at $\lambda_z/2$, i.e. half a spanwise wavelength apart. While the early breakdown stage closely resembles that of the ideal-gas case TadIG, the Λ-vortices become more elongated in the streamwise direction from $Re_x/10^5 \approx 5.2$ onwards, coinciding with the large amplitude of 3-D modes $(3/2,1)$ and $(0,2)$ in Fig. 6.10(b). This elongation of the Λ-vortices, along with longitudinal structures on their sides, is particularly visible for $5.2 \leq Re_x/10^5 \leq 6$ in Fig. 6.12(a), which shows a horizontal flow snapshot (xz-plane) of the streamwise velocity at $y/\delta_{99,0} = 0.49$. In contrast, the staggered Λ-vortex arrangement in case TadIG (Fig. 6.12b) breaks down more rapidly during the transitional stage.

Compared to the subcritical state, figures 6.11(b,c) reveal distinct vortical structures in the transcritical-heating state. During the early stage of breakdown, dominated by mode $(1,0)$, 2-D billow structures with near-wall separation zones (highlighted in cyan) are convected downstream. At later stages, cases Tw110-LA and Tw110-IA exhibit fundamentally different breakdown dynamics. In Tw110-LA, the forced 3-D mode $(1/2,1)$ rapidly grows from 0.01% to 13% between $Re_x/10^5 \approx 6$ and 7.3, leading to the sudden appearance of staggered Λ-vortices lifting off from the billow roll-ups. Unlike the elongated staggered alignment observed in Tw095-LA, Λ-vortices here emerge more abruptly and locally, with secondary structures forming at half a spanwise wavelength apart (see Sec. 6.5.2.1). By $Re_x/10^5 \approx 7.5$, where mode $(0,0)$ reaches approximately 30%, the first row of hairpin vortices becomes visible, with small-scale structures at their legs. Farther downstream, the complete breakdown of the preceding 2-D billow roll-up becomes evident, characterised by near-wall longitudinal structures between $Re_x/10^5 \approx 7.5$ and 7.7.

In contrast, case Tw110-IA exhibits a delayed breakdown of each 2-D billow, as indicated by the extended near-wall separation zones. The onset of three-dimensionality is significantly delayed, consistent with the more gradual growth of 3-D modes in Fig. 6.10(d). Λ-like vortices emerge within the 2-D billow roll-ups, initially displaying an aligned peak–valley splitting, characteristic of the fundamental K-type breakdown (see Sec. 6.5.2.2). The Λ-

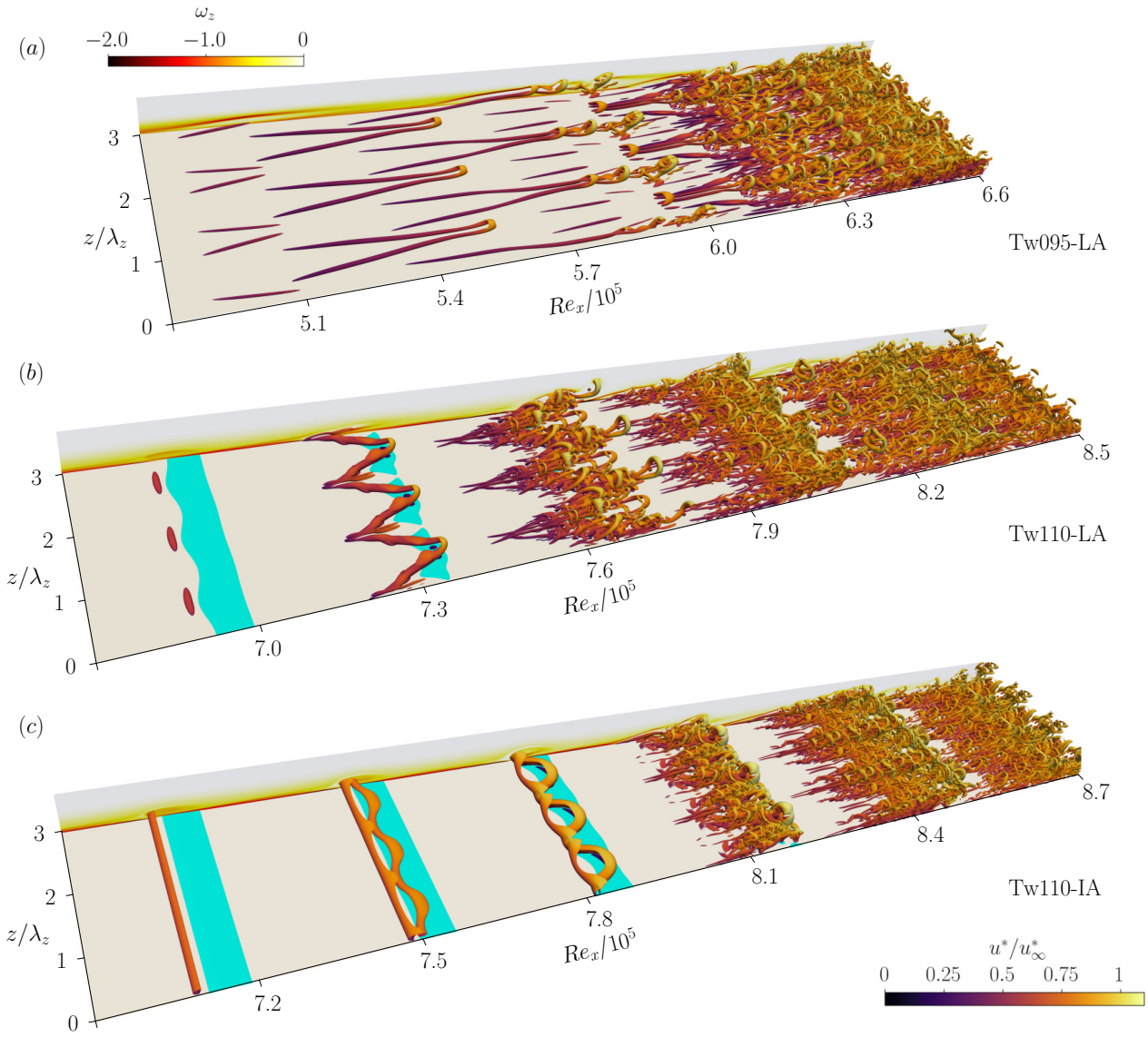

Figure 6.11: Instantaneous isosurfaces of the Q-criterion, coloured by the streamwise velocity magnitude: (a) case Tw095-LA (Q = 0.015) at t/T_0 = 0, (b) case Tw110-LA (Q = 0.020) at t/T_0 = 0.5, and (c) case Tw110-IA (Q = 0.020) at t/T_0 = 0.5. Here, T_0 is the period of the fundamental wave. The side xy-plane shows the instantaneous spanwise vorticity ω_z. Isosurfaces of the separation zones, i.e. regions with $u < 0$, are coloured in cyan. For better visualisation, the domain is copied twice in the spanwise direction. Supplementary movies are available at `https://github.com/pcboldini/DNSvisualisation`.

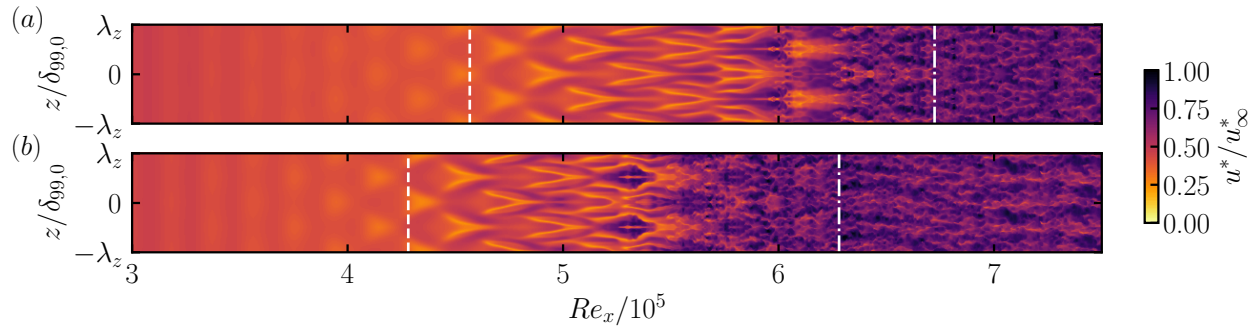

Figure 6.12: Contours of instantaneous streamwise velocity (xz-plane at $y/\delta_{99,0} = 0.49$): (a) Tw095-LA and (b) TadIG. The dashed and dash-dotted white vertical lines represent the locations of $C_{f,min} = \min\{C_f\}$ and $C_{f,max} = \max\{C_f\}$, respectively. For better visualisation, the domain is copied once in the spanwise direction.

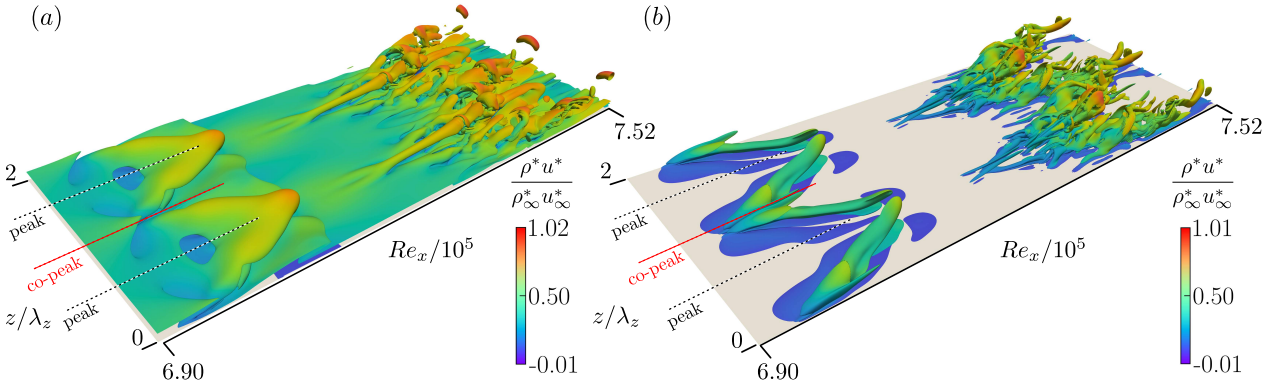

Figure 6.13: Case Tw110-LA. Instantaneous isosurfaces of (a) spanwise vorticity $|\omega_z| = 0.45$ and (b) streamwise vorticity $|\omega_x| = 0.45$, coloured by the streamwise momentum ρu magnitude at $t/T_0 = 0.5$. Here, T_0 is the period of the fundamental wave. For better visualisation, the domain is copied once in the spanwise direction.

vortices exhibit a shorter streamwise than spanwise wavelength, consistent with the large amplitude of mode $(2,1)$ in the early breakdown stage in Fig. 6.10(d). No strong lift-up of hairpin-like vortices is observed; however, near-wall longitudinal structures, resembling those in Tw110-LA, gradually emerge. Ultimately, each billow independently breaks into small-scale turbulent structures, eventually merging with the turbulent structures originating from the previous billow. From $Re_x/10^5 \approx 8.0$ onwards, as mode $(0,0)$ reaches an amplitude of $\sim$30%, the resulting turbulent flow pattern resembles that of Tw110-LA between $Re_x/10^5 \approx 7.5$ and 7.7, as shown in Fig. 6.11(b).

6.5.2.1 Case Tw110-LA: detailed breakdown analysis

Figure 6.13 shows close-up views of the initial breakdown region in case Tw110-LA ($6.90 \leq Re_x/10^5 \leq 7.52$), with isosurfaces of spanwise ω_z and streamwise ω_x vorticity in Figs. 6.13(a,b), respectively, at the same time instant as in Fig. 6.11(b). The visualisation spans two spanwise wavelengths to capture the full structure. The ω_z-distribution reveals a delta-wing-like shear

layer at $z = 0.5\lambda_z, 1.5\lambda_z, ...$ (dashed black lines), with peak spanwise vorticity at its tip. These structures, featuring round, slightly inclined heads, are aligned above the oppositely-signed ω_x-legs of the Λ-shaped vortex (Fig. 6.13b). At these locations, referred to hereafter as 'peak' locations, the strongest u' and ρ' perturbations occur with $u'_{rms} \approx 0.2$ and $\rho'_{rms} \approx 0.18$. This layer is hereafter referred to as the 'upper' high-shear layer and is denoted as 'UL'. Half a spanwise length apart, at $z = 0, \lambda_z, ...$ (dashed red line), u' and ρ', unlike in case Tw095-LA, do not decay but exhibit the second-largest r.m.s. amplitudes in the spanwise direction. This location is thus referred to hereafter as the 'co-peak'; cf. the ideal-gas APG case (Kloker 1993; Kloker & Fasel 1995; Kosorygin 1994). Here, the adjacent Λ-vortices are more closely spaced than in cases TadIG and Tw095-LA, consistent with a delta-wing-like topology (Kloker & Fasel 1995), and a secondary streamwise vortical structure develops between them.

The origin of the secondary vortex system is illustrated in Fig. 6.14, which shows instantaneous contours of ω_z in longitudinal planes (between $Re_x/10^5 = 6.90$ and 7.52) at five time steps ($t/T_0 = [0, 0.25, 0.5, 0.75, 1.0]$). At the 'co-peak' plane ($z/\lambda_z = 0$, Figs. 6.14a,c,e,g,i), a local maximum of ω_z forms near the wall, hereafter referred to as the 'inverted lower' high-shear layer and labelled as 'IL', resembling that of the ideal-gas APG case. Its origin is linked to the downstream-convected near-wall separation zone (highlighted in cyan) below the 2-D billow trough, which induces a local high-shear velocity profile (see Sec. 6.4.2 in Fig. 6.9a). This layer is unstable to 3-D perturbations (cf. stationary laminar separation bubble; Maucher *et al.* (2000)) due to strong near-wall u'-disturbances (see inset in Fig. 6.14c), which are transported downstream with the shear layer. Similar to the 2-D investigation (Fig. 6.9c), they correspond to a strong near-wall amplitude of mode $(1, 0)$ and its higher harmonics. Mode $(1/2, 1)$, which was absent in Sec. 6.4.2, reaches its peak at $y/\delta_{99,0} \approx 1$ (not shown). Over time, the 'inverted lower' layer evolves: its head is pushed towards the wall, while its leg is lifted upward (Fig. 6.14e). The secondary vortex system shown in Fig. 6.13(b) then develops above it, again reminiscent of the ideal-gas APG case. The two oppositely signed vortical structures transport low-velocity, low-density fluid upwards, as seen in the ρu-contours in Fig. 6.13(b). At later times (Figs. 6.14g and 6.14i), the 'inverted lower' layer merges with a second high-shear layer, crossing the entire boundary layer.

At $t/T_0 = 1$, the flow structures at the 'co-peak' location match those at the 'peak' location at $t/T_0 = 0$ in Fig. 6.14(b), indicating the staggered, periodic breakdown pattern of case Tw110-LA. The newly formed shear layer initially consists of two adjacent, streamwise-aligned, counter-rotating vortex filaments. As it becomes increasingly unstable in Figs. 6.14(b,d,f), it rolls up and breaks into small-scale structures (see the secondary vortex system at 'peak' locations near $Re_x/10^5 \approx 7.35$ in Fig. 6.13). Simultaneously, the 'upper' high-shear layer ('UL' in Figs. 6.14b,d,f), also destabilises and breaks up into numerous small vortical structures (Figs. 6.14h and 6.14j), generating an isolated hairpin-like vortex, captured by the ω_z-isocontours at $Re_x/10^5 \approx 7.5$ in Fig. 6.13(a). Note that the breakdown to turbulence is initiated by the earlier break-up of the 'inverted lower' layer at the 'co-peak' positions, which precedes the break-up of the 'upper' layer at the 'peak' positions. This sequence is also evident in Fig. 6.11(b), where near-wall turbulence triggered by the

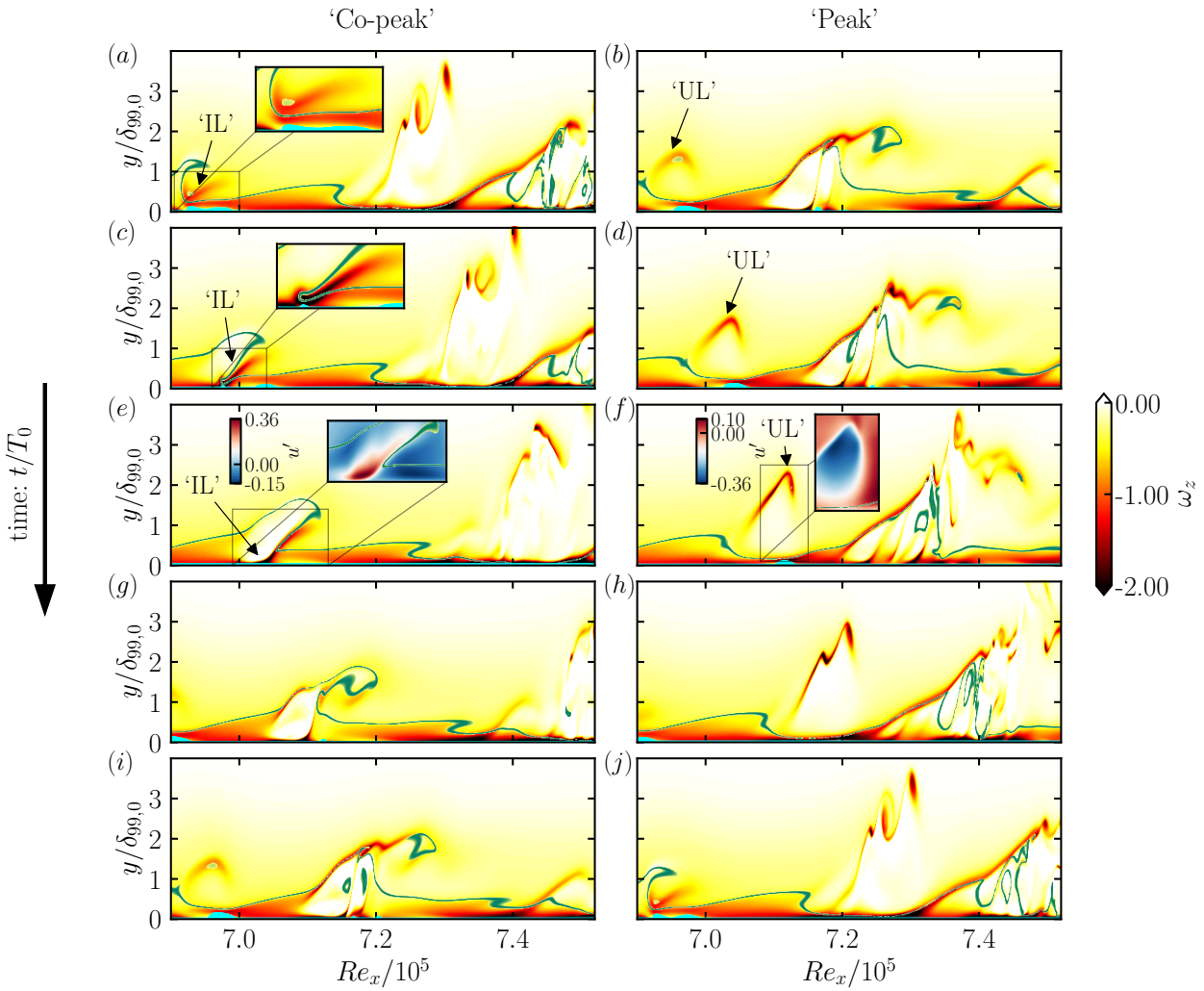

Figure 6.14: Case Tw110-LA. Instantaneous contours of spanwise vorticity ω_z in the Re_x–$y/\delta_{99,0}$ plane at: (a,b) $t/T_0 = 0$, (c,d) $t/T_0 = 0.25$, (e,f) $t/T_0 = 0.5$, (g,h) $t/T_0 = 0.75$, and (i,j) $t/T_0 = 1.0$. Here, T_0 is the period of the fundamental wave. The first column (a,c,e,g,i) corresponds to the spanwise 'co-peak' location at $z/\lambda_z = 0$ (see Fig. 6.13), while the second column in (b,d,f,h,j) corresponds to the spanwise 'peak' location at $z/\lambda_z = 0.5$ (see Fig. 6.13). The 'upper' and 'inverted lower' high-shear layers are labeled as 'UL' and 'IL', respectively. The near-wall region for which $u < 0$ is coloured in cyan. The Widom line $y = y_{WL}$ lies within the green region, i.e. between $95\% \max\{c_p\}$ and $\max\{c_p\}$.

'inverted lower' layer emerges significantly farther upstream than the small-scale structures in the boundary-layer core, which are caused by the break-up of the 'upper' layer.

6.5.2.2 Case Tw110-IA: detailed breakdown analysis

Figures 6.15(a,b) show isocontours of ω_z and ω_x for case Tw110-IA, respectively, at the same time step as in Fig. 6.11(c). The visualisation spans two spanwise wavelengths to capture the full structure. Unlike case Tw110-LA, mode $(1,0)$ retains a high amplitude over a longer streamwise distance, allowing the 2-D billow roll-ups to grow farther downstream, with intensified billow crests and larger near-wall separation zones. A key difference between

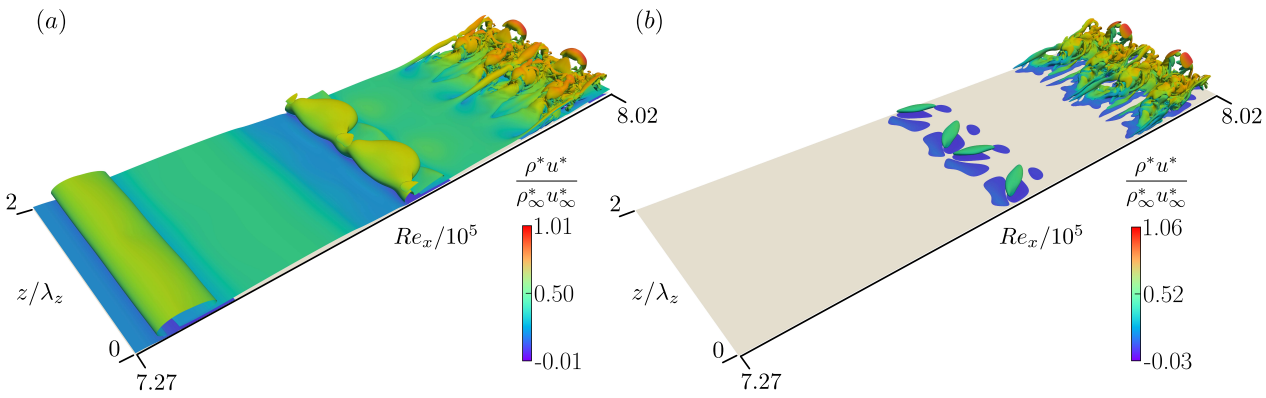

Figure 6.15: Case Tw110-IA. Instantaneous isosurfaces of (a) spanwise vorticity $|\omega_z| = 0.45$ and (b) streamwise vorticity $|\omega_x| = 0.45$, coloured by the streamwise momentum ρu magnitude at $t/T_0 = 0.5$. Here, T_0 is the period of the fundamental wave. For better visualisation, the domain is copied once in the spanwise direction.

Tw110-IA and Tw110-LA lies in the 3-D disturbance evolution during the breakdown. In the former, following the nonlinear amplification of 3-D modes, Λ-like vortices (see Fig. 6.15) form gradually inside each streamwise-convected 2-D billow roll-up. Unlike the abrupt, staggered onset in case Tw110-LA, these vortices emerge naturally in an aligned formation without the external forcing of modes $(0, 1)$ or $(1, \pm 1)$, cf. Rist & Fasel (1995). This development inside the single billow roll-up is highlighted in Fig. 6.16 between $t/T_0 = 0.5$ and $t/T_0 = 1.0$ ($7.42 \leq Re_x/10^5 \leq 7.79$). As the billow roll-up travels downstream, the separation zone at the spanwise 'peak' location weakens (see inset of Fig. 6.16b) due to the recirculation of high-velocity fluid towards the wall by the Λ-vortex legs. The rapid growth of the 3-D modes around $Re_x/10^5 \approx 7.6$ intensifies the 'upper' layers at the 'peak' locations ($z = 0.5\lambda_z, 1.5\lambda_z, ...$), which emerge from the billow crest. Meanwhile, the near-wall separation zones generate small, oppositely-signed longitudinal vortices (inset of Fig. 6.16c). At $t/T_0 = 1$, the spanwise 'peak' features an 'upper' high-shear Λ-shaped layer (see $|\omega_z|$ = const.-contours in Fig. 6.16e), which enhances the spanwise flow modulation, while its legs are pushed closer to the wall, giving rise to regions of high ω_z and additional secondary vortical structures; cf. Rist & Fasel (1995). This 'upper' layer is analogous to that of case Tw110-LA in Fig. 6.14. Upstream, the 'inverted lower' layer develops inside the boundary layer in a manner analogous to that observed in case Tw110-LA, transforming the initial 'peak'–'valley' splitting into a 'peak'–'co-peak' breakdown scenario. This high-shear layer originates at the trough of the billow roll-up and generates strong secondary low-density co-rotating vortices at the intermediate spanwise 'co-peak' locations (Figs. 6.16g,h), which travel faster than the flow in the near-wall region of the spanwise 'peak'. These longitudinal structures, visible in Fig. 6.15 around $Re_x/10^5 \approx 7.8$, break up earlier than the far-wall hairpin-like vortices, and contribute to the formation of turbulent structures also at the spanwise 'co-peak' locations.

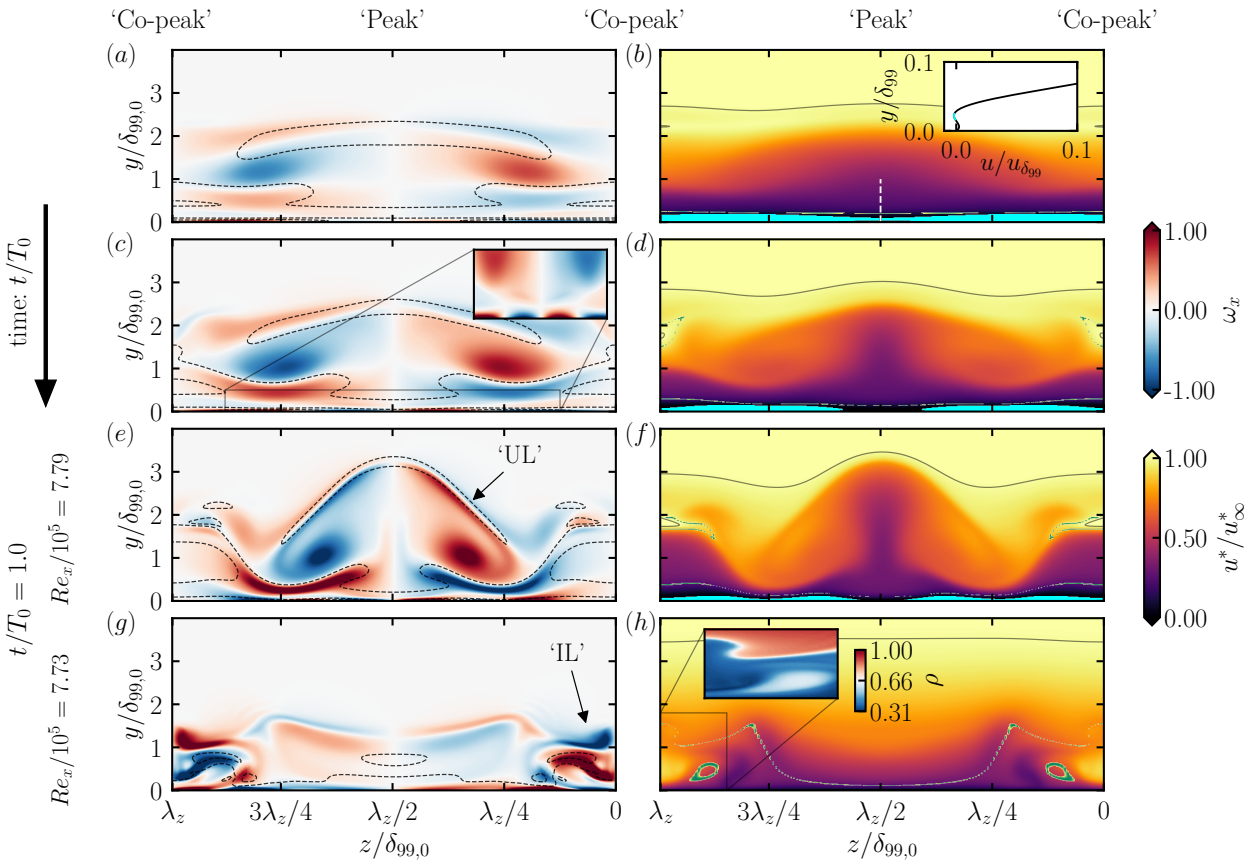

Figure 6.16: Case Tw110-IA. Instantaneous contours of streamwise vorticity ω_x and velocity u^*/u^*_∞ in the $z/\delta_{99,0}$-$y/\delta_{99,0}$ plane at (a,b) $t/T_0 = 0.5$ ($Re_x/10^5 = 7.62$), (c,d) $t/T_0 = 0.75$ ($Re_x/10^5 = 7.70$), and (e–h) $t/T_0 = 1.0$. T_0 is the period of the fundamental wave. The dashed black line in (a,c,e,g) indicates contours of $|\omega_z| = 0.45$, while the black line in (b,d,f,h) corresponds to δ_{99}. The 'upper' and 'inverted lower' high-shear layers are labeled as 'UL' and 'IL', respectively. The near-wall region for which $u < 0$ is coloured in cyan. The Widom line $y = y_{WL}$ lies within the green region, i.e. between $95\% \max\{c_p\}$ and $\max\{c_p\}$.

6.5.3 Integral quantities

To illustrate the transition process, Fig. 6.17 presents isocontours of time- and spanwise-averaged streamwise velocity and density. The velocity profiles in Figs. 6.17(a,b) illustrate the transition to turbulence for cases Tw095-LA and Tw110-LA, respectively. In the latter, the near-wall separation zones are absent, as they are convected downstream and disappear on average. In the turbulent regime, the velocity and density profiles of both cases become qualitatively similar, regardless of whether the fluid is weakly or strongly non-ideal. In the strongly non-ideal case Tw110-LA, after transition to turbulence, the Widom line (coloured in green in Fig. 6.17d) shifts significantly closer to the wall, considerably reducing the height of the vapour-like region compared with the laminar regime. The implications of this shift on the turbulent boundary layer are discussed in Sec. 6.6.

To quantitatively characterise the transitional boundary layers following the qualitative analysis in Sec. 6.5.2, the streamwise evolution of the time- and spanwise-averaged skin-

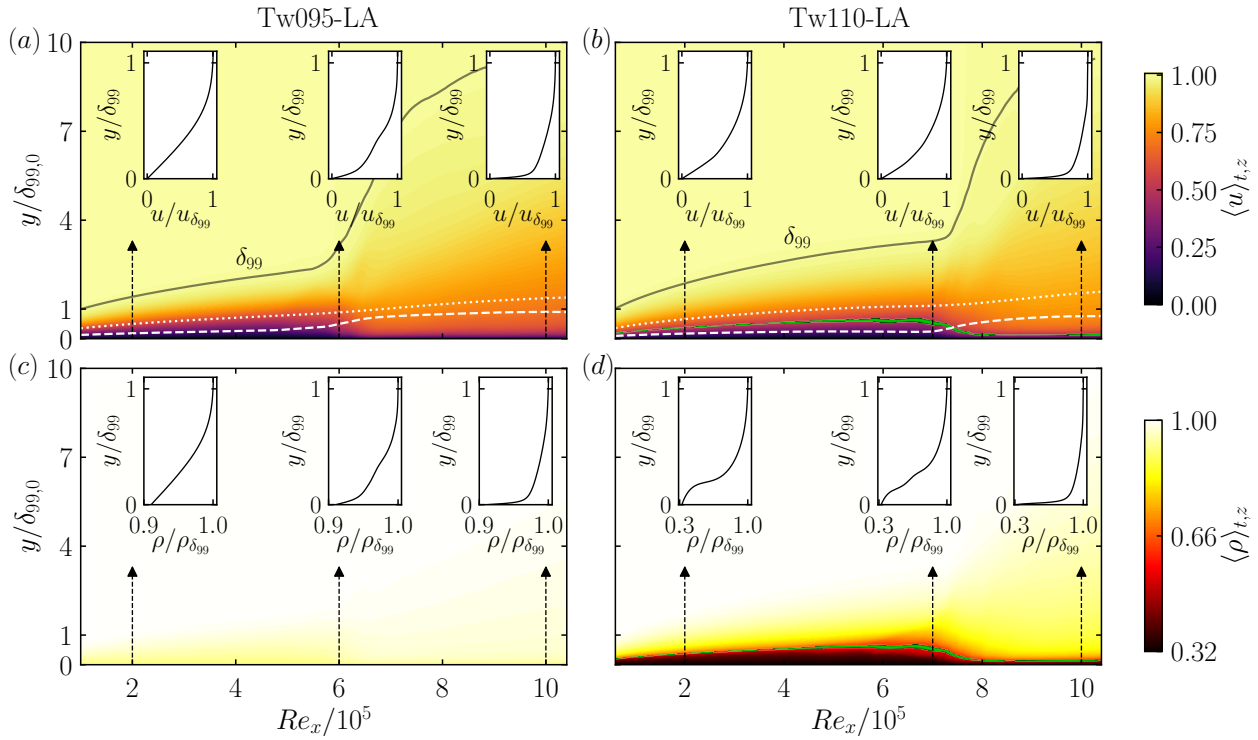

Figure 6.17: Contours of the time- and spanwise-averaged (a,b) streamwise velocity $\langle u \rangle_{t,z}$ and (c,d) density $\langle \rho \rangle_{t,z}$ for (a,c) case Tw095-LA and (b,d) case Tw110-LA. In (a,b), the displacement thickness δ_1 and momentum thickness θ are indicated by a white dotted and dashed lines, respectively. Insets in (a,b) show selected streamwise velocity profiles normalised by the corresponding $u(\delta_{99}) = 0.99$. The insets in (c,d) depict selected density profiles normalised by the corresponding $\rho(\delta_{99})$. In (b) and (d), the Widom line $y = y_{WL}$ lies within the green-shaded region, i.e. between $95\% \max\{c_p\}$ and $\max\{c_p\}$.

friction coefficient C_f and the Stanton number St is examined. These quantities are defined in dimensionless form as

$$C_f = \frac{\overline{\tau}^*_w}{0.5\rho^*_\infty u^{*2}_\infty} = \frac{2\overline{\tau}_w}{Re}, \quad St = \frac{\overline{q}^*_w}{\rho^*_\infty u^*_\infty (h^*_{aw} - h^*_w)} = \frac{\overline{q}_w}{RePr_\infty Ec_\infty (h_{aw} - h_w)}, \tag{6.1a,b}$$

where the non-dimensional characteristic parameters are defined in Eqs. (2.8*a–d*). The adiabatic wall enthalpy, $h^*_{aw} = h^*_\infty + ru^{*2}_\infty/2$, where the recovery factor $r = (h_{aw} - h_\infty)/(h_0 - h_\infty)$ (h_0 is the total enthalpy) is given as $Pr^{1/3}_\infty = 1$ (White 2006), can be expressed in reduced form as $h_{r,aw} = h_{r,\infty} + rM^2_\infty a^2_{r,\infty}/2$, where the free-stream reduced enthalpy is defined as $h_{r,\infty} = e_{r,\infty} + p_{r,\infty}/\rho_{r,\infty}$. It is important to note that the assumption $r \approx 1$ has been verified in the laminar boundary layer under transcritical conditions (not shown). Figures 6.18(a,b) show the streamwise evolutions of C_f and St, respectively, for all cases in Tab. 6.2. The theoretical laminar curves, $C_{f,lam.}$ and $St_{lam.}$, for a non-ideal fluid are derived from Eq. (6.1*a,b*) using the self-similar Lees–Dorodnitsyn variables as

$$C_{f,lam.} = \frac{\sqrt{2}C_w}{Re}\left.\frac{\partial u}{\partial \eta}\right|_w, \quad St_{lam.} = \frac{1}{\sqrt{2}ReEc_\infty(h_{aw} - h_w)}\frac{C_w\, c_{p,r,w}}{Pr_w\, c_{p,r,\infty}}\left.\frac{\partial T}{\partial \eta}\right|_w, \tag{6.2a,b}$$

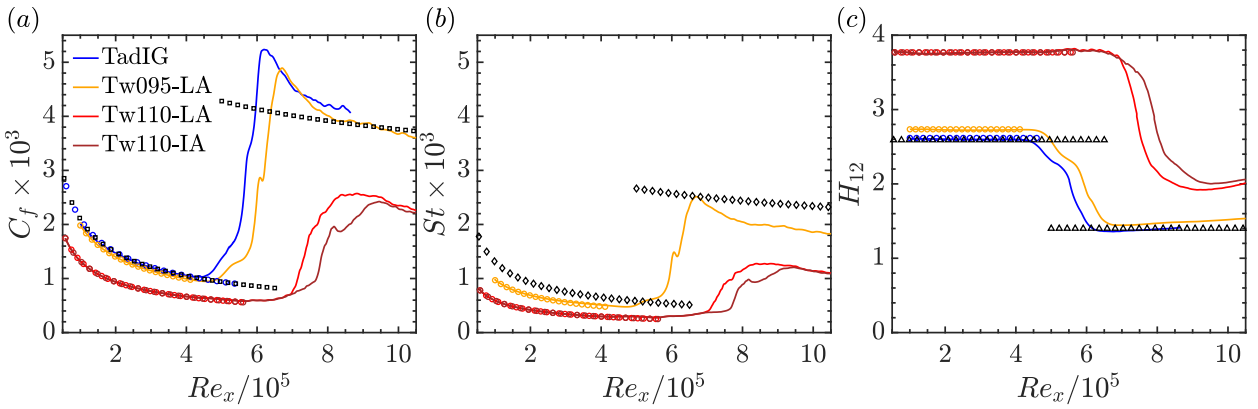

Figure 6.18: Time- and spanwise-averaged: (a) skin-friction coefficient C_f, (b) Stanton number St, and (c) shape factor H_{12}, as functions of Re_x. Solid lines denote DNS results, while circle (∘) symbols represent the self-similar laminar correlations from Eq. (6.2*a*,*b*) with initial conditions as in Sec. 6.3.1. In (a,b), the theoretical incompressible skin-friction coefficient and the theoretical incompressible Stanton number using the Reynolds analogy $St = 0.5 C_f Pr_\infty^{-2/3}$ are represented by square (▫) and diamond (⋄) black symbols, respectively (White 2006). Note that for TadIG, $St = 0$ due to adiabatic wall conditions. In (c), the theoretical incompressible shape factor is indicated with triangle (▵) black symbols (White 2006).

where $\partial u/\partial\eta|_w$ and $\partial T/\partial\eta|_w$ are the wall-normal gradients of the laminar streamwise velocity and temperature in Fig. 6.2, respectively, and $C_w = \rho_w\mu_w$ is the Chapman-Rubesin parameter at the wall. In contrast, turbulent correlations for non-ideal wall-bounded flows are not yet available. An estimation is presented in Sec. 6.6, where we introduce an accurate estimation solver.

The skin-friction and Stanton-number curves initially follow the laminar trend in all cases. In Tw095-LA, both $\partial u/\partial\eta|_w$ and C_w in Eqs. (6.2*a*,*b*) resemble the ideal-gas case, resulting in a $C_{f,lam.}$ distribution that closely matches the ideal-gas case. In contrast, for both Tw110-LA and Tw110-IA, despite a fuller laminar velocity profile, C_w is significantly below unity due to density and viscosity stratification. Thus, $C_{f,lam.}^{\mathrm{Tw110}} < C_{f,lam.}^{\mathrm{Tw095}}$. A similar trend holds for St in Fig. 6.18(b). In Tw095-LA, St closely matches the incompressible limit, i.e. $St = 0.332 Pr^{-2/3}/Re$. In Tw110-LA and Tw110-IA, the enthalpy difference $(h_{aw} - h_w)$ is significantly larger, yielding $St_{lam.}^{\mathrm{Tw110}} < St_{lam.}^{\mathrm{Tw095}}$.

In Tw095-LA, transition begins as mode $(1/2, 1)$ overtakes $(1, 0)$ and its amplitude exceeds 1%. Between $Re_x/10^5 \approx 5.3$ and 6.0 coinciding with the saturation of $(1/2, 1)$ and other 3-D modes, both C_f and St level off as elongated Λ-vortices become the predominant flow structures. At $Re_x/10^5 \approx 6.0$, a sharp rise in C_f and St is observed, as the amplification of modes $(1/2, 1)$, $(0, 2)$, and higher 3-D modes leads to strong MFD and the roll-up of the Λ-vortices into hairpin vortices that evolve into ring-like structures. Consequently, both C_f and St overshoot, consistent with the ideal-gas case TadIG.

In Tw110-LA and Tw110-IA, transition is delayed. The C_f and St curves begin to deviate from the laminar predictions around $Re_x/10^5 \approx 5.7$, following the subharmonic resonance of modes $(1, 0)$ and $(2, 0)$ and the appearance of near-wall separation zones. However, these

separation zones are convected downstream such that the average C_f remains positive, unlike a classic laminar separation bubble, where a negative C_f is observed due to a larger, steady separation zone (Alam & Sandham 2000). The C_f and St curves for cases Tw110-LA and Tw110-IA remain identical up to $Re_x/10^5 \approx 6.9$, beyond which Tw110-LA exhibits a rapid rise in C_f due to the abrupt amplification of 3-D disturbances. In contrast, Tw110-IA shows a sharp increase in both C_f and St only at $Re_x/10^5 \approx 7.65$, followed by a kink in their evolutions around $Re_x/10^5 \approx 8.2$, associated with the strong saturation of the steady modes $(0,1)$ and $(0,2)$. Qualitatively, the minor decrease in C_f and St corresponds to the region between the break-up of two spanwise rollers, where no prominent vortical structures are observed (see Fig. 6.11(c) between $Re_x/10^5 \approx 8.0$ and 8.1). Further downstream, the distributions of both transcritical cases gradually level off without a pronounced overshoot. Although mode $(0,0)$, representing the wall-normal amplitude maximum, is approximately as large as in the subcritical case, the longitudinal vortex mode $(0,2)$ is significantly smaller, and no distinct overshoot appears. Accordingly, the reduction in C_f and St is more pronounced in the turbulent regime than in the laminar region, when compared to the subcritical case. The contribution of $\overline{\mu' \partial u'/\partial y|_w}$ to the wall shear stress $\overline{\tau}_w$ is found to be negligible. Despite different initial forcings, the C_f and St curves of Tw110-LA and Tw110-IA converge as expected towards the same turbulent values.

The streamwise development of the shape factor $H_{12} = \delta_1/\theta$, where $\delta_1 = \int_0^\infty (1-\rho u)\,\mathrm{d}y$ is the displacement thickness and $\theta = \int_0^\infty (\rho u)(1-u)\,\mathrm{d}y$ is the momentum thickness, is shown in Fig. 6.18(c). In the transcritical cases, the increase of H_{12} ($H_{12} \approx 3.76$) in the laminar boundary layer is driven by a significant rise in δ_1, caused by the reduction in streamwise momentum ρu in the near-wall vapour-like state, and a decrease in θ resulting from the fuller velocity profile compared to the subcritical case. Before H_{12} drops to approximately 2.0, primarily due to the sharp rise in the turbulent θ-value (see Fig. 6.17b), it exhibits minor oscillations between $Re_x/10^5 \approx 5.0$ and 6.0, attributed to the localised increase and decrease in δ_1 over the near-wall separation zones.

6.6 Turbulent boundary layer

After breakdown, we apply mean-flow scaling theories to the turbulent boundary layers in the subcritical case Tw095-LA and the transcritical case Tw110-LA (see Tab. 6.1). Specifically, we examine whether the velocity profiles, after transformation, collapse onto the velocity profile of a constant-property boundary layer. If such a collapse is observed, then the transformed profiles will be used to estimate the turbulent skin-friction coefficient C_f and Stanton number St, to assess whether these parameters can be predicted for fluids at supercritical pressure.

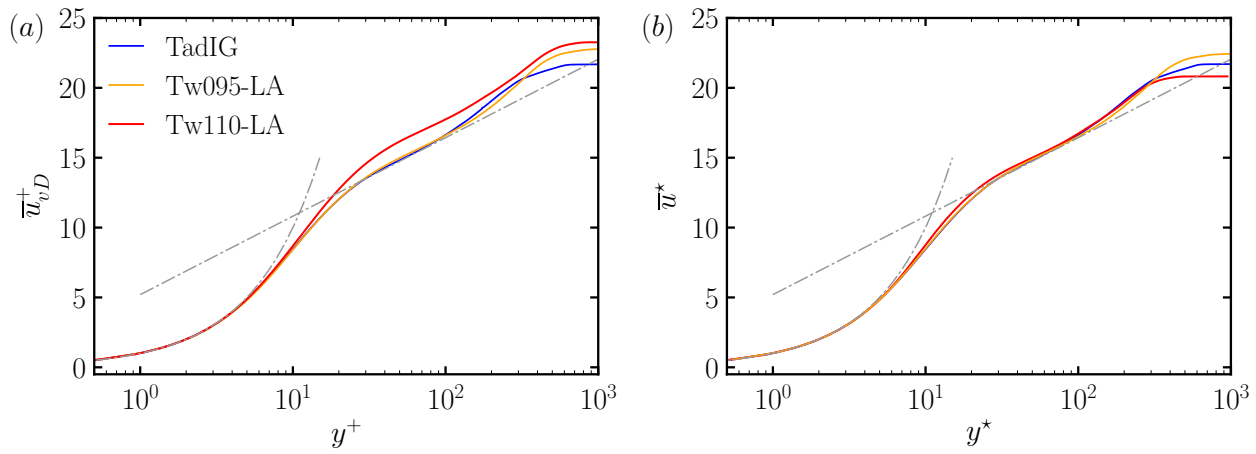

Figure 6.19: Wall-normal profiles of the transformed streamwise velocity using (a) van Driest (1951) and (b) Patel *et al.* (2016). Cases Tw095-LA and Tw110-LA are shown in orange at $Re_\theta = 1387$ ($Re_x = 1.0{\cdot}10^6$) and in red at $Re_\theta = 881$ ($Re_x = 1.06{\cdot}10^6$), respectively. Grey dash-dotted lines denote the linear and logarithmic laws ((a): $(1/\kappa)\log y^+ + C$, (b): $(1/\kappa)\log y^\star + C$) with $\kappa = 0.41$ and $C = 5.2$. Blue shows the ideal-gas case TadIG at $Re_\theta = 1190$ ($Re_x = 0.8{\cdot}10^6$).

6.6.1 Mean velocity and enthalpy–velocity transformations

We consider the transformation proposed by Patel *et al.* (2016) and Trettel & Larsson (2016), which extends the van Driest (1951) velocity transformation (subscript $(\cdot)_{vD}$) defined as $\overline{u}^+_{vD} = \int_0^{\overline{u}^+} \sqrt{\overline{\rho}/\overline{\rho}_w}\,\mathrm{d}\overline{u}^+$, by accounting for spatial variations in the viscous length scale $\delta_v^\star$ in the near-wall region. It is formulated as

$$\overline{u}^\star = \int_0^{\overline{u}^+} \left(1 - \frac{y}{\delta_v^\star}\frac{\mathrm{d}\delta_v^\star}{\mathrm{d}y}\right) \underbrace{\frac{u_\tau}{u_\tau^\star}\,\mathrm{d}\overline{u}^+}_{\mathrm{d}\overline{u}^+_{vD}}, \tag{6.3}$$

where the superscripts $(\cdot)^+$ and $(\cdot)^\star$ indicate non-dimensionalisation by the viscous length scale δ_v and friction velocity u_τ (as defined in Appendix C.1), and by the semi-local viscous length scale $\delta_v^\star = \overline{\mu}/(\overline{\rho}u_\tau^\star)$ and semi-local friction velocity $u_\tau^\star = \sqrt{\overline{\tau}_w/\overline{\rho}}$, respectively. The Reynolds (time and spanwise) average of a given variable χ is expressed as $\overline{\chi} = \chi - \chi'$, with χ' denoting the corresponding fluctuation. It is worth noting that the semi-local Mach number $M_\tau = u_\tau/\overline{a}_w$ remains much smaller than unity across the entire domain (with a maximum value of 0.025). Therefore, the transformation recently proposed by Hasan *et al.* (2023), which extends Eq. (6.3) to account for intrinsic compressibility effects, would yield results equivalent to $\overline{u}^\star$.

Figures 6.19(a,b) show the transformed Reynolds-averaged mean velocity profiles for $\overline{u}^+_{vD}$ and $\overline{u}^\star$ on logarithmic scales of y^+ and $y^\star$, respectively. The turbulent profiles are extracted near the end of the computational domains to ensure well-developed turbulent boundary layers: for Tw095-LA at $Re_\theta = 1387$ ($Re_x = 1.0 \cdot 10^6$), for Tw110-LA at $Re_\theta = 881$ ($Re_x = 1.06 \cdot 10^6$), and for TadIG at $Re_\theta = 1190$ ($Re_x = 0.8 \cdot 10^6$). As expected, both velocity transformations of the subcritical case Tw095-LA show good collapse with the velocity of the constant-property turbulent boundary layer (case TadIG), due to the low variation of

thermophysical properties across the boundary layer. In contrast, the van Driest (1951) scaling shows a large offset in the logarithmic region for the transcritical case Tw110-LA. For this case, the large near-wall variation of the viscous length scale must be taken into account. With this correction, Eq. (6.3) clearly improves the collapse with the constant-property boundary layer (see Fig. 6.19b).

Contrary to the findings of Kawai (2019), this collapse is achieved for the following reasons: in case Tw110-LA, the wall-normal velocity in the boundary layer remains relatively small, with $\overline{v}/u_\infty \approx 0.2\%$. Furthermore, the density and viscosity fluctuations, which peak in the buffer layer, are moderate, of the order of $\sqrt{\overline{\rho'\rho'}}/\overline{\rho}$ and $\sqrt{\overline{\mu'\mu'}}/\overline{\mu} \approx 0.3$, respectively. By contrast, in the transcritical case investigated by Kawai (2019) at a higher reduced pressure ($p_r \approx 1.28$) but significantly larger wall-to-free-stream temperature ratios ($T_w^*/T_\infty^* \approx 4$–$8$), the wall-normal velocity reached approximately 1.5%, while the density and viscosity fluctuations reached $\sqrt{\overline{\rho'\rho'}}/\overline{\rho} \approx 1.0$, and $\sqrt{\overline{\mu'\mu'}}/\overline{\mu} \approx 0.4$, particularly in the logarithmic layer. These strong fluctuations led to large near-wall convective flux and an overshoot of the Reynolds shear stress surpassing unity in the logarithmic region, ultimately causing the failure of the velocity transformation. In our case, however, the total stress balance, on which the Patel *et al.* (2016) transformation relies, is still mainly governed by the viscous and turbulent stresses under transcritical conditions. Overall, the transformed velocity profiles indicate that the flow has transitioned into the fully turbulent regime by the end of the computational domain.

Next, we focus on estimating the mean thermodynamic properties to develop a predictive model for C_f and St, which remains unknown for turbulent boundary layers with highly non-ideal fluids. One possible approach is to directly integrate the total heat flux from the wall to the free stream to reconstruct the temperature field. However, this method is cumbersome, as it requires an iterative procedure on the heat flux to match the prescribed wall-to-free-stream temperature ratio, combined with a turbulence model that itself depends on the velocity field as well as the density- and temperature-dependent thermodynamic properties. As a more practical alternative, we examine the mean temperature–velocity correlations, which offer a simpler route. When non-ideal-gas effects become significant, enthalpy-based relations must be employed, as enthalpy is no longer a linear function of T but instead depends on another thermodynamic property. Furthermore, classical enthalpy-based relations such as Crocco–Busemann (Smits & Dussauge 2006), or the relations of Walz (1969) and Duan & Martín (2011), assume a constant mixed Prandtl number Pr_m ($Pr_m = 1$ in Crocco–Busemann), defined as

$$Pr_m = \frac{(\overline{\mu} + \mu_t)\overline{c}_p}{\overline{\kappa} + \kappa_t}, \quad \text{with: } \mu_t = \frac{-\overline{\rho}\widetilde{u''v''}}{\partial\widetilde{u}/\partial y} \text{ and } \kappa_t = \frac{-\overline{c}_p\overline{\rho}\widetilde{v''T''}}{\partial\widetilde{T}/\partial y}, \tag{6.4}$$

where μ_t and κ_t are the eddy viscosity and eddy conductivity, respectively. Note that $\widetilde{\chi} = \overline{\rho\chi}/\overline{\rho}$ denotes the Favre average, with χ'' as the Favre fluctuation.

The mixed Prandtl number Pr_m, turbulent Prandtl number $Pr_t = \mu_t\overline{c}_p/\kappa_t$, and molecular Prandtl number $\overline{Pr}$ are plotted in Figs. 6.20(a–c), respectively, for the subcritical and transcritical cases. In case Tw095-LA, the mixed Prandtl number remains approximately constant and close to unity across the boundary layer ($Pr_{m,w} \approx 1.06$), despite the turbulent

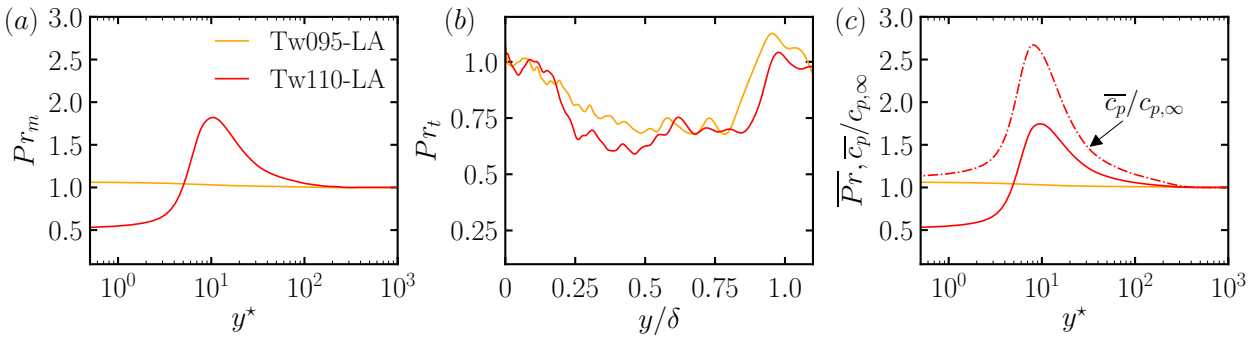

Figure 6.20: Case Tw095-LA (Re_θ = 1387) in orange and Tw110-LA (Re_θ = 881) in red: (a) mixed Prandtl number Pr_m, (b) turbulent Prandtl number Pr_t, and (c) mean molecular Prandtl number $\overline{Pr}$ and $\overline{c}_p/c_{p,\infty}$ (red dash-dotted line) for case Tw110-LA.

Prandtl number decreasing to approximately 0.7 in the outer region (see Fig. 6.20b). The evolution of Pr_m confirms the assumption underlying the aforementioned enthalpy-based relations with a constant Prandtl number. Under transcritical conditions, however, Pr_m deviates from unity in the logarithmic region, reaching 1.84 in the buffer layer before dropping below unity in the viscous sub-layer ($Pr_{m,w} \approx 0.51$). Observing the mean molecular Prandtl number $\overline{Pr}$ in Fig. 6.20(c), its behaviour shows that the evolution of the Pr_m is dominated by molecular diffusion. The strong increase and subsequent decrease of Pr_m towards the wall are proportional to the variation of $\overline{c}_p$, indicating that the Widom line is predominantly located in the buffer layer in the turbulent regime. In contrast, the turbulent Prandtl number moderately decreases from unity in the near-wall region to approximately 0.6.

To address the variable Pr_m in the highly non-ideal case Tw110-LA, we consider the variable-Prandtl-number theory of van Driest (1955). For a turbulent boundary layer in mean steady state over a ZPG flat plate, it holds that

$$\left(\frac{\bar{i}'}{Pr_m}\right)' + (1 - Pr_m)\,\frac{\tau'}{\tau}\left(\frac{\bar{i}'}{Pr_m}\right) = -\frac{u_\infty^2}{h_\infty}, \tag{6.5}$$

where $\bar{i} = \overline{h}/h_\infty$ is the mean enthalpy ratio, τ is the total shear stress, and the superscript $(\cdot)'$ indicates differentiation with respect to $\overline{u}_r = \overline{u}/u_\infty$. Integrating Eq. (6.5) yields

$$\bar{i} = \frac{h_w}{h_\infty} - \frac{\mathcal{S}}{\mathcal{S}_\infty}\left(\frac{h_w}{h_\infty} - 1\right) + \frac{u_\infty^2}{h_\infty}\left[\frac{\mathcal{S}}{\mathcal{S}_\infty}\mathcal{R}_\infty - \mathcal{R}\right], \tag{6.6}$$

where the functions $\mathcal{S}$ and $\mathcal{R}$ are defined as:

$$\mathcal{S} = \int_0^{\overline{u}_r} Pr_m \cdot \exp\left[-\int_{\tau_w}^{\tau} \frac{(1 - Pr_m)}{\tau}\mathrm{d}\tau\right]\mathrm{d}\overline{u}_r,$$

$$\mathcal{R} = \int_0^{\overline{u}_r} Pr_m \cdot \exp\left[-\int_{\tau_w}^{\tau} \frac{(1 - Pr_m)}{\tau}\mathrm{d}\tau\right]\left\{\int_0^{\overline{u}_r} \exp\left(\int_{\tau_w}^{\tau} \frac{(1 - Pr_m)}{\tau}\mathrm{d}\tau\right)\mathrm{d}\overline{u}_r\right\}\mathrm{d}\overline{u}_r. \tag{6.7a,b}$$

Note that for $Pr_m = 1$ and $Pr_m = \text{const.}$, the classical relations of Crocco–Busemann (Smits & Dussauge 2006) and Walz (1969) are recovered, respectively.

Figures 6.21(a,b) compare Eq. (6.6) against DNS data for the heated case Tw095-LA (T_w^*/T_∞^* = 1.056) and Tw110-LA (T_w^*/T_∞^* = 1.222), respectively. For the subcritical case, the

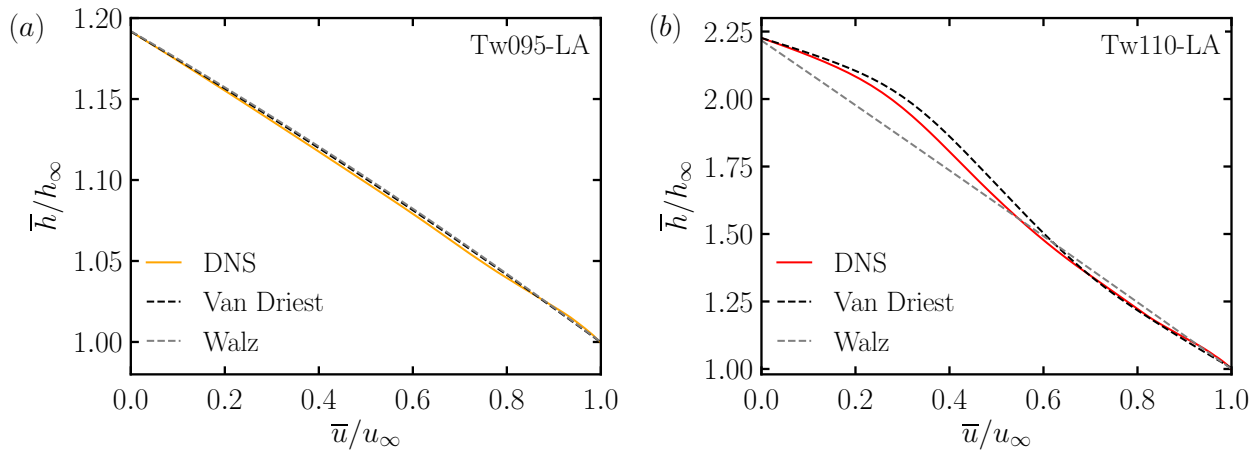

Figure 6.21: Reynolds-averaged mean enthalpy from the variable-Prandtl theory of van Driest (1955) in black for (a) Tw095-LA at $Re_\theta = 1387$ (DNS profile in orange) and (b) Tw110-LA at $Re_\theta = 881$ (DNS profile in red). In grey is shown the relation of Walz (1969) as $\overline{h}/h_\infty = h_w/h_\infty + (h_{aw} - h_w)(\overline{u}/u_\infty)/h_\infty - r u_\infty^2 (\overline{u}/u_\infty)^2/(2h_\infty)$.

van Driest relation accurately predicts $\overline{h}/h_\infty$ and aligns with the Walz relation as $Pr_m \approx$ const. However, for the highly non-ideal fluid with strongly varying mixed Prandtl number, as seen in Fig. 6.20(a), the Walz's relation becomes particularly inaccurate in the inner layer. From $\overline{u}/u_\infty \approx 0.6$, or $y^\star \approx 20$, the enthalpy undergoes a significant increase, which only the van Driest relation is able to capture in good agreement with the DNS data.

6.6.2 Estimating mean profiles and fluxes

We now follow the approach of Hasan *et al.* (2024) to predict the drag and heat transfer and compare the results to the available DNS data (see Fig. 6.18). In this approach, the mean shear is integrated from the wall to the free stream to obtain the streamwise velocity, using a combination of inner- and outer-layer modelling approximations. The inner-layer eddy viscosity is modelled using the Johnson–King mixing-length formulation (Johnson & King 1985), accounting for variations in viscous length and velocity scales, while the outer layer is described by Coles' law of the wake (Coles 1956), modified to include mean density variations. The corresponding thermodynamic properties, e.g. ρ, T, μ, κ, and Pr, are computed using the VdW EoS, under the assumption of constant thermodynamic pressure, and the JST model, with both expressed as functions of the enthalpy obtained via van Driest variable-Prandtl theory. Note that two additional assumptions are made: (i) $Pr_m \approx \overline{Pr}$ (compare Figs. 6.20a,c), and (ii) the shear distribution follows van Driest (1955), i.e. $\tau/\tau_w \approx 1 - \exp[-\kappa/\sqrt{C_f/2}(1 - \overline{u}_r)]$, with $\kappa = 0.41$ as the von Kármán constant. For further details on the analytical solver, refer to the source code available on GitHub (`https://github.com/pcboldini/DragAndHeatTransferEstimation_NonIdealFluids`).

Figure 6.22 presents the predicted temperature, density, viscosity, and velocity profiles from the analytical solver ('Estimation') compared with the DNS profiles for cases Tw095-LA and Tw110-LA. In the subcritical case, the estimated profiles are in very good agreement

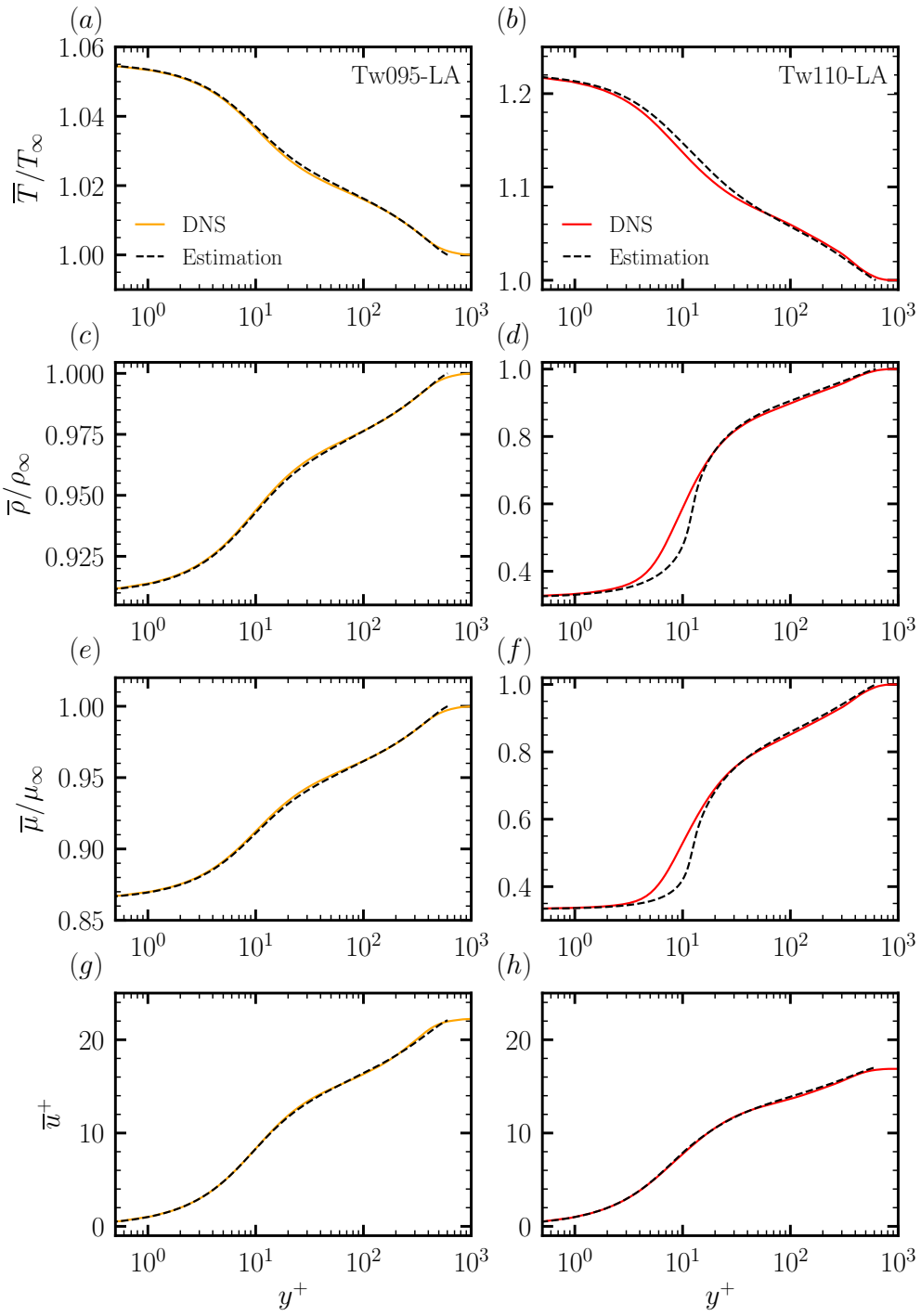

Figure 6.22: Estimated mean (a,b) temperature $\overline{T}/T_\infty$, (c,d) density $\overline{\rho}/\rho_\infty$, (e,f) viscosity $\overline{\mu}/\mu_\infty$, and (g,h) streamwise velocity $\overline{u}^+$ profiles (dashed grey lines) compared to DNS results (solid lines, case Tw095-LA ($Re_\theta = 1387$) in orange, and case Tw110-LA ($Re_\theta = 881$) in red).

with the DNS solution. In the transcritical case, the temperature profile in Fig. 6.22(b) shows minimal deviations in the buffer layer but successfully approximates the wall heat flux $\overline{q}_w$. The estimated profiles for density (Fig. 6.22d) and viscosity (Fig. 6.22f) differ significantly only in the buffer layer, where the largest discrepancies in $\overline{h}$ are observed. Note that Jensen's inequality, i.e. $\overline{\chi} \neq \chi(\overline{h}, \overline{p})$, applies to these thermophysical quantities (Nemati *et al.* 2015), due to their sharp curvature around the pseudo-critical point, i.e. $\max\{c_p\}$, and their large

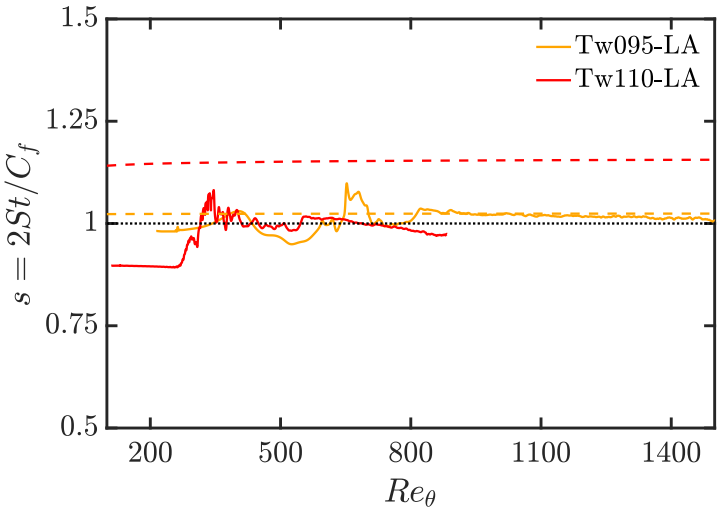

Figure 6.23: Reynolds analogy factor $s = 2St/C_f$ as a function of the momentum-thickness Reynolds number Re_θ: case Tw095-LA (orange) and Tw110-LA (red). Solid lines correspond to the DNS results, while dashed lines represent the turbulent Reynolds analogy factor, $s = \mathcal{S}_\infty$, according to the variable-Prandtl theory of van Driest (1955). The Reynolds analogy is indicated by a black dotted line.

fluctuations present specifically in the buffer layer. Conversely, the estimated velocity profile agrees very well with the DNS solution, as it results from integration across both inner and outer layers.

Before addressing the prediction of the skin-friction coefficient and Stanton number, we first examine the Reynolds analogy, which relates skin friction and heat transfer. Using the Reynolds analogy factor, $s = 2St/C_f = \overline{q}^*_w u^*_\infty/(\overline{\tau}^*_w(h^*_{aw}-h^*_w))$, we investigate how non-ideal-gas effects may disrupt the classical coupling between momentum and thermal transport. The impact of the Reynolds analogy is shown in Fig. 6.23. In the laminar boundary layer, strong property variations in the transcritical state reduce the Reynolds analogy factor below unity ($s \approx 0.89$). In the transitional region, the value of s rises above unity in both thermodynamic states due to the gradual development of turbulent structures. Interestingly, s appears largely insensitive to the degree of fluid non-ideality in the turbulent boundary layer. Here, the Reynolds analogy holds in both thermodynamic states, with $s \approx 1$. The behaviour aligns with trends observed in ideal-gas turbulent boundary layers, where s was found to be unaffected by variations in wall temperature and Mach number (Wenzel *et al.* 2021). Nevertheless, a more comprehensive investigation over a broader Reynolds-number range would be needed to extend the applicability of these results to other non-ideal fluid flows. Note that the turbulent Reynolds analogy factor, calculated according to the variable-Prandtl theory of van Driest (1955) in Eq. (6.5), with $s = \mathcal{S}_\infty$, follows the DNS results only in the subcritical state. In the transcritical state, larger deviations in the estimation of τ are observed.

In Figs. 6.24(a,b), the DNS and estimated values of the skin-friction coefficient, C_f, and Stanton number, St, are plotted as functions of Re_θ. The predictions of C_f show good agreement with the DNS curves beyond the respective overshoots. Moreover, the less pronounced

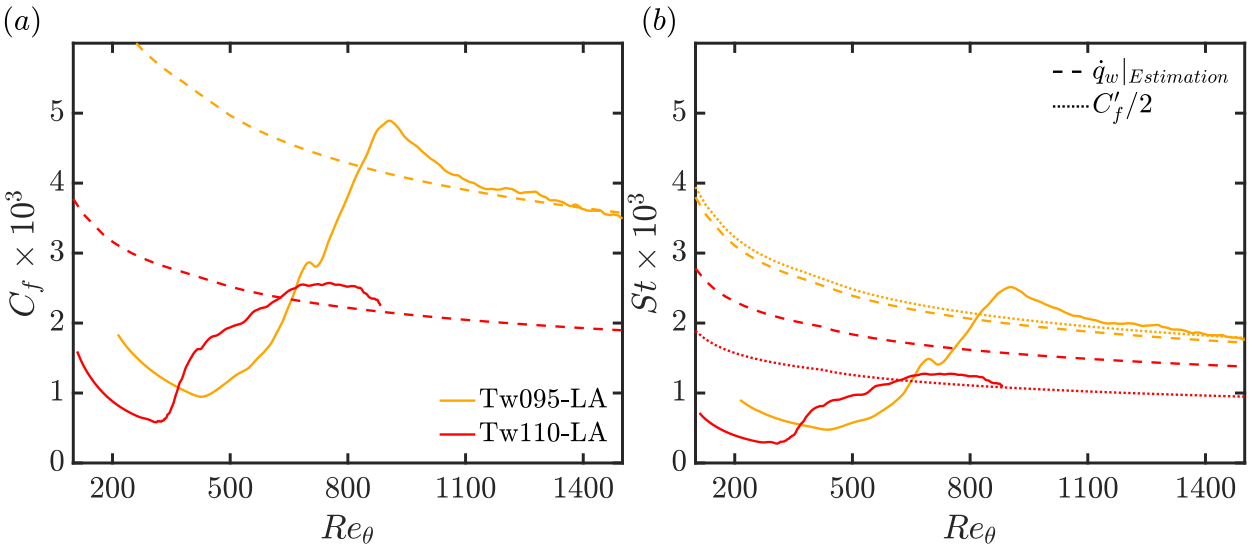

Figure 6.24: Case Tw095-LA (orange) and Tw110-LA (red): (a) skin-friction coefficient C_f and (b) Stanton number St as functions of the momentum-thickness Reynolds number Re_θ. In (a,b), solid lines correspond to the DNS results, while dashed lines denote the analytical estimations. In (b), dotted lines represent $St = C'_f/2$ ($Pr_\infty = 1$) according to the Reynolds analogy, where C'_f is the analytical prediction from (a).

overshoot in C_f for case Tw110-LA is confirmed. In contrast, the St prediction reveals good accuracy only for the subcritical case Tw095-LA. For the highly non-ideal case Tw110-LA, the St number is over-predicted by about 30% at $Re_\theta = 881$ due to a slightly higher estimated wall heat flux in Fig. 6.22(b). Note that the error in the Stanton number prediction using the relation of Walz (1969) reaches about 200% at $Re_\theta = 881$. Interestingly, when applying the Reynolds analogy $St = C'_f/2$ for $Pr_\infty = 1$, verified in Fig. 6.23, and using C'_f from the analytical prediction in Fig. 6.24(a), the estimated St curve closely agrees with the DNS results in the turbulent regime. In conclusion, this behaviour suggests that even under the examined transcritical conditions with variable mixed Prandtl number, the Reynolds analogy may remain a robust tool for predicting the turbulent heat transfer in ZPG flat-plate boundary layers.

6.7 Conclusions

Direct Numerical Simulations (DNS) are performed to investigate the laminar-to-turbulent transition of zero-pressure-gradient flat-plate boundary layers at supercritical pressure with wall heating to trigger Mode-II instability. Two flow cases are defined based on the pseudo-critical temperature T^*_{pc}, both featuring a liquid-like free stream ($T^*_\infty < T^*_{pc}$): one in the subcritical, liquid-like state with $T^*_w < T^*_{pc}$, and one in the transcritical (pseudo-boiling) state with a vapour-like near-wall region ($T^*_w > T^*_{pc}$).

First, only a single fundamental 2-D wave is excited. Under linear forcing, the Mode-II instability in boundary layers is shown to result from the combination of shear and baroclinic

effects, producing two out-of-phase vorticity waves around the critical layer. This confirms the model proposed by Bugeat *et al.* (2024) in plane Couette flow. As the 2-D wave forcing is increased, nonlinearity saturates the unstable 2-D wave in the subcritical state, case Tw095. Conversely, in the transcritical-heating state, case Tw110, nonlinear excitation of higher harmonics emerges in the vicinity of the forcing strip. The first higher harmonic $(2,0)$ outgrows the primary mode $(1,0)$ further downstream. A strong modal interaction follows, leading to the development of subharmonic resonance of mode $(1,0)$ relative to the now dominant $(2,0)$ mode. This resonant interaction, similar to the vortex pairing in mixing layers, accelerates the nonlinear breakdown and induces the billowing motion of the Widom line within the boundary layer. The resulting behaviour closely resembles the classical Kelvin-Helmholtz instability in shear layers, generating a sequence of billow structures that grow within the boundary layer in the streamwise direction. In addition, large velocity perturbations near the wall cause periodic, localised flow reversal, with a generalised inflection point and a density-weighted vorticity maximum, indicative of inviscid instability. The formation of localised separation zones, absent under weakly non-ideal-gas conditions, is analogous to that observed in the ideal-gas state with a prescribed (strong) Adverse Pressure Gradient (APG).

Subsequently, the Three-Dimensional (3-D) breakdown to turbulence is investigated by building upon the 2-D nonlinear analyses of both subcritical and transcritical cases. In addition to the large-amplitude 2-D wave, a pair of subharmonic oblique waves at half the frequency of the primary wave is introduced. The amplitude of the oblique waves is either infinitesimally small ('IA') or finitely large ('LA').

In the subcritical state, case Tw095-IA reveals that infinitesimal 3-D perturbations fail to trigger transition within the considered Reynolds number range. Conversely, in Tw095-LA, the classical H-type breakdown is triggered with a sharp skin-friction overshoot, resembling the ideal-gas reference case of Sayadi *et al.* (2013). However, the onset of the staggered, streamwise-elongated Λ-vortices is delayed compared to the ideal-gas case.

In the transcritical heating state, despite stronger primary-wave growth, transition to turbulence is delayed compared to the subcritical state, given the same forcing parameters. In analogy with the 2-D nonlinear analysis, spanwise-oriented billows initially dominate the early transitional stage, with downstream-convected near-wall separation zones causing a moderate rise in C_f and St, neither of which becomes negative. In Tw110-LA, subharmonic resonance emerges only after vortex pairing between mode $(1,0)$ and its first higher harmonic $(2,0)$. Once the 3-D subharmonic reaches finite amplitude, all 3-D modes undergo abrupt nonlinear amplification. This leads to the formation of alternating high-shear layers at spanwise 'peak' and 'co-peak' (half a spanwise wavelength apart) positions, similar to the K-type breakdown with Adverse Pressure Gradient (APG) (Kloker 1993; Kloker & Fasel 1995). The 'co-peak' high-shear layer, induced by near-wall separation, breaks up first, triggering near-wall longitudinal structures ahead of the outer-region hairpin-like vortices.

In contrast, case Tw110-IA, with infinitesimally low subharmonic 3-D forcing, reveals that no oblique-wave forcing is needed to trigger transition, despite its onset shifting slightly

downstream compared to Tw110-LA. As a result, the primary 2-D wave is amplified to higher amplitude levels, initiating a rapid fill-up of the spectrum of all 3-D modes from the low numerical background noise, with a fundamental-resonance/breakdown mechanism emerging. In other words, subharmonic resonance is no longer the dominant secondary-instability mechanism under low-noise conditions. Three-dimensionality within each spanwise-oriented billow develops gradually, with aligned Λ-vortices progressively forming and breaking up similar to case Tw110-LA.

The C_f and St curves of both transcritical cases are characterised by: (i) the absence of a sharp skin-friction overshoot, due to the lack of strong hairpin-like structures; (ii) lower transitional momentum-thickness Reynolds numbers; and (iii) significantly higher shape factors, H_{12}, compared to the subcritical case.

In the turbulent regime under transcritical conditions, the Patel *et al.* (2015) scaling collapses the velocity profiles well. For predicting the mean enthalpy profile under transcritical conditions, the classical enthalpy–velocity relations fail to reproduce the rapid inner-layer enthalpy rise due to strong variations of the molecular Prandtl number. Instead, the theory of van Driest (1955) for variable Prandtl number agrees well with the DNS data. Based on these results, a predictive model for the turbulent skin-friction coefficient and Stanton number for non-ideal fluid flows is developed, demonstrating good agreement with the DNS results.

The findings in this work highlight the sensitivity of the laminar-to-turbulent transition to both the amplitude of the 3-D perturbations and the thermodynamic state. Due to the presence of the Widom line (pseudo-boiling effect), 2-D waves can be strongly amplified, similar to the ideal-gas mixing layer, and may trigger transition to turbulence from 3-D numerical background noise alone. The resulting K-type breakdown features resemble those observed in the ideal-gas APG case, a scenario absent under ideal-gas and weakly non-ideal-gas conditions without a streamwise pressure gradient.

Finally, these DNS investigations of controlled laminar-to-turbulent transition pave the way for future studies of free-stream-turbulence-induced transition that may be encountered in experimental facilities or industrial applications under pseudo-boiling conditions.

Bibliography

Alam, M. & Sandham, N. D. 2000 Direct numerical simulation of 'short' laminar separation bubbles with turbulent reattachment. *J. Fluid Mech.* **410**, 1–28.

Babucke, A., Kloker, M. & Rist, U. 2007 Direct numerical simulation of a serrated nozzle end for jet-noise reduction. In *Transactions of the High Performance Computing Center, Stuttgart (HLRS) 2007*, p. 319–337.

Bae, J. H., Yoo, J. Y. & Choi, H. 2005 Direct numerical simulation of turbulent supercritical flows with heat transfer. *Phys. Fluids* **17**, 105104.

Bake, S., Meyer, D. G. W. & Rist, U. 2002 Turbulence mechanism in Klebanoff transition: a quantitative comparison of experiment and direct numerical simulation. *J. Fluid Mech.* **459**, 217–243.

Banuti, D. T. 2015 Crossing the Widom-line – Supercritical pseudo-boiling. *J. Supercrit. Fluids* **98**, 12–16.

Boldini, P. C., Bugeat, B., Peeters, J. W. R., Kloker, M. & Pecnik, R. 2024 Transient growth in diabatic boundary layers with fluids at supercritical pressure. *Phys. Rev. Fluids* **9**, 083901.

Boldini, P. C., Bugeat, B., Peeters, J. W. R., Kloker, M. & Pecnik, R. 2026 Direct numerical simulations of K-type transition in a flat-plate boundary layer with supercritical fluids. In *Proceedings of the 10th IUTAM Symposium on Laminar-Turbulent Transition* (ed. Kentaro Kato, Ayumu Inasawa & Masaharu Matsubara), pp. 255–261. Singapore: Springer Nature Singapore.

Boldini, P. C., Hirai, R., Costa, P., Peeters, J. W. R. & Pecnik, R. 2025 CUBENS: A GPU-accelerated high-order solver for wall-bounded flows with non-ideal fluids. *Comput. Phys. Commun.* **309**, 109507.

Bugeat, B., Boldini, P. C., Hasan, A. M. & Pecnik, R. 2024 Instability in strongly stratified plane Couette flow with application to supercritical fluids. *J. Fluid Mech.* **984**, A31.

Bugeat, B., Boldini, P. C. & Pecnik, R. 2022 On the new unstable mode in the boundary layer flow of supercritical fluids. In *Proceedings of the 12th International Symposium on Turbulence and Shear Flow Phenomena (TSFP-12)*.

Candler, G. V. 2019 Rate effects in hypersonic flows. *Annu. Rev. Fluid Mech.* **51**, 379–402.

Cao, L. Y., Xu, R. N., Yan, J. J., He, S. & Jiang, X. P. 2021 Direct numerical simulation of convective heat transfer of supercritical pressure CO2 in a vertical tube with buoyancy and thermal acceleration effect. *J. Fluid Mech.* **927**, A29.

Chang, C. L. & Malik, M. R. 1994 Oblique-mode breakdown and secondary instability in supersonic boundary layers. *J. Fluid Mech.* **273**, 323–360.

Coles, D. 1956 The law of the wake in the turbulent boundary layer. *J. Fluid Mech.* **1** (2), 191–226.

Craik, D. D. A. 1971 Nonlinear resonant instability in boundary layers. *J. Fluid Mech.* **50**, 393–413.

van Driest, E. R. 1951 Turbulent boundary layer in compressible fluids. *J. Aeronaut. Sci.* **18**, 145–160.

van Driest, E. R. 1955 The turbulent boundary layer with variable Prandtl number. In *50 Jahre Grenzschichtforschung: Eine Festschrift in Originalbeiträgen* (ed. H. Görtler & W. Tollmien), p. 257–271. Vieweg+Teubner Verlag.

Duan, L. & Martín, M. P. 2011 Direct numerical simulation of hypersonic turbulent boundary layers. Part 4. Effect of high enthalpy. *J. Fluid Mech.* **684**, 25–59.

Fasel, H. F., Rist, U. & Konzelmann, U. 1990 Numerical investigation of the three-dimensional development in boundary-layer transition. *AIAA J.* **28**, 29–37.

Fedorov, A. 2011 Transition and stability for high-speed boundary layers. *Ann. Rev. Fluid Mech.* **43**, 79–95.

Fezer, A. & Kloker, M. 1999 Spatial direct numerical simulation of transition phenomena in supersonic flat-plate boundary layers. In *Laminar–Turbulent Transition (ed. R. Kobayashi)*, p. 415–420. Springer.

Franko, K. J. & Lele, S. K. 2013 Breakdown mechanisms and heat transfer overshoot in hypersonic zero pressure gradient boundary layers. *J. Fluid Mech.* **730**, 491–532.

Gloerfelt, X., Bienner, A. & Cinnella, P. 2023 High-subsonic boundary-layer flows of an organic vapour. *J. Fluid Mech.* **971**, A8.

Govindarajan, R. & Sahu, K. C. 2014 Instabilities in viscosity-stratified flow. *Ann. Rev. Fluid Mech.* **46**, 331–353.

Guardone, A., Colonna, P., Pini, M. & Spinelli, A. 2024 Nonideal compressible fluid dynamics of dense vapors and supercritical fluids. *Annu. Rev. Fluid Mech.* **56** (1), 241–269.

Guo, J., Yang, X. I. A. & Ihme, M. 2022 Structure of the thermal boundary layer in turbulent channel flows at transcritical conditions. *J. Fluid Mech.* **934**, A45.

Hader, C. & Fasel, H. F. 2019 Direct numerical simulations of hypersonic boundary-layer transition for a flared cone: fundamental breakdown. *J. Fluid Mech.* **869**, 341–384.

Hasan, A. M., Larsson, J., Pirozzoli, S. & Pecnik, R. 2023 Incorporating intrinsic compressibility effects in velocity transformations for wall-bounded turbulent flows. *Phys. Rev. Fluids* **8**, L112601.

Hasan, A. M., Larsson, J., Pirozzoli, S. & Pecnik, R. 2024 Estimating mean profiles and fluxes in high-speed turbulent boundary layers using inner/outer-layer scalings. *AIAA J.* **62** (2), 848–853.

He, J., Tian, R., Jiang, P. X. & He, S. 2021 Turbulence in a heated pipe at supercritical pressure. *J. Fluid Mech.* **920**, A45.

Herbert, T. 1988 Secondary instability of boundary layers. *Annu. Rev. Fluid Mech.* **20**, 487–526.

Johnson, D. A. & King, L. 1985 A mathematically simple turbulence closure model for attached and separated turbulent boundary layers. *AIAA J.* **23** (11), 1684–1692.

Jossi, A. J., Stiel, L. I. & Thodos, G. 1962 The viscosity of pure substances in the dense gaseous and liquid phases. *AIChE J.* **8**, 59–63.

Kachanov, Yu. S. 1994 Physical mechanisms of laminar-boundary-layer transition. *Annu. Rev. Fluid Mech.* **26**, 411–482.

Kachanov, Yu. S. & Levchenko, V. Ya. 1984 The resonant interaction of disturbances at laminar-turbulent transition in a boundary layer. *J. Fluid Mech.* **138**, 209–247.

Kawai, S. 2019 Heated transcritical and unheated non-transcritical turbulent boundary layers at supercritical pressures. *J. Fluid Mech.* **865**, 563–601.

Kim, K., Hickey, J.-P. & Scalo, C. 2019 Pseudophase change effects in turbulent channel flow under transcritical temperature conditions. *J. Fluid Mech.* **871**, 52–91.

Klaassen, G. P. & Peltier, W. R. 1985 The onset of turbulence in finite-amplitude Kelvin-Helmholtz billows. *J. Fluid Mech.* **155**, 1–35.

Klebanoff, P. S., Tidstrom, K. D. & Sargent, L. M. 1962 The three-dimensional nature of boundary-layer instability. *J. Fluid Mech.* **12**, 1–34.

Kloker, M. 1993 Direkte numerische Simulation des laminar-turbulenten Strömungsumschlages in einer stark verzögerten Grenzschicht. PhD thesis, University of Stuttgart.

Kloker, M. 2024 A note on the flow topology during laminar-turbulent transition induced by Tollmien–Schlichting waves. ResearchGate, Report Number: IAG-TN-2024-LTT-02, available at: https://www.researchgate.net/publication/385746142.

Kloker, M. & Fasel, H. 1995 Direct numerical simulation of boundary-layer transition with strong adverse pressure gradient. In *Laminar-Turbulent Transition* (ed. Ryoji Kobayashi), pp. 481–488. Berlin, Heidelberg: Springer Berlin Heidelberg.

Kosorygin, V. S. 1994 Stability and transition to turbulence in 2-D boundary layer under the influence of adverse pressure gradients. In *Nonlinear Instability of Nonparallel Flows*. IUTAM-Sym., Potsdam, USA, 1993.

Lemmon, E. W., Huber, M. L. & Mclinden, M. O. 2013 NIST Standard Reference Database 23: Reference Fluid Thermodynamic and Transport Properties - REFPROP, Version 9.1. Available at: `http://www.nist.gov/srd/nist23.cfm`.

Li, F., Guo, J., Bai, B. & Ihme, M. 2023 Analysis of real-fluid thermodynamic effects on turbulent statistics in transcritical channel flows. *Phys. Rev. Fluids* **8**, 024605.

Li, F., Zhang, W., Bai, B. & Ihme, M. 2024 Small-scale turbulent characteristics in transcritical wall-bounded flows. *J. Fluid Mech.* **986**, A36.

Liu, C.-L., Kaminski, A. & Smyth, W. D. 2023 The effects of boundary proximity on Kelvin–Helmholtz instability and turbulence. *J. Fluid Mech.* **966**, A2.

Luhar, M., Sharma, A. S. & McKeon, B. J. 2014 On the structure and origin of pressure fluctuations in wall turbulence: predictions based on the resolvent analysis. *J. Fluid Mech.* **751**, 38–70.

Ma, P. C., Yang, X. I. A. & Ihme, M. 2018 Structure of wall-bounded flows at transcritical conditions. *Phys. Rev. Fluids* **3**, 034609.

Mani, A. 2012 Analysis and optimization of numerical sponge layers as a nonreflective boundary treatment. *J. Comput. Phys.* **231**, 704–716.

Maucher, U., Rist, U., Kloker, M. & Wagner, S. 2000 DNS of laminar-turbulent transition in separation bubbles. In *High Performance Computing in Science and Engineering '99 (ed. E Krause, W. Jäger (Eds.))*, p. 279–294. Springer-Verlag, Berlin.

Monkewitz, P. A. 1988 Subharmonic resonance, pairing and shredding in the mixing layer. *J. Fluid Mech.* **188**, 223–252.

Morellina, S., Bellan, J. & Cutts, J. 2020 Global thermodynamic, transport-property and dynamic characteristics of the Venus lower atmosphere below the cloud layer. *Icarus* **350**, 113761.

Morkovin, M. V. 1969 On the many faces of transition. In *Viscous Drag Reduction* (ed. C. S. Wells), p. 1–31. Springer.

Nemati, H., Patel, A., Boersma, B. J. & Pecnik, R. 2015 Mean statistics of a heated turbulent pipe flow at supercritical pressure. *Int. J. Heat Mass Transf.* **83**, 741–752.

Nemati, H., Patel, A., Boersma, B. J. & Pecnik, R. 2016 The effect of thermal boundary conditions on forced convection heat transfer to fluids at supercritical pressure. *J. Fluid Mech.* **800**, 531–556.

Okong'o, N. & Bellan, J. 2002 Consistent boundary conditions for multicomponent real gas mixtures based on characteristic waves. *J. Comput. Phys.* **176**, 330–344.

Okong'o, N. & Bellan, J. 2010 Small-scale dissipation in binary-species, thermodynamically supercritical, transitional mixing layers. *Comp. Fluids* **39** (7), 1112–1124.

Patel, A., Boersma, B. J. & Pecnik, R. 2016 The influence of near-wall density and viscosity gradients on turbulence in channel flows. *J. Fluid Mech.* **809**, 793–820.

Patel, A., Peeters, J. W. R., Boersma, B. J. & Pecnik, R. 2015 Semi-local scaling and turbulence modulation in variable property turbulent channel flows. *Phys. Fluids* **27**, 095101.

Peeters, J. W. R., Pecnik, R., Rohde, M., van der Hagen, T. H. J. J. & Boersma, B. J. 2016 Turbulence attenuation in simultaneously heated and cooled annular flows at supercritical pressure. *J. Fluid Mech.* **799**, 505–540.

Ren, J. & Kloker, M. 2022 Instabilities in three-dimensional boundary-layer flows with a highly non-ideal fluid. *J. Fluid Mech.* **951**, A9.

Ren, J., Marxen, O. & Pecnik, R. 2019 Boundary-layer stability of supercritical fluids in the vicinity of the Widom line. *J. Fluid Mech.* **871**, 831–864.

Rist, U. & Fasel, H. 1995 Direct numerical simulation of controlled transition in a flat-plate boundary layer. *J. Fluid Mech.* **298**, 211–248.

Robinet, J.-C. & Gloerfelt, X. 2019 Instabilities in non-ideal fluids. *J. Fluid Mech.* **880**, 1–4.

Saric, W. S., Reed, H. L. & Kerschen, E. J. 2002 Boundary-layer receptivity to freestream disturbances. *Annu. Rev. Fluid Mech.* **34**, 291–319.

Sayadi, T., Hamman, C. W. & Moin, P. 2013 Direct numerical simulation of complete H-type and K-type transitions with implications for the dynamics of turbulent boundary layers. *J. Fluid Mech.* **724**, 480–509.

Schmid, P. J. & Henningson, D. S. 2001 *Stability and transition in shear flows*. Springer.

Sciacovelli, L., Gloerfelt, X., Passiatore, D., Cinnella, P. & Grasso, F. 2020 Numerical investigation of high-speed turbulent boundary layers of dense gases. *Flow Turbul. Combust.* **105**, 555–579.

Sharan, N. & Bellan, J. 2021 Investigation of high-pressure turbulent jets using direct numerical simulation. *J. Fluid Mech.* **922**, A24.

Sivasubramanian, J. & Fasel, H. F. 2015 Direct numerical simulation of transition in a sharp cone boundary layer at Mach 6: fundamental breakdown. *J. Fluid Mech.* **768**, 175–218.

Smits, A. J. & Dussauge, J.-P. 2006 *Turbulent Shear Layers in Supersonic Flow*. Springer Science & Business Media.

Stiel, L. I. & Thodos, G. 1964 The thermal conductivity of nonpolar substances in the dense gaseous and liquid regions. *AIChE J.* **10**, 26–30.

Taylor, G. I. 1936 Statistical theory of turbulence. Part V. Effect of turbulence on boundary layer. Theoretical discussion of relationship between scale of turbulence and critical resistance of spheres. *Proc. R. Soc. Lond. A.* **156**, 307–317.

Trettel, A. & Larsson, J. 2016 Mean velocity scaling for compressible wall turbulence with heat transfer. *Phys. Fluids* **28** (2), 026102.

Unnikrishnan, S. & Gaitonde, D. V. 2020 Linear, nonlinear and transitional regimes of second-mode instability. *J. Fluid Mech.* **905**, A25.

Van der Waals, J. D. 1873 Over de continuïteit van den gas- en vloeistoftoestand. PhD thesis, Hoogeschool te Leiden.

Walz, A. 1969 *Boundary Layers of Flow and Temperature*. MIT Press, Cambridge.

Wang, X. & Yang, V. 2017 Supercritical mixing and combustion of liquid-oxygen/kerosene bi-swirl injectors. *J. Propul. Power* **33**, 316–322.

Wenzel, C., Gibis, T., Kloker, M. & Rist, U. 2021 Reynolds analogy factor in self-similar compressible turbulent boundary layers with pressure gradients. *J. Fluid Mech.* **907**, R4.

White, F. M. 2006 *Viscous Fluid Flow, 3rd Edition*. Boston: McGraw-Hill.

Yoo, J. Y. 2013 The turbulent flows of supercritical fluids with heat transfer. *Annu. Rev. Fluid Mech.* **45**, 495–525.

Zhong, X. 1998 High-order finite-difference schemes for numerical simulation of hypersonic boundary-layer transition. *J. Comput. Phys.* **144** (2), 662–709.

7

SECONDARY SUBHARMONIC INSTABILITY

This chapter reports unpublished work that builds upon the results of Chapter 6 and is currently being prepared for submission.

This chapter investigates secondary subharmonic instability in zero-pressure-gradient flat-plate boundary layers with a fluid at supercritical pressure. Three thermodynamic states are examined: subcritical, supercritical, and transcritical temperature conditions, the latter involving pseudo-boiling as the Widom line is crossed. Secondary instability theory based on Floquet analysis is extended to non-ideal gases and employed alongside direct numerical simulations. In non-transcritical states, two-dimensional subharmonic resonance between the primary Tollmien–Schlichting wave and its subharmonic does not occur at moderate primary-wave amplitudes, consistent with classical ideal-gas behaviour; given the sharp cut-off at low spanwise wavenumbers, a finite spanwise wavenumber is required for subharmonic resonance. In contrast, under transcritical conditions, the strong Mode-II instability enables two-dimensional subharmonic resonance at primary-wave amplitudes as low as 0.6%, a threshold substantially lower than the approximately 4% threshold typical of ideal-gas adverse-pressure-gradient boundary layers. This low threshold under pseudo-boiling conditions is attributed to the elevated location of the shear layer associated with the Widom line, which reduces the wall-damping effect on the two-dimensional vortex pairing mode. The phase shift between primary and subharmonic forcing waves has only a weak influence on the two-dimensional subharmonic resonance. Three-dimensional simulations with finite-amplitude two-dimensional subharmonic forcing confirm that, although two-dimensional subharmonic resonance is active under transcritical conditions, the fundamental-resonance wave–vortex triad ultimately drives a K-type-like breakdown. These results demonstrate that pseudo-boiling makes two-dimensional vortex pairing accessible at moderate disturbance amplitudes, while preserving the inherently three-dimensional nature of the final breakdown process.

7.1 Introduction

As explained in Chapter 1, transition to turbulence is a highly complex process, primarily due to its pronounced nonlinearity and sensitivity to a wide range of influencing factors. Following 'Path A' (Morkovin 1969), once a downstream-amplifying Two-Dimensional (2-D) Tollmien–Schlichting (TS) wave exceeds a threshold amplitude, typically around 0.1%, secondary instability may arise. At this point, the base flow, which has been modulated by the TS wave, becomes highly susceptible to secondary instabilities, particularly to small Three-Dimensional (3-D) disturbances spanning a broad range of spanwise wavenumbers.

This behaviour is well captured by the Secondary Instability Theory (SIT) of Herbert (1988). The theory is based on investigating the stability of a modified base flow, comprising a superposition of the laminar boundary-layer solution and a finite-amplitude 2-D TS wave, with respect to infinitesimal 3-D disturbances. Because the base flow is streamwise periodic, the resulting fourth-order linear differential system is solved using Floquet analysis, which enables a systematic treatment of secondary instabilities in periodic flows. This approach yields local growth rates for the 3-D disturbances as functions of the amplitude of the 2-D primary wave, its frequency, and the spanwise wavenumber of the secondary modes. The analysis distinguishes between fundamental and subharmonic modes, depending on their resonance relation with the primary wave. For the growth rates in these two canonical cases, good quantitative agreement with experiments has been achieved; see Klebanoff *et al.* (1962) for fundamental resonance (K-type) and Kachanov & Levchenko (1984) for subharmonic resonance (H-type). The fundamental modes correspond to primary resonance in the Floquet system, whereas subharmonic modes arise from principal parametric resonance. In addition, detuned modes (Jouin *et al.* 2024), associated with off-resonant or combination resonances, naturally arise within the broader Floquet spectrum and may become relevant depending on the disturbance environment.

In incompressible boundary layers, the selection between subharmonic (H-type) and fundamental (K-type) resonance has been extensively investigated. Subharmonic resonance is observed both in experiments and in the SIT predictions when the TS wave amplitude remains below approximately 1–2%; in this regime, the SIT indicates that subharmonic resonance exhibits higher growth rates than fundamental resonance in a Zero-Pressure-Gradient (ZPG) boundary layer (Herbert 1984). If the TS amplitude is larger, or if additional longitudinal vortices are present, introduced in experiments, for example, by a spanwise row of small, elevated, periodically interrupted strips, the fundamental resonance mechanism sets in Klebanoff *et al.* (1962); Rist & Fasel (1995). However, it still remains unclear why a specific secondary instability mechanism initiates transition in a given boundary-layer flow; the dominant type appears to depend strongly on the nature of the incoming flow and the surrounding flow conditions. A detailed overview is provided in Herbert (1988).

In compressible boundary layers, early SIT-based studies by Masad & Nayfeh (1990) and El-Hady (1991) demonstrated that subharmonic and fundamental resonances persist, with compressibility shifting instability thresholds. Building on the work of Ng & Erlebacher

(1992), who analysed secondary instabilities up to Mach 4.5, recent research (Xu *et al.* 2020; Kumar & Prakash 2021; Chen *et al.* 2021) has increasingly addressed high-temperature effects in high-speed flows (Candler 2019). In parallel, Direct Numerical Simulations (DNS) studies have explored secondary instabilities in supersonic flat-plate boundary layers (Chang & Malik 1994; Adams & Kleiser 1995; Fezer & Kloker 1999; Mayer & Fasel 2008; Marxen *et al.* 2014) and over sharp cones (Sivasubramanian & Fasel 2014 2015), though all under the ideal-gas assumption. Until now, no studies have investigated secondary instability mechanisms in fluids exhibiting non-ideal thermodynamic behaviour (Guardone *et al.* 2024).

A recent study of the nonlinear regime in a ZPG boundary layer with a fluid at supercritical pressure (Boldini *et al.* 2025*a*) revealed behaviour analogous to that of boundary layers subjected to a (strong) Adverse Pressure Gradient (APG) in the ideal-gas state (see also Chapter 6). Under pseudo-boiling conditions, the billowing of the Widom line induces localised separation zones, with the boundary layer characterised by a Generalised Inflection Point (GIP) (Bugeat *et al.* 2024), leading to highly unstable velocity profiles at high Reynolds numbers. Moreover, 2-D subharmonic resonance was found between the first higher harmonic and the primary wave. For ideal gas, the APG effect on the secondary subharmonic instability was studied by Herbert & Bertolotti (1985) and Kloker (1993). With increasing deceleration of the boundary layer, the growth rates of both primary and secondary disturbances rise significantly, while the range of unstable spanwise wavenumbers remains essentially unchanged. At extremely large TS amplitudes of around 30%, still assuming a fixed wave shape and neglecting mean-flow distortion, the flow was found to be unstable also to a 2-D subharmonic mode, similar to a spatially periodic free-shear layer (Pierrehumbert & Widnall 1982). At this large amplitude of the primary wave, 2-D vortex pairing dominates the transition process. However, TS amplitudes above 10% clearly violate the underlying assumptions of the SIT; see Kloker (2024). Such limitations do not apply to DNS investigations, which do not rely on assumptions regarding the disturbance development. In classical ZPG ideal-gas boundary layers, a distinction must also be made between fundamental and subharmonic secondary instabilities: while fundamental (K-type) resonance admits a 2-D secondary mode, it requires a finite TS-wave amplitude, typically several percent (e.g. 4% in Kloker (1993)), before becoming unstable.

Building on these observations, the main focus of this work is to investigate secondary subharmonic resonance in ZPG flat-plate boundary layers with a fluid above the thermodynamic critical point. The APG-like behaviour induced by pseudo-boiling suggests that Mode II may fundamentally alter the secondary-instability dynamics. In classical ideal-gas boundary layers, subharmonic resonance becomes active at moderate TS-wave amplitudes, but a 2-D subharmonic mode requires extremely large primary-wave amplitudes before becoming unstable. Under pseudo-boiling conditions, however, the strong Mode-II instability may enable 2-D subharmonic resonance at far lower amplitudes, making its role in the transition process particularly relevant. We therefore aim to clarify how Mode II influences or enhances subharmonic secondary-instability growth. To investigate these effects, the wall temperature is set in the vapour-like state, such that the flow crosses the pseudo-critical

(Widom) line from a liquid-like free stream at supercritical pressure. First, non-ideal gas effects are included in the SIT analysis based on Floquet theory, which serves as a preliminary analysis. To overcome the multiple assumptions of SIT, DNS analyses are employed to fully account for the nonlinearity of Mode II. The subharmonic resonance calculations reported in this work emphasise the key role of 2-D perturbations in flat-plate boundary layers under pseudo-boiling conditions. Secondary instability analysis is applied here for the first time to fluids at supercritical pressure, providing new insights into resonant interactions in non-ideal fluid flows.

The work is organised as follows. Section 7.2 introduces the governing equations, with particular emphasis on the secondary-instability-theory solver. The flow conditions, secondary instability analysis framework, and DNS computational setup are presented in Sec. **??**. Subsequently (Sec. 7.4), secondary instability analysis is performed for three boundary-layer flow cases at a free-stream pressure of $p^*_\infty/p^*_c = 1.10$, where p^*_c denotes the thermodynamic critical pressure, within a narrow temperature range. The cases differ in wall-heating conditions, namely below, above, and across the Widom line, corresponding to subcritical, supercritical, and transcritical states (the latter involving pseudo-boiling (Banuti 2015)), respectively. The transcritical case is specifically designed to trigger Mode II instability. Section 7.5.1 deals with the 2-D DNS investigations of the subharmonic resonance, while Sec. 7.5.2 focuses on the full breakdown to turbulence through subharmonic resonance. The work is concluded in Sec. 7.6.

7.2 Methodology

This section provides a concise description of the governing equations and the DNS framework; further details are given in Chapters 2 and 6. In contrast, the methodology of the SIT analysis is presented in more detail.

7

7.2.1 Governing equations

The single-phase, non-reacting flow of supercritical fluids is governed by the fully compressible Navier–Stokes (NS) equations, see Eq. (2.1). For its non-dimensionalisation and reference quantities based on free-stream conditions, we refer to the previous chapters, see Chapters 5 and 6. Two standard assumptions are considered in this work: (i) a zero bulk viscosity (Stokes' hypothesis) in agreement with Sciacovelli *et al.* (2017a); Ren *et al.* (2019*a*), and (ii) a zero buoyancy force induced by stratification effects. Similar to Chapter 6, the reduced Van der Waals (VdW) cubic Equation of State (EoS) (see Sec. 2.2.2) is chosen, consistent with the principle of corresponding states. The analytical expressions of Jossi *et al.* (1962) and Stiel & Thodos (1964) for the transport properties (see Sec. 2.3.2) are selected.

7.2.2 Secondary instability analysis

For the secondary instability analysis, the Floquet-based SIT of Ng & Erlebacher (1992) is employed. The basic flow $\mathbf{q}_b$ is constructed as the superposition of: (i) the self-similar laminar flow $\mathbf{q}_0$, which is based on the self-similar solution of the compressible boundary-layer equations with non-ideal thermophysical properties and diabatic wall (Ren *et al.* 2019*b*; Boldini *et al.* 2024) (see Sec. 2.4), and (ii) a finite-amplitude one-dimensional (1-D) primary disturbance $\mathbf{q}_1$ in the Linear Stability Theory (LST) framework, see Chapter 3. Thus, flow variables are decomposed as:

$$\mathbf{q}(x,y,z,t) = \mathbf{q}_b(x,y,t) + \epsilon\mathbf{q}_2'(x,y,z,t), \tag{7.1}$$

where $\epsilon \ll 1$ and $\mathbf{q}_2'$ denotes the secondary disturbance. The basic flow, denoted by $(\cdot)_b$, is then written as

$$\mathbf{q}_b(x,y,t) = \mathbf{q}_0(y) + A_0\left[\hat{\mathbf{q}}_1(y)e^{\mathrm{i}\theta} + \text{c.c.}\right], \tag{7.2}$$

where $\theta = \alpha x - \omega t$, A_0 is the primary-wave amplitude, and subscript $(\cdot)_0$ denotes the base-flow quantities. Substituting the decomposition in Eq. (7.1) into the NS equations in Eq. (2.1) and subtracting the basic flow yields the disturbance equations governing the secondary instability. They read:

$$\frac{\partial\rho_2'}{\partial t} + \nabla\cdot(\rho_b\mathbf{u}_2') + \nabla\cdot(\rho_2'\mathbf{u}_b) = 0, \tag{7.3a}$$

$$\begin{aligned}\rho_b\left[\frac{\partial\mathbf{u}_2'}{\partial t} + (\mathbf{u}_b\cdot\nabla)\,\mathbf{u}_2' + (\mathbf{u}_2'\cdot\nabla)\,\mathbf{u}_b\right] + \rho_2'\Big[(\mathbf{u}_b\cdot\nabla)\,\mathbf{u}_b\Big] &= -\nabla p_2' \\ + \frac{1}{Re}\left\{\nabla\cdot\left[\mu_b\left(\nabla\mathbf{u}_2' + (\nabla\mathbf{u}_2')^{\mathrm{T}}\right)\right] + \nabla\cdot\left[\mu_2'\left(\nabla\mathbf{u}_b + (\nabla\mathbf{u}_b)^{\mathrm{T}}\right)\right]\right\} \\ + \frac{1}{Re}\left\{\nabla\cdot\left[\lambda_b\left(\nabla\cdot\mathbf{u}_2'\right)\mathbf{I} + \lambda_2'\left(\nabla\cdot\mathbf{u}_b\right)\mathbf{I}\right]\right\},\end{aligned} \tag{7.3b}$$

$$\begin{aligned}\rho_b\left[\frac{\partial e_2'}{\partial t} + (\mathbf{u}_b\cdot\nabla)\,e_2' + (\mathbf{u}_2'\cdot\nabla)\,e_b\right] + \rho_2'\left[\frac{\partial e_b}{\partial t} + (\mathbf{u}_b\cdot\nabla)\,e_b\right] &= p_2'\nabla\mathbf{u}_b + p_b\nabla\mathbf{u}_2' \\ + \frac{1}{RePr_\infty Ec_\infty}\Big[\nabla\cdot(\kappa_b\nabla T_2' + \kappa_2'\nabla T_b)\Big] + \frac{1}{Re}\Phi_2',\end{aligned} \tag{7.3c}$$

with

$$\begin{aligned}\Phi_2' \quad &= \lambda_b\left[2\left(\nabla\cdot\mathbf{u}_b\right)\left(\nabla\cdot\mathbf{u}_2'\right)\right] + \lambda_2'\left[\left(\nabla\cdot\mathbf{u}_b\right)\left(\nabla\cdot\mathbf{u}_b\right)\right] \\ &+\mu_b\left[\left(\nabla\mathbf{u}_b + (\nabla\mathbf{u}_b)^{\mathrm{T}}\right)\left(\nabla\mathbf{u}_2' + (\nabla\mathbf{u}_2')^{\mathrm{T}}\right)\right] + \frac{\mu_2'}{2}\left[\left(\nabla\mathbf{u}_b + (\nabla\mathbf{u}_b)^{\mathrm{T}}\right)^2\right].\end{aligned} \tag{7.4}$$

In the following, the SIT analysis is performed under the assumptions that: (a) the base flow is locally parallel, (b) self-interaction of the primary wave does not cause a significant mean-flow distortion or modify the wave shape, (c) terms of $O(\epsilon A_0^2, \epsilon A_0^2/Re)$ are neglected (Masad & Nayfeh 1990), (d) the fluctuating secondary thermodynamic and transport properties (e.g., $\rho_2', \mu_2', \kappa_2'$) depend nonlinearly on two independent thermodynamic variables (typically

p_2' and T_2'). After a first-order Taylor expansion, for example, the viscosity perturbation μ_2' can be written as:

$$\begin{aligned}\mu_2' = \quad & \left.\frac{\partial \bar{\mu}_b}{\partial \bar{p}_b}\right|_{\bar{T}_b} p_2' + \left.\frac{\partial \bar{\mu}_b}{\partial \bar{T}_b}\right|_{\bar{p}_b} T_2' = \\ & p_2'\left(\left.\frac{\partial \bar{\mu}_0}{\partial \bar{p}_0}\right|_{\bar{T}_0} + A_0 \left.\frac{\partial^2 \bar{\mu}_0}{\partial \bar{p}_0^2}\right|_{\bar{T}_0} p_1' + A_0 \left.\frac{\partial^2 \bar{\mu}_0}{\partial \bar{p}_0 \partial \bar{T}_0}\right|_{\bar{p}_0} T_1'\right) + \\ & T_2'\left(\left.\frac{\partial \bar{\mu}_0}{\partial \bar{T}_0}\right|_{\bar{p}_0} + A_0 \left.\frac{\partial^2 \bar{\mu}_0}{\partial \bar{T}_0^2}\right|_{\bar{p}_0} T_1' + A_0 \left.\frac{\partial^2 \bar{\mu}_0}{\partial \bar{p}_0 \partial \bar{T}_0}\right|_{\bar{T}_0} p_1'\right).\end{aligned} \tag{7.5}$$

Regarding the primary-wave amplitude A_0, its definition depends on the considered thermodynamic state. In non-transcritical states, the dominant perturbation is the streamwise velocity perturbation, and therefore

$$\max_{0\le y<\infty}\{|\hat{u}_1(y)|^2\} = 1/2, \tag{7.6}$$

consistent with the subsonic, ideal-gas convention (Masad & Nayfeh 1990; Ng & Erlebacher 1992). In this case, the primary amplitude is denoted with $A_{0,u'}$. In contrast, this normalisation becomes inaccurate in the transcritical (pseudo-boiling) state, where LST results show that the peak density fluctuation exceeds the peak velocity by more than an order of magnitude (see Chapters 3 and 6). Therefore, for transcritical cases, the amplitude A_0 (here denoted as $A_{0,\rho'}$) is defined based on the maximum root mean square (rms) value of the density perturbation as

$$\max_{0\le y<\infty}\{|\hat{\rho}_1(y)|^2\} = 1/2, \tag{7.7}$$

to avoid inconsistency in the basic-flow decomposition in Eq. (7.2). By moving with the phase speed of the primary wave, the secondary disturbance in the periodic streamwise direction, i.e. $\tilde{x} = x - ct$, can be expressed in Floquet form as

$$\mathbf{q}_2'(x,y,z,t) = e^{\gamma\tilde{x}+\sigma t} e^{\mathrm{i}\beta_2 z} e^{\mathrm{i}\epsilon_d \theta} \sum_{n=-\infty}^{\infty} \hat{\mathbf{q}}_{2,n}(y) e^{\mathrm{i}n\theta}, \tag{7.8}$$

where ϵ_d is the detuning parameter ($\epsilon_d = 0.5$ for subharmonic modes), $n \in \mathbb{Z}$ is the Floquet mode index, $\gamma = \gamma_r + \mathrm{i}\gamma_i$ and $\sigma = \sigma_r + \mathrm{i}\sigma_i$ represent the characteristic exponents, and β_2 is the spanwise wavenumber. In the spatial framework considered here, $\sigma = 0$ and γ_r corresponds to the spatial secondary growth rate. For practical calculations, Eq. (7.8) is truncated to N_m modes (m denotes the truncated Floquet harmonic index in the finite-mode expansion) as follows:

$$\mathbf{q}_2'(x,y,z,t) = e^{\gamma\tilde{x}} e^{\mathrm{i}\beta_2 z} e^{\mathrm{i}\epsilon_d\theta} \times \begin{cases} \displaystyle\sum_{m=-\frac{N_m-1}{2}}^{\frac{N_m-1}{2}} \hat{\mathbf{q}}_{2,m}(y)\, e^{\mathrm{i}m\theta}, & \text{for odd } N_m, \\ \displaystyle\sum_{m=-\frac{N_m}{2}}^{\frac{N_m-2}{2}} \hat{\mathbf{q}}_{2,m}(y)\, e^{\mathrm{i}m\theta}, & \text{for even } N_m. \end{cases} \tag{7.9}$$

For the case of secondary subharmonic disturbances, the lowest sufficient number of Fourier modes is $N_m = 2$ for a 2-D primary wave. In this case, the Floquet expansion in Eq. (7.9) becomes:

$$\mathbf{q}_2'(x,y,z,t) = e^{\gamma\tilde{x}} e^{\mathrm{i}\beta_2 z}\left[\hat{\mathbf{q}}_{2,-1}(y) e^{-\mathrm{i}\theta/2} + \hat{\mathbf{q}}_{2,0}(y) e^{\mathrm{i}\theta/2}\right]. \tag{7.10}$$

After replacing Eq. (7.10) into the secondary disturbance equations, Eq. (7.3), the resulting system can be written as a complex eigenvalue problem of the form

$$\mathbf{B}_0\hat{\mathbf{q}}_2 = \gamma\mathbf{B}_\gamma\hat{\mathbf{q}}_2 + \gamma^2\mathbf{B}_{\gamma^2}\hat{\mathbf{q}}_2, \tag{7.11}$$

where $\mathbf{B}_0$, $\mathbf{B}_\gamma$, and $\mathbf{B}_{\gamma^2}$ are the global matrices of the non-ideal gas formulation, each depending on the basic flow $\mathbf{q}_b$. The vector $\hat{\mathbf{q}}_2$ is the global eigenvector that contains the modal amplitudes $\hat{\mathbf{q}}_{2,-1}$ and $\hat{\mathbf{q}}_{2,0}$. To solve the quadratic eigenvalue problem in Eq. (7.11), a linear reformulation is employed, consistent with the LST methodology described in Sec. 3.2.1. Both the primary and secondary eigenvalue problems are solved using the LAPACK implementation of the QZ algorithm (generalised Schur decomposition). A pseudo-spectral collocation method based on Chebyshev collocation points with near-wall grid clustering is used to discretise the wall-normal direction, following Schmid & Henningson (2001). The validation of the SIT solver is presented hereafter.

Validation of the secondary instability theory solver

The secondary instability analysis presented in this work is validated by reproducing the ideal-gas temporal results of Ng & Erlebacher (1992) (adiabatic wall, $M_\infty = 1.6$, $Pr_\infty = 0.72$, $c_p^*/c_v^* = 1.4$, $Re = 613.24$, $\alpha = 0.0879$, $\beta_2 = 0.1464$, $\epsilon_d = 0.5$) in Fig. 7.1(a) and the ideal-gas spatial results of Masad & Nayfeh (1990) (adiabatic wall, $M_\infty = 0.8$, $Pr_\infty = 0.72$, $c_p^*/c_v^* = 1.4$, $Re = 850$, $F = 60 \times 10^{-6}$, $A_{0,u'} = 0.01$, $\epsilon_d = 0.5$) in Fig. 7.1(b). Note that the frequency parameter F and the spanwise-wavenumber parameter b are defined as $F = \omega/Re_0$ and $10^3\beta_2/Re_0$, respectively. The latter describes a wave of fixed physical spanwise wavenumber as it travels downstream (Herbert 1984). In both cases, very good agreement is obtained for the secondary subharmonic growth rate (temporal: growth rate σ_r and $\gamma = 0$, spatial: growth rate γ_r and $\sigma = 0$). To obtain a grid-independent solution under non-ideal-gas conditions, the influence of mesh size N_y and mesh height y_{max} on the subharmonic growth rate is examined. The transcritical T09w110 case, see Sec. 7.3 or Chapter 6, is considered at $Re = 606$ and $A_{0,\rho'} = 10\%$. The results shown in Fig. 7.1(c) for varying N_y indicate that a resolution of $N_y = 200$ together with a domain height of $y_{max} = 50$ (not shown) is required to achieve mesh independence. This numerical setup is therefore adopted throughout the secondary-instability calculations presented in this chapter.

7.2.3 DNS solver

The DNS analysis is performed using the CUBENS solver (Boldini *et al.* 2025*b*), see Chapter 5 for details. The same numerical setup as described in Sec. 6.2 is employed. The time step Δt is selected based on the frequency of the primary-wave disturbance, ω_1, as $\Delta t = 2\pi/(\omega_1 LP)$. The parameter LP is chosen such that the maximum Courant–Friedrichs–Lewy number remains below 0.8 in all spatial directions. In the streamwise direction, the wall-normal maximum amplitudes of the mass-flux perturbation $(\rho u)' = \bar{\rho}u' + \bar{u}\rho' + \rho' u'$ are used to quantify the disturbance amplitudes.

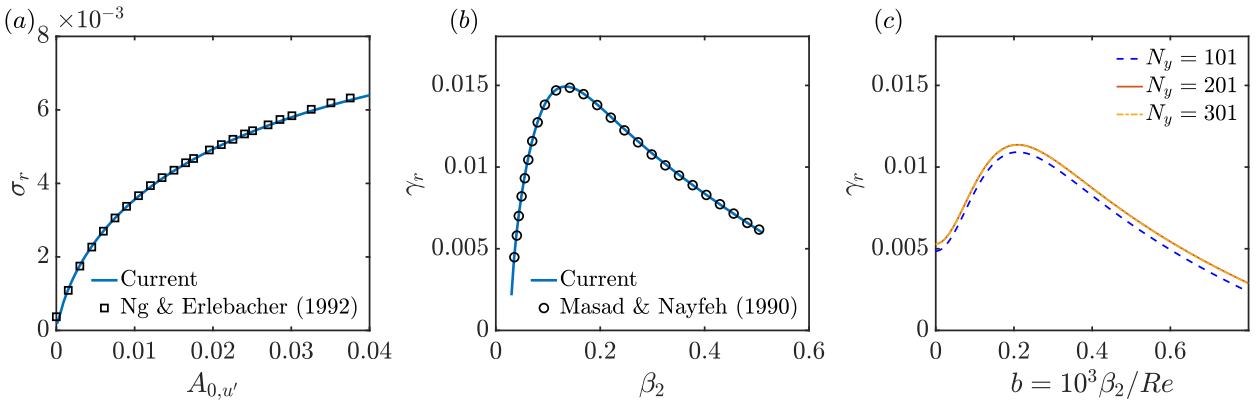

Figure 7.1: Validation of the secondary–instability solver. (a) Ideal-gas temporal secondary subharmonic growth rate σ_r as a function of the primary-wave amplitude $A_{0,u'}$: comparison between the present results (solid line) and Ng & Erlebacher (1992) (black (□) symbols). (b) Ideal-gas spatial secondary subharmonic growth rate γ_r as a function of the spanwise wavenumber β_2: comparison between the present results (solid line) and Masad & Nayfeh (1990) (black (○) symbols). (c) Transcritical case T09w110: influence of wall-normal mesh size N_y on the spatial amplification rate γ_r for N_y = 101, 201, and 301.

7.3 Flow cases and DNS setup

The flow parameters of the ZPG boundary-layer flows considered in this chapter are summarised below. These thermodynamic conditions were previously employed by Boldini *et al.* (2025*a*) (see Chapter 6). A free-stream reduced pressure of $p_{r,\infty}$ = 1.10 is selected, while the Mach number is set to 0.2 in alignment with Sayadi *et al.* (2013). With respect to the pseudo-critical temperature T^*_{pc} (T^*_{pc}/T^*_c = 1.024 at p_r = 1.10), three different thermodynamic states at supercritical pressure are examined. All cases feature a heated wall (subscript $(\cdot)_w$) to trigger Mode-II instability. A (i) subcritical-temperature case (T09w095), where the temperature is entirely in the liquid-like state from the free stream ($T_{r,\infty}$ = 0.90) to the wall ($T_{r,w}$ = 0.95); a (ii) supercritical-temperature case (T11w120), where the temperature is entirely in the vapour-like state from the free stream ($T_{r,\infty}$ = 1.10) to the wall ($T_{r,w}$ = 1.20); and a (iii) transcritical-temperature case (T09w110), where the temperature crosses the pseudo-critical value with a liquid-like free stream ($T_{r,\infty}$ = 0.90) and a vapour-like wall ($T_{r,w}$ = 1.10). To illustrate these three thermodynamic states, Fig. 7.2 shows the reduced temperature-pressure (T_r–p_r) diagram with selected isolines of reduced density $\rho_r = \rho^*/\rho^*_c$. All relevant flow parameters are listed in Tab. 7.1.

7.3.1 DNS setup and disturbance strip

The NS equations are integrated in a Cartesian coordinate system over the flat plate. The computational domain starts downstream of the leading edge at x_0 with inlet Reynolds number $Re_{x,0}$. The reference length scale is the boundary-layer thickness at the domain inlet, $\delta^*_{99}(x_0) = \delta^*_{99,0}$. Non-reflecting boundary conditions for single-phase non-ideal-fluid flows

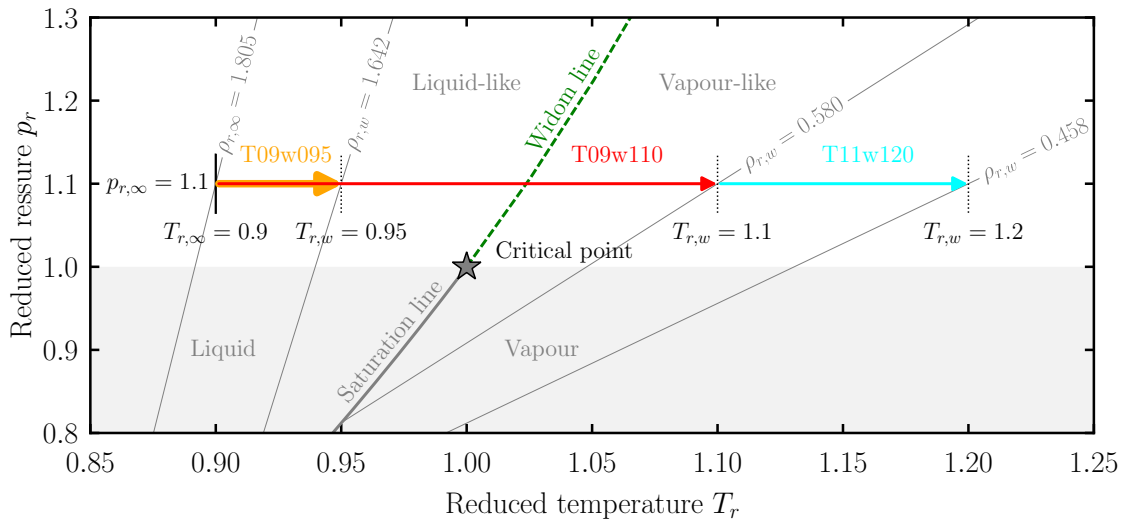

Figure 7.2: Reduced temperature-pressure (T_r–p_r) diagram with isolines of reduced density ρ_r. Isobar at $p_{r,\infty} = 1.10$ indicating the three supercritical cases listed in Tab. 7.1: T09w095 (→), T09w110 (→), and T11w120 (→). The saturation line and pseudo-critical (Widom) line, defined as the locus of the maxima of the specific isobaric heat capacity, follow the approximate generalised equation $p_r = \exp\{(T_r - 1)A_{VdW}/\min(T_r, 1)\}$ with $A_{VdW} = 4$ (Banuti 2015).

Case	T09w095	T11w120	T09w110
State	subcrit. temp.	supercrit. temp.	transcrit. temp.
Wall	isotherm	isotherm	isotherm
T_w^*/T_c^*	0.95	1.20	1.10
T_w^*/T_∞^*	1.056	1.091	1.222
Line style	—	—	—

Table 7.1: Thermodynamic conditions for the three flow cases with free-stream reduced pressure $p_\infty^*/p_c^* = 1.10$ and free-stream reduced temperature $T_\infty^*/T_c^* = 0.90$. For all cases, the Mach number is $M_\infty = 0.2$. The wall temperature is denoted by T_w^*. The non-ideal-flow cases correspond to the thermodynamic states represented in the reduced temperature-pressure (T_r–p_r) diagram in Fig. 7.2.

(Okong'o & Bellan 2002), together with numerical sponge zones (Mani 2012), are applied at the boundaries. At the wall, the no-slip and no-penetration conditions are prescribed, and the wall is isothermal. The grid is equidistant in the streamwise and spanwise (periodic) directions with N_x and N_z points, respectively. In the wall-normal direction, grid stretching is applied to N_y grid points. For the streamwise resolution used here, we ensure a sufficient amount of grid points per streamwise wavelength of the primary wave. Periodic boundary conditions are employed in the spanwise direction, while for 2-D simulations, the number of spanwise computational points equals unity. The initial condition follows the self-similar

Case	L_x	L_y	$N_x \times N_y$	σ	$Re_{x,0}/10^5$	$Re_{x,mid}/10^5$
T09w095	378.3	20.0	3000×600	4.0	0.9	1.3
T11w120	590.3	20.0	3000×600	4.0	0.4	0.78
T09w110	703.8	40.0	3000×600	10.0	0.58	0.96

Table 7.2: Main numerical parameters for the 2-D simulations presented in this work. L_x and L_y denote the streamwise and wall-normal domain sizes, and N_x and N_y are the corresponding numbers of grid points. The stretching factor σ controls the near-wall mesh refinement (Boldini *et al.* 2025*b*). $Re_{x,0}$ and $Re_{x,mid}$ denote the inlet and mid-point disturbance-strip Reynolds numbers, respectively.

laminar boundary-layer profiles based on Lees–Dorodnitsyn variables (Ren *et al.* 2019*b*; Boldini *et al.* 2024). A summary of the main numerical parameters can be found in Tab. 7.2 for the 2-D simulations.

Once the laminar base flow has reached a steady-state solution, disturbances are prescribed at the wall via a blowing/suction disturbance strip as a function of the wall-normal velocity

$$v(x, y = 0, z, t) = f(x)\left[A_1 \sin(\omega_1 t) + A_2 \sin(\omega_2 t + \phi)\right], \tag{7.12}$$

where $A_1 = A_1^*/u_\infty^*$ and $A_2 = A_2^*/u_\infty^*$ are the 2-D wave amplitudes of the primary and secondary waves, respectively. Note that the physically appropriate disturbance is in fact ρv, and if different thermodynamic states with different wall-temperature cases, i.e. different v_w are compared, an equal v-amplitude at the wall does not imply an equal physical perturbation amplitude. Similarly, $\omega_1 = \omega_1^* \delta_{99,0}^*/u_\infty^*$ and $\omega_2 = \omega_2^* \delta_{99,0}^*/u_\infty^*$ are the corresponding primary and secondary frequencies. As this study targets the secondary subharmonic resonance characteristic of Mode II, the forcing frequencies are chosen such that $\omega_2 = 0.5\omega_1$. The spanwise wavenumber β_0 is set to zero, whereas ϕ indicates the phase shift between the fundamental and subharmonic waves. The function $f(x) = 15.1875\xi^5 - 35.4375\xi^4 + 20.25\xi^3$ in Eq. (7.12), with $\xi = (x - x_1)/(x_{mid} - x_1)$ for $x_1 < x < x_{mid}$ and $\xi = (x_2 - x)/(x_2 - x_{mid})$ for $x_{mid} < x < x_2$, where $x_{mid} = (x_1 + x_2)/2$ corresponds to $Re_{x,mid}$, accounts for the streamwise variation. The time step Δt for all simulations is defined based on the frequency of the primary disturbance ω_1 of the disturbance-strip forcing.

7.3.2 Primary instability

Linear stability analysis is performed for the cases listed in Tab. 7.1. Figure 7.3 displays the growth rate $-\alpha_i$ in the Re–F stability diagram, where $Re = \sqrt{Re_x}$. As investigated by Ren *et al.* (2019*b*); Boldini *et al.* (2024), wall heating towards $T_{r,pc}$ in the subcritical state (Fig. 7.3a) has the opposite effect of wall heating away from $T_{r,pc}$ in the supercritical state (Fig. 7.3b). The latter behaves similarly to the ideal-gas conditions with the same T_w^*/T_∞^*-ratio (blue dotted line). The transcritical state in Fig. 7.3(c), featuring the dual-mode instability (Mode I and II) is taken from Boldini *et al.* (2025*a*) (Chapter 6). Moreover,

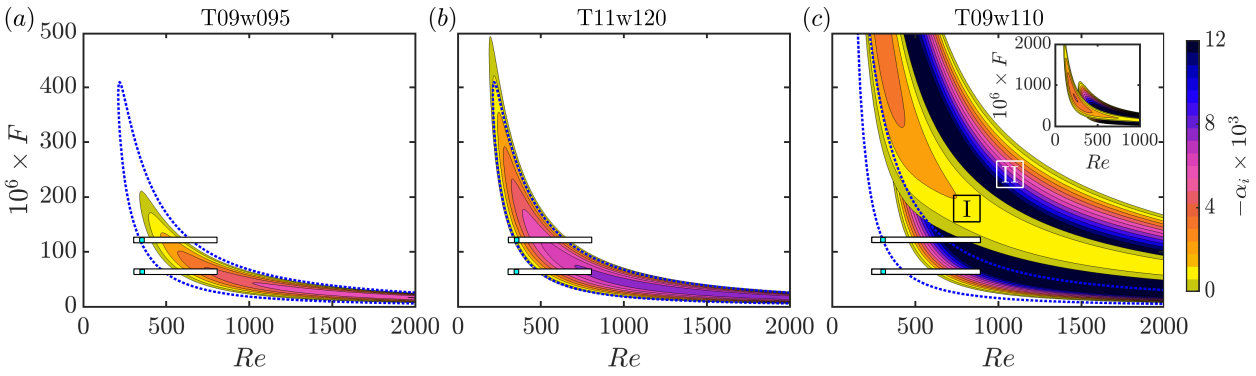

Figure 7.3: Growth-rate ($-\alpha_i$) contours in the Re–F stability diagram: (a) T09w095, (b) T11w120, and (c) T09w110 (Mode I and II). The blue dotted lines indicate the ideal-gas neutral stability curve corresponding to the same T_w^*/T_∞^*-ratio. The inset in panel (c) highlights the broad frequency band over which Mode I and II band coexist. The 2-D DNS domain and perturbation strip used for subharmonic resonance, i.e. $F_1 = 124\times10^{-6}$ and $F_2 = 62\times10^{-6}$, are shown by the white-black and cyan bars, respectively.

in accordance with Boldini *et al.* (2025*a*), the primary TS wave is selected with $F_1 = \omega_1/Re_0 = 124 \times 10^{-6}$. This frequency was used in the H-type breakdown experiments of Kachanov & Levchenko (1984) and has since become a standard choice in studies of subharmonic secondary instabilities in the ideal-gas regime (Herbert 1984 1988). For the 2-D DNS investigation in Sec. 7.5, the DNS domain, indicated by rectangular bars in Fig. 7.3, is placed within the linearly unstable region, with the disturbance strip (coloured in cyan) positioned somewhat upstream of, or close to, Re_{cr} (branch I).

7.4 Secondary instability analysis

A preliminary analysis of the secondary subharmonic instability in the non-ideal-gas cases of Tab. 7.1 is performed. A fixed Re-location and frequency $F = 124 \times 10^{-6}$ for various amplitudes A_0 of the primary wave and spanwise wavenumber $b = 10^3\beta_2/Re$ are considered. The chosen Reynolds number for the SIT analysis is based on the stability diagrams for the primary instability in Fig. 7.3. For the non-transcritical cases, the neutral point at branch II of the stability diagram is selected, $Re = 606$ (with an N-factor of $N = \int_{x_0} -\alpha_i = 0.67$) for case T09w095 and $Re = 660$ ($N = 2.66$) for case T11w120, respectively. Here, the following hold: (i) $|-\alpha_i| \ll |\gamma|$, (ii) the temporal and spatial SIT frameworks yield identical results, and (iii) the TS-wave amplitude is largest (Herbert 1984). For the transcritical case, the second neutral point at $F = 124 \times 10^{-6}$, i.e. at branch II, is only reached at large Reynolds numbers, where breakdown to turbulence has already occurred (Boldini *et al.* 2025*a*). Therefore, a point within the unstable region is selected at $Re = 606$, with the eigenvalue of $\alpha = 0.179 - 0.0095\mathrm{i}$, corresponding to an N-factor of 1.49. Because of the large TS-wave amplitude in this case, unstable modes may not be tuned (i.e. may have a complex γ) to the TS wave and therefore may not propagate at the same phase velocity. In any case,

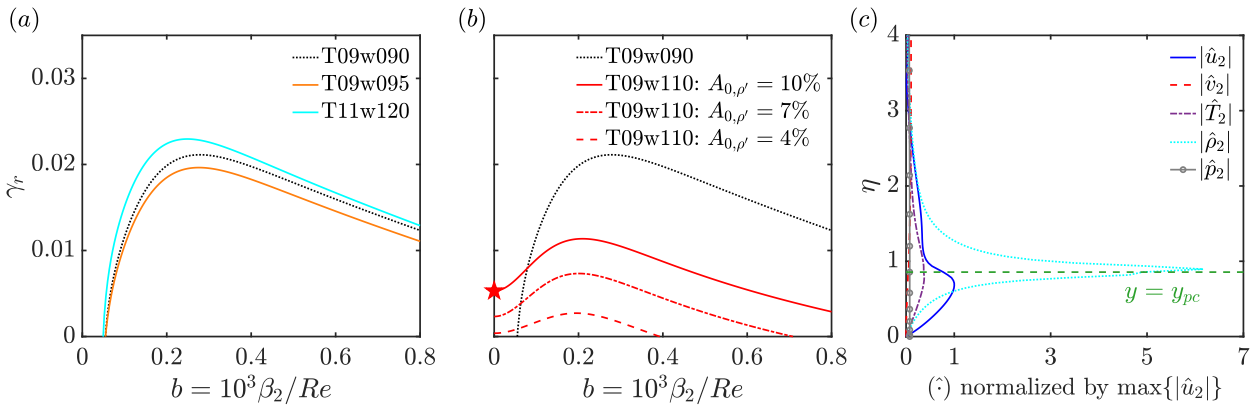

Figure 7.4: (a,b) SIT secondary subharmonic growth rates γ_r as a function of the spanwise wavenumber parameter b. (a) Case T09w090 (incompressible) at Re = 606, T09w095 (subcritical) at Re = 606, and T11w120 (supercritical) at Re = 660 with $A_{0,u'}$ = 1%. (b) Case T09w090 at Re = 606 and case T09w110 with $A_{0,\rho'} = [10\%, 7\%, 4\%]$ at Re = 606. (c) Secondary eigenfunctions, normalised by max{$|\hat{u}|$}, for case T09w110 with $A_{0,\rho'}$ = 10% at b = 0 (see red diamond in panel (b)). The location of the pseudo-critical point $y = y_{pc}$, i.e. where $\bar{T}^* = T^*_{pc}$, is indicated in green (- -).

the mode with the largest real part, i.e. max{γ_r}, is initially considered in the following. In Figs. 7.4(a,b), the influence of the spanwise wavenumber on the amplification of subharmonic disturbances is shown. Figure 7.4(a) displays the growth rate γ_r at $A_{0,u'}$ = 1% for the non-transcritical cases together with the incompressible boundary layer (case T09w090 with T^*_w/T^*_∞ = 1). The amplification decreases with increasing wall temperature in the liquid-like state (see case T09w095), whereas it increases in the vapour-like state (see case T11w120). The maximum amplification shifts from $b \approx 0.3$ (incompressible state) to lower values in both non-transcritical states. For small spanwise wavenumbers, the amplification drops, and there are no weakly 3-D and, in particular, no 2-D subharmonic modes that resonate with the 2-D primary wave, regardless of its amplitude. This behaviour is markedly different for the transcritical case T09w110 in Fig. 7.4(b). Already at moderate primary-wave amplitudes ($A_{0,\rho'}$ = 4%), subharmonic amplification at b = 0 becomes active. This confirms the similarity of a transcritical boundary-layer profile to a strongly decelerated flow (Herbert & Bertolotti 1985) and free-shear layer (Pierrehumbert & Widnall 1982), yet with a substantially lower amplitude-threshold of the primary wave. Note that $A_{0,\rho'}$ = 4% corresponds to $A_{0,u'}$ = 0.57%, as max{$\hat{\rho}_2$} $\approx$ 7 × max{$\hat{u}_2$}. Nonetheless, the largest subharmonic amplification occurs at finite b, i.e. $b_{max} \approx 0.2$ (wave angle $\theta = \arctan(\beta_2/0.5\alpha_r) \approx 53°$). In Fig. 7.4(c), the corresponding subharmonic eigenfunctions $\hat{\mathbf{q}}_2$ are shown for case T09w110 with $A_{0,\rho'}$ = 10%. A similar shape to that of $\hat{\mathbf{q}}_1$ (see Fig. 6.4c) is found for all secondary eigenfunctions, together with a vanishing spanwise velocity perturbation.

This preliminary, localised investigation reveals the possibility of moderate secondary-instability growth under the assumptions of SIT; see Ng & Erlebacher (1992); Herbert (1988) for details. Furthermore, under pseudo-boiling conditions, Boldini *et al.* (2025*a*) observed that higher harmonics actively contribute to the nonlinear destabilisation of the primary wave,

violating SIT assumptions once again. For these reasons, the full spatial development of 2-D subharmonic disturbances is investigated next using DNS. In Sec. 7.5, we present controlled 2-D simulations employing the disturbance-strip parameters introduced in Sec. 7.3.1.

7.5 DNS results

7.5.1 2-D analysis

We perform 2-D forced DNS for the cases reported in Tab. 7.1. The wall-normal forcing at the disturbance strip is applied according to Eq. (7.12). Two 2-D waves are considered: one with varying amplitude A_1, and one with fixed amplitude A_2. The remaining forcing parameters are chosen such that $\omega_1 = 2\omega_2$, ensuring subharmonic resonance, and the phase shift is set initially to $\phi = 0$ in Eq. (7.12). The spanwise wavenumber of all disturbances is zero.

Figure 7.5 shows the results for the non-transcritical cases. The forcing modes $(1,0)$ and $(1/2,0)$ are shown for $A_1 = 7.5\times10^{-3}$ and $A_2 = 8.5\times10^{-5}$ (blue curves) and for $A_1 = 7.5\times10^{-4}$ and $A_2 = 8.5\times10^{-5}$ in red. The subcritical case T09w095 is shown in Fig. 7.5(a), and the supercritical case T11w120 in Fig. 7.5(b). Because the growth of secondary subharmonic instability depends primarily on the amplitude of the primary wave, we increase A_1 by one order of magnitude, from $A_1 = 7.5\times10^{-4}$ to 7.5×10^{-3}. Nevertheless, no 2-D secondary subharmonic growth is observed, in agreement with the SIT analysis in Fig. 7.4. For $A_1 = 7.5\times10^{-4}$, the evolution of modes $(1,0)$ and $(1/2,0)$ largely follows the LST predictions, whereas nonlinear effects destabilise the primary wave, which subsequently influences the behaviour of the subharmonic mode $(1/2,0)$. This effect is more pronounced for the supercritical case T11w120, where the linear growth of the primary wave is stronger (see stability diagram in Figs. 7.3a,b), reaching amplitudes of approximately 7.5% at $Re \approx 680$ before becoming nonlinearly unstable. We conclude that, in the non-transcritical states, subharmonic resonance does not occur for purely 2-D disturbances at moderate primary-wave amplitudes, similarly to the ideal-gas results. A finite spanwise wavenumber is required for resonance.

The transcritical case T09w110 is presented in Fig. 7.6. Together with the primary and secondary waves, higher harmonics are also shown, since they actively participate in the nonlinear stages of transition (Boldini *et al.* 2025*a*). In Fig. 7.6(a), the primary amplitude A_1 is initially set to 7.5×10^{-5}, while the secondary-wave amplitude is kept fixed at $A_2 = 8.5\times10^{-5}$, as in the non-transcritical cases. The growth of modes $(1,0)$ and $(1/2,0)$ follows the LST prediction throughout the DNS domain up to $Re \approx 750$, where mode $(1/2,0)$ departs from its linear behaviour and begins to grow rapidly. When the primary forcing amplitude is increased by one order of magnitude (Fig. 7.6b), a stronger subharmonic amplification is obtained, and the onset of the 2-D subharmonic resonance shifts upstream to approximately $Re \approx 700$, occurring once the amplitude of mode $(1,0)$ exceeds approximately 0.6%. In Fig. 7.6(c), further increasing A_1 results in a pronounced growth of the higher harmonics of Mode II, which are unstable according to LST (Fig. 7.3). These harmonics exceed the amplitude of

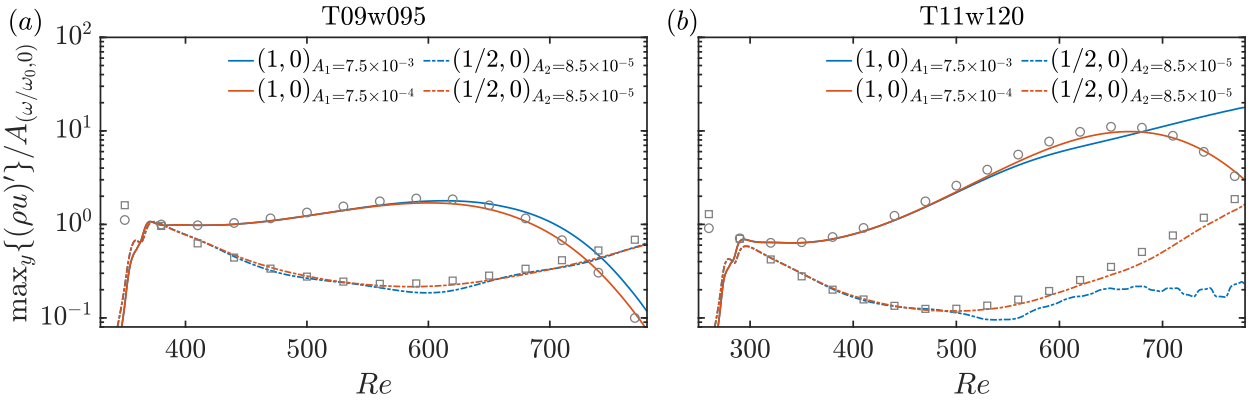

Figure 7.5: Streamwise evolution of the y-maximum disturbance amplitudes $(\rho u)'$, normalised by the corresponding forcing amplitude $A_{(\omega/\omega_0,0)}$, for (a) subcritical case T09w095 ($T_w^*/T_\infty^* = 1.056$) and (b) supercritical case T11w120 ($T_w^*/T_\infty^* = 1.091$). Forcing amplitudes are: $A_1 = 7.5\times10^{-3}$ and $A_2 = 8.5\times10^{-5}$ (blue); $A_1 = 7.5\times10^{-4}$ and $A_2 = 8.5\times10^{-5}$ (red). LST predictions for modes $(1,0)$ and $(1/2,0)$ are shown with grey circles (○) and squares (□), respectively.

the primary mode. In this scenario, which was studied in detail by Boldini *et al.* (2025*a*) for the single-frequency case, mode $(2,0)$ overtakes mode $(1,0)$ and saturates nonlinearly around $Re \approx 700$. Upstream of this location, once mode $(1,0)$ surpasses approximately 0.6%, the 2-D subharmonic resonance sets in, producing a noticeable kink in the growth of $(1/2,0)$ near $Re \approx 650$, associated with the saturation of $(1,0)$. It is evident that an increase of the primary-wave amplitude leads to an earlier onset of subharmonic resonance. A further modification of the growth of mode $(1/2,0)$ occurs downstream, after the resonance between modes $(2,0)$ and $(1,0)$ and the consequent destabilisation of the primary wave. Around $Re \approx 750$, mode $(1/2,0)$ reaches its peak, coinciding with mode $(1,0)$ attaining a 10%-amplitude. At this stage, nonlinear interactions between mode $(3,0)$ and its subharmonic $(3/2,0)$ also appear. Note that, as soon as secondary growth develops, oscillations appear in the evolution of mode $(1/2,0)$. These oscillations are likely linked to a modal shift from Mode II to subharmonic secondary growth, and they become less pronounced as A_1 increases, as seen in Fig. 7.6(c).

In Fig. 7.7, the corresponding amplitude distributions of the secondary disturbances at $Re = 700$ are shown as a function of the primary-wave amplitudes used in Fig. 7.6. For $A_1 = 7.5\times10^{-5}$, where no subharmonic growth is active at $Re = 700$, the secondary disturbance closely follows the LST prediction. When the primary amplitude is increased to $A_1 = 7.5\times10^{-4}$, for which subharmonic growth is present, the secondary amplitude functions become noticeably modified near the peak of $\rho^{(1/2,0)}$ due to the nonlinear self-interaction of the primary wave. For the largest primary amplitude, i.e. $A_1 = 7.5\times10^{-3}$, strong nonlinear effects shift the location of the maximum of the streamwise-velocity amplitude upward, while the density-amplitude profile exhibits two peaks, corresponding to the two wall-normal locations where c_p reaches a maximum. The SIT prediction (black dotted line) for $A_1 = 7.5\times10^{-3}$ clearly demonstrates the breakdown of SIT under these transcritical flow conditions; see Sec. 7.4 for the SIT assumptions.

The 2-D nature of the secondary instability associated with Mode II may also depend

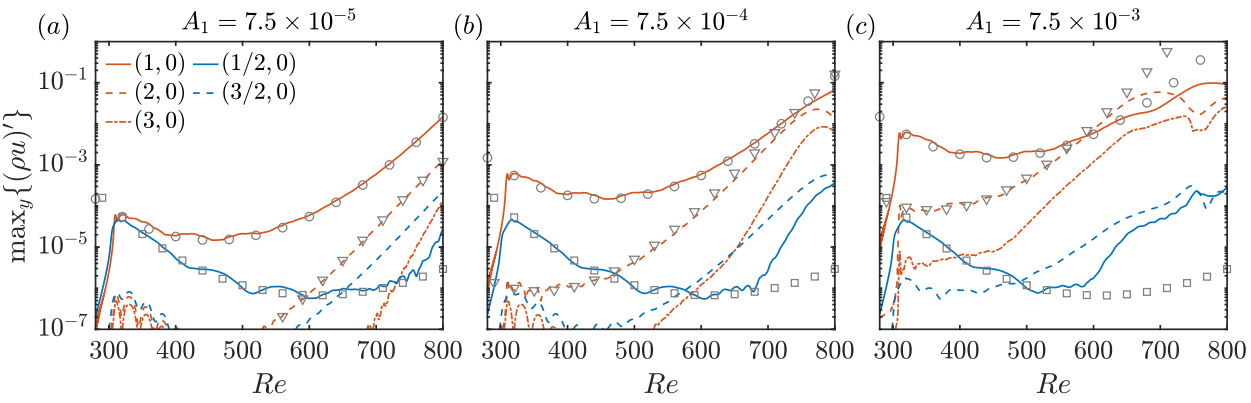

Figure 7.6: Streamwise development of the y-maximum $(\rho u)'$ disturbance amplitudes for case T09w110 (T_w^*/T_∞^* = 1.222). The forcing amplitudes are: (a) $A_1 = 7.5\times10^{-5}$ and $A_2 = 8.5\times10^{-5}$, (b) $A_1 = 7.5 \times 10^{-4}$ and $A_2 = 8.5 \times 10^{-5}$, (c) $A_1 = 7.5 \times 10^{-3}$ and $A_2 = 8.5 \times 10^{-5}$. The LST predictions for mode $(1, 0)$ and $(1/2, 0)$ are represented with (○) and (□), respectively.

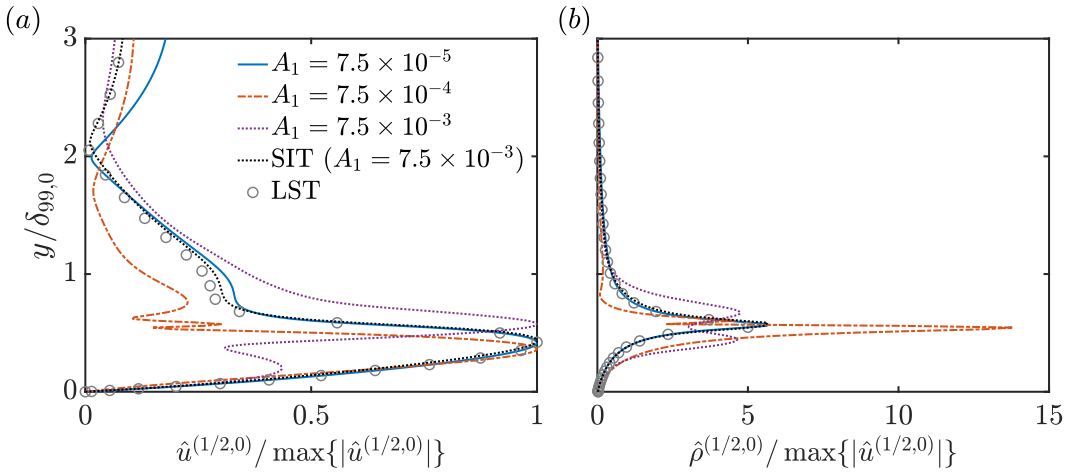

Figure 7.7: DNS results at Re = 700 for case T09w110 with $A_2 = 8.5 \times 10^{-5}$: (a) streamwise-velocity and (b) density perturbation of the subharmonic mode as a function of the wall-normal coordinate $y/\delta_{99,0}$ ($\delta_{99,0}$ is the inlet boundary-layer thickness) normalised by their respective $\max\{|\hat{u}^{(1/2,0)}|\}$. The primary amplitudes are $A_1 = 7.5 \times 10^{-5}$ (blue), $A_1 = 7.5 \times 10^{-4}$ (red), and $A_1 = 7.5 \times 10^{-3}$ (purple). LST predictions are shown with grey (○) symbols.

sensitively on the phase shift between the primary and secondary forcing waves, and, more significantly, on the increase of wall temperature during the supercritical-state transition (crossing the Widom line). Both effects are examined in the following.

Two-dimensional phase-shift effect in the transcritical state

Monkewitz (1988) and Dong *et al.* (2019) demonstrated, both mathematically and numerically, that the phase shift between the Kelvin–Helmholtz mode and its subharmonic strongly influences vortex pairing in stratified shear flows, with increasing phase difference delaying the pairing process. In a related study, Liu *et al.* (2023) showed that, when an isolated shear layer is placed near a solid boundary, the phase difference can vary significantly during

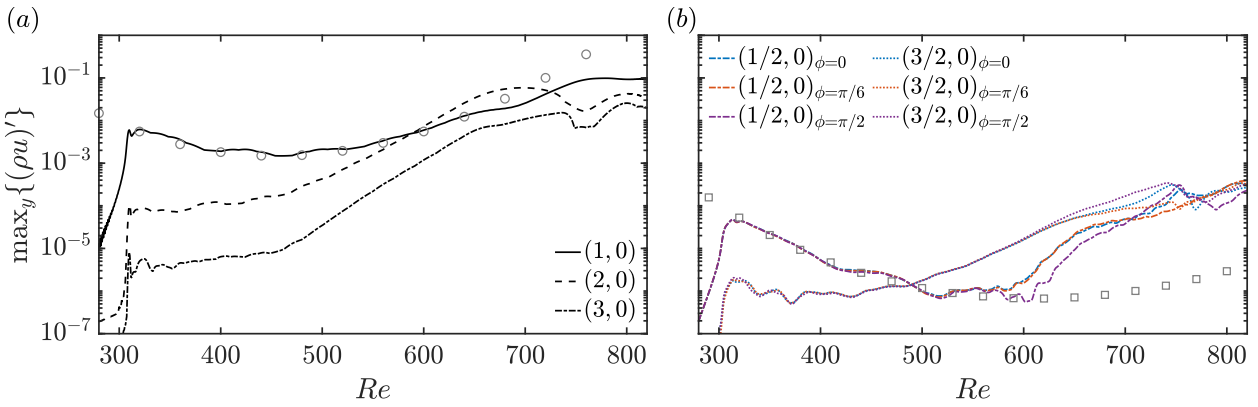

Figure 7.8: Influence of the phase shift ϕ on the streamwise development of the y-maximum $(\rho u)'$ disturbance amplitudes for case T09w110: (a) modes $(1,0)$, $(2,0)$, and $(3,0)$; (b) modes $(1/2,0)$ and $(3/2,0)$. LST predictions for modes $(1,0)$ and $(1/2,0)$ are shown with grey circles ($\circ$) and squares ($\square$), respectively.

the resonance (lock-on) process. For TS waves in a non-self-similar boundary layer, (Würz *et al.* 2012) found that frequency-detuned and spanwise-wavenumber-detuned subharmonic resonances have an extremely large spectral width; however, no resonant interaction between a 2-D primary wave and 2-D subharmonics was observed.

In this section, we examine whether a similar behaviour holds for flat-plate boundary layers under transcritical conditions. Complementary 2-D forced DNS are performed as in Sec. 7.5.1, varying only the phase shift ϕ in Eq. (7.12) between the primary wave and its subharmonic. In Fig. 7.8(a), the evolution of mode $(1,0)$ and its higher harmonics is essentially unaffected by the phase shift. In contrast, Fig. 7.8(b) shows that the phase shift has a larger influence on the 2-D subharmonic mode $(1/2,0)$ and its higher harmonic. As the phase shift increases from $\phi = 0$ to $\pi/2$, the onset of subharmonic resonance $(1/2,0)$ moves slightly downstream. Conversely, the higher harmonic $(3/2,0)$ persists over a longer streamwise distance at $\phi = \pi/2$, reaching its largest amplitude around $Re \approx 740$. Near this Reynolds number, mode $(1/2,0)$ saturates only for $\phi = 0$ and $\pi/2$ before growing again farther downstream. For $\phi = \pi/6$, the growth of the subharmonic mode is smoother and closely follows that of mode $(3/2,0)$. Overall, the influence of the phase shift on the subharmonic resonance is weak. As in the findings of Liu *et al.* (2023), the proximity of the wall in this boundary-layer configuration likely suppresses strong phase-shift effects on phase locking and 2-D vortex pairing.

Wall-temperature effect from subcritical to transcritical state

In Sec. 7.5.1, we identified the presence of 2-D subharmonic resonance in a boundary layer at supercritical-pressure and transcritical-temperature states. Under these flow conditions, which are characterised by the appearance of a GIP, Mode II becomes the dominant instability mechanism. This raises the question of whether unstable 2-D subharmonic modes should always be expected once the Widom line is crossed and pseudo-boiling conditions are reached.

To examine this, we start from the subcritical case T09w095 and gradually increase the

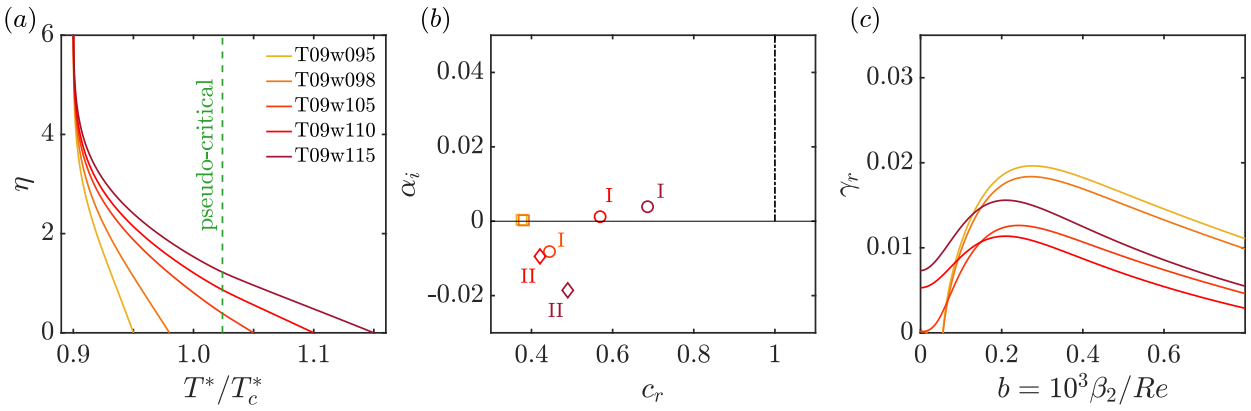

Figure 7.9: (a) Base-flow temperature profiles as a function of the self-similar wall-normal coordinate η. The pseudo-critical point, i.e. the location where $T^* = T^*_{pc}$, is indicated by a green dashed line (– –). (b) Discrete modes of the primary wave at $Re = 606$ and $F = 124 \times 10^{-6}$; squares, circles, and diamonds denote the subcritical TS-like mode, Mode I, and transcritical Mode II, respectively; the black dash-dotted line denotes the continuous entropy/vorticity branch according to Tumin (2007)). (c) Secondary spatial growth rates (γ_r) as a function of the spanwise-wavenumber parameter b. All SIT calculations are performed with the normalisation $A_{0,u'}\,\hat{u}_1 = 0.01$.

wall temperature, transitioning to the transcritical state (T09w110) and beyond, as shown in Fig. 7.9(a). The corresponding discrete modes of the primary wave at $Re = 606$ and $F = 124 \times 10^{-6}$ are shown in Fig. 7.9(b), while Fig. 7.9(c) reports the spatial growth rates of the associated subharmonic secondary mode. All SIT calculations use the most unstable discrete mode, with the primary eigenfunctions normalised such that $A_{0,u'}\hat{u}_1 = 0.01$. In the subcritical state (cases T09w095 and T09w098 marked by square symbols in Fig. 7.9b), increasing the wall temperature reduces the maximum secondary growth rate, $\max\{\gamma_r\}$, while the sharp cut-off near $b \approx 0.05$ remains essentially unchanged. Once the supercritical-state transition is reached, Mode I becomes increasingly destabilised (circle symbols in Fig. 7.9b) up to case T09w105, where the modal amplification is largest. Simultaneously, the cut-off spanwise wavenumber for the subharmonic instability shifts towards $\beta_2 = 0$, although the overall maximum γ_r decreases. For cases T09w110 and T09w115, the transcritical Mode II is the most unstable mode (diamond symbols in Fig. 7.9b). At these conditions, the entire $\gamma_r(b)$ curve in Fig. 7.9(c) shifts to larger spatial growth rates, with a significant contribution of the vortex-pairing mechanism at $b = 0$. This behaviour can be understood by noting that, as the wall temperature increases beyond the pseudo-critical value, the height at which $y = y_{pc}$, in other words, the height of the Widom line, increases. The nonlinear evolution of Mode II generates localised flow reversals near the wall, above which a shear layer forms (see Sec. 6.4.2). As the Widom line moves further from the wall, so does this shear layer. The elevated position of this shear layer reduces the wall-damping effect on the 2-D vortex pairing mode, analogous to the mechanism identified by Herbert & Bertolotti (1985) for ideal-gas boundary layers approaching separation. Here, very large primary-wave amplitudes are required to overcome the wall damping and trigger the 2-D subharmonic resonance.

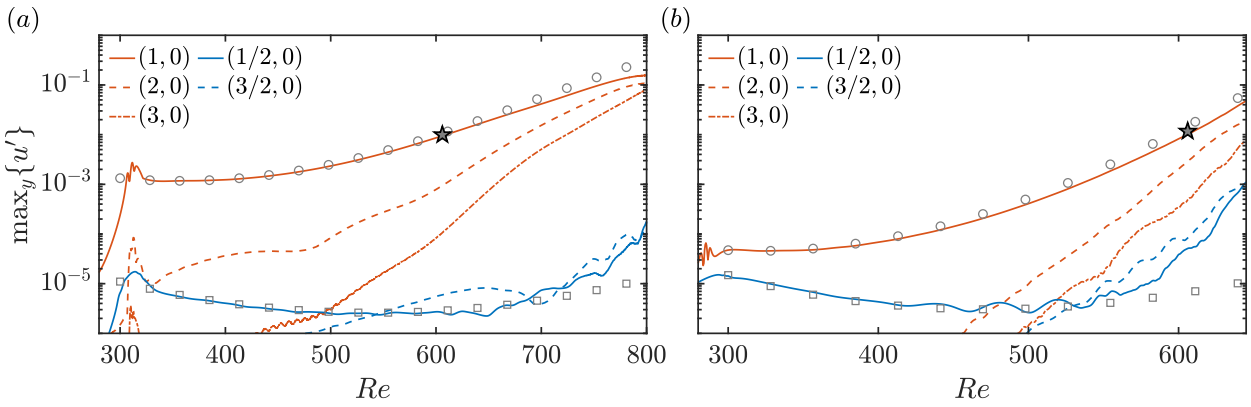

Figure 7.10: Streamwise development of the y-maximum of the streamwise-velocity disturbance u' for (a) case T09w105 ($T_w^*/T_\infty^* = 1.167$) and (b) case T09w115 ($T_w^*/T_\infty^* = 1.278$). LST predictions for modes $(1,0)$ and $(1/2,0)$ are shown with grey circles (○) and squares (□), respectively. The location of the SIT analysis in Fig. 7.9(c), with $A_{0,u'}\hat{u}_1 = 0.01$, is indicated by the star (☆) symbol.

In addition to the SIT calculations, we perform 2-D forced DNS for two selected transcritical cases, i.e. T09w105, which shows no evidence of 2-D vortex pairing at $Re = 606$, and T09w115, which exhibits the strongest subharmonic resonance among all cases at $b = 0$ in Fig. 7.9(c). Except for the wall-temperature variation, all flow conditions and numerical settings match those of case T09w110 in Fig. 7.6. The forcing amplitude of the 2-D primary wave is adjusted to reproduce the same amplitude normalisation used in the SIT analysis, i.e. $A_{0,u'}\,\hat{u}_1 = 0.01$ at $Re = 606$. Figures 7.10(a,b) show the corresponding streamwise amplitude developments for cases T09w105 and T09w115, respectively. The simulations confirm the observations previously obtained by the SIT analysis. For case T09w105, the 2-D subharmonic resonance requires a larger primary-wave amplitude at $Re = 606$, as no subharmonic growth of mode $(1/2,0)$ is observed in Fig. 7.10(a). Notably, a moderate 2-D resonance between modes $(3/2,0)$ and $(1/2,0)$ appears only further downstream, at $Re \approx 640$, causing a slight destabilisation of $(1/2,0)$. In contrast, for case T09w115 in Fig. 7.10(b), 2-D subharmonic resonance occurs at the same primary-wave amplitude as in Fig. 7.10(a), but now begins as early as $Re \approx 530$. At $Re \approx 650$, the secondary growth of $(1/2,0)$ reaches levels that are one to two orders of magnitude smaller than those of the first and second higher harmonics of the primary mode $(1,0)$. The earlier onset is likely linked to the increased primary density perturbations ρ_1', caused by the higher wall temperature, which significantly strengthens the primary wave. Although the velocity-based amplitude $A_{0,u'}\,\hat{u}_1 = 0.01$ remains nominally within the linear range, the associated density fluctuations are much larger, so nonlinear terms involving ρ_1' can already trigger nonlinear effects.

7.5.2 3-D analysis

After confirming the presence of 2-D secondary subharmonic growth in 2-D DNS configurations under transcritical conditions, we extend the study to 3-D DNS and investigate the

L_x	L_y	L_z	$N_x \times N_y \times N_z$	$Re_{x,0}/10^5$	Δx^+_{max}	$\Delta y^+_{w,max}$	Δz^+_{max}	$Re_{\theta,max}$
977.43	40.0	9.63	$14000 \times 900 \times 150$	0.58	4.54	0.49	4.17	799

Table 7.3: Case 'Tw110-LA2D': numerical parameters of the 3-D DNS configuration corresponding to the 2-D case T09w110 listed in Tab. 7.2. Here, L_x, L_y, and L_z are the sizes of the computational domain in the streamwise, wall-normal, and spanwise directions, respectively; N_x, N_y, and N_z denote the number of grid points in the corresponding directions; $Re_{x,0}$ is the inlet Reynolds number; Δx^+_{max}, $\Delta y^+_{w,max}$, and Δz^+_{max} are the maximum grid spacings in the x-, y-, and z-directions relative to the maximum viscous length scale in the domain, $\overline{\mu}_w/(\overline{\rho}_w u_\tau)$.

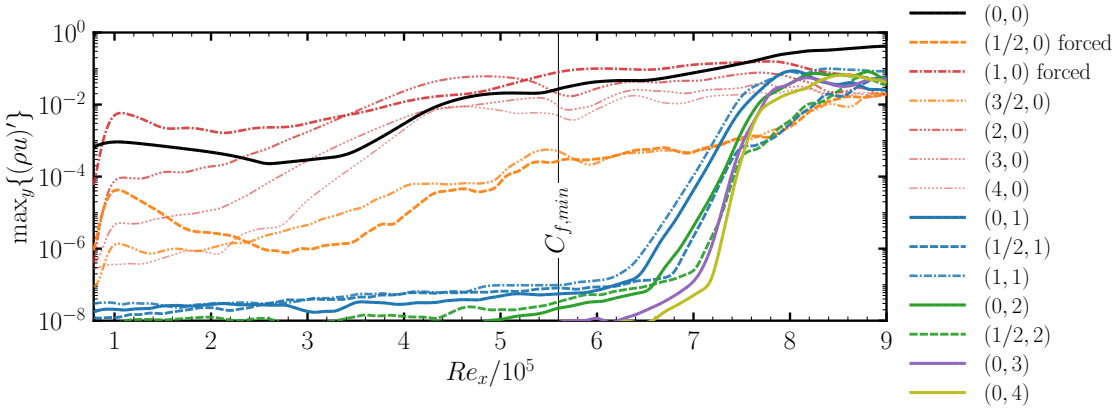

Figure 7.11: Streamwise evolution of the y-maximum of $(\rho u)'$ for the most relevant modes $(\omega/\omega_{2\text{-D}}, \beta/\beta_0)$ for case Tw110-LA2D. The minimum value of the time- and spanwise-averaged skin-friction coefficient is indicated as $C_{f,min} = \min\{C_f\}$.

full breakdown to turbulence via 2-D subharmonic resonance. The forcing parameters are taken from the 2-D DNS case T09w110 in Fig. 7.6(c) with $A_1 = 7.5 \times 10^{-3}$, $F_1 = 124 \times 10^{-6}$, $A_2 = 8.5 \times 10^{-5}$, and $F_2 = 62 \times 10^{-6}$ ($\beta_0 = 0$). These correspond to the transcritical case 'Tw110' in Chapter 6. The only difference lies in the spanwise wavenumber imposed at the disturbance strip, which is set to $\beta_0 = 0$ here. The numerical parameters of the 3-D DNS setup, hereafter referred to as case 'Tw110-LA2D', are reported in Tab. 7.3.

Figure 7.11 illustrates the modal evolution. In this configuration, mode $(1/2, 0)$ is forced at the same amplitude as $(1/2, 1)$ in case Tw110-LA (see Fig. 6.10), while no oblique subharmonic is introduced. The evolution of the fundamental wave $(1, 0)$ and its higher harmonics follows the same development as in the other Tw110 cases up to saturation. Mode $(1/2, 0)$ undergoes 2-D subharmonic resonance with the primary wave, as predicted by the SIT and 2-D DNS under transcritical conditions, with $(1/2, 0)$ and $(3/2, 0)$ growing rapidly beyond $Re_x/10^5 \approx 4.5$. This confirms that the 2-D subharmonic instability mechanism, typically inactive in ideal-gas boundary layers, is indeed active under pseudo-boiling conditions. However, its growth rate remains lower than that of the fundamental-resonance wave–vortex triad $(1, 0)$–$(0, 1)$–$(1, 1)$. Consequently, before the 2-D subharmonic can reach nonlinear satura-

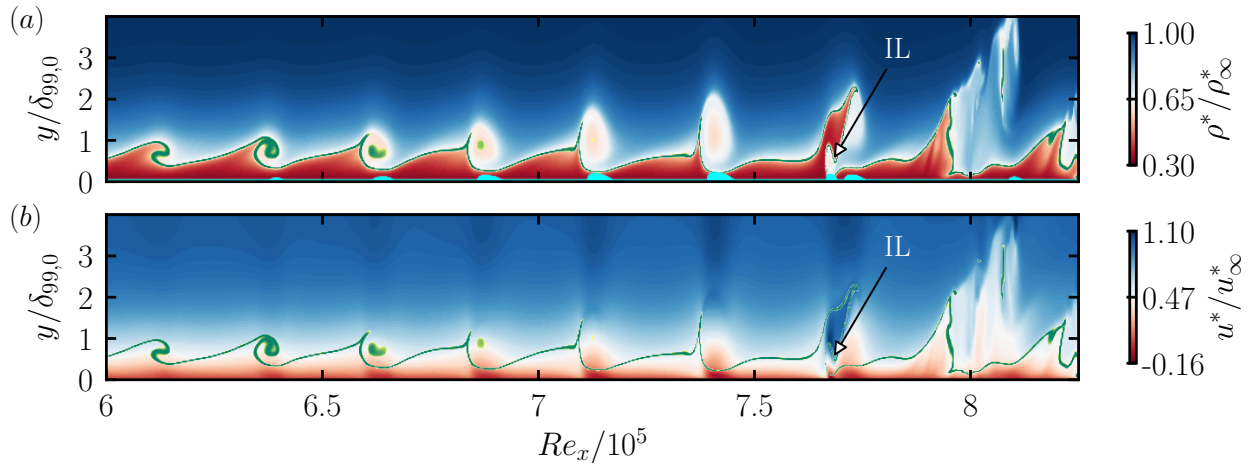

Figure 7.12: Instantaneous contours in the wall-normal xy-plane of (a) density and (b) streamwise velocity. In (a), the near-wall region for which $u < 0$ is coloured in cyan. The Widom line $y = y_{WL}$ lies within the green region, i.e. between $95\%\max\{c_p\}$ and $\max\{c_p\}$. The 'inverted lower' high-shear layer is labelled as 'IL' similarly to Sec. 6.5.2.

tion, the oblique modes $(1,1)$ and $(0,1)$ are nonlinearly amplified and drive the breakdown to turbulence, following the same fundamental-resonance pathway observed in case Tw110-IA. Notably, as in case Tw110-IA, modes $(1,1)$ and $(0,1)$ arise initially from numerical background noise and only begin to behave as discrete boundary-layer wave modes further downstream, once the wave–vortex triad with $(1,0)$ is established. This confirms that the fundamental-resonance mechanism is more robust than the 2-D subharmonic one, even when the latter is explicitly forced at finite amplitude. The 2-D subharmonic thus represents an additional instability mechanism unique to transcritical boundary layers, but does not bypass the inherently 3-D nature of the final breakdown process.

Snapshots of density and streamwise velocity in the boundary-layer xy-plane at a constant spanwise location of $z/\delta_{99,0} = 0$ are shown in Figs. 7.12(a,b). In Fig. 7.12(a), the initial spanwise-invariant billow roll-ups of Mode II are visible, with regions of flow reversals (coloured in cyan) forming near the troughs. As the billows grow in the streamwise direction, the flow-reversal pockets expand. Consistent with the findings in Sec. 6.5.2, an 'inverted lower' high-shear layer (denoted as 'IL') develops above these flow-reversal regions as the mean-flow profile becomes strongly inflectional. The appearance of this 'IL' layer occurs in Fig. 7.12 at $Re_x/10^5 \approx 7.7$ and marks the onset of its propagation through the boundary layer, eventually breaking down into oppositely-signed longitudinal vortices. These flow structures are consistent with the modal analysis in Fig. 7.11, where the fundamental wave $(1,0)$ and its harmonics dominate the nonlinear development, while the 2-D subharmonic $(1/2,0)$ remains at linear amplitude levels and does not significantly alter the breakdown.

Figures 7.13(a–c) present the streamwise development of the skin-friction coefficient C_f, Stanton number St, and shape factor H_{12}, respectively. For comparison, the additional transcritical cases discussed in Chapter 6 are included. The global quantities for case Tw110-LA2D closely follow those of case Tw110-IA up to $Re_x/10^5 \approx 8.0$, consistent with the similar

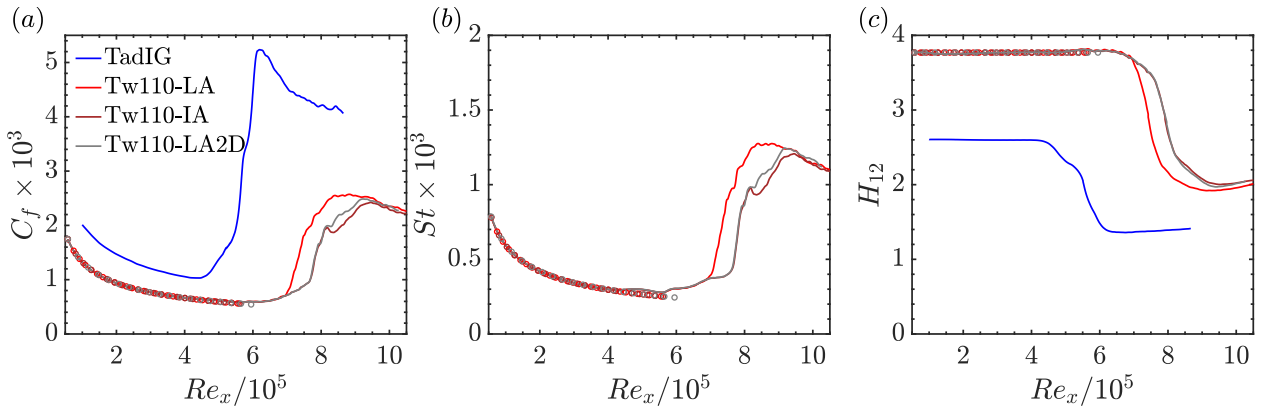

Figure 7.13: Time- and spanwise-averaged: (a) skin-friction coefficient C_f, (b) Stanton number St, and (c) shape factor H_{12} as functions of Re_x. Solid lines denote DNS results, while circle ($\circ$) symbols represent the self-similar laminar correlations from Eq. (6.2a,b) with initial transcritical conditions as in Sec. 6.3.1. Cases TadIG, Tw110-LA, and Tw110-IA are discussed in Chapter 6.

breakdown pathway identified in the modal analysis: both cases transition via fundamental resonance of the $(1,0)$–$(0,1)$–$(1,1)$ triad rather than through subharmonic mechanisms. Beyond this location, C_f and St for case Tw110-LA2D no longer exhibit the plateau observed in case Tw110-IA but continue to rise towards their fully turbulent values. This is attributed to the stronger amplification of the steady mode $(0,1)$ in case Tw110-LA2D, as evident from the modal analysis in Fig. 7.11: nonlinear interactions between the 2-D subharmonic $(1/2,0)$ and the fundamental wave $(1,0)$ feed energy into the wave–vortex triad $(1,0)$–$(0,1)$–$(1,1)$, accelerating the breakdown to turbulence compared to case Tw110-IA. The distribution of the shape factor H_{12} closely resembles that of case Tw110-IA, further confirming that the 2-D subharmonic disturbance, despite being active as predicted by the Floquet analysis, does not contribute significantly to the mean-flow distortion. This is consistent with mode $(1/2,0)$ remaining at linear amplitudes up to the late breakdown stage, while the nonlinear dynamics are essentially governed by the fundamental wave and its 3-D breakdown.

7.6 Conclusions

Secondary subharmonic resonance in zero-pressure-gradient wall-heated flat-plate boundary layers with supercritical fluids has been investigated using both Floquet-based Secondary Instability Theory (SIT) and Direct Numerical Simulations (DNS). Three thermodynamic states at supercritical pressure (p_r = 1.10) were examined: a subcritical-temperature case (T09w095) with the flow entirely in the liquid-like state ($T^* < T^*_{pc}$), a supercritical-temperature case (T11w120) entirely in the vapour-like state ($T^* > T^*_{pc}$), and a transcritical case (T09w110) where the temperature crosses the pseudo-critical temperature T^*_{pc} from a liquid-like free stream to a vapour-like near-wall region.

To capture non-ideal gas effects, the Floquet-based SIT framework of Ng & Erlebacher

(1992) was extended to account for the nonlinear dependence of thermodynamic and transport properties on pressure and temperature perturbations. This required a modified amplitude normalisation based on density fluctuations rather than velocity for the transcritical case, where density perturbations exceed velocity perturbations by more than an order of magnitude. The SIT analysis is complemented by DNS using the open-source GPU-accelerated solver CUBENS to account for the mean-flow distortion and higher-harmonic interactions that violate SIT assumptions under pseudo-boiling conditions.

The SIT analysis revealed that secondary subharmonic instability characteristics depend strongly on wall temperature and primary-wave amplitude. In the non-transcritical cases, subharmonic amplification decreases in the liquid-like state ($T_w^*/T_\infty^* = 1.056$) and increases in the vapour-like state ($T_w^*/T_\infty^* = 1.091$) relative to the incompressible (ideal-gas) boundary layer, with the most amplified spanwise wavenumber for secondary instability shifting towards smaller values. Crucially, in these states, Two-Dimensional (2-D) subharmonic modes exhibit no resonance with the 2-D primary wave at moderate amplitudes – consistent with classical ideal-gas boundary-layer behaviour.

For the transcritical case ($T_w^*/T_\infty^* = 1.222$), the SIT analysis reveals a fundamentally different behaviour. At primary-wave amplitudes as low as $A_{0,\rho'} = 4\%$ (corresponding to only $A_{0,u'} = 0.57\%$), 2-D subharmonic disturbances become unstable at zero spanwise wavenumber – behaviour reminiscent of free shear layers and strongly decelerated boundary layers, yet occurring at substantially lower amplitude thresholds than previously reported for ideal-gas flows. This low threshold is attributed to the inflectional velocity profile induced by pseudo-boiling: the shear layer associated with the Widom line is elevated away from the wall, reducing the wall-damping effect on the 2-D vortex-pairing mode. Nevertheless, the maximum subharmonic growth rate still occurs at finite spanwise wavenumber parameters ($b_{max} \approx 0.2$) corresponding to a wave angle of approximately 53°), and the secondary eigenfunctions retain a structure similar to the primary Mode II disturbance, with the density fluctuation peaking at the Widom line.

The DNS investigations confirmed the SIT predictions for the non-transcritical cases: no 2-D subharmonic resonance occurs, and three-dimensional (3-D) modes are required for secondary instability growth. In the transcritical case, however, significant 2-D subharmonic amplification was observed, with resonance setting in once the primary wave exceeds approximately 0.6% of the free-stream mass flux. The onset location shifts upstream with increasing forcing amplitude. Higher harmonics, particularly mode $(2, 0)$, grow rapidly to nonlinear amplitudes, eventually exceeding the primary wave and invalidating the SIT assumptions. The secondary eigenfunctions develop pronounced nonlinear features, including multi-peaked velocity and density disturbance profiles. A phase-shift analysis indicates that 2-D subharmonic growth depends only weakly on the relative phase between primary and secondary waves, in contrast to the strong phase dependence observed in free shear layers. A parametric study of wall temperature revealed that 2-D subharmonic resonance at zero spanwise wavenumber emerges only when the Widom line is sufficiently far from the wall. As wall temperature increases beyond the pseudo-critical value, the high-shear region associated

with the Widom line rises, reducing the wall-damping effect on the vortex-pairing mode and enabling 2-D subharmonic growth at progressively lower primary-wave amplitudes.

The 3-D DNS of the transcritical case with explicit 2-D subharmonic forcing confirmed that this instability mechanism is active under pseudo-boiling conditions: modes $(1/2, 0)$ and $(3/2, 0)$ undergo resonance with the primary wave, as predicted by the SIT analysis and 2-D DNS. However, despite the 2-D subharmonic resonance, the $(1/2, 0)$ mode remains at linear amplitude levels up to the late breakdown stage. Its growth rate is lower than that of the fundamental-resonance wave–vortex triad $(1, 0)$–$(0, 1)$–$(1, 1)$, which arises from numerical background noise and drives the breakdown to turbulence following the same K-type-like scenario observed in case Tw110-IA of Chapter 6. Nonetheless, nonlinear interactions between the 2-D subharmonic and the fundamental wave strengthen the $(0, 1)$ mode, resulting in slightly earlier transition compared to the case Tw110-IA with infinitesimal 3-D forcing. The 2-D subharmonic thus represents an additional instability mechanism unique to transcritical boundary layers, but does not bypass the inherently 3-D nature of the final breakdown process.

Bibliography

Adams, N. A. & Kleiser, L. 1995 Subharmonic transition to turbulence in a flat-plate boundary layer at Mach number 4.5. *J. Fluid Mech.* **317**, 301–335.

Banuti, D. T. 2015 Crossing the Widom-line – Supercritical pseudo-boiling. *J. Supercrit. Fluids* **98**, 12–16.

Boldini, P. C., Bugeat, B., Peeters, J. W. R., Kloker, M. & Pecnik, R. 2024 Transient growth in diabatic boundary layers with fluids at supercritical pressure. *Phys. Rev. Fluids* **9**, 083901.

Boldini, P. C., Bugeat, B., Peeters, J. W. R., Kloker, M. & Pecnik, R. 2025*a* Direct numerical simulation of complete transition to turbulence with a fluid at supercritical pressure. *J. Fluid Mech.* **1025**, A59.

Boldini, P. C., Hirai, R., Costa, P., Peeters, J. W. R. & Pecnik, R. 2025*b* CUBENS: A GPU-accelerated high-order solver for wall-bounded flows with non-ideal fluids. *Comput. Phys. Commun.* **309**, 109507.

Bugeat, B., Boldini, P. C., Hasan, A. M. & Pecnik, R. 2024 Instability in strongly stratified plane Couette flow with application to supercritical fluids. *J. Fluid Mech.* **984**, A31.

Candler, G. V. 2019 Rate effects in hypersonic flows. *Annu. Rev. Fluid Mech.* **51**, 379–402.

Chang, C. L. & Malik, M. R. 1994 Oblique-mode breakdown and secondary instability in supersonic boundary layers. *J. Fluid Mech.* **273**, 323–360.

Chen, X., Wang, L. & Fu, S. 2021 Secondary instability of the hypersonic high-enthalpy boundary layers with thermal–chemical nonequilibrium effects. *Phys. Fluids* **33**, 034132.

Dong, W., Tedford, E. W., Rahmani, M. & Lawrence, G. A. 2019 Sensitivity of vortex pairing and mixing to initial perturbations in stratified shear flows. *Phys. Rev. Fluids* **4**, 063902.

El-Hady, N. M. 1991 Spatial three-dimensional secondary instability of compressible boundary layer flows. *AIAA J.* **29** (5), 688–696.

Fezer, A. & Kloker, M. 1999 Spatial direct numerical simulation of transition phenomena in supersonic flat-plate boundary layers. In *Laminar–Turbulent Transition (ed. R. Kobayashi)*, p. 415–420. Springer.

Guardone, A., Colonna, P., Pini, M. & Spinelli, A. 2024 Nonideal compressible fluid dynamics of dense vapors and supercritical fluids. *Annu. Rev. Fluid Mech.* **56** (1), 241–269.

Herbert, T. 1984 Analysis of the subharmonic route to transition in boundary layers. *AIAA Pap.* **84**, 0009.

Herbert, T. 1988 Secondary instability of boundary layers. *Annu. Rev. Fluid Mech.* **20**, 487–526.

Herbert, T. & Bertolotti, F. P. 1985 The effect of pressure gradients on the growth of subharmonic disturbances in boundary layers. In *Conference Low Reynolds Number Airfoil Aerodynamics (Notre Dame University)*, pp. 65–76.

Jossi, A. J., Stiel, L. I. & Thodos, G. 1962 The viscosity of pure substances in the dense gaseous and liquid phases. *AIChE J.* **8**, 59–63.

Jouin, A., Ciola, N., Cherubini, S. & Robinet, J.-C. 2024 Detuned secondary instabilities in three-dimensional boundary-layer flow. *Phys. Rev. Fluids* **9**, 043901.

Kachanov, Yu. S. & Levchenko, V. Ya. 1984 The resonant interaction of disturbances at laminar-turbulent transition in a boundary layer. *J. Fluid Mech.* **138**, 209–247.

Klebanoff, P. S., Tidstrom, K. D. & Sargent, L. M. 1962 The three-dimensional nature of boundary-layer instability. *J. Fluid Mech.* **12**, 1–34.

Kloker, M. 1993 Direkte numerische Simulation des laminar-turbulenten Strömungsumschlages in einer stark verzögerten Grenzschicht. PhD thesis, University of Stuttgart.

Kloker, M. 2024 A note on the flow topology during laminar-turbulent transition induced by Tollmien–Schlichting waves. ResearchGate, Report Number: IAG-TN-2024-LTT-02, available at: https://www.researchgate.net/publication/385746142.

Kumar, C. & Prakash, A. 2021 Secondary subharmonic instability of hypersonic boundary layer in thermochemical equilibrium over a flat plate. *Phys. Fluids* **33**, 024107.

Liu, C.-L., Kaminski, A. & Smyth, W. D. 2023 The effects of boundary proximity on Kelvin–Helmholtz instability and turbulence. *J. Fluid Mech.* **966**, A2.

Mani, A. 2012 Analysis and optimization of numerical sponge layers as a nonreflective boundary treatment. *J. Comput. Phys.* **231**, 704–716.

Marxen, O., Iaccarino, G. & Magin, T. E. 2014 Direct numerical simulations of hypersonic boundary-layer transition with finite-rate chemistry. *J. Fluid Mech.* **755**, 35–49.

Masad, J. A. & Nayfeh, A. H. 1990 Subharmonic instability of compressible boundary layers. *Phys. Fluids* **2** (8), 1380–1392.

Mayer, C. S. J. & Fasel, H. F. 2008 Investigation of asymmetric subharmonic resonance in a supersonic boundary layer at Mach 2 using dns. *AIAA Pap.* p. 0591.

Monkewitz, P. A. 1988 Subharmonic resonance, pairing and shredding in the mixing layer. *J. Fluid Mech.* **188**, 223–252.

Morkovin, M. V. 1969 On the many faces of transition. In *Viscous Drag Reduction* (ed. C. S. Wells), p. 1–31. Springer.

Ng, L. L. & Erlebacher, G. 1992 Secondary instabilities in compressible boundary layers. *Phys. Fluids* **4**, 710–726.

Okong'o, N. & Bellan, J. 2002 Consistent boundary conditions for multicomponent real gas mixtures based on characteristic waves. *J. Comput. Phys.* **176**, 330–344.

Pierrehumbert, R. T. & Widnall, S. E. 1982 The two- and three-dimensional instabilities of a spatially periodic shear layer. *J. Fluid Mech.* **114**, 59–82.

Ren, J., Fu, S. & Pecnik, R. 2019*a* Linear instability of Poiseuille flows with highly non-ideal fluids. *J. Fluid Mech.* **859**, 89–125.

Ren, J., Marxen, O. & Pecnik, R. 2019*b* Boundary-layer stability of supercritical fluids in the vicinity of the Widom line. *J. Fluid Mech.* **871**, 831–864.

Rist, U. & Fasel, H. 1995 Direct numerical simulation of controlled transition in a flat-plate boundary layer. *J. Fluid Mech.* **298**, 211–248.

Sayadi, T., Hamman, C. W. & Moin, P. 2013 Direct numerical simulation of complete H-type and K-type transitions with implications for the dynamics of turbulent boundary layers. *J. Fluid Mech.* **724**, 480–509.

Schmid, P. J. & Henningson, D. S. 2001 *Stability and transition in shear flows*. Springer.

Sciacovelli, L., Cinnella, P. & Gloerfelt, X. 2017a Direct numerical simulations of supersonic turbulent channel flows of dense gases. *J. Fluid Mech.* **821**, 153–199.

Sivasubramanian, J. & Fasel, H. F. 2014 Numerical investigation of the development of three-dimensional wavepackets in a sharp cone boundary layer at Mach 6. *J. Fluid Mech.* **756**, 600–649.

Sivasubramanian, J. & Fasel, H. F. 2015 Direct numerical simulation of transition in a sharp cone boundary layer at Mach 6: fundamental breakdown. *J. Fluid Mech.* **768**, 175–218.

Stiel, L. I. & Thodos, G. 1964 The thermal conductivity of nonpolar substances in the dense gaseous and liquid regions. *AIChE J.* **10**, 26–30.

Tumin, A. 2007 Three-dimensional spatial normal modes in compressible boundary layers. *J. Fluid Mech.* **586**, 295–322.

Würz, W., Sartorius, D., Kloker, M., Borodulin, V. I., Kachanov, Y. S. & Smorodsky, B. V. 2012 Detuned resonances of Tollmien-Schlichting waves in an airfoil boundary layer: experiment, theory, and direct numerical simulation. *Phys. Fluids* **24** (9), 094103.

Xu, J., Lu, J., Mughal, S., Yu, P. & Bai, J. 2020 Secondary instability of Mack mode disturbances in hypersonic boundary layers over micro-porous surface. *Phys. Fluids* **32**, 044105.

8

CONCLUSIONS AND FUTURE RESEARCH

'Non quia difficilia sunt non audemus,
sed quia non audemus difficilia sunt.'

Seneca the Younger, Moral Letters to Lucilius

The final chapter summarises the overall findings of this thesis and highlights its contribution to advancing the field. Based on these results, recommendations are provided for future research directions.

8.1 Conclusions

The investigations conducted in this work aimed to develop a comprehensive understanding of the laminar-to-turbulent transition in zero-pressure-gradient boundary layers with fluids at supercritical pressure. To this end, a systematic framework combining modal stability theory (including both primary and secondary instabilities), non-modal stability analysis, and Direct Numerical Simulations (DNS) has been established. The high-fidelity, cost-effective, and energy-efficient numerical simulations, which cover transitional to fully turbulent wall-bounded flows, were enabled by a newly developed high-order, GPU-accelerated solver tailored for fluids in non-ideal thermodynamic states. This framework has enabled a detailed investigation of the mechanisms driving both linear and nonlinear disturbance amplification across various stages of transition to turbulence in the non-ideal, single-phase thermodynamic region, particularly near the pseudo-critical (Widom) line, where the ideal-gas assumption breaks down and thermophysical properties vary sharply. Based on the theoretical analyses and numerical simulations, the following main conclusions can be drawn:

Modal stability analysis (Chapters 3 and 7)

- Under pseudo-boiling conditions (crossing of the pseudo-critical temperature) in the zero-Eckert-number limit: (i) with wall heating, the transcritical Mode II found by Ren *et al.* (2019) is recovered; and (ii) with wall cooling, not previously examined, the Tollmien–Schlichting-like Mode I is found to be entirely suppressed, consistent with the well-known stabilising effect of cooling on viscous instabilities, while an inviscid mode with characteristics similar to Mode II emerges instead. Inviscid stability calculations confirm the existence of this unstable mode in the presence of a Generalised Inflection Point (GIP). The GIP's origin is then linked to a minimum in kinematic viscosity at the Widom line. This finding is universal for non-polar supercritical fluids under pseudo-boiling conditions.

- The same Mode-II instability is recovered using reduced cubic equations of state (e.g. Van der Waals), confirming that the physical mechanism is not tied to a specific fluid model.

- Oblique modal stability analysis shows that, in the zero-Eckert-number limit, Two-Dimensional (2-D) modes dominate both local and integral amplification across all thermodynamic states. With increasing compressibility, neutral 2-D waves of inviscid Mode II become destabilised, causing Three-Dimensional (3-D) perturbations to become more unstable than their 2-D counterparts. Extending the inviscid framework of Lees & Lin (1946) to non-ideal gases reveals that this behaviour originates from a

critical-layer mechanism, consistent with the generalised Fjørtoft criterion, that emerges at finite Mach number and promotes oblique-wave amplification.

- A simplified plane Couette flow model with strong density and viscosity stratifications, typical of supercritical fluids, demonstrates that an inviscid instability arises from a localised maximum of density-weighted vorticity. This maximum satisfies the generalised Fjørtoft criterion. The instability consists of two phase-locked vorticity waves generated by shear and baroclinic effects around the kinematic-viscosity minimum.

- Floquet-based secondary instability analysis reveals that, under pseudo-boiling conditions, 2-D subharmonic modes can become unstable even at moderate primary-wave amplitudes – a behaviour reminiscent of free shear layers or strongly decelerated flows.

Non-modal stability analysis (Chapter 4)

- To account for non-ideal gas behaviour, a new energy norm is derived. The norm reduces to Chu's (Chu 1965) and Mack's (Hanifi *et al.* 1996) norms under the ideal-gas assumption.

- Under pseudo-boiling conditions, the presence of transcritical Mode II leads to an optimal energy growth driven by the combined effects of the lift-up and Orr mechanisms. The resulting streaks are streamwise-modulated, at an angle scaling like Re^{-1}, and exhibit strong thermal components.

- Under pseudo-boiling conditions, non-modal N-factors resemble those induced by an adverse pressure gradient in incompressible ideal-gas boundary layers. Cooling beyond the Widom line greatly enhances optimal growth but is accompanied by a strong inviscid instability (inflectional profile). Conversely, heating beyond the Widom line yields sufficiently large optimal growth to potentially trigger transition, especially under high free-stream turbulence.

CUBic Equation of state Navier–Stokes solver (Chapter 5)

- The open-source, high-order CUBic Equation of state Navier–Stokes (CUBENS) solver has been developed for DNS of transitional and turbulent flows with compressible non-ideal fluids. CUBENS is the first open-source, GPU-accelerated, high-order solver capable of simulating wall-bounded flows in the supercritical fluid region, incorporating cubic equations of state and transport-property models with a kinetic-energy- and entropy-preserving (KEEP) discretisation for numerical stability under strong property variations.

- CUBENS efficiently operates on the latest-generation GPU-accelerated clusters and is fully compatible with the two leading architectures, NVIDIA and AMD. In multi-node and multi-GPU configurations ranging from 2 to 128 compute nodes (8 to 512 GPUs),

it achieves a strong-scaling speed-up factor of around 52% and a weak-scaling efficiency of 0.88 with 1024^3 points per GPU.

- The solver has been validated against various benchmark cases, including the compressible Taylor–Green vortex, stratified and unstratified controlled boundary-layer transition scenarios, and turbulent boundary layers, demonstrating accuracy and robustness across ideal- and non-ideal-fluid states.

Direct numerical simulations (Chapter 6)

- Under pseudo-boiling conditions, nonlinear forcing of a single 2-D wave excites higher harmonics near the forcing region, triggering resonant interactions that cause billowing of the Widom line and generate Kelvin–Helmholtz-like structures. Large near-wall velocity perturbations induce periodic, localised separation zones with a generalised inflection point, linked to inviscid instability, and similar to effects seen under strong adverse pressure gradients in ideal-gas boundary layers.

- Regarding the breakdown to turbulence in the absence of pseudo-boiling, the addition of a pair of subharmonic oblique waves to a large-amplitude 2-D wave shows that infinitesimal 3-D perturbations fail to trigger transition, while finite-amplitude 3-D forcing leads to H-type breakdown with the formation of Λ-vortices and a sharp skin-friction overshoot resembling the ideal-gas reference case.

- Under pseudo-boiling conditions (wall heating), transition can occur relatively early via a naturally selected fundamental (K-type) breakdown, even without oblique wave forcing, as a single amplified 2-D wave is sufficient to trigger nonlinearities by amplifying background noise. The breakdown to turbulence is abrupt, without a marked skin-friction overshoot, but is characterised by lower transitional momentum-thickness Reynolds numbers.

- In the fully turbulent region, a predictive tool is developed that accurately captures mean velocity and temperature profiles, enabling estimation of skin-friction and heat-transfer coefficients using variable-property scaling theories. Notably, the Reynolds analogy is found to hold under pseudo-boiling conditions.

8.2 Future research

While the results presented in this thesis advance our understanding of transition mechanisms in supercritical fluids, they represent only a first step. One important effect not considered here is buoyancy. The strong density variations that occur near the pseudo-critical point may give rise to significant buoyancy effects, which can substantially influence flow stability depending on wall thermal conditions. In transcritical wall-heating scenarios, where the near-wall region enters a vapour-like regime, the buoyancy force tends to be destabilising.

Conversely, in transcritical wall-cooling cases, where the near-wall region remains in a liquid-like regime, this force is stabilising. Under such conditions, the Oberbeck–Boussinesq approximation, commonly used in stratified flows, becomes largely inaccurate due to the strong property variations near the pseudo-critical point. One approach to overcome this limitation is to employ a fully compressible formulation that includes the gravitational source term in the wall-normal (y) momentum equation of the Navier–Stokes equations, as initially implemented in the CUBENS solver (see Chapters 2 and 5) but intentionally neglected for the studies presented in this thesis. As reported by Zonta & Soldati (2018) for closed-flow configurations, inertial, buoyancy, and viscous forces ultimately determine whether the laminar flow is stabilised or destabilised, or whether the turbulent flow is turbulence- or buoyancy-dominated. For horizontal boundary layers, the influence of buoyancy on the stability and transition to turbulence, both with and without pseudo-boiling, remains largely unexplored and thus constitutes a relevant direction for future research. After the study on incompressible stratified boundary layers by Parente *et al.* (2020), a further step was taken by Boldini *et al.* (2025), who investigated buoyancy effects on modal instabilities in weakly and strongly stratified flow cases. The key contribution is an original perturbative framework under the general non-Oberbeck–Boussinesq formulation, which predicts how buoyancy modifies modal instabilities without re-solving the eigenvalue problem and links the buoyancy sensitivity directly to the perturbation energy budget. The framework enables fast N-factor predictions for buoyant boundary layers across wide ranges of Prandtl number, temperature ratio, and Mach number. Beyond ideal-gas flows, the framework provides the first-ever assessment of buoyancy effects on Mode-II instability in supercritical fluids.

Several other open questions regarding transition in supercritical fluids remain. Beyond the various combinations of operating conditions, such as pressure, temperature, and wall thermal conditions, that may promote different routes to laminar-to-turbulent transition, several fundamental research challenges arise; among them, the most relevant are outlined below:

1. Impact of wall cooling under pseudo-boiling conditions: this effect has been investigated only in the linear regime in the present work, yielding significantly larger modal and non-modal N-factors than wall heating. Given also the broader frequency range of the Mode-II-like instability at play, complex nonlinear interactions between the different modes could be even more relevant, followed by rapid saturation and accelerated secondary instability, leading to an abrupt transition to turbulence at lower Reynolds numbers. The findings will offer critical insight into the early onset of turbulence in wall-cooled systems operating near the pseudo-boiling point, which is of particular importance for applications such as supercritical fuel injection in rocket engines or regenerative cooling channels in high-performance propulsion systems (Li *et al.* 2025).

2. Free-Stream-Turbulence (FST) transition and receptivity: the ‘controlled’ breakdown simulations performed in this research neglected the effect of FST and the associated natural receptivity process. However, for sufficiently high FST intensity (of order

Tu ~ $O(1\%)$) (Brandt 2003), the exponential growth of TS waves, and potentially that of inviscid Mode II, can be bypassed, leading to the formation of Klebanoff streaks that undergo secondary instability and break down into turbulent spots. This 'bypass' scenario is particularly relevant in turbomachinery flows, such as in turbine blades and cascades (Bhaskaran & Lele 2010; Sandberg & Michelassi 2022). For instance, recent studies on the dense vapour Novec649 in mildly non-ideal gas conditions (Gloerfelt *et al.* 2023; Bienner *et al.* 2023) have shown that, due to the very high Reynolds number, even the classical 'bypass' scenario can itself be bypassed by a nonlinear receptivity mechanism. Such behaviour should also be studied under pseudo-boiling conditions, along with a detailed analysis of the receptivity process (Saric *et al.* 2002). In 'natural' or uncontrolled flow conditions, typical of conventional 'noisy' wind tunnels, background disturbances are more broadband, and the flow naturally selects the dominant frequencies and wavenumbers from the free-stream spectrum. This selection process is likely to be fundamentally altered by the strong property gradients present in boundary layers at supercritical pressure, along with the influence of leading-edge effects and surface inhomogeneities on the receptivity under such conditions.

3. Complex geometries: the current study focused on zero-pressure-gradient flat-plate boundary layers. However, realistic engineering applications involving supercritical fluids often employ curved surfaces (e.g. turbine blades), 3-D flows, leading-edge effects, pressure gradients, and surface roughness, which give rise to additional instability mechanisms, including attachment-line, modified streamwise, centrifugal, and cross-flow (CF) instabilities (Saric *et al.* 2003). A first attempt to understand and control CF instability was undertaken by Ren & Kloker (2022) on a swept flow with favourable pressure gradient (e.g. over a swept wing). Since their analysis focused on linear modal instabilities (i.e. steady and unsteady CF modes), a recommendation for future work should explore the nonlinear regime and investigate secondary instability of CF vortices using the nonlinear parabolised stability equation (NPSE) (Malik *et al.* 1999) or nonlinear harmonic Navier–Stokes (Westerbeek *et al.* 2024), and up to the turbulent breakdown with DNS under pseudo-critical conditions (cf. the ideal-gas study of Bonfigli & Kloker (2007), resembling the DLR-Göttingen swept flat-plate experiment (Bippes 1999)). Note that, to enable high-fidelity simulations in complex geometries with the CUBENS solver, the current Cartesian framework must either be replaced with a boundary-conforming curvilinear coordinate system or extended through an immersed boundary method.

Finally, building upon the theoretical and computational framework presented in this thesis, a complementary experimental campaign has been initiated through the development and operation of a natural-circulation loop with supercritical carbon dioxide at the Process & Energy Laboratory of the Delft University of Technology (Draskic 2025). The loop includes an optically accessible horizontal plate heat-exchanger test section that enables controlled investigation of buoyancy-induced thermal stratification in supercritical flows under pseudo-

boiling. This facility thus offers a promising platform for future investigations of instability growth and laminar–to-turbulent transition with fluids at supercritical pressure. Systematic comparisons between experimental measurements and high-fidelity simulations will be essential to validate the computational predictions and enhance understanding of the transition mechanisms in non-ideal fluid flows.

Bibliography

Bhaskaran, R. & Lele, SK. 2010 Large eddy simulation of free-stream turbulence effects on heat transfer to a high-pressure turbine cascade. *J. Turbulence* **11**, N6.

Bienner, A., Gloerfelt, X. & Cinnella, P. 2023 Leading-edge effects on freestream turbulence induced transition of an organic vapor. *Flow Turbul. Combust.* **112**, 1–29.

Bippes, H. 1999 Basic experiments on transition in three-dimensional boundary layers dominated by crossflow instability. *Prog. Aerosp. Sci.* **35**, 363–412.

Boldini, P. C., Hirai, R., Bugeat, B. & Pecnik, R. 2025 First-order buoyancy correction of modal instabilities in stratified boundary layers. Submitted to J. Fluid Mech., arXiv: 2511.21130.

Bonfigli, G. & Kloker, M. 2007 Secondary instability of crossflow vortices: validation of the stability theory by direct numerical simulation. *J. Fluid Mech.* **583**, 229–272.

Brandt, L. 2003 Numerical studies of bypass transition in the Blasius boundary layer. PhD thesis, KTH Royal Institute of Technology.

Chu, T. B. 1965 On the energy transfer to small disturbances in fluid flow (part I). *Acta Mech.* **1**, 215–234.

Draskic, M. 2025 Buoyancy-dominated flows of supercritical carbon dioxide: mixed convection and natural circulation at supercritical pressures. PhD thesis, Delft University of Technology.

Gloerfelt, X., Bienner, A. & Cinnella, P. 2023 High-subsonic boundary-layer flows of an organic vapour. *J. Fluid Mech.* **971**, A8.

Hanifi, A., Schmid, P. J. & Henningson, D. S. 1996 Transient growth in compressible boundary layer flow. *Phys. Fluids* **8**, 826–837.

Lees, L. & Lin, C. C. 1946 Investigation of the stability of the laminar boundary layer in a compressible fluid. *NACA Tech. Note* 1115.

Li, Z., Banuti, D. T., Ren, J., Lyu, J., Wang, H. & Chu, X. 2025 A review of microscale physics and macroscale convective heat transfer in supercritical fluids for energy and propulsion systems. *Appl. Therm. Eng.* **272**, 126380.

Malik, M. R., Li, F., Choudhari, M. M. & Chang, C. L. 1999 Secondary instability of crossflow vortices and swept-wing boundary-layer transition. *J. Fluid Mech.* **399**, 85–115.

Parente, E., Robinet, J. C., De Palma, P. & Cherubini, S. 2020 Modal and nonmodal stability of a stably stratified boundary layer flow. *Phys. Rev. Fluids* **5**, 113901.

Ren, J. & Kloker, M. 2022 Instabilities in three-dimensional boundary-layer flows with a highly non-ideal fluid. *J. Fluid Mech.* **951**, A9.

Ren, J., Marxen, O. & Pecnik, R. 2019 Boundary-layer stability of supercritical fluids in the vicinity of the Widom line. *J. Fluid Mech.* **871**, 831–864.

Sandberg, R. D. & Michelassi, A. 2022 Fluid dynamics of axial turbomachinery: Blade- and stage-level simulations and models. *Annu. Rev. Fluid Mech.* **54**, 255–285.

Saric, W. S., Reed, H. L. & Kerschen, E. J. 2002 Boundary-layer receptivity to freestream disturbances. *Annu. Rev. Fluid Mech.* **34**, 291–319.

Saric, W. S., Reed, H. L. & White, E. B. 2003 Stability and transition of three-dimensional boundary layers. *Annu. Rev. Fluid Mech.* **35**, 413–440.

Westerbeek, S., Hulshoff, S., Schuttelaars, H. & Kotsonis, M. 2024 DeHNSSo: The Delft Harmonic Navier–Stokes Solver for nonlinear stability problems with complex geometric features. *Comput. Phys. Commun.* **302**, 109250.

Zonta, F. & Soldati, A. 2018 Stably stratified wall-bounded turbulence. *Appl. Mech. Rev.* **70**, 040801.

NOMENCLATURE

Acronyms

1-D, 2-D, 3-D	One-, Two-, and Three-Dimensional
APG	Adverse Pressure Gradient
BC	Boundary Condition
BL	Boundary Layer
CO_2	Carbon Dioxide
CPU	Central Processing Unit
CUBENS	CUBic Equation of state Navier–Stokes
DNS	Direct Numerical Simulation
EoS	Equation of State
FFT	Fast-Fourier Transformed
GIP	Generalised Inflection Point
GPU	Graphics Processing Unit
HPC	High-Performance Computing
IG	Ideal Gas
IP	Inflection Point
KEEP	Kinetic-Energy and Entropy Preserving
KH	Kelvin–Helmholtz
LST	Linear Stability Theory
MFD	Mean-Flow Distortion
MPEoS	Multi-Parameter Equations of State
MPI	Message Passing Interface
NS	Navier–Stokes
OS	Orr–Sommerfeld
PR	Peng–Robinson
SIT	Secondary Instability Theory
TS	Tollmien–Schlichting
VdW	Van der Waals
ZPG	Zero Pressure Gradient

Greek Symbols

α	streamwise wavenumber
α_υ	thermal expansion coefficient
β	spanwise wavenumber
γ	heat capacity ratio; spatial growth rate (SIT)
$\Delta x, \Delta y, \Delta z$	grid spacing in streamwise, wall-normal, spanwise direction
Δt	time step
δ	Blasius length scale
δ_1	displacement thickness
δ_{99}	boundary-layer thickness
$\delta_{99,0}$	boundary-layer thickness at the computational domain inlet
δ_υ	viscous length scale at the wall
ϵ_d	detuning parameter (SIT)
η	self-similar wall-normal coordinate
θ	momentum thickness
κ	von Kármán constant; thermal conductivity
κ_t	eddy conductivity
λ	wavelength; Lamé's constant
μ	dynamic viscosity
μ_t	eddy viscosity
ν	kinematic viscosity
ξ	self-similar streamwise coordinate; disturbance vorticity
ρ	density
σ	temporal growth rate (SIT)
τ	shear stress
τ_w	wall shear stress
υ	specific volume
χ	generic flow quantity
Φ	density-weighted vorticity
Ψ	wave angle
Ω	base-flow vorticity
ω	angular frequency
$\omega_x, \omega_y, \omega_z$	streamwise, wall-normal, spanwise vorticity
$\bar{\omega}$	acentric factor

Latin Symbols

A	amplitude
a	speed of sound
C	Chapman–Rubesin parameter
C_f	skin-friction coefficient

c	phase speed
c_p	isobaric heat capacity
c_v	isochoric heat capacity
e	specific internal energy
e_0	specific total energy
E	energy norm
Ec	Eckert number
F	non-dimensional frequency parameter
Fr	Froude number
G	optimal energy amplification
g^*	gravitational acceleration
H_{12}	boundary-layer shape factor
h	specific enthalpy; timewise harmonic
i	mean enthalpy ratio
i	imaginary unit
k	index of spanwise modes
L^*_{ref}	reference length
M	Mach number
M_r	relative Mach number
N	N-factor
N_x, N_y, N_z	grid points in streamwise, wall-normal, spanwise direction
p	pressure
Pr	Prandtl number
Pr_m	mixed Prandtl number
$\mathbf{Q}$	state vector of conservative variables
$\mathbf{q}$	state vector of primitive variables
R_g	specific gas constant
Re	Reynolds number
Re_0	Reynolds number at the computational domain inlet
Re_τ	friction Reynolds number
Ri	Richardson number
s	Reynolds analogy factor; specific entropy
St	Stanton number
T	temperature
T_0	fundamental period
t	time
Tu	turbulence level
u, v, w	streamwise, wall-normal, spanwise velocity
u_τ	friction velocity
x, y, z	streamwise, wall-normal, spanwise direction
Z	compressibility factor

Subscripts and Superscripts

$(\cdot)^*$	dimensional quantity
$(\cdot)^+$	wall-scaled quantity
$(\cdot)'$	disturbance quantity
$(\cdot)^\star$	semi-local quantity
$(\cdot)^{\mathrm{T}}$	transpose of a vector or matrix
$\bar{(\cdot)}$	base-flow quantity
$\hat{(\cdot)}$	disturbance eigenfunction
$\overline{(\cdot)}$	Reynolds-averaged quantity
$\widetilde{(\cdot)}$	Favre-averaged quantity
$(\cdot)_0$	quantity evaluated at the computational-domain inlet
$(\cdot)_c$	quantity evaluated at the vapour–liquid critical point
$(\cdot)_{cr}$	quantity evaluated at the (hydrodynamic) critical layer
$(\cdot)_{crit}$	quantity evaluated at the (hydrodynamic) critical Reynolds number
$(\cdot)_\infty$	free-stream quantity
$(\cdot)_{pc}$	quantity evaluated at the pseudo-critical point (pseudo-boiling)
$(\cdot)_r$	reduced (non-dimensional) quantity, normalised with critical values
$(\cdot)_{ref}$	reference quantity
$(\cdot)_s$	quantity evaluated at the generalised inflection point (GIP)
$(\cdot)_{vD}$	Van Driest's quantity
$(\cdot)_w$	quantity evaluated at the wall

ACKNOWLEDGEMENTS

There are far too many people to thank properly, and my memory, much like a typical CUBENS run, is firmly memory-bandwidth-bounded. If I forget to mention someone by name, please accept my apologies in advance and interpret it as a limitation of the model rather than of my gratitude. Even so, these memories will stay with me forever. This journey started in the strange, quiet "laminar" phase of the COVID lockdowns and continued into the more "turbulent" post-COVID years, and I am truly thankful to all the people who, in one way or another, helped me make it to the end of this "big yellow book". In the same spirit, the acknowledgements could only end up being almost as long as the thesis itself.

First of all, I have to start with **Prof. dr. Rene Pecnik**. Rene, you know I would have written this in German, but I do not even know where to begin thanking you. Let me start from our first meeting when you invited me to Delft; there was already a spark. Since then, our long discussions, whether planned or spontaneous, have always been intense and inspiring, whether we talked about science or about something completely different. Your passion for research, from the smallest details to the bigger picture, your constant motivation, and your incredible availability have helped me enormously throughout these years. This thesis has been profoundly shaped by your mentorship and support. I am especially grateful for the time we spent together debugging CUBENS, trying to craft the "perfect" plot (and you know exactly what I mean by "perfect"), or finding the correct eigenvalue with Python. You always had an *offenes Ohr* for all my little remarks and complaints, and your wise suggestions were crucial in steering this work, and my future steps, in the right direction. I could go on, at great length as always, but as we usually end up joking anyway, I will just finish by remarking that Jannik Sinner is Italian, unlike me, apparently. *Dankeschön, auf gut Österreichisch,* for everything.

Next, I would like to thank my co-promotor, **Dr. ir. Jurriaan W. R. Peeters** who, although formally second on the list, has been equally important throughout this journey. I will try to be as Dutch with you as you were with me: direct and to the point. You carefully read through my papers and thesis draft and always gave clear, honest, and very wise recommendations, especially when it came to structure, clarity, and feasibility. Your sense of what was realistic and well-planned often saved me from disappearing into yet another rabbit hole of ideas. I am also very grateful for the opportunity you gave me to be a teaching assistant for two years in a row for the "Advanced Heat Transfer" course, which ended up being something

I genuinely enjoyed and learned a lot from. Your directness and your willingness to make time, even when you were extremely busy, taught me how to keep this thesis on a realistic and workable path. *Dankjewel* for everything.

I owe a special debt of gratitude to **Dr. Benjamin Bugeat**. Ben, your rigorous comments, your way of building arguments from first principles, and your patience in explaining subtle points have helped me sharpen my thinking in countless ways. Many of the "unstable" ideas benefited from our very long discussions, sometimes in the office we shared, sometimes online, and sometimes in front of far too many equations, even after your move across the Channel. You were, in many ways, like having a co-supervisor. Thank you for always taking the time, for your honesty when something still had "just a few tiny mistakes", and for the humour that often softened our scientific frustrations. And beyond the physics, thank you for the beers after work, the food, the tennis matches, and the many conversations that made these years lighter and genuinely enjoyable. *Merci beaucoup* for everything.

My sincere thanks also go to **Dr.-Ing. Markus J. Kloker**, whose work has inspired me since my student time in Stuttgart. Markus, your lectures on transition and hypersonic flows first sparked my fascination for boundary-layer instabilities and high-speed flows, and it has been a pleasure and an honour to continue discussing stability and transition with you at conferences and beyond, both in the classical and in the "non-ideal" context. Although I ultimately could not continue my PhD in Stuttgart, the foundation you provided has accompanied me throughout this project. Your historical view on the field, your detailed focus on the physics, and your insights on DNS studies have left a clear mark on this thesis and on future work, continuing in the spirit of Stuttgart's strong tradition in transition research after your well-deserved retirement. *Dankschee* for everything.

I am also very thankful to **Dr. Pedro Costa** for both the scientific and non-scientific discussions. Pedro, your help with code development and GPU optimisation took me from essentially zero to something at least vaguely resembling a GPU hero like you, and your guidance saved me countless hours of wandering blindly through OpenACC programming guides and lines of code. I also appreciated your help with the HPC facilities, the Icelandic GPU, your own GPU, and, of course, the regular debates about football and food. *Muito obrigado* for everything.

Within the ERC Critical project, I was lucky to share this journey with wonderful PhD and postdoc colleagues: **Asif**, **Ben** (see above), **Marko**, **Ryo**, and **Sanath**. Working with you all was both scientifically rewarding and genuinely fun! Marko, your daily perseverance and grasp of experimental setups have been truly impressive, already from the very first day as we sat in that weird office. Our long discussions about basketball and the NBA (with a special mention for your true idol Jokić and coach Dušan) were great part of our

days at P&E. Just keep working on your German, though, as I will do with my Dutch (see corrected *Samenvatting*). Asif, your depth of understanding and your confidence in challenging ideas have been very inspiring; I really enjoyed our conversations about the States, your idol Cristiano Ronaldo (pronounced with Pedro's accent), healthy food, but also the APS conference in Washington, which I will always remember not just for that memorable hypersonic presentation, but also for that famous unexpected pizza. Ryo, you were not only a colleague but also an amazing office mate, always incredibly kind and generous. I particularly appreciated your calmness, the excellent organisation, and consistently clear presentations. Your help in navigating the Japanese Shinkansen system and the streets of Nagano made my life noticeably easier when visiting your beautiful country. Sanath, your directness and humour made you a fantastic sparring partner when it came to numerical simulations. The DLES conference in Erlangen, with endless hours of biking and sitting next to the "turbulence gods", will always remain among my favourite memories from the PhD.

I also want to thank the master's students I supervised during these years, **Francisco**, **Jiayu**, **Pranav**, and **Romain**. I hope I was a decent supervisor, talking not too much but also not too harsh. Your daily efforts and profound contributions, from the stability analyses to the numerical simulations, have been a great help and have contributed significantly to this thesis.

A big thank you as well to the core of the people from the "Heat-Transfer Hotshots" group (those who are in it know who we are). So, thank you to **An** (I know that your bonsai will live forever), **Anna**, **Atharv**, **Baptiste**, **Bartu**, **Bergmann**, **Giandomenico**, **Mammad**, **Rafael**, and **Teja**. Our discussions about sports (including the memorable football prediction games), life, jokes, the evenings together with delicious food and beers, and the scientific discussions that somehow always followed made this period much more enjoyable, both inside and outside the office.

I would also like to thank several other colleagues at P&E, or who already left P&E, by name: **Arvind**, **Fatma**, **Heng**, **Hugo**, **Irem**, **Jesse**, **Julien**, **Luis**, **Mengmeng**, **Parsa**, **Rishabh**, **Robin**, **Rumen**, **Simone**, **Sowmya**, **Stephan**, and **Suriya**, for the many lunches, Secret Santas, P&E events, and countless coffee breaks we shared. I am also grateful to the support staff **Rob**, **Caroline**, **Eveline**, and **Linda**, for their patience with my Dutch emails and for their help with the many administrative tasks that kept my PhD running smoothly, especially during COVID times.

Another special thank you goes to the support teams of the DelftBlue and Snellius (SURF) HPC infrastructures for their continuous assistance in keeping the simulations running smoothly. In particular, I would like to personally thank **Dr. ir. Mathieu Pourquie** for his prompt technical support and **Dr. Benjamin Czaja** for the discussions on energy optimisation.

From my short but meaningful time in Stuttgart at IAG, I would like to thank in particular **Prof. Dr.-Ing. Ulrich Rist** (and, above all, his "Wisdom line" suggestion), **Priv.-Doz. Dr.-Ing. Christoph Wenzel**, **Dr.-Ing. Duncan Ohno**, **Jason Appelbaum**, **Dr.-Ing. Johannes Peter**, **Dr.-Ing. Louis Gagnon**, **Dr.-Ing. Tobias Gibis**, **Tristan Römer**, and **Zhengfei Guo**. Your encouragement during those early steps of my academic journey, the many discussions in the one and only corridor, and the supportive atmosphere at the institute played a key role in shaping the direction of this thesis.

Outside science, a big part of my life in Delft was shaped by **Punch Basketball**. Long hours of trainings, games around the Netherlands, and the many wins and losses, where we even came close to promotion to the Eerste Divisie, were the perfect counterbalance to the long days sitting in the office. In particular, I want to thank coach **Jurriaan**, **Amélie**, **Burak**, **Gaetano**, **Jacopo**, **Jasper**, **Marco**, **Mario**, **Niccolò**, **Thijs**, and **Tommaso**.

Before I come to friends and family, I should say a few words about **Delft** and **the Netherlands**, which managed to become "home" despite the weather and the lack of good Italian food (the cheese, however, is excellent). My first year (and more) here was shaped by the quiet strangeness of the COVID period, when empty streets, closed university buildings, and everything moving online, became part of daily life. In that period, the Delftse Methode, Arjen Lubach, and Nieuwsuur became my unexpected Dutch teachers, and the language, and the country, began to feel familiar. The bike rides along canals, the unpredictable but on-average grey skies, and the direct yet genuinely kind people, especially those at the Saturday market, all shaped my life in Delft. Entering the old town always felt a bit like returning home to Venice, just with *fietsen* and without *gondole*.

Finally, a word of *grazie, dankeschön, thanks, dankjewel, gracias, merci,* 谢谢, ... to my **friends** and my **family**. To my friends in Mirano, in Venice, in Germany, and elsewhere: thank you for your patience over these years, especially when I was not particularly quick in answering messages or not very present during the Christmas holidays. When simulations and deadlines kept me distracted, you remained patient and made every reunion feel as easy as if no time had passed. To my family — my *zie*, *zii*, *cugini*, *cugine*, and my *nonni e nonne*, including those who are no longer with us — thank you for your support and for following this long path with interest, although we were rarely in the same place at the right time. To my *mamma* and *papà*, *grazie di tutto*. Thank you for the weekly calls, the continuous "bothering" about how things were going and when this thesis would finally be finished, while I kept postponing the call. Among many other things, you taught me curiosity and perseverance since the beginning; I am deeply grateful for everything you have done for me. To my dear *Jiaxin*: thank you for your daily patience, your steadiness, and your understanding through the busiest stretches of these years, especially when plans run late and *Deutsche Bahn* was delayed as usual. Thank you for making the hard days lighter and the good days even better. I hope the next chapter is a closer one with you.

CURRICULUM VITAE

Pietro Carlo Boldini was born in Pisa, Italy, on 8 November 1993. After completing the Liceo E. Majorana – E. Corner in Mirano, Venice, in 2012, he moved to Germany to pursue a Bachelor's degree in Aerospace Engineering at the University of Stuttgart. His bachelor's thesis was entitled "Optimum Design of the Intake for an Atmosphere-Breathing Electric Propulsion System". In 2018, he obtained a Master's degree with distinction in Aerospace Engineering from the University of Stuttgart. During his studies, he developed a strong interest in fluid mechanics and aerothermodynamics, with a particular focus on compressible flows and flow instability phenomena. His master's thesis, entitled 'Effects of Thermal Non-Equilibrium on Hypersonic Boundary-Layer Transition', was carried out at the Laboratory for Advanced Simulation of Turbulence (LAST) at Tsinghua University, Beijing, under the supervision of Prof. Song Fu. It investigated high-temperature gas effects on the stability of hypersonic boundary layers. In 2019, he worked as a Research Associate at the University of Stuttgart's Institute of Aerodynamics and Gas Dynamics, Germany, under the supervision of Dr.-Ing. Markus J. Kloker, investigating hypersonic boundary-layer transition and control on conical geometries.

In late 2020, Pietro began his PhD at Delft University of Technology, the Netherlands, joining the Process & Energy Department under the supervision of Prof. dr. Rene Pecnik. His research focused on the stability and transition to turbulence of boundary-layer flows at supercritical pressure, which exhibit strong variations in properties such as viscosity and density. The work combined high-fidelity simulations and high-performance computing with hydrodynamic stability analysis methods. During his PhD, he presented his work at various international conferences and online seminars, and published several articles in peer-reviewed journals. He also contributed to student education as a teaching assistant in the master's course 'Advanced Heat Transfer' and supervised various master's students.

This thesis is the result of his research as a doctoral candidate at Delft University of Technology.

LIST OF PUBLICATIONS

Journal publications

P. C. Boldini, B. Bugeat, J. W. R. Peeters, M. Kloker, R. Pecnik, *Subharmonic resonance of two-dimensional boundary-layer modes in fluids at supercritical pressure*, in preparation for submission (Chapter 7).

P. C. Boldini, R. Hirai, B. Bugeat, R. Pecnik, *First-order buoyancy correction of modal instabilities in stratified boundary layers*, submitted to Journal of Fluid Mechanics, 2025 (not included in the dissertation).

P. C. Boldini, B. Bugeat, J. W. R. Peeters, M. Kloker, R. Pecnik, *Direct numerical simulation of complete transition to turbulence with a fluid at supercritical pressure*, Journal of Fluid Mechanics, Volume 1025, A59, 2025 (Chapter 6).

P. C. Boldini, R. Hirai, P. Costa, J. W. R. Peeters, R. Pecnik, *CUBENS: A GPU-accelerated high-order solver for wall-bounded flows with non-ideal fluids*, Computer Physics Communications, Volume 309, 109507, 2025 (Chapters 2 and 5).

P. C. Boldini, B. Bugeat, J. W. R. Peeters, M. Kloker, R. Pecnik, *Transient growth in diabatic boundary layers with fluids at supercritical pressure*, Physical Review Fluids 9, 083901, 2024 (Chapters 3 and 4).

B. Bugeat, **P. C. Boldini**, A. M. Hasan, R. Pecnik, *Instability in strongly stratified plane Couette flow with application to supercritical fluids*, Journal of Fluid Mechanics, Volume 984, A31, 2024 (Chapter 3).

Conference publications

P. C. Boldini, B. Bugeat, J. W. R. Peeters, M. Kloker, R. Pecnik, *Direct Numerical Simulations of K-type transition in a flat-plate boundary layer with supercritical fluids*, In Proceedings of the 10th IUTAM Symposium on Laminar-Turbulent Transition, (ed. K. Kato, A. Inasawa & M. Matsubara), pp. 255–261, Springer Nature Singapore, 2026. (not included in the dissertation).

P. C. Boldini, R. Gaspar, B. Bugeat, P. Costa, J. W. R. Peeters, R. Pecnik, *Direct numer-*

ical simulation of H-type transition in a flat-plate boundary layer with supercritical fluids, In Proceedings of 14th International ERCOFTAC Symposium on Engineering Turbulence Modelling and Measurements (ETMM14), Barcelona, Spain, September 6-8, 2023 (not included in the dissertation).

B. Bugeat, **P. C. Boldini**, R. Pecnik, *On the new unstable mode in the boundary layer flow of supercritical fluids*, In Proceedings of the 12th International Symposium on Turbulence and Shear Flow Phenomena (TSFP-12), Osaka, Japan (Online), 2022 (Chapter 3).

Conference and seminar presentations

P. C. Boldini, B. Bugeat, J. W. R. Peeters, M. Kloker, R. Pecnik, *Widom-line effect on the boundary-layer transition with a highly non-ideal fluid*, 16th ERCOFTAC SIG33 WORKSHOP: Progress in Flow Instability, Transition and Control, Cagliari, Italy, 2025.

P. C. Boldini, *CUBENS: A GPU-accelerated high-order solver for wall-bounded flows with non-ideal fluids*, Computer Physics Communications Seminar Series, Online, `https://doi.org/10.52843/cassyni.gwmx6m`, 2025.

R. Hirai, **P. C. Boldini**, R. Pecnik, *Direct numerical simulation of H-type transition in stratified horizontal boundary layers*, 77th Annual Meeting of the APS Division of Fluid Dynamics, Salt Lake City, UT, USA, 2024.

P. C. Boldini, B. Bugeat, J. W. R. Peeters, M. Kloker, R. Pecnik, *DNS of K-type transition in a flat-plate boundary layer with supercritical fluids*, 1st European Fluid Dynamics Conference (EFDC1), Aachen, Germany, 2024.

P. C. Boldini, B. Bugeat, J. W. R. Peeters, M. Kloker, R. Pecnik, *DNS of K-type transition in a flat-plate boundary layer with supercritical fluids*, 10th IUTAM Symposium on Laminar-Turbulent Transition, Nagano, Japan, 2024.

P. C. Boldini, R. Hirai, B. Bugeat, P. Costa, J. W. R. Peeters, R. Pecnik, *Research on transitional boundary layers with fluids at supercritical pressure*, Burgers Symposium, Lunteren, the Netherlands, 2024.

P. C. Boldini, R. Hirai, P. Costa, J. W. R. Peeters, R. Pecnik, *GPU-accelerated DNS of diabatic transitional boundary layers at supercritical pressures*, DLES – Direct and Large Eddy Simulation 14, Erlangen, Germany, 2024.

P. C. Boldini, B. Bugeat, P. Costa, J. W. R. Peeters, R. Pecnik, *DNS of K- and H-type transitions in a flat-plate boundary layer with supercritical fluids*, 76th Annual Meeting of the APS Division of Fluid Dynamics, Washington D.C., USA, 2023.

P. C. Boldini, B. Bugeat, P. Costa, J. W. R. Peeters, R. Pecnik, *Direct numerical simulation of H-type transition in a flat-plate boundary layer with supercritical fluids*, 21. STAB-Workshop DLR Göttingen, Göttingen, Germany, 2023.

P. C. Boldini, R. Gaspar, B. Bugeat, P. Costa, J. W. R. Peeters, R. Pecnik, *Direct numerical simulation of H-type transition in a flat-plate boundary layer with supercritical fluids*, The 14th International ERCOFTAC Symposium on Engineering Turbulence Modelling and Measurements, Barcelona, Spain, 2023.

P. C. Boldini, B. Bugeat, J. W. R. Peeters, R. Pecnik, *Transient growth in flat-plate boundary layers with a highly non-ideal fluid*, 15th ERCOFTAC SIG33 WORKSHOP: Progress in Flow Instability, Transition and Control, Alghero, Italy, 2023.

P. C. Boldini, R. Gaspar, B. Bugeat, P. Costa, J. W. R. Peeters, R. Pecnik, *Direct numerical simulation of H-type transition in a flat-plate boundary layer with supercritical fluids*, Burgers Symposium, Lunteren, the Netherlands, 2023.

APPENDIX

'Se vogliamo che tutto rimanga com'è, bisogna che tutto cambi.' (La tesi.)

G. Tomasi di Lampedusa, Il Gattopardo

R_g^* (J/(kg K))	p_c^* (bar)	T_c^* (K)	ρ_c^* (kg/m^3)
188.9	73.9	304.1	467.6

Table A.1.1: Thermodynamic properties of CO_2: specific gas constant (R_g^*), critical pressure (p_c^*), critical temperature (T_c^*), and critical density (ρ_c^*).

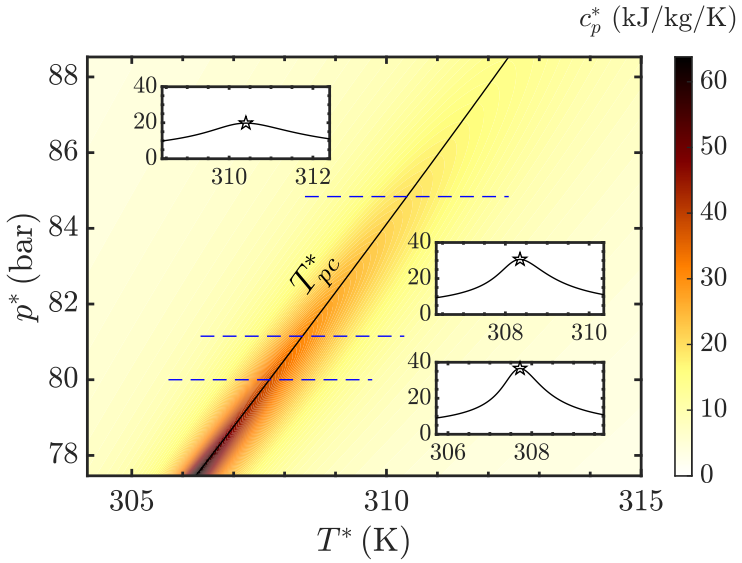

Figure A.1.1: Supercritical CO_2: contours of the specific isobaric heat capacity c_p^* in the T^*–p^* plane, together with the evolution of the pseudo-critical temperature T_{pc}^* (—). Insets display one-dimensional profiles of $c_p^*(T^*)$ along isobars (- - -) at $p^* = 80$ bar ($T_{pc}^* = 307.7$ K), $p^* = 81.15$ bar ($T_{pc}^* = 308.3$ K), and $p^* = 84.8$ bar ($T_{pc}^* = 310.4$ K). In each inset, the c_p^*-peak location (⋆) marks T_{pc}^*.

A.1 Supercritical CO_2

The material-dependent parameters of CO_2 are provided in Tab. A.1.1. The evolution of the pseudo-critical temperature (black solid line) as a function of pressure is plotted in Fig. A.1.1 along with contours of c_p^*.

The evolution of the viscosity gradients with respect to temperature and density, $\partial\bar{\mu}/\partial\bar{T}\big|_{\bar{\rho}}$ and $\partial\bar{\mu}/\partial\bar{\rho}|_{\bar{T}}$, is shown in the dimensional p^*–T^* diagram in Fig. A.1.2.

A.2 Thermodynamic identities

The first law of thermodynamics can be written in terms of $\rho = 1/v$ and specific internal energy e as:

$$T\,\mathrm{d}s = \mathrm{d}e - \frac{p}{\rho^2}\mathrm{d}\rho, \tag{A.1}$$

where s is the specific entropy. The four Maxwell relations are obtained from the exact differentials of the internal energy, Helmholtz free energy, enthalpy, and Gibbs free energy,

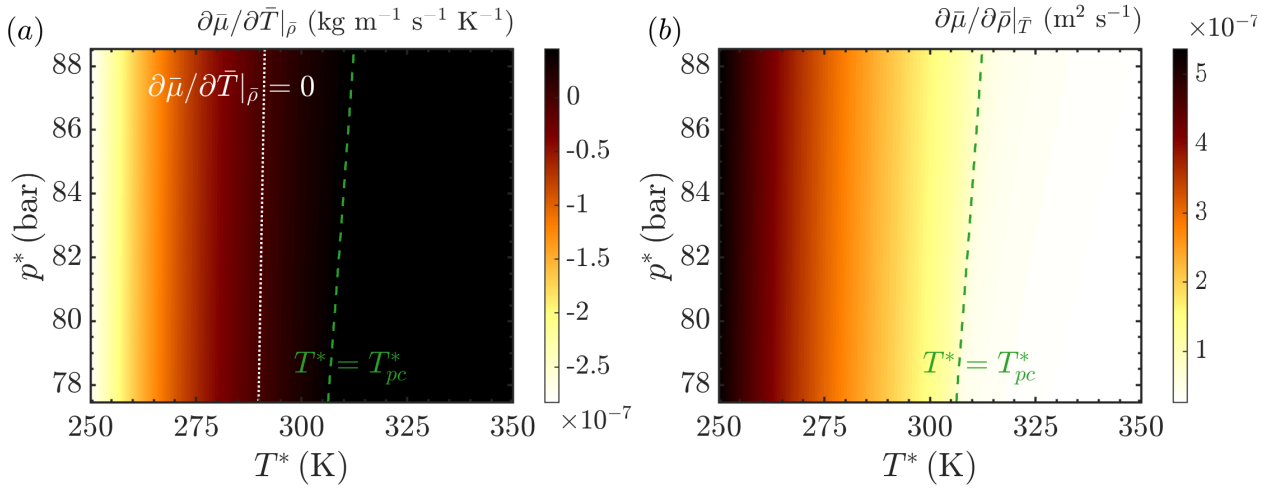

Figure A.1.2: Dimensional viscosity gradients: (a) $\partial\bar{\mu}/\partial\bar{T}\big|_{\bar{\rho}}$ and (b) $\partial\bar{\mu}/\partial\bar{\rho}|_{\bar{T}}$ as functions of the supercritical pressure p^* and temperature T^* in the proximity of the Widom line (indicated by the dashed green line at $T^* = T^*_{pc}$). In (a), the location where $\partial\bar{\mu}/\partial\bar{T}\big|_{\bar{\rho}} = 0$ is marked by a white dotted line.

expressed here in terms of (ρ, T, p, s):

$$\rho^2 \frac{\partial T}{\partial \rho}\bigg|_s = \frac{\partial p}{\partial s}\bigg|_\rho, \tag{A.2}$$

$$\rho^2 \frac{\partial s}{\partial \rho}\bigg|_T = \frac{\partial p}{\partial T}\bigg|_\rho, \tag{A.3}$$

$$-\rho^2 \frac{\partial T}{\partial p}\bigg|_s = \frac{\partial \rho}{\partial s}\bigg|_p, \tag{A.4}$$

$$\rho^2 \frac{\partial s}{\partial p}\bigg|_T = \frac{\partial \rho}{\partial T}\bigg|_p. \tag{A.5}$$

The total differential of a quantity χ as a function of the independent quantities Y and Z can be expressed as:

$$\mathrm{d}\chi = \frac{\partial \chi}{\partial Y}\bigg|_Z \mathrm{d}Y + \frac{\partial \chi}{\partial Z}\bigg|_Y \mathrm{d}Z. \tag{A.6}$$

Moreover, the triple product rule holds as

$$\frac{\partial Y}{\partial \chi}\bigg|_Z \frac{\partial \chi}{\partial Z}\bigg|_Y \frac{\partial Z}{\partial Y}\bigg|_\chi = -1, \tag{A.7}$$

and the reciprocity rule holds as

$$\frac{\partial Y}{\partial \chi}\bigg|_Z = \frac{1}{\dfrac{\partial \chi}{\partial Y}\Big|_Z} = \frac{\partial \chi}{\partial Y}\bigg|_Z^{-1}, \tag{A.8}$$

and the chain rule holds as

$$\left.\frac{\partial \chi}{\partial Y}\right|_Z = \left.\frac{\partial \chi}{\partial Y_2}\right|_Z \left.\frac{\partial Y_2}{\partial Y}\right|_Z = \frac{\left.\frac{\partial \chi}{\partial Y_2}\right|_Z}{\left.\frac{\partial Y}{\partial Y_2}\right|_Z}, \tag{A.9}$$

where Y_2 is another independent variable.

A.3 Thermodynamic partial derivatives

The partial derivatives of the considered cubic equations of state in Sec. 2.2, which are required for the stability analysis, are presented hereafter.

A.3.1 Van der Waals

The required partial derivatives in reduced form are

$$\left.\frac{\partial p_r}{\partial T_r}\right|_{\rho_r} = \frac{8\rho_r}{3-\rho_r}, \quad \left.\frac{\partial p_r}{\partial \rho_r}\right|_{T_r} = \frac{24T_r}{(3-\rho_r)^2} - 6\rho_r, \tag{A.10}$$

$$\left.\frac{\partial^2 p_r}{\partial T_r^2}\right|_{\rho_r} = 0, \quad \left.\frac{\partial^2 p_r}{\partial \rho_r^2}\right|_{T_r} = -6 + \frac{48T_r}{(3-\rho_r)^3}, \tag{A.11}$$

$$\left.\frac{\partial}{\partial \rho_r}\right|_{T_r}\left(\left.\frac{\partial p_r}{\partial T_r}\right|_{\rho_r}\right) = \left.\frac{\partial}{\partial T_r}\right|_{\rho_r}\left(\left.\frac{\partial p_r}{\partial \rho_r}\right|_{T_r}\right) = \frac{24}{(3-\rho_r)^2}, \tag{A.12}$$

$$\left.\frac{\partial e_r}{\partial T_r}\right|_{\rho_r} = \frac{c_{v,r}}{Z_c}, \quad \left.\frac{\partial e_r}{\partial \rho_r}\right|_{T_r} = -3. \tag{A.13}$$

A.3.2 Peng–Robinson

The required partial derivatives in reduced form are

$$\left.\frac{\partial p_r}{\partial T_r}\right|_{\rho_r} = K\sqrt{\frac{\alpha}{T_r}}\frac{a_r\rho_r^2 Z_c^{-2}}{1+2b_r Z_c^{-1}\rho_r - b_r^2 Z_c^{-2}\rho_r^2} - \frac{\rho_r Z_c^{-1}}{b_r Z_c^{-1}\rho_r - 1}, \tag{A.14}$$

$$\left.\frac{\partial p_r}{\partial \rho_r}\right|_{T_r} = \frac{Z_c^{-1}T_r}{(\rho_r b_r Z_c^{-1}-1)^2} - a_r\alpha Z_c^{-2}\frac{(2\rho_r + 2b_r Z_c^{-1}\rho_r^2)}{\left[1+2b_r Z_c^{-1}\rho_r - \rho_r^2 b_r^2 Z_c^{-2}\right]^2}, \tag{A.15}$$

$$\left.\frac{\partial^2 p_r}{\partial T_r^2}\right|_{\rho_r} = -\frac{K(K+1)}{2\sqrt{T_r^3}}\frac{a_r Z_c^{-2}\rho_r^2}{1+2b_r Z_c^{-1}\rho_r - \rho_r^2 b_r^2 Z_c^{-2}}, \tag{A.16}$$

$$\left.\frac{\partial^2 p_r}{\partial \rho_r^2}\right|_{T_r} = \frac{2b_r Z_c^{-2}T_r}{(1-b_r Z_c^{-1}\rho_r)^3} - 2\alpha a_r Z_c^{-2}\frac{(2b_r^3 Z_c^{-3}\rho_r^3 + 3b_r^2 Z_c^{-2}\rho_r^2 + 1)}{(1+2b_r Z_c^{-1}\rho_r - b_r^2 Z_c^{-2}\rho_r^2)^3}, \tag{A.17}$$

$$\begin{aligned}&\left.\frac{\partial}{\partial \rho_r}\right|_{T_r}\left(\left.\frac{\partial p_r}{\partial T_r}\right|_{\rho_r}\right) = \left.\frac{\partial}{\partial T_r}\right|_{\rho_r}\left(\left.\frac{\partial p_r}{\partial \rho_r}\right|_{T_r}\right) = \\ &\frac{Z_c^{-1}}{(b_r Z_c^{-1}\rho_r - 1)^2} + 2a_r K Z_c^{-2}\sqrt{\frac{\alpha}{T_r}}\frac{b_r Z_c^{-1}\rho_r^2 + \rho_r}{(-b_r^2 Z_c^{-2}\rho_r^2 + 2b_r Z_c^{-1}\rho_r + 1)^2},\end{aligned} \tag{A.18}$$

$$\left.\frac{\partial e_r}{\partial T_r}\right|_{\rho_r} = c_{v,r}Z_c^{-1} - \frac{a_r Z_c^{-1}}{4\sqrt{2}b_r}\left[\frac{K(K+1)}{\sqrt{T_r}}\right]\ln\left(\frac{1+b_r Z_c^{-1}\rho_r(1-\sqrt{2})}{1+b_r Z_c^{-1}\rho_r(1+\sqrt{2})}\right), \tag{A.19}$$

$$\left.\frac{\partial e_r}{\partial \rho_r}\right|_{T_r} = -\frac{a_r Z_c^{-2}}{1+2b_r Z_c^{-1}\rho_r - b_r^2 Z_c^{-2}\rho_r^2}\left[(K+1)^2 - K(K+1)\sqrt{T_r}\right]. \tag{A.20}$$

A.4 Stability matrices for modal analysis

A.4.1 Viscous instability

The base-flow matrices $\mathbf{L_t}$, $\mathbf{L_x}$, $\mathbf{L_y}$, $\mathbf{L_z}$, $\mathbf{L_q}$, $\mathbf{V_{xx}}$, $\mathbf{V_{yy}}$, $\mathbf{V_{zz}}$, $\mathbf{V_{xy}}$, $\mathbf{V_{xz}}$, and $\mathbf{V_{yz}}$ in Eq. (3.5) are of size 5×5 and their non-zero elements are given below:

$$\left.\begin{aligned} &L_t(1,1) = \bar{\rho}_{\bar{p}}, \quad L_t(1,5) = \bar{\rho}_{\bar{T}}, \\ &L_t(2,2) = L_t(3,3) = L_t(4,4) = \bar{\rho}, \\ &L_t(5,1) = \bar{\rho}\bar{e}_{\bar{p}}, \quad L_t(5,5) = \bar{\rho}\bar{e}_{\bar{T}}, \end{aligned}\right\} \tag{A.21}$$

$$\left.\begin{aligned} &L_x(1,1) = \bar{u}\bar{\rho}_{\bar{p}}, \quad L_x(1,2) = \bar{\rho}, \quad L_x(1,5) = \bar{u}\bar{\rho}_{\bar{T}}, \\ &L_x(2,1) = 1, \quad L_x(2,2) = \bar{\rho}\bar{u}, \quad L_x(2,3) = -\frac{1}{Re}\bar{\mu}_y, \\ &L_x(3,1) = -\frac{1}{Re}\bar{\mu}_{\bar{p}}\bar{u}_y, \quad L_x(3,2) = -\frac{1}{Re}\bar{\lambda}_y, \\ &L_x(3,3) = L_x(4,4) = \bar{\rho}\bar{u}, \quad L_x(3,5) = -\frac{1}{Re}\bar{\mu}_{\bar{T}}\bar{u}_y, \\ &L_x(5,1) = \bar{\rho}\bar{u}\bar{e}_{\bar{p}}, \quad L_x(5,2) = \bar{p}, \quad L_x(5,3) = -\frac{2\bar{\mu}}{Re}\bar{u}_y, \quad L_x(5,5) = \bar{\rho}\bar{u}\bar{e}_{\bar{T}}, \end{aligned}\right\} \tag{A.22}$$

$$\left.\begin{aligned} &L_y(1,3) = \bar{\rho}, \\ &L_y(2,1) = -\frac{1}{Re}\bar{\mu}_{\bar{p}}\bar{u}_y, \quad L_y(2,2) = -\frac{1}{Re}\bar{\mu}_y, \quad L_y(2,5) = -\frac{1}{Re}\bar{\mu}_{\bar{T}}\bar{u}_y, \\ &L_y(3,1) = 1, \quad L_y(3,3) = -\frac{1}{Re}\bar{\lambda}_y - \frac{2}{Re}\bar{\mu}_y, \\ &L_y(4,4) = -\frac{1}{Re}\bar{\mu}_y, \\ &L_y(5,1) = -\frac{1}{ReEc_\infty Pr_\infty}\bar{T}_y\bar{\kappa}_{\bar{p}}, \quad L_y(5,2) = -\frac{2\bar{\mu}}{Re}\bar{u}_y \quad L_y(5,3) = \bar{p}, \\ &L_y(5,5) = -\frac{1}{ReEc_\infty Pr_\infty}\left(\bar{T}_y\bar{\kappa}_{\bar{T}} + \bar{\kappa}_y\right), \end{aligned}\right\} \tag{A.23}$$

$$\left.\begin{aligned} &L_z(1,4) = \bar{\rho}, \\ &L_z(3,4) = -\frac{1}{Re}\bar{\lambda}_y, \\ &L_z(4,1) = 1, \quad L_z(4,3) = -\frac{1}{Re}\bar{\mu}_y, \\ &L_z(5,4) = \bar{p}, \end{aligned}\right\} \tag{A.24}$$

$$
\left.
\begin{aligned}
&L_{q'}(1,3) = \bar{\rho}_y, \\
&L_{q'}(2,1) = -\frac{1}{Re}\bar{\mu}_{\bar{p}}\bar{u}_{yy} - \frac{1}{Re}\bar{u}_y\left[\bar{\mu}_{\bar{p}\bar{p}}\bar{p}_y + \bar{\mu}_{\bar{p}\bar{T}}\bar{T}_y\right], \quad L_{q'}(2,3) = \bar{\rho}\bar{u}_y, \\
&L_{q'}(2,5) = -\frac{1}{Re}\bar{\mu}_{\bar{T}}\bar{u}_{yy} - \frac{1}{Re}\bar{u}_y\left[\bar{\mu}_{\bar{T}\bar{T}}\bar{T}_y + \bar{\mu}_{\bar{p}\bar{T}}\bar{p}_y\right], \\
&L_{q'}(5,1) = -\frac{1}{Re}\bar{\mu}_{\bar{p}}\bar{u}_y^2 - \frac{1}{ReEc_\infty Pr_\infty}\left[\bar{T}_{yy}\bar{\kappa}_{\bar{p}} + \bar{T}_y\left(\bar{\kappa}_{\bar{p}\bar{T}}\bar{T}_y + \bar{\kappa}_{\bar{p}\bar{p}}\bar{p}_y\right)\right], \\
&L_{q'}(5,3) = \bar{\rho}\bar{e}_y, \\
&L_{q'}(5,5) = -\frac{1}{Re}\bar{\mu}_{\bar{T}}\bar{u}_y^2 - \frac{1}{ReEc_\infty Pr_\infty}\left[\bar{T}_{yy}\bar{\kappa}_{\bar{T}} + \bar{T}_y\left(\bar{\kappa}_{\bar{p}\bar{T}}\bar{p}_y + \bar{\kappa}_{\bar{T}\bar{T}}\bar{T}_y\right)\right],
\end{aligned}
\right\} \tag{A.25}
$$

$$
\left.
\begin{aligned}
&V_{xx}(2,2) = V_{yy}(3,3) = V_{zz}(4,4) = -\frac{\bar{\lambda}}{Re} - \frac{2\bar{\mu}}{Re}, \\
&V_{xx}(3,3) = V_{xx}(4,4) = -\frac{\bar{\mu}}{Re}, \quad V_{yy}(2,2) = V_{yy}(4,4) = -\frac{\bar{\mu}}{Re}, \\
&V_{zz}(2,2) = V_{zz}(3,3) = -\frac{\bar{\mu}}{Re}, \\
&V_{xx}(5,5) = V_{yy}(5,5) = V_{zz}(5,5) = -\frac{\bar{\kappa}}{ReEc_\infty Pr_\infty}, \\
&V_{xy}(2,3) = V_{xy}(3,2) = -\frac{\bar{\lambda}}{Re} - \frac{\bar{\mu}}{Re}, \quad V_{xz}(2,4) = V_{xz}(4,2) = -\frac{\bar{\lambda}}{Re} - \frac{\bar{\mu}}{Re}, \\
&V_{yz}(3,4) = V_{yz}(4,3) = -\frac{\bar{\lambda}}{Re} - \frac{\bar{\mu}}{Re}.
\end{aligned}
\right\} \tag{A.26}
$$

For simplicity, the derivative of a thermodynamic quantity with respect to $\bar{p}$ at constant $\bar{T}$, and vice versa, is denoted as $(\cdot)_{\bar{p}}$ and $(\cdot)_{\bar{p}\bar{p}}$ instead of $\partial/\partial\bar{p}|_{\bar{T}}$ and $\partial^2/\partial\bar{p}^2|_{\bar{T}\bar{T}}$, and as $(\cdot)_{\bar{T}}$ and $(\cdot)_{\bar{T}\bar{T}}$ instead of $\partial^2/\partial\bar{T}^2|_{\bar{p}\bar{p}}$, respectively. With the same formulation, the first- and second-order derivatives in wall-normal direction $\mathrm{d}(\cdot)/\mathrm{d}y$ and $\mathrm{d}^2(\cdot)/\mathrm{d}y^2$ are expressed as $(\cdot)_y$ and $(\cdot)_{yy}$, respectively. All derivatives of thermodynamic and transport properties with respect to $\bar{p}$ and $\bar{T}$ are calculated as a function of the EoS and transport properties employed.

A.4.2 Inviscid instability

The base-flow matrices $\mathbf{R_{inv.}}$, $\mathbf{S_{inv.}}$, $\mathbf{M_{inv.}}$, $\mathbf{N_{inv.}}$, and $\mathbf{P_{inv.}}$ in Eq. (3.22) are of size 2×2 and their non-zero elements are given as

$$
\left.
R_{inv.}(1,2) = -\bar{\rho}\mathrm{i}\omega, \quad R_{inv.}(2,1) = \mathrm{i}\left(\omega^2 - \bar{a}^2\beta_r^2\right),
\right\} \tag{A.27}
$$

$$
\left.
S_{inv.}(1,1) = 1, \quad S_{inv.}(2,2) = -\bar{\rho}\bar{a}^2\omega,
\right\} \tag{A.28}
$$

$$M_{inv.}(1,2) = -\bar{\rho}\bar{u}\mathrm{i}, \quad M_{inv.}(2,1) = 2\bar{u}\mathrm{i}\omega, \quad M_{inv.}(2,2) = \bar{\rho}\bar{a}^2\bar{u}_y, \Big\} \tag{A.29}$$

$$N_{inv.}(2,2) = -\bar{\rho}\bar{u}\bar{a}^2, \tag{A.30}$$

$$P_{inv.}(2,1) = \mathrm{i}\left(\bar{a}^2 - \bar{u}^2\right), \tag{A.31}$$

where the first-order derivatives in wall-normal direction $\mathrm{d}(\cdot)/\mathrm{d}y$ are expressed as $(\cdot)_y$. The matrix $\mathbf{A_{inv.}}$ in Eq. (3.23) is of size 2×2 and its non-zero elements are given as

$$\left.\begin{aligned} A_{inv.}(1,2) &= -\bar{\rho}\mathrm{i}(\alpha\bar{u} - \omega), \\ A_{inv.}(2,1) &= \frac{\mathrm{i}(\alpha^2 + \beta_r^2)}{\bar{\rho}(\alpha\bar{u} - \omega)}\left(1 - M_r^2\right), \quad A_{inv.}(2,2) = \frac{\alpha\bar{u}_y}{\alpha\bar{u} - \omega}. \end{aligned}\right\} \tag{A.32}$$

where the first-order derivatives in wall-normal direction $\mathrm{d}(\cdot)/\mathrm{d}y$ are expressed as $(\cdot)_y$.

B.1 Stability matrices for non-modal analysis

The base-flow matrices in Appendix A.4 are adjusted for the considered non-dimensionalisation of the Navier–Stokes equations in non-conservative form (see Eq. (4.1)). Only the modified terms in the linearised stability equations (see Eq. (3.5)) are reported hereafter. The modified base-flow matrices are:

$$L_x(5,2) = Ec_\infty\bar{p}, \quad L_x(5,3) = -\frac{2Ec_\infty\bar{\mu}}{Re}\bar{u}_y, \Big\} \tag{B.1}$$

$$\left.\begin{aligned} L_y(5,1) &= -\frac{1}{RePr_\infty}\bar{\kappa}_{\bar{p}}\bar{T}_y, \quad L_y(5,2) = -\frac{2Ec_\infty\bar{\mu}}{Re}\bar{u}_y, \\ L_y(5,3) &= Ec_\infty\bar{p}, \quad L_y(5,5) = -\frac{1}{RePr_\infty}\left(\bar{\kappa}_y + \bar{\kappa}_{\bar{T}}\bar{T}_y\right), \end{aligned}\right\} \tag{B.2}$$

$$L_z(5,4) = Ec_\infty\bar{p}, \tag{B.3}$$

$$\left.\begin{aligned} L_{q'}(5,1) &= -\frac{Ec_\infty}{Re}\bar{\mu}_{\bar{p}}\bar{u}_y^2 - \frac{1}{RePr_\infty}\left[\bar{T}_{yy}\bar{\kappa}_{\bar{p}} + \bar{T}_y\left(\bar{\kappa}_{\bar{p}\bar{T}}\bar{T}_y + \bar{\kappa}_{\bar{p}\bar{p}}\bar{p}_y\right)\right], \\ L_{q'}(5,5) &= -\frac{Ec_\infty}{Re}\bar{\mu}_{\bar{T}}\bar{u}_y^2 - \frac{1}{RePr_\infty}\left[\bar{T}_{yy}\bar{\kappa}_{\bar{T}} + \bar{T}_y\left(\bar{\kappa}_{\bar{p}\bar{T}}\bar{p}_y + \bar{\kappa}_{\bar{T}\bar{T}}\bar{T}_y\right)\right], \end{aligned}\right\} \tag{B.4}$$

$$V_{xx}(5,5) = V_{yy}(5,5) = V_{zz}(5,5) = -\frac{\bar{\kappa}}{RePr_\infty}. \Big\} \tag{B.5}$$

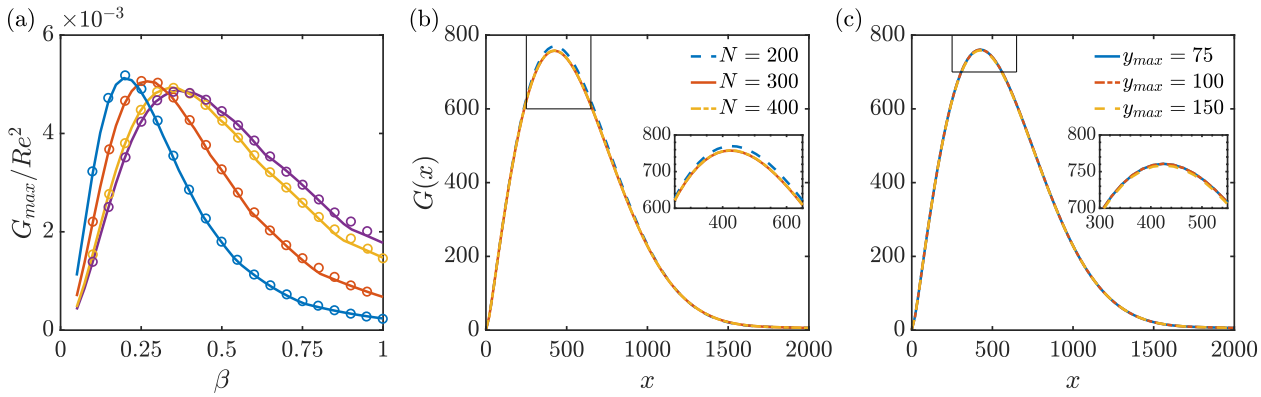

Figure B.2.1: (a) ideal gas, comparison of maximum energy amplification: $M_\infty = 0.5$ (—), and $M_\infty = 1.0$ (—), $M_\infty = 2.0$ (—), $M_\infty = 3.0$ (—), Tumin & Reshotko (2001) marked by a coloured circle (∘); (b) non-ideal gas, influence of mesh size N on the energy amplification $G(x)$: $N = 200$ (– –), $N = 300$ (—), and $N = 400$ (– ·); (c) non-ideal gas, influence of mesh height y_{max} on the energy amplification $G(x)$: $y_{max} = 75$ (—), $y_{max} = 100$ (– ·), and $y_{max} = 150$ (– –).

B.2 Transient growth: validation

The transient-growth analysis presented in this work is validated by reproducing the spatial results of Tumin & Reshotko (2001) for an ideal gas (adiabatic wall, $T_0^* = 333\,\mathrm{K}$, $Pr_\infty = 0.70$, $c_p^*/c_v^* = 1.40$, $\omega = 0$, $Re = 300$). A good agreement is observed in Fig. B.2.1(a) at different Mach numbers. To obtain a grid-independent solution when using a non-ideal gas, the influence of mesh size N and mesh height y_{max} is investigated. A transcritical wall-heating reference case at constant supercritical pressure is chosen: $p_\infty^* = 80\,\mathrm{bar}$, $T_\infty^*/T_{pc}^* = 0.90$, an isothermal wall with $T_w^*/T_{pc}^* = 1.05$, $M_\infty = 10^{-3}$, $Pr_\infty = 2.11$, $\omega = 0.013$, $\beta = 0.45$, and $Re = 300$. The results, shown in Fig. B.2.1(b) for N and Fig. B.2.1(c) for y_{max}, respectively, reveal that a value of $N = 300$ and $y_{max} = 75$ is necessary for mesh independence. Hence, this numerical set-up is retained throughout the non-modal calculations in this study.

B.3 Temporal vs. spatial transient growth

So far, spatial optimal growth has been analysed for its simpler interpretation in experimental facilities (Tumin & Reshotko 2001). However, it is noteworthy to investigate whether similar non-modal behaviour is obtained regardless of the considered optimisation procedure. For the temporal analysis, initial disturbances are optimised at $t = 0$ in order to achieve the maximum temporal energy growth at a later time t_{max} over β and streamwise wavenumber α (Hanifi *et al.* 1996). The case selected for the comparison is the transcritical case T09w105, where oblique disturbances are optimal. Figs. B.3.1(a,b) and B.3.1(c,d) display the maximum energy amplification G_{max} and the maximum location x_{max} and time t_{max}, respectively, for both the spatial and temporal analysis of case T09w105. The qualitative behaviour of G_{max} is nearly identical for low values of ω and α for both Fig. B.3.1(a) and B.3.1(b). At large ω and α,

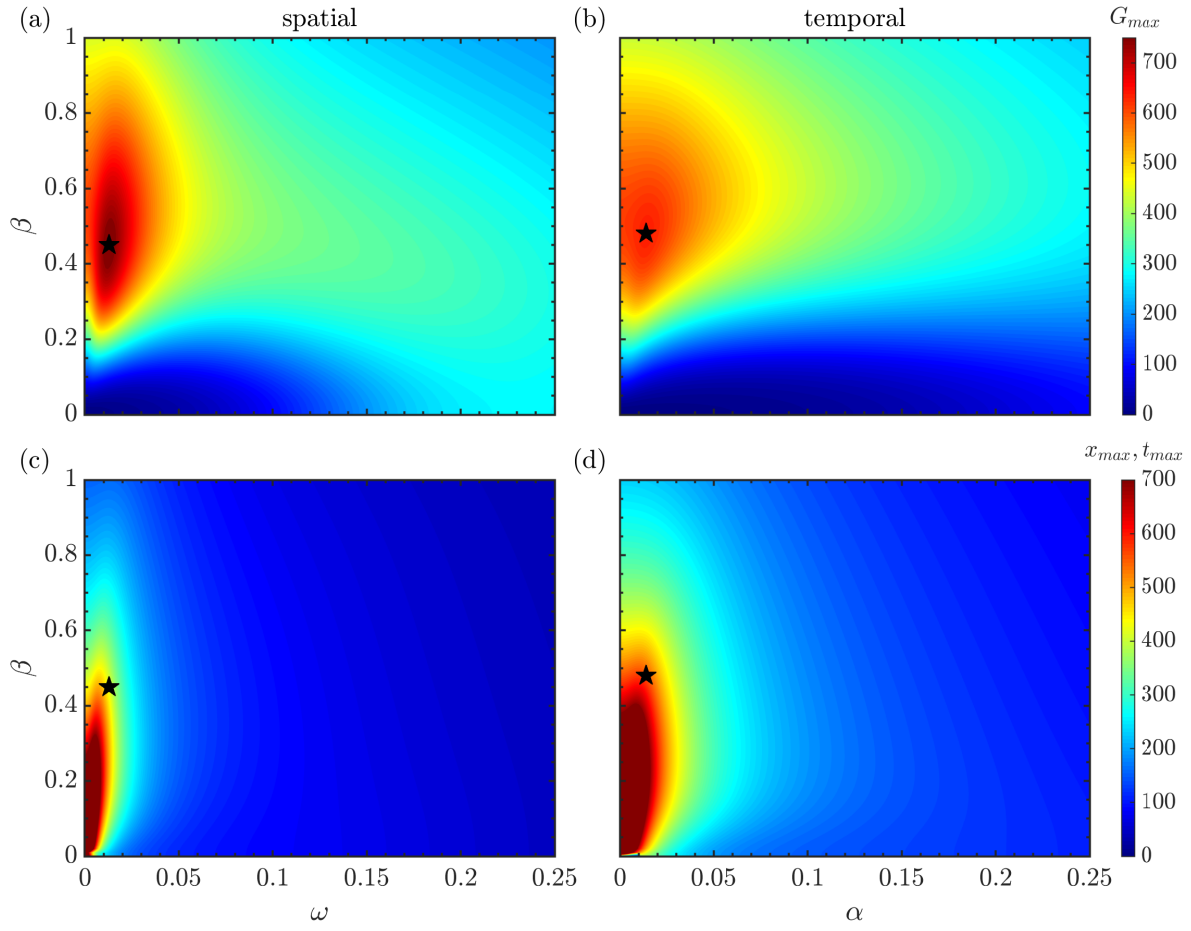

Figure B.3.1: Transcritical case T09w105: (a) contour plots of $G_{max}(\omega, \beta)$, (b) contour plots of $G_{max}(\alpha, \beta)$, (c) contour plots of $x_{max}(\omega, \beta)$, and (d) contour plots of $t_{max}(\alpha, \beta)$. G_{opt} is denoted with a black star ($\star$) symbol.

the spatial framework reveals a larger suboptimal growth near the ω-axis, which is negligible in the temporal framework. In the latter, the location of G_{opt}, defined as $\max\{G_{max}(\alpha, \beta)\}$, is found at $\beta_{opt} = 0.48$ and $\alpha_{opt} = 0.014$. This confirms the observation of Bitter (2015), in which most of the modes contributing to the optimal growth belong to the vorticity and entropy branches of the eigenspectrum. In fact, the phase speed $c_{ph,opt}$, obtained as the ratio between ω_{opt} and α_{opt}, is nearly unity. With respect to the value of G_{opt} for both frameworks, a difference of about 15% is found. In conclusion, the same physical mechanisms can be observed for both the temporal and spatial analysis.

B.4 The choice of energy norm

All non-modal optimisations presented in Sec. 4.4 are performed with the new energy norm introduced in Sec. 4.2.3. This norm considers both the kinetic and internal energy of a perturbation in a non-ideal gas flow. One can now question whether the energy amplification is dependent on the choice of the norm. To answer this question and analyse the sensitivity of the results in Sec. 4.4, the energy norm in Eq. (4.10) is modified. When choosing only the

kinetic energy, i.e. $\mathbf{M} = \mathrm{diag}\,(0, \bar{\rho}, \bar{\rho}, \bar{\rho}, 0)$, an infinite, and thus unphysical, energy amplification is achieved. Instead, the internal energy content is intentionally altered by considering: (1) frozen internal energy, i.e. $\mathbf{M} = \mathrm{diag}\,(1, \bar{\rho}, \bar{\rho}, \bar{\rho}, 1)$, (2) internal energy according to ideal gas, e.g. $\mathbf{M} = \mathrm{diag}\left(R_g\bar{T}/\bar{\rho}, \bar{\rho}, \bar{\rho}, \bar{\rho}, \bar{\rho}\,c_v/(Ec_\infty\bar{T})\right)$. Another alternative, hereafter (3), is to take the non-ideal optimal perturbations obtained in Sec. 4.2.3 and re-scale them by the kinetic energy norm. Thus, following Eq. (4.16), the new optimal amplification for (3) is

$$G_{(3)} = \max \frac{\|\mathbf{F}_{(3)}\mathbf{\Lambda}\boldsymbol{\kappa}(0)\|_2^2}{\|\mathbf{F}\boldsymbol{\kappa}(0)\|_2^2}, \quad \boldsymbol{\kappa}(0) = \mathbf{F}^{-1}\mathbf{r}, \tag{B.5a,b}$$

where $\mathbf{F}$, $\mathbf{\Lambda}$, $\mathbf{F}^{-1}$, $\mathbf{r}$ (right singular eigenvector) are obtained with $\mathbf{M}$ as in Eq. (4.13), whereas $\mathbf{F}_{(3)}$ is the Cholesky decomposition of $\mathbf{A}_{(3)} = \mathbf{F}_{(3)}^H\mathbf{F}_{(3)}$ (with $\mathbf{A}_{(3),kl} = \int_0^\infty \hat{\mathbf{q}}_k^H\mathbf{M}_{(3)}\hat{\mathbf{q}}_l\,\mathrm{d}y$) as a function of the kinetic energy norm matrix $\mathbf{M}_{(3)} = \mathrm{diag}\,(0, \bar{\rho}, \bar{\rho}, \bar{\rho}, 0)$. Energy norms based on (1) and (2) were previously used in Ren *et al.* (2019*a*). In order to account for the largest non-ideal effects on the norm, the two transcritical cases of Tab. 4.1, with their optimal growth reported in Tab. 4.2, are examined. In Fig. B.4.1(a), the maximum energy amplification $G_{max}(\omega)$ at constant $\beta = \beta_{opt}$, i.e. $\beta_{opt} = 0.45$, is shown for case T09w105. The optimal energy amplification is found, independently of the energy norm adopted, around $\omega = 0.013$ (marked by a coloured star ($\star$) symbol). The non-ideal energy norm yields the largest transient growth (blue dash-dotted line). The shape of optimal perturbations displayed in Fig. 4.8 is not affected by the energy-norm modifications (not presented here for the sake of brevity). In Fig. B.4.1(b), the maximum energy amplification $G_{max}(\beta)$ at constant $\omega = \omega_{opt}$, i.e. $\omega_{opt} = 0$, is presented for case T11w095. Here, we notice a greater dependence on the energy norm, especially when the internal energy is kept constant (case (1), yellow continuous line). In this case, there is an actual increase in the internal energy compared to the other norms. Moreover, a shift of the maximum energy amplification is notable. Similar to the transcritical T09w105 case, the shape of the optimal perturbations remains intact except for the density perturbations, where a smaller $\hat{\rho}$-amplitude in case (1) is observed. Overall, energy amplifications with the re-scaled energy norm (case (3), purple dotted line) show an analogous transient growth as the ideal-gas norm cases (case (2), red dashed line).

B.5 Inviscid vorticity perturbation equation

The equation for the wall-normal vorticity perturbation ω_y' is obtained hereafter. The wall-normal vorticity is split as $\omega_y = \bar{\omega}_y + \omega_y'$ and inserted into Eq. (4.18). Subsequently, the following assumptions, in agreement with Sec. 4.2.3, are drawn: (1) Two-Dimensional (2-D) base flow and locally parallel flow, i.e. $\bar{\omega}_y = \bar{v} = \bar{w} = 0, \partial(\bar{\cdot})/\partial x = 0, \partial(\bar{\cdot})/\partial z = 0$, (2) base-flow wall-normal pressure gradient $\partial\bar{p}/\partial y$ is 0, (3) linearisation, i.e. $q_i^2 = q_iq_j = 0$. After subtraction of the base flow, the baroclinic term in Eq. (4.18) becomes:

$$\frac{1}{\rho^2}\left(\frac{\partial\rho}{\partial z}\frac{\partial p}{\partial x} - \frac{\partial\rho}{\partial x}\frac{\partial p}{\partial z}\right) \quad\Longrightarrow\quad \frac{1}{\bar{\rho}^2}\left(\frac{\partial\rho'}{\partial z}\frac{\partial\bar{p}}{\partial x} + \frac{\partial\bar{\rho}}{\partial z}\frac{\partial p'}{\partial x} - \frac{\partial\bar{\rho}}{\partial x}\frac{\partial p'}{\partial z} - \frac{\partial\rho'}{\partial x}\frac{\partial\bar{p}}{\partial z}\right) = 0. \tag{B.6}$$

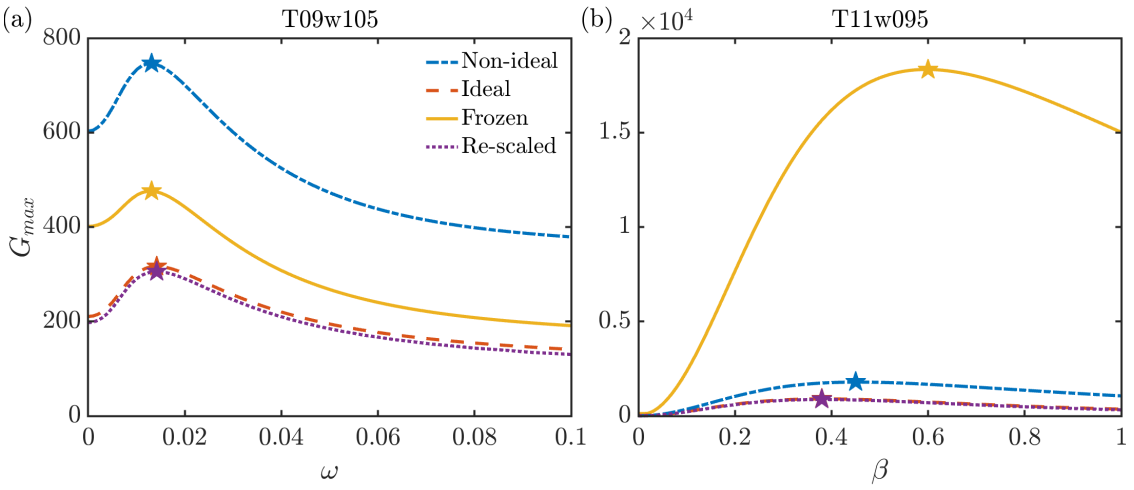

Figure B.4.1: Effect of the energy norm on the energy amplification: non-ideal energy norm, ideal-gas energy norm (2), frozen internal energy norm (1), re-scaled non-ideal energy norm by the kinetic energy norm (3). (a) T09w105, as a function of ω for $\beta = \beta_{opt}$; (b) T11w095, as a function of β for $\omega = 0$. The maximum energy amplification is indicated with a coloured star ($\star$) symbol.

Thus, the final expression of the wall-normal vorticity perturbation equation is

$$\frac{\partial \omega_y'}{\partial t} + \bar{u}\frac{\partial \omega_y'}{\partial x} = -\frac{\partial v'}{\partial z}\frac{\partial \bar{u}}{\partial y}, \tag{B.7}$$

with absent baroclinic influence.

B.6 Influence of the pressure on the transient growth

The influence of the reduced pressure, $p_r = p^*/p_c^*$, on transient growth is investigated. As one approaches the critical point, the gradients of thermophysical properties are more pronounced near the Widom line (e.g. c_p^* in Fig. A.1.1), making the base flow become more inflectional and enhancing modal growth (Ren *et al.* 2019*b*), thus enhancing the likelihood of transition below the critical Reynolds number. To assess whether transient growth could be the critical transition mechanism, the supercritical pressure is increased from a constant pressure of $p^* = 80\,\text{bar}$ (i.e. $p_r = 1.083$) to 81.15 bar ($p_r = 1.10$) and 84.84 bar ($p_r = 1.15$) for cases T09w105 and T11w095. Other base-flow parameters in Tab. 4.1 are marginally influenced by this pressure variation due to the Mach number of $M_\infty = 10^{-3}$. In Fig. B.6.1, the base-flow profiles of $\mathrm{d}/\mathrm{d}y(\bar{\rho}\,\mathrm{d}\bar{u}/\mathrm{d}y)$ decrease with increasing reduced pressure for both transcritical cases. In this regard, the location of the GIP is barely modified. For case T11w095 in Fig. B.6.1(b), the IP location (coloured star ($\star$) symbol) shifts slightly away both from the wall and the Widom line, where $y_{pc} \approx y_{GIP}$. For each reduced pressure, the same analysis conducted in Fig. 4.27 is performed and displayed in Fig. B.6.2. Firstly, regardless of the selected supercritical pressure, the same optimal growth mechanisms for the transcritical regime as previously analysed in Sec. 4.4.2 are observed: lift-up and Orr mechanisms for T09w105, and

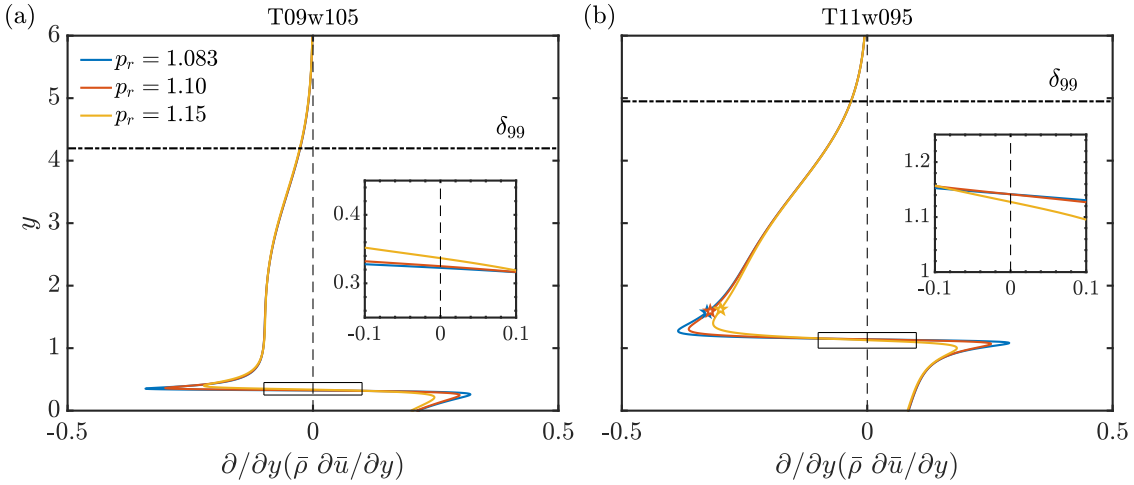

Figure B.6.1: Generalised inflection point of the boundary-layer profile at different reduced pressures, $p_r = (1.083, 1.10, 1.15)$: (a) case T09w105, and (b) case T11w095. Note that δ_{99} is not altered by a pressure change.

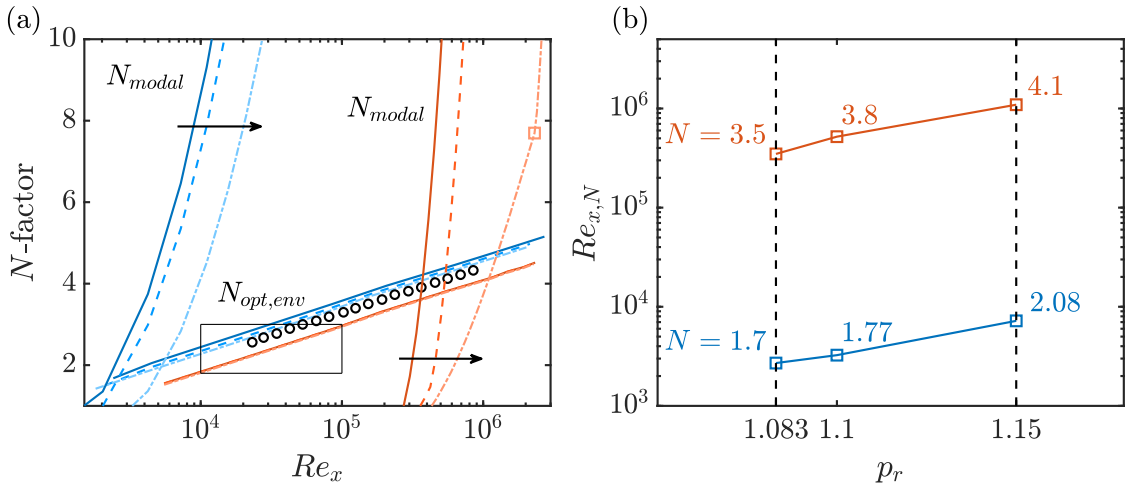

Figure B.6.2: Effect of p_r-increase on the envelope curves of optimal non-modal and modal growth: case T09w105 (—), and case T11w095 (—). In (a), $p_r = 1.083$: continuous lines, $p_r = 1.10$: dashed lines, and $p_r = 1.15$: dash-dotted lines. In (a), black arrows indicate an increase in reduced pressure. The black circle (∘) symbol refers to the adverse pressure case of Levin & Henningson (2003). In (b), N-factors are indicated at the Reynolds number $Re_{x,N}$ where $N_{modal} = N_{opt}$.

only lift-up effect for T11w095. Fig. B.6.2(a) presents the envelope curves for modal and non-modal growth, verifying the robustness of transient growth with respect to a thermodynamic variation. $N_{opt,env}$ is slightly affected by the pressure change, negligible for the transcritical wall-heating case T09w105. Regarding modal growth in case T09w105 (Fig. B.6.1a), the base-flow profile becomes less inflectional with increased reduced pressure, stabilising Mode II while Mode I remains nearly unchanged. At $p_r = 1.15$, Mode I dominates until $Re_x \approx 2.2\times10^6$, marked by a kink in the N-factor curve (coloured (□) symbol). Subsequently, the Reynolds number $Re_{x,N}$ at which $N_{modal} = N_{opt}$ is displayed in Fig. B.6.2(b). $Re_{x,N}$ grows linearly

Case	L_x	L_y	L_z	$N_x \times N_y \times N_z$	$Re_{x,0}/10^5$	Δx^+_{max}	$\Delta y^+_{w,max}$	Δz^+_{max}	$Re_{\theta,max}$
Tw095	724.3	40.0	9.63	$13550 \times 600 \times 180$	1.0	4.48	0.63	4.48	1509
Tw110	1078.0	40.0	9.63	$20150 \times 900 \times 180$	0.58	3.49	0.49	3.49	885
TadIG	515.0	20.0	9.63	$4000 \times 600 \times 150$	1.0	10.0	0.59	4.9	1229

Table C.1.1: Numerical parameters for the 3-D simulations (Sec. 6.5) of the flow cases listed in Tab. 6.1: L_x, L_y, and L_z are the sizes of the computational domain in the streamwise, wall-normal, and spanwise directions, respectively; N_x, N_y, and N_z denote the numbers of grid points in the corresponding directions; $Re_{x,0}$ is the inlet Reynolds number; Δx^+_{max}, $\Delta y^+_{w,max}$, and Δz^+_{max} are the maximum grid sizes in the x-, y-, and z-directions relative to the maximum viscous length scale in the domain, $\overline{\mu}_w/(\overline{\rho}_w u_\tau)$. In addition, the momentum Reynolds number is defined as $Re_\theta = \rho^*_\infty u^*_\infty \theta^*/\mu^*_\infty$, based on the local momentum thickness θ^* and free-stream properties. Note that case Tw110 here corresponds to case Tw110-LA in Tab. 6.2, whereas case Tw110-IA differs in $\Delta y^+_{w,max} \approx 0.48$, $\Delta x^+ \approx \Delta z^+ \approx 3.39$, and $Re_{\theta,max} = 837$.

by a factor of 3 from $p_r = 1.084$ to 1.15 (red line), but non-modal amplification remains moderate. In case T11w095, a similar behaviour is observed (Fig. B.6.2a). The increase of the inflectional location, i.e. $\mathrm{d}^2\bar{u}/\mathrm{d}y^2 = 0$, weakly stabilises modal instability, while non-modal amplification is almost unaffected by the pressure change. Hence, $Re_{x,N}$ more than doubles from $p_r = 1.083$ to 1.15 (blue line), but near the flat-plate leading edge, N_{opt} remains too low for transition below the critical Reynolds number. In conclusion, for a transcritical wall-cooled boundary layer, modal growth dominates near the critical point. For transcritical wall-heating, with large free-stream disturbances as in Levin & Henningson (2003), bypassing the exponential growth of Mode I and II is more likely when the gradients of thermophysical properties are no longer abrupt.

C.1 DNS set-ups and grid-resolution analysis

The grid resolution, with $N_x \times N_y \times N_z$ grid points, varies for each case. The grid is uniform in the streamwise (x) and spanwise (z) directions, and stretched in the wall-normal (y) direction according to $y = y_e[K_1\eta + (1-K_1)(1+\tanh(0.5\sigma(\eta-1)/\tanh(0.5\sigma)))]$, where $\eta = 0,\ldots,1$ and $K_1 = 0.6(N_y-1)/(Re_{\tau,0}y_e)$. The stretching factor σ and the inlet friction Reynolds number $Re_{\tau,0} = \delta_{99,0}/\delta_{99,v}$ – with $\delta_{99,v} = \overline{\mu}_w/(\overline{\rho}_w u_\tau)$, and $u_\tau = \sqrt{\overline{\tau}_w/\overline{\rho}_w}$ and $\overline{\tau}_w$ being the friction velocity and the wall shear stress, respectively – are chosen such that the first grid cell in the wall-normal direction, Δy^+_w, (superscript $(\cdot)^+$ denotes viscous units), remains below unity throughout the domain. At the inlet x_0, the laminar boundary layer is resolved with approximately 140 grid points in the wall-normal direction for both supercritical cases. Tables C.1.1 and C.1.2 summarise the relevant grid parameters for the Three-Dimensional (3-D) (Sec. 6.5) and 2-D (Sec. 6.4) simulations, respectively.

One-dimensional non-reflecting boundary conditions for non-ideal flows (Okong'o & Bel-

Case	L_x	L_y	$N_x \times N_y$	$Re_{x,0}/10^5$
Tw095	378.3	20.0	2000×400	0.9
Tw110	703.8	40.0	4000×800	0.58

Table C.1.2: Numerical parameters for the 2-D simulations (Sec. 6.4) of the flow cases listed in Tab. 6.1: L_x and L_y are the sizes of the computational domain in the streamwise and wall-normal directions, respectively; N_x and N_y denote the numbers of grid points in the corresponding directions; $Re_{x,0}$ is the inlet Reynolds number.

lan 2002) are applied at: (i) the subsonic inlet ($x = x_0$); (ii) the outlet ($x = x_e$), with the incoming wave amplitude set to zero; (iii) the top boundary ($y = y_e$), with constant pressure $p_{r,\infty}$, and (iv) the wall ($y = 0$), where no-slip and no-penetration conditions are imposed, except in the disturbance-strip region (see Sec. 6.3.2). In addition, sponge zones are applied at the inlet, outlet, and top boundaries to minimise spurious acoustic reflections (Mani 2012), with the local solution gradually dampened towards the laminar boundary-layer profile. The inflow sponge length ($x_0 < x < x_0 + 20.0$) and damping strength ($\sigma_p = 0.5$) are the same for all simulations. For case Tw110, both the outlet ($x_e - 50.0 < x < x_e$, $\sigma_p = 0.5$) and top sponge zones ($y_e - 13.3 < y < y_e$, $\sigma_p = 1.0$) are extended to account for the strong fluctuation intensity, e.g. $\rho'/\overline{\rho} \approx O(1)$ (Kawai 2019). For cases Tw095 and TadIG, sponge zones are active in the regions $x_e - 20.0 < x < x_e$ ($\sigma_p = 0.5$) and $y_e - 1.0 < y < y_e$ ($\sigma_p = 0.5$). A sensitivity analysis of the grid resolution for transcritical case Tw110 (the most computationally expensive case) is performed in the following.

The baseline computational grid of case Tw110 (hereafter referred to as the 'fine grid'), reported in Tab. C.1.1, is coarsened by factors of approximately 1.44, 1.2, and 1.2 in the streamwise, wall-normal, and spanwise directions, respectively, resulting in a grid of $14000 \times 750 \times 150$ points, hereafter referred to as the 'coarser mesh'. Uniform spacing is applied in the streamwise and spanwise directions, while the same wall-normal grid-clustering and $\Delta y^+_{w,max}$ as the fine grid are retained. Figures C.1.1 and C.1.2 show that the modal evolution, skin-friction coefficient, and Stanton number remain largely insensitive to changes in grid resolution, confirming the robustness of the 3-D simulations.

C.2 Laminar boundary layer at supercritical pressure

For supercritical cases Tw095 and Tw110 in Tab. 6.1, a comparison is made between the initial solution described in Sec. 6.3.1 and the steady, fully developed 2-D DNS. Note that the disturbance strip is not active in these simulations. The DNS boundary-layer profiles in Fig. C.2.1 are in strong agreement with the self-similar profiles for streamwise velocity, temperature, and density in both regimes. Minor deviations in wall-normal velocity emerge upon crossing the Widom line (Boldini *et al.* 2025), caused by the non-zero DNS wall-normal pressure gradient retained in the numerical integration of Eq. (2.1). In fact, the pressure

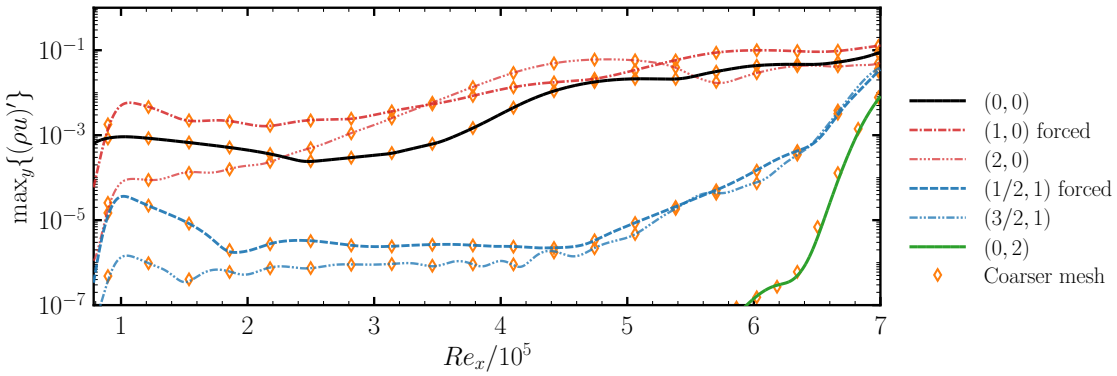

Figure C.1.1: Case Tw110-LA: streamwise development of the y-maximum $(\rho u)'$ disturbance amplitudes of the most relevant modes $(\omega/\omega_{2\text{-D}}, \beta/\beta_0)$. Coarser-mesh results are marked with ◊.

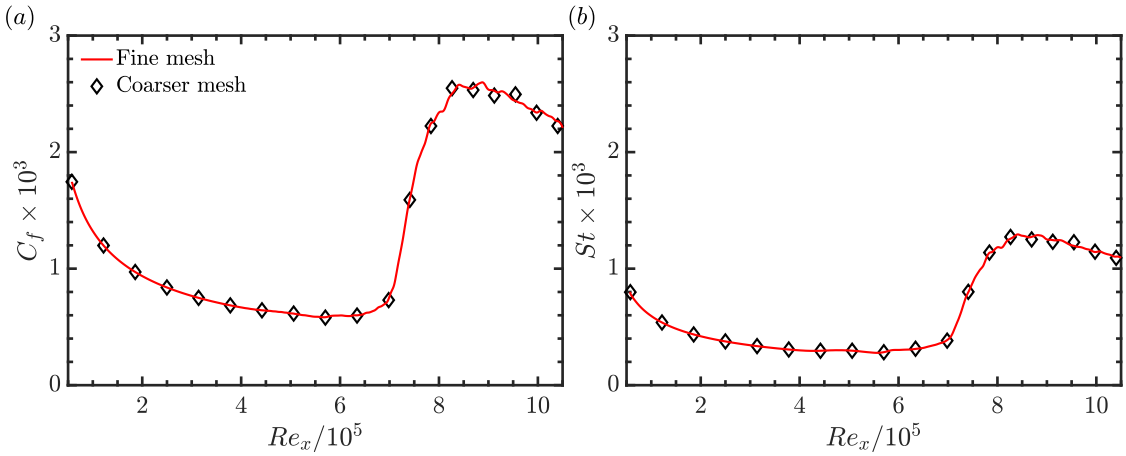

Figure C.1.2: Case Tw110-LA: time- and spanwise-averaged (a) skin-friction coefficient and (b) Stanton number. Coarser-mesh results are marked with ◊.

boundary-layer profile shown in the inset of Fig. C.2.1 reveals a bump at the height of the pseudo-critical point. This phenomenon arises due to the dependence of p on both ρ and T. Thus, the resulting pressure gradient is expressed as $\partial p/\partial y \propto \partial p/\partial \rho\, \partial \rho/\partial y + \partial p/\partial T\, \partial T/\partial y$. Both terms reach their maximum at the pseudo-critical point and nearly cancel each other out. As a result, the deviation from the conventional boundary-layer assumption of $\partial p/\partial y = 0$ remains minimal, thereby justifying the validity of the self-similar boundary-layer solution used in Sec. 6.3.1.

C.3 Linear disturbance evolution: LST versus DNS

To compare DNS with LST results in Sec. 6.4.1, the disturbances are Fourier transformed in time. The normalised disturbance growth rate and phase speed of the fundamental wave are calculated as

$$\alpha_i(x) = -\frac{Re}{Re_0}\frac{1}{\hat{u}^{max}}\frac{\partial \hat{u}^{max}}{\partial x}, \quad c_r(x) = \frac{\omega_{2\text{-D}} Re_0}{Re}\left(\frac{\partial \hat{\phi}}{\partial x}\right)^{-1}, \tag{C1a,b}$$

C

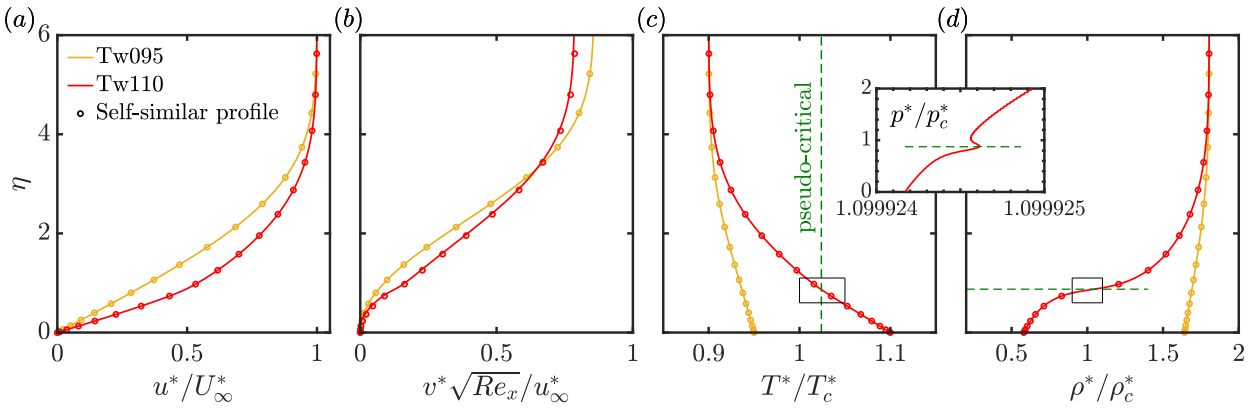

Figure C.2.1: 2-D DNS laminar profiles for cases Tw095 and Tw110: (a) streamwise velocity, (b) wall-normal velocity, (c) reduced temperature, and (d) reduced density plotted against the self-similar wall-normal coordinate η. The laminar self-similar solutions are indicated by circles (∘). The DNS reduced pressure p^*/p^*_c is plotted in the inset. The dashed green line (– –) indicates the pseudo-critical point, i.e. where $T^* = T^*_{pc}$.

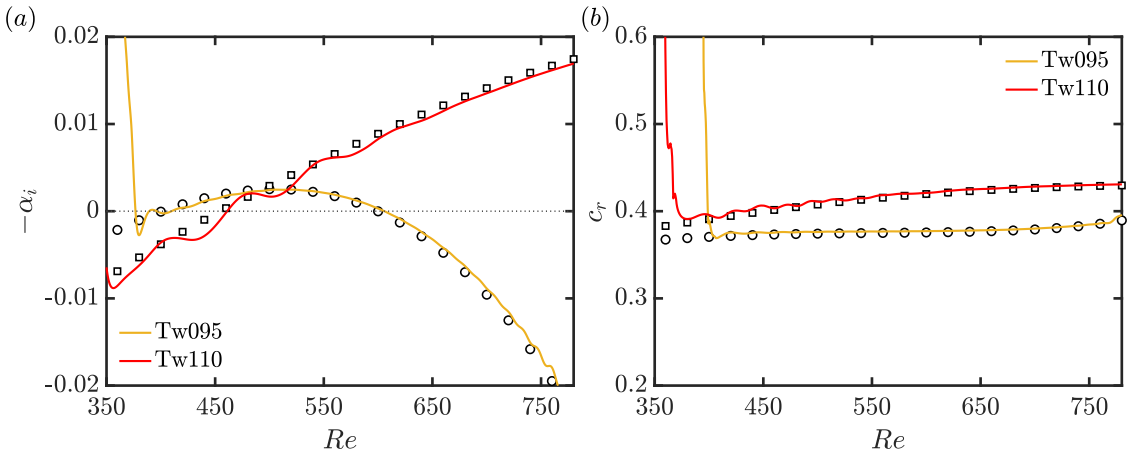

Figure C.3.1: Comparison between low-amplitude DNS (lines) and LST (symbols) for a 2-D wave at $F_{2\text{-D}} = 124 \times 10^{-6}$: (a) growth rate ($-\alpha_i$) and (b) phase speed c_r. Cases Tw095 and Tw110 (Mode II) in orange and red, respectively.

where $\hat{u}^{max}(x) = \max\{|\hat{u}(x = \text{const.}, y)|\}$ and $\hat{\phi}$ is the phase angle $\arg(\hat{p}_{1,w})$, with $\hat{p}_w$ being the wall pressure. Figure C.3.1 compares the spatial amplification rate $-\alpha_i$ and phase speed c_r for cases Tw095 and Tw110. The results reveal very good agreement between DNS and LST, with the phase speed being less sensitive to the criterion used in Eq. (C1*a*,*b*). However, for α_i in Fig. C.3.1(a), a moderate modulation near the disturbance strip is observed, caused by the excitation of damped waves before the most unstable mode dominates. This behaviour is more pronounced for case Tw110. A smaller disturbance strip and a further upstream disturbance-strip location reduce the modulation (not shown). Thus, for case Tw110, $Re_{x,mid}$ is shifted upstream relative to that in case Tw095 (see Tab. C.1.1).

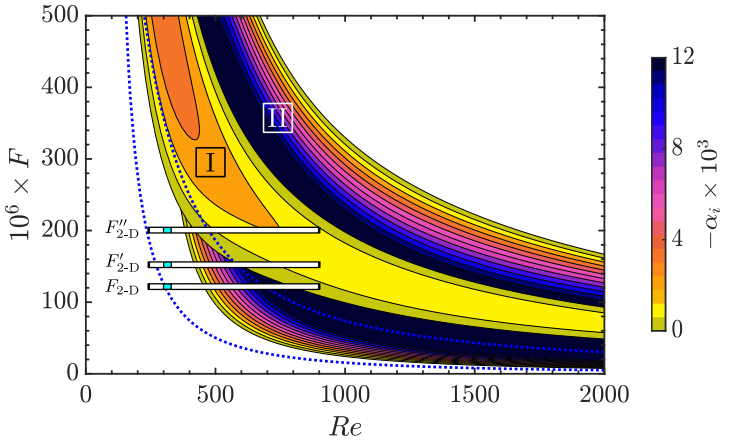

Figure C.4.1: Growth-rate ($-\alpha_i$) contours in the Re–F stability diagram for case Tw110. Three different fundamental forcing frequencies are selected, $F_{2\text{-D}} = 124 \times 10^{-6}$, $F'_{2\text{-D}} = 150 \times 10^{-6}$, and $F''_{2\text{-D}} = 200 \times 10^{-6}$. The locations of the DNS domain and perturbation strip are marked by white and cyan bars, respectively. The dotted blue line represents the ideal-gas neutral stability at equal T^*_w/T^*_∞-ratio.

C.4 Effect of the fundamental forcing frequency

We perform additional 2-D simulations of the transcritical boundary layer (case Tw110) at higher fundamental forcing frequencies. The simulations are conducted over the same Reynolds-number range using two higher fundamental forcing amplitudes, $F'_{2\text{-D}} = 150 \times 10^{-6}$ and $F''_{2\text{-D}} = 200 \times 10^{-6}$, in addition to the baseline value $F_{2\text{-D}} = 124 \times 10^{-6}$ used in Sec. 6.4.2. The forcing amplitude remains unchanged at $A_{2\text{-D}} = 7.5 \times 10^{-3}$. For clarity, we show below the Re–F stability diagram in Fig. C.4.1, with the location of the DNS domain and perturbation strip indicated by white and cyan bars, respectively. The numerical setup can be found in Tab. C.1.2 and is identical for all three simulations.

The nonlinear response of the boundary layer to the finite-amplitude perturbation is shown in Fig. C.4.2 for $F'_{2\text{-D}} = 150 \times 10^{-6}$ (panel a) and $F''_{2\text{-D}} = 200 \times 10^{-6}$ (panel b). Similar to Figs. 6.7(b,d), nonlinear excitation of higher harmonics emerges in the vicinity of the forcing strip. For $F'_{2\text{-D}} = 150 \times 10^{-6}$, the amplified mode $(2,0)$ slightly surpasses mode $(1,0)$ at $Re \approx 600$ before saturating. Subharmonic resonance between $(1,0)$ and $(2,0)$ sets in at $Re \approx 700$, where mode $(1,0)$ is further destabilised, leading to a strong increase of the mean-flow distortion (MFD) $(0,0)$ which reaches up to 10% at $Re \approx 800$. For comparison, the amplitude of $(0,0)$ in Fig. 6.7(b) remains around 5%. For $F''_{2\text{-D}} = 200 \times 10^{-6}$, the MFD is even higher, reaching about 1%, already at $Re \approx 600$. In this case, mode $(2,0)$ does not surpass mode $(1,0)$, but contributes to its further downstream amplification in subharmonic fashion. Note that around $Re \approx 400$, the contribution of the unstable Mode I becomes visible, showing a local increase in amplitude (deviation from LST of Mode II).
Overall, as for the frequency $F_{2\text{-D}} = 124 \times 10^{-6}$, we observe strong modal interaction between the higher harmonics and the fundamental mode, together with subharmonic resonance between $(2,0)$ and $(1,0)$, analogous to vortex pairing in mixing layers.

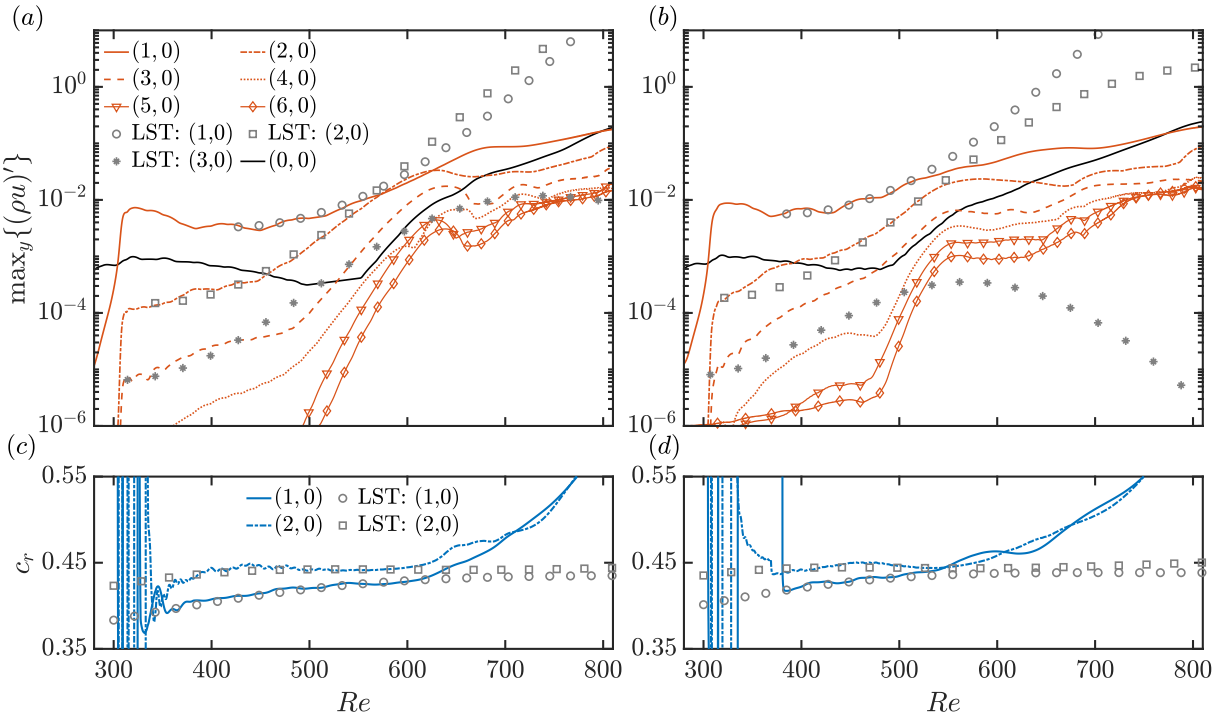

Figure C.4.2: Case Tw110: (a,c) $F'_{2\text{-D}} = 150\times10^{-6}$ and (b,d) $F''_{2\text{-D}} = 200\times10^{-6}$; (a,b) maximum wall-normal mass-flux amplitude for mode $(1,0)$ (solid line), $(2,0)$ (dash-dotted line), $(3,0)$ (dashed line), $(4,0)$ (dotted line), $(5,0)$ (solid line with $\triangledown$), and $(6,0)$ (solid line with $\diamond$); (c,d) phase speed c_r for mode $(1,0)$ (solid line) and $(2,0)$ (dash-dotted line). The mean-flow distortion $(0,0)$ is indicated with a black solid line. The LST solution is represented with circle ($\circ$) symbols for mode $(1,0)$, square ($\square$) symbols for mode $(2,0)$, and asterisk ($*$) symbols for mode $(3,0)$.

The nonlinear evolution of the density field is shown in Fig. C.4.3 for two different forcing frequencies. Similar to Fig. 6.8 for $F_{2\text{-D}} = 124\times10^{-6}$, a train of streamwise-growing density billows appears, induced by the billowing motion of the Widom line within the boundary layer. Moreover, travelling regions of flow reversal (highlighted in cyan) are present below the Widom-line troughs, indicating localised near-wall separation. For a detailed discussion of these mechanisms, we refer to Sec. 6.4.2. In addition, for higher forcing frequencies, the localised separation zones appear earlier upstream (cf. Fig. 6.8) and the billows grow faster in the streamwise direction; these behaviours are directly linked to the larger amplitude of mode $(0,0)$, the MFD, as discussed in Fig. C.4.2.

In conclusion, the results in Figs. C.4.2 and C.4.3 demonstrate that the same physical mechanisms are recovered at higher fundamental forcing frequencies in the nonlinear regime at pseudo-boiling conditions, namely: (i) modal interaction with higher harmonics, (ii) subharmonic resonance between the first-higher harmonic and fundamental mode, (iii) Widom-line billowing, and (iv) the formation of near-wall separation zones.

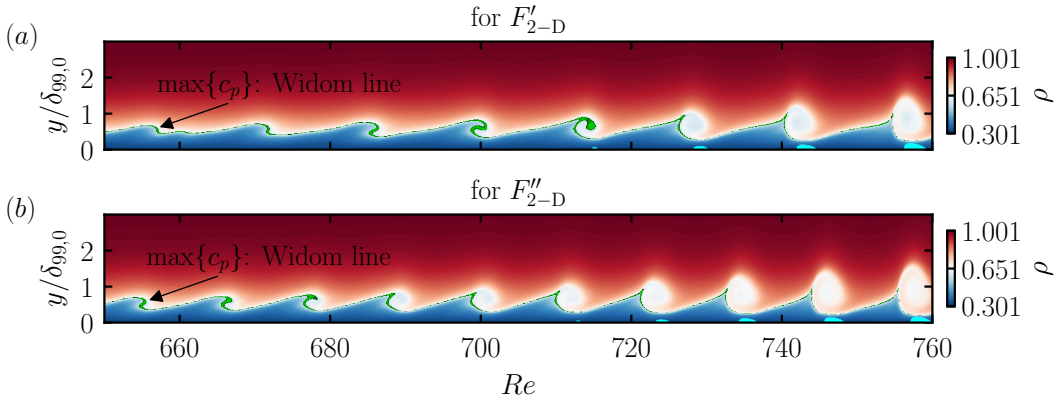

Figure C.4.3: Case Tw110. Instantaneous contours of density ρ at $T/T_0 = 0$, where $T_0 = 2\pi/\omega_0$ (fundamental frequency ω_0), with $A^{(1,0)}_{2\text{-D}} = 7.5 \times 10^{-3}$: (a) $F'_{2\text{-D}} = 150 \times 10^{-6}$ (fundamental frequency ω'_0), (b) $F''_{2\text{-D}} = 200 \times 10^{-6}$ (fundamental frequency ω''_0). The Widom line $y = y_{WL}$ lies within the green region, i.e. between $98\%\max\{c_p\}$ and $\max\{c_p\}$. The near-wall region for which $u < 0$ is coloured in cyan.

Bibliography

Bitter, N. P. 2015 Stability of Hypervelocity Boundary Layers. PhD thesis, California Institute of Technology.

Boldini, P. C., Hirai, R., Costa, P., Peeters, J. W. R. & Pecnik, R. 2025 CUBENS: A GPU-accelerated high-order solver for wall-bounded flows with non-ideal fluids. *Comput. Phys. Commun.* **309**, 109507.

Hanifi, A., Schmid, P. J. & Henningson, D. S. 1996 Transient growth in compressible boundary layer flow. *Phys. Fluids* **8**, 826–837.

Kawai, S. 2019 Heated transcritical and unheated non-transcritical turbulent boundary layers at supercritical pressures. *J. Fluid Mech.* **865**, 563–601.

Levin, O. & Henningson, D. S. 2003 Exponential vs algebraic growth and transition prediction in boundary layer flow. *Flow Turbul. Combust.* **70**, 183–210.

Mani, A. 2012 Analysis and optimization of numerical sponge layers as a nonreflective boundary treatment. *J. Comput. Phys.* **231**, 704–716.

Okong'o, N. & Bellan, J. 2002 Consistent boundary conditions for multicomponent real gas mixtures based on characteristic waves. *J. Comput. Phys.* **176**, 330–344.

Ren, J., Fu, S. & Pecnik, R. 2019*a* Linear instability of Poiseuille flows with highly non-ideal fluids. *J. Fluid Mech.* **859**, 89–125.

Ren, J., Marxen, O. & Pecnik, R. 2019*b* Boundary-layer stability of supercritical fluids in the vicinity of the Widom line. *J. Fluid Mech.* **871**, 831–864.

Tumin, A. & Reshotko, E. 2001 Spatial theory of optimal disturbances in boundary layers. *Phys. Fluids* **13**, 2097–2104.

C

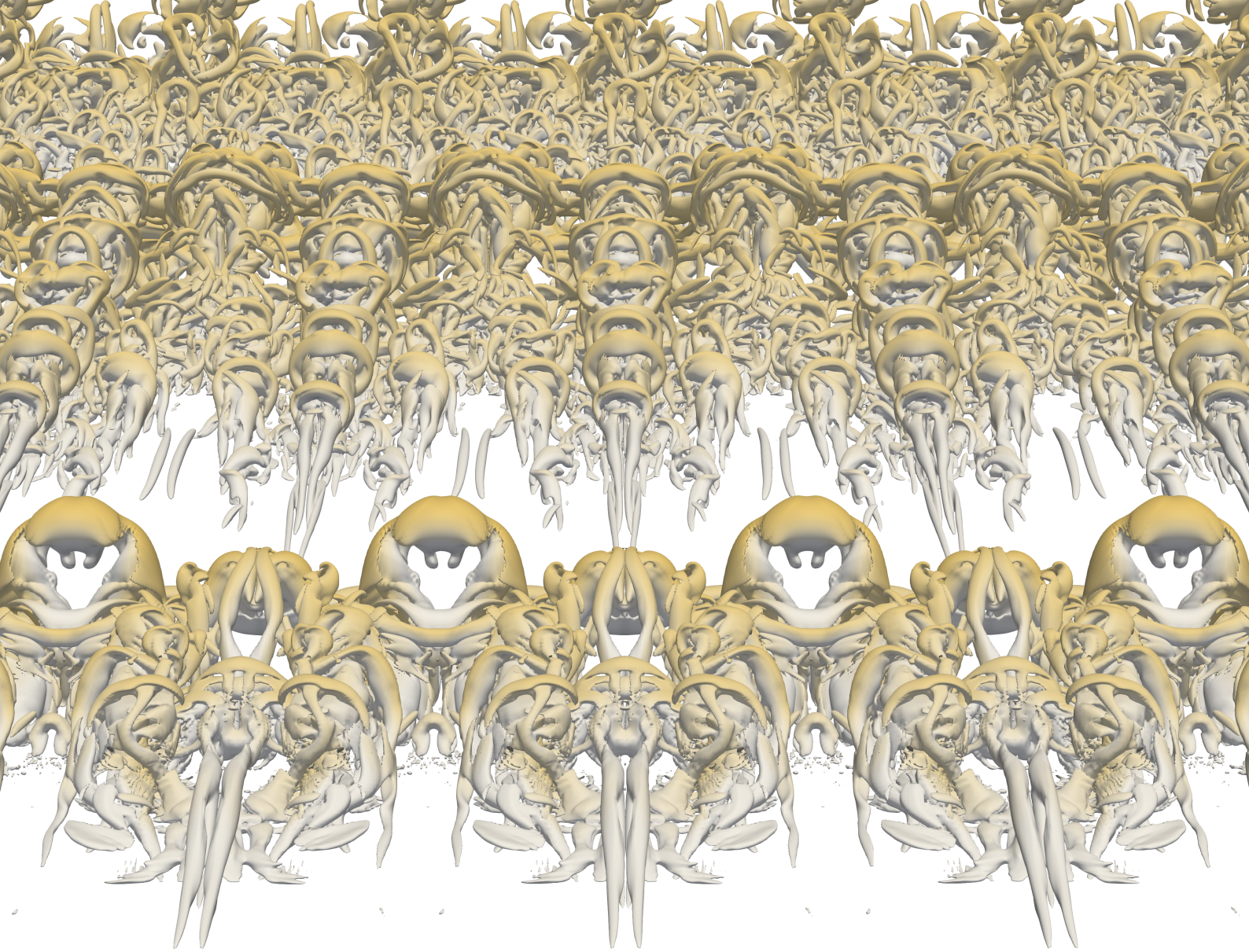

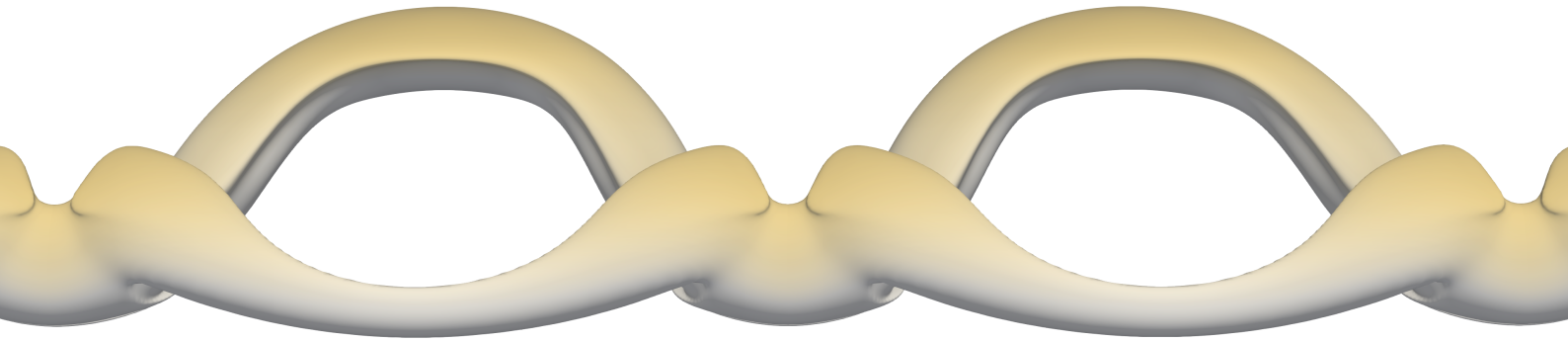

TU Delft